Metall-organische Gerüstverbindungen und deren Polymerkomposite für potenzielle Gas- und Dampfadsorptionsanwendungen

Dissertation

zur Erlangung des Doktorgrades

Dr. rer. nat.

der Mathematisch-Naturwissenschaftlichen Fakultät

der Heinrich-Heine-Universität Düsseldorf

vorgelegt von

Christian Jansen

aus Brüggen

Düsseldorf, Oktober 2022

aus dem Institut für nanoporöse und nanoskalierte Materialien
der Heinrich-Heine-Universität Düsseldorf

Gedruckt mit der Genehmigung der

Mathematisch-Naturwissenschaftlichen Fakultät der

Heinrich-Heine-Universität Düsseldorf

Berichterstatter:

1. Prof. Dr. Christoph Janiak

2. Prof. Dr. Christian Ganter

Tag der mündlichen Prüfung: 09.12.2022

Eidesstattliche Erklärung

Ich versichere an Eides statt, dass die Dissertation von mir selbstständig und ohne unzulässige fremde Hilfe unter der Beachtung der „Grundsätze zur Sicherung guter wissenschaftlicher Praxis" an der Heinrich-Heine-Universität Düsseldorf erstellt worden ist.

Die aus fremden Quellen direkt oder indirekt übernommenen Gedanken sind als solche kenntlich gemacht.

Die Arbeit wurde bisher weder im Inland noch im Ausland in gleicher oder ähnlicher Form einer anderen Prüfungsbehörde vorgelegt. Es wurden keine früheren erfolglosen Promotionsversuche unternommen.

_____ _____

Ort, Datum Unterschrift

Probleme kann man niemals mit derselben Denkweise lösen, durch die sie entstanden sind.

Albert Einstein

Danksagung

An dieser Stelle möchte ich mich bei verschiedenen Personen bedanken, die mich während der gesamten Studien- und Promotionszeit begleitet und unterstützt haben und auf die ich immer zählen konnte.

Zuallererst gilt mein Dank Herrn Prof. Dr. Christoph Janiak für die Möglichkeit einer Promotion in seinem Arbeitskreis. Vielen Dank für die interessanten Aufgabenstellungen und die kompetente und zuverlässige Hilfe, die bei aufgetretenen Problemen zu einer Lösung führten, im und abseits des Mitarbeiterseminars.

Herrn Prof. Dr. Christian Ganter danke ich herzlich für die Übernahme des Koreferats und für die interessanten Hinweise, Fragen und Anregungen im Mitarbeiterseminar.

Herrn Prof. Dr. Peter Proksch danke ich für die zur Verfügung gestellten Pilzkulturen und für die Anfertigung der Tests zur mikrobiellen Beständigkeit. Hier sei besonders Herr Dr. Nam Michael Tran-Cong erwähnt für das praktische Durchführen der Tests. Diese Arbeiten haben zu einem erheblichen Teil einer Publikation beigetragen.

Herrn Prof. Dr. Vladimir Pankov danke ich für die Möglichkeit der Kooperation, die in einer Veröffentlichung gemündet ist.

Aus dem Kreis der Festangestellten danke ich Birgit Tommes, Annette Ricken, Marcell Demandt und Jutta Bourgeois für verschiedenste Messungen (IR oder AAS) und für die Unterstützung nach dem Auftreten von Problemen mit verschiedenen Geräten oder Ähnlichem.

Mein Dank gilt ebenso verschiedenen Kollegen, die für mich Messungen angefertigt haben, wie Alex Spieß, Dennis Dietrich und Carsten Schlüsener für die aufgenommenen REM-Bilder. Ebenso danke ich Alexa Schmitz, Dennis Woschko und Moritz Steinert für die TGA-Analysen.

Meinem Bachelorstudenten Nabil Assahub und meinem Masterstudenten Tim Müller danke ich für ihre fleißige Arbeitsweise, während der Anfertigung ihrer Abschlussarbeiten und für die Beiträge, die sie zu dieser Arbeit geleistet haben.

Den Kollegen im Arbeitskreis danke ich für die nette Aufnahme, das gute Arbeitsklima und die Hilfe bei sämtlichen Fragestellungen.
Hierbei möchte ich besonders Niels Tannert und Bastian Moll danken, die mich schon während der Bachelor- bzw. Masterarbeit in die Gepflogenheiten dieses Arbeitskreises eingeführt haben.
Des Weiteren möchte ich Jun Liang für die gemeinsame Zeit im Labor danken und seine fachliche Kompetenz. Ebenso Philipp Brandt für die Einführung in den Bereich der

theoretischen Berechnungen, bzgl. IAST und Adsorptionsenthalpien. Ebenso möchte ich Yangyang Sun danken für die Hilfe bei unserem gemeinsamen Lieblingsgerät dem V-Star, welches wir nicht nur einmal gemeinsam auseinanderbauen durften.
Für die gesamte Zeit meiner Promotion bin ich einer Reihe von Leuten sehr dankbar, die diese Zeit einmalig gemacht haben und denen ich noch nicht im Einzelnen gedankt habe: Anna Goldman, Alexander Nuhnen, Serkan Gökpinar, Dennis Dietrich, Stefanie Bügel, Simon Millan, Tobie Matemb Ma Ntep, Dustin Jordan, Dietrich Püschel, Ishtvan Boldog, Hai Yen Beglau, Tobias Heinen, Robert Oestreich, Daniel Komisarek und der gesamten Nano-Gang auf dem anderen Flur.

Besonders danken möchte ich meinen Bürokollegen, die mich während der Zeit hier begleitet haben. Besonders hervorzuheben ist Emrah Hastürk für die Hilfe bei Fragen zu den Sorptionsmessungen und den Geräten und meinen weiteren Bürokollegen Marcus Fetzer, Simon-Patrick Höfert, Vasily Gvilava und Alex Spieß für die angenehme Atmosphäre. Hierbei sind besonders Alex und Vasily hervorzuheben, die auch im Kellerbüro für eine angenehme Ablenkung gesorgt haben und meine nicht-existenten erdkundlichen Fähigkeiten gnadenlos bei Geotastic ausgenutzt haben, außer Marcus (ohne Kellerbeteiligung) der ebenfalls eine gewisse erdkundliche Inkompetenz ausstrahlt (vor allem bei Flaggen der Länder).
Wir drei Kellerkinder hatten auch ab und an mal produktive Phasen, als wir noch oben waren, wie die Betreuung des Analytik-Praktikums oder die gemeinsame Vorlesung zum Praktikum, die aber trotzdem viel Spaß gemacht haben und sich meistens nicht nach Arbeit angefühlt haben.

Ein besonderer Dank gilt Alex Spieß, der mich seit Tag 1 an der HHU begleitet und durch den die diversen Vorlesungen, die diversen Praktika, die Bachelor- und die Masterarbeit deutlich angenehmer gestaltet wurden, ebenso wie die gesamte Promotion.

Meiner Freundin Pauline bin ich zutiefst dankbar, dass du meinen Eigenheiten mit einer konstanten Ruhe und Gelassenheit gegenübergetreten bist. Du hast mir in allen Phasen der Promotion geholfen, auch selbst, wenn ich keine Hilfe annehmen wollte. Ebenso danke ich dir für das Zuhören, wenn ich über den Chemie-Kram erzählt habe, auch wenn du es wahrscheinlich gar nicht hören wolltest.

Meiner Familie, besonders meinen Eltern möchte ich für die unendliche Geduld danken, die sie während des gesamten Studiums und der Promotion aufgebracht haben. Ihr wart immer für mich da und habt mich immer unterstützt. Ohne euch wäre diese gesamte Zeit niemals möglich gewesen.

Für meine Familie

I. Kurzzusammenfassung

Im Zuge dieser Arbeit wurden die Sorptionseigenschaften von Metall-organischen Gerüstverbindungen mit verschiedenen Metallen und Linkern untersucht. Das Ziel war es MOFs für verschiedene sorptionsbasierte Anwendungen zu untersuchen. Ebenso wurden in dieser Arbeit auch Kompositmaterialien aus Metall-organischen Gerüstverbindungen und verschiedenen Polymeren für diese sorptionsbasierten Anwendungen erforscht. Dies geschah unter verschiedenen Gesichtspunkten und war unter anderem abhängig von den verwendeten Polymeren.

Die Grundlage dieser Arbeit basierte auf der Verwendung von stabilen Metall-organischen Gerüstverbindungen, die durch das HSAB-Konzept als stabile Bindungsformen klassifiziert wurden. So wurden höher geladene Kationen (+ III und + IV) mit carbonsäurebasierten Liganden umgesetzt, oder niedriger geladene Kationen (+ II) mit Imidazolatliganden. Diese Kombinationen sind laut HSAB-Konzept als hart-hart oder weich-weich einzustufen.

Die synthetisierten Verbindungen wurden für verschiedene Adsorptionsanwendungen untersucht, diese beinhalteten unter anderem die Wasseraufnahme oder die Adsorption von flüchtigen organischen Verbindungen. Der Großteil der Messungen wurde im relativen Druckbereich bis $p\,p_0^{-1} = 0.9$ untersucht und gilt als Standard in der Forschung für Dampfadsorption, um eine Kondensation der Dämpfe in der Pore zu verhindern.

Aufbauend auf den reinen Dampfadsorptionsergebnissen wurden weitergehende Untersuchungen durchgeführt, die thematisch an die Sorptionsdaten anschließen. Hierunter fallen zum Beispiel die Kontrolle der Stabilität der MOFs mittels Pulverröntgendiffraktometrie und Stickstoffsorptionen. Dies sollte eine weiterbestehende Kristallinität und Porosität nach den durchgeführten Dampfsorptionsexperimenten überprüfen und gewährleisten.

Ein weiteres wichtiges Feld der Forschung waren theoretischen Rechnungen, die auf den experimentellen Daten basieren, wie die Kalkulation von IAST-Selektivitäten oder das Berechnen der Adsorptionsenthalpien. Diese theoretisch berechneten Daten sind wichtig, um die Eignung einer Metall-organischen Gerüstverbindung für eine potenzielle Anwendung bewerten zu können.

Die im weiteren Verlauf dieser Arbeit untersuchten Kompositmaterialien wurden, wie oben bereits beschrieben, nach erfolgreicher Dampfsorption weiteren Experimenten unterzogen, die abhängig von den eingesetzten Polymeren waren. Es wurden beispielweise die MOF@Chitosan-Komposite zum Einsatz in adsorptionsgetriebenen Wärmetransformationsgeräten getestet. Im Detail wurde hierbei die Stabilität bzw. die Widerstandsfähigkeit der Komposite gegenüber Pilzen getestet. Diese können in den Geräten hervorragende Wachstumsbedingungen vorfinden, aufgrund der hohen Feuchtigkeit und Wärme, daher müssen potenzielle Arbeitsmittel dagegen resistent sein.

II. Abstract

In the course of this work, the sorption properties of metal-organic frameworks with different metals and linkers were investigated. The aim was to investigate MOFs for various sorption-based applications. Similarly, composites of metal organic frameworks and various polymers were also explored in this work for these sorption-based applications. This was done from different aspects and was dependent on the polymers used, among other factors.

The premise of this work was based on the use of stable metal organic frameworks classified as stable bonding forms by the HSAB concept. Thus, higher charged cations (+ III and + IV) were combined with carboxylic acid based ligands, or lower charged cations (+ II) with imidazolate ligands. According to the HSAB concept, these combinations can be classified as hard hard or soft soft.

The synthesized compounds were studied for various adsorption applications, these included water uptake or adsorption of volatile organic compounds. The majority of the measurements were studied in the relative pressure range up to p p_0^{-1} = 0.9 which is considered the standard in vapor adsorption research to prevent vapor condensation in the pore.

Based on the vapor adsorption results, more advanced studies were conducted that thematically follow the sorption data. These include, for example, monitoring the stability of the MOFs, using powder X-ray diffraction and nitrogen sorptions. This was to verify and ensure the crystallinity and porosity after the vapor sorption experiments.

Another important field of research were theoretical calculations based on the experimental data, such as the calculation of IAST selectivities or the calculation of adsorption enthalpies. These theoretically calculated data are important to evaluate the suitability of a metal-organic framework for a potential application.

The composite materials investigated in the process of this work, as described above, were also used for further experiments after successful vapor sorption, depending on the polymers used. For example, the MOF@Chitosan composites were tested for use in adsorption-driven heat transformation devices. In detail, the stability and resistance of the composites to fungi were tested. These can find excellent growth conditions in the equipment, due to the high humidity and heat, so potential working materials must be resistant towards them.

III. Publikationsliste

Niels Tannert, Christian Jansen, Sandra Nießing, Christoph Janiak: „Robust synthesis routes and porosity of the Al-based metal-organic frameworks Al-fumarate, CAU-10-H and MIL-160"

Dalton Trans. **2019**, *48*, 2967–2976.

Christian Jansen, Nam Michael Tran-Cong, Carsten Schlüsener, Alexa Schmitz, Peter Proksch, Christoph Janiak: „MOF@chitosan Composites with Potential Antifouling Properties for Open-Environment Applications of Metal-Organic Frameworks"

Solids **2022**, *3*, 35-54

Tatsiana Shutava, Christian Jansen, Kanstantsin Livanovich, Vladimir Pankov, Christoph Janiak: „Metal organic framework/polyelectrolyte composites for water vapor sorption applications"

Dalton Trans. **2022**, *51*, 7053-7067

Christian Jansen, Niels Tannert, Dirk Lenzen, Marco Bengsch, Simon Millan, Anna Goldman, Dustin Nils Jordan, Linda Sondermann, Norbert Stock, Christoph Janiak: „Unravelling gas sorption in the aluminum metal-organic framework CAU-23: CO_2, H_2, CH_4, SO_2 sorption isotherms, enthalpy of adsorption and mixed-adsorptive calculations"

Z. Anorg. Allg. Chem. **2022**, *648*, e202200170

Christian Jansen, Nabil Assahub, Alex Spieß, Jun Liang, Alexa Schmitz, Shanghua Xing, Serkan Gökpinar, Christoph Janiak: „The Complexity of Comparative Adsorption of C_6 Hydrocarbons (Benzene, Cyclohexane, *n*-Hexane) at Metal-Organic Frameworks"

Nanomaterials **2022**, *12*, 3614

Niels Tannert, Sebastian-Johannes Ernst, Christian Jansen, Hans-Jörg Bart, Stefan K. Henninger, Christoph Janiak: „Evaluation of the highly stable metal-organic framework MIL-53(Al)-TDC (TDC = 2,5-thiophenedicarboxylate) as a new and promising adsorbent for heat transformation applications"

J. Mater. Chem. A **2018**, *6,* 17706-17712

Yangyang Sun, Alex Spieß, Christian Jansen, Alexander Nuhnen, Serkan Gökpinar, Raphael Wiedey, Sebastian-Johannes Ernst, Christoph Janiak: „Tunable LiCl@UiO-66 composites for water sorption-based heat transformation applications"

J. Mater. Chem. A **2020**, *8*, 13364-13375

Jun Liang, Vasily Gvilava, Christian Jansen, Secil Öztürk, Alex Spieß, Jingxiang Lin, Shanghua Xing, Yangyang Sun, Hao Wang, Christoph Janiak: „Cucurbituril-Encapsulating Metal–Organic Framework via Mechanochemistry: Adsorbents with Enhanced Performance"

Angew. Chem. Int. Ed. **2021**, *60*, 15365-15370

Abkürzungsverzeichnis

BET	Brunauer, Emmett, Teller
Bspw.	Beispielsweise
BTEX	Benzol, Toluol, Ethylbenzol, Xylol
Bzw.	Beziehungsweise
CAU	Christian-Albrechts-Universität
CPO	Coordination Polymer of Oslo
Deion.	Deionisiertes
DGC	Dry-gel conversion Trockengelsynthese
DMF	Dimethylformamid
DUT	Dresden University of Technology Dresden Universität der Technologie
EEA	European Environment Agency Europäische Umweltagentur
Engl.	Englisch
EPA	Enviromental Protection Agency Umweltschutzbehörde
Et al.	Et alii Und andere
HKUST	Hong Kong University of Science and Technology Hongkong Universität der Wissenschaft und Technologie
HoA	Heat of adsorption Adsorptionswärme
HPLC	High-pressure liquid chromatography Hochdruckflüssigkeitschromatographie
HSAB	Hard and soft acid and bases Harte und weiche Säuren und Basen

IAST	Ideal adsorbed solution theory Theorie zur idealen adsorbierten Lösung
IRMOF	Isoreticular metal-organic framework Isoretikuläre Metall-organische Gerüstverbindungen
IUPAC	International Union of Pure and Applied Chemistry Internationale Union für reine und angewandte Chemie
MIL	Matériaux de l'Institut Lavoisier Materialien des Instituts Lavoisier
MOF	Metal-organic framework Metall-organische Gerüstverbindungen
NMR	Nuclear magnetic resonance Kernspinresonanz
NMVOC	non-methane volatile organic compounds nicht-methanhaltige flüchtige organische Verbindungen
OFAST	osmotic framework adsorbed solution theory
OMS	open metal sites ungesättigte Metallknotenpunkte
PVA	Polyvinylalkohol
PXRD	Powder X-ray diffraction Pulverröntgendiffraktometrie
REM	Rasterelektronenmikroskopie
SDA	Structure-directing agents strukturgebendes Mittel
SEM	Scanning electron microscope (REM)
SOD	Sodalith
Sog.	Sogenannten
SVOC	Semi volatile organic compounds Schwerflüchtige organische Verbindungen
TGA	Thermogravimetrische Analyse

UiO	Universitetet i Oslo Universität Oslo
Verd.	Verdünnt
VOC	Volatile organic compounds flüchtige organische Verbindungen
VVOC	Very volatile organic compounds Sehr flüchtige organische Verbindungen
WHO	World Health Organization Weltgesundheitsorganisation
ZIF	Zeolitic imidazolate framework Zeolitische Imidazolat Gerüstverbindungen

Inhaltsverzeichnis

1. Einleitung

1.1 Metall-organische Gerüstverbindungen

Metall-organische Gerüstverbindungen (engl. *metal-organic frameworks*, kurz MOFs) sind eine Unterkategorie der Koordinationspolymere. Sie bestehen aus anorganischen und organischen Teilen, weshalb sie als Hybridmaterialien bezeichnet werden.[1] Der exakte Aufbau der MOFs besteht aus metallischen Knotenpunkten, die durch verbrückende organische Liganden, auch Linker genannt, verbunden werden. Die exakte IUPAC-Definition (*International Union of Pure and Applied Chemistry, deutsch* Internationale Union für reine und angewandte Chemie) lautet daher auch, dass „MOFs Koordinationsnetzwerke sind mit organischen Liganden, die potenzielle Hohlräume beinhalten“. Diese kurz gehaltene Definition umschließt eine große Vielzahl an Materialien, so sind auch dynamische Systeme als MOF definiert, die unter äußerem Einfluss ihre Struktur verändern können und dann Porosität erlangen. Dies kann bedeuten, dass MOFs nicht zwangsläufig kristallin sein müssen.[2]

Der strukturelle Aufbau, mit möglichen Hohlräumen, führt zu einer theoretischen Porosität der Materialien und macht diese für eine große Anzahl an potenziellen Anwendungen interessant.[3] Dies unterscheidet MOFs von reinen Koordinationspolymeren, die auch in eindimensionaler Kettenstruktur vorliegen können. Dies Unterscheidung bzw. Klassifizierung wird in der nachfolgenden Abbildung 1 schematisch verdeutlicht.[4]

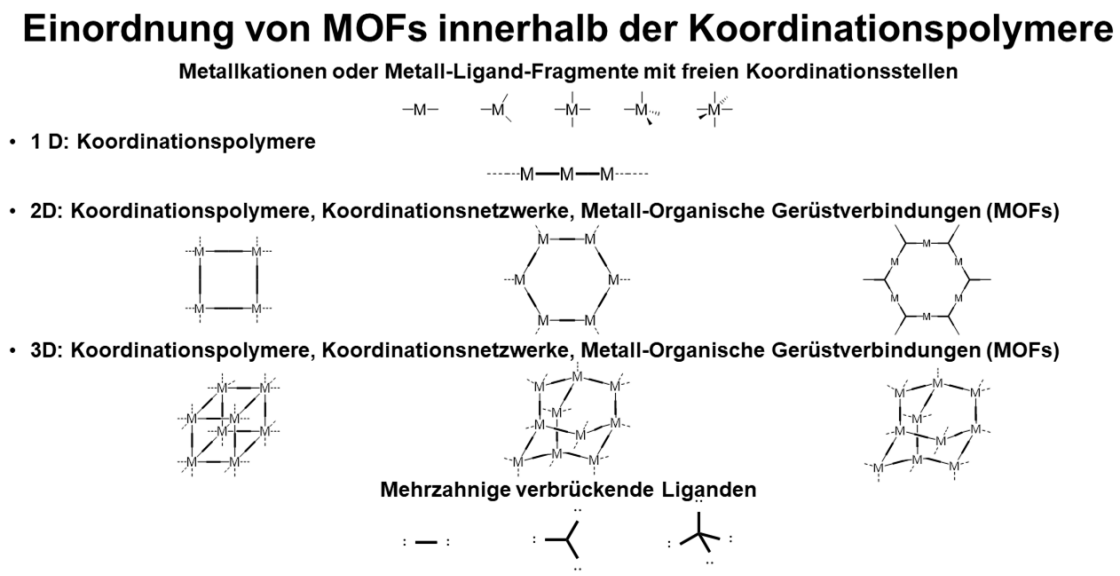

Abbildung 1: *Schematische Darstellung von Koordinationspolymeren aus Metallionen bzw. Metall-Ligand-Fragmenten und multidentaten, verknüpfenden Liganden und Einordnung von MOFs als Unterkategorie der Koordinationspolymere bzw. der Koordinationsnetzwerke. Nachbildung und ins deutsche übersetzt von Ref. 4 mit Genehmigung, © 2010, The Royal Society of Chemistry.*

Die in der Abbildung 1 gezeigten Metallionen bzw. Metall-Ligand-Fragmente bestehen aus Metallkationen bzw. aus Metall-Sauerstoff-Clustern, den sog. *secondary building units* (kurz SBUs).[5] Diese Cluster werden mit den Linkern zu Netzwerken aufgespannt, wobei die Linker

sowohl zwei- als auch mehr zähnige (bidentat oder multidentat) Liganden sein können,[6] also dementsprechende verknüpfende bzw. funktionelle Gruppen tragen können.[7] Die Verwendung von diversen funktionellen Gruppen ist möglich, wie z. B. Carboxylate,[8] Phosphonate,[9] oder auch Liganden mit Stickstoffatomen z. B. Imidazole.[10] Somit können, unter Verwendung des HSAB-Konzepts (*hard and soft acid and bases*),[11] zwischen harten und weichen Liganden unterschieden werden.[12,13] In Kombination mit der großen Anzahl an Metallatomen und Oxidationsstufen kann die hohe Stabilität mancher MOFs sehr gut mit dem HSAB-Konzept erklärt werden. Die MOFs könne so gezielt für Anwendungen mit hohem Stabilitätsanspruch ausgewählt und synthetisiert werden.

Des Weiteren können auch bifunktionelle Liganden, Linker mit Heteroatomen,[14] oder mit zusätzlichen funktionellen Gruppen,[15] die nicht verbrückend im Gerüst eingebaut sind, verwendet werden.[16] Diese große Auswahl und Art der Funktionalisierung ist ein wichtiger Vorteil, um ein Material bzw. die Pore für eine spezielle Anwendung maßzuschneidern bzw. zu synthetisieren.[17] Ebenso kann die Pore vergrößert werden, indem ein größerer Linker eingesetzt wird. Geschieht dies unter Beibehalten der Netzwerkstruktur, wird von einer isoretikulären Verlängerung des MOFs gesprochen.[18] Zusätzlich können auch flexible Liganden verwendet werden, die es möglich machen neuartige kristalline Gerüstmaterialien aufzuspannen.[19]

Die folgende Abbildung 2 stellt einen Auszug der möglichen Metallkationen und potenzieller linker dar, mit der Einordnung in das HSAB-Konzept. Diese Einordnung ermöglicht eine gewisse Vorhersagbarkeit in Bezug auf die Stabilität der resultierenden MOFs aus der jeweiligen Metall-Linker-Kombination.

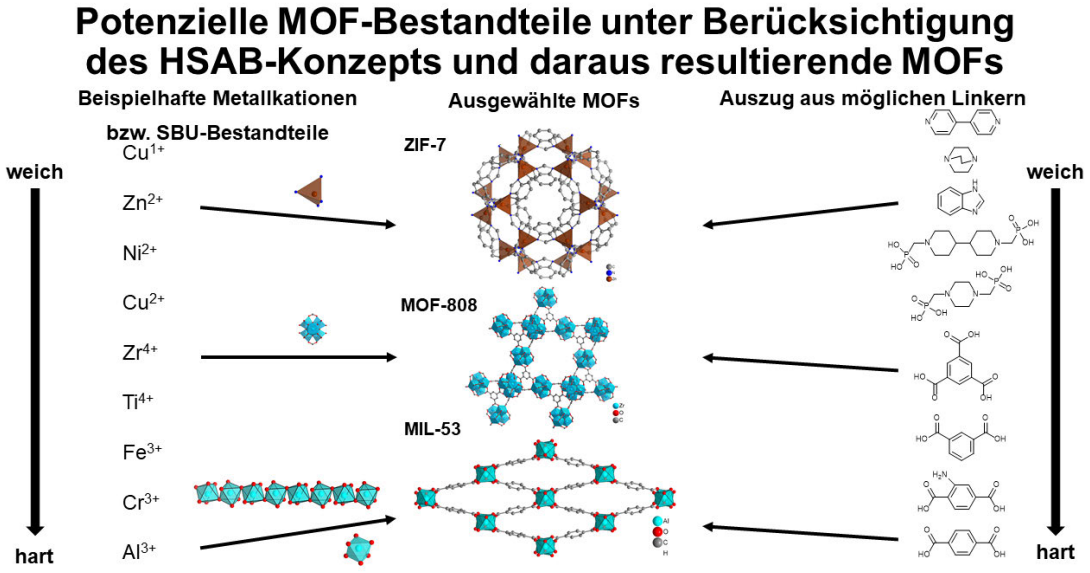

Abbildung 2: *Potenzielle Bestandteile von MOFs, inklusive der Einteilung in harte und weiche Komponenten mittels des HSAB-Konzept und eine beispielhafte resultierende MOF-Auswahl. Die CCDC-Nummern der gezeigten MOFs inkl. Referenzen: 602541 (ZIF-7),[20] 1002672 (MOF-808),[21] 220477 (MIL-53).[22]*

Der Begriff m*etal-organic frameworks* wurde erstmals im Jahr 1995 von Yaghi *et al.* verwendet, um die damals neuartigen Verbindungen bestehend aus Kupfer und 4,4´-Bipyridin,[23] bzw. aus Kobalt und 1,3,5-Benzoltricarboxylat (Trimesinsäure) zu beschreiben.[24] Diese wurden erstmals als poröse 3D-Gerüstverbindungen bezeichnet.

MOF-Verbindungen gehen auf unterschiedliche anorganisch-organische Hybridmaterialien zurück, wie die Werner-Komplexe, die Hofmann-Clathrate oder Berliner Blau. Diese Materialien sind ebenfalls geeignet kleine Moleküle reversibel aufzunehmen und können daher als die Vorläufermaterialien von MOFs bezeichnet werden.[25]

Eine der wichtigsten „frühen" MOF-Verbindungen ist MOF-5 und besteht aus Zink und 1,4-Benzoldicarboxylat (Terephthalat), mit im Gerüst eingebauten Dimethylformamid (kurz DMF), und wurde 1996 von Yaghi *et al.* erstmals synthetisiert und 1999 erstmalig MOF-5 genannt.[26,27] 1998 wurde anhand von MOF-5 zum ersten Mal die Porosität mittels einer Gassorptionsisotherme an einem MOF untersucht und in diesem Forschungsgebiet als gängige Methode etabliert.[28]

Die Nomenklatur von MOFs ist nicht abschließend definiert und macht eine Zuordnung des MOFs anhand des Namens unmöglich, wie es bereits 2013 von Batten *et al.* angemerkt wurde. Neuartige MOFs werden häufig nur mit der Abkürzung MOF und einer fortlaufenden Nummer angegeben, wie es bei MOF-5 der Fall ist, oder mit dem Kürzel der Universität an der es erstmals synthetisiert wurde, in Kombination mit Nummern bzw. Ziffern.[2] Ein weiterer wichtiger struktureller Aspekt ist, wie oben bereits erwähnt, die Ausdehnung des Netzwerks unter Verwendung eines verlängerten Linkers. Diese isoretikuläre Verlängerung eines MOFs wird häufige auch in der Benennung des MOFs deutlich. So bildet das mehrfach erwähnte MOF-5 den Ausgangspunkt für eine große Anzahl an porösen isoretikulär vergrößerten MOFs. MOF-5 wird in dieser Reihe auch als IRMOF-1 (*isoreticular metal-organic framework,* deutsch isoretikuläre Metall-organische Gerüstverbindungen) bezeichnet. Die zugehörigen MOFs mit gleicher Struktur, aber unterschiedlichen Linkern dementsprechend durchnummeriert.[29]

Neben den MOFs sind eine weitere wichtige strukturelle Klasse der porösen Materialien die zeolitischen Imidazolat Gerüstverbindungen (engl. z*eolitic imidazolate frameworks,* kurz ZIFs). Sie werden als eine Unterklasse der MOFs angesehen und bestehen aus einem Metall (meist Zink oder Kobalt) und einer verbrückenden Imidazolverbindung als Ligand.[30] ZIFs wurden erstmals im Jahr 2002 von Tian *et al.* Beschrieben. Die hergestellte Verbindung besteht aus Kobalt und Imidazol, welche in Piperazin miteinander umgesetzt worden sind.[31] Die strukturelle Besonderheit von ZIFs, im Vergleich mit MOFs, ist ihr Aufbau, der Zeolithen gleicht, also kristallinen Aluminosilikaten. Das Metallkation ist analog zum Silicium bzw. zum Aluminium koordiniert, jedoch handelt es sich um Imidazolliganden und nicht um Sauerstoff. Dennoch kombinieren ZIFs viele Eigenschaften der MOFs und der Zeolithe, wie die hohe thermische und chemische Stabilität und machen sie daher interessant für die Forschung.[30]

Die große Vielfalt an möglichen Verbindungen wird durch eine große Anzahl an Syntheserouten bzw. -bedingungen ermöglicht, da diese ein breites Spektrum an Varianten aufweisen.[32] Die ersten MOFs wurden meist, wie die bereits oben Genannten, unter solvothermalen Bedingungen hergestellt.[33] Solvothermal bedeutet, dass die Edukte und das Lösemittel bzw. das Lösemittelgemisch unter hohem Druck und hohen Temperaturen in einem geschlossenem System zur Reaktion gebracht werden.[32] Die Löslichkeit der Edukte in dem jeweiligen Lösemittel soll hiermit erhöht werden und Reaktion ermöglichen, die unter Normalbedingungen nicht stattfinden würden. Weitere mögliche Reaktions- bzw. Synthesebedingungen sind in der nachfolgenden Abbildung 3 gezeigt, die aus Stock *et al.* übernommen und ins Deutsche übersetzt wurde.[32]

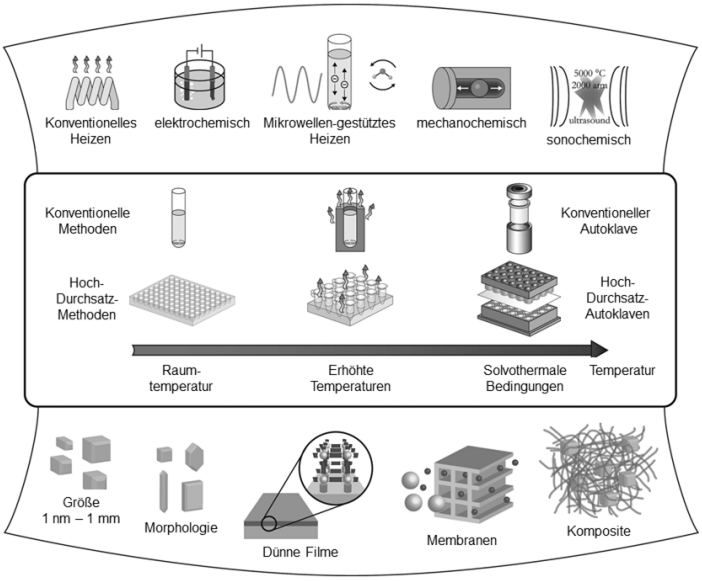

Abbildung 3: *Auszug aus möglichen Synthesemethoden (obiger Teil), inklusive Reaktionstemperaturbereichen (mittlerer Teil) und zugehörigen Reaktionsprodukten, unterteilt in Größe, Morphologie und Produktart (unterer Teil). Nachdruck (ins Deutsche übersetzt) von Ref. 32 mit Genehmigung, © 2012, American Chemical Society.*

Ebenso wie die MOFs sind auch die Synthesemethoden weiterentwickelt worden. Es wurde versucht diese am Grundsatz der „grünen“ Chemie auszurichten.[34] Dies beschreibt den Ansatz bei der Synthese neuartiger chemischer Produkte die Verwendung oder die Erzeugung gefährlicher Substanzen zu verringern oder vollständig zu vermeiden.[35]

Für MOFs wird zusätzlich die Aufgabe definiert neue Syntheserouten zu suchen, die weniger schädliche Lösemittel einsetzen bzw. unter Umständen vollständig auf diese verzichten. Dieser Ansatz der „grünen“ Synthese für MOFs wird im Review von Reinsch umfassend dargelegt und analysiert. Die wichtigsten Erkenntnisse sind die Verringerung des Lösemittelgebrauchs, die Auswahl nicht toxischer Metallsalze und die Skalierbarkeit der Ansätze hin zu einem industriellen Niveau.[36]

Dies kann durch andere Syntheserouten erreicht werden, die ebenfalls bei Stock *et al.*

dargestellt werden.[32] So weisen mechanochemische Synthesen eine gute Skalierbarkeit auf und verzichten nahezu oder vollständig auf Lösemittel. Crawford *et al.* synthetisierten auf diese Weise 2015 drei unterschiedliche MOFs im größeren Maßstab mit einem Schneckenextruder. Hierbei konnten zwei der hergestellten MOFs vollständig ohne Lösemittel synthetisiert werden. Bei der dritten Verbindung wurde der Einsatz von Lösemittel deutlich reduziert, im Vergleich mit der in der Literatur eingesetzten Menge. Diese Synthesebedingungen führten dennoch zu einer hohen Kristallinität, sowie einer großen Porosität der Produkte.[37]

Ein weitere Synthesemethoden ist die Herstellung von MOFs unter elektrochemischen Bedingungen. Eine solche kann zu einer Verkürzung der Reaktionszeiten und zu milderen Reaktionsbedingungen führen.[38] Joaristi *et al.* haben 2012 mehrere wichtige prototypische MOFs mit dieser Syntheseroute hergestellt, mit verschiedenen Metallkationen, wie Zn^{2+}, Cu^{2+} oder Al^{3+}. Ebenfalls untersuchten sie den Einfluss von Lösemitteln, Temperatur und der Stromdichte.[39] Mikrowellensynthesen sind eine zusätzliche Option bei der Herstellung von MOFs und können das konventionelle Heizen in Öfen, bei solvothermalen Synthesen, ersetzen. Hierdurch kann die Reaktionszeit erheblich verkürzt und Energie eingespart werden.[40] Dies konnte von Choi *et al.* an dem bereits erwähnten prototypischen MOF-5 gezeigt werden. Sowohl die Kristallinität, als auch die Porosität des MOFs wurde beibehalten und der Einfluss von Metall-Ligand-Verhältnis, Temperatur und Zeit variiert und überprüft.[41]

Die Trockengelsynthese (engl. *dry-gel conversion*, kurz DGC) ist eine Synthesevariante bei der die Edukte vorgelegt werden und diese im Dampf des Lösemittels miteinander reagieren. Hierdurch kann deutlich weniger Lösemittel eingesetzt und anschließend wiederverwendet und die Größe der Reaktionsapparaturen verkleinert werden.[42]

Bei der Kombination unterschiedlicher Methoden können die gesamten Vorteile der jeweiligen Syntheserouten genutzt werden, um die Herstellung von verschiedenen MOFs zu verbessern. So haben Tannert und Gökpinar *et al.* bei der DGC-Methode das konventionelle Heizen des Syntheseofens durch eine Mikrowelle ersetzt und konnten so verschiedene MOFs in kurzer Zeit, mit guten Ausbeuten und in mit der Literatur vergleichbarer Qualität synthetisieren.[43]

Eine der häufigsten, eingesetzten Methoden bei der MOF-Synthese ist weiterhin die Rückflussmethode, da hierbei die Parameter Metallsalzquelle, Konzentrationsverhältnisse, Lösemittel oder die zeitverzögerte Zugabe eines Eduktes umfassend analysiert werden können. Zusätzlich können bei dieser Synthesemethode die Ansätze leicht vergrößert und der Einfluss des Maßstabs auf Kristallinität und Porosität, in Hinblick auf eine Verwendung in der Industrie, bewertet werden.[44]

Zusätzlich zu den Syntheserouten spielt die Auswahl der Edukte, vor allem des Metallsalzes, genauer gesagt des Gegenions, eine entscheidende Rolle im Verlauf der Reaktion, wie bereits oben erwähnt.[45] Die Wahl der Edukte und des Lösemittels und somit auch indirekt der pH-Wert, kann die Produktbildung, neben weiteren Faktoren, erheblich beeinflussen, im

Hinblick auf die Kristallinität und die Porosität, oder sogar zu einem anderen Produkt führen.[46] So können sog. polymorphe Verbindungen, wie zum Beispiel bei der Reaktion von einem Aluminiumsalz mit Trimesinsäure synthetisiert werden. Es können die drei unterschiedliche Verbindungen MIL-100 (*Matériaux de l'Institut Lavoisier*),[47] MIL-110,[48] und MIL-96,[49] mit unterschiedlicher Netzwerkstruktur und Porosität entstehen. Die Reaktionsbedingungen sind entscheidend dafür, welche der drei Verbindungen erhalten wird. Mittels Pulverröntgendiffraktometrie (engl. *powder X-ray diffraction*, kurz PXRD) und Rasterelektronenmikroskopie (kurz, REM; engl. *scanning electron microscope*, kurz SEM) konnten die unterschiedlichen Phasen identifiziert werden. MIL-100 wurde als die kinetische Phase und MIL-96 als das thermodynamische Produkt identifiziert, MIL-110 wiederum entsteht nur in stark saurer Umgebung.[50] Trotz der gleichen Ausgangsmaterialien sind die Eigenschaften der drei MOFs im Hinblick auf die Porosität deutlich verschieden. So weichen sowohl die Oberflächen, als auch die Porengrößen sehr stark voneinander ab, was auf den unterschiedlichen Aufbau der drei Verbindungen zurückzuführen ist.[47,48,49]

Ein weiterer wichtiger Faktor bei den Synthesen der MOFs sind Modulatoren,[51] *mineralizer*,[32] oder *strucuture-directing agents/architecture-directing agents* (kurz SDAs, deutsch strukturgebendes Mittel),[52] um die gewünschten Produkte zu erhalten und ihre Eigenschaften zu verbessern.[32] Hierbei nehmen die drei Substanzklassen eine unterschiedliche Funktion in der Synthese wahr.

Modulatoren werden eingesetzt um die Eigenschaften des MOFs zu verändern. Hierbei können Modulatoren sowohl die Größe, als auch die Morphologie der Partikel verändern und die Synthesen reproduzierbarer machen.[53,54,55] Die Einteilung von Modulatoren kann in zwei größere Kategorien erfolgen, die Modulatoren, welche für die Koordination des Netzwerks oder für die Deprotonierung in der Synthese zuständig sind. Erstere lassen sich nochmal in Monocarbonsäuren und Salzsäure unterscheiden.[51] Im weiteren Verlauf wird auf die Wirkung der Monocarbonsäure und der Salzsäure in der MOF-Synthese detaillierter eingegangen, um die unterschiedliche Wirkungsweise zu erläutern. Monocarbonsäuren stehen in Konkurrenz zum Linker und koordinieren ebenfalls am Metallzentrum und verursachen so, dass weniger Ligand in das MOF eingebaut wird und verlangsamen dadurch die Kristallisation.[56] Salzsäure hingegen dient in der Synthese als Reaktionsbeschleuniger und erhöht die Löslichkeit der Liganden, vor allem in der Synthese von MOFs der UiO-Reihe (*Universitetet i Oslo*).[57]

Ein weiterer wichtiger Aspekt bei Modulatoren ist das Einbauen von Defektstellen in das Netzwerk. Hierbei kann zwischen Linker- und Clusterdefekten unterschieden werden, also entweder dem Austausch von Liganden gegen Modulatoren, oder dem Absättigen des Netzwerks mit Modulatoren und dem Verlust der Konnektivität mit einer SBU.[58] Die Überprüfung der Defektstellen wird mittels der thermogravimetrischen Analyse (kurz TGA) und NMR (*nuclear magnetic resonance*, deutsch Kernspinresonanz) durchgeführt.[59,60]

Mineralizer sollen die Löslichkeit der Edukte erhöhen und die Kristallisation fördern. Dieser Ansatz wurde bei der Synthese von Zeolithen angewendet und für MOFs mit carbonsäure-haltigen Liganden übernommen. Ein vor allem in frühen MOF-Synthesen eingesetzter *mineralizer* ist Flusssäure, wobei das enthaltene Fluorid in die MOF-Strukturen eingebaut wird.[61] Jedoch wurde es erfolgreich durch ungefährlichere Stoffe ersetzt und Alternativen sind Salpetersäure oder Essigsäure, beispielweise bei der Synthese von MIL-101(Cr).[62]

Structure-directing agents wurden ebenfalls bei der Synthese von Zeolithen verwendet und sollen die Produktbildung begünstigen.[63] Bei der Synthese von MOFs können unterschiedliche Chemikalien als SDAs verwendet werden, wie Linker-Analoga,[64] Benzol oder organische Amine.[32]

Ein wichtiger Aspekt bei MOFs ist die Aktivierung, um die potenzielle Porosität des Netzwerks vollständig nutzen zu können. Hierbei müssen mehrere Faktoren berücksichtigt werden, wie die vollständige Entfernung der in den Poren verbleibenden Moleküle, bspw. nicht eingebauter Linker oder Nebenprodukte aus der Synthese.[65] Dies soll durch einen mehrfachen Lösemittelaustausch gewährleistet werden, bei dem zu niedriger siedenden Lösemittel hin ausgetauscht wird, oder bis hin zu überkritischem Kohlenstoffdioxid. Anschließend können MOFs noch, unter zu Hilfenahme von Vakuum, thermisch aktiviert werden.[66]

Die vollständige Aktivierung des MOFs ist notwendig, um es für die breiten Anwendungsmöglichkeiten bestmöglich zu nutzen. Ein Auszug aus möglichen Anwendungsgebieten ist in der folgenden Abbildung 4 dargestellt.

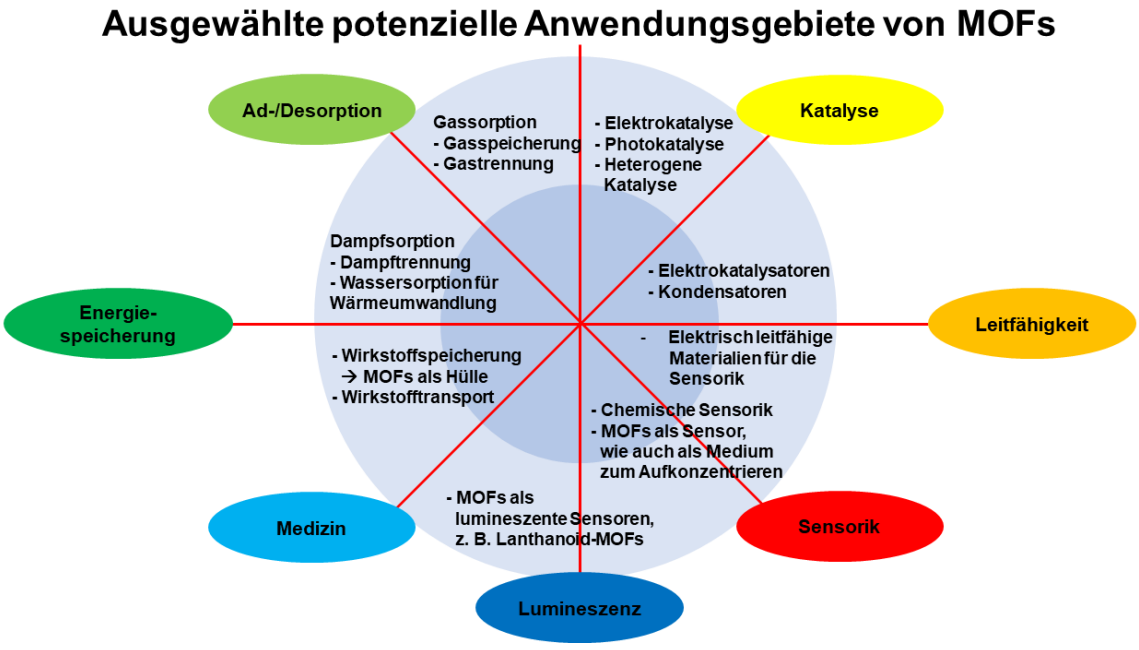

Abbildung 4: *Ausgewählte potenzielle Anwendungsgebiete von MOFs außerhalb des Kreises dargestellt und spezifische Ausprägungen in der Mitte des Kreises, mit gebietsübergreifenden Anwendungsmethoden. Diese Abbildung wurde eigenständig erstellt und ist angelehnt an die Graphiken aus Ref. 4 und Ref. 67.*

Die möglichen Anwendungen von MOFs sind sehr vielfältig und hängen mit gezielten Synthesemöglichkeiten für unterschiedlichen Bereiche zusammen.

Zwei wichtige Bereiche für MOFs, die durch ihre poröse Struktur begründet sind, sind die Gasspeicherung und -trennung bzw. gilt dies auch für Dämpfe. Dieses auf Adsorptions- und Desorptionsprozessen basierende Themengebiet ist eine der am besten untersuchte Anwendungen, was durch die hohen Oberflächen und die großen Poren begründet ist. [68] In Kapitel 1.3 Gas-/Dampfsorption wird detailliert auf die Sorptionsmechanismen und die gesamte Thematik rund um die Porosität und die Oberflächen eingegangen.

MOFs können ebenfalls gezielt im Bereich der heterogenen Katalyse eingesetzt werden und bieten eine Vielzahl von Vorteilen gegenüber homogenen Metall-Katalysatoren, wie die einfache Handhabung durch Abtrennen und Recyclen, breites chemisches Variantenreichtum und damit verbundene hohe Selektivität.[69,70]

Ein weiteres breit gefächertes Einsatzgebiet für MOFs ist der Einsatz in der Sensorik, z. B. in wässrigen Lösungen oder in der Gasphase. Der Nachweis durch einen MOF-Sensor kann hierbei sehr unterschiedlich erfolgen, so gibt es Sensoren die auf den lumineszenten Eigenschaften von MOFs basieren oder auf einer Redoxreaktion in einem elektrochemischen System.[71]

Zusätzlich wird in der Forschung der Einsatz von MOFs in der Medizin, für bildgebende Verfahren in der Diagnostik,[72] oder als Material für den Wirkstofftransport untersucht.[73] Die bildgebenden Verfahren, wie für die Magnetresonanztomographie oder die Computertomographie basieren darauf, dass MOFs Bildgebungsmittel aufnehmen und so die Aufnahmen möglich machen. Ein weiterer Vorteil ist das gleichzeitige Beladen der MOFs mit Bildgebungsmitteln und Wirkstoffen, womit die Wirkung von Medikamenten direkt beobachtet werden kann.[72]

Für die gezielte Anwendung von MOFs ist die Kristallit-Form und die davon abhängige Beschaffenheit des Produkts essentiell. So ist bei MOFs zu unterscheiden, ob das Material als mikrokristallines Pulver oder einkristallin vorliegt. Diese unterschiedlichen Ausgangsmaterialien (MOFs), für spezielle Kompositmaterialien oder im weiteren für die Anwendungsmöglichkeiten, können meist durch gezielte Variation der Synthese erhalten werden.[53] Für die Aufklärung der Struktur bei neuen Verbindungen sind einkristalline MOF-Produkte vorteilhaft,[74] wohingegen für potenzielle Anwendungen die Form des mikrokristallinen Pulvers zur Weiterverarbeitung bevorzugt wird.[75]

Wird eine weitere Ebene der MOF Architektur betrachtet, wird untersucht in welchem hierarchischen Verhältnis MOFs aufgebaut werden können, um diese für vielfältige Zwecke maßzuschneidern. Hierbei werden drei Arten der Hierarchie in MOFs unterschieden, die sich auf die poröse, die architektonische und die kompositorische Hierarchie beziehen. Hierbei ist besonders die poröse Hierarchie relevant, welche in Kapitel 1.3 Gas-/Dampfsorption näher

erläutert wird. Die anderen beiden Bereiche beziehen sich auf kombinierte MOF-Materialien und deren gezielte Synthese.[76]

Weitere Aspekte, die bei der gezielten Synthese von MOFs untersucht werden, sind das Einbauen von ungesättigten Metallknotenpunkten (engl. *open metal sites*, kurz OMS),[69] oder die Verwendung von zwei unterschiedlichen Liganden in einer Struktur, sogenannte *Mixed-Linker* MOFs.[77,78] Ungesättigte Metallknotenpunkte können entstehen, wenn an den Knotenpunkten koordiniertes Lösemittel entfernt wird. Dies geschieht mit verschiedenen Methoden, wie dem Lösemittelaustausch mit anschließender thermischer Aktivierung oder alternativ photothermischer Aktivierung, ohne vorher einen Austausch des Lösemittels durchzuführen.[69] Sind anschließend die metallischen Knotenpunkte ungesättigt und somit zugänglich können diese z. B. für eine bessere katalytische Aktivität sorgen,[79] die Sorptionskapazitäten erhöhen,[80] oder für eine gezielte Trennung von Gasen genutzt werden.[81]

Bei MOFs mit zwei unterschiedlichen Liganden, die in das Netzwerk eingebaut werden, wird der Ansatz verfolgt durch das Einfügen von einem zweiten Liganden, aber zum Beispiel mit einer funktionellen Gruppe, das MOF für eine gewisse Anwendung maßzuschneidern.[82] So konnten sowohl Schlüsener *et al.*, als auch Tan *et al.* unabhängig voneinander zeigen, dass durch die Verwendung von zwei Liganden und Variation der Verhältnisse die Aufnahme bei der Wassersorption gezielt zu hydrophileren oder hydrophoberen Bereichen verschoben werden kann.[77,78,83] Schlüsener *et al.* konnten zusätzlich zeigen, dass die erfolgreiche Synthese mit zwei unterschiedlichen Linkern und die daraus resultierende Struktur erheblich vom Öffnungswinkel des Moleküls abhängig sind, welcher in diesem Fall zwischen den zwei Carboxylaten entsteht.[78] Die verwendeten Strukturen basieren auf unterschiedlichen Aluminium-haltigen MOFs, die in der Forschung eine besondere Rolle einnehmen und im folgenden Kapitel näher erläutert werden.

1.1.1 Aluminiumbasierte MOFs

Aluminiumbasierte MOFs sind aufgrund ihrer hohen Stabilität von großem Interesse. Die Stabilität geht auf die starke Aluminium-Sauerstoff-Bindung zwischen den Metallknotenpunkte und den Carbonsäure-funktionalisierten Liganden zurück. Diese beiden Komponenten werden im HSAB-Konzept (vgl.: Abbildung 2) als besonders hart eingestuft und formen damit eine besonders stabile Bindung.[84] Weitere wichtige Punkte bei Aluminium-MOFs sind die zumeist einfachen Syntheserouten,[85] und die vielfältige Varianz von einsetzbaren Liganden.[86] Zusätzlich ist Aluminium ein verhältnismäßig günstiges Metall mit einem hohen natürlichem Vorkommen und geringer Toxizität und macht damit die daraus synthetisierten MOFs für eine potenzielle Massenproduktion interessant.[87] Wenn diese MOFs noch mit nachhaltig hergestellten Liganden produziert werden, wie zum Beispiel bei MIL-160 mit dem Linker 2,5-Furandicarbonsäure, ist es ein weiterer Schritt in Richtung „grüner“ Chemie. Der Linker wird mittels Oxidation aus 5-Hydroxymethylfurfural synthetisiert, welches aus erneuerbarer

Biomasse gewonnen wird.[88]

Ein interessanter struktureller Aspekt bei der Großzahl der Aluminium-MOFs, im Vergleich zu MOFs mit anderen Metallen ist der Aufbau der Metallknotenpunkte, die aus wiederholenden Al-O-verknüpften Oktaedern bestehen, die zu Ketten aufgereiht werden. Die Verknüpfung dieser Oktaeder kann in unterschiedlichen Konfigurationsisomeren erfolgen, in cis- und/oder trans-Anordnung, die Möglichkeiten sind in Abbildung 5 dargestellt.[78]

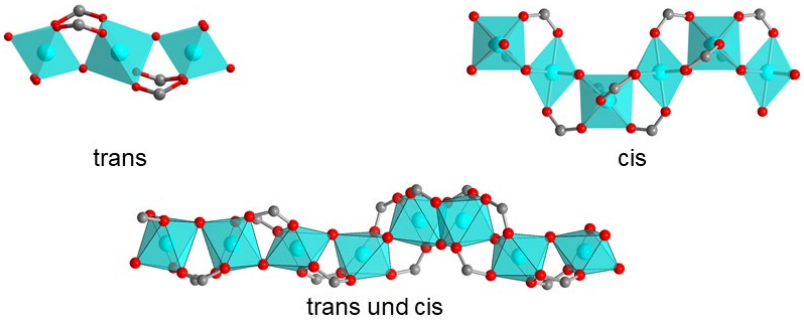

Abbildung 5: *Verknüpfung der Al-O-Oktaeder mit den wiederholenden Einheiten, die zu unterschiedlichen Konfigurationsisomeren aufgespannt werden (cis und/oder trans). Die Strukturen wurden mit Diamond[89] eigenständig erstellt (CSD-Nummer: 1051975 (trans),[90] 1828695 (cis),[91] 1878820 (trans/cis)[92]).*

Die Verknüpfung der Al-O-Oktaeder und ihre Anordnung in cis- und/oder trans-Isomerie wird durch den Öffnungswinkel der Liganden bestimmt, wie Schlüsener *et al.* in ihrem *Mixed-Linker*-Ansatz zeigen konnten.[78] Dies ermöglicht die Strukturen potenzieller neuer Aluminium-MOFs in gewissem Maße hervorzusagen. Jedoch gibt es mit gleicher Verknüpfung dennoch mehrere unterschiedliche Strukturen, wie die cis-verknüpften MOFs MIL-160[88] und CAU-10-H (Christian-Albrechts-Universität),[93] oder die trans-verknüpften MOFs MIL-53[22] und DUT-4/5 (Dresden University of Technology).[94] Ein Aluminium-MOF, das eine Struktur mit beiden Konfigurationsisomeren zeigt, wie in Abbildung 5 unten dargestellt, ist das von Lenzen *et al.* synthetisierte CAU-23. Dieses MOF besteht aus den gleichen Edukten (Aluminiumsalz und dem Linker 2,5-Thiophendicarbonsäure), wie sein Isomer MIL-53-TDC, welches aus reiner trans-Verknüpfung aufgebaut ist. [95]

Im Gegensatz zu den kettenförmig aufgebauten Aluminium-MOFs gibt es auch MOFs mit einer SBU, die durch Liganden verbrückt wird, wie in MIL-100(Al).[47] Im Fall von MIL-100(Al) besteht die Struktur aus dreikernigen, oktaedrisch koordinierten Aluminiumbausteinen, die einen Supertetraeder bilden, die durch den Linker Trimesinsäure verknüpft sind.[96]

Das Aluminium-MOF MIL-53 zeigt eine Besonderheit, im Vergleich zu anderen Aluminium-MOFs, den sogenannten *breathing-effect* (deutsch Atmungseffekt). Hierbei verändert sich die Porenöffnung des MOFs in Abhängigkeit von den Molekülen in der Pore.[22] Dieser Effekt wird auch bei MIL-47(V) beobachtet, einem isotypischen bzw. isostrukturellen MOF, zu MIL-53.[97] Bei diesen MOFs wird zwischen drei Phasen unterschieden, der

Hochtemperatur-, der Niedrigtemperatur- und der synthetisieren Phase.[22] Diese Phasen können im PXRD unterschieden werden und durch Aufreinigen und Ausheizen/Aktivieren des MOFs gezielt erhalten werden. Die Hochtemperatur-Phase ist besonders für Adsorptionsanwendungen interessant und wichtig, da die Pore frei von Lösemittel oder Edukten vorliegt.[22]

Wichtige potenzielle Anwendungen von Aluminium-MOFs basieren meist auf deren Sorptionseigenschaften und deren hohen Stabilität gegenüber Wasser und der Atmosphäre. Diese Stabilität wird häufig für Wassersorptionsexperimente eingesetzt, die in Kapitel 1.3.3 Wassersorption näher erläutert werden.

1.1.2 MOFs mit anderen Metallen

Zusätzlich zu den aluminiumbasierten MOFs gibt es eine Vielzahl von weiteren Metallen, die eine wichtige Rolle in der MOF-Forschung einnehmen. Viele prototypische MOFs wurden erstmalig mit anderen hochwertigen Metall-Kationen synthetisiert und nicht mit Al^{3+}. Hierzu zählen zum Beispiel Cr^{3+},[61] Zr^{4+},[98] und Ti^{4+},[99] die im Verlauf dieser Arbeit weitergehend untersucht werden, aber auch niedrigwertige Metall-Kationen, wie Zn^{2+},[27] oder Cu^{2+}.[100]

Eines der meist untersuchten MOFs ist MIL-101(Cr), welches aus Cr^{3+}-Kationen und dem Linker Terephthalsäure besteht.[61] Die Cr^{3+}-Kationen bilden mit Sauerstoff Oktaeder, die zu einer trimeren SBU verknüpft werden, welche mit den Liganden die Poren aufspannen. Durch diese Anordnung besteht MIL-101 aus einem Netzwerk mit zwei unterschiedlich großen Poren mit einem Durchmesser von 29 und 34 Å und einer Porenfenstergröße von 12 und 16/17 Å (Abbildung 6).[62] Ein großer Vorteil von MIL-101 ist die große Variation des Liganden mit funktionellen Gruppen,[101] die eine gezielte Synthese zur Anwendung ermöglichen und miteinander kombiniert werden können, wie Lammert *et al.* in ihrer Untersuchung zeigen konnten.[102] Die Eigenschaften bzw. die möglichen Anwendungsmöglichkeiten von MIL-101(Cr) sind sehr gut untersucht und basieren auf der hohen Porosität bzw. den großen Poren des MOFs.[61] Die potenziell untersuchten Anwendungen von funktionalisiertem MIL-101(Cr) sind zum Beispiel der Einsatz als (heterogener) Katalysator,[103,104] die CO_2-Speicherung,[105] oder die Sorption von N/S-Heteroaromatischen Verbindungen.[106] Das unfunktionalisierte MIL-101(Cr) wird sehr häufig zur Wassersorption eingesetzt. Der Mechanismus der Wasseraufnahme wurde mit Hilfe molekularer Simulation untersucht.[107]

Ein weiteres interessantes und gut untersuchtes MOF ist UiO-66 und besteht aus dem Kation Zr^{4+} und Terephthalsäure. Die SBU von UiO-66 ist aus $Zr_6O_4(OH)_4$-Einheiten aufgebaut, die durch den Liganden verbrückt sind. Die Sauerstoff- bzw. Hydroxy-Gruppen liegen auf den Flächen des Oktaeders, während die Zr-Atomen die Ecken des Oktaeders bilden.[108] Das aufgespannte UiO-66-Netzwerk bildet zwei unterschiedliche Poren aus mit einem Porendurchmesser von 6 Å für die kleinere tetraedrische Pore und 11 Å für die größere oktaedrische Pore, mit dreieckigen Porenfenstern von 6 Å (Abbildung 6).[109]

UiO-66 hat aufgrund der hohen Stabilität der Zr-O-Bindung eine große Beständigkeit gegenüber Lösemitteln und im sauren pH-Bereich.[110] Eine Besonderheit bei UiO-66 ist das gezielte Einbauen von Defekten, welches, wie bereits erwähnt, zwischen Linker- und Clusterdefekten unterscheidet.[58,59,60] Das Auftreten dieser Defekte wurde erstmals von Valenzano *et al.* im Jahr 2011 untersucht.[111] Nachfolgend wurden von Shearer *et al.* Methoden zur Bestimmung der Defekte etabliert. Die Analysen bzw. die Defektbestimmungen erfolgten, wie bereits in Kapitel 1.1 Metall-organische Gerüstverbindungen erwähnt, mittels NMR und TGA.[58,59,60] Bei der TGA bildet die Annahme einer vollständige Verbrennung des Zr-MOFs UiO-66 zu Zirconiumoxid (ZrO_2) die Grundlage. Aus dieser idealisierten Verbrennung kann zwischen der realen/tatsächlichen und der idealen Menge unterschieden werden, um hieraus die Defekte zu berechnen. Hierbei ist zu beachten, dass mit dieser Methode nur fehlende Liganden in der Struktur analysiert werden können und keine fehlenden Metallknotenpunkte bzw. SBUs.[112] Die fehlenden Liganden werden häufig durch Modulatoren oder Lösemittel ersetzt.[58,59,60]

Diese Besonderheiten in der Struktur bei UiO-66 und den isoretikulär verlängerten oder den funktionalisierten UiOs , in Kombination mit der hohen Stabilität, machen diese interessant für eine Vielzahl von möglichen Anwendungen.[113] So wurde unfunktionalisiertes UiO-66 für unterschiedliche Sorptionsexperimente verwendet, wie bei der Hochdruck-Adsorption von CO_2 und CH_4,[114] der Adsorption von Wasser,[115] oder dem Entfernen von giftigen Chemikalien.[116] Die funktionalisierten UiO-66 wurden ebenfalls für eine Vielzahl unterschiedlicher Anwendungen untersucht, wie dem Einsatz als fluoreszenter pH-Sensor,[117] für die Verwendung als Material bei der Gassorption und -trennung,[118] oder ebenfalls bei der Entfernung von giftigen Chemikalien.[119]

Ein weiteres MOF ist MIL-125 und hat den gleichen Liganden wie UiO-66 Terephthalsäure und als Metallkation das kleinere Ti^{4+}.Titan ist interessant aufgrund der geringen Toxizität, der Redoxaktivität und der photokatalytischen Eigenschaften.[99] Die Struktur von MIL-125 und seinem amino-funktionalisierten Derivat NH_2-MIL-125 ist aufgebaut aus acht TiO_6-Oktaeder, die zu einem zyklischen Oktamer aufgespannt werden und durch die Liganden verknüpft sind.[120] Hierdurch entstehen Poren mit einem Durchmesser von 12.55 Å und 6.13 Å und Porenfenstern von 5-7 Å (Abbildung 6).[99] Die potenziellen Anwendungen von MIL-125 und NH_2-MIL-125 wurden sowohl im Bereich der Sorption,[121,122] als auch im katalytischen Bereich erforscht.[123,124]

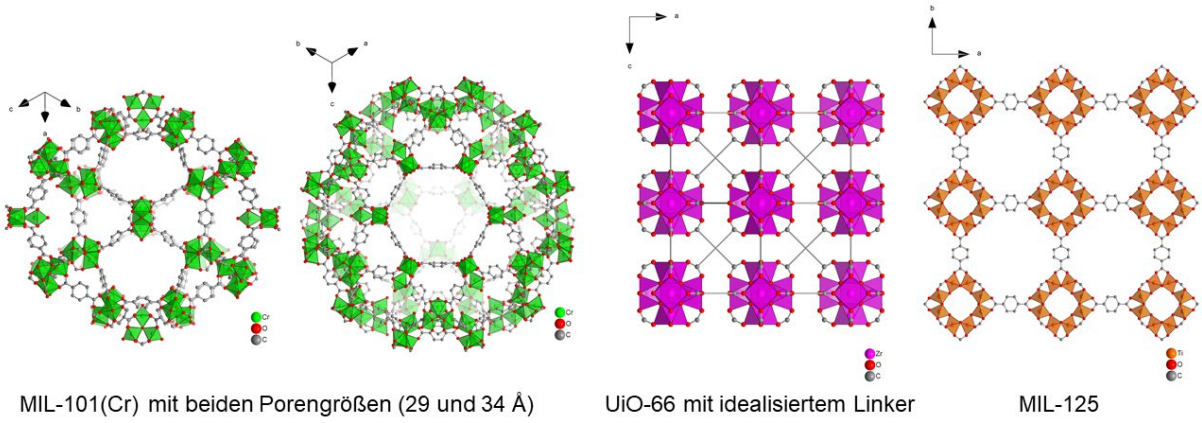

Abbildung 6: *Drei prototypische MOFs mit ihren Poren (MIL-101(Cr), UiO-66, MIL-125). Die Strukturen wurden eigenständig mit Diamond[89] erstellt (CSD-Nummer: 605510 (MIL-101),[61] 733458 (UiO-66),[108] 751157(MIL-125)[99])*

Zwei weitere wichtige MOFs sind das bereits erwähnte MOF-5 und HKUST-1 (*Hong Kong University of Science and Technology*), die aus den zweiwertigen Metall-Kationen Zn^{2+},[27] und Cu^{2+} bestehen,[100] welche mit den jeweiligen Dicarbonsäuren ein Netzwerk aufspannen. Die Kombination der weicheren Metalle mit einer Carbonsäure (hart) beeinflusst die Stabilität der Materialien erheblich gegenüber Luftfeuchtigkeit und Sauerstoff bzw. der Atmosphäre und ist somit im Einklang mit dem HSAB-Konzept.[13] Stabilere Verbindungen mit zweiwertigen Metall-Kation bilden die ZIFs, die im nächsten Kapitel 1.1.3 ZIFs näher erläutert werden.

1.1.3 ZIFs

ZIFs sind eine Unterkategorie der MOFs mit einer Zeolith-artigen Topologie und herausragender thermischer und chemischer Stabilität,[125] die durch das HSAB-Konzept ebenfalls begründet ist.[12]

Eines der am häufigsten, untersuchten ZIFs ist ZIF-8 bestehend aus dem Zn^{2+}-Kation und dem Liganden 2-Methylimidazol. Die Struktur von ZIF-8 ist aufgebaut aus tetraedrischen mit Stickstoff koordinierten Zn-Atomen, die Tetraeder sind über die Liganden verknüpft. Dieses aufgespannte Netzwerk beinhaltet eine Pore mit einem Durchmesser von 12 Å und einer Porenöffnung von 3.4 Å.[126] Die Synthese von ZIF-8 macht das MOF für mögliche industrielle Anwendungen interessant, da es bei Raumtemperatur in wässriger Lösung, mit einem Überschuss an Linker, synthetisiert werden kann.[127] ZIF-8 ist eines der wenigen MOFs, das schon im industriellen Maßstab durch die BASF synthetisiert und vertrieben worden ist, als Basolite® Z1200.[128] Die in der Literatur untersuchten Anwendungen sind vielfältig, wie zum Beispiel die Trennung von Ethanol und Wasser durch Adsorption,[129] oder die Gastrennung für eine Vielzahl von Gemischen.[130]

Zwei weitere für diese Arbeit relevanten ZIFs werden aus denselben Edukten synthetisiert, ZIF-7 und ZIF-11. [20] Beide werden aus einem Zn-Salz und Benzimidazol hergestellt. Die Reaktionsbedingungen beeinflussen die Produktbildung und ermöglichen somit eine gezielte

Synthese des gewünschten Produkts. ZIF-11 kristallisiert in der RHO-Topologie aus mit Zn^{2+}-Kationen, die von 4 Stickstoff-Atomen aus den Liganden tetraedrisch koordiniert werden. Hierbei ergeben sich Poren mit einem Durchmesser von 14.6 Å und einem Porenfenster mit 3.0 Å. ZIF-7 bildet strukturell die SOD-Topologie (Sodalith) aus, die ebenfalls aus Zn-N-verknüpften Tetraedern aufgebaut ist, jedoch mit einer anderen Verknüpfung. Hiermit ergibt sich eine Pore mit einem Durchmesser von 4.3 Å und einem Porenfenster von 2.9 Å.[131] Die beiden ZIFs mit ihrer Porenstruktur sind in Abbildung 7 dargestellt.

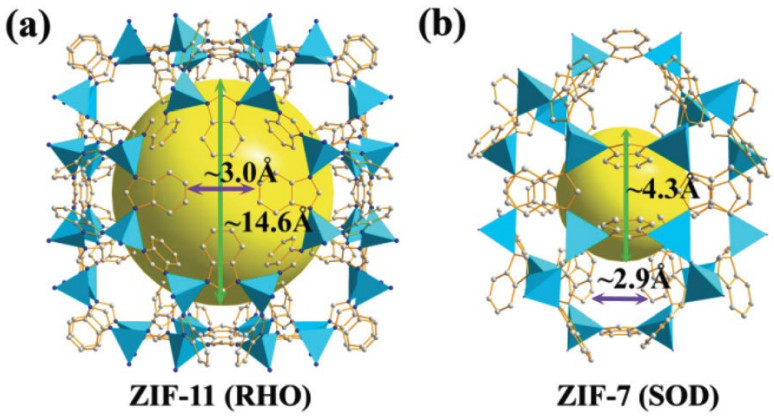

Abbildung 7: *Kristallstrukturen der ZIFs ZIF-11 (a) und ZIF-7 (b) mit den Poren als gelbe Kugeln dargestellt und den zugehörigen Porendurchmessern und Porenfenster, entnommen aus Ref. 131 mit Genehmigung © 2013, The Royal Society of Chemistry.*

Eine strukturelle Besonderheit von ZIFs ist der sogenannte *gate-opening-effect* (deutsch Türöffnungseffekt), der auch bei ZIF-7 beobachtet wird. Hierbei öffnet sich die Pore in Abhängigkeit von äußeren Einflüssen, wie der Affinität für ein Molekül oder durch Druck.[132] Im Fall von ZIF-7 findet eine Änderung statt und der Benzol-Ring im Linker dreht aus der Porenöffnung heraus und erweitert hierbei die Porenöffnung.[133]

Die hohe Stabilität und die strukturellen Besonderheiten machen ZIF-11 und ZIF-7 für eine Vielfalt von Anwendungen interessant. ZIF-11 wurde beispielsweise für die Alkohol/Wasser-Trennung untersucht,[134] oder für H_2/CO_2-Sorptionsexperimente bei unterschiedlichen Drücken.[135] Die potenziellen Anwendungen für ZIF-7 sind sehr breit gefächert, wie die Untersuchung von Gasadsorptionsphänomenen,[136,137] die Verwendung als elektrochemischer Biosensor,[138] oder die Adsorption von flüchtigen organischen Verbindungen zeigt.[139]

1.2 Kompositmaterialien mit MOFs

MOFs sind, wie bereits erwähnt, für viele Anwendungsbereiche interessant, jedoch liegen diese in Form von Einkristallen oder mikrokristallinen Pulvern vor. Dies ist für die meisten Anwendungen ein Nachteil im Hinblick auf die Handhabbarkeit der Materialien. Durch Kombination von MOFs mit weiteren Materialien kann dieses Problem behoben und zusätzlich noch positive Materialeigenschaften von allen, im Verbund beinhalteten, Stoffen genutzt werden.[140] Diese Art von Materialien werden Komposite bzw. Kompositmaterialien bezeichnet. Hier wird zwischen zwei bis drei Arten von MOF-Materialien unterschieden, was auf den Aufbau der Komposite zurückzuführen ist. Eines der beiden Materialien wird in das Andere eingearbeitet und bekommt somit eine übergeordnete Struktur vorgegeben. So kann zwischen MOF@Matrix/Stoff und Stoff@MOF differenziert werden, je nach Aufgabe des MOFs und der Beschaffenheit der anderen Bestandteile. Wobei vor allem bei MOF@Matrix/Stoff noch ein spezieller Aufbau-Typ entsteht, wenn MOFs gezielt auf einer Oberfläche aufwachsen, so entsteht ein Komposit mit einer Grenzschicht zwischen den Materialien. Zusätzlich gibt es noch MOF *core-shell*-Komposite (deutsch Kern-Schale-Komposite), wobei MOFs sowohl Kern, als auch Hülle sein können.[141] Die detaillierte Unterscheidung zwischen den einzelnen Kompositmaterialien und ihre potenzielle Anwendung wird in den beiden Unterkapiteln 1.2.1 MOF@Matrix/Stoff und 1.2.2 Stoff@MOF tiefergehend erläutert. Zusätzlich wird auf die vielfältigen Syntheserouten eingegangen mit denen die einzelnen Kompositmaterialien hergestellt werden können.[142]

1.2.1 MOF@Matrix/Stoff

Eine Gruppe der MOF@Matrix/Stoff-Komposite bestehen aus MOFs und Polymeren und ist, im Hinblick auf verschiedenste Aspekte und Anwendungen, sehr gut in der Literatur untersucht. Bei diesen Kompositen muss zwischen vielen Aspekten unterschieden werden, wie der Art der Polymere,[143] der Syntheseroute,[142] der Struktur bzw. der Form des Komposits,[143] und abschließend die erhofften Synergie-Effekte[142] für die vielfältigen Anwendungen.[144]

Vor allem die verwendeten Polymere haben einen Einfluss auf die Synthese der Kompositmaterialien, da diese durch unterschiedliche Methoden erst verarbeitet werden können. Im Folgenden wird exemplarisch anhand verschiedener Polymere ein Bereich der möglichen Syntheserouten dargestellt.

Das erste betrachtete Polymer ist Polyvinylalkohol (kurz PVA), hierbei handelt es sich um ein kommerziell hergestelltes, hydrophiles Polymer, welches häufig zur Kompositsynthese eingesetzt wird. In einer möglichen Syntheseroute haben Hastürk *et al.* das PVA in Wasser homogen verteilt und bei 80 °C gelöst und anschließend den Polymermonolith mit dem Anti-Solvent Aceton ausgefällt. Hierbei ergibt sich durch Wahl des Reaktionsgefäßes die Struktur des Monoliths. Durch dispergieren des MOFs in der Polymer-Wasser-Lösung, mit

anschließendem Ausfällen, werden die Kompositmaterialien hergestellt.[145] Bei einer weiteren Synthesemöglichkeit werden mittels Tropfen der MOF-Polymer-Dispersion in flüssigen Stickstoff PVA-Komposite erhalten, wie es Khabzina *et al.* für UiO-Komposite durchgeführt haben. Die in flüssigen Stickstoff getropften Kügelchen, werden durch Sublimation des Lösemittels getrocknet und in Form gehalten.[146] Diese Methode wird auch als *freeze-casting* (Formgebung durch Einfrieren) bezeichnet und häufig in Kombination mit anschließendem *freeze-drying* (Gefriertrocknung) verwendet. So konnten Hastürk *et al.* viele unterschiedliche MOF-Polymer-Komposite erhalten, mit MIL-101(Cr) als verwendetem MOF und verschiedenen synthetischen Polymeren.[147]

Eine weitere große Gruppe sind die natürlich vorkommenden Polymere, wie beispielsweise Chitin,[148] bzw. Chitosan,[149] Alginat,[150] oder auch Agar.[151] Chitosan und Alginat sind zwei natürliche Polymere, die durch eine weitere Chemikalie quervernetzt werden können und so stabile Materialien ausbilden. Da Chitosan im weiteren Verlauf der Arbeit verwendet wurde, wird auf diesen Prozess des Quervernetzens näher eingegangen.

Das Quervernetzen eines Polymers erfolgt durch einen sogenannten *crosslinker* (deutsch Quervernetzer). Im Falle von Chitosan ist es beispielsweise Pentanatriumtriphosphat ($Na_5P_3O_{10}$),[152] Glutaraldehyd,[153] oder Ethylenglykoldiglycidylether.[154] Alginat wird meist mit einer Calciumnitrat-Lösung quervernetzt.[155]

Die Synthese dieser quervernetzten natürlichen Polymere ist abhängig von der vernetzenden Chemikalie. So erfolgt das Vernetzen mit Glutaraldehyd und Ethylenglykoldiglycidylether über einen längeren Zeitraum durch Homogenisieren der Probe, mittels Rühren, und beispielweise anschließender Gefriertrocknung.[156] Die Quervernetzung mit Pentanatriumtriphosphat für Chitosan und mit Calcium-Nitrat für Alginat erfolgt deutlich schneller und ermöglicht so eine andere Syntheseroute. Hierbei werden Polymer- bzw. MOF-Polymer-Kügelchen erstellt, indem das Polymer gelöst wird und MOF homogen dispergiert wird. Anschließend werden die Dispersionen in die Quervernetzer-Lösungen getropft und es entstehen sofort stabile Kugeln, die von außen nach innen weiter quervernetzt werden, wie es Liang *et al.* für MIL-125@Chitosan-Komposite gemacht haben,[157] oder Dasgupta *et al.* für CPO-27-Ni@Alginat-Komposite mit Ba^{2+} (*Coordination Polymer of Oslo*) als Quervernetzer.[158]

Die aus diesen unterschiedlichen Synthesemethoden erstellten Kompositmaterialien haben deutlich verschiedene Strukturen, wie Kügelchen,[157] Monolithe,[159] oder Membranen,[160] wobei die letzten beiden Strukturen die Form durch die ausgewählten Reaktionsgefäße vorgegeben bekommen. Durch die Wahl der Synthese kann somit theoretisch die optimale Form für eine potenzielle Anwendung ausgewählt werden.

Die Anwendungen von MOF@Matrix/Stoff-Kompositen sind sehr vielfältig und hängen stark von der MOF-Matrix-Kombination ab, da beide entscheidend zu den geforderten Anwendungseigenschaften beitragen können, mit Ausnahme von Kompositen bei denen zum

Beispiel das Polymer nur die Struktur bzw. die Form vorgeben soll.
So wurden die bereits erwähnten UiO@PVA-Komposite für die Aufreinigung von Luft verwendet, indem mit diesen Materialien eine Aufreinigung gegenüber Ammoniak erfolgt.[146] Eine weitere Einsatzmöglichkeit von MOF@PVA-Kompositen ist die Verwendung als Extraktionsmittel für nicht-steroidale entzündungshemmende Medikamente aus Wasser.[161] Ein für diese Arbeit ebenso wichtiges Polymer ist das bereits erwähnte Chitosan und dessen Anwendungsmöglichkeiten, die unter anderem auf der besonderen antimikrobiellen und antifugalen Eigenschaft beruhen können.[162,163] Nun kann versucht werden diese Eigenschaft auch auf Kompositmaterialien mit Chitosan zu übertragen, oder generell dieses natürliche nicht toxische Polymer als Matrix einzusetzen. Dies ist vor allem für den Wirkstofftransport, in Kombination mit MOFs, interessant, um die Verträglichkeit mit dem Organismus zu gewährleisten.[164] Ebenso häufig werden die MOF@Chitosan-Kompositmaterialien in der Wasseraufreinigung eingesetzt, da die Materialien über eine hohe Stabilität gegenüber Wasser verfügen.[165,166]
Bei den Kompositmaterialien für den Wirkstofftransport gibt es eine weitere Unterscheidung zu den bereits angesprochenen Kompositen. So werden die Wirkstoffe häufig in die MOFs eingelagert, sodass die MOFs die Hülle des Komposits darstellen. Dieser Teil der Materialien wird im nächsten Kapitel 1.2.2 Stoff@MOF detaillierter erläutert.

1.2.2 Stoff@MOF

Stoff@MOF-Kompositmaterialien werden für unterschiedliche Anwendungen verwendet und hängen von den eingelagerten Materialien und dem verwendeten MOF, also der Matrix, ab. Die einzulagernden Stoffe und vor allem deren Größe haben entscheidenden Einfluss auf die Synthese der Komposite. Hierbei kann zwischen zwei Synthesemethoden unterschieden werden, wobei nur die erste Methode als Synthese im engeren Sinne zu bezeichnen ist. Gemeint ist die *in situ*-Synthese, bei dieser Synthesevariante werden sowohl die einzulagernden Stoffe oder deren Edukte und die Ausgangstoffe der MOFs vorgelegt und die Stoffe während der Synthese eingelagert.[140] Die andere Möglichkeit ist die postsynthetische Einlagerung der Stoffe in MOFs. Der limitierende Faktor bei dieser Art der Einlagerung ist die Größe des Porenfensters in Relation zum einzulagernden Stoff, da Moleküle nicht eingelagert werden können, wenn diese größer sind als die Öffnung der Pore, auch wenn der Porendurchmesser groß genug wäre.[142]
Die Anwendungsmöglichkeiten für Stoff@MOF-Komposite sind ebenfalls breit gefächert. Dies ist bedingt durch die große Bandbreite an potenziellen einzulagernden Stoffen, wie beispielsweise den erwähnten Wirkstoffen.[167] Ebenso wichtig zu nennen, ist die Einlagerung von Nanopartikeln in MOFs, wie beispielsweise bei Li *et al.* für die Herstellung von Au@ZIF-8-Kompositen für katalytische Zwecke.[168] Zusätzlich werden häufig auch unterschiedliche kohlenstoffbasierte Materialien eingelagert, um die Adsorptionskapazitäten

zu erhöhen, wie gegenüber Aceton,[169] Kohlenstoffdioxid oder Methan.[170]
Die Grundlage der MOF-Komposite und der MOFs ist zu großen Anteilen in ihrer außergewöhnlichen Porosität begründet. Die Ermittlung und Klassifizierung werden im nächsten Kapitel 1.3 Gas-/Dampfsorption tiefergehend erläutert.

1.3 Gas-/Dampfsorption

Die Porosität der MOFs ist eine der wichtigsten Eigenschaften der Verbindungen und wird durch die Aufnahme von Gasen bestimmt. Dies ist das vergleichende Kriterium für die erfolgreiche Synthese von MOFs in Kombination mit einem PXRD.
Dieses vergleichende Kriterium zeigt sich in der Oberfläche der Materialien und wird im nächsten Kapitel 1.3.1 Oberflächenbestimmung detailliert vorgestellt.

1.3.1 Oberflächenbestimmung

Die Grundlage für die Oberflächenbestimmung von porösen Materialien, nicht nur von MOFs, sind die BET-Theorie (Brunauer, Emmett, Teller) aus dem Jahr 1938,[171] und die Langmuir-Theorie aus dem Jahr 1932.[172] Die beiden Theorien unterscheiden sich in den vorausgesetzten Grundlagen und liefern unterschiedliche Oberflächen-Werte für dasselbe Material.
Für die Einordnung dieser Methoden in den Bereich der Sorptionen müssen zuerst gewisse Begrifflichkeiten eingeführt und unterschieden werden. So beruhen beide Theorien auf der Physiosorption von einem Stoff (meist ein Gas) auf einer Oberfläche. Jedoch ist die Physiosorption gegenüber der Chemisorption abzugrenzen. [173] Bei der Chemisorption werden Bindungen zwischen dem Stoff und der Oberfläche ausgebildet, was häufig auch irreversibel ist.[174] Die Physiosorption basiert auf schwächeren Wechselwirkungen zwischen dem anzulagernden Stoff (dem Adsorptiv) und der Oberfläche (dem Adsorbens). Die angelagerten bzw. adsorbierten Teilchen werden als Adsorbat bezeichnet.[173]
Die BET-Theorie basiert auf dem Aufbau von Multilagen des Adsorptivs am Adsorbens und ist eine Generalisierung der Langmuir-Theorie, die auf der Monolagen Adsorption beruht, also dem Unterschied in wie vielen Schichten die Adsorptive angelagert und zu Adsorbaten werden.[171] Weitere Voraussetzungen für die BET-Theorie und die genaue Bestimmung von Oberflächen beziehen sich auf das verwendete Gas und auf die Beschaffenheit der zu vermessenden Probe. Die Adsorptive, die meist verwendet werden, sind Stickstoff und Argon, wobei im Optimalfall jeweils am Siedepunkt der Gase gemessen wird (77 K für Stickstoff und 87 K für Argon), da die Wechselwirkungen zum Ausbilden einer Monolage des Gases am Adsorbens und dem weiteren Ausbilden der Multilagen am stärksten sind. Die Unterschiede zwischen den beiden Gasen hängen mit ihren chemischen Eigenschaften zusammen. So ist Argon kein diatomares Molekül, sondern ein Atom und besitzt kein Quadrupol-Moment, was bedeutende Vorteile sind. Jedoch wird meist Stickstoff in der Literatur verwendet, da die

Messungen mit einem Aufbau mit flüssigem Stickstoff in einem Dewar-Gefäß, um die Messtemperatur zu gewährleisten, einfacher durchführbar sind. Dies ist bei Argon und 87 K nur mittels einem Kühlgeräts möglich, welches im kryogenen Bereich arbeitet.[175] Generell wird bei der Physiosorption zwischen drei unterschiedlichen Porengrößen unterschieden, den Mikro- (<2 nm), den Meso- (2-50 nm) und den Makroporen (>50 nm).[173] Bei MOFs mit Mikro- bzw. Mesoporen ist bei der Bestimmung der Oberfläche mittels BET-Theorie eine Besonderheit zu beachten. Die Ausbildung einer Multilagen-Adsorption kann unter Umständen nicht stattfinden, da kleine Poren in diesem Bereich bereits vollständig gefüllt sind. Dies kann die Oberflächenbestimmung verfälschen und der Auswertebereich muss angepasst werden.[176] Die Aufnahme bzw. die aufgenommene Menge des Adsorptivs am Adsorbens führt aufgetragen gegen den Druck oder den relativen Druck zu einer Sorptionsisotherme. Diese Sorptionsisotherme liefert Rückschlüsse auf die Porenstruktur bzw. -größe des zu analysierenden Materials, wobei die IUPAC zwischen sechs Isothermentypen unterscheidet.[175] Diese sechs Isothermentypen wurden in weiteren Arbeiten, um weitere Isothermenarten ergänzt, die detaillierter auf flexible Strukturen eingehen.[177] Die ursprünglichen sechs Sorptionsisothermen sind in der folgenden Abbildung 8 dargestellt.

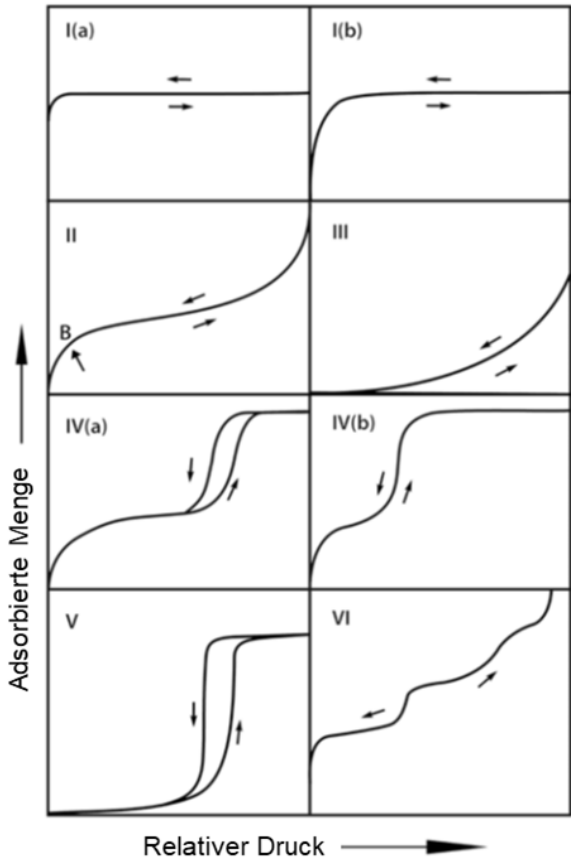

Abbildung 8: *Einordnung und Unterscheidung der sechs Sorptionsisothermen laut IUPAC, entnommen und übersetzt aus Ref. 175 mit Genehmigung © 2015 De Gruyter, IUPAC.*

Die unterschiedlichen Isothermentypen werden durch die Porengrößen des Materials vorgegeben und lassen sich wie folgt klassifizieren. Die Typ I-Isothermen in der ersten Zeile der vorherigen Abbildung 8 entstehen bei vornehmlich mikroporösen Adsorbenzien, wobei zwischen den reversiblen Typen I(a) und I(b) unterschieden wird. Der Isothermentyp I(a) beschreibt ein rein mikroporöses Material mit einer geringen externen Oberfläche (zwischen den Partikeln) und ist durch den starken Anstieg im niedrigen relativen Druckbereich definiert. Dieser ist bei der Typ I(b)-Isotherme weniger stark ausgeprägt und hängt mit der breiteren Porengrößen-Verteilung zusammen, die breitere Mikroporen und schmalen Mesoporen (<2.5 nm) beinhalten kann. Der reversible Isothermentyp II umfasst die Physiosorption von nicht-porösen oder makroporösen Materialien und beinhaltet den als B markierten Punkt, der den starken Anstieg der aufgenommenen Menge beendet und die Linearisierung der Isotherme einleitet. Dieser Punkt fehlt bei Typ III-Isothermen, die eine konstante, nicht endende Aufnahme zeigen, bis zu einem relativen Druck von 1. Typ IV-Isothermen können in Typ (a) und (b) unterschieden werden und beschreiben mesoporöse Adsorbenzien. Hierbei ist es Kombination von Mono- und Multilagen-Adsorption und anschließender Kondensation des Adsorptivs in der Pore. Typ IV(a) zeigt jedoch bei der Desorption, also der Abgabe des Gases, eine Hysterese und Typ IV(b) nicht. Eine Hysterese ist eine verzögerte bzw. erschwerte Abgabe des Adsorptiv. Bei schwachen Adsorbenz-Adsorbat-Wechselwirkung kann eine Typ V-Isotherme ausgebildet werden, die bei hohen relativen Drücken eine vollständige Porenfüllung zeigt und eine Hysterese. Der letzte Isothermentyp ist Typ VI, eine reversible, stufenförmige Isotherme. Diese beschreibt die Aufnahme eines Adsorptivs an einer gleichmäßigen nicht-porösen Oberfläche.[175]

Die flexiblen Isothermentypen lassen sich in fünf verschiedene Formen unterteilen und basieren auf der flexiblen, porenöffnenden Struktur eines Materials. Hierbei werden die Art und Weise der Porenöffnung mit Hilfe verschiedener Isothermen klassifiziert. So kann zwischen der Öffnung von einer kleinen zu einer großen Pore (Typ I oder II) oder zwischen der Öffnung eines nicht-porösen zu einem porösen Material (Typ III oder IV) differenziert werden und zusätzlich bei welchem relativen Druck diese Öffnung stattfindet. Ein besonderer Fall der flexiblen Isothermentypen beschreibt die Änderung bzw. Anpassung der Sorptionsisotherme beim Durchlaufen mehrerer Zyklen, was als *shape memory effect* (deutsch Form-Gedächtnis-Effekt) bezeichnet (Typ V) wird.[177]

Wie bereits erwähnt werden die Bestimmungen der Oberflächen der Materialien mit Stickstoff oder Argon durchgeführt. Dennoch gibt es eine große Anzahl von weiteren Gasen, die untersucht werden. Dieser Aspekt wird im nächsten Kapitel 1.3.2 Gassorption näher beleuchtet und steht nicht im Zusammenhang mit der Bestimmung der Porosität.

1.3.2 Gassorption

Zusätzlich zu den bereits erwähnten Gasen Stickstoff und Argon gibt es eine Vielzahl von weiteren Gasen, die mit MOFs adsorbiert worden sind, um MOFs für verschiedene Anwendungsmöglichkeiten zu testen.[178] Hierbei ist in erster Linie zu unterscheiden bei welchen Drücken die Gassorptionen stattfinden, also beim Sättigungsdruck, beim Umgebungsdruck oder unter Hochdruck.

Bei Sorptionen unter Normaldruck oder Sättigungsdruck sind eine Vielzahl von Gasen bereits untersucht worden, wie beispielsweise Kohlenstoffdioxid (CO_2),[179,180,181] Kohlenstoffmonoxid (CO),[182] Methan (CH_4),[183] Schwefeldioxid (SO_2),[184,185,186,187] Schwefelwasserstoff (H_2S),[188] Ammoniak (NH_3),[189] oder diverse Stickoxide (NO_x).[190] Andere Gase, wie zum Beispiel Wasserstoff (H_2) werden meist unter Hochdruck untersucht, da die potenziellen Anwendungsbedingungen und die Handhabbarkeit dies erfordern. Im Fall von Wasserstoff ist es meist die Speicherung in porösen Materialien.[3] Dennoch wurden auch weitere Gase unter Hochdruckbedingungen untersucht, wie Kohlenstoffdioxid, Propen oder Methan.[191]

Die Sorptionsbedingungen hängen von den Gasen und den potenziellen Anwendungen ab, für die MOFs und deren Sorptionseigenschaften eingesetzt werden sollen. Diese sind sehr breit gefächert, wie z. B. die bereits erwähnte Gasspeicherung, Gastrennung oder der Einsatz als Filtermaterialien, wobei dies als Erweiterung der allgemeinen Gastrennung zu sehen ist. Li *et al.* untersuchten die mögliche Anwendung von MOFs im Bereich der Reduktion von Kohlenstoffdioxid, um dem Klimawandel entgegenzuwirken und erforschten die Gasspeicherung im niedrigen Druckbereich, um die geringen, aber schädlichen, Konzentration zu simulieren, in Abhängigkeit von anderen Bestandteilen der Luft.[180]

Ein neueres, in der Literatur untersuchtes, Feld ist die potenzielle Anwendung von MOFs in der Rauchgasentschwefelung, also der Einsatz von MOFs für die SO_2/CO_2-Trennung, wie von Brandt *et al.* Untersucht.[184,185,186] Alternativ wurde ebenfalls die Detektion bzw. Speicherung von Schwefeldioxid von López-Olvera *et al.* Betrachtet mit Untersuchung des Einflusses eines starren und eines flexiblen Gerüsts.[187] Weitere mögliche Anwendungsgebiete für MOFs sind die bereits angesprochenen Verwendungen als Filtermaterialien, nicht nur gegenüber Schwefeldioxid in der Rauchgasentschwefelung, sondern auch gegenüber Nervengasen oder anderen chemischen Kampfstoffen. Hierzu haben beispielsweise Montoro *et al.* den potenziellen Einsatz von MOF-5 gegenüber Nervengas, wie Senfgas und dessen Analoga theoretisch analysiert,[192] oder Plonka *et al.* den möglichen Einsatz von zirconiumbasierten MOFs gegenüber chemischen Kampfstoffen durch katalytische Zersetzung des jeweiligen Stoffes.[193]

Im nächsten Kapitel 1.3.3 Wassersorption soll der Fokus von der reinen Gassorption auf die Dampfsorption gelenkt werden, beziehungsweise soll ein Sonderfall der Dampfsorption näher beleuchtet werden, der eine Vielzahl von Anwendungsmöglichkeiten beinhaltet.

1.3.3 Wassersorption

Die Wassersorptionen von MOFs sind ein sehr breit gefächertes und gut untersuchtes Feld in der Literatur. Wie bereits erwähnt, eignen sie sich aufgrund ihrer hohen Porosität und Stabilität und den gezielten, maßgeschneiderten Synthese gut für dieses Einsatzgebiet.

Zwei wichtige Anwendungsgebiete der Wassersorption sind die adsorptionsgetriebene Wärmetransformation,[194,195] und die Wasserspeicherung aus der Umgebungsluft.[196]

Adsorptionsgetriebene Kältemaschinen bzw. Wärmepumpen basieren auf einem thermodynamischen Prozess, der in der folgenden Abbildung 9 visualisiert ist.[197]

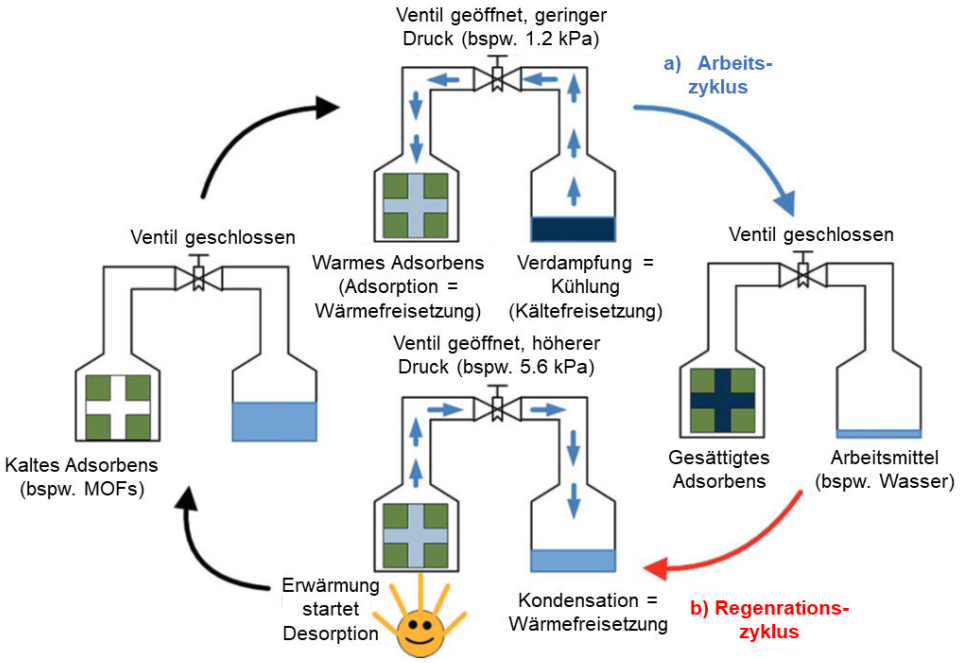

Abbildung 9: *Darstellung des Grundprinzips von adsorptionsgetriebenen Kältemaschinen und Wärmepumpen, entnommen und übersetzt aus Ref. 197 mit Genehmigung © 2012, Wiley-VCH.*

Das Arbeitsprinzip der mit Feststoff befüllten Wärmetransformationssysteme, aus thermodynamischer Sicht, kann als Kombination eines Wärmemotors und einer Wärmepumpe beschrieben werden, wobei die freigesetzte Energie des Wärmemotors die Wärmepumpe antreibt.[197]

Der Arbeitszyklus (a) beschreibt die Aufnahme eines Arbeitsmittels, beispielsweise Wasser (oder auch Alkohole), durch das MOF. Daraus resultiert Adsorptionswärme, wobei das Adsorptiv der Umgebung Wärme entzieht. Der zweite Teil des Zyklus (b) ist der Regenerationszyklus. Hierbei wird das MOF wieder getrocknet, die Erwärmung startet also die Desorption. Das Adsorptiv wird dabei verdampft und kondensiert wieder aus, wobei Kondensationswärme frei wird.[120]

In der Literatur sind mehrere Beispiele für diese zyklisch betriebenen Systeme bekannt, wie der mit Aluminiumfumarat bzw. Basolite® A520 beschichtete Wärmetauscher von Kummer *et al.* aus dem Jahr 2017.[198] Häufig werden bei dieser Art der Anwendung auch

Kompositmaterialien eingesetzt, wie die MOF@PVA-Komposite von Gökpinar *et al.* aus dem Jahr 2019, um dem MOF eine handhabbare Form zu geben.[199]

Die Auswahl des Adsorbens und die Formgebung bei dieser Art der Anwendung sind sehr vielfältig.[200] So können die bereits genannten Kompositmaterialien eingesetzt werden oder auch eine spezielle Form des Komposits die sogenannten *coatings* (deutsch Beschichtungen) mit einem Bindemittel.[201] Des Weiteren wird in der Literatur versucht die Kapazitäten von bestehenden Materialien zu erhöhen, wie es beispielweise Sun *et al.* bei UiO-66 erfolgreich durch den Einsatz von Lithiumchlorid (LiCl) in ihren LiCl@UiO-66-Kompositen gezeigt haben. Anschließend wurde auch die Zyklenstabilität der Materialien nachgewiesen, ohne eine Abnahme in der Wasser-Aufnahmekapazität über 10 Zyklen.[202]

Das zweite oben genannte Einsatzgebiet für MOFs im Bereich der Wassersorption behandelt das Speichern von Wasser aus der Umgebungsluft (engl. *water harvesting*) und wurde erstmal von Furukawa und Yaghi *et al.* im Jahr 2014 für MOFs beschrieben.[21] Der Einsatz von MOFs erscheint für diese Anwendung in dürren und wasserarmen Gebieten von Vorteil, da diese gezielt für eine hohe Maximalbeladung, in einem definierten Druck- und Temperaturbereich, synthetisiert werden können.[203,204]

So haben Kim *et al.* gezeigt, dass Zirconiumfumarat (MOF-801) in der Lage ist, Wasser aus der Luft zu speichern, auch bei einer sehr geringen relativen Luftfeuchtigkeit von nur 20 %. Die Regeneration des Materials erfolgte mit natürlichem Sonnenlicht, wodurch 2.8 Liter Wasser mit einem Kilogramm MOF gewonnen werden konnten.[196] In einer weiteren Arbeit wurden acht hydrothermal stabile MOFs in einer Umgebungsfeuchte untersucht, die gute Sorptionskapazitäten bei mittlerer und hoher Luftfeuchtigkeit zeigen, wegen ihren hohen Oberflächen.[205]

Eine Anwendungsmöglichkeit, die ähnliche Voraussetzungen aber ein anderes Ziel hat, wie die Wasserspeicherung, ist die autonome Kontrolle der Luftfeuchtigkeit im Inneren von Gebäuden. So konnten Tsobnang *et al.* zwei neue MOFs mit Kupfer und Chrom oder Eisen synthetisieren, die die Luftfeuchtigkeit im Versuchsaufbau zwischen 15 und 25 % regulieren bzw. halten und gleichzeitig im niedrigen Druckbereich Stickstoff und Kohlenstoffdioxid ausschließen konnten.[206]

Die Wassersorption ist ein wichtiger Teil der Dampfsorption, vor allem in den bereits erwähnten Anwendungen, jedoch gibt es eine weitere Reihe von Dämpfen (und Gasen) die von MOFs aufgenommen werden können. Hierunter fallen die im nächsten Kapitel 1.3.4 VOC-Sorption erwähnten Verbindungen, wobei teilweise in Kapitel 1.3.2 Gassorption schon auf ausgewählte Verbindungen hingewiesen wurde.

1.3.4 VOC-Sorption

Ein großer Teil in der Literatur der Gas- bzw. Dampfsoprtionen beschäftigt sich mit den *volatile organic compounds* (deutsch flüchtige organische Verbindungen, kurz VOCs). Diese

umfassen, je nach Definition, unterschiedliche Substanzen bzw. werden differenziert aufgegliedert. Die folgenden Unterkapitel umfassen die unterschiedlichen, in der Literatur verbreiteten, Definitionen und die Herkunft der meisten VOCs sowohl natürlicher als auch anthropogener Herkunft und den Einsatz von MOFs gegenüber VOCs.

1.3.4.1 Definition und Einteilung der VOCs

Die Definitionen für VOCs sind sehr vielfältig und werden von den Behörden unterschiedlich ausgelegt. Die EPA (*Enviromental Protection Agency*, deutsch Umweltschutzbehörde) definiert VOCs als „jede Verbindung aus Kohlenstoff, ausgeschlossen Kohlenstoffmonoxid, Kohlenstoffdioxid, Kohlensäure, Metallcarbide, oder Carbonate und Ammoniumcarbonate, die an photochemischen Reaktionen in der Atmosphäre beteiligt sind“.[207,208] Die EEA (*European Environment Agency*, deutsch Europäische Umweltagentur) hingegen definiert VOCs, gemäß der Richtlinie 2004/42/EG, als „organische Verbindung mit einem Anfangssiedepunkt von höchstens 250 °C bei einem Standarddruck von 101.3 kPa“.[209]

Die WHO (*World Health Organization*, deutsch Weltgesundheitsorganisation) beschreibt und teilt VOCs in unterschiedliche Kategorien ein, die nach Siedepunkten bzw. Siedebereichen aufgegliedert sind.[210] Diese Definition gilt vorrangig für die Bestandteile in der Luft in Innenräumen und ist in Tabelle 1 dargestellt.

Tabelle 1: *Einteilung und Beschreibung von VOCs anhand der Siedebereiche, gemäß der WHO.*[210]

Abkürzung/Einteilung	Beschreibung/Übersetzung	Siedebereich
VVOC (very volatile organic compounds)	Sehr flüchtige organische Verbindungen	<0 bis 50 … 100 °C
VOC (volatile organic compounds)	Flüchtige organische Verbindungen	50 … 100 °C bis 240 … 260 °C
SVOC (semi volatile organic compounds)	Schwerflüchtige organische Verbindungen	240 … 260 bis 380 … 400 °C

Unabhängig von den verschiedenen Definitionen liegt das Problem von VOCs in der Flüchtigkeit und dem negativen Einfluss auf die menschliche Gesundheit und die Umwelt, da diese als giftig, krebserregend und erbgutveränderd gelten und dies bereits bei sehr geringen Konzentrationen.[211] Die Herkunft der VOCs ist ebenso vielfältig, wie die unterschiedlichen Stoffklassen, die als VOCs kategorisiert werden können.[178] Zusätzlich zu den VOCs können auch noch weitere Substanzen zu den schädlichen Stoffen hinzugezählt werden, wie die bereits erwähnten NO_x, SO_x, CO_x oder H_2S oder auch stickstoff-, oder schwefelhaltige

Verbindungen, Farbstoffe, Pharmazeutika und Pflegeprodukte des täglichen Bedarfs, da Teile davon einen negativen Einfluss auf Mensch und Umwelt haben.[212]

Die Ursachen von VOCs und anderen giftigen Stoffen sind sehr vielfältig und sowohl natürlicher Herkunft, also auch von Menschen verantwortet. Dies ist der bedeutend größere Anteil, der aufgereinigt oder gar verhindert werden muss.[208,211] Die Verteilung und die Menge der VOCs sind stark abhängig von der Region und deren landwirtschaftlichen oder industriellen Gegebenheiten.[208,211,213]

Die Verteilung der VOCs ohne Methan für Deutschland, auch als NMVOCs (*non-methane volatile organic compounds*, deutsch nicht-methanhaltige flüchtige organische Verbindungen) bezeichnet, sind in der folgenden Abbildung 10 dargestellt. Der ausgewertete Zeitraum beginnt im Jahr 1990 und endet im Jahr 2020. Die Graphik schlüsselt die entstandenen VOCs nach Quellkategorien auf.[214]

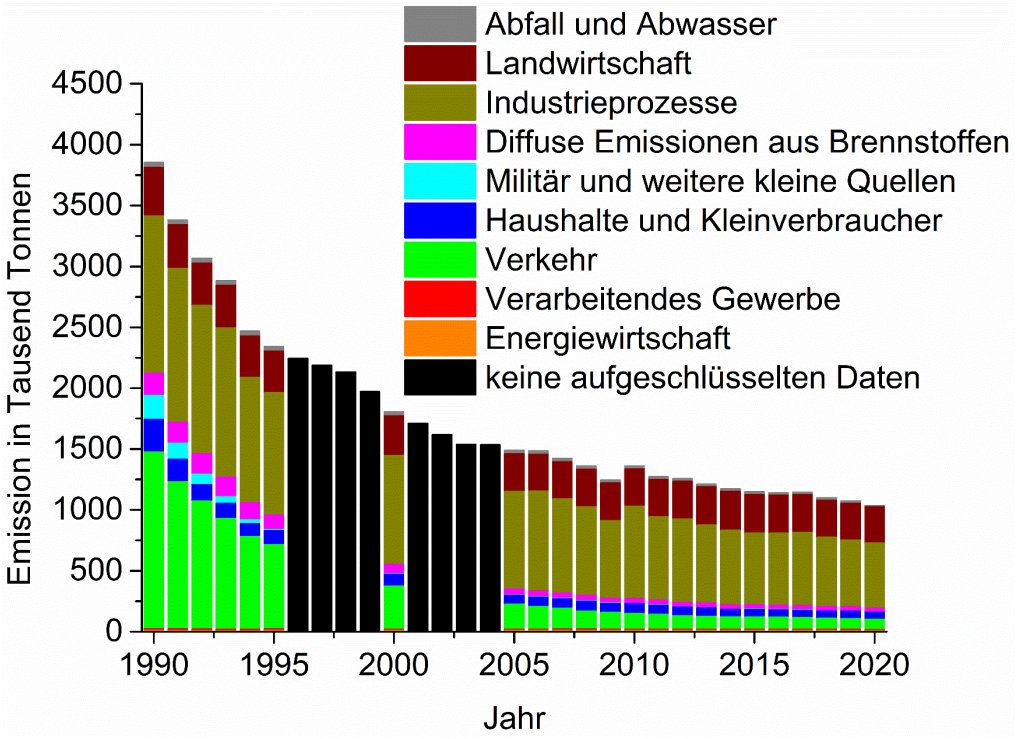

Abbildung 10: *Emissionen flüchtiger organischer Verbindungen ohne Methan (NMVOC) aufgeteilt nach Quellkategorien.[214] Für die Jahre 1996-1999 und 2001-2004 waren keine aufgeschlüsselten Daten aufruf- bzw. abrufbar.*

Die Studie zeigt einen deutlichen Rückgang der NMVOC Emissionen von 3892 Tausend Tonnen im Jahr 1990 zu 1036 Tausend Tonnen im Jahr 2020.[214]

1.3.4.2 Arten der VOC-Sorption

Dieser stetige Rückgang von NMVOCs bzw. VOCs im Allgemeinen ist auf einen sensibleren Umgang mit der Umwelt zurückzuführen, im Hinblick auf immer strengere Auflagen für die Entstehung bei Produktionsprozessen und deutlich verbesserte Methoden zur Reduktion der VOCs beim Ausstoß in die Umwelt. Dieses Kapitel behandelt den Einsatz von MOFs in

unterschiedlichen Applikationen für die Reduktion von VOCs mittels verschiedener Methoden. Zusätzlich soll ein kurzer Vergleich mit anderen Materialien gezogen werden.[211]

Der Einsatz von MOFs gegen VOCs erfolgt häufig durch die Sorption von VOCs und bildet den Schwerpunkt des Kapitels,[215] jedoch können MOFs auch zur katalytischen Zersetzung und Umwandlung von VOCs eingesetzt werden.[216]

Alternative Materialien die industriell hergestellt werden und in Konkurrenz zu MOFs stehen, sind beispielsweise Zeolithe, Silica oder Aktivkohle.[217] So haben Hunter-Sellars *et al.* die VOC-Adsorption verschiedener industrieller Materialien getestet, in Abhängigkeit von der relativen Luftfeuchtigkeit. Hierfür wurde sowohl die Wassersorption der Materialien, als auch die Sorption verschiedener VOCs getestet und in Relation zueinander gesetzt.[218]

Der bereits mehrfach erwähnte Vorteil von MOFs gegenüber den industriell hergestellten und verwendeten Materialien ist die gezielte Synthese mit funktionellen Gruppen oder angepassten Porenmerkmalen/-größen, die die Adsorption für bestimmte VOCs selektiv machen können oder sollen.[219] Dieser Vorteil wird auch in den adsorptionsbasierten Anwendungsmöglichkeiten deutlich (Abbildung 11), die häufig eine Trennung von zwei oder mehr VOCs zur Grundlage haben,[220,221] oder das Filtern von Luft in Innenräumen oder Abgasströmen.[215] Zusätzlich wird der Einsatz von MOFs in der Sensorik untersucht.[222]

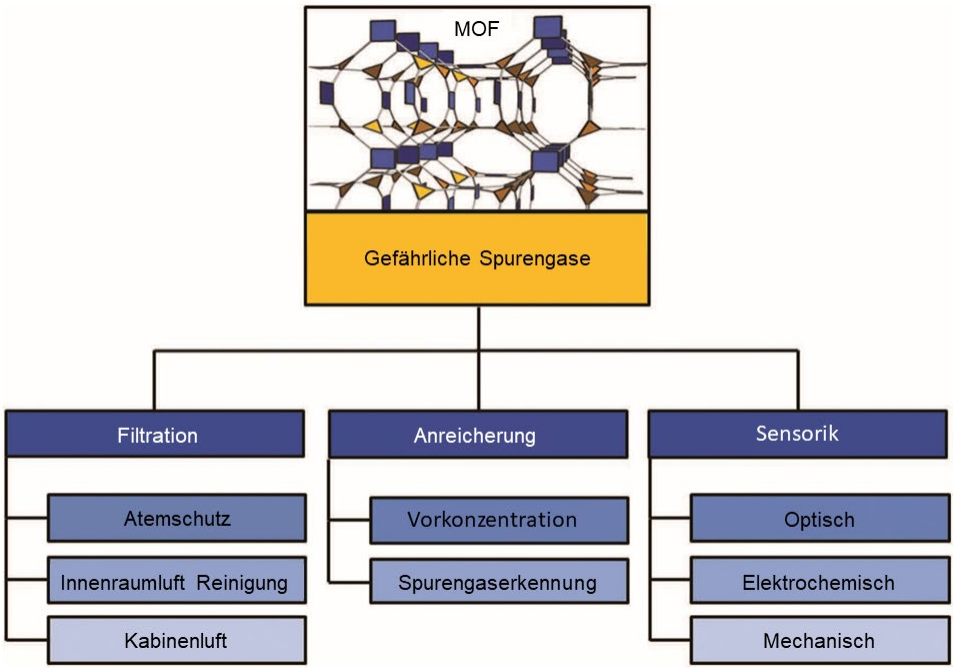

Abbildung 11: *Schematische Übersicht potenzieller Anwendungsmöglichkeiten von MOFs im Bereich der Filtration, der Anreicherung und der Sensorik, entnommen und übersetzt aus Ref. 222 mit Genehmigung © 2018, Wiley-VCH.*

Die Trennung der VOCs kann hierbei mit MOFs sowohl in der Gas- bzw. Dampfphase, als auch in der flüssigen Phase untersucht werden und ist abhängig von der potenziellen Anwendung und den damit verbundenen Gegebenheiten.[223,224]

Bei den VOCs gibt es eine Vielzahl von Gemischen, die für eine industrielle Trennung relevant

sind und dabei der Einsatz von MOFs als Trennmittel untersucht wurde. Häufig untersuchte Gemische sind die BTEX (Benzol, Toluol, Ethylbenzol und Xylole),[225] die Xylole,[226] Benzol/Cyclohexan,[227] oder lineare Alkane.[228] Die Trennung der VOCs erfolgt durch verschiedene Eigenschaften der MOFs und basiert beispielweise auf Wechselwirkungen des MOFs bzw. genauer einer funktionellen Gruppe des Linkers mit dem VOC oder mit den offenen Koordinationsstellen, den OMS.[229,230] Die Trennung kann alternativ auch durch reinen Größenausschluss des VOCs erfolgen, durch die Porengröße des Netzwerks bzw. durch die Größe des Porenfensters.[231] Macreadie *et al.* haben sogar gezeigt, dass die Wechselwirkungen in Kombination mit der Porenumgebung zu einer selektiven Adsorption von Benzol oder Cyclohexan führen können. Interessanterweise sind die MOFs so konzipiert, dass das aliphatische MOF selektiv für einen aromatischen Gast ist und das aromatische MOF selektiv für einen aliphatischen Gast.[232] Santra *et al.* hingegen argumentieren, dass das untersuchte Kupfer-Anthracenylterpyridin-MOF selektiv für Benzol ist, aufgrund der C-H-π bzw. π-π Wechselwirkungen.[233] Diese unterschiedlichen Herangehensweisen zeigen, dass die Trennung von VOCs äußerst komplex ist und viele Aspekte, sowohl in der Dampf-, als auch in der Flüssigphase betrachtet bzw. beachtet werden müssen. Die größenbasierte Trennung von Molekülen, wie bei der Trennung der Xylol-Isomere, oder der Hexan-Isomere ist meist in Kombination mit der optimalen Packung der VOC-Moleküle korreliert.[226,234] Diese Art der Trennung wird auch *molecular sieve separation* (deutsch Siebtrennung auf Molekülebene) genannt und wurde für die Trennung von *n*-Hexan, *3*-Methylpentan und *2,2*-Dimethylbutan mittels einem mikroporösen Einsen-MOFs von Lv *et al.* erforscht. Hierbei konnte gezeigt werden, dass die Trennleistung mit dem sterischen Unterschied zwischen den Substanzen, wie erwartet, steigt.[235]

Ist die Trennung von Substanzen nicht direkt experimentell durchführbar, wie beispielsweise mit chromatographischen Methoden,[236] oder mit Durchbruchmessungen (engl. *breakthrough measurements*),[237] kann auch auf theoretische Berechnungen zurückgegriffen werden. Diese Berechnungen können zum einen die Selektivität von einem Material gegenüber Gemischen ermitteln, zum anderen die Wechselwirkungen der Oberfläche des Adsorbens mit dem Adsorptiv kalkulieren. Beide Arten der theoretischen Berechnungen werden im folgenden Kapitel 1.4 Theoretische Berechnungen detailliert erläutert, sowie die Voraussetzungen dargelegt.

1.4 Theoretische Berechnungen

Die theoretischen Berechnungen bzw. die indirekt experimentell ermittelten Daten, die in diesem Kapitel und den zwei Unterkapiteln vorgestellt und beschrieben werden, basieren auf der Auswertung von einzelnen Sorptionsisothermen und dienen als Ausgangsgrundlage für die Berechnung. Somit kann mit einer theoretischen Berechnung die erste Näherung für die Selektivität von zwei Materialien oder die Stärke der Wechselwirkung eines Adsorbens-/Adsorptiv-Paares ermittelt werden, ohne einen experimentellen Aufbau und Aufwand.

Die theoretischen Berechnungen sind zum einen die *isosteric heat/enthalpy of adsorption* (kurz HoA, deutsch Adsorptionswärme bzw. Adsorptionsenthalpie) und die *ideal adsorbed solution theory* (kurz IAST, deutsch Theorie zur idealen adsorbierten Lösung). Die Berechnungen zur HoA basieren auf mindestens zwei Adsorptionsisothermen, die bei unterschiedlichen Temperaturen aufgenommen wurden,[238] wohingegen die berechneten IAST-Selektivitäten auf mindestens zwei Adsorptionsisothermen beruhen, die bei derselben Temperatur aufgenommen wurden, jedoch mit unterschiedlichen Adsorptiven.[239]

1.4.1 Heat of Adsorption

Die Adsorptionswärme oder die Adsorptionsenthalpie können, laut Nuhnen *et al.*, indirekt experimentell ermittelt werden, wenn verschiedene Voraussetzungen für die gemessenen Adsorptionsisothermen vorliegen. Zu beachten ist, dass die Begrifflichkeiten Adsorptionswärme und Adsorptionsenthalpie häufig identisch verwendet werden, jedoch ist die Adsorptionswärme ein positiver und die Adsorptionsenthalpie ein negativer Wert. Werden die Grundlagen zur Berechnung betrachtet, müssen die Isothermen mit demselben Gerät gemessen werden und mindestens zwei Isothermen mit einem Temperaturunterschied von 10 bis 20 K oder, im Optimalfall, drei Isothermen mit Temperaturunterschieden von je 10 K gemessen werden (bei gleichem Adsorptiv). Das Verwenden von drei Isothermen zur Berechnung wird empfohlen, um die statistische Signifikanz zu erhöhen und eine Fehlerberechnung durchführen zu können.[238] In der Literatur sind eine Vielzahl von Gasen und Dämpfen, in Kombination mit MOFs, mit dieser Art der Berechnung der Wechselwirkungen untersucht worden, wie beispielsweise CO_2,[240,241,242] SO_2,[184] CH_4,[243] oder Benzol.[244]

Wichtig zu beachten, bei der Berechnung der Adsorptionswärme bzw. Adsorptionsenthalpie, ist die Anpassung eines theoretischen Isothermenmodells an die gemessene Adsorptionsisothermen. Hierzu stellen Nuhnen *et al.* verschiedene mögliche Modelle vor, wie Freundlich-Langmuir, in Kombination mit Clausius-Clapeyron, oder die Virial-Anpassung, wobei bei beiden Modelle hervorzuheben ist, dass eine Berechnung der Adsorptionswärme oder Adsorptionsenthalpie nur über den Bereich durchgeführt werden darf in dem experimentelle Messpunkte vorhanden sind und keine Extrapolation der Daten erfolgen sollte. Dies wird geraten, um keinen zu hohen Fehler bei der Berechnung zu generieren. Ebenso ist

zu erwähnen, dass das Freundlich-Langmuir Modell ein Adsorptionsmodell mit physikalischen Grundlagen ist, im Gegensatz zum Virial-Modell, welches auf mathematischer Anpassung der Isothermen beruht mit einer erweiterbaren Anzahl an Virial-Koeffizienten.[238]

1.4.2 Ideal Adsorbed Solution Theory

Die Berechnung von Selektivitäten mit IAST bzw. die Beschreibung des Modells erfolgte erstmals im Jahr 1965 von Myer und Prausnitz, am Beispiel von Methan/Ethan, Kohlenstoffmonoxid/Sauerstoff, Propan/Propen und Ethen/Kohlenstoffdioxid mit verschiedenen Adsorbenzien und liefert die mathematischen und physikalischen Grundlagen.[239]

MOFs gelten als vielversprechende, energie-effiziente Alternative zu konventionellen, in der Industrie eingesetzten, Trennmethoden, wie beispielsweise die Destillation. Aufgrund der bereits beschriebenen Eigenschaften ist es daher von Interesse die Trenneigenschaften von MOFs zu analysieren. IAST ist hierfür eine geeignete Methode, die aus experimentellen einzelnen Gassorptionsisothermen Trennungsleistung bzw. Selektivitäten simulieren kann.[245] Eine Erweiterung des IAST Modells für flexible MOFs, das OFAST Modell (*osmotic framework adsorbed solution theory*) wurde ebenfalls eingeführt, um eine bessere Simulation des Verhaltens von flexiblen Strukturen gegenüber Gemischen zu erhalten.[246,247]

Die Voraussetzungen für die Berechnungen der IAST-Selektivitäten ähneln denen für die HoA, da das gleiche Sorptionsgerät verwendet werden muss, jedoch hierbei dieselbe Temperatur und zwei unterschiedliche Adsorptive. Zusätzlich sollten die Adsorptive keine stark unterschiedliche Polarität aufweisen. Die Methode ist zusätzlich limitiert bei der Simulation von Selektivitäten bei zu hohen Drücken.[248] Die Berechnung erfolgt analog zur HoA im ersten Schritt mit dem Anwenden eines Isothermenmodells auf die gemessenen, einzelnen Sorptionsisothermen, wobei auch hier zu beachten ist, dass die Isothermen mit demselben Modell beschrieben bzw. angepasst werden, da die gleichen Parameter zu weiteren Berechnung nötig sind.[184]

Die Formel für die Selektivitäten lautet:

$$S = \frac{x_1/x_2}{y_1/y_2}$$

mit x_i als adsorbierter Gas-/Dampfmenge und y_i als die Molfraktion des jeweiligen Adsorptivs.[184,239]

Die in der Literatur betrachteten Gemische sind sehr vielfältig und behandeln sowohl Gase, als auch Dämpfe, wie SO_2/CO_2,[184,185,186] CO_2/CH_4,[243] CO_2/N_2,[249] oder Benzol/Cyclohexan.[250]

2. Zielsetzung und Motivation

Der Einsatz von Metall-organischen Gerüstverbindungen in potenziellen Anwendungen, die auf der Dampfsorption aufbauen, sind ein wichtiges und breites Forschungsgebiet. Wie in der Einleitung erläutert, eignen sich MOFs für diese Zwecke besonders gut. Sie weisen eine hervorragende thermische und chemische Stabilität vor und sind durch ihre großes Variantenreichtum für verschiedene Anwendungen gezielt synthetisierbar. Dies unterscheidet die Metall-organischen Gerüstverbindungen von den aktuell in der Industrie eingesetzten Arbeitsmitteln erheblich und ist als ihr größter Vorteil anzusehen.

Das Ziel dieser Arbeit war die Untersuchung der Dampfsorptionseigenschaften von verschiedenen MOFs und die anschließende Überprüfung der Stabilität. Basierend auf diesen Ergebnissen sollen weitere Experimente mit diesen porösen Materialien durchgeführt werden. Hierbei soll die Arbeit nicht nur auf reine Metall-organische Gerüstverbindungen beschränkt sein, sondern auch mögliche Kompositmaterialien mit natürlichen oder synthetischen Polymeren untersuchen.

Hauptteil der vorliegenden Arbeit soll die Untersuchung von Dampfsorptionen an Metall-organischen Gerüstverbindungen sein. Hierzu sollen diese mit einem volumetrischen Gas-/Dampfsorptionsgerät untersucht werden und die jeweiligen MOFs im relativen Druckbereich des zu adsorbierenden Dampfes vermessen werden. Die zu untersuchenden MOFs sollen hinsichtlich einer möglichen Verwendung in den verschiedenen potenziellen Anwendungsgebieten ausgesucht werden. Daher soll der Fokus auf möglichst stabilen Metall-organischen Gerüstverbindungen liegen und diese unter anderem nach dem HSAB-Konzept ausgewählt werden. Des Weiteren soll bei der Auswahl der Metallkationen auf eine gewisse Umweltverträglichkeit und potenzielle Kosten geachtet werden, weshalb ein Großteil der untersuchten Metall-organischen Gerüstverbindungen auf Aluminium und Zirconium basieren sollen. Dennoch sollen diese möglichst mit „Standard“-Verbindungen oder kommerziell erhältlichen Verbindungen verglichen werden.

Ein weiteres wichtiges Feld der Forschung sind theoretischen Rechnungen, die auf den experimentellen Daten basieren, wie die Kalkulation von IAST-Selektivitäten oder das Berechnen der Adsorptionsenthalpien. Diese theoretisch berechneten Daten sind wichtig, um die Eignung einer Metall-organischen Gerüstverbindung für eine potenzielle Anwendung bewerten zu können. Daher sollen die erhaltenen Ergebnisse auch hierhin weitergehend untersucht werden.

Zusätzlich soll die Formgebung der Metall-organischen Gerüstverbindungen ebenfalls ein Teilgebiet dieser Arbeit sein, da diese immens wichtig für potenzielle Anwendungen ist. Die pulverförmig synthetisierten Produkte lassen sich meist nur schwer in Anwendungen einsetzen. Durch die Formgebung, beispielsweise mit natürlichen oder synthetischen Polymeren, soll dieses Problem umgangen oder behoben werden.

3. Kumulativer Teil

Ein Teil der Ergebnisse dieser Dissertation wurde bereits in fünf Publikationen in internationalen Journalen veröffentlicht. Die fünf Erstautorschaften werden in den folgenden Kapiteln 3.1, 3.2, 3.3, 3.4 und 3.5 mit einer kurzen Zusammenfassung beschrieben und die eigenen Anteile an der jeweiligen Publikation aufgeführt. Jede Publikation steht mit einer eigenen Aufzählung für sich. Abbildungen, Tabellen und Schemata folgen hierbei nicht dem Haupttext. Zudem ist für jede Publikation die Literatur in einem separaten Quellenverzeichnis aufgeführt, sowohl für den Haupttext, als auch für die unterstützenden Informationen zum Haupttext. Die Publikationen sind in chronologischer Reihenfolge aufgeführt. Für Veröffentlichungen als Co-Autor sind jeweils kurze Zusammenfassungen gegeben und die eigenen Anteile an der Publikation werden aufgezeigt. Weitere Ergebnisse, welche bislang nicht publiziert sind, werden in den Kapiteln 4 und 5 beschrieben, wobei Kapitel 4 die Ergebnisse beschreibt und erläutert und Kapitel 5 die Synthesen, Geräte und Methoden nähergehend beschreibt. Weitere ergänzende Daten zu diesen unveröffentlichten Ergebnissen sind zusätzlich im Anhang gegeben.

3.1 Robust synthesis routes and porosity of the Al-based metal-organic frameworks Al-fumarate, CAU-10-H and MIL-160

Niels Tannert, Christian Jansen, Sandra Nießing, Christoph Janiak

Dalton Trans. **2019**, *48*, 2967–2976.

DOI: 10.1039/c8dt04688c

Impact-Faktor: 4.569 (2021)

Kurzzusammenfassung:

Aluminiumbasierte MOFs haben sich zu einer Gruppe der vielversprechendsten MOFs für potenzielle Anwendungen entwickelt, aufgrund ihrer besonderen hydrothermalen Stabilität, der einfachen Synthese und der hohen Verfügbarkeit des preiswerten und nicht-toxischen Metalls. In dieser Veröffentlichung werden im Besonderen die drei MOFs Aluminiumfumarat, CAU-10-H und MIL-160 untersucht, zusammen mit ihren kommerziell erhältlichen Liganden Fumar-, Isophthal-, und Furandicarbonsäure. Diese drei MOFs sind aufgrund ihrer hydrothermalen Stabilität und ihrer Wasseraufnahme mögliche Kandidaten für die Anwendung als Materialien für die Wärmetransformation. Gleichzeitig ist für die Verwendung in potenziellen Anwendungen besonders wichtig, dass die Synthese und die Porosität der MOFs eine hohe Reproduzierbarkeit besitzen. Die für diese MOFs typischen Synthesen in Lösungen, aus der Literatur, sind gut reproduzierbar und ebenso leichte Variationen dieser Synthesen

führen zu einer vergleichbaren Porosität. Die Trockengelsynthesen wurden für diese drei MOFs implementiert und führten zu Produkten mit höheren absoluten Porenvolumen, da die Produkte eine stärkere Agglomeration der Partikel zeigen. Die Evaluation der Daten und unsere ergänzte Synthesemethode zeigen, dass die MOFs sehr gut reproduziert werden können und unabhängig von der Syntheseroute sind. Dies führt zu einer generell guten potenziellen Verwendung für die oben genannte Anwendungsmöglichkeit.

Anteile an der Publikation:

- Idee der Publikation in Zusammenarbeit mit Herrn Niels Tannert
- Konzept, experimentelle Arbeiten und Analytik (bis auf unten gelistete Ausnahmen) in Zusammenarbeit mit Herrn Niels Tannert
- Aufarbeitung der Ergebnisse, Verfassen des Manuskripts und das Erstellen der Abbildungen und Tabellen
- Korrekturen und Verschriftlichung und Revision durch Herr Prof. Dr. Christoph Janiak
- REM-Aufnahmen durch Frau Sandra Nießing

Dalton Transactions

PAPER

View Article Online
View Journal | View Issue

Cite this: *Dalton Trans.*, 2019, **48**, 2967

Robust synthesis routes and porosity of the Al-based metal–organic frameworks Al-fumarate, CAU-10-H and MIL-160†

Niels Tannert, ‡ Christian Jansen, ‡ Sandra Nießing and Christoph Janiak *

Aluminum-based metal–organic frameworks, Al-MOFs, have developed into one of the most promising MOFs for potential applications because of, *inter alia*, their hydrothermal stability and comparatively easy synthesis, and the availability of abundant, inexpensive and non-poisonous metal. Here, we evaluate the synthesis and porosity properties of the three MOFs aluminum fumarate (Alfum), CAU-10-H and MIL-160 involving the commercially readily available ligands fumaric, isophthalic and furandicarboxylic acid, respectively. The three Al-MOFs exhibit proven hydrothermal stability and water uptake to make them eligible for heat transformation applications. At the same time, it is important for applications that the synthesis and porous properties of these MOFs are robust, that is readily reproducible within certain limits. The typical solution synthesis of these MOFs was carried out with slight variations and compared with the literature to check if indeed the reported porosity data can readily be reproduced. Furthermore, dry-gel conversion (DGC) was implemented here for the synthesis of these MOFs and yielded products with higher total pore volumes due to the inherent aggregate formation under dry-gel synthesis conditions. The evaluation and our added syntheses ascertain that these Al-MOFs can be reproducibly synthesized with robust porosity properties, which are independent of the synthesis method, underscoring the potential of these MOFs for applications.

Received 27th November 2018,
Accepted 28th January 2019

DOI: 10.1039/c8dt04688c

rsc.li/dalton

Introduction

Metal–organic frameworks (MOFs) are crystalline coordination networks, built up by metal nodes[1] and bridging organic ligands ("linkers")[2] that are receiving steady attention as porous materials, owing to their high specific surface areas[3] and chemical variability to modulate their properties.[4] MOFs appear to be interesting in a wide range of potential applications, such as catalysis,[5,6] sensing,[7] gas separation[8,9] and storage,[10] drug delivery[11] and heat transformation processes.[12,13]

The diversity of synthesis methods for MOFs[14] has steadily increased within the last few years.[15–17] Besides the first solvothermal methods,[18] there are now syntheses under ambient pressure and even ambient temperature.[19] There are electro-[20] and sonochemical,[21] microwave,[22] flow reactor,[18,23] mechanochemical,[24] dry-gel conversion (DGC) syntheses[25] and combinations thereof.[26]

At the same time, it is now becoming clear that the synthesis method of a MOF may lead to material variations, which in turn can have stark effects on the MOF properties, such as porosity and gas uptake.[27–29]

Aluminum-based MOFs like MIL-53,[30] Al-fumarate (Alfum, Basolite A520),[31,32] CAU-10-H,[33] and MIL-160[34] can be considered among the most promising MOFs with regard to applications. Al-MOFs typically display (helical) chains with either *trans*- (MIL-53 and Alfum) or *cis*- (CAU-10-H and MIL-160) corner-sharing AlO_6 octahedra, in which the shared corners are OH-anions or oxygen atoms from the carboxylate groups of the organic linker molecules (Fig. 1, see the ESI† for further structure images and details).

Al-MOFs display microporous, narrow pore size distributions originating from parallel one-dimensional square-to-rhombus-shaped channels. One advantage of Al-MOFs is their high chemical and hydrothermal stability,[35–38] which makes them prone to realistic applications where water content or humidity cannot be avoided. Alfum and CAU-10-H have demonstrated stability over 4500 and 10 000 water adsorption and desorption cycles, respectively.[36,38] Both exhibit the desired steep s-shaped water sorption isotherm with uptake in a relatively low partial pressure range.[36,38] Besides, aluminum is considered non-toxic and is one of the most abundant (8.3% by weight in the Earth's crust) and inexpensive metals.

Institut für Anorganische Chemie und Strukturchemie, Heinrich-Heine-Universität Düsseldorf, 40204 Düsseldorf, Germany. E-mail: janiak@uni-duesseldorf.de

† Electronic supplementary information (ESI) available: The background of the presented MOFs, details of materials and methods, synthesis protocols and optimizations, work-up procedures, additional PXRDs, nitrogen and water sorption analyses, SEMs, and TGAs. See DOI: 10.1039/c8dt04688c

‡ These authors contributed equally.

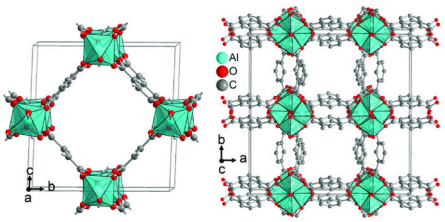

Fig. 1 Unit-cell content of Alfum (left) and CAU-10-H (right, corresponding to MIL-160) with the Al atoms in polyhedral presentation. See Fig. S2–S4 in the ESI† for further information.

Al-MOFs have received attention in hierarchical porosity,[39] gas storage and gas separation,[40] adsorption of organics,[41] catalysis,[42] mechanical energy storage,[43] water and air purification/remediation,[44] water harvesting,[45] desalination,[46] sensing,[47] proton conductivity,[48] mixed-matrix membranes (MMMs)[49] and in heat transformation applications.[36,38,50–55] In the last few years, Alfum and CAU-10-H have therefore moved from basic research materials to adsorbents in pre-industrial full-scale devices.[50,54,55]

In view of the importance of Al-MOFs, it seems crucial that the material properties are robust, within certain limits to variations in syntheses. Here we critically assess the different synthesis methods together with the porosity properties of Alfum, CAU-10-H and MIL-160 for their robustness. We carried out the typical solution synthesis of these MOFs with a slight variation compared to the literature to check if the reported data can be readily reproduced.

We also extended the syntheses towards more novel dry-gel conversion (DGC) in order to try minimizing the often high solvent consumption in MOF syntheses following our earlier work on this technique[26,56] towards more sustainable MOF synthesis procedures.[57] DGC is attributed to the reduced amounts of solvent used and waste due to the physical separation of the solvent and reactant mixture.[26,58] This separation results in the advantage of DGC that only enough solvent for the wetting of the reactants is needed and that after the reaction, the solvent can be recovered largely uncontaminated and could be used for further reaction runs. Hence, DGCs result in drastically reduced amounts of contaminated solvent which need to be disposed of.[26,59]

To the best of our knowledge, this is the first wider testing of DGC in Al-MOF synthesis, following our recent DGC synthesis report of Alfum (see Fig. 1 in the ESI† for details on the DGC apparatus).[26]

Experimental

Materials and instrumentation

All chemicals were used as received from the suppliers (see section S1 in the ESI†).

Powder X-ray diffraction (PXRD) was performed at ambient temperature on a D2 phaser (Bruker, Billerica, US) using Cu-K_α radiation (λ = 1.54182 Å) between 5° < 2Θ < 50° at a scanning rate of 0.0125° s^{-1} (300 W, 30 kV, 10 mA). Analyses of the diffractograms were carried out with Match 3.11 software. All PXRD patterns are obtained in section S6 in the ESI.†

Thermogravimetric analysis (TGA) was performed on a Netzsch TG209 F3 Tarsus (Netzsch, Selb, Germany) device under a synthetic air atmosphere, ramping with 5 K min^{-1} from 25 °C to 600 °C. TGA curves are given in section S7 in the ESI.†

SEM images were acquired on a JEOL JSM-6510 advanced electron microscope (Jeol, Akishima, Japan) with a LaB_6 cathode at 5–20 keV. The microscope was equipped with an Xflash 410 (Bruker, Billerica, US) silicon drift detector. SEM images are obtained in section S8 in the ESI.†

The surface area (Brunauer–Emmett–Teller,[60] BET) was determined by nitrogen (purity 99.999%, 5.0) sorption experiments at T = 77 K, using liquid nitrogen and *ca.* 20–50 mg of the sample and performing on a Quantachrome NOVA-4000e (Quantachrome, Odelzhausen, Germany) instrument within the partial pressure range of pp_0^{-1} = 10^{-3}–1 bar. Each sample was degassed under vacuum (<10^{-2} mbar) at 150 °C for *ca.* 3 h prior to measurement. All surface areas (BET) were calculated from five adsorption points by applying Roquerol plots (r > 0.998). For the pressure ranges of five-point-BET calculations of each MOF, see section S9 in the ESI.† Total pore volumes were calculated from the N_2 sorption isotherm at pp_0^{-1} = 0.95. NLDFT calculations for pore size distributions were done with NovaWin 11.03 software using the 'N_2 at 77 K on carbon, slit pore, NLDFT equilibrium' model. All N_2 sorption isotherms are shown in section S9 in the ESI.†

Water sorption experiments were carried out on a Quantachrome VStar4 (Quantachrome, Odelzhausen, Germany) instrument within the partial pressure range of pp_0^{-1} = 10^{-3}–1 bar. Each sample was degassed under vacuum (<10^{-3} mbar) at 150 °C for *ca.* 3 h prior to measurement, using a FloVac (Quantachrome, Odelzhausen, Germany) degasser. All water sorption isotherms are depicted in section S10 in the ESI.†

Solution syntheses

In brief, the solution synthesis of Alfum was carried out as described in the patented route. The solution of fumaric acid and NaOH was added dropwise to the aluminum sulfate solution at 60 °C (further details in section S3, ESI†).[31]

The solution synthesis of CAU-10-H was carried out in accordance with a report by Reinsch *et al.*[33] Aluminum sulfate and isophthalic acid were reacted in an autoclave in a water/dimethylformamide (DMF) mixture (further details in section S3, ESI†).

The solution synthesis of MIL-160 was carried out following a modified protocol of Cadiau *et al.*,[34] who used 1 eq. of NaOH, whereas we used 2 eq. of NaOH for full deprotonation of 1 eq. of the dicarboxylate linker. To the deprotonated acid solution, dissolved aluminum chloride was added and then the mixture was refluxed (further details in section S3, ESI†).

Dry-gel conversion (DGC)

In brief, DGC syntheses were performed in a Teflon reactor using a temperature programmable oven (see Fig. S1† for

images of the reactor and section S4 for details of the experimental setup).

In a typical synthetic procedure, we rapidly ground aluminum sulfate octadecahydrate ($Al_2(SO_4)_3{\cdot}18H_2O$) or aluminum chloride hexahydrate ($AlCl_3{\cdot}6H_2O$) (1 eq.), with fumaric acid (2 eq.), isophthalic acid (1 eq.) or 2,5-furandicarboxylic acid (1 eq.) and sodium hydroxide (NaOH) (4, 0 or 2 eq.) in a mortar and placed the mixture on a DGC sieve with water (2 mL) or water/DMF (4 : 1, 2 mL) at the bottom of a Teflon reactor. DGCs were carried out at varying temperatures and conversion times. The white products were washed three times with water (10 mL each), recovered by centrifugation each time and finally dried under vacuum (80 °C, 24 h).

From both synthesis routes, the product crystallinity together with phase identification was verified by PXRD (section S6, ESI†), surface areas with pore volumes (BET) were determined by N_2 sorption at 77 K (section S9, ESI†) and water sorption isotherms were measured at 20 °C (section S10, ESI†).

Results and discussion

Table 1 summarizes the synthesis conditions, porosity properties and yields of Alfum, CAU-10-H and MIL-160 given in the literature, supplemented by our modified solution and dry-gel conversion synthesis.

There are synthesis routes in solution using beakers, Pyrex tubes, round bottom flasks, Teflon-lined autoclaves, or even a flow reactor as stated in the literature protocols. In a singular case, an extruder was used for Alfum albeit no pore volume of the product was reported.[74]

The BET surface area, (micro)pore volume and yield were chosen to assess the product quality and synthesis conditions. We note that the pore volume was not always given and the yield was missing frequently. Thus, a consistent comparison of pore volumes and yields is difficult. For the pore volume it was noted whenever possible if the value refers to the micropore volume calculated from the N_2 adsorption isotherm at pp_0^{-1} = 0.1 for pores with $d \leq 2$ nm (20 Å) or the total pore volume at pp_0^{-1} = 0.95 for pores ≤20 nm.

There are even synthesis reports stating neither surface area nor pore volume nor yield.[50,61–65] These reports are not included in Table 1.

For Alfum and CAU-10-H aluminum sulfate, $Al_2(SO_4)_3$ is mostly used as the Al source, while for MIL-160 aluminum trichloride, $AlCl_3$ is chosen. We see no special reasoning for this choice of aluminum starting material as $AlCl_3$ or $NaAlO_2$ for Alfum and basic aluminum acetate $Al(OH)(CH_3COO)_2$ for MIL-160 gave similar results. For Alfum with $AlCl_3$, the solvent DMF apparently had to be used. It is evident that Alfum synthesis with $AlCl_3$ did not yield very high surface areas.

For Alfum and MIL-160, deprotonation of the dicarboxylic acid is achieved with added NaOH. The reaction of $Al_2(SO_4)_3$ with isophthalic acid to CAU-10-H works without the addition of a base, but with the use of DMF.

The syntheses are mostly carried out in aqueous solution at temperatures ranging from 60 °C to reflux (100 °C) and with DMF up to 135 °C. Reaction times can be as short as 1 min for Alfum in a continuous reactor system,[66] but also last about 100 or more hours. A special or beneficial effect of long reaction times is not evident.

For Alfum there is a particular wide range of surface areas reported between 723 and 1333 $m^2\ g^{-1}$. For CAU-10-H and MIL-160, the range is more narrow with 525 to 656 $m^2\ g^{-1}$ and 1070 to 1150 $m^2\ g^{-1}$, respectively.

In general, the degree of crystallinity of the Al-MOFs as observed by powder X-ray diffractometry is comparable to that in the literature. The same accounts for the SEM images of Al-MOFs, which typically show intergrown agglomerates of varying sizes independent of the synthesis method. Al-MOFs do not tend to grow larger crystallites, so that no single-crystal X-ray structures have been obtained until today. The reported structures of Alfum, CAU-10-H and MIL-160 are based on Rietveld refinements.[32–34]

Alfum

As shown in Table 1, the synthesis literature on aluminum fumarate is extensive. Furthermore, the MOF is commercially available, which underlines the importance of aluminum fumarate.[67] Different aluminum salts and both water (with NaOH) and DMF as the solvent were used. Temperature and reaction time were varied widely, from 60 to 150 °C and from one minute to four days. A difference from other MOFs is the large-scale synthesis of aluminum fumarate as was patented by BASF. This is related to the simple method of preparation, which makes it possible to also produce the MOF in a flow reactor or an extruder.[66,74]

The patent of commercial Basolite A520 stated only the Langmuir surface area.[31] We drew four samples from the same commercial batch to obtain the BET surface area of 1033 ± 7 $m^2\ g^{-1}$, which is in very good accordance with that in other reports.[31,32] We could readily obtain Alfum with a very similar yield, surface area and pore volume when we repeated the synthesis protocol from the BASF patent, except that stirring was continued for a further 2 hours after combining the solutions (details in section S3, ESI†).

Within the DGC synthesis (see section S4.1, ESI† for detailed information) we found 100 °C and 6 h to be the optimal conditions. Wetting of the precursor mixture was not necessary because of the good solubility of fumaric acid with NaOH. With DGC, the surface areas and pore volumes were consistent with the other synthesis literature. The yields of the DGC are lower, because of the loss of the starting material or product through the sieve to the bottom of the autoclave.

When comparing the Alfum DGC synthesis with the continuous solution synthesis route, it should be noted that such continuous solution syntheses involve large amounts of solvents. The patented synthesis procedure for continuous production of Alfum demonstrates different methods with varying space–time–yields (STYs) from 2032 to 5339 kg m^{-3} day^{-1}.[31]

Table 1 Synthesis, porosity parameters and yields of Alfum, CAU-10-H and MIL-160

Al-MOF	Reactants	Conditions	BET surface area[a] [$m^2 g^{-1}$]	Pore volume [$cm^3 g^{-1}$]	Yield [%] for STY [$kg m^{-3} day^{-1}$]	Ref.
Alfum	$Al_2(SO_4)_3$, fumaric acid, NaOH	65 °C, 1 min residence time (continuous)	1054	n.a.	STY: 97159	18
	$Al_2(SO_4)_3$, fumaric acid, NaOH	65 °C, 1 min residence time (continuous)	1015–1084	n.a.	74–85	66
	$Al_2(SO_4)_3$, fumaric acid, NaOH	60 °C, 3 h (solution)	1156	n.a.	74	44*b*
	Purchased from MOF Technologies[67]	Purchased from MOF Technologies[67]	1021	0.44	Purchased	46
			894	n.a.	Purchased	68
	$AlCl_3$, fumaric acid, DMF	130 °C, 4 d (solution)	1021	0.48	90	36
			792	0.93 (total)	n.a.	69
	$AlCl_3$, fumaric acid, DMF	130 °C, 96 h (solution)	792	0.43	n.a.	70
			792	0.48	n.a.	71
	$Al_2(SO_4)_3$, fumaric acid, NaOH	60 °C, 30 min (solution)	1025	0.47	96	32
	$Al_2(SO_4)_3$, fumaric acid, NaOH	90 °C, 60 min (solution)	821	0.44	n.a.	71
	$NaAlO_2$, fumaric acid	90 °C, 30 min (solution)	925	0.65 (total)	74	72
			980	1.42 (total)	n.a.	73
	$Al_2(SO_4)_3$, fumaric acid, NaOH	150 °C, (twin screw extrusion)	1010	n.a.	STY: 27000	74
	$Al_2(SO_4)_3$, fumaric acid, NaOH (1 : 2 : 4)	100 °C, 1 h, 800 W (MW-DGC), 6 h (DGC)	983–1189	0.43–0.61 (micropore)	58–71	26
	$Al_2(SO_4)_3$, fumaric acid, NaOH	RT, 60 °C, 0.17, 0.27, 0.5 h (solution)	723–1333[d,L]	0.47 (micropore)[32]	76–98	31
		Basolite A520			STY: 2032–5339 [d]	
			880 (Argon)	n.a.	n.a.	75
			965–971	0.85–0.91/0.38 (micropore)	Purchased	76
			999–1040[e]	0.51–0.63 (micropore)[b,e]	n.a.	This work
	$Al_2(SO_4)_3$, fumaric acid, NaOH (1 : 2 : 4)	60 °C, 150 min (solution)	780–1254	0.36–0.72 (micropore)[b]	73–85	This work
	$Al_2(SO_4)_3$, fumaric acid, NaOH (1 : 2 : 4)	80, 100, 120 °C, 6, 12, 24 h (DGC)	983–1189[c]	0.51–0.61[b]	23–53	This work
CAU-10-H	$Al_2(SO_4)_3$, isophthalic acid (1 : 1)	Reflux, 117 h (solution)	564	0.26	91	38
	$NaAlO_2$, $Al_2(SO_4)_3$, sodium iosophthalate (1 : 1,5 : 4)	Reflux, 10 h (solution)	n.a.	n.a.	93	54
	$Al_2(SO_4)_3$, isophthalic acid (1 : 1), DMF	135 °C, 12 h (solution in autoclave)	635	0.25 (micropore)	60–70	48 and 33
			525	0.27	n.a.	37
			656	0.25 (micropore)	n.a.	42*a*
			640	0.25 (micropore)	n.a.	77
			615	n.a.	89	78
	$Al_2(SO_4)_3$, isophthalic acid (1 : 1), DMF	135 °C, 12 h (solution in autoclave)	415–484	0.25–0.27[b]	35–42	This work
	$Al_2(SO_4)_3$, isophthalic acid (1 : 1), DMF	115, 135, 155 °C, 6, 12, 24 h (DGC)	285–560[c]	0.24–0.47[b]	22–44	This work
MIL-160	$Al(OH)(CH_3COO)_2$, 2,5-furandicarboxylic acid (1 : 1)	Reflux, 24 h (solution)	1150	0.48	93	79
	$AlCl_3$, 2,5-furandicarboxylic acid, NaOH (1 : 1 : 1)	Reflux, 24 h (solution)	1070	0.40 (micropore)	n.a.	34
	$Al(OH)(CH_3COO)_2$, 2,5-furandicarboxylic acid (1 : 1)	100 °C, 96 h (solution in Pyrex tube)	1098	0.41 (micropore)	n.a.	83
	$AlCl_3$, 2,5-furandicarboxylic acid, NaOH (1 : 1 : 1)	Reflux, 24 h (solution)	1148	0.46 (total)	n.a.	80
	$AlCl_3$, 2,5-furandicarboxylic acid, NaOH (1 : 1 : 2)	Reflux, 24 h (solution)	1178	0.42[b]	55	This work
	$AlCl_3$, 2,5-furandicarboxylic acid, NaOH (1 : 1 : 1 or 2)	80, 100, 120 °C, 12, 24, 48 h (DGC)	968–1180[c]	0.54–0.56[b]	22–50	This work

[a] BET surface areas were obtained from five adsorption points in the individual MOF pressure range (section S9, ESI). [b] This work: Calculated using the NLDFT model for carbon (slit pore), with pp_0^{-1} = 0.95 for total pore volume and pp_0^{-1} = 0.5 for micropore volume. [c] This work; the range of at least three samples. [d] Stated in the patent.[31] [e] Range of five individual measurements from the same batch (this work, Table S9, ESI) and in good agreement with values in the literature.[31,32] [L] Langmuir surface area. All values are rounded.

The most effective STY of 3615 kg m^{-3} day^{-1} achieves 4.1 wt% of the product in the dispersion/solution, which in turn means 95.9 wt% of the mother liquor. Thus, 3615 kg Alfum product per day from a 4.1 wt% dispersion would go along with 3615 × 100/4.1 = 88 170 kg (= 88.17 tons) mother liquor waste per day.

Fig. 2a depicts the exemplary PXRD patterns of Alfum samples obtained *via* our solution synthesis, by optimized DGC, from commercial Basolite A520 and the theoretical pattern.

Fig. 2b shows the N_2 sorption isotherms of different Alfum samples, underscoring the similar porosity properties of the samples from solution synthesis, DGC and commercial Basolite A520 (Table 1). The observed steep rise at high partial pressures ($pp_0^{-1} > 0.9$) in the DGC product can be attributed to a larger inter-particle volume of aggregated crystallites, which result in the dry-gel formation. The latter promotes (meso-) to macroporous cavities,[26] as the residual water in the DGC process forms such voids in the gel.[81] This property is a common feature within our presented DGC results, since it could be observed in any DGC isotherm of all three presented Al-MOFs and can therefore be declared as highly reproducible and a unique feature of DGC for Al-MOFs. Therefore, the total pore volume at $pp_0^{-1} = 0.95$ will always be superior in DGC syntheses compared to solution-based approaches.

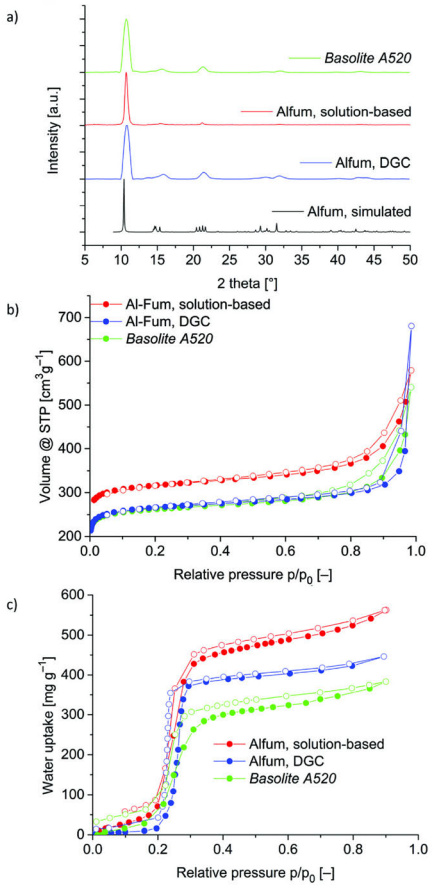

Fig. 2 Comparison of Alfum from solution synthesis, DGC and commercial Basolite A520: (a) PXRDs. The simulated pattern was calculated using CSD-Refcode DOYBEA.[32] (b) Nitrogen sorption isotherms (T = 77 K). (c) Water sorption isotherms (T = 20 °C). Filled circles depict adsorption; unfilled circles indicate desorption.

The SEM images of Alfum (Fig. S14, ESI†) show the typical intergrown agglomerates of varying sizes independent of the synthesis method.

Thermogravimetric analysis (TGA) of the Alfum samples (Fig. S11, ESI†) revealed mostly comparable thermal stability to over 400 °C among all samples, which is in agreement with the literature, where around 400 °C is typically given as thermal stability.[32]

Water uptake capacities correlate with the porosity of the sample, and it is worth noting that the DGC product has a higher uptake than commercial Basolite A520 (Fig. 1c).

CAU-10-H

CAU-10-H syntheses are mainly carried out in autoclaves and under reflux. The most commonly followed synthesis route was first published by Reinsch *et al.*,[33] which used an autoclave at 135 °C for 12 h and provided surface areas of 525 to 656 $m^2\ g^{-1}$. For the reflux synthesis yield, over 90% can be reached albeit at very long reaction times of up to 117 h.

We repeated here the synthesis in solution from the work of Reinsch *et al.* using an autoclave at 135 °C for 12 h. The surface areas and yields from our syntheses are below the literature values. For the DGC synthesis (see section S4.2, ESI† for detailed information), 155 °C and 12 h were found to be the optimal conditions. Wetting of the precursor mixture with a small amount of DMF was necessary to ensure proper phase formation since the linker isophthalic acid possesses poor solubility in water.[82] The DGC surface areas and pore volumes were consistent with those mentioned in the literature. The yields of the DGC are lower due to the loss of the starting material or product when falling through the sieve.

The PXRDs show no crystallinity differences between the products from solution synthesis and moistened DGC (Fig. 3a).

The nitrogen sorption isotherm of the CAU-10-H samples obtained by DGC again indicates the more pronounced inter-particle volume (Fig. 3b). Nitrogen sorption further revealed comparable BET surface areas from both routes, however with higher values and a wider range within DGC (Table 1). TGA showed comparable stability (~380 °C) for both CAU-10-H samples (Fig. S12, ESI†) which agrees with the thermal stability values mentioned in the literature from TGA at around 400 °C.[33] The SEM images confirm the formation of seemingly macroporous agglomerates by DGC (Fig. S15, ESI†). The water uptake capacity correlates with the porosity of the individual sample with the expected S-shaped isotherms below $pp_0^{-1} = 0.2$.[37,38]

MIL-160

MIL-160 is a new Al-MOF whose first published synthesis dated from 2015.[34] Only two different sources of aluminum

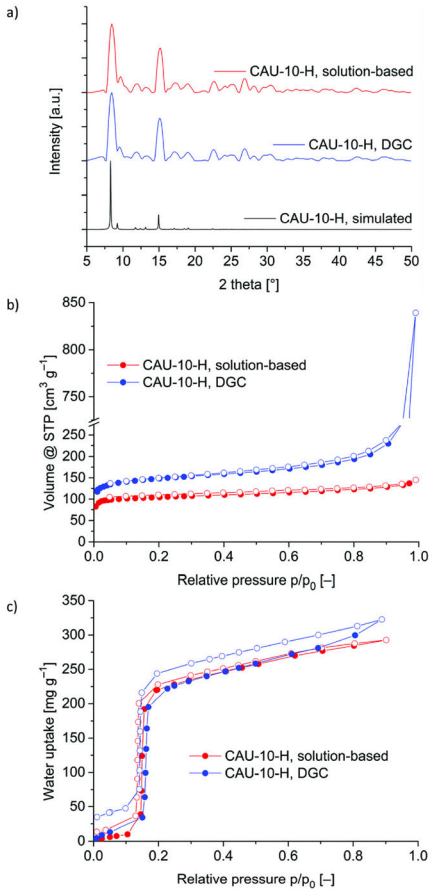

Fig. 3 Comparison of CAU-10-H from solution and DGC synthesis: (a) PXRDs. The simulated pattern was calculated using CSD-Refcode QQOBUT.[36] (b) Nitrogen sorption isotherms (T = 77 K). (c) Water sorption isotherms (T = 20 °C). Filled circles depict adsorption; unfilled circles indicate desorption.

were used and the conditions of synthesis appear to have not differed much or even systematically investigated. Most publications use the reflux synthesis by Cadiau *et al.*[34] Only one publication reported the production of MIL-160 in a Pyrex tube at 100 °C for 96 h.[83]

In our work, the solution synthesis is also based on the work by Cadiau *et al.*, but we used twice the molar amount of NaOH to achieve the complete deprotonation of the acid. With this synthesis modification, we achieved the same results as Cadiau *et al.* The use of only 1 mol NaOH for 1 mol of furandicarboxylic acid gave considerably lower surface areas of 135–451 $m^2 g^{-1}$ (moistened).

DGC synthesis (see section S4.3, ESI† for details) gave optimum samples at 100 °C and 48 h reaction time. Wetting of the precursor mixture showed no particular improvement. The use of 2 mol NaOH for each mol of linker yielded a higher surface area.

From the typical PXRD patterns given in Fig. 4a, MIL-160 samples obtained from the solution synthesis gave a better match to the simulated pattern, while samples from DGC showed additional reflections.

Fig. 4b shows the N_2 sorption isotherms of MIL-160 samples obtained by DGC and a solution-based approach.

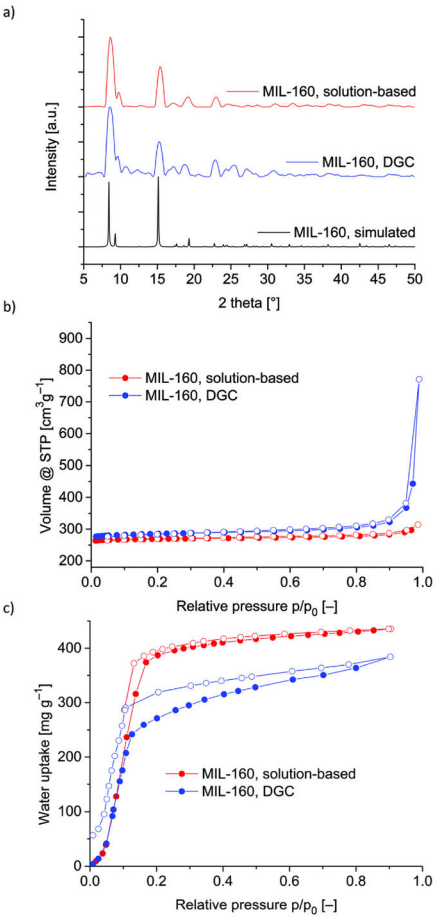

Fig. 4 Comparison of MIL-160 from solution and DGC synthesis: (a) PXRDs. Simulated pattern was calculated using CSD-Refcode PIBZOS.[83] (b) Nitrogen sorption isotherms (T = 77 K). (c) Water sorption isotherms (T = 20 °C). Filled circles depict adsorption; unfilled circles indicate desorption.

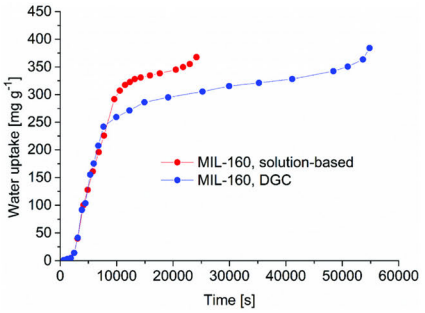

Fig. 5 Water uptake *versus* equilibration time for each data point for MIL-160 from solution and DGC synthesis.

Once again, the steep uptake at $pp_0^{-1} > 0.9$ is evident for the DGC product and, consequently, total pore volumes of DGC syntheses are reproducibly higher than from the solution synthesis. Other than this, DGC surface areas and pore volumes were consistent with the literature. Water sorption isotherms are depicted in Fig. 4c.

The additional pore volume in MIL-160-DGC is due to mesopores. The *V*–*t*-plot method determined the micropore *versus* total pore volume to be 0.40/0.42 for MIL-160-solution and 0.28/0.54 for MIL-160-DGC. It can be assumed that the meso-microporosity should also affect the water sorption kinetics, such that a hierarchical macro-meso-microporosity may be expected to lead to fast adsorption into the micropores. We have exemplarily plotted the water uptake *versus* time for the two MIL-160 probes to check for a kinetic water adsorption effect in view of the increased total pore volume and higher mesopore content for MIL-160-DGC (Fig. 5). Yet, and maybe in contrast to expectation, the smaller micropore filling occurs at the same rate. The filling of the larger micropores requires more time but is still faster in the overall microporous MIL-160-solution sample. The mesopore filling in MIL-160-DGC then becomes very time consuming. This may be rationalized by a non- or even inverse-hierarchical nature of the micro-mesopores. Internal mesopores, which are only accessible by micropores leading to them, will require extended equilibration times.

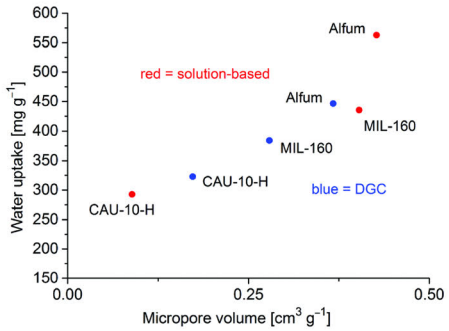

Fig. 6 Water uptake *versus* micropore volume (by *V*–*t*-plot method) for solution and DGC samples.

TGA revealed comparable stability for both samples (>300 °C), with the DGC product decomposing at slightly lower temperatures (Fig. S13, ESI†). According to the literature, MIL-160 is temperature stable up to 400 °C.[34] SEM images (Fig. S16, ESI†) show the typical morphology with intergrown crystallites in samples of both synthesis routes.

Conclusion

Al-MOFs present a most promising class of MOFs for diverse applications due to their ease of synthesis and hydrothermal stability. Their synthesis procedures and porosity properties appear to be rather robust, that is, BET surface areas were rather independent of the synthesis route and readily reproducible from standard literature synthesis protocols. The same can be seen for the pore volume and yield for CAU-10-H and MIL-160, which can be traced to essentially one primary synthesis procedure. For Alfum, the pore volume and yield (if given) varied widely due to the large differences in the synthesis conditions concerning starting materials, solvent, temperature, time and method.

Dry-gel conversion could be introduced as an alternative synthesis procedure for Al-MOFs, where as an ecological benefit, only low amounts of solvent are needed. The crystallinity and microporosity of all optimized DGC products were in the range of solution-based materials (Table 1), while the BET surface areas of DGC products reached or even outperformed those of solution-based products. We found that DGCs of Al-MOFs reproducibly led to products with higher total pore volumes due to the inherent aggregate formation in the dry-gel synthesis process. The latter promotes water-filled voids within the gel and agglomeration that results in large interparticle volumes after activation. Depending on the literature source, water uptake may be correlated with total pore volume (calculated at $pp_0^{-1} = 0.95$).[84] When plotting the water uptake at $pp_0^{-1} = 0.95$ *versus* the total pore volume at $pp_0^{-1} = 0.95$ (Fig. S20, ESI†), it is evident that for MIL-160 the trend is reversed; that is, the solution-based MIL-160 product with a lower pore volume has a higher water uptake. However, from our experience the micropore volume (Table S10, ESI†) has a more decisive role in determining the water uptake. A plot of the water uptake *versus* micropore volume indeed presents a more convincing trend: for chemically identical MOFs a higher micropore volume is followed by a higher water uptake (Fig. 6).

In conclusion, DGC was proven to be a sustainable alternative for the robust syntheses of sorption-active Al-MOFs. In the future, attention should be paid to developing continuous (non-autoclave) processes for the Al-MOFs CAU-10-H and MIL-160, as exist already for Alfum.

Conflicts of interest

There are no conflicts of interest to declare.

Acknowledgements

The authors gratefully acknowledge the financial support from the Federal German Ministry of Education and Research (BMBF) for the project Optimat under grant no. 03SF0492C.

References

1 J. Zhou, H. Li, H. Zhang, H. Li, W. Shi and P. Cheng, *Adv. Mater.*, 2015, **27**, 7072–7077.
2 F. A. Almeida Paz, J. Klinowski, S. M. F. Vilela, J. P. C. Tome, J. A. S. Cavaleiro and J. Rocha, *Chem. Soc. Rev.*, 2012, **41**, 1088–1110.
3 G. Maurin, C. Serre, A. Cooper and G. Férey, *Chem. Soc. Rev.*, 2017, **46**, 3104–3107.
4 R. Haldar and T. K. Maji, *CrystEngComm*, 2013, **15**, 9276–9295.
5 Y.-B. Huang, J. Liang, X.-S. Wang and R. Cao, *Chem. Soc. Rev.*, 2017, **46**, 126–157.
6 A. Herbst and C. Janiak, *CrystEngComm*, 2017, **19**, 4092–4117.
7 W. P. Lustig, S. Mukherjee, N. D. Rudd, A. V. Desai, J. Li and S. K. Ghosh, *Chem. Soc. Rev.*, 2017, **46**, 3242–3285.
8 J.-R. Li, R. J. Kuppler and H.-C. Zhou, *Chem. Soc. Rev.*, 2009, **38**, 1477–1504.
9 J. Dechnik, J. Gascon, C. J. Doonan, C. Janiak and C. J. Sumby, *Angew. Chem., Int. Ed.*, 2017, **56**, 9292–9310.
10 K. Adil, Y. Belmabkhout, R. S. Pillai, A. Cadiau, P. M. Bhatt, A. H. Assen, G. Maurin and M. Eddaoudi, *Chem. Soc. Rev.*, 2017, **46**, 3402–3430; C. Petit, *Curr. Opin. Chem. Eng.*, 2018, **20**, 132–142.
11 P. Horcajada, R. Gref, T. Baati, P. K. Allan, G. Maurin, P. Couvreur, G. Férey, R. E. Morris and C. Serre, *Chem. Rev.*, 2012, **112**, 1232–1268.
12 F. Jeremias, D. Fröhlich, C. Janiak and S. K. Henninger, *New J. Chem.*, 2014, **38**, 1846–1852.
13 M. F. de Lange, K. J. F. M. Verouden, T. J. H. Vlugt, J. Gascon and F. Kapteijn, *Chem. Rev.*, 2015, **115**, 12205–12250.
14 N. Stock and S. Biswas, *Chem. Rev.*, 2012, **112**, 933–969.
15 J. Ren, X. Dyosiba, N. M. Musyoka, H. W. Langmi, M. Mathe and S. Liao, *Coord. Chem. Rev.*, 2017, **352**, 187–219.
16 T. Ogawa, K. Iyoki, T. Fukushima and Y. Kajikawa, *Materials*, 2017, **10**, 1428–1448; S. Barman, H. Furukawa, O. Blacque, K. Venkatasan, O. M. Yaghi, G.-X. Jin and H. Berke, *Chem. Commun.*, 2011, **47**, 11882–11884.
17 H. Reinsch and N. Stock, *Dalton Trans.*, 2017, **46**, 8339–8349.
18 M. Rubio-Martinez, C. Avci-Camur, A. W. Thornton, I. Imaz, D. Maspoch and M. R. Hill, *Chem. Soc. Rev.*, 2017, **46**, 3453–3480.
19 M. Sánchez-Sánchez, N. Getachew, K. Díaz, M. Díaz-García, Y. Chebude and I. Díaz, *Green Chem.*, 2015, **17**, 1500–1509; F. Jeremias, S. K. Henninger and C. Janiak, *Dalton Trans.*, 2016, **45**, 8637–8644.
20 R. Ameloot, L. Stappers, J. Fransaer, L. Alaerts, B. F. Sels and D. E. de Vos, *Chem. Mater.*, 2009, **21**, 2580–2582.
21 W.-J. Son, J. Kim, J. Kim and W.-S. Ahn, *Chem. Commun.*, 2008, **47**, 6336–6338; N. Abdollahi, M. Y. Masoomi, P. C. Junk and J. Wang, *Ultrason. Sonochem.*, 2018, **45**, 50–56; N. A. Khan and S. H. Jhung, *Coord. Chem. Rev.*, 2015, **285**, 11–23.
22 I. Thomas-Hillman, A. Laybourn, C. Dodds and S. W. Kingman, *J. Mater. Chem. A*, 2018, **6**, 11564–11581; M. Taddei, D. A. Steitz, J. A. van Bokhoven and M. Ranocchiari, *Chem. – Eur. J.*, 2016, **22**, 3245–3249.
23 P. A. Bayliss, I. A. Ibarra, E. Pérez, S. Yang, C. C. Tang, M. Poliakoff and M. Schröder, *Green Chem.*, 2014, **16**, 3796–3802.
24 K. Užarević, T. C. Wang, S.-Y. Moon, A. M. Fidelli, J. T. Hupp, O. K. Farha and T. Friščić, *Chem. Commun.*, 2016, **52**, 2133–2136.
25 Q. Shi, Z. Chen, Z. Song, J. Li and J. Dong, *Angew. Chem., Int. Ed.*, 2011, **123**, 698–701; A. K. Das, R. S. Vemuri, I. Kutnyakov, B. P. McGrail and R. K. Motkuri, *Sci. Rep.*, 2016, **6**, 28050; J. Kim, Y.-R. Lee and W.-S. Ahn, *Chem. Commun.*, 2013, **49**, 7647–7649.
26 N. Tannert, S. Gökpinar, E. Hastürk, S. Nießing and C. Janiak, *Dalton Trans.*, 2018, **47**, 9850–9860.
27 M. Peplow, *Chem. World*, 2018, 13; S. Goldie, *Chem. World*, 2018, 5.
28 J. Park, J. D. Howe and D. S. Sholl, *Chem. Mater.*, 2017, **29**, 10487–10495.
29 T. Tian, Z. Zeng, D. Vulpe, M. E. Casco, G. Divitini, P. A. Midgley, J. Silvestre-Albero, J.-C. Tan, P. Z. Moghadam and D. Fairen-Jimenez, *Nat. Mater.*, 2018, **17**, 174–180.
30 F. Millange, C. Serre and G. Férey, *Chem. Commun.*, 2002, 822–823; T. Loiseau, C. Serre, C. Huguenard, G. Fink, F. Taulelle, M. Henry, T. Bataille and G. Férey, *Chem. – Eur. J.*, 2004, **10**, 1373–1382.
31 C. Kiener, U. Müller and M. Schubert, *Germany Pat*, WO2007/118841A2, BASF SE, 2007; C. Kiener, U. Müller and M. Schubert, *US Pat*, 12/297666, BASF SE, 2012; E. Leung, U. Müller, N. Trukhan, H. Mattenheimer and G. Cox, *US Pat*, 13/249943, BASF SE, 2012.
32 E. Alvarez, N. Guillou, C. Martineau, B. Bueken, B. Van de Voorde, C. Le Guillouzer, P. Fabry, F. Nouar, F. Taulelle, D. de Vos, J.-S. Chang, K. H. Cho, N. Ramsahye, T. Devic, M. Daturi, G. Maurin and C. Serre, *Angew. Chem., Int. Ed.*, 2015, **54**, 3664–3668.
33 H. Reinsch, M. A. van der Veen, B. Gil, B. Marszalek, T. Verbiest, D. de Vos and N. Stock, *Chem. Mater.*, 2013, **25**, 17–26.

34 A. Cadiau, J. S. Lee, D. Damasceno Borges, P. Fabry, T. Devic, M. T. Wharmby, C. Martineau, D. Foucher, F. Taulelle, C.-H. Jun, Y. K. Hwang, N. Stock, M. F. De Lange, F. Kapteijn, J. Gascon, G. Maurin, J.-S. Chang and C. Serre, *Adv. Mater.*, 2015, **27**, 4775–4780.
35 M. Gaab, N. Trukhan, S. Maurer, R. Gummaraju and U. Müller, *Microporous Mesoporous Mater.*, 2012, **157**, 131–136.
36 F. Jeremias, D. Fröhlich, C. Janiak and S. K. Henninger, *RSC Adv.*, 2014, **4**, 24073–24082.
37 D. Fröhlich, S. K. Henninger and C. Janiak, *Dalton Trans.*, 2014, **43**, 15300–15304.
38 D. Fröhlich, E. Pantatosaki, P. D. Kolokathis, K. Markey, H. Reinsch, M. Baumgartner, M. A. van der Veen, D. E. de Vos, N. Stock, G. K. Papadopoulos, S. K. Henninger and C. Janiak, *J. Mater. Chem. A*, 2016, **4**, 11859–11869.
39 W. Liang, L. Li, J. Hou, N. D. Shepherd, T. D. Bennett, D. M. D'Alessandro and V. Chen, *Chem. Sci.*, 2018, **9**, 3508–3516; L. Feng, S. Yuan, L.-L. Zhang, K. Tan, J.-L. Li, A. Kirchon, L.-M. Liu, P. Zhang, Y. Han, Y. J. Chabal and H.-C. Zhou, *J. Am. Chem. Soc.*, 2018, **140**, 2363–2372; U. Betke, M. Klaus, J. G. Eggebrecht, M. Scheffler and A. Lieb, *Microporous Mesoporous Mater.*, 2018, **265**, 43–56.
40 D. Damasceno Borges, P. Normand, A. Permiakova, R. Barbaro, N. Heymans, D. S. Galvao, C. Serre, G. De Weireld and G. Maurin, *J. Phys. Chem. C*, 2017, **121**, 26822–26832.
41 S. Couck, Y.-Y. Liu, K. Leus, G. V. Baron, P. Van der Voort and J. F. M. Denayer, *Microporous Mesoporous Mater.*, 2015, **206**, 217–225.
42 (*a*) A. Dhakshinamoorthy, N. Heidenreich, D. Lenzen and N. Stock, *CrystEngComm*, 2017, **19**, 4187–4193; (*b*) L. M. Aguirre-Díaz, D. Reinares-Fisac, M. Iglesias, E. Gutiérrez-Puebla, F. Gándara, N. Snejko and M. Á. Monge, *Coord. Chem. Rev.*, 2017, **335**, 1–27.
43 P. G. Yot, L. Vanduyfhuys, E. Alvarez, J. Rodriguez, J.-P. Itié, P. Fabry, N. Guillou, T. Devic, I. Beurroies, P. L. Llewellyn, V. Van Speybroek, C. Serre and G. Maurin, *Chem. Sci.*, 2016, **7**, 446–450.
44 (*a*) Y. Belmabkhout, R. S. Pillai, D. Alezi, O. Shekhah, P. M. Bhatt, Z. Chen, K. Adil, S. Vaesen, G. de Weireld, M. Pang, M. Suetin, A. J. Cairns, V. Solovyeva, A. Shkurenko, O. E. Talll, G. Maurin and M. Eddaoudi, *J. Mater. Chem. A*, 2017, **5**, 3293–3303; (*b*) S. Karmakar, J. Dechnik, C. Janiak and S. De, *J. Hazard. Mater.*, 2016, **303**, 10–20; (*c*) M. Mon, R. Bruno, J. Ferrando-Soria, D. Armentano and E. Pardo, *J. Mater. Chem. A*, 2018, **6**, 4912–4947.
45 M. J. Kalmutzki, C. S. Diercks and O. M. Yaghi, *Adv. Mater.*, 2018, **30**, 1704304; H. Kim, S. Yang, S. R. Rao, S. Narayanan, E. A. Kapustin, H. Furukawa, A. S. Umans, O. M. Yaghi and E. N. Wang, *Science*, 2017, **356**, 430–434; F. Trapani, A. Polyzoidis, S. Loebbecke and C. G. Piscopo, *Microporous Mesoporous Mater.*, 2016, **230**, 20–24.
46 E. Elsayed, R. Al-Dadah, S. Mahmoud, P. A. Anderson, A. Elsayed and P. G. Youssef, *Desalination*, 2017, **406**, 25–36.
47 A. Weiss, N. Reimer, N. Stock, M. Tiemann and T. Wagner, *Phys. Chem. Chem. Phys.*, 2015, **17**, 21634–21642.
48 N. Reimer, B. Bueken, S. Leubner, C. Seidler, M. Wark, D. De Vos and N. Stock, *Chem. – Eur. J.*, 2015, **21**, 12517–12524.
49 S. Karmakar, S. Bhattarcharjee and S. De, *J. Environ. Chem. Eng.*, 2017, **5**, 6087–6097.
50 M. F. de Lange, T. Zeng, T. J. H. Vlugt, J. Gascon and F. Kapteijn, *CrystEngComm*, 2015, **17**, 5911–5920; M. F. de Lange, C. P. Ottevanger, M. Wiegman, T. J. H. Vlugt, J. Gascon and F. Kapteijn, *CrystEngComm*, 2015, **17**, 281–285.
51 J. Canivet, A. Fateeva, Y. Guo, B. Coasne and D. Farrusseng, *Chem. Soc. Rev.*, 2014, **53**, 5594–5617.
52 N. C. Burtch, H. Jasuja and K. S. Walton, *Chem. Rev.*, 2014, **114**, 10575–10612.
53 N. Tannert, S.-J. Ernst, C. Jansen, S. Nießing, H.-J. Bart, S. K. Henninger and C. Janiak, *J. Mater. Chem. A*, 2018, **6**, 17706–17712; M. F. de Lange, B. L. van Velzen, C. P. Ottevanger, K. J. F. M. Verouden, L.-C. Lin, T. J. H. Vlugt, J. Gascon and F. Kapteijn, *Langmuir*, 2015, **31**, 12783–12796.
54 D. Lenzen, P. Bendix, H. Reinsch, D. Fröhlich, H. Kummer, M. Möllers, P. P. C. Hügenell, R. Gläser, S. Henninger and N. Stock, *Adv. Mater.*, 2017, **30**, 1705869.
55 H. Kummer, F. Jeremias, A. Warlo, G. Füldner, D. Fröhlich, C. Janiak, R. Gläser and S. K. Henninger, *Ind. Eng. Chem. Res.*, 2017, **56**, 8393–8398.
56 S. Gökpinar, T. Diment and C. Janiak, *Dalton Trans.*, 2017, **46**, 9895–9900.
57 H. Reinsch, *Eur. J. Inorg. Chem.*, 2016, 4290–4299; H. Reinsch, S. Waitschat, S. M. Chavan, K. P. Lillerud and N. Stock, *Eur. J. Inorg. Chem.*, 2016, 4490–4498.
58 I. Ahmed, J. Jeon, N. A. Khan and S. H. Jhung, *Cryst. Growth Des.*, 2012, **12**, 5878–5881.
59 N. Yang, M. Yue and Y. Wang, *Prog. Chem.*, 2012, **24**, 253–261.
60 M. Thommes, K. Kaneko, A. V. Neimark, J. P. Olivier, F. Rodriguez-Reinoso, J. Rouquerol and K. S. Sing, *Pure Appl. Chem.*, 2015, **87**, 1051–1069.
61 Y. Wang, Q. Qu, G. Liu, V. S. Battaglia and H. Zheng, *Nano Energy*, 2017, **39**, 200–210.
62 H. Jin, A. Wollbrink, R. Yao, Y. Li, J. Caro and W. Yang, *J. Membr. Sci.*, 2016, **513**, 40–46.
63 D. Damasceno Borges, P. Normand, A. Permiakova, R. Babarao, N. Heymans, D. S. Galvao, C. Serre, G. de Weireld and G. Maurin, *J. Phys. Chem. C*, 2017, **121**, 26822–26832.
64 D. D. Borges, G. Maurin and D. S. Galvao, *MRS Adv.*, 2017, **2**, 519–524.
65 J. Caro, X. Wu, W. Wan, J. Jiang and A. Huang, *Angew. Chem., Int. Ed.*, 2018, **57**, 1–5.
66 M. Rubio-Martinez, T. D. Hadley, M. P. Batten, K. Constanti-Carey, T. Barton, D. Marley, A. Mönch, K.-S. Lim and M. R. Hill, *ChemSusChem*, 2016, **9**, 938–941.
67 http://www.moftechnologies.com/products/(10-12-2018).

68 E. Elsayed, R. AL-Dadah, S. Mahmoud, A. Elsayed and P. A. Anderson, *Appl. Therm. Eng.*, 2016, **99**, 802–812.
69 H. W. B. Teo, A. Chakraborty, Y. Kitagawa and S. Kayal, *Int. J. Heat Mass Transfer*, 2017, **114**, 621–627.
70 H. W. B. Teo, A. Chakraborty and S. Kayal, *Microporous Mesoporous Mater.*, 2018, **272**, 109–116.
71 S. Kayal, A. Chakraborty and H. W. B. Teo, *Mater. Lett.*, 2018, **221**, 165–167.
72 L. Zhou, X. Zhang and Y. Chen, *Mater. Lett.*, 2017, **197**, 224–227.
73 R. Kashanaki, H. Ebrahimzadeh and M. Moradi, *New J. Chem.*, 2018, **42**, 5806–5813.
74 D. Crawford, J. Casaban, R. Haydon, N. Giri, T. McNally and S. L. James, *Chem. Sci.*, 2015, **6**, 1645–1649.
75 B. Bozbiyik, J. Lannoeye, D. E. de Vos, G. V. Baron and J. F. M. Denayer, *Phys. Chem. Chem. Phys.*, 2016, **18**, 3294–3301.
76 J. A. Coelho, A. M. Ribeiro, A. F. P. Ferreira, S. M. P. Lucena, A. E. Rodrigues and D. C. S. de Azevedo, *Ind. Eng. Chem. Res.*, 2016, **55**, 2134–2143.
77 H. Reinsch, S. Waitschat and N. Stock, *Dalton Trans.*, 2013, **42**, 4840–4847.
78 V. B. López-Cervantes, E. Sánchez-González, T. Jurado-Vázquez, A. Tejeda-Cruz, E. González-Zamora and I. A. Ibarra, *Polyhedron*, 2018, **155**, 163–169.
79 A. Permyakova, O. Skrylnyk, E. Courbon, M. Affram, S. Wang, U.-H. Lee, A. H. Valekar, F. Nouar, G. Mouchaham, T. Devic, G. de Weireld, J.-S. Chang, N. Steunou, M. Frère and C. Serre, *ChemSusChem*, 2017, **10**, 1419–1426.
80 A. Permyakova, S. Wang, E. Courbon, F. Nouar, N. Heymans, P. D'Ans, N. Barrier, P. Billemont, G. de Weireld, N. Steunou, M. Frère and C. Serre, *J. Mater. Chem. A*, 2017, **5**, 12889–12898.
81 R. Cai, Y. Liu, S. Gu and Y. Yan, *J. Am. Chem. Soc.*, 2010, **132**, 12776–12777.
82 B.-W. Long, L.-S. Wang and J.-S. Wu, *J. Chem. Eng. Data*, 2005, **50**, 136–137.
83 M. Wahiduzzaman, D. Lenzen, G. Maurin, N. Stock and M. T. Wharmby, *Eur. J. Inorg. Chem.*, 2018, 3626–3632.
84 S. M. T. Abtab, D. Alezi, P. M. Bhatt, A. Shkurenko, Y. Belmabkhout, H. Aggarwal, Ł. J. Weseliński, N. Alsadun, U. Samin, M. N. Hedhili and M. Eddaoudi, *Chem*, 2017, **4**, 94–105.

ELECTRONIC SUPPORTING INFORMATION (ESI)

Robust synthesis routes and porosity of Al-based metal-organic frameworks Al-fumarate, CAU-10-H and MIL-160†

*Niels Tannert, Christian Jansen, Sandra Nießing and Christoph Janiak**

*Institut für Anorganische Chemie und Strukturchemie, Heinrich-Heine-Universität Düsseldorf, Universitätsstraße 1, 40225 Düsseldorf, Germany. *E-mail: janiak@uni-duesseldorf.de*

Emails:

niels.tannert@hhu.de; christian.jansen@hhu.de; sandra.niessing@hhu.de

Keywords
Metal-Organic Frameworks, Synthesis Optimization, Dry-Gel Conversion, Al-MOFs, [Al(OH)(Linker)], Aluminum fumarate (Alfum), CAU-10-H, MIL-160, Solvent Re-use

Table of Contents

S1. Materials and equipment

All chemicals were used as received by the supplier (*cf.* Table 1).

Table 1: Used chemicals, supplier and purities.

Chemical	Supplier	Purity
$AlCl_3$ * 6 H_2O	Janssen Chimica	99%
$Al(SO)_4$*18H_2O	AppliChem	not specified
$Al(OH)(acetate)_2$	AlfaAesar	not specified
Basolite™ *A520*	Sigma Aldrich	not specified
Dimethylformamide	Fischer Chemicals	99.99
Ethanol	Sigma Aldrich	> 99.8%
Fumaric acid	Alfa Aesar	99%
2,5-furandicarboxylic acid	OxChem	95%
Isopththalic acid	AlfaAesar	99%
NaOH (microgranulate)	Chem Solute	not specified

Dry-gel conversion, DGC inlays were self-built. The full equipment was made of Teflon. The holes in DGC sieves had a diameter of 0.5 mm. The ring inlays, shown in Figure S1, can have various heights for height adjustment. We thank the mechanics workshop of Heinrich-Heine-University Düsseldorf for the manufacturing of the DGC container set.

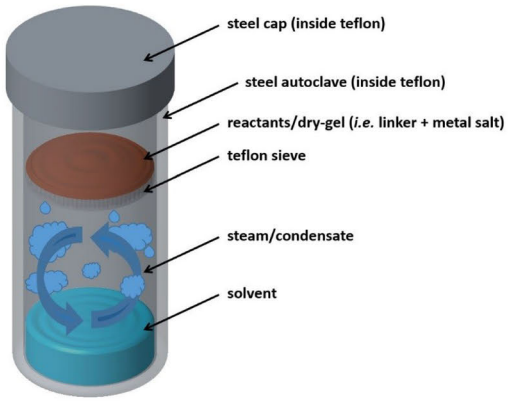

Figure S1 *Top left: Full Teflon autoclave set for DGC with container, three inlay rings for height adjustment, DGC sieve and cap (from left to right). Top right: Close-up view of a DGC sieve. Bottom: Schematic illustration of the working principle of dry-gel conversion.*

S2. Additional information on Alfum, CAU-10-H and MIL-160

Aluminum fumarate (Alfum)

Aluminum fumarate was first described in the patent literature in 2013.[1,2] It was the first MOF synthesized on a ton scale and it is marketed by BASF under the name *Basolite*™ *A520*. Figure S2 shows the structural features of Alfum.

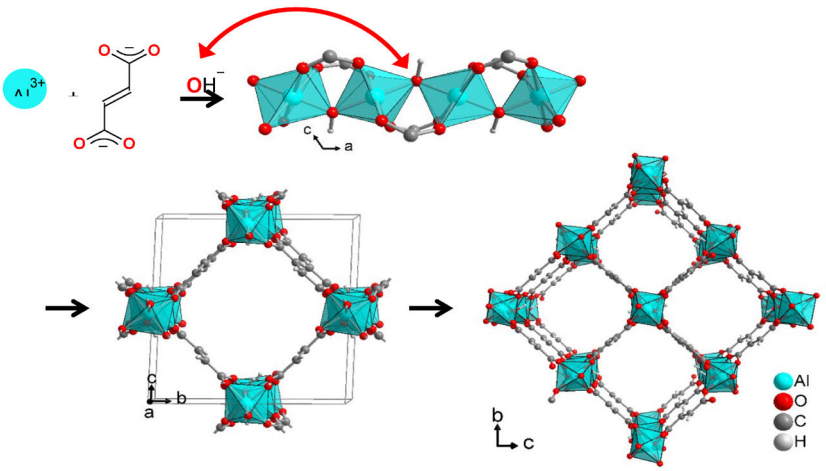

Figure S2 *Al^{3+}, hydroxide and fumarate building blocks of Alfum, from which in analogy to the structure of MIL-53 a chain of trans-μ-OH-connected vertex-bridged {AlO_6} octahedra is formed. These chains run along the crystallographic a direction and are connected through the fumarate linkers along the bc diagonal. Graphic produced by software Diamond[3] from cif-file for Basolite A520 (CSD-Refcode DOYBEA).[4]*

Aluminum fumarate resembles the MIL-53 topology with its infinite Al-OH-Al chains, bridged by fumarate linkers. It presents the chemical formula $[Al(OH)(O_2C\text{-}CH{=}CH\text{-}CO_2) \cdot n\ H_2O]_m$ and displays microporous, rhombohedral channels with *ca.* 5.7 x 6.0 Å^2 free dimensions.[4,5] The BET surface area (*Brunauer-Emmett-Teller*) ranges from 925 to 1212 m^2 g^{-1}.[6,7] The material exhibits high hydrothermal stability, which is attributed to its aqueous synthesis route and the good hydrolytic stability of the Al-carboxylate bond.

Besides the patented solution-based route, it can as well be prepared in continuous flow reactors,[8] or *via* mechanochemical procedures such as extrusion.[9] Thereby, 27 000 kg m^{-3} day^{-1} space-time-yields (STY) were calculated to be feasible.[10] Continuous flow methods achieved even STYs up to 97 159 kg m^{-3} day^{-1} at 5.6 kg h^{-1} and *ca.* 1000-1100 m^{2}g^{-1}.[8] Other synthetic routes comprise for example spray drying,[11] and our recently proposed technique or microwave assisted-dry gel conversion, MW-DGC.[12]

Aluminum fumarate is one of the most promising MOFs for application,[4,13,14] mostly due to its hydrothermal stability and water sorption properties, but also due to an environmentally friendly synthesis route with water as single solvent, inexpensive and abundant metal cation, and a "green" linker from renewable biomass.[15,16] Gaab *et al.* proved its applicability as storage container for natural gas, used as fuel in a vehicle, with 40% increased cruising distance.[16] Moreover, Alfum was proven to be a very promising candidate for implementation as adsorbent in heat transformation applications,[14,17] since it displays suitable water sorption characteristics (desired s-shaped isotherm with steep loading lift, absence of hysteresis, reasonable isosteric heat of adsorption).[4,14] Alfum is applicable as adsorbent for removal of fluoride from water,[18] in desalination processes,[7] in mixed-

matrix-membranes (MMMs)[19] and it was proposed to be the best porous solid for mechanical energy storage.[20] Latest contributions to Alfum included defective engineering/modulation,[21] modelling,[22] adsorption of volatile organic compounds,[6] and kinetics of water sorption.[23]

CAU-10-H

In 2012 Reinsch and co-workers described the synthesis of CAU-10-H (Fig. S3) (CAU = *Christian-Albrechts-Universität*) out of a water-dimethylformamide (DMF) mixture of isophthalic acid and aluminum sulfate, applying solvothermal conditions (135 °C, 12 h).[24]

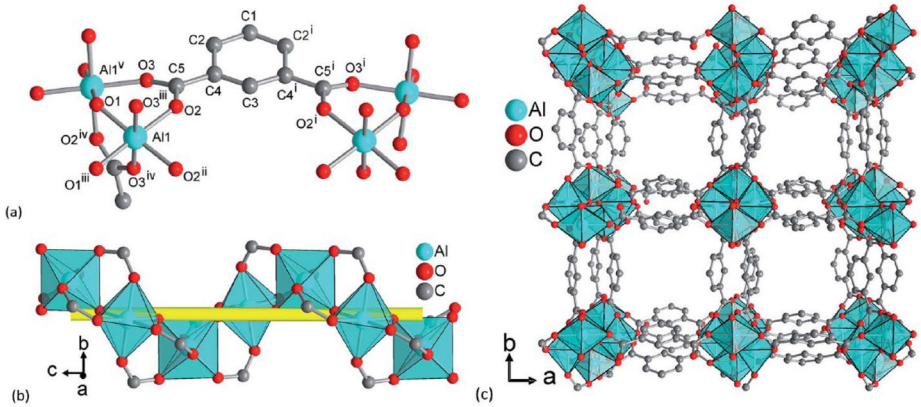

Figure S3 *Structural elements in CAU-10-H. (a) Extended asymmetric unit with full Al coordination spheres and full ligand bridging mode. Symmetry transformations i = 1–x, y, z; ii = x, –y, –z; iii = 0.25+y, 0.25–x, –0.25+z; iv = 0.25+y, –0.25+x, 0.25–z; v = 0.25–y, –0.25+x, 0.25+z. (b) The inorganic building unit, a fourfold helical chain of cis vertex-bridged {AlO_6}-polyhedra winding around the four-fold axis (yellow line). (c) The 3D framework structure exhibits square shaped one-dimensional channels. Graphic produced by software Diamond[3] from cif-file for CAU-10-H (CSD-Refcode OQOBUT).[25]*

CAU-10-H features *cis*-μ-OH connected {AlO_6}-polyhedra, that form helical chains, running along the crystallographic *c* direction. Along *a* and *b* the chains are connected by the isophthalate linkers. The material builds up one-dimensional channels, resulting in a surface area of 535-625 $m^2\ g^{-1}$ (BET) and a pore volume of 0.25 $cm^3\ g^{-1}$.[24] The latter is in good agreement with single point adsorption simulation by force-field methods (0.23 $cm^3\ g^{-1}$),[26] although theoretical calculations suggested a surface area of 713 $m^2\ g^{-1}$ and a pore volume of 0.43 $cm^3\ g^{-1}$ (Cadiau *et al.* [27]: 0.35 $cm^3\ g^{-1}$).[28] The 5-position of the aromatic ring can bear various substituents, yielding chemical formulas corresponding to $[Al(OH)(O_2C\text{-}C_6XH_3\text{-}CO_2) \cdot n\ H_2O]_m$ (with X = -H, -OH, $-OCH_3$, $-NH_2$, $-NO_2$, $-CH_3$, -F, -Br, $-SO_3H$),[24,29,30,31] going along with variegated properties of the resulting material (*e.g.* sorption characteristics of water vapor, CO_2- and H_2). Also various mixed-linker approaches were carried out.[30,31,32]

In terms of different synthesis routes, CAU-10-MOFs were always obtained out of water-DMF mixtures under solvothermal conditions (135 °C, 12 h). Besides the common approach, de Lange *et al.* obtained CAU-10-H in a microwave synthesis within 1 h heating.[33] Although the synthesis requires DMF, both aluminum sources and isophthalic acid are produced on an industrial scale, are toxicologically harmless and rather inexpensive.[33,34] Therefore, CAU-10-H represents a most marketable material.[33] To the best of our knowledge, there is no report for alternative synthesis routes to the solvothermal and microwave conditions.

CAU-10-H is a very good candidate for heat transformation applications,[17] as it represents nearly perfect hydrothermal stability,[35] which is underlined by no structural degradation of the material over 700 repeated adsorption/desorption cycles.[35] It has a higher volumetric adsorption capacity (0.38 $cm^3\ g^{-1}$ at $pp_0^{-1} = 0.26$)[24] and thermodynamic efficiency for water than commercially adsorbents (*e.g.* SAPO-34),[33,36] possessing an isosteric heat of adsorption of *ca.* 54 kJ mol^{-1} (theoretically -49 kJ mol^{-1}, predicted by GCMC simulations.[37] Accordingly, dense coatings of CAU-10-H were employed on different substrates with the purpose of heat transformation.[38] Due to its properties, it was also addressed to be suitable for humidity sensing by impedance spectroscopy,[31] investigated in terms of proton conductivity and catalytic activity,[32] as well as gas adsorption and separation.[39]

MIL-160

A rather new Al-MOF material is MIL-160 (*Matériaux Institut Lavoisier*), which was described by Cadiau *et al.* in 2015.[27] They obtained the MOF by applying reflux conditions for aqueous solutions of 2,5-furandicarboxylic acid, sodium hydroxide and aluminum chloride. MIL-160 is constructed identical to CAU-10-H by cis-μ-OH-connected, vertex-sharing {AlO_6} octahedra, that form helical chains, which are then joined by the linker 2,5-furandicarboxylate (Fig. S4).

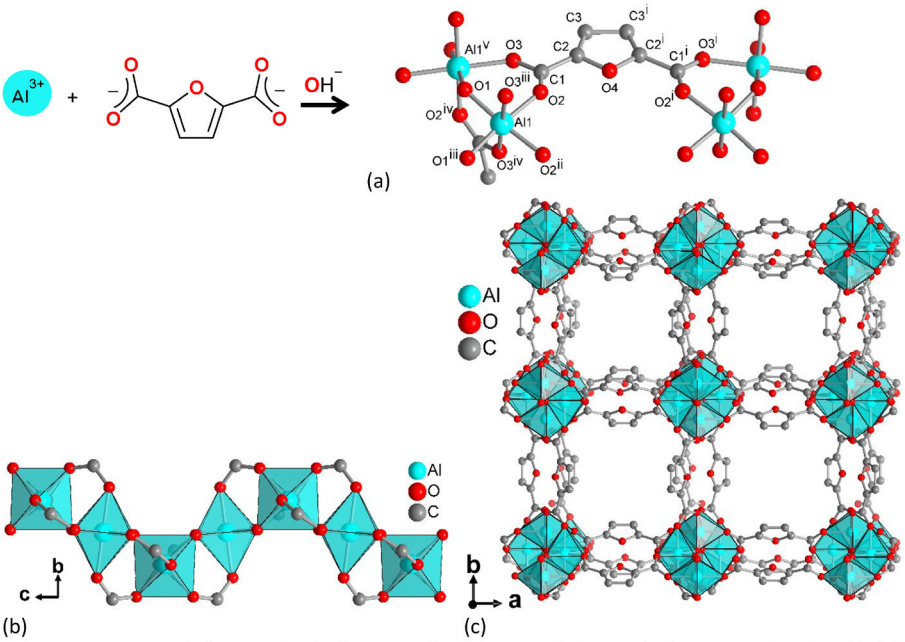

Figure S4 *Structural elements in the framework of MIL-160: (a) Extended asymmetric unit with full Al coordination spheres and full ligand bridging mode. Symmetry transformations i = 1–x, y, z; ii = x, –y, –z; iii = 0.25+y, 0.25–x, –0.25+z; iv = 0.25+y, –0.25+x, 0.25–z; v = 0.25–y, –0.25+x, 0.25+z. (b) Helical chains of cis vertex-bridged {AlO_6}-polyhedra and (c) surrounded by the carboxylates ligands, to yield square-shaped one dimensional channels; compare to the closely related structure of CAU-10-H in Fig. S3. Graphic produced by software Diamond[3] from cif-file for MIL-160 (CSD-Refcode PIBZOS).[40]*

MIL-160 is reported to be isostructural to CAU-10-H, having chains of {AlO_6}-polyhedra that are surrounded by linker molecules.[27] This results in a chemical formula of $[Al(OH)(O_2C\text{-}C_4H_2O\text{-}CO_2) \cdot n\ H_2O]_m$ and microporous square-shaped channels of 5 Å edge length.[27,41] The material exhibits a surface

area of 1070 $m^2 g^{-1}$ and a pore volume of 0.40 $cm^3 g^{-1}$ from $AlCl_3$ and NaOH (theoretically: 1250 $m^2 g^{-1}$, 0.48 $cm^3 g^{-1}$),[27] respectively 1150 $m^2 g^{-1}$ and 0.46 $cm^3 g^{-1}$, from $Al(OH)(CH_3COO)_2$,41 although very recent theoretical calculations suggested a surface area of 776 $m^2 g^{-1}$ and a pore volume of 0.45 $cm^3 g^{-1}$.[28]

The hydrophilic character of the MOF is also due to the heteroatom in the furan moiety of the linker. This resulted in a highly hydrothermally stable material with promising water sorption characteristics. Very recently, the MOF was advantageously synthesized from basic aluminum acetate (*i.e.* $Al(OH)(CH_3COO)_2$) in a scale-up.[41] The synthesis route of MIL-160 is environmentally friendly, since the linker is already on the way to being produced from renewable biomass *via* oxidation of 5-(hydroxy-methyl)furfural (5-HMF) on a very large industrial scale and water is the single solvent.[42,43] Hence, the production costs for MIL-160 may decline further within the next years. MIL-160 is quite a new material, there are – to the best of our knowledge - only the aforementioned two reports for different synthesis routes, mainly varying in the aluminum source and scale of synthesis.[27,41] A most recent and third report on MIL-160 focusses on structural refinements and flexibility upon N_2 and H_2O sorption.[40]

Cadiau *et al.* denoted MIL-160 as the most promising Al-MOF for heat pump applications.[27] In comparison to CAU-10-H, slightly higher desorption temperatures are required; nevertheless, it outperforms both Alfum and CAU-10-H in terms of gravimetric water loadings.[27] In detail, it submits distinctively higher performance in terms of the loading spread (*i.e.* mass of adsorbed water vapor per mass of adsorbent) for the desired lift phase 1 (*i.e.* according to Henninger *et al.*: desired loading at low pp_0^{-1}, depending on driving temperature).[27,44,45,46] Permyakova *et al.* investigated MIL-160 with respect to shaping into granules and heat reallocation.[41] Their report suggests similar properties to the ones reported by Cadiau *et al.* and underlines the suitability of the material for heat transformation application.

S3. Reflux-based syntheses for comparison

Alfum was synthesized according to the patented approach:[1,2] for solution 1, sodium hydroxide (0.2803 g, 7.01 mmol, 4 eq) and fumaric acid (0.3863 g, 3.33 mmol, 2 eq) were dissolved in water (6 mL). For solution 2, aluminum sulfate octadecahydrate (1.171 g, 1.76 mmol, 1 eq) was diluted in water (5 mL) at 60 °C. Over the course of 30 min, solution 1 was dropped into solution 2 and further stirred (60 °C, 2 h). The product was centrifuged (2000 U/min, 15 min) and decanted, subsequently washed with water (50 mL). The latter step was repeated. Subsequently, the product was dried overnight (80 °C, 1 - 10 mbar), yielding a white powder (0.4104 g, 74% yield, BET = 1131 $m^2 g^{-1}$).

CAU-10-H was synthesized according to a protocol by Reinsch *et al.*: Aluminum sulfate octadecahydrate (0.8005 g, 4.82 mmol, 1 eq) and isophthalic acid (0.2000 g, 5.00 mmol, 1 eq) were transferred into a Teflon-lined autoclave (37 mL reactor volume) with water (4 mL) and DMF (1 mL). After 5 min of stirring, the autoclave was closed and heated (3 h heating, 12 h at 135 °C, 1 h cooling). Afterwards, the reaction mixture was decanted, washed with water three times (30 mL each), centrifuged (2000 U/min, 30 min), decanted and re-dispersed each time. Subsequently, the product was dried overnight (80 °C, 1 - 10 mbar), yielding a white powder (0.2122 g, 42% yield, BET = 435 $m^2 g^{-1}$).

MIL-160 was synthesized in a modified protocol of Cadiau *et al.*, who used 1 eq NaOH, whereas we used 2 eq NaOH to deprotonate the linker fully: 2,5-furandicarboxylic acid (0.3123 g, 2.0 mmol, 1 eq) and sodium hydroxide (0.1603 g, 4.0 mmol, 2 eq) were converted in water (10 mL, 2 h). Aluminum chloride hexahydrate (0.4826 g, 2.0 mmol, 1 eq) was added and reflux (24 h, 100 °C) was initiated. After decantation, the product was washed with water three times (30 mL each), centrifuged (2000 U/min, 30 min), decanted and re-dispersed each time. Subsequently, the product was dried overnight (80 °C, 1 - 10 mbar), yielding a white powder (0.2184 g, 55% yield, BET = 1178 $m^2 g^{-1}$).

S4. Dry-gel conversions: Syntheses optimizations

In order to find reliable DGC synthesis routes for the three presented MOFs, we carried out profound synthesis optimizations for each MOF individually: In a first approach, we assumed the stated synthesis temperatures and conversion times according to the reflux-based syntheses described in the literature for each MOF. Subsequently, we varied the temperature to one elevated and one lower level to find an optimal synthesis temperature. By applying the most suitable temperature, we varied time by choosing one longer and one shorter protocol.

The details and results of these time and temperature variations are summarized in Table S2, S4 and S7 for Alfum, CAU-10-H and MIL-160, respectively.

In each synthesis, one approach was carried with dry starting materials, another with wetted reactants. Thereby, we checked if wetting of the precursor mixture before conversion may be supportive for crystallinity and/or BET surface areas of the presented MOFs (*cf.* Figures S5-S12 and Figures S17-S19). Thereby, we were able to assure best and most efficient DGCs of the presented MOFs. The criteria yield, crystallinity, BET surface area and pore volume, as well as water sorption behavior were taken into account for synthesis optimizations towards first DGCs of Al-MOFs in general.

For CAU-10-H the DGC synthesis is based on the autoclave solution synthesis of Reinsch *et al.* using the same molar ratios of aluminum sulfate and isophthalic acid.[24] The reaction conditions of 135 °C for 12 h were taken as a starting point and the time and temperature were systematically varied.

For MIL-160 we have used the reaction conditions of Cadiau *et al.* as a starting point, that is 100 °C and 24 h.[27] From this starting point we have chosen a higher and lower temperature and at the medium temperature we varied the reaction to longer and shorter times than the literature. Furthermore, we investigate the use of 1 or 2 eq NaOH.

PXRD plots and nitrogen sorption isotherms that were taken into account as key-factors for synthesis optimizations are depicted in the respective Sections S4.1, S4.2 and S4.3.

Alfum

In a typical synthetic procedure, we rapidly ground aluminum sulfate octadecahydrate ($Al_2(SO_4)_3 \cdot 18H_2O$) (159 mg, 0.24 mmol, 1 eq), fumaric acid (H_2fum) (53 mg, 0.48 mmol, 2 eq) and sodium hydroxide (NaOH) (40 mg, 1.02 mmol, 4 eq) in a mortar and placed the mixture on a DGC sieve with water (5 mL) at the bottom of a Teflon reactor. DGCs were carried out at varying temperatures and conversion times. The white products were washed three times with water (10 mL each), recovered by centrifugation each time and finally dried under vacuum (80 °C, 24 h).

CAU-10-H

In a typical synthetic procedure, we rapidly ground aluminum sulfate octadecahydrate ($Al_2(SO_4)_3 \cdot 18H_2O$) (169 mg, 0.25 mmol, 1 eq), isopththalic acid (H_2BDC) (42 mg, 0.25 mmol, 1eq) in a mortar and placed the mixture on a DGC sieve with water/DMF (4:1, 5 mL) at the bottom of a Teflon reactor. DGCs were carried out at varying temperatures and conversion times. The white products were washed three times with water (10 mL each), recovered by centrifugation each time and finally dried under vacuum (80 °C, 24 h).

MIL-160

In a typical synthetic procedure, we rapidly ground aluminum chloride hexahydrate ($AlCl_3 \cdot 6H_2O$) (144 mg, 0.60 mmol, 1 eq), 2,5-furandicarboxylic acid (H_2FDC) (93 mg, 0.60 mmol, 1 eq) and sodium hydroxide (NaOH) (1 or 2 eq) in a mortar and placed the mixture on a DGC sieve with water (5 mL) at the bottom of a Teflon reactor. DGCs were carried out at varying temperatures and conversion times. The white products were washed three times with water (10 mL each), recovered by centrifugation each time and finally dried under vacuum (80 °C, 24 h).

S4.1. Dry-gel conversions: Synthesis optimizations -- Alfum

Table S2. Listing of DGC synthesis conditions for Alfum with variation of time and temperature.

Aluminum fumarate						
Conditions	**Not Moistened**					
80 °C; 12 h	**Starting Materials**	**Initial Weight**	**Molar Amount**	**Equivalents**	**Product**	
	Aluminum Sulfate	0.1559 g	0.23 mmol	1 eq	**Yield**	0.0516 g (70 %)
	Fumaric acid	0.0542 g	0.47 mmol	2 eq		
	NaOH	0.0400 g	1.00 mmol	4 eq	**Surface**	630 m^2/g
	Water	2 ml	-	-		
100 °C; 12 h	**Starting Materials**	**Initial Weight**	**Molar Amount**	**Equivalents**	**Product**	
	Aluminum Sulfate	0.1597 g	0.24 mmol	1 eq	**Yield**	0.0524 g (69 %)
	Fumaric acid	0.0555 g	0.48 mmol	2 eq		
	NaOH	0.0409 g	1.02 mmol	4 eq	**Surface**	795 m^2/g
	Water	2 ml	-	-		
120 °C; 12 h	**Starting Materials**	**Initial Weight**	**Molar Amount**	**Equivalents**	**Product**	
	Aluminum Sulfate	0.1571 g	0.24 mmol	1 eq	**Yield**	0.0609 g (82 %)
	Fumaric acid	0.0546 g	0.47 mmol	2 eq		
	NaOH	0.0403 g	1.01 mmol	4 eq	**Surface**	749 m^2/g
	Water	2 ml	-	-		
100 °C; 6 h	**Starting Materials**	**Initial Weight**	**Molar Amount**	**Equivalents**	**Product**	
	Aluminum Sulfate	0.1573 g	0.24 mmol	1 eq	**Yield**	0.0500 g (67 %)
	Fumaric acid	0.0547 g	0.47 mmol	2 eq		
	NaOH	0.0404 g	1.01 mmol	4 eq	**Surface**	1037 m^2/g
	Water	2 ml	-	-		
100 °C; 24 h	**Starting Materials**	**Initial Weight**	**Molar Amount**	**Equivalents**	**Product**	
	Aluminum Sulfate	0.1590 g	0.24 mmol	1 eq	**Yield**	0.0532 g (71 %)
	Fumaric acid	0.0553 g	0.48 mmol	2 eq		
	NaOH	0.0408 g	1.02 mmol	4 eq	**Surface**	1129 m^2/g
	Water	2 ml	-	-		
Conditions	**Moistened**					
80 °C; 12 h	**Starting Materials**	**Initial Weight**	**Molar Amount**	**Equivalents**	**Product**	
	Aluminum Sulfate	0.1550 g	0.23 mmol	1 eq	**Yield**	0.0468 g (64 %)
	Fumaric acid	0.0539 g	0.46 mmol	2 eq		
	NaOH	0.0397 g	0.99 mmol	4 eq	**Surface**	1004 m^2/g
	Water	1.8 + 0.2 ml	-	-		
100 °C; 12 h	**Starting Materials**	**Initial Weight**	**Molar Amount**	**Equivalents**	**Product**	
	Aluminum Sulfate	0.1593 g	0.24 mmol	1 eq	**Yield**	0.0460 g (61 %)
	Fumaric acid	0.0554 g	0.48 mmol	2 eq		
	NaOH	0.0408 g	1.02 mmol	4 eq	**Surface**	604 m^2/g
	Water	1.8 + 0.2 ml	-	-		
120 °C; 12 h	**Starting Materials**	**Initial Weight**	**Molar Amount**	**Equivalents**	**Product**	
	Aluminum Sulfate	0.1564 g	0.23 mmol	1 eq	**Yield**	0.0663 g (89 %)
	Fumaric acid	0.0544 g	0.47 mmol	2 eq		
	NaOH	0.0402 g	1.01 mmol	4 eq	**Surface**	577 m^2/g
	Water	1.8 + 0.2 ml	-	-		
100 °C; 6 h	**Starting Materials**	**Initial Weight**	**Molar Amount**	**Equivalents**	**Product**	
	Aluminum Sulfate	0.1591 g	0.24 mmol	1 eq	**Yield**	0.0435 g (58 %)
	Fumaric acid	0.0553 g	0.48 mmol	2 eq		
	NaOH	0.0409 g	1.02 mmol	4 eq	**Surface**	1284 m^2/g
	Water	1.8 + 0.2 ml	-	-		
100 °C; 24 h	**Starting Materials**	**Initial Weight**	**Molar Amount**	**Equivalents**	**Product**	
	Aluminum Sulfate	0.1590 g	0.24 mmol	1 eq	**Yield**	0.0280 g (37 %)
	Fumaric acid	0.0553 g	0.48 mmol	2 eq		
	NaOH	0.0408 g	1.02 mmol	4 eq	**Surface**	575 m^2/g
	Water	1.8 + 0.2 ml	-	-		

Section S4.1.1. Dry-gel conversions: Synthesis optimizations -- Alfum solvent re-use

Table S3. Listing of DGC synthesis conditions for Alfum and solvent re-use.

Aluminum fumarate						
Conditions	**Not moistened**					
100 °C; 6 h	**Starting Materials**	**Initial Weight**	**Molar Amount**	**Equivalents**	**Product**	
	Aluminum Sulfate	0.1676 g	0.25 mmol	1 eq	**Yield**	0.0386 g (49 %)
	Fumaric acid	0.0587 g	0.51 mmol	2 eq		
	NaOH	0.0406 g	1.02 mmol	4 eq	**Surface**	924 m^2/g
	Water	2 ml	-	-		
100 °C; 6 h	**Starting Materials**	**Initial Weight**	**Molar Amount**	**Equivalents**	**Product**	
	Aluminum Sulfate	0.1670 g	0.25 mmol	1 eq	**Yield**	0.0326 g (41 %)
	Fumaric acid	0.0579 g	0.50 mmol	2 eq		
	NaOH	0.0423 g	1.06 mmol	4 eq	**Surface**	1076 m^2/g
	Water	2 ml	-	-		
100 °C; 6 h	**Starting Materials**	**Initial Weight**	**Molar Amount**	**Equivalents**	**Product**	
	Aluminum Sulfate	0.1672 g	0.25 mmol	1 eq	**Yield**	0.0390 g (49 %)
	Fumaric acid	0.0588 g	0.51 mmol	2 eq		
	NaOH	0.0405 g	1.01 mmol	4 eq	**Surface**	1045 m^2/g
	Water	2 ml	-	-		
100 °C; 6 h	**Starting Materials**	**Initial Weight**	**Molar Amount**	**Equivalents**	**Product**	
	Aluminum Sulfate	0.1673 g	0.25 mmol	1 eq	**Yield**	0.0364 g (46 %)
	Fumaric acid	0.0582 g	0.50 mmol	2 eq		
	NaOH	0.0437 g	1.09 mmol	4 eq	**Surface**	1032 m^2/g
	Water	2 ml	-	-		
Conditions	**Moistened**					
100 °C; 6 h	**Starting Materials**	**Initial Weight**	**Molar Amount**	**Equivalents**	**Product**	
	Aluminum Sulfate	0.1673 g	0.25 mmol	1 eq	**Yield**	0.0377 g (48 %)
	Fumaric acid	0.0592 g	0.51 mmol	2 eq		
	NaOH	0.0410 g	1.02 mmol	4 eq	**Surface**	983 m^2/g
	Water	1.8 + 0.2 ml	-	-		
100 °C; 6 h	**Starting Materials**	**Initial Weight**	**Molar Amount**	**Equivalents**	**Product**	
	Aluminum Sulfate	0.1650 g	0.25 mmol	1 eq	**Yield**	0.0413 g (53 %)
	Fumaric acid	0.0579 g	0.50 mmol	2 eq		
	NaOH	0.0422 g	1.06 mmol	4 eq	**Surface**	991 m^2/g
	Water	1.8 + 0.2 ml	-	-		
100 °C; 6 h	**Starting Materials**		**Molar Amount**	**Equivalents**	**Product**	
	Aluminum Sulfate	0.1661 g	0.25 mmol	1 eq	**Yield**	0.0180 g (23 %)
	Fumaric acid	0.0586 g	0.50 mmol	2 eq		
	NaOH	0.0401 g	1.00 mmol	4 eq	**Surface**	1189 m^2/g
	Water	1.8 + 0.2 ml	-	-		
100 °C; 6 h	**Starting Materials**		**Molar Amount**	**Equivalents**	**Product**	
	Aluminum Sulfate	0.1691 g	0.25 mmol	1 eq	**Yield**	0.0404 g (50 %)
	Fumaric acid	0.0590 g	0.51 mmol	2 eq		
	NaOH	0.0427 g	1.07 mmol	4 eq	**Surface**	1089 m^2/g
	Water	1.8 + 0.2 ml	-	-		

S4.2. Dry-gel conversions: Synthesis optimizations -- CAU-10-H

Table S4. Listing of DGC synthesis conditions for CAU-10-H with variation of time and temperature.

CAU-10-H						
Conditions	**Not Moistened**					
115 °C; 12 h	**Starting Materials**	**Initial Weight**	**Molar Amount**	**Equivalents**	**Product**	
	Aluminum Sulfate	0.2065 g	0.31 mmol	1 eq	**Yield**	-
	Isophthalic Acid	0.0517 g	0.31 mmol	1 eq		
	N,N-Dimethylformamide	0.4 ml	-	-	**Surface**	-
	Water	1.6 ml	-	-		
135 °C; 12 h	**Starting Materials**	**Initial Weight**	**Molar Amount**	**Equivalents**	**Product**	
	Aluminum Sulfate	0.2001 g	0.30 mmol	1 eq	**Yield**	0.0362 g (29 %)
	Isophthalic Acid	0.0509 g	0.31 mmol	1 eq		
	N,N-Dimethylformamide	0.4 ml	-	-	**Surface**	33 m^2/g
	Water	1.6 ml	-	-		
155 °C; 12 h	**Starting Materials**	**Initial Weight**	**Molar Amount**	**Equivalents**	**Product**	
	Aluminum Sulfate	0.1920 g	0.29 mmol	1 eq	**Yield**	0.0783 g (65 %)
	Isophthalic Acid	0.0481 g	0.29 mmol	1 eq		
	N,N-Dimethylformamide	0.4 ml	-	-	**Surface**	13 m^2/g
	Water	1.6 ml	-	-		
135 °C; 6 h	**Starting Materials**	**Initial Weight**	**Molar Amount**	**Equivalents**	**Product**	
	Aluminum Sulfate	0.2002 g	0.30 mmol	1 eq	**Yield**	-
	Isophthalic Acid	0.0502 g	0.30 mmol	1 eq		
	N,N-Dimethylformamide	0.4 ml	-	-	**Surface**	-
	Water	1.6 ml	-	-		
135 °C; 24 h	**Starting Materials**	**Initial Weight**	**Molar Amount**	**Equivalents**	**Product**	
	Aluminum Sulfate	0.1642 g	0.25 mmol	1 eq	**Yield**	0.0487 g (48 %)
	Isophthalic Acid	0.0411 g	0.25 mmol	1 eq		
	N,N-Dimethylformamide	0.4 ml	-	-	**Surface**	1 m^2/g
	Water	1.6 ml	-	-		
Conditions	**Moistened**					
115 °C; 12 h	**Starting Materials**	**Initial Weight**	**Molar Amount**	**Equivalents**	**Product**	
	Aluminum Sulfate	0.2062 g	0.31 mmol	1 eq	**Yield**	0.0460 g (36 %)
	Isophthalic Acid	0.0517 g	0.31 mmol	1 eq		
	N,N-Dimethylformamide	0.4 ml	-	-	**Surface**	168 m^2/g
	Water	1.6 ml	-	-		
135 °C; 12 h	**Starting Materials**	**Initial Weight**	**Molar Amount**	**Equivalents**	**Product**	
	Aluminum Sulfate	0.1999 g	0.30 mmol	1 eq	**Yield**	0.0590 g (47 %)
	Isophthalic Acid	0.0508 g	0.31 mmol	1 eq		
	N,N-Dimethylformamide	0.4 ml	-	-	**Surface**	398 m^2/g
	Water	1.6 ml	-	-		
155 °C; 12 h	**Starting Materials**	**Initial Weight**	**Molar Amount**	**Equivalents**	**Product**	
	Aluminum Sulfate	0.1690 g	0.25 mmol	1 eq	**Yield**	0.0552 g (52 %)
	Isophthalic Acid	0.0423 g	0.25 mmol	1 eq		
	N,N-Dimethylformamide	0.4 ml	-	-	**Surface**	472 m^2/g
	Water	1.6 ml	-	-		
135 °C; 6 h	**Starting Materials**	**Initial Weight**	**Molar Amount**	**Equivalents**	**Product**	
	Aluminum Sulfate	0.2015 g	0.30 mmol	1 eq	**Yield**	0.0373 g (30 %)
	Isophthalic Acid	0.0506 g	0.30 mmol	1 eq		
	N,N-Dimethylformamide	0.4 ml	-	-	**Surface**	255 m^2/g
	Water	1.6 l	-	-		
135 °C; 24 h	**Starting Materials**	**Initial Weight**	**Molar Amount**	**Equivalents**	**Product**	
	Aluminum Sulfate	0.1707 g	0.26 mmol	1 eq	**Yield**	0.0484 g (45 %)
	Isophthalic Acid	0.0427 g	0.26 mmol	1 eq		
	N,N-Dimethylformamide	0.4 ml	-	-	**Surface**	250 m^2/g
	Water	1.6 ml	-	-		

S.4.2.1. Dry-gel conversions: Synthesis optimizations -- CAU-10-H solvent re-use

Table S5. Listing of DGC synthesis conditions for CAU-10-H and solvent re-use.

CAU-10-H						
Conditions	**Not Moistened**					
155 °C; 12 h	**Starting Materials**	**Initial Weight**	**Molar Amount**	**Equivalents**	**Product**	
	Aluminum Sulfate	0.1987 g	0.30 mmol	1 eq	**Yield**	0.0643 g (52 %)
	Isophthalic Acid	0.0502 g	0.30 mmol	1 eq		
	N,N-Dimethylformamide	0.4 ml	-	-	**Surface**	67m^2/g
	Water	1.6 ml	-	-		
155 °C; 12 h	**Starting Materials**	**Initial Weight**	**Molar Amount**	**Equivalents**	**Product**	
	Aluminum Sulfate	0.1998 g	0.30 mmol	1 eq	**Yield**	0.0606 g (49 %)
	Isophthalic Acid	0.0500 g	0.30 mmol	1 eq		
	N,N-Dimethylformamide	0.4 ml	-	-	**Surface**	23 m^2/g
	Water	1.6 ml	-	-		
155 °C; 12 h	**Starting Materials**	**Initial Weight**	**Molar Amount**	**Equivalents**	**Product**	
	Aluminum Sulfate	0.1982 g	0.30 mmol	1 eq	**Yield**	0.0387 g (31 %)
	Isophthalic Acid	0.0505 g	0.30 mmol	1 eq		
	N,N-Dimethylformamide	0.4 ml	-	-	**Surface**	232 m^2/g
	Water	1.6 ml	-	-		
155 °C; 12 h	**Starting Materials**	**Initial Weight**	**Molar Amount**	**Equivalents**	**Product**	
	Aluminum Sulfate	0.1990 g	0.30 mmol	1 eq	**Yield**	0.0408 g (33 %)
	Isophthalic Acid	0.0503 g	0.30 mmol	1 eq		
	N,N-Dimethylformamide	0.4 ml	-	-	**Surface**	20 m^2/g
	Water	1.6 ml	-	-		
Conditions	**Moistened**					
155 °C; 12 h	**Starting Materials**	**Initial Weight**	**Molar Amount**	**Equivalents**	**Product**	
	Aluminum Sulfate	0.2008 g	0.30 mmol	1 eq	**Yield**	0.0071 g (6 %)
	Isophthalic Acid	0.0503 g	0.30 mmol	1 eq		
	N,N-Dimethylformamide	0.4 ml	-	-	**Surface**	285 m^2/g
	Water	1.6 ml	-	-		
155 °C; 12 h	**Starting Materials**	**Initial Weight**	**Molar Amount**	**Equivalents**	**Product**	
	Aluminum Sulfate	0.1994 g	0.30 mmol	1 eq	**Yield**	0.0376 g (30 %)
	Isophthalic Acid	0.0496 g	0.30 mmol	1 eq		
	N,N-Dimethylformamide	0.4 ml	-	-	**Surface**	348 m^2/g
	Water	1.6 ml	-	-		
155 °C; 12 h	**Starting Materials**	**Initial Weight**	**Molar Amount**	**Equivalents**	**Product**	
	Aluminum Sulfate	0.1974 g	0.30 mmol	1 eq	**Yield**	0.0362 g (29 %)
	Isophthalic Acid	0.0503 g	0.30 mmol	1 eq		
	N,N-Dimethylformamide	0.4 ml	-	-	**Surface**	560 m^2/g
	Water	1.6 ml	-	-		
155 °C; 12 h	**Starting Materials**	**Initial Weight**	**Molar Amount**	**Equivalents**	**Product**	
	Aluminum Sulfate	0.2005 g	0.30 mmol	1 eq	**Yield**	0.0114 g (9 %)
	Isophthalic Acid	0.0515 g	0.31 mmol	1 eq		
	N,N-Dimethylformamide	0.4 ml	-	-	**Surface**	42 m^2/g
	Water	1.6 l	-	-		

S4.2.2. Dry-gel conversions: Synthesis optimizations -- CAU-10-H solvent re-use (less DMF)

Table S6. Listing of DGC synthesis conditions for CAU-10-H and solvent re-use with less DMF.

CAU-10-H						
Conditions	**Not Moistened**					
155 °C; 12 h	**Starting Materials**	**Initial Weight**	**Molar Amount**	**Equivalents**	**Product**	
	Aluminum Sulfate	0.2023 g	0.30 mmol	1 eq	**Yield**	0.0706 g (56 %)
	Isophthalic Acid	0.0515 g	0.31 mmol	1 eq		
	N,N-Dimethylformamide	0.4 ml	-	-	**Surface**	8 m^2/g
	Water	1.6 ml	-	-		
155 °C; 12 h	**Starting Materials**	**Initial Weight**	**Molar Amount**	**Equivalents**	**Product**	
	Aluminum Sulfate	0.2008 g	0.30 mmol	1 eq	**Yield**	0.0588 g (47 %)
	Isophthalic Acid	0.0492 g	0.30 mmol	1 eq		
	N,N-Dimethylformamide	0.4 ml	-	-	**Surface**	15 m^2/g
	Water	1.6 ml	-	-		
155 °C; 12 h	**Starting Materials**	**Initial Weight**	**Molar Amount**	**Equivalents**	**Product**	
	Aluminum Sulfate	0.1999 g	0.30 mmol	1 eq	**Yield**	0.0565 g (45 %)
	Isophthalic Acid	0.0502 g	0.30 mmol	1 eq		
	N,N-Dimethylformamide	0.4 ml	-	-	**Surface**	0 m^2/g
	Water	1.6 ml	-	-		
155 °C; 12 h	**Starting Materials**	**Initial Weight**	**Molar Amount**	**Equivalents**	**Product**	
	Aluminum Sulfate	0.2004 g	0.30 mmol	1 eq	**Yield**	0.0547 g (44 %)
	Isophthalic Acid	0.0505 g	0.30 mmol	1 eq		
	N,N-Dimethylformamide	0.4 ml	-	-	**Surface**	10 m^2/g
	Water	1.6 ml	-	-		
Conditions	**Moistened**					
155 °C; 12 h	**Starting Materials**	**Initial Weight**	**Molar Amount**	**Equivalents**	**Product**	
	Aluminum Sulfate	0.2000 g	0.30 mmol	1 eq	**Yield**	0.0547 g (44 %)
	Isophthalic Acid	0.0484 g	0.29 mmol	1 eq		
	N,N-Dimethylformamide	0.4 ml	-	-	**Surface**	317 m^2/g
	Water	1.6 ml	-	-		
155 °C; 12 h	**Starting Materials**	**Initial Weight**	**Molar Amount**	**Equivalents**	**Product**	
	Aluminum Sulfate	0.2008 g	0.30 mmol	1 eq	**Yield**	0.0434 g (35 %)
	Isophthalic Acid	0.0496 g	0.30 mmol	1 eq		
	N,N-Dimethylformamide	0.4 ml	-	-	**Surface**	497 m^2/g
	Water	1.6 ml	-	-		
155 °C; 12 h	**Starting Materials**	**Initial Weight**	**Molar Amount**	**Equivalents**	**Product**	
	Aluminum Sulfate	0.1998 g	0.30 mmol	1 eq	**Yield**	0.0093 g (7 %)
	Isophthalic Acid	0.0500 g	0.30 mmol	1 eq		
	N,N-Dimethylformamide	0.4 ml	-	-	**Surface**	10 m^2/g
	Water	1.6 ml	-	-		
155 °C; 12 h	**Starting Materials**	**Initial Weight**	**Molar Amount**	**Equivalents**	**Product**	
	Aluminum Sulfate	0.2026 g	0.30 mmol	1 eq	**Yield**	0.0277 g (22 %)
	Isophthalic Acid	0.0500 g	0.30 mmol	1 eq		
	N,N-Dimethylformamide	0.4 ml	-	-	**Surface**	312 m^2/g
	Water	1.6 l	-	-		

S4.3. Dry-gel conversions: Synthesis optimizations -- MIL-160

Table S7. Listing of DGC synthesis conditions for MIL-160 with variation of time and temperature.

MIL-160						
Conditions	**Not Moistened**					
80 °C; 24 h	**Starting Materials**	**Initial Weight**	**Molar Amount**	**Equivalents**	**Product**	
	Aluminium Chloride	0.1391 g	0.58 mmol	1 eq	**Yield**	0.0313 g (27 %)
	2,5-Furandicarboxylic Acid	0.0899 g	0.58 mmol	1 eq		
	NaOH	0.0230 g	0.58 mmol	1 eq	**Surface**	264 m^2/g
	Water	2 ml	-	-		
100 °C; 24 h	**Starting Materials**	**Initial Weight**	**Molar Amount**	**Equivalents**	**Product**	
	Aluminium Chloride	0.1927 g	0.80 mmol	1 eq	**Yield**	0.0416 g (26 %)
	2,5-Furandicarboxylic Acid	0.1242 g	0.80 mmol	1 eq		
	NaOH	0.0326 g	0.82 mmol	1 eq	**Surface**	57 m^2/g
	Water	2 ml	-	-		
120 °C; 24 h	**Starting Materials**	**Initial Weight**	**Molar Amount**	**Equivalents**	**Product**	
	Aluminium Chloride	0.1439 g	0.60 mmol	1 eq	**Yield**	0.0162 g (14 %)
	2,5-Furandicarboxylic Acid	0.0929 g	0.60 mmol	1 eq		
	NaOH	0.0238 g	0.60 mmol	1 eq	**Surface**	101 m^2/g
	Water	2 ml	-	-		
100 °C; 12 h	**Starting Materials**	**Initial Weight**	**Molar Amount**	**Equivalents**	**Product**	
	Aluminium Chloride	0.1465 g	0.61 mmol	1 eq	**Yield**	0.0227 g (19 %)
	2,5-Furandicarboxylic Acid	0.0947 g	0.61 mmol	1 eq		
	NaOH	0.0243 g	0.61 mmol	1 eq	**Surface**	394 m^2/g
	Water	2 ml	-	-		
100 °C; 48 h	**Starting Materials**	**Initial Weight**	**Molar Amount**	**Equivalents**	**Product**	
	Aluminium Chloride	0.1395 g	0.58 mmol	1 eq	**Yield**	0.0237 g (21 %)
	2,5-Furandicarboxylic Acid	0.0902 g	0.58 mmol	1 eq		
	NaOH	0.0232 g	0.58 mmol	1 eq	**Surface**	119 m^2/g
	Water	2 ml	-	-		
Conditions	**Moistened**					
80 °C; 24 h	**Starting Materials**	**Initial Weight**	**Molar Amount**	**Equivalents**	**Product**	
	Aluminium Chloride	0.1402 g	0.58 mmol	1 eq	**Yield**	0.0216 g (19 %)
	2,5-Furandicarboxylic Acid	0.0906 g	0.58 mmol	1 eq		
	NaOH	0.0232 g	0.58 mmol	1 eq	**Surface**	135 m^2/g
	Water	1.8 + 0.2 ml	-	-		
100 °C; 24 h	**Starting Materials**	**Initial Weight**	**Molar Amount**	**Equivalents**	**Product**	
	Aluminium Chloride	0.1931 g	0.80 mmol	1 eq	**Yield**	0.0765 g (48 %)
	2,5-Furandicarboxylic Acid	0.1244 g	0.80 mmol	1 eq		
	NaOH	0.0327 g	0.82 mmol	1 eq	**Surface**	354 m^2/g
	Water	1.8 + 0.2 ml	-	-		
120 °C; 24 h	**Starting Materials**	**Initial Weight**	**Molar Amount**	**Equivalents**	**Product**	
	Aluminium Chloride	0.1444 g	0.60 mmol	1 eq	**Yield**	0.0902 g (76 %)
	2,5-Furandicarboxylic Acid	0.0933	0.60 mmol	1 eq		
	NaOH	0.0239	0.60 mmol	1 eq	**Surface**	402 m^2/g
	Water	1.8 + 0.2 ml	-	-		
100 °C; 12 h	**Starting Materials**	**Initial Weight**	**Molar Amount**	**Equivalents**	**Product**	
	Aluminium Chloride	0.1475 g	0.61 mmol	1 eq	**Yield**	0.0099 g (7 %)
	2,5-Furandicarboxylic Acid	0.0954 g	0.61 mmol	1 eq		
	NaOH	0.0245 g	0.61 mmol	1 eq	**Surface**	249 m^2/g
	Water	1.8 + 0.2 ml	-	-		
100 °C; 48 h	**Starting Materials**	**Initial Weight**	**Molar Amount**	**Equivalents**	**Product**	
	Aluminium Chloride	0.1391 g	0.58 mmol	1 eq	**Yield**	0.0066 g (6 %)
	2,5-Furandicarboxylic Acid	0.0899 g	0.58 mmol	1 eq		
	NaOH	0.0231 g	0.58 mmol	1 eq	**Surface**	451 m^2/g
	Water	1.8 + 0.2 ml	-	-		

S4.3.1. Dry-gel conversions: Synthesis optimizations -- MIL-160 solvent re-use

Table S8. Listing of DGC synthesis conditions for MIL-160 and solvent re-use.

MIL-160						
Conditions	**Not Moistened**					
100 °C; 24 h	**Starting Materials**	**Initial Weight**	**Molar Amount**	**Equivalents**	**Product**	
	Aluminum Chloride	0.0980 g	0.41 mmol	1 eq	**Yield**	0.0336 g (42 %)
	2,5-Furandicarboxylic Acid	0.0637 g	0.41 mmol	1 eq		
	NaOH	0.0332 g	0.83 mmol	2 eq	**Surface**	438 m^2/g
	Water	2 ml	-	-		
100 °C; 24 h	**Starting Materials**	**Initial Weight**	**Molar Amount**	**Equivalents**	**Product**	
	Aluminum Chloride	0.0993 g	0.41 mmol	1 eq	**Yield**	0.0294 g (36 %)
	2,5-Furandicarboxylic Acid	0.0646 g	0.41 mmol	1 eq		
	NaOH	0.0343 g	0.85 mmol	2 eq	**Surface**	435 m^2/g
	Water	2 ml	-	-		
100 °C; 24 h	**Starting Materials**	**Initial Weight**	**Molar Amount**	**Equivalents**	**Product**	
	Aluminum Chloride	0.1005 g	0.42 mmol	1 eq	**Yield**	0.0413 g (50 %)
	2,5-Furandicarboxylic Acid	0.0622 g	0.40 mmol	1 eq		
	NaOH	0.0323 g	0.81 mmol	2 eq	**Surface**	370 m^2/g
	Water	2 ml	-	-		
100 °C; 24 h	**Starting Materials**	**Initial Weight**	**Molar Amount**	**Equivalents**	**Product**	
	Aluminum Chloride	0.0988 g	0.41 mmol	1 eq	**Yield**	0.0295 g (36 %)
	2,5-Furandicarboxylic Acid	0.0624 g	0.40 mmol	1 eq		
	NaOH	0.0315 g	0.79 mmol	2 eq	**Surface**	891 m^2/g
	Water	2 ml	-	-		
Conditions	**Moistened**					
100 °C; 24 h	**Starting Materials**	**Initial Weight**	**Molar Amount**	**Equivalents**	**Product**	
	Aluminum Chloride	0.0966 g	0.40 mmol	1 eq	**Yield**	0.0302 g (38 %)
	2,5-Furandicarboxylic Acid	0.0614 g	0.40 mmol	1 eq		
	NaOH	0.0337 g	0.84 mmol	2 eq	**Surface**	995 m^2/g
	Water	1.8 + 0.2 ml	-	-		
100 °C; 24 h	**Starting Materials**	**Initial Weight**	**Molar Amount**	**Equivalents**	**Product**	
	Aluminum Chloride	0.0987 g	0.41 mmol	1 eq	**Yield**	0.0244 g (30 %)
	2,5-Furandicarboxylic Acid	0.0659 g	0.42 mmol	1 eq		
	NaOH	0.0333 g	0.83 mmol	2 eq	**Surface**	968 m^2/g
	Water	1.8 + 0.2 ml	-	-		
100 °C; 24 h	**Starting Materials**	**Initial Weight**	**Molar Amount**	**Equivalents**	**Product**	
	Aluminum Chloride	0.1010 g	0.42 mmol	1 eq	**Yield**	0.0379 g (46 %)
	2,5-Furandicarboxylic Acid	0.0625 g	0.40 mmol	1 eq		
	NaOH	0.0344 g	0.86 mmol	2 eq	**Surface**	1180 m^2/g
	Water	1.8 + 0.2 ml	-	-		
100 °C; 24 h	**Starting Materials**	**Initial Weight**	**Molar Amount**	**Equivalents**	**Product**	
	Aluminum Chloride	0.0989 g	0.41 mmol	1 eq	**Yield**	0.0177 g (22 %)
	2,5-Furandicarboxylic Acid	0.0631 g	0.40 mmol	1 eq		
	NaOH	0.0321 g	0.80 mmol	2 eq	**Surface**	980 m^2/g
	Water	1.8 + 0.2 ml	-	-		

S5. Solvent re-use for Alfum, CAU-10-H and MIL-160

We carried out solvent re-use experiments over four repeated DGC runs with the same solvent and fresh reactant mixture on the sieve at the head of the DGC autoclave (*cf.* Figure S1).

The details and results of these solvent re-use experiments are summarized in Table S3, S5, S6 and S8 for Alfum, CAU-10-H and MIL-160, respectively.

Figure S5-S8 graphically depict the results of solvent re-use with respect to BET surface area and yield.

Alfum

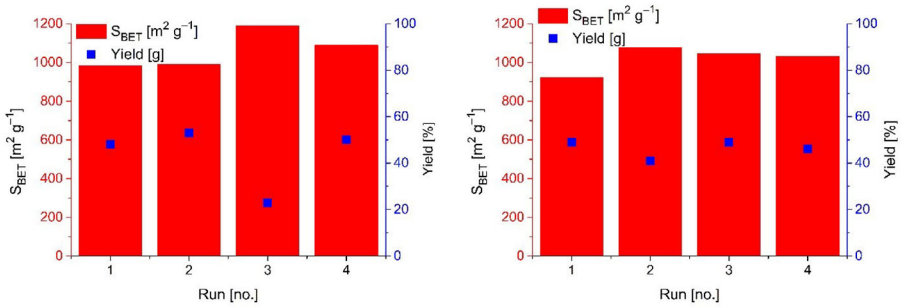

Figure S5 *Solvent re-use over four DGC runs for Alfum, with BET surface area (red bars) and yields (blue squares). Left: wetted precursor mixture, right: dry precursor mixture. Minor yields, e.g. 20% in run 3, due to washing off/falling down of the product during handling of the DGC setup.*

CAU-10-H, repetition with wetting of neat DMF

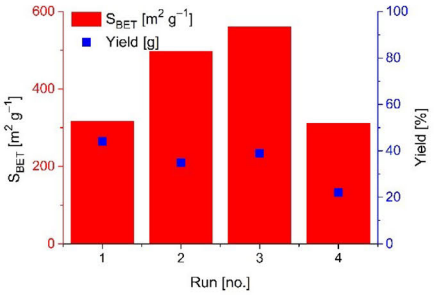

Figure S6 *Solvent re-use over four DGC runs for CAU-10-H, with BET surface area (red bars) and yields (blue boxes). A wetted (neat DMF) precursor mixture was used. Minor yields, due to washing off/falling down of the product during handling of the DGC setup.*

MIL-160

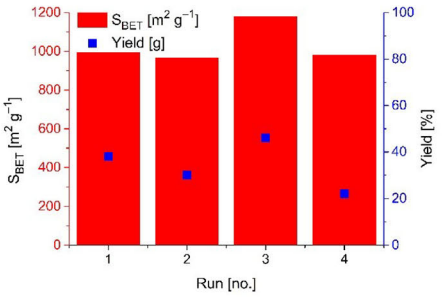

Figure S7 *Solvent re-use over four DGC runs for MIL-160, with BET surface area (red bars) and yields (blue boxes). A wetted precursor mixture was used. Minor yields, due to washing off/falling down of the product during handling of the DGC setup.*

S6. PXRD measurements

Crystallinity was proven with powder X-ray diffractometry (PXRD), using a *Bruker D2 Phaser* diffractometer with a flat silicon, low background sample holder and Cu-K_α radiation (λ = 1.54184 Å) at 30 kV and 0.04 ° s^{-1} in the 2θ = 5-50 ° range.

Figure S8-S12 depict PXRD patterns of all obtained samples Alfum, CAU-10-H and MIL-160 samples within solvent re-use in comparison with each simulated pattern.

Alfum

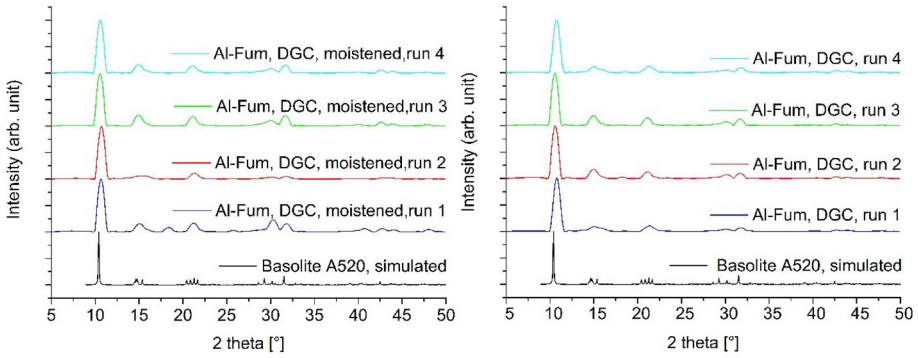

Figure S8 *PXRD patterns of Alfum samples obtained by synthesis runs with solvent re-use, in comparison with simulated pattern (CDS-Refcode DOYBEA).[4] Left: wetted precursor mixture, right: dry precursors. Figure 1 in the main manuscript shows a comparison with the industrial benchmark Basolite A520.*

CAU-10-H, repetition with wetting of neat DMF

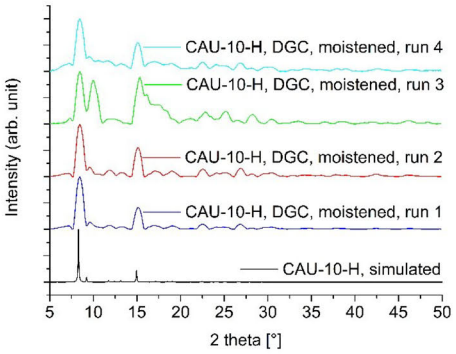

Figure S9 *PXRD patterns of aluminum CAU-10-H samples obtained by synthesis runs with solvent re-use, in comparison with simulated pattern (CCDC CSD-Refcode QQOBUT).[25] A wetted (neat DMF) precursor mixture was used.*

MIL-160

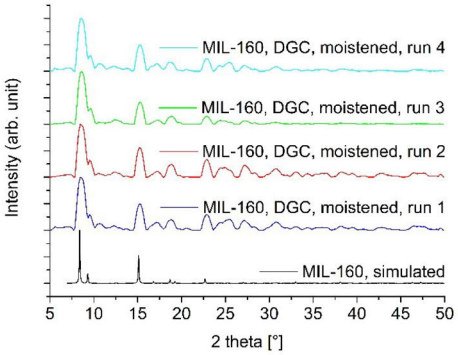

Figure S10 *PXRD patterns of MIL-160 samples obtained by synthesis runs with solvent re-use, in comparison with simulated pattern (CCDC PIBZOS).*[40] *A wetted precursor mixture was used.*

S7. Thermogravimetric Analysis (TGA)

Exemplarily, we performed thermogravimetric analyses (TGA) of samples obtained *via* DGC of each of the presented MOFs. Figure S11-S15 depict TGA curves of Alfum, CAU-10-H and MIL-160 samples.

Alfum

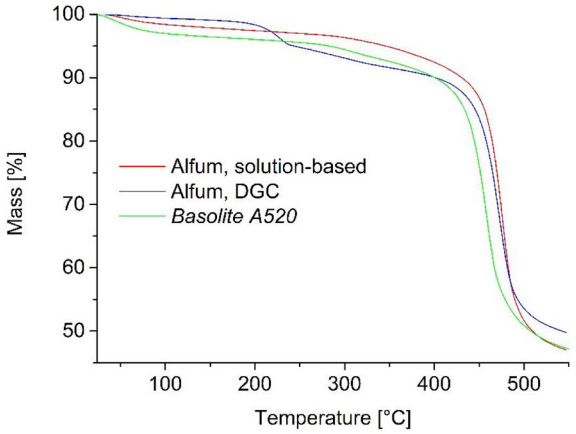

Figure S11 TG curve of Alfum samples from DGC (blue) and from solution-based synthesis (red) in comparison with industrial benchmark *Basolite A520*.

CAU-10-H

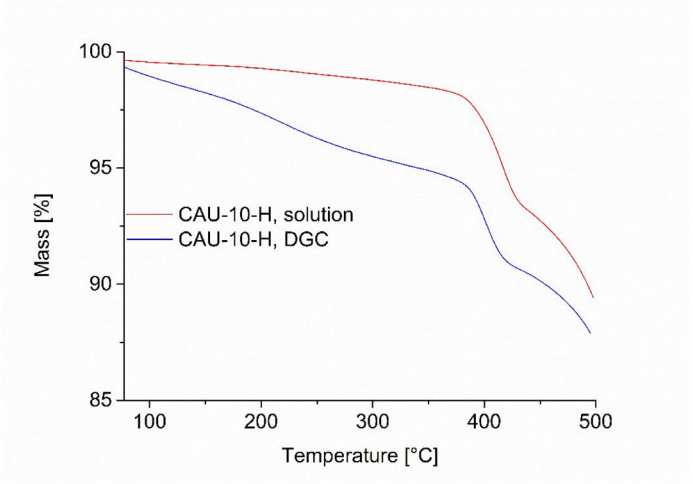

Figure S12 TG curve of CAU-10-H samples from DGC (blue) and from solution-based synthesis (red).

MIL-160

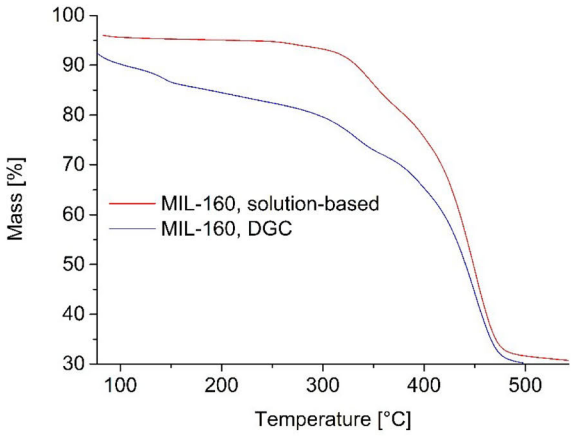

Figure S13 TG curve of MIL-160 samples from DGC (blue) and from solution-based synthesis (red).

S8. Scanning electron microscopy (SEM)

For control of morphology we recorded SEM images using a *JEOL JSM-6510 advanced electron microscope* with a LaB_6 cathode at 20 keV.

Figure S14-S18 exemplarily depict SEM images of selected samples of the three presented MOFs.

Alfum

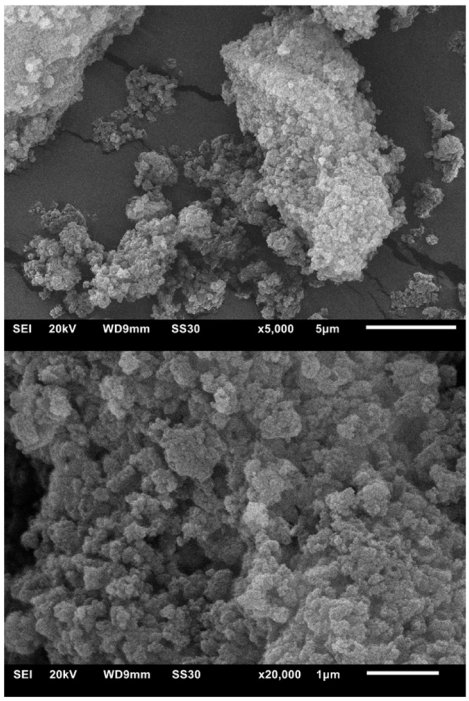

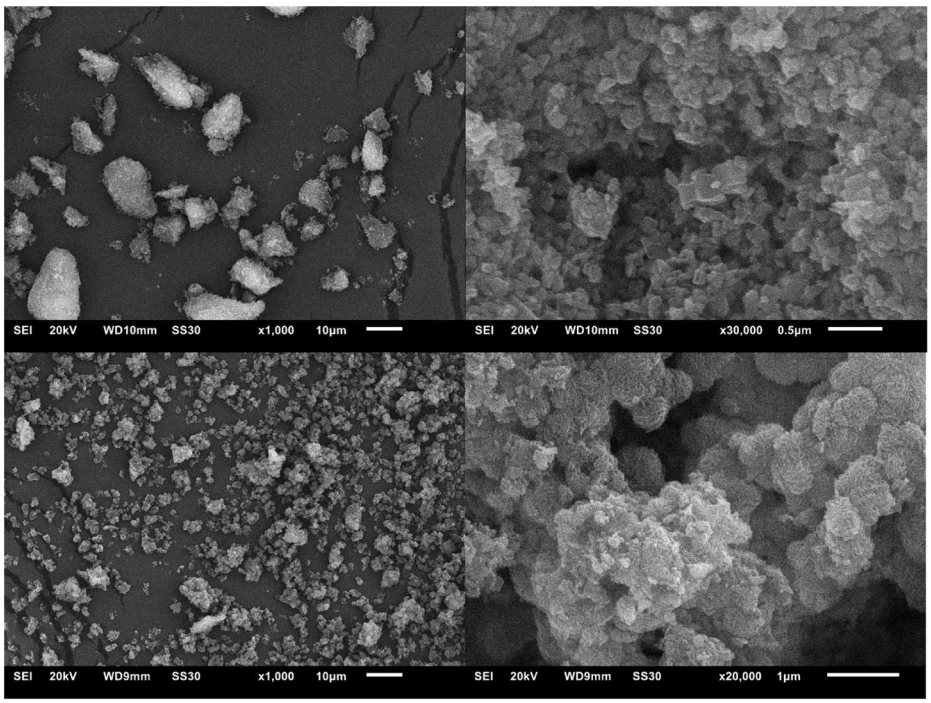

Figure S14 *SEM images of different Alfum samples at different magnifications (left: overview, right: close-up). Top: Basolite A520. Middle: Alfum from DGC. Bottom: Alfum from solution-based synthesis*

CAU-10-H

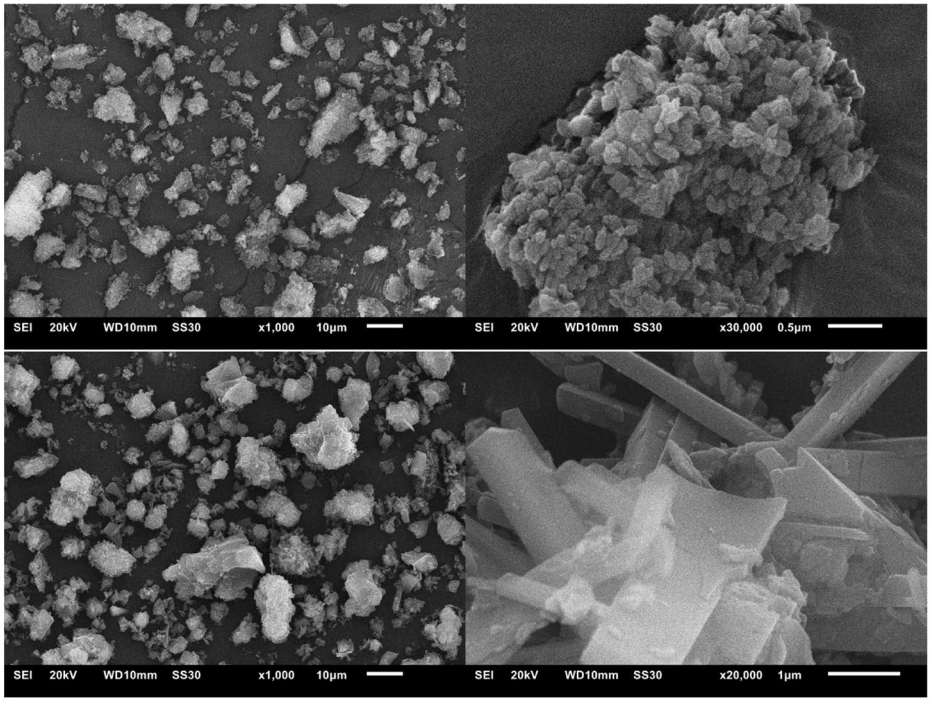

Figure S15 *SEM images of different CAU-10-H samples at different magnifications (left: overview, right: close-up). Top: CAU-10-H from DGC. Bottom: CAU-10-H from solution-based synthesis.*

MIL-160

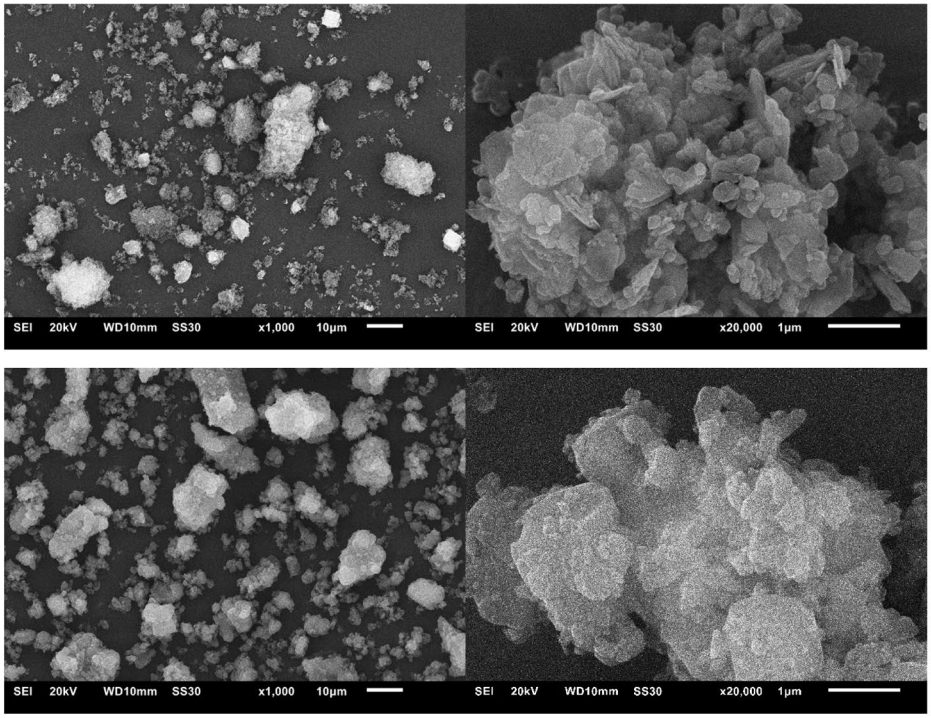

Figure S16 *SEM images of MIL-160 samples at different magnifications (left: overview, right: close-up). Top: MIL-160 from DGC. Bottom: MIL-160 from solution-based synthesis.*

S9. Nitrogen sorption experiments solvent re-use (T = 77 K)

Surface areas (BET) were determined by nitrogen (purity 99.999%) sorption experiments at 77.35 K using a *Quantachrome NOVA-4000e* instrument within a partial pressure range of $pp_0^{-1} = 10^{-3}$-1 bar. Each sample was degassed under vacuum (< 10^{-2} mbar) at 100 °C (MIL-100(Fe)), respectively 150 °C (Alfum) for *ca.* 3 h, prior to measurement. All surface areas (BET) were calculated from five adsorption points in the pressure range pp_0^{-1} = 0.009 - 0.041 bar for samples of Alfum, pp_0^{-1} = 0.004 - 0.125 bar for samples of CAU-10-H and pp_0^{-1} = 0.014 - 0.052 bar for samples of MIL-160. This range is indeed not recommended by IUPAC (International Union of Pure and Applied Chemistry) for BET surface determination, but rather suitable for microporous materials.[47]

Figure S17-S19 depict the nitrogen sorption isotherms of all obtained MOF samples during DGCs with solvent re-use over four DGC runs.

Aluminum fumarate

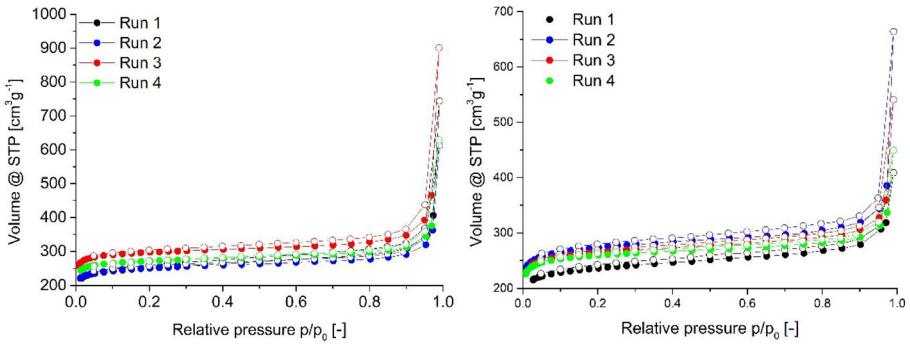

Figure S17 *Nitrogen sorption (77 K) isotherms of aluminum fumarate samples obtained by synthesis runs with solvent re-use. Left: wetted precursor mixture, right: dry precursor mixture.*

CAU-10-H, repetition with wetting of neat DMF

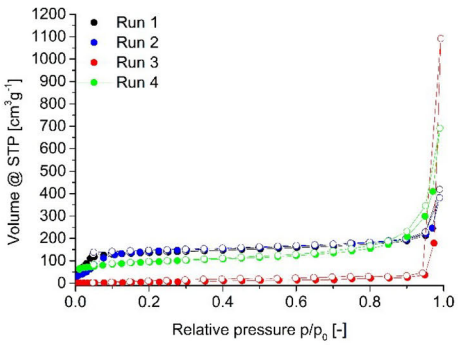

Figure S18 *Nitrogen sorption (77 K) isotherms of CAU-10-H samples obtained by synthesis runs with solvent re-use. A wetted (neat DMF) precursor mixture was used.*

MIL-160

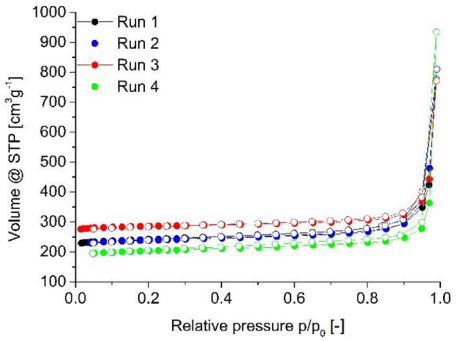

Figure S19 *Nitrogen sorption (77 K) isotherms of MIL-160 samples obtained by synthesis runs with solvent re-use. A wetted (neat DMF) precursor mixture was used.*

Table S9 summarizes repeated N_2 sorption results of the industrial benchmark *Basolite A520* using the same batch, but not the same sample.

Table S9 *Repeated determination of BET areas of Basolite A520 using nitrogen sorption (T = 77 K).*

Benchmark	No. of measurement	BET [$m^2\ g^{-1}$]
Basolite A520	1	1030
	2	1038
	3	999
	4	1040
	5	1026

S10. Water sorption experiments (T = 20 °C)

Water sorption experiments were carried out on a *Quantachrome VStar4* (QUANTACHROME, Odelzhausen, Germany) instrument within a partial pressure range of $pp_0^{-1} = 10^{-3}$-1 bar. Each sample was degassed under vacuum (< 10^{-3} mbar) at 150 °C for *ca.* 3 h prior to measurement, using a *FloVac* (QUANTACHROME, Odelzhausen, Germany) degasser.

All water sorption isotherms are depicted in Figures 2c) ,3c),4c) in the main manuscript.

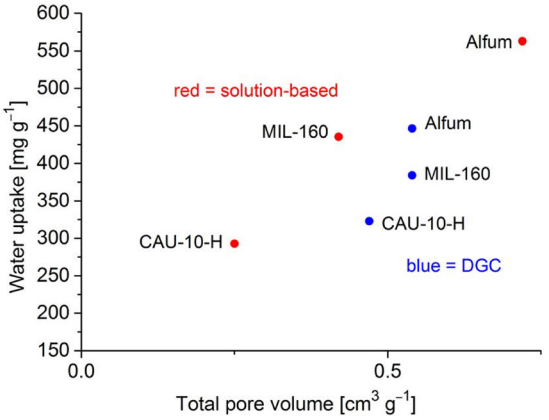

Fig. S20 Water uptake (at $p/p_0 = 0.95$) versus the total pore volume (at $p/p_0 = 0.95$) for solution and DGC samples.

Table S10 *Microporosity characteristics for solution and DGC samples from V-t-plot method.*

Sample	Micropore surface area [m² g⁻¹]	External and mesopore surface area [m² g⁻¹]	Micropore volume [cm³ g⁻¹]
Alfum solution-based	1112	141	0.427
DGC	941	104	0.367
CAU-10-H solution-based	378	192	0.089
DGC	437	129	0.173
MIL-160 solution-based	1067	30	0.403
DGC	899	81	0.279

S11. References

[1] E. Leung, U. Müller, N. Trukhan, H. Mattenheimer, G. Cox and S. Blei, *Process for preparing porous metal-organic frameworks based on aluminum fumarate*, U.S. Patent No. 8,524,932, BASF SE, 3 Sep. 2013.

[2] C. Kiener, U. Müller, and M. Schubert, *Method of using a metal organic frameworks based on aluminum fumarate*, U.S. Patent No. 8,518,264, BASF SE, 27 Aug. 2013.

[3] K. Brandenburg, Diamond 4.3.1, Crystal and Molecular Structure Visualization, Crystal Impact - K. Brandenburg & H. Putz GbR, Bonn, Germany, 2009.

[4] E. Alvarez, N. Guillou, C. Martineau, B. Bueken, B. Van de Voorde, C. Le Guillouzer, P. Fabry, F. Nouar, F. Taulelle, D. de Vos, J.-S. Chang, K. H. Cho, N. Ramsahye, T. Devic, M. Daturi, G. Maurin and C. Serre, *Angew. Chem. Int. Ed.*, 2015, **54**, 3664-3668.

[5] T. Loiseau, C. Volkringer, M. Haouas, F. Taulelle and G. Férey, *C. R. Chim.* 2015, **18**, 1350-1369.

[6] L. Zhou, X. Zhang and Y. Chen, *Mater. Lett.*, 2017, **197**, 224-227.

[7] E. Elsayed, R. Al-Dadah, S. Mahmoud, P. A. Anderson, A. Elsayed and P. G. Youssef, *Desalination*, 2017, **406**, 25-36.

[8] M. Rubio-Martinez, T. D. Hadley, M. P. Batten, K. Constanti-Carey, T. Barton, D. Marley, A. Mönch, K-S. Lim and M. R. Hill, *ChemSusChem*, 2016, **9**, 938-941.

[9] D. E. Crawford and J. Casaban, *Adv. Mater.*, 2016, **28**, 5747-5754.

[10] D. Crawford, J. Casaban, R. Haydon, N. Giri, T. McNally and S. L. James, *Chem. Sci.*, 2015, **6**, 1645-1649.

[11] M. Rubio-Martinez, C. Avci-Camur, A. W. Thornton, I. Imaz, D. Maspoch, M. R. Hill, *Chem. Soc. Rev.* **2017**, *46*, 3453–3480.

[12] N. Tannert, S. Gökpinar, E. Hastürk, S. Nießing and C. Janiak, *Dalton Trans.*, 2018, **47**, 9850-9860.

[13] B. Yilmaz, N. Trukhan and U. Müller, *Chin. J. Catal.*, 2012, **33**, 3-10.

[14] F. Jeremias, D. Fröhlich, C. Janiak and S. K. Henninger, *RSC Adv.*, 2014, **4**, 24073-24082.

[15] J. Chen, K. Shen and Y. Li, *ChemSusChem*, 2017, **10**, 3165-3187.

[16] M. Gaab, N. Trukhan, S. Maurer, R. Gummaraju and U. Müller, *Micropor. Mesopor. Mater.*, 2012, **157**, 131-136.

[17] S. K. Henninger, S.-J. Ernst, L. Gordeeva, P. Bendix, D. Fröhlich, A. D. Grekova, L. Bonaccorsi, Y. Aristov and J. Jaenchen, *Renew. Energ.*, 2017, **110**, 59-69.

[18] S. Karmakar, J. Dechnik, C. Janiak and S. De, *J. Hazard. Mater.*, 2016, **303**, 10-20.

[19] S. Karmakar, S. Bhattarcharjee and S. De, *J. Env. Chem. Eng.*, 2017, **5**, 6087-6097.

[20] P. G. Yot, L. Vanduyfhuys, E. Alvarez, J. Rodriguez, J.-P. Itié, P. Fabry, N. Guillou, T. Devic, I. Beurroies, P. L. Llewellyn, V. Van Speybroek, C. Serre and G. Maurin, *Chem. Sci.*, 2016, **7**, 446-450.

[21] H. W. B. Teo, A. Chakraborty and S. Kayal, *Micropor. Mesopor. Mater.*, 2018, **272**, 109-116.

[22] T. Splith, D. Fröhlich, S. K. Henninger and F. Stallmach, *J. Magn. Reson.*, 2018, **291**, 40-46.

[23] H. W. B. Teo, A. Chakraborty, Y. Kitagawa and S. Kayal, *Int. J. Heat Mass Tran.*, 2017, **114**, 621-629.

[24] H. Reinsch, M. A. van der Veen, B. Gil, B. Marszalek, T. Verbiest, D. de Vos and N. Stock, *Chem. Mater.*, 2012, **25**, 17-26.

[25] D. Fröhlich, E. Pantatosaki, P. D. Kolokathis, K. Markey, H. Reinsch, M. Baumgartner, M. A. van der Veen, D. E. de Vos, N. Stock, G. K. Papadopoulos, S. K. Henninger and C. Janiak, *J. Mater. Chem. A*, 2016, **4**, 11859-11869.

[26] H. Reinsch, M Krüger, J. Wack, J. Senker, F. Salles, G. Maurin and N. Stock, *Micropor. Mesopor. Mater.*, 2012, **157**, 50-55.

[27] A. Cadiau, J. S. Lee, D. D. Borges, P. Fabry, T. Devic, M. T. Wharmby, C. Martineau, D. Foucher, F. Taulelle, C.-H. Jun, Y. K. Hwang, N. Stock, M. F. De Lange, F. Kapteijn, J. Gascon, G. Maurin, J.-S. Chang and C. Serre, *Adv. Mater.*, 2015, **27**, 4775-4780.

[28] D. D. Borges, G. Maurin and D. S. Galvao, *MRS Adv.*, 2017, **2**, 519-524.

[29] M. F. de Lange, C. P. Ottevanger, M. Wiegmann, T. J. H. Vlugt, J. Gascon and F. Kapteijn, *CrystEngComm*, 2015, **17**, 281-285.

[30] H. Reinsch, S. Waitschat and N. Stock, *Dalton Trans.*, 2013, **42**, 4840-4847.

[31] A. Weiss, N. Reimer, N. Stock, M. Tiemann and T. Wagner, *Micropor. Mesopor. Mater.*, 2016, **220**, 39-43.
[32] N. Reimer, B. Bueken, S. Leubner, C. Seidler, M. Wark, D. De Vos and N. Stock, *Chem. Eur. J.*, 2015, **21**, 12517-12524.
[33] M. F. de Lange, T. Zeng, T. J. H. Vlugt, J. Gascon and F. Kapteijn, *CrystEngComm*, 2015, **17**, 5911-5920.
[34] R. J. Sheehan, *Ullmann's Encyclopedia of Industrial Chemistry*, Wiley-VCH Verlag GmbH & Co., Weinheim, Germany 2000.
[35] D. Fröhlich, S. K. Henninger and C. Janiak, *Dalton Trans.*, 2014, **43**, 15300-15304.
[36] M. Goldsworthy, *Micropor. Mesopor. Mate*r., 2014, **196**, 59-67.
[37] A. Cadiau, J. S. Lee, D. Damasceno Borges, P. Fabry, T. Devic, M. T. Wharmby, C. Martineau, D. Foucher, F. Taulelle, C.-H. Jun et al., *Adv. Mater.* **2015**, *27*, 4775–4780.
[38] H. Kummer, F. Jeremias, A. Warlo, G. Füldner, D. Fröhlich, C. Janiak, R. Gläser and S. K. Henninger, *Ind. Eng. Chem. Res.*, 2017, **56**, 8393-8398.
[39] A. D. Wiersum, C. Giovannangeli, D. Vincent, E. Bloch, H. Reinsch, N. Stock, J. S. Lee, J.-S. Chang and P. L. Llewellyn, *ACS Comb. Sci.*, 2013, **2**, 111-119.
[40] M. Wahiduzzaman, D. Lenzen, G. Maurin, N. Stock and M. T. Wharmby, *Eur. J. Inorg. Chem.*, 2018, 3626-3632.
[41] A. Permyakova, O. Skrylnyk, E. Courbon, M. Affran, S. Wang, U-H. Lee, A. H. Valekar, F. Nouar, G. Mouchaham, T. Devic, G. De Weireld, J.-S. Chang, N. Steunou, M. Frère and C. Serre, *ChemSusChem*, 2017, **10**, 1419-1426.
[42] http://avantium.com/yxy/yxy-technology.html; accessed 01.08.2017, 01:54 h.
[43] Press releases: 'Synvina: Jointventure of BASF and Avantium established', 2016.
[44] S. K. Henninger, H. A. Habib and C. Janiak, *J. Am. Chem. Soc.*, 2009, **131**, 2776-2777.
[45] S. K. Henninger, F. P. Schmidt and H.-M. Henning, *Appl. Therm. Eng.*, 2010, **30**, 1692-1702.
[46] S. K. Henninger, F. Jeremias, H. Kummer, P. Schossig and H.-M. Henning, *Energy Proc.*, 2012, **30**, 279-288.
[47] M. Thommes, K. Kaneko, A. V. Neimark, J. P. Olivier, F. Rodriguez-Reinoso, J. Rouquerol and K. S. Sing, *Pure Appl. Chem.*, 2015, **87**, 1051-1069.

3.2 MOF@chitosan Composites with Potential Antifouling Properties for Open-Environment Applications of Metal-Organic Frameworks

Christian Jansen, Nam Michael Tran-Cong, Carsten Schlüsener, Alexa Schmitz, Peter Proksch, Christoph Janiak

Solids **2022**, *3*, 35-54

DOI: 10.3390/solids3010004

Impact-Faktor: -

Kurzzusammenfassung:

MOFs sind, aufgrund ihrer einfachen Synthese und der hohen Variabilität, die durch die organischen Liganden gegeben ist, geeignete Kandidaten für eine Vielzahl von Anwendungen. Für Anwendungen in der Umwelt können die MOFs, aufgrund ihres organischen Anteils, anfällig sein für die Bildung von Fäulnisbefall bzw. der Bildung von Biofilmen. Dies kann die potenzielle poröse Struktur der MOFs zerstören oder die Sorptionskapazitäten verringern. Daher ist ein besonderes Augenmerk auf das Verhindern des Biofilm- bzw. Mikroorganismus-Wachstums zu richten. Eine Möglichkeit hierfür ist die Verwendung von Chitosan, einem Polysaccharid-Biopolymer. Dieses wird durch basische Deacetylierung von Chitin gewonnen, das wiederum der Hauptbestandteil von Krustentierschalen ist. Chitosan ist bekannt für seine antifugalen Eigenschaften und daher ein geeigneter Kandidat für Kompositmaterialien mit MOFs. In unserem Fall wird das Chitosan als Matrix für die MOF@Chitosan-Komposite genutzt und verschiedene aluminiumbasierte MOFs verwendet. Anschließend wird der antifugale Effekt der Komposite untersucht, mit verschiedenen Kompositen mit einer maximalen MOF-Beladung bis hin zu 90 %. Die Komposite und ihre Ausgangsmaterialien wurden nach der DIN EN ISO 846 untersucht und die Materialeigenschaften gegenüber den Pilzen *Chaetomium globosum* und *Aspergillus falconensis* bewertet.

Anteile an der Publikation:

- Idee der Publikation in Zusammenarbeit mit Herrn Prof. Dr. Christoph Janiak
- Konzept, experimentelle Arbeiten und Analytik (bis auf unten gelistete Ausnahmen)
- Aufarbeitung der Ergebnisse, Verfassen des Manuskripts und das Erstellen der Abbildungen und Tabellen
- Korrekturen und Verschriftlichung und Revision durch Herr Prof. Dr. Christoph Janiak
- Korrekturen durch Herr Prof. Dr. Peter Proksch

- REM-Aufnahmen durch Herr Carsten Schlüsener
- TGAs durch Frau Alexa Schmitz
- Stabilitätstests der MOFs und der Komposite gegenüber den Pilzen durch Herr Nam Michael Tran-Cong

solids

MDPI

Article

MOF@chitosan Composites with Potential Antifouling Properties for Open-Environment Applications of Metal-Organic Frameworks

Christian Jansen [1], Nam Michael Tran-Cong [2], Carsten Schlüsener [1], Alexa Schmitz [1], Peter Proksch [2] and Christoph Janiak [1,*]

[1] Institut für Anorganische Chemie und Strukturchemie, Heinrich-Heine-Universität, D-40204 Düsseldorf, Germany; Christian.Jansen@hhu.de (C.J.); Carsten.Schluesener@hhu.de (C.S.); alexa.schmitz@hhu.de (A.S.)

[2] Institut für Pharmazeutische Biologie und Biotechnologie, Heinrich-Heine-Universität, D-40204 Düsseldorf, Germany; Nam.Tran-Cong@hhu.de (N.M.T.-C.); Proksch@uni-duesseldorf.de (P.P.)

* Correspondence: Janiak@hhu.de

Abstract: Metal-organic frameworks (MOFs) are promising materials for a myriad of applications because of their easy synthesis and large variability through the organic linker. For open-environment applications, the organic content can, however, give rise to fouling, that is, biofilm formation. Biofilms can destroy the MOF and reduce the sorption capacity. Therefore, it is necessary to formulate MOFs for open-environment application to avoid the growth of microorganisms. Chitosan is a polysaccharide biopolymer, obtained from chitin shells of shrimps by alkaline deacetylation, and has known fungistatic properties. Here, chitosan is used as a matrix for MOF@chitosan composites with different aluminum-based MOFs to implement the fungistatic effect of chitosan to MOFs. The obtained composites with the highest possible MOF loadings of up to 90% were tested according to DIN EN ISO 846 to examine the fungistatic material properties against the fungi *Chaetomium globosum* and *Aspergillus falconensis*.

Keywords: metal-organic frameworks; Al-MOFs; chitosan; aluminum fumarate; MIL-160; antifouling; *Chaetomium globosum*; *Aspergillus falconensis*

Citation: Jansen, C.; Tran-Cong, N.M.; Schlüsener, C.; Schmitz, A.; Proksch, P.; Janiak, C. MOF@chitosan Composites with Potential Antifouling Properties for Open-Environment Applications of Metal-Organic Frameworks. *Solids* **2022**, 3, 35–54. https://doi.org/10.3390/solids3010004

Academic Editor: Mirosław Mączka

Received: 28 December 2021
Accepted: 21 January 2022
Published: 27 January 2022

1. Introduction

Metal-organic frameworks (MOFs) consist of metal clusters, also called secondary building units (SBUs), and bridging organic ligands, also called linkers [1,2]. MOFs are microporous materials with highly tunable properties through their broad variability of metals and linkers [3,4] and a wide field of potential applications [5], such as gas separation [6,7], and storage [8], drug delivery [9,10], catalysis [11], heat transformation, etc. [12–20]. Still, for realistic applications, the initially microcrystalline MOF powders must be formulated or shaped into composites with polymers [21–25]. Furthermore, for the application of porous MOFs under ambient, open-environment conditions in the presence of air and moisture, not only must their hydrothermal stability be considered but also their resistance to antifouling needs to be addressed. A particularly relevant case for the antifouling behavior of MOFs is their use for cyclic water sorption from air for dehumidification [26], including water-harvesting. A recently advocated potential open-environment application is the use of porous materials to capture and release ('harvest') water vapor under atmospheric conditions without external power sources as a promising methodology for obtaining drinking water in arid or desert regions of the world. The potential of metal-organic frameworks to adsorb and desorb water for fresh water production in regions with medium or high humidity conditions during the night was probably first investigated by Kim et al. [27] and Trapani et al. in 2016 [28], and followed-up by Yaghi and others in 2017, until now [29,30].

So far, the antifouling properties of MOFs have rarely been addressed; Cu-BTC (HKUST-1; Hong Kong University of Science and Technology) and derivative materials were found to inhibit the spore growth of *Aspergillus niger*, *Aspergillus oryzae,* and *Fusarium oxysporum* [31], as well as *Fusarium solani* and *Penicillium chrysogenum* [32]. Another approach is the use of silver-based materials, like Ag-MOFs [33].

Most promising MOFs for cyclic water sorption applications are aluminum-based MOFs (Al-MOFs), such as aluminum fumarate (Alfum, Basolite® A520) [34–37], CAU-10-H (Christian-Albrechts-Universität) [38–40], CAU-23 [41], MIL-160 (Matériaux de l'Institut Lavoisier, Material Institute Lavoisier) [42,43], and MIL-53-TDC [44,45] because of their proven hydrothermal stability [45,46], low metal toxicity, and good water uptake characteristics. The hydrothermal stability has been demonstrated for some Al-MOFs over more than 40 cycles, e.g., Alfum [37], CAU-10-H [47], MIL-160 [42], and MIL-100 [48]. Yet, it must also be ensured that the largely organic MOFs will not be prone to fouling through the colonialization and digestion by fungal organism.

Chitosan (CTS) is derived from a natural, non-toxic, biodegradable polymer as the deacetylated derivative of chitin, which is the main constituent of the shell or exoskeleton of insects, crabs, and shrimp [49,50]. As such, chitosan is obtained from the chitin shells of shrimps by alkaline deacetylation. Chitosan offers antifouling effects [51], both against bacteria and against fungi. The antifouling effect depends on the degree of deacetylation and mostly on the molecular weight [52]. MOF@chitosan composite materials are already tested for *inter alia*, the extraction of ions from aqueous systems [53], the treatment of waste water [54], the use as bio-compatible nanocarriers [55], the separation of water-ethanol mixtures [56], the storage of CO_2 [57], or the adsorption of pharmaceutical products [58]. MOFs for chitosan composites are MIL-101(Cr) [59], MIL-101(Fe) [60], MIL-68(Al) [53], MIL-100(Fe) [55], NH2-MIL-88 [61], MIL-125 [62], or UiO-66 (Universitetet i Oslo) [54]. Antifouling properties of these MOF@chitosan composites were, however, not investigated.

Organic materials can be especially suitable habitats for microorganisms living on their surfaces. Many microorganisms tend to form biofilms, attracting other microorganisms to colonize a material's surface using quorum sensing [63]. Fungi can appear as symbionts, decomposers, or pathogens living in biofilms [64]. Fungi, especially of the genus *Aspergillus, Chaetomium,* and *Penicillium,* can act as opportunistic pathogens causing severe mycosis [65–70]. Further, these species are known for their abilities to produce mycotoxins. Due to their spores, these fungi are ubiquitous. High humidity offers appropriate biotopes. Also, medical devices, such as vapor chambers or steam sterilization machines, are possible biotopes for fungi, increasing infection risks [71,72]. From a biofilm, fungi can sporulate, i.e., release massive amounts of spores that can induce allergic asthma by constant immune response [65,73].

To prevent fungal colonization, antifungal agents can be added [74]. Another approach is to design materials with surfaces where microorganisms are not able to grow [75].

Here we investigate the antifouling properties of Al-MOF@chitosan composites with the MOFs Alfum and MIL-160 (Figure 1, further chemical details on the MOFs are given in Section S1, Supplementary Information) against the fungi *Chaetomium globosum* and *Aspergillus falconensis*, thereby also focusing on retaining the MOF porosity. The composites with polyvinylalcohol (PVA) and Silikophen® were tested as references. The DIN EN ISO (Deutsches Institut für Normung, European Norm, International Organization for Standardization) standard for the action of microorganisms on plastics was followed, which describes how tests must be carried out to determine the resistance of materials against microorganisms [76]. *Chaetomium globosum* is one of five fungi named in the DIN EN ISO standard and *Aspergillus falconensis* was chosen because of its lower toxicity compared to *Aspergillus niger*, which is also named in the ISO standard.

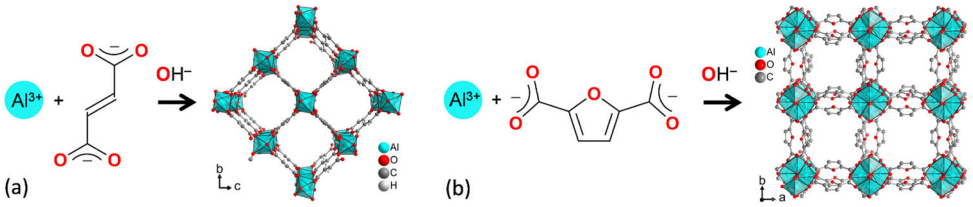

Figure 1. Schematic formation of (**a**) aluminum fumarate (Alfum) from Al^{3+} and fumarate and (**b**) MIL-160 from Al^{3+} and 2,5-furandicarboxylate (see Section S1, Figures S1 and S2, Supplementary Information for further details).

2. Material and Methods

2.1. Materials and Instrumentation

All chemicals were used as received by suppliers (see Section S1 in the Supplementary Information). The aluminum fumarate was received from BASF, known as Basolite® A520. Aluminum chloride hexahydrate, $AlCl_3 \cdot 6H_2O$, was purchased from Fluka Analytical; 2,5-furandicarboxylic acid, 'chitosan medium molecular weight', Mowiol 20–98 (PVA) M_w ~125.000, and Tween80 from Sigma Aldrich; NaOH and ethanol (p. a.) from Chem Solute; ethanol (p. a.) from Riedel de Haën; acetic acid (99.9%) and acetone from VWR Chemical; and sodium triphosphate, glutaraldehyde (25 aq.), and agar from Alfa Aesar. Silikophen® P50/X was obtained from Evonik; xylene (p. a.) and DMF from Fischer Chemical; $NaNO_3$ (p. a.), KCl (p. a.), and KH_2PO_4 (p. a.) from Appli Chem; K_2HPO_4 (p. a.) and $MgSO_4$ * 7 H_2O (p. a.) from Merck; $FeSO_4 \cdot 7\ H_2O$ (99.5%) from Grüssing (the CAS numbers are given in Table S1 in the Supplementary Information).

Powder X-ray diffractometry (PXRD) was performed at ambient temperature on a *Bruker D2 phaser* (BRUKER, Billerica, MA, USA) using Cu-K_α radiation (λ = 1.54182 Å) between 5° < 2θ < 50° with a scan rate of 0.0125 s^{-1} (300 W, 30 kV, 10 mA) and a step size of 0.15 and 0.05° per step, giving a typical total measurement time of 6 min for a diffractogram. In Figures S3 and S4, the PXRDs of the neat MOFs were also measured with a *Rigaku Miniflex 600* (RIGAKU, Tokio; Japan) using Cu-Kα radiation (λ = 1.54182 Å) between 5° < 2θ < 50° with a scan rate of 0.083 s^{-1} (600 W, 40 kV, 15 mA) and a step size of 0.01° per step, giving a total measurement time of 10 min for a diffractogram. Analyses of the diffractograms were carried out with *Match 3.11* software. All PXRD patterns are collected in Section S5 in the Supplementary Information. The broadening of the PXRDs, obtained on the Bruker D2 phaser, is related to the short measurement time, which was selected due to the high number of samples.

Thermogravimetric analysis (TGA) was measured on a *Netzsch TG209 F3 Tarsus* (NETZSCH, Selb, Germany) device under synthetic air atmosphere, ramping 10 K min^{-1} to 600 °C. TGA curves are given in Section S7 in the Supplementary Information.

SEM images were acquired on a *JEOL JSM-6510 Advanced electron microscope* (JEOL, Akishima, Japan) with a LaB_6 cathode at 5–20 keV. The microscope was equipped with an *Xflash 410* (Bruker, Billerica, MA, USA) silicon drift detector. SEM images are presented in Section S8 in the Supplementary Information.

Surface areas (*Brunauer-Emmett-Teller* [77], BET) were determined by nitrogen (purity 99.999%, 5.0) sorption experiments at T = 77 K, using liquid nitrogen and ca. 20–50 mg of sample and performing on a *Quantachrome Autosorp 6* (QUANTACHROME, Odelzhausen, Germany) instrument within a partial pressure range of $pp_0{}^{-1} = 10^{-3} - 1$ bar. Each sample was degassed under a vacuum (<10^{-2} mbar) at 120 °C for ca. 3 h prior to measurement. All surface areas (BET) were calculated from five adsorption points applying Rouquerol plots ($r > 0.998$). For pressure ranges of five-point BET calculations of each MOF, see Section S9 in the Supplementary Information. All N_2 sorption isotherms are shown in Section S9 in the Supplementary Information.

Water sorption experiments were performed on a *Quantachrome VStar4* (QUANTACHROME, Odelzhausen, Germany) instrument within a partial pressure range of $pp_0{}^{-1} = 10^{-3} - 1$ bar. Each sample was degassed under a vacuum (<10^{-3} mbar) at 120 °C for ca. 3 h prior to measurement, using a *FloVac* (QUANTACHROME, Odelzhausen, Germany) degasser. All water sorption isotherms are depicted in Section S10 in the Supplementary Information.

FT-IR spectra were measured in KBr-mode on a Bruker TENSOR 37 IR (BRUKER, Billerica, MA, USA) spectrometer in the range of 4000–400 cm^{-1}. All IR spectra are depicted in Section S6 in the Supplementary Information.

Conventional drying was carried out using a vacuum oven (Vacutherm oven, HERAEUS, Hanau, Germany) and a Büchi glass oven B-560 (Büchi, Flawil, Switzerland).

Supercritical drying was carried out using an ethanol-washed sample still dispersed in ethanol in an automated critical point dryer Leica EM CPD300 (LEICA, Wetzlar, Germany) which was set to perform 99 exchange cycles of CO_2 at slow speed and 100% stirring.

The samples for the tests for microbial metabolism were prepared on a laminar air flow bench of the type Laminar Air Flow (HERAEUS, Hanau, Germany). For this, petri dishes, needles, and an inoculating loop (SARSTEDT, Nümbrecht, Germany) were used. The tests were carried out in an Incu-Line Incubator (VWR, Radnor, PA, USA) and examined with an eyepiece microscope (WILD HEERBRUGG, Heerbrugg, Switzerland).

2.2. Syntheses

2.2.1. MIL-160 Synthesis

MIL-160 was synthesized under reflux according to the literature Cadiau et al. [42]. Instead of 1 eq NaOH, we used 2 eq NaOH to ensure full deprotonation of the linker 2,5-furandicarboxylic acid. 2,5-Furandicarboxylic acid (4.68 g, 30 mmol, 1 eq) and sodium hydroxide (2.4 g, 60 mmol, 2 eq) were dissolved in water (150 mL). Aluminum chloride hexahydrate (7.24 g, 30 mmol, 1 eq) was added and the mixture refluxed (24 h, 100 °C). After centrifugation, the product was washed three times with water (160 mL), centrifuged, and redispersed each time. Finally, the product was dried overnight (80 °C, 1–10 mbar), yielding a white powder (3.9 g, 66% yield, BET = 1186 $m^2\ g^{-1}$) (further details in Section S2, Supplementary Information).

2.2.2. Chitosan Bead Synthesis

Chitosan beads were synthesized according to the literature of Bodmeier et al. and Wu et al. [78,79]. Chitosan solutions were prepared with different concentrations by dissolving chitosan flakes in 2 wt-% (weight-%) acetic acid. Thus, the following four concentrations of 6, 20, 30, and 40 g L^{-1} were obtained. For preparing beads, the chitosan solutions were taken up with a 1 mL syringe and added dropwise to a 10 wt-% $Na_5P_3O_{10}$ solution. Subsequently, the particles were washed with water and dried overnight (80 °C, 1–10 mbar) (further details in Section S2, Supplementary Information).

2.2.3. Synthesis of MOF@chitosan

MOF@chitosan beads were synthesized according to the literature of Zhuo et al. [58]. Different MOF loadings were prepared, up to a maximum of 90 wt-%. Composite materials were prepared with chitosan solutions of 6 or 20 g L^{-1} (corresponding to 10 and 20 or 3 and 6 mL of solution, cf. Table 1). The solid MOF was added into the chitosan solution (chitosan dissolved in 2 wt-% acetic acid) and stirred for 3 h. This mixture, drawn in portions of 1 mL in a 1 mL syringe and from there the portion of 1 mL, was added quickly dropwise (within 30 s) into a 10 wt-% $Na_5P_3O_{10}$ solution with constant stirring at room temperature for 15 min. The synthesized beads were collected and washed with Milli-Q water and dried overnight (80 °C, 1–10 mbar) (further details in Table 1 and Section S3, Supplementary Information). Figure 2 illustrates the synthesis process.

Table 1. Details of the relative and absolute MOF and polymer amounts.

Composite	Crosslinker [a]	MOF Amount	Polymer Amount	Solution Volume and Concentration
MOF60@Chitosan	$Na_5P_3O_{10}$	60% (180 mg)	40% (120 mg)	20 or 6 mL, 6 or 20 g L^{-1}
MOF80@Chitosan	$Na_5P_3O_{10}$	80% (240 mg)	20% (60 mg)	10 or 3 mL, 6 or 20 g L^{-1}
MOF90@Chitosan	$Na_5P_3O_{10}$	90% (540 mg)	10% (60 mg)	10 or 3 mL, 6 or 20 g L^{-1}
MOF@PVA	-	80% (480 mg)	20% (120 mg)	2 mL, 60 g L^{-1}
MOF@Silikophen®	-	High	low only on surface [b]	10 mL of Silikophen in 30 mL of xylene

[a] 10 wt% solution. [b] Amount of polymer cannot be determined due to the dip coating process.

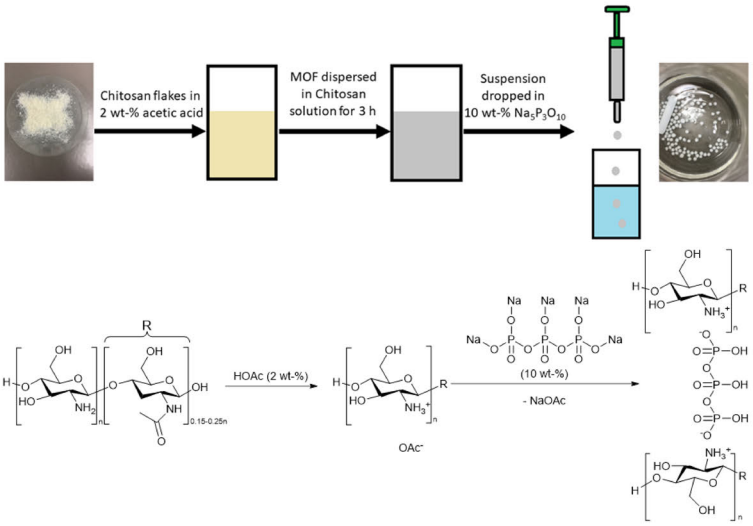

Figure 2. Synthesis process of the MOF@chitosan composites and reaction scheme of the crosslinking process below (both with $Na_5P_3O_{10}$).

2.2.4. Synthesis of MOF@PVA

MOF@PVA beads were synthesized according to a synthesis of Khabzina et al. [80] with MOF loadings of up to 80 wt-%. A PVA solution (60 g L^{-1}) was prepared by dissolving PVA powder in water at 80 °C for 24 h by constant stirring until a homogeneous solution was obtained. Then the MOF (480 mg) was added into the PVA solution (120 mg in 2 mL water) and stirred for 24 h to get a homogeneous suspension. The MOF@PVA suspension was, dropwise, added into liquid nitrogen to form composite beads. These beads were collected and stored in acetone for 24 h, followed by washing three times with acetone (150 mL) and drying overnight (80 °C, 1–10 mbar) (further details in Table 1 and Section S3, Supplementary Information).

2.2.5. Synthesis of MOF@Silikophen®

MOF@Silikophen® composites were synthesized according to the literature of Jeremias et al. [37]. Silikophen® P50/X (10 mL) was dissolved in xylene (30 mL). MOF tablets were prepared by

using an IR-press with 2 tons of surface pressure (further details in Section S3, Supplementary Information). MOF tablets were dipped into the Silikophen® solution, removed after 20 s, and dried at RT in air over night. Afterwards, the tablets were tempered according to the following program: 2 h/50 °C; 2 h/105 °C; 3 h/250 °C; and then cooled to RT (further details in Table 1 and Section S3, Supplementary Information).

2.3. Antifouling Tests

The procedure is based on method A of DIN EN ISO 846 (10/1997) (testing for resistance to fungi) [76], using a low-carbon nutrient medium. The composition of the nutrient medium can be taken from Table S5 in the Supplementary Information. The mineral salts are dissolved in 2000 mL of water and form the basis for the fungus tests. A total of 1000 mL of this stock mineral salt solution is mixed with 0.1 g of a non-toxic wetting agent (Tween80). The carbon source-free (incomplete) culture medium for the actual tests is obtained by adding 10 g agar (20 g L^{-1}) to 500 mL of the stock mineral salt solution. The fungus tests were carried out according to the following protocol:

First, the samples were immersed for 1 min in an ethanol-water mixture (70:30), air dried, and stored in a closed container at RT until use. The test specimens were disinfected before the test by means of water-steam sterilization (121 °C, 2 bar). The complete culture medium was filled after heating in sterile petri dishes and cured. The samples were placed as flat as possible on the incomplete nutrient medium. Spores of the fungi to be used were taken from the respective spore turf and combined with the mineral salt solution with a wetting agent additive to form a spore suspension. The spore suspensions were placed on the incomplete nutrient media and the petri dishes were sealed. The samples were incubated with the fungi at 24 ± 1 °C for up to four weeks.

The preparation of a spore suspension was carried out with the following fungi: *Chaetomium globosum* and *Aspergillus falconensis* (further details in Section S4, Supplementary Information).

Method A of the DIN EN ISO 846 [76] test describes five fungi (*Aspergillus niger, Penicillium funiculosum, Paecilomyces varioti, Gliocladium virens,* and *Chaetomium globosum*). Our labs only support risk group 1 organisms, according to the TRBA 460 "Classification of fungi in risk groups"; therefore, we decided to test our composites with two fungi classified as risk group 1 organisms: *Aspergillus falconensis* (as a substitute for *Aspergillus niger*, which belongs to risk group 2) and *Chaetomium globosum.* To better assess whether the used chitosan is digested or overgrown, the two mentioned fungi were examined individually (unlike the DIN EN ISO standard).

Figure 3 shows two examples of two used composites that did not pass the overgrow tests. Due to the morphological appearances of the fungi, they could be distinguished easily from the composites.

All samples were tableted to obtain a uniform shape and surface area for the fungi growth and to facilitate visual assessment. This ensured that fungi growth would not be influenced by the shape or surface area of powders versus granules with larger and smaller outer-surface areas. However, during surface sterilization, some tablets degraded. Pieces of such degraded tablets were still used.

The evaluation of the samples was carried out by means of visual classification, which is also specified in the DIN EN ISO standard (cf. Table 2). Over the time of 15 or 27 days, photographic images of the antifouling tests were taken 1 to 6 days apart (Section S11, Supplementary Information). The basis for the assessment was always the final image of the test series (day 15 for *Chaetomium globosum* and day 27 for *Aspergillus falconensis*; Section S11, Supplementary Information) and the associated microscopic observation of the growth intensity (Table 2). Growth experiments with *Aspergillus falconensis* were carried out in triplicate to ensure reproducibility.

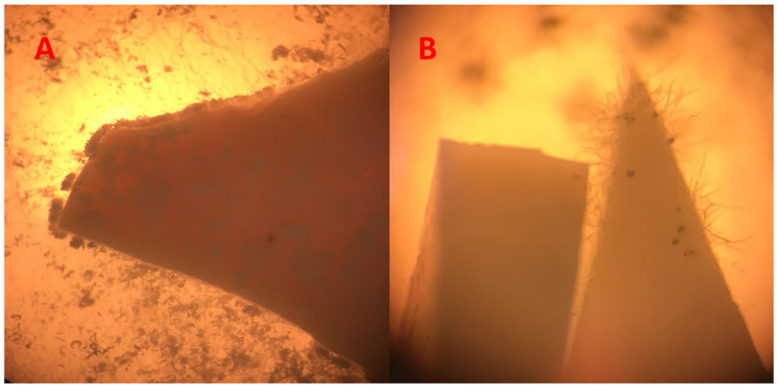

Figure 3. Image (**A**) shows overgrown composites with *Chaetomium globosum*; Image (**B**) shows several spores of *Aspergillus falconensis*, including heads. (64-fold enlargement of two composites during the growth tests).

Table 2. Evaluation of the growth strength for the visual assessment, based on DIN EN ISO 846.

Method	Category	Growth Intensity, Observation	Assessment of the Sample Material
A	0	no growth visible under microscopic observation	material does not serve as a nutrient for microorganisms; it is "inert" or "fungistatic"
	1	no growth visible with the naked eye, but clearly visible under the microscope at 50 times magnification	material contains nutrients or is only slightly soiled, so that only slight growth is possible
	2	growth visible to the naked eye, up to 25% of the sample surface overgrown	material is not resistant to fungal attack and contains nutrients for the development of microorganisms
	3	growth visible to the naked eye, up to 50% of the sample surface overgrown	
	4	significant growth, over 50% of the sample surface overgrown	
	5	strong growth, entire sample surface overgrown	

3. Results and Discussion

The aluminum fumarate (Alfum) used for the composite materials was supplied by BASF as Basolite® A520. The synthesis of MIL-160 was based on a procedure by Cadiau et al. [42], except that twice the amount of sodium hydroxide was used to achieve complete deprotonation of the 2,5-furandicarboxylic acid. For comparison with the MOF@chitosan composites, both Alfum and MIL-160 were characterized by PXRD (Figures S3 and S4), SEM (Figures S17 and S18), IR (Figure S8), N_2-sorption (Figures S26 and S27), H_2O-sorption (Figures S34 and S35), and TGA (Figure S11, Supplementary Information).

The used chitosan (medium molecular weight) was purchased from Sigma Aldrich, with a specified molecular weight dispersion of 190 to 310 kDa and a degree of deacetylation of 75–85% (from the data sheet of the manufacturer). The chitosan was received as flakes, which have a white-beige to brownish color. The crosslinked chitosan particles with different chitosan concentrations had BET-surface areas between 144 and 233 $m^2\ g^{-1}$.

3.1. MOF@chitosan Composites

The soluble chitosan was crosslinked in the presence of the MOF, and to precipitate the MOF@chitosan composite Glutaraldehyde (1 mL of an 83 g L^{-1} solution) and sodium triphosphate ($Na_5P_3O_{10}$, 10 wt-% solution) were tested as crosslinkers. Glutaraldehyde

bonds connect covalently to chitosan (Figure S42, Supplementary Information), whereas $Na_5P_3O_{10}$ connects the chitosan chains by ionic bonds through the protonated amino group (Figure 2). $Na_5P_3O_{10}$ proved to be the better crosslinker, due to its non-toxicity and easier handling, regarding synthesis, compared to glutaraldehyde. Hence, the use of glutaraldehyde was not pursued any further, also because of its toxicity. Furthermore, the syntheses of the composite materials with glutaraldehyde required considerably more time for the gelation and aging so that only monoliths, no beads, could be obtained and MOF loadings up to 90% could not be achieved (Section S2 and S3, Supplementary Information).

The composite formation does not affect the particle size of the MOF. The MOF peak widths in the PXRD patterns (albeit already high due to instrument effects; see below) did not change. The higher background is related to the amount of amorphous chitosan inside the composite. There should be no change in MOF particle size because ultrasound, which is known to decrease the particle size, was not used for composite formation.

3.1.1. Alfum@chitosan

For the Alfum@chitosan composites, several syntheses were carried out in which the MOF content was systematically varied, and two different chitosan concentrations (6 and 20 g L^{-1}) were used. The MOF content was 60, 80, and 90 wt-% in relation to the all the composite material. Even higher loading was not possible because the volume of the chitosan solution eventually became too low and no longer produced a homogeneous dispersion; therefore, it became impossible to add it dropwise into the $Na_5P_3O_{10}$ solution. The diffraction patterns of the Alfum@chitosan composites confirm the retention of MOF crystallinity (Figures 4 and S5, Supplementary Information).

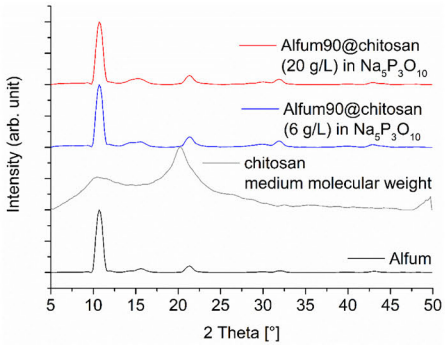

Figure 4. PXRD patterns of Alfum90@chitosan composites for a MOF content of 90 wt-%, prepared with different chitosan concentrations. The diffraction patterns for 60 and 80 wt-% Alfum@chitosan are shown in Figure S5 (Supplementary Information). The broad contribution from amorphous chitosan is only seen at lower MOF wt-% (Figure S5). The broadening of the PXRDs is related to the short measurement time of 6 min on the Bruker D2 phaser, which was used due to the large number of samples and is not related to a low crystallinity of the MOF (cf. Figure S3 in the Supplementary Information with the sharper reflexes measured on a Rigaku Miniflex). The PXRD of Alfum was obtained from the purchased MOF from BASF.

The pore accessibility of Alfum within the Alfum@chitosan composite materials was investigated by nitrogen and water sorption (Figures 5, S29 and S37, Supplementary Information).

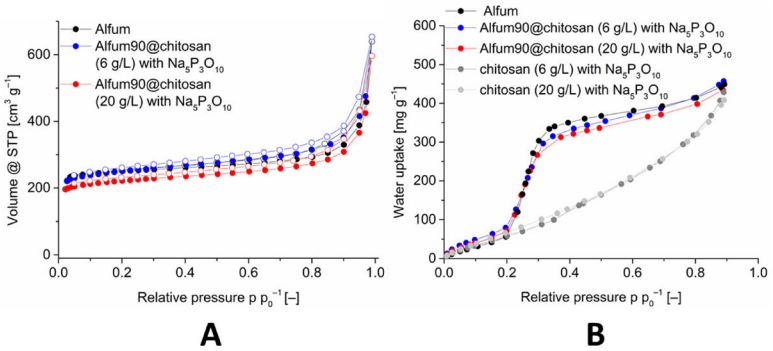

Figure 5. Image (**A**): Nitrogen sorption (77 K) isotherm of Alfum90@chitosan composites with different chitosan concentrations, in comparison with Alfum. Image (**B**): Water adsorption (293 K) isotherms of Alfum90@chitosan composites with different chitosan concentrations, in comparison with Alfum and crosslinked chitosan. The isotherms for 60 and 80 wt-% Alfum@chitosan are shown in Figures S29 and S37 (Supplementary Information).

The porosity, that is, BET-surface areas, pore volumes and water uptake values decrease disproportionately high with the decrease in the Alfum in the composite. Table 3 lists the porosity data in comparison with the calculated (expected) values, which are mass-corrected for the wt-% of the MOFs and the chitosan in the composite. The measured values also become much lower than the calculated (expected) BET-surface areas and the water uptake values. Thus, the composite materials with 60% MOF have a significantly lower surface than the materials with 80% and 90% MOF. Only when the composite was dried supercritically for activation prior to the sorption measurements the expected BET-surface area could be obtained. During the normal thermal/vacuum drying process, the beads of the Alfum@chitosan composite shrink considerably (decrease in diameter from 3.5 mm to 3.0 mm (20 g L^{-1}) and 2.5 mm to 2.4 mm (6 g L^{-1}), Figure S41, Supplementary Information) whereas during supercritically drying the beads retain the original size but become mechanically fragile. Hence, the solvent plays a role of a pore-forming agent by creating an interfacial volume between the MOF and the chitosan layer. When the solvent is removed by thermal/vacuum drying, the chitosan layer apparently covers and blocks part of the pores. Supercritical drying retains the interfacial volume and, thereby, prevents pore blocking but at the expense of mechanical stability. The beads break apart. The composite material with 90% MOF and a chitosan concentration of 6 g L^{-1} provides the best result with a BET-surface area of 964 m^2 g^{-1}.

Scanning electron microscopy (SEM) images with energy-dispersive X-ray spectroscopic (EDX) element mapping (Figure 6) reveal a very good superposition, which suggests that both aluminum and phosphorus (from cross-linked chitosan) are evenly distributed in the bead.

A magnified view of the surface of the beads does not allow differentiation between the agglomerated particles of Alfum and the chitosan since Alfum does not have a well-defined morphology.

Table 3. BET-surface areas, pore volumes, and water uptake values of the composite materials and the educts.

Educt/Composite Materials	CTS Conc. [g L^{-1}]	BET-Surface [m^2 g^{-1}]		Pore Volume [cm^3 g^{-1}] [a]		Water Uptake [mg g^{-1}] at 0.9 p p_0^{-1}	
		Meas. (% of Calc.)	Calc. [b]	Meas. (% of Calc)	Calc. [b]	Meas. (% of Calc.)	Calc. [a]
chitosan	6	144	-	0.30	-	428	-
chitosan	20	230	-	0.46	-	408	-
chitosan	30	220	-	0.45	-	-	-
chitosan	40	202	-	0.40	-	-	-
Alfum (Basolite® A520)	-	988	-	0.51	-	449	-
Alfum60@chitosan	6	20 (3)	650	0.23 (53)	0.43	-	-
Alfum60@chitosan	20	294 (43)	685	0.18 (37)	0.49	-	-
Alfum60@chitosan	30	202 (30)	681	0.16 (33)	0.49	-	-
Alfum60@chitosan	40	26 (4)	674	0.43 (91)	0.47	-	-
Alfum80@chitosan	6	474 (58)	819	0.29 (62)	0.47	393 (88)	445
Alfum80@chitosan	20	587 (70)	836	0.35 (70)	0.50	468 (106)	441
Alfum80@chitosan d.s. [c]	6	844 (103)	819	0.67 (143)	0.47	-	-
Alfum80@chitosan d.s. [c]	20	893 (107)	836	0.58 (116)	0.50	-	-
Alfum90@chitosan	6	964 (107)	904	0.54 (110)	0.49	457 (102)	447
Alfum90@chitosan	20	856 (94)	912	0.48 (94)	0.51	434 (98)	445
MIL-160	-	1186	-	0.48	-	368	-
MIL-160(60)@chitosan	6	32 (4)	769	0.22 (54)	0.41	-	-
MIL-160(60)@chitosan	20	138 (17)	804	0.47 (100)	0.47	-	-
MIL-160(80)@chitosan	6	720 (74)	978	0.34 (77)	0.44	347 (91)	380
MIL-160(80)@chitosan	20	610 (61)	995	0.29 (60)	0.48	370 (98)	376
MIL-160(80)@chitosan d.s. [c]	6	858 (88)	978	0.46 (105)	0.44	-	-
MIL-160(80)@chitosan d.s. [c]	20	918 (92)	995	0.47 (98)	0.48	-	-
MIL-160(90)@chitosan	6	1068 (99)	1082	0.44 (96)	0.46	395 (106)	374
MIL-160(90)@chitosan	20	964 (88)	1090	0.41 (85)	0.48	392 (105)	372

[a] Pore volume at 0.9 p p_0^{-1}. [b] The calculated (expected) mass-corrected BET surfaces (1), pore volumes (2), and the water uptake values (3) were derived as the sum of the mass-weighted S_{BET}, V_{pore}, or H_2O uptake of the MOFs and S_{BET}, V_{pore}, or H_2O uptake of the chitosan with the following three formulas: $S_{BET}^{calc} = wt\text{-}\%_{MOF} * S_{BET}^{MOF} + wt\text{-}\%_{Chitosan} * S_{BET}^{Chitosan}$ (1); $V_{pore}^{calc} = wt\text{-}\%_{MOF} * V_{pore}^{MOF} + wt\text{-}\%_{Chitosan} * V_{pore}^{Chitosan}$ (2); $H_2O\ uptake^{calc} = wt\text{-}\%_{MOF} * H_2O\ uptake^{MOF} + wt\text{-}\%_{Chitosan} * H_2O\ uptake^{Chitosan}$ (3). with S_{BET}(Alfum) = 988 m^2 g^{-1}, S_{BET}(MIL-160) = 1186 m^2 g^{-1}, etc. [c] d.s. = dried supercritically for activation prior to sorption measurements.

3.1.2. MIL-160@chitosan

The MIL-160 composite materials were prepared and characterized like the composite materials with Alfum. The same percentages of MOF and chitosan were used to ensure comparability. The PXRDs of the composite materials point out the reflexes of the MIL-160. Only the diffractogram of the spheres with 60% has a stronger background due to the high amorphous content of chitosan, shown in the ESI. The PXRDs of 80% and 90% composite materials do not have a strong background and correlate with the MOF content, shown in Figure 7 for the composite material with 90% MIL-160. In addition, the reflections match the MOF and the diffractogram has no impurities.

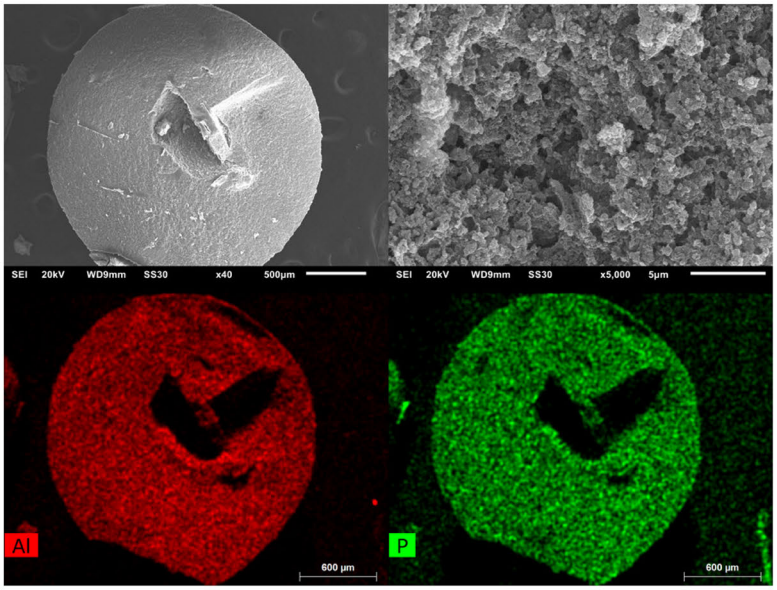

Figure 6. SEM images of Alfum80@chitosan at different magnifications (left: overview, right: close-up). EDX-element mapping for aluminum and phosphorus (bottom) for the particle in the overview at top left. The dark features in the element maps, that is, the lower amount of Al and P in the center and to the upper right of the bead are due to X-ray blocking by the groove in the bead surface so that the generated element-specific X-rays cannot be detected.

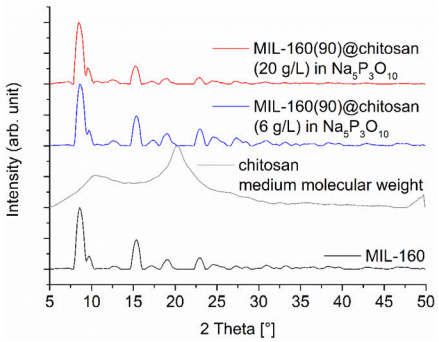

Figure 7. PXRD patterns of MIL-160(90)@chitosan composites for a MOF content of 90 wt-%, prepared with different chitosan concentrations. The diffraction patterns for 60 and 80 wt-% MIL-160@chitosan are shown in Figure S6 (Supplementary Information). The broad contribution from amorphous chitosan is only seen at lower MOF wt-% (Figure S6). The broadening of the PXRDs are related to the short measurement time of 6 min on the Bruker D2 phaser, which was used due to the large number of samples and is not related to a low crystallinity of the MOF (cf. Figure S4 in the Supplementary Information with the sharper reflexes measured on a Rigaku Miniflex).

The sorption properties were investigated analogously to the other composite materials with nitrogen sorption and water sorption. The nitrogen sorptions are shown in Figure 8.

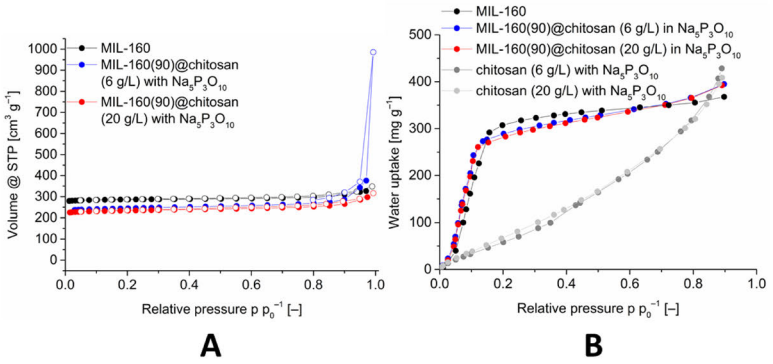

Figure 8. Image (**A**): Nitrogen sorption (77 K) isotherm of MIL-160(90)@chitosan composites with different chitosan concentrations, in comparison with MIL-160. Image (**B**): Water adsorption (293 K) isotherms of MIL-160(90)@chitosan composites with different chitosan concentrations, in comparison with MIL-160 and crosslinked chitosan. The isotherms for 60 and 80 wt-% MIL-160@chitosan are shown in Figures S30 and S38 (Supplementary Information).

The nitrogen adsorption isotherms and the associated BET-surface areas correlate with the percentage of MOF (cf. Table 3). Thus, the composite materials with 60% MOF have a significantly lower surface area than the materials with 80% and 90% MOF. The composite material with 90% MOF and a chitosan concentration of 6 g L^{-1} gives the best result with a BET-surface area of 1068 m^2 g^{-1}. The associated water sorption isotherms are shown in Figure 8 and in the ESI and were measured for the composite materials with an MOF content of 80% and 90%. The S-shaped water sorption isotherm with little-to-no uptake at low p $p_0{}^{-1}$ and a sudden rise in a small p $p_0{}^{-1}$ interval correspond to Type V isotherms [77] and are typical for the adsorption of water vapor at MOFs [15].

The maximum adsorption of the composite material is above the maximum uptake of MIL-160. This can be attributed to the polymer because it has a higher water uptake at a relative pressure of 0.9. This higher uptake is characteristic for polymers, and it is due to swelling. To verify the cross-linking of the composite and the MOF in the material, an EDX mapping for aluminum and phosphorus was performed and presented in Figure 9.

The EDX mapping shows that, in the complete area of the sphere, aluminum, and thus MOF and phosphorus, and thus cross-linked chitosan, are present. The lower amounts of Al and P in the middle right of the mapping is due to the particle geometry. The hollow in the middle of the particle blocks the X-rays, and they cannot be detected. In addition to the analytical methods described, TGA and IR, shown in the ESI, were recorded on selected samples.

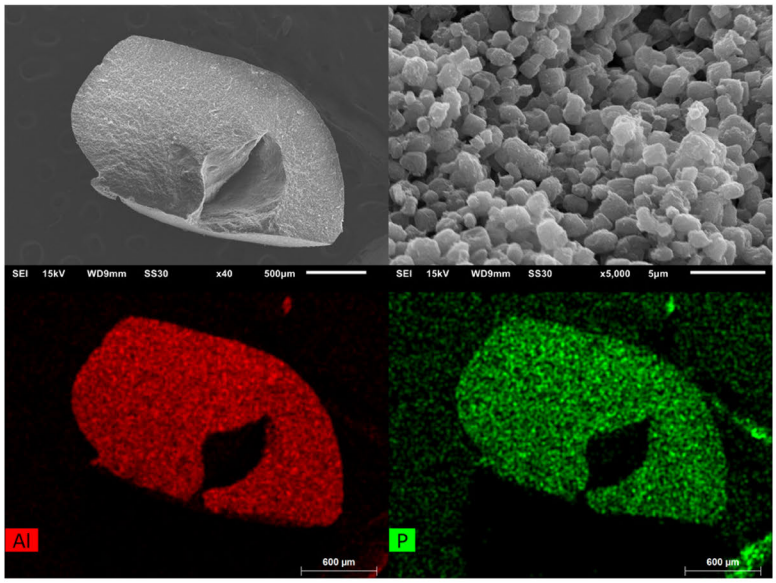

Figure 9. SEM images of MIL-160(90)@chitosan at different magnifications (left: overview; right: close-up). EDX-mapping measurement for aluminum and phosphorus (bottom). The dark features in the element maps, that is, the lower amounts of Al and P in the center and to the upper right of the bead are due to X-ray blocking by the groove in the bead surface so that the generated element-specific X-rays cannot be detected.

3.2. MOF@PVA Composites and MOF@Silikophen® Composites

The MOF@PVA composite materials, as well as the Silikophen® composite materials, were used as reference materials for the antifouling tests of MOF@chitosan. Silikophen® is a phenylmethylpolysiloxane resin and, unlike the chitosan and PVA polymers, was not used as a matrix but as a coating. For coating, tablets of the two MOFs were pressed and immersed for 20 s in a Silikophen®-xylene mixture, then dried in the air, transferred to a Büchi glass oven, and tempered. The PVA and Silikophen® composites were characterized by PXRD (Figures S8 and S9), SEM (Figures S22–S25), N_2-sorption (Figures S32 and S33), H_2O-sorption (Figure S40), and TGA (Figure S16).

3.3. Antifouling Tests

The evaluation of the samples was conducted by visual examination according to DIN EN ISO 846 [76]. *Chaetomium globosum* grows faster than *Aspergillus falconensis* and can fully overgrow composites within 15 days (Section S11, Supplementary Information), so that incubation with *Chaetomium globosum* was stopped after this time while incubation with *Aspergillus falconensis* was continued for 27 days. Table 4 lists the results of the microbial metabolism tests with *Aspergillus falconensis*. None of composites exhibited an inhibitory effect toward *Chaetomium globosum*. Fully overgrown and colonized composites with *Chaetomium globosum* were observed in all samples (Section S11, Supplementary Information).

Table 4. Comparison of the results of the tests for microbial metabolism for *Aspergillus falconensis*.

Composite Material	*Aspergillus falconensis* $n = 3$		
	1	**2**	**3**
chitosan medium molecular weight	3	5	5
chitosan crosslinked with $Na_5P_3O_{10}$	0	5	5
Alfum60@chitosan	0	0	0
Alfum80@chitosan	0	0	0
Alfum90@chitosan	2	0	0
MIL-160(60)@chitosan	2	0	0
MIL-160(80)@chitosan	1	0	0
MIL-160(90)@chitosan	2	0	0
Alfum	3	5	5
MIL-160	1	1	1
Alfum@PVA	2	3	3
MIL-160@PVA	0	2	2
Alfum@Silikophen®	5	5	5
MIL-160@Silikophen®	1	2	2

Figures 10–12 show examples of the spread of the fungus *Aspergillus falconensis* on different samples and the respective assessment according to the DIN EN ISO standard.

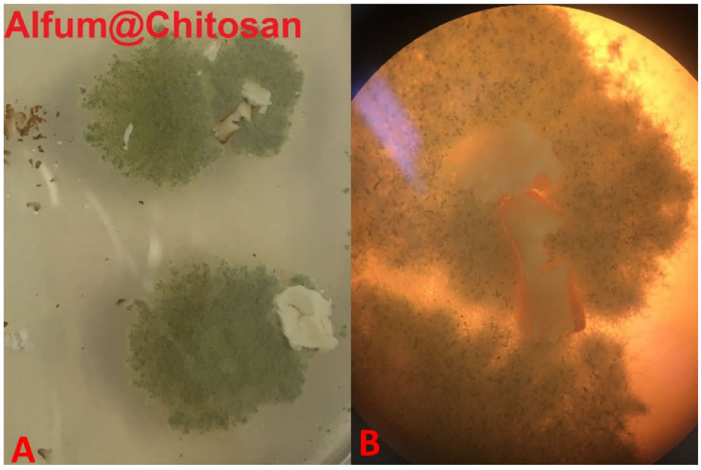

Figure 10. Pictures of the Alfum80@chitosan composite materials in the fungus test with *Aspergillus falconensis*. (Image (**A**): Visual naked-eye observation; Image (**B**): microscopic image).

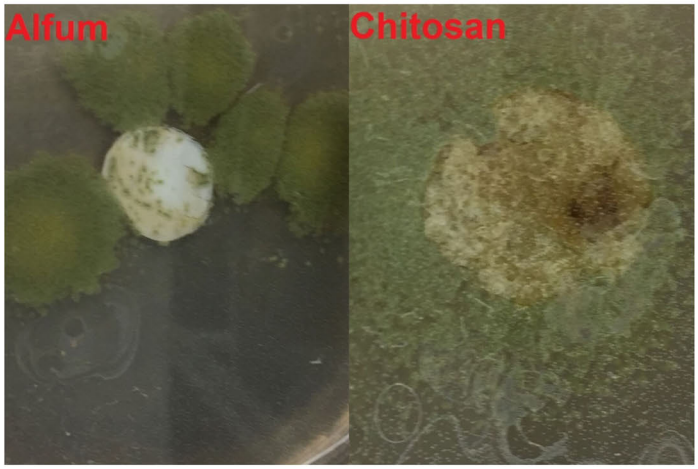

Figure 11. Representative pictures of Alfum and crosslinked chitosan materials in the fungus test with *Aspergillus falconensis*. (Visual naked-eye observation). The diameter of the pressed white composite pellet is 1.3 cm.

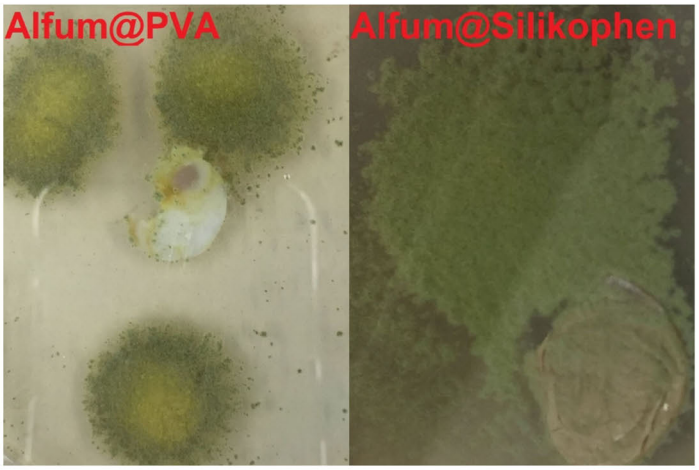

Figure 12. Pictures of the Alfum@PVA and Alfum@Silikophen® materials in the fungus test with *Aspergillus falconensis*. (Visual naked-eye observations).

In all figures, the growth of the fungus is clearly recognizable and due to the green color of the fungus it can be distinguished from the white composite material (cf.). Visually, no growth of the fungus can be seen on top of the material surface in Figure 10. This is also confirmed by the microscopic image. The fungus grows to the vertical edges of the composite material but does not overgrow it. An overgrowth of the composite material, as it is needed for the categories 2–5 (Table 2), can be seen for Alfum and crosslinked chitosan alone (Figure 11) and the PVA and Silikophen® composites (Figure 12).

It is noteworthy that the separate Alfum MOF and chitosan did not show an inhibitory effect towards *Aspergillus falconensis*. Only the combination of Alfum and chitosan exhibited a higher resistance to the fungus. The distance from the start of fungus growth to the

composite materials plays a major role and may explain the slight differences between the three replicate experiments. It is difficult to ensure that the composite materials always grow the same distance from where the fungus is placed on the nutrient medium because the fungus does not grow in a defined direction. During incubation, we ensured that all tablets had a chance to get in contact with the fungus by adding water to prevent the nutrient medium from running dry and making it useless for examination over the time of 15 or 27 days.

The reference composite material Alfum@PVA shows a low degree of overgrowth, and it can also be clearly seen that the sample is not central to fungal growth. The composite Alfum@Silikophen® is assigned to category 5, as over 50% of the sample surface is covered with the fungus. From this it can be concluded that the Silikophen® binder has no anti-fouling effect and thus serves well as a comparison material.

We observed that the *Aspergillus falconensis* can experience two quite different growth states. The fungus can strongly overgrow the Alfum@PVA and MIL-160@Silikophen® composites. For the MOF@chitosan composite, no growth is visible under microscopic observation, hence the material can be considered fungistatic and does not serve as a nutrient for microorganisms.

4. Conclusions

In this work, we were able to synthesize porous MOF@chitosan composite materials with different loadings. Alfum and MIL-160 were embedded in a chitosan matrix for the first time. The chitosan cross-linking was carried out in situ with $Na_5P_3O_{10}$, whereby the chitosan concentrations were systematically varied in order to ensure a homogeneous dispersion necessary for the synthesis and thus to obtain the desired properties of the composite materials. Spherical particles could be obtained by the very reproducible drop casting method.

In addition, tests were performed on the microbial metabolism of the composites. An anti-fouling effect of the chitosan composites against *Aspergillus falconensis* could be detected whereas *Chaetomium globosum* proved to be more aggressive and could overgrow the chitosan composite materials. Further, the chitosan composite materials show a significantly higher resistance to *Aspergillus falconensis* than the composites with PVA and Silikophen®. All MOF@chitosan composite materials could be classified as "inert" or "fungistatic" against *Aspergillus falconensis*. Another interesting observation was the behavior of pure MOF tablets where MIL-160 had a higher resistance than Alfum. In follow-up work, this suggests the need to investigate different MOF linkers and Al-MOFs with a wider variety of linkers for their fungistatic effects.

Supplementary Materials: The following are available online https://www.mdpi.com/article/10.3390/solids3010004/s1. S1. Materials and equipment, S2. MOF and Chitosan Synthesis, S3 Composite Synthesis, S4 Antifouling Tests, S5 PXRD Measurements, S6 Infrared spectra, S7 Thermogravimetric Analysis (TGA), S8 Scanning electron microscopy (SEM), S9 Nitrogen sorption experiments (T = 77 K), S10 Water sorption experiments (T = 293 K), S11 Antifouling tests series (images), S12 Images of the MOF@chitosan composites, S13 Reaction scheme of chitosan and glutaraldehyde, S14 Graphics, S15 References.

Author Contributions: Conceptualization: C.J. (Christian Jansen) and C.J. (Christoph Janiak); methodology: C.J. (Christian Jansen); validation: C.J. (Christian Jansen) and N.M.T.-C.; formal analysis: C.J. (Christian Jansen), N.M.T.-C., C.S., and A.S.; investigation: C.J. (Christian Jansen), N.M.T.-C., C.S., and A.S.; resources: P.P. and C.J. (Christoph Janiak); data curation: C.J. (Christian Jansen); visualization: C.J. (Christian Jansen); writing—original draft preparation: C.J. (Christian Jansen); writing—review and editing: C.J. (Christian Jansen), P.P., and C.J. (Christoph Janiak); Supervision: C.J. (Christoph Janiak); project administration: P.P. and C.J. (Christoph Janiak); funding acquisition: P.P. and C.J. (Christoph Janiak). All authors have read and agreed to the published version of the manuscript.

Funding: C.J. (Christoph Janiak) is indebted to the DFG for funding within the priority program SPP 1928 "COORNET" (grant Ja466–43/1).

Data Availability Statement: The data presented in this study are available on request from the corresponding author.

Conflicts of Interest: The authors declare that they have no known competing financial interests or personal relationships that could have appeared to influence the work reported in this paper.

References

1. Batten, S.R.; Champness, N.R.; Chen, X.-M.; Garcia-Martinez, J.; Kitagawa, S.; Öhrström, L.; O'Keeffe, M.; Paik Suh, M.; Reedijk, J. Terminology of metal–organic frameworks and coordination polymers (IUPAC Recommendations 2013). *Pure Appl. Chem.* **2013**, *85*, 1715–1724. [CrossRef]
2. Zhou, H.-C.J.; Kitagawa, S. Metal-organic frameworks (MOFs). *Chem. Soc. Rev.* **2014**, *43*, 5415–5418. [CrossRef] [PubMed]
3. Farha, O.K.; Hupp, J.T. Rational design, synthesis, purification, and activation of metal-organic framework materials. *Acc. Chem. Res.* **2010**, *43*, 1166–1175. [CrossRef] [PubMed]
4. Taddei, M. When defects turn into virtues: The curious case of zirconium-based metal-organic frameworks. *Coord. Chem. Rev.* **2017**, *343*, 1–24. [CrossRef]
5. Evans, J.D.; Garai, B.; Reinsch, H.; Li, W.; Dissegna, S.; Bon, V.; Senkovska, I.; Fischer, R.A.; Kaskel, S.; Janiak, C.; et al. Metal–organic frameworks in Germany: From synthesis to function. *Coord. Chem. Rev.* **2019**, *380*, 378–418. [CrossRef]
6. Nuhnen, A.; Dietrich, D.; Millan, S.; Janiak, C. Role of Filler Porosity and Filler/Polymer Interface Volume in Metal-Organic Framework/Polymer Mixed-Matrix Membranes for Gas Separation. *ACS Appl. Mater. Interfaces* **2018**, *10*, 33589–33600. [CrossRef]
7. Aykac Ozen, H.; Ozturk, B. Gas separation characteristic of mixed matrix membrane prepared by MOF-5 including different metals. *Sep. Purif. Technol.* **2019**, *211*, 514–521. [CrossRef]
8. He, Y.; Zhou, W.; Qian, G.; Chen, B. Methane storage in metal-organic frameworks. *Chem. Soc. Rev.* **2014**, *43*, 5657–5678. [CrossRef]
9. Karimzadeh, Z.; Javanbakht, S.; Namazi, H. Carboxymethylcellulose/MOF-5/Graphene oxide bio-nanocomposite as antibacterial drug nanocarrier agent. *BioImpacts* **2019**, *9*, 5–13. [CrossRef]
10. Abánades Lázaro, I.; Forgan, R.S. Application of zirconium MOFs in drug delivery and biomedicine. *Coord. Chem. Rev.* **2019**, *380*, 230–259. [CrossRef]
11. Rogge, S.M.J.; Bavykina, A.; Hajek, J.; Garcia, H.; Olivos-Suarez, A.I.; Sepúlveda-Escribano, A.; Vimont, A.; Clet, G.; Bazin, P.; Kapteijn, F.; et al. Metal-organic and covalent organic frameworks as single-site catalysts. *Chem. Soc. Rev.* **2017**, *46*, 3134–3184. [CrossRef] [PubMed]
12. Solovyeva, M.V.; Gordeeva, L.G.; Aristov, Y.I. "MIL-101(Cr)–methanol" as working pair for adsorption heat transformation cycles: Adsorbent shaping, adsorption equilibrium and dynamics. *Energy Convers. Manag.* **2019**, *182*, 299–306. [CrossRef]
13. Hastürk, E.; Ernst, S.-J.; Janiak, C. Recent advances in adsorption heat transformation focusing on the development of adsorbent materials. *Curr. Opin. Chem. Eng.* **2019**, *24*, 26–36. [CrossRef]
14. Gordeeva, L.G.; Aristov, Y.I. Adsorptive heat storage and amplification: New cycles and adsorbents. *Energy* **2019**, *167*, 440–453. [CrossRef]
15. Liu, X.; Wang, X.; Kapteijn, F. Water and Metal-Organic Frameworks: From Interaction toward Utilization. *Chem. Rev.* **2020**, *120*, 8303–8377. [CrossRef] [PubMed]
16. Steinert, D.M.; Ernst, S.-J.; Henninger, S.K.; Janiak, C. Metal-Organic Frameworks as Sorption Materials for Heat Transformation Processes. *Eur. J. Inorg. Chem.* **2020**, *2020*, 4502–4515. [CrossRef]
17. Jeremias, F.; Fröhlich, D.; Janiak, C.; Henninger, S.K. Water and methanol adsorption on MOFs for cycling heat transformation processes. *New J. Chem.* **2014**, *38*, 1846–1852. [CrossRef]
18. Rieth, A.J.; Wright, A.M.; Rao, S.; Kim, H.; LaPotin, A.D.; Wang, E.N.; Dincă, M. Tunable Metal-Organic Frameworks Enable High-Efficiency Cascaded Adsorption Heat Pumps. *J. Am. Chem. Soc* **2018**, *140*, 17591–17596. [CrossRef]
19. Elsayed, E.; AL-Dadah, R.; Mahmoud, S.; Elsayed, A.; Anderson, P.A. Aluminium fumarate and CPO-27(Ni) MOFs: Characterization and thermodynamic analysis for adsorption heat pump applications. *Appl. Therm. Eng.* **2016**, *99*, 802–812. [CrossRef]
20. AL-Dadah, R.; Mahmoud, S.; Elsayed, E.; Youssef, P.; Al-Mousawi, F. Metal-organic framework materials for adsorption heat pumps. *Energy* **2020**, *190*, 116356. [CrossRef]
21. O'Neill, L.D.; Zhang, H.; Bradshaw, D. Macro-/microporous MOF composite beads. *J. Mater. Chem.* **2010**, *20*, 5720. [CrossRef]
22. Rowe, M.D.; Thamm, D.H.; Kraft, S.L.; Boyes, S.G. Polymer-modified gadolinium metal-organic framework nanoparticles used as multifunctional nanomedicines for the targeted imaging and treatment of cancer. *Biomacromolecules* **2009**, *10*, 983–993. [CrossRef] [PubMed]
23. Hastürk, E.; Höfert, S.-P.; Topalli, B.; Schlüsener, C.; Janiak, C. Shaping of MOFs via freeze-casting method with hydrophilic polymers and their effect on textural properties. *Microporous Mesoporous Mater.* **2020**, *295*, 109907. [CrossRef]
24. Hastürk, E.; Schlüsener, C.; Quodbach, J.; Schmitz, A.; Janiak, C. Shaping of metal-organic frameworks into mechanically stable monoliths with poly(vinyl alcohol) by phase separation technique. *Microporous Mesoporous Mater.* **2019**, *280*, 277–287. [CrossRef]
25. Gökpinar, S.; Ernst, S.-J.; Hastürk, E.; Möllers, M.; El Aita, I.; Wiedey, R.; Tannert, N.; Nießing, S.; Abdpour, S.; Schmitz, A.; et al. Air-Con Metal–Organic Frameworks in Binder Composites for Water Adsorption Heat Transformation Systems. *Ind. Eng. Chem. Res.* **2019**, *58*, 21493–21503. [CrossRef]

26. Tsobnang, P.K.; Hastürk, E.; Fröhlich, D.; Wenger, E.; Durand, P.; Ngolui, J.L.; Lecomte, C.; Janiak, C. Water Vapor Single-Gas Selectivity via Flexibility of Three Potential Materials for Autonomous Indoor Humidity Control. *Cryst. Growth Des.* **2019**, *19*, 2869–2880. [CrossRef]
27. Kim, S.-I.; Yoon, T.-U.; Kim, M.-B.; Lee, S.-J.; Hwang, Y.K.; Chang, J.-S.; Kim, H.-J.; Lee, H.-N.; Lee, U.-H.; Bae, Y.-S. Metal–organic frameworks with high working capacities and cyclic hydrothermal stabilities for fresh water production. *Chem. Eng. J.* **2016**, *286*, 467–475. [CrossRef]
28. Trapani, F.; Polyzoidis, A.; Loebbecke, S.; Piscopo, C.G. On the general water harvesting capability of metal-organic frameworks under well-defined climatic conditions. *Microporous Mesoporous Mater.* **2016**, *230*, 20–24. [CrossRef]
29. Kim, H.; Yang, S.; Rao, S.R.; Narayanan, S.; Kapustin, E.A.; Furukawa, H.; Umans, A.S.; Yaghi, O.M.; Wang, E.N. Water harvesting from air with metal-organic frameworks powered by natural sunlight. *Science* **2017**, *356*, 430–434. [CrossRef]
30. Hanikel, N.; Prévot, M.S.; Fathieh, F.; Kapustin, E.A.; Lyu, H.; Wang, H.; Diercks, N.J.; Glover, T.G.; Yaghi, O.M. Rapid Cycling and Exceptional Yield in a Metal-Organic Framework Water Harvester. *ACS Cent. Sci.* **2019**, *5*, 1699–1706. [CrossRef]
31. Bouson, S.; Krittayavathananon, A.; Phattharasupakun, N.; Siwayaprahm, P.; Sawangphruk, M. Antifungal activity of water-stable copper-containing metal-organic frameworks. *R. Soc. Open Sci.* **2017**, *4*, 170654. [CrossRef] [PubMed]
32. Celis-Arias, V.; Loera-Serna, S.; Beltrán, H.I.; Álvarez-Zeferino, J.C.; Garrido, E.; Ruiz-Ramos, R. The fungicide effect of HKUST-1 on Aspergillus niger, Fusarium solani and Penicillium chrysogenum. *New J. Chem.* **2018**, *42*, 5570–5579. [CrossRef]
33. Firouzjaei, M.D.; Shamsabadi, A.A.; Aktij, S.A.; Seyedpour, S.F.; Sharifian Gh, M.; Rahimpour, A.; Esfahani, M.R.; Ulbricht, M.; Soroush, M. Exploiting Synergetic Effects of Graphene Oxide and a Silver-Based Metal-Organic Framework to Enhance Antifouling and Anti-Biofouling Properties of Thin-Film Nanocomposite Membranes. *ACS Appl. Mater. Interfaces* **2018**, *10*, 42967–42978. [CrossRef] [PubMed]
34. Alvarez, E.; Guillou, N.; Martineau, C.; Bueken, B.; Van de Voorde, B.; Le Guillouzer, C.; Fabry, P.; Nouar, F.; Taulelle, F.; Vos, D.D.; et al. The structure of the aluminum fumarate metal-organic framework A520. *Angew. Chem.* **2015**, *54*, 3664–3668. [CrossRef] [PubMed]
35. Leung, E.; Müller, U.; Trukhan, N.; Mattenheimer, H.; Cox, G.; Blei, S. Process for Preparing Porous Metal-Organic Framework Based on Aluminium Fumarate. U.S. Patent 2012/0082864 A1, 30 September 2011.
36. Kummer, H.; Jeremias, F.; Warlo, A.; Füldner, G.; Fröhlich, D.; Janiak, C.; Gläser, R.; Henninger, S.K. A Functional Full-Scale Heat Exchanger Coated with Aluminum Fumarate Metal–Organic Framework for Adsorption Heat Transformation. *Ind. Eng. Chem. Res.* **2017**, *56*, 8393–8398. [CrossRef]
37. Jeremias, F.; Fröhlich, D.; Janiak, C.; Henninger, S.K. Advancement of sorption-based heat transformation by a metal coating of highly-stable, hydrophilic aluminium fumarate MOF. *RSC Adv.* **2014**, *4*, 24073–24082. [CrossRef]
38. Reinsch, H.; Waitschat, S.; Stock, N. Mixed-linker MOFs with CAU-10 structure: Synthesis and gas sorption characteristics. *Dalton Trans.* **2013**, *42*, 4840–4847. [CrossRef]
39. Fröhlich, D.; Pantatosaki, E.; Kolokathis, P.D.; Markey, K.; Reinsch, H.; Baumgartner, M.; van der Veen, M.A.; de Vos, D.E.; Stock, N.; Papadopoulos, G.K.; et al. Water adsorption behaviour of CAU-10-H: A thorough investigation of its structure–property relationships. *J. Mater. Chem. A* **2016**, *4*, 11859–11869. [CrossRef]
40. Lenzen, D.; Bendix, P.; Reinsch, H.; Fröhlich, D.; Kummer, H.; Möllers, M.; Hügenell, P.P.C.; Gläser, R.; Henninger, S.; Stock, N. Scalable Green Synthesis and Full-Scale Test of the Metal-Organic Framework CAU-10-H for Use in Adsorption-Driven Chillers. *Adv. Mater.* **2018**, *30*. [CrossRef]
41. Lenzen, D.; Zhao, J.; Ernst, S.-J.; Wahiduzzaman, M.; Ken Inge, A.; Fröhlich, D.; Xu, H.; Bart, H.-J.; Janiak, C.; Henninger, S.; et al. A metal-organic framework for efficient water-based ultra-low-temperature-driven cooling. *Nat. Commun.* **2019**, *10*, 3025. [CrossRef]
42. Cadiau, A.; Lee, J.S.; Damasceno Borges, D.; Fabry, P.; Devic, T.; Wharmby, M.T.; Martineau, C.; Foucher, D.; Taulelle, F.; Jun, C.-H.; et al. Design of hydrophilic metal organic framework water adsorbents for heat reallocation. *Adv. Mater.* **2015**, *27*, 4775–4780. [CrossRef]
43. Permyakova, A.; Skrylnyk, O.; Courbon, E.; Affram, M.; Wang, S.; Lee, U.-H.; Valekar, A.H.; Nouar, F.; Mouchaham, G.; Devic, T.; et al. Synthesis Optimization, Shaping, and Heat Reallocation Evaluation of the Hydrophilic Metal-Organic Framework MIL-160(Al). *Chem. Sus. Chem.* **2017**, *10*, 1419–1426. [CrossRef] [PubMed]
44. Tschense, C.B.L.; Reimer, N.; Hsu, C.-W.; Reinsch, H.; Siegel, R.; Chen, W.-J.; Lin, C.-H.; Cadiau, A.; Serre, C.; Senker, J.; et al. New Group 13 MIL-53 Derivates based on 2,5-Thiophenedicarboxylic Acid. *Z. Anorg. Allg. Chem.* **2017**, *643*, 1600–1608. [CrossRef]
45. Tannert, N.; Ernst, S.-J.; Jansen, C.; Bart, H.-J.; Henninger, S.K.; Janiak, C. Evaluation of the highly stable metal–organic framework MIL-53(Al)-TDC (TDC = 2,5-thiophenedicarboxylate) as a new and promising adsorbent for heat transformation applications. *J. Mater. Chem. A* **2018**, *6*, 17706–17712. [CrossRef]
46. Gaab, M.; Trukhan, N.; Maurer, S.; Gummaraju, R.; Müller, U. The progression of Al-based metal-organic frameworks—From academic research to industrial production and applications. *Microporous Mesoporous Mater.* **2012**, *157*, 131–136. [CrossRef]
47. Fröhlich, D.; Henninger, S.K.; Janiak, C. Multicycle water vapour stability of microporous breathing MOF aluminium isophthalate CAU-10-H. *Dalton Trans.* **2014**, *43*, 15300–15304. [CrossRef]
48. Jeremias, F.; Khutia, A.; Henninger, S.K.; Janiak, C. MIL-100(Al, Fe) as water adsorbents for heat transformation purposes—a promising application. *J. Mater. Chem.* **2012**, *22*, 10148–10151. [CrossRef]

49. Wisser, D.; Wisser, F.M.; Raschke, S.; Klein, N.; Leistner, M.; Grothe, J.; Brunner, E.; Kaskel, S. Biological Chitin-MOF Composites with Hierarchical Pore Systems for Air-Filtration Applications. *Angew. Chem.* **2015**, *54*, 12588–12591. [CrossRef]
50. Percot, A.; Viton, C.; Domard, A. Optimization of chitin extraction from shrimp shells. *Biomacromolecules* **2003**, *4*, 12–18. [CrossRef]
51. Islam, S.; Bhuiyan, M.A.R.; Islam, M.N. Chitin and Chitosan: Structure, Properties and Applications in Biomedical Engineering. *J. Polym. Environ.* **2017**, *25*, 854–866. [CrossRef]
52. Goy, R.C.; de Britto, D.; Assis, O.B.G. A review of the antimicrobial activity of chitosan. *Polimeros* **2009**, *19*, 241–247. [CrossRef]
53. Asiabi, M.; Mehdinia, A.; Jabbari, A. Spider-web-like chitosan/MIL-68(Al) composite nanofibers for high-efficient solid phase extraction of Pb(II) and Cd(II). *Microchim. Acta* **2017**, *184*, 4495–4501. [CrossRef]
54. Fu, Q.; Wen, L.; Zhang, L.; Chen, X.; Pun, D.; Ahmed, A.; Yang, Y.; Zhang, H. Preparation of Ice-Templated MOF-Polymer Composite Monoliths and Their Application for Wastewater Treatment with High Capacity and Easy Recycling. *ACS Appl. Mater. Interfaces* **2017**, *9*, 33979–33988. [CrossRef]
55. Hidalgo, T.; Giménez-Marqués, M.; Bellido, E.; Avila, J.; Asensio, M.C.; Salles, F.; Lozano, M.V.; Guillevic, M.; Simón-Vázquez, R.; González-Fernández, A.; et al. Chitosan-coated mesoporous MIL-100(Fe) nanoparticles as improved bio-compatible oral nanocarriers. *Sci. Rep.* **2017**, *7*, 43099. [CrossRef] [PubMed]
56. Li, Q.; Liu, Q.; Zhao, J.; Hua, Y.; Sun, J.; Duan, J.; Jin, W. High efficient water/ethanol separation by a mixed matrix membrane incorporating MOF filler with high water adsorption capacity. *J. Membr. Sci.* **2017**, *544*, 68–78. [CrossRef]
57. Singo, M.C.; Molepo, X.C.; Oluwasina, O.O.; Daramola, M.O. Chitosan-impregnated Sod-Metal Organic Frameworks (Sod-ZMOF) for CO_2 Capture: Synthesis and Performance Evaluation. *Energy Procedia* **2017**, *114*, 2429–2440. [CrossRef]
58. Zhuo, N.; Lan, Y.; Yang, W.; Yang, Z.; Li, X.; Zhou, X.; Liu, Y.; Shen, J.; Zhang, X. Adsorption of three selected pharmaceuticals and personal care products (PPCPs) onto MIL-101(Cr)/natural polymer composite beads. *Sep. Purif. Technol.* **2017**, *177*, 272–280. [CrossRef]
59. Liu, L.; Ge, J.; Yang, L.-T.; Jiang, X.; Qiu, L.-G. Facile preparation of chitosan enwrapping Fe_3O_4 nanoparticles and MIL-101(Cr) magnetic composites for enhanced methyl orange adsorption. *J. Porous Mater.* **2016**, *23*, 1363–1372. [CrossRef]
60. Asiabi, M.; Mehdinia, A.; Jabbari, A. Electrospun biocompatible Chitosan/MIL-101 (Fe) composite nanofibers for solid-phase extraction of Δ9-tetrahydrocannabinol in whole blood samples using Box-Behnken experimental design. *J. Chromatogr. A* **2017**, *1479*, 71–80. [CrossRef]
61. Sivakumar, P.; Priyatharshni, S.; Nagashanmugam, K.B.; Thanigaivelan, A.; Kumar, K. Chitosan capped nanoscale Fe-MIL-88B-NH 2 metal-organic framework as drug carrier material for the pH responsive delivery of doxorubicin. *Mater. Res. Express* **2017**, *4*, 85023. [CrossRef]
62. Liang, X.-X.; Wang, N.; Qu, Y.-L.; Yang, L.-Y.; Wang, Y.-G.; Ouyang, X.-K. Facile Preparation of Metal-Organic Framework (MIL-125)/Chitosan Beads for Adsorption of Pb(II) from Aqueous Solutions. *Molecules* **2018**, *23*, 1524. [CrossRef] [PubMed]
63. Kirisits, M.J.; Parsek, M.R. Does Pseudomonas aeruginosa use intercellular signalling to build biofilm communities? *Cell. Microbiol.* **2006**, *8*, 1841–1849. [CrossRef] [PubMed]
64. Ramage, G.; Rajendran, R.; Gutierrez-Correa, M.; Jones, B.; Williams, C. Aspergillus biofilms: Clinical and industrial significance. *FEMS Microbiol. Lett.* **2011**, *324*, 89–97. [CrossRef]
65. Greenberger, P.A. Allergic bronchopulmonary aspergillosis. *J. Allergy Clin. Immunol.* **2002**, *110*, 685–692. [CrossRef] [PubMed]
66. Ustianowski, A.P.; Sieu, T.P.M.; Day, J.N. Penicillium marneffei infection in HIV. *Curr. Opin. Infect. Dis.* **2008**, *21*, 31–36. [CrossRef]
67. Duong, T.A. Infection Due to Penicillium marneffei, an Emerging Pathogen: Review of 155 Reported Cases. *Clin. Infect. Dis.* **1996**, *23*, 125–130. [CrossRef]
68. Supparatpinyo, K.; Khamwan, C.; Baosoun, V.; Nelson, K.E.; Sirisanthana, T. Disseminated Penicillium marneffei infection in Southeast Asia. *Lancet* **1994**, *344*, 110–113. [CrossRef]
69. Naidu, J.; Singh, S.M.; Pouranik, M. Onychomycosis caused by Chaetomium globosum Kunze. *Mycopathologia* **1991**, *113*, 31–34. [CrossRef]
70. Abbott, S.P.; Sigler, L.; McAleer, R.; McGough, D.A.; Rinaldi, M.G.; Mizell, G. Fatal cerebral mycoses caused by the ascomycete Chaetomium strumarium. *J. Clin. Microbiol.* **1995**, *33*, 2692–2698. [CrossRef]
71. McFeters, G.A.; Bazin, M.J.; Mirelman, D.; Bryers, J.D.; Mitchell, R.; Caldwell, D.E.; Schubert, R.H.W.; Characklis, W.G.; Tanaka, T.; Lund, D.B.; et al. Biofilm Development and Its Consequences. In *Microbial Adhesion and Aggregation: Report of the Dahlem Workshop on Microbial Adhesion and Aggregation Berlin 1984, January 15–20*; Marshall, K.C., Ed.; Springer: Berlin/Heidelberg, Germany, 1984; pp. 108–124, ISBN 978-3-642-70139-9. [CrossRef]
72. Characklis, W.G. Bioengineering report: Fouling biofilm development: A process analysis. *Biotechnol. Bioeng.* **1981**, *23*, 1923–1960. [CrossRef]
73. Herxheimer, H.; Hyde, H.; Williams, D. Allergic asthma caused by fungal spores. *Lancet* **1966**, *1*, 572–573. [CrossRef]
74. Baillie, G.S.; Douglas, L.J. Matrix polymers of Candida biofilms and their possible role in biofilm resistance to antifungal agents. *J. Antimicrob. Chemother.* **2000**, *46*, 397–403. [CrossRef] [PubMed]
75. Teughels, W.; van Assche, B.; Sliepen, I.; Quirynen, M. Effect of material characteristics and/or surface topography on biofilm development. *Clin. Oral Imp. Res.* **2006**, *17*, 68–81. [CrossRef] [PubMed]
76. Deutsches Institut für Normung. *DIN EN ISO 846 Plastics—Evaluation of the Action of Microorganisms*; Beuth: Berlin, Germany, 2018.

77. Thommes, M.; Kaneko, K.; Neimark, A.V.; Olivier, J.P.; Rodriguez-Reinoso, F.; Rouquerol, J.; Sing, K.S.W. Physisorption of gases, with special reference to the evaluation of surface area and pore size distribution (IUPAC Technical Report). *Pure Appl. Chem.* **2015**, *87*, 1051–1069. [CrossRef]
78. Bodmeier, R.; Oh, K.-H.; Pramar, Y. Preparation and Evaluation of Drug-Containing Chitosan Beads. *Drug Dev. Ind. Pharm.* **1989**, *15*, 1475–1494. [CrossRef]
79. Wu, S.-J.; Liou, T.-H.; Yeh, C.-H.; Mi, F.-L.; Lin, T.-K. Preparation and characterization of porous chitosan-tripolyphosphate beads for copper(II) ion adsorption. *J. Appl. Polym. Sci.* **2013**, *127*, 4573–4580. [CrossRef]
80. Khabzina, Y.; Dhainaut, J.; Ahlhelm, M.; Richter, H.-J.; Reinsch, H.; Stock, N.; Farrusseng, D. Synthesis and Shaping Scale-up Study of Functionalized UiO-66 MOF for Ammonia Air Purification Filters. *Ind. Eng. Chem. Res.* **2018**, *57*, 8200–8208. [CrossRef]

Supplementary Materials (SM)

MOF@chitosan composites with potential antifouling properties for open-environment applications of metal-organic frameworks

Christian Jansen[a], Nam Michael Tran-Cong[b], Carsten Schlüsener[a], Alexa Schmitz[a], Peter Proksch[b], Christoph Janiak[a,]*

*[a]Institut für Anorganische Chemie und Strukturchemie, Heinrich-Heine-Universität, D-40204, Düsseldorf, Germany. *E-Mail: Janiak@hhu.de*
[b]Institut für Pharmazeutische Biologie und Biotechnologie, Heinrich-Heine-Universität, D-40204, Düsseldorf, Germany

Emails:

Christian.Jansen@hhu.de, Nam.Tran-Cong@hhu.de, Carsten.Schluesener@hhu.de, alexa.schmitz@hhu.de, Proksch@uni-duesseldorf.de, Janiak@hhu.de

Keywords

Metal-Organic frameworks, Al-MOFs, Chitosan, Aluminum fumarate, MIL-160, Anti-Fouling, *Chaetomium globosum*, *Aspergillus falconensis*

Table of Contents

S1. Materials and equipment

All chemicals were used as received by the supplier (*cf.* Table S1).

Table S1: Used chemicals, supplier and purities.

Chemical	**CAS number:**	**Supplier**	**Purity [%]**
Acetic acid	64-19-7	VWR Chemical	99.9
Acetone	67-64-1	VWR Chemical	p.a.
Agar	9002-18-0	Alfa Aesar	not specified
Aluminum chloride hexahydrate	7784-13-6	Fluka	not specified
Aluminum fumarate (Basolite® A520)	not specified	BASF	not specified
Chitosan medium molecular weight	9012-76-4	Sigma Aldrich	not specified
Dipotassium phosphate	7758-11-4	Merck	p.a.
Ethanol	64-17-5	Chem Solute	p.a.
Ethanol	64-17-5	Riedel de Haën	p.a.
Glutaraldehyde	111-30-8	Alfa Aesar	25 aq.
Iron(II) sulfate heptahydrate	7782-63-0	Grüssing	99.5
Monopotassium phosphate	7778-77-0	Appli Chem	p.a.
Magnesium sulfate heptahydrate	10034-99-8	Merck	p.a.
Methanol	67-56-1	Fischer Chemical	p.a.
Mowiol 20-98 (PVA) M_w~125.000	9002-89-5	Sigma Aldrich	not specified
N,N-Dimethylformamide	68-12-2	Fischer Chemical	not specified
Potassium chloride	7447-40-7	Appli Chem	p.a.
Sodium hydroxide	1310-73-2	Chem Solute	not specified
Sodium nitrate	7631-99-4	Appli Chem	p.a.
Sodium triphosphate	7758-29-4	Alfa Aesar	not specified
Silikophen® P50/X	not specified	Evonik	not specified
Tween80	9005-65-6	Sigma Aldrich	not specified
Xylene	1330-20-7	Fischer Chemical	p.a.
2,5-Furandicarboxylic acid	3238-40-2	Sigma Aldrich	not specified

Basolite® A520; Aluminum fumarate (Alfum)

Aluminum fumarate was first described in the patent literature in 2013 [1,2]. It was the first MOF synthesized on a ton scale and it is marketed by BASF under the name *Basolite® A520*. Figure S1 shows the structural features of Alfum.

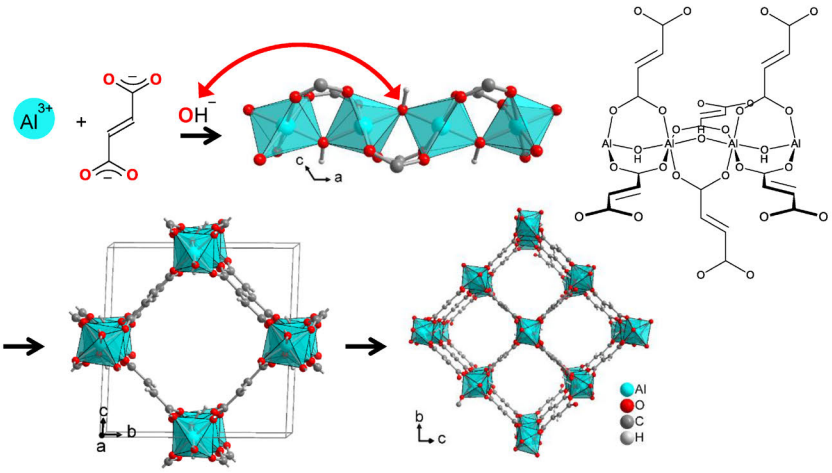

Figure S1: Al^{3+}, hydroxide and fumarate building blocks of Alfum, which give a chain of trans-μ-OH-connected vertex-bridged {AlO_6} octahedra. These chains run along the crystallographic a direction and are connected through the fumarate linkers along the bc diagonals. Graphic produced by software Diamond [3] from cif-file for Basolite A520 (CSD-Refcode DOYBEA) [4].

MIL-160

MIL-160 (*Matériaux Institut Lavoisier*) was described by Cadiau *et al.* in 2015 [5]. The MOF was obtained under reflux conditions from aqueous solutions of 2,5-furandicarboxylic acid, sodium hydroxide and aluminum chloride. MIL-160 is constructed by cis-μ-OH-connected, vertex-sharing {AlO_6} octahedra, that form helical chains, which are then joined by the linker 2,5-furandicarboxylate (Figure S2).

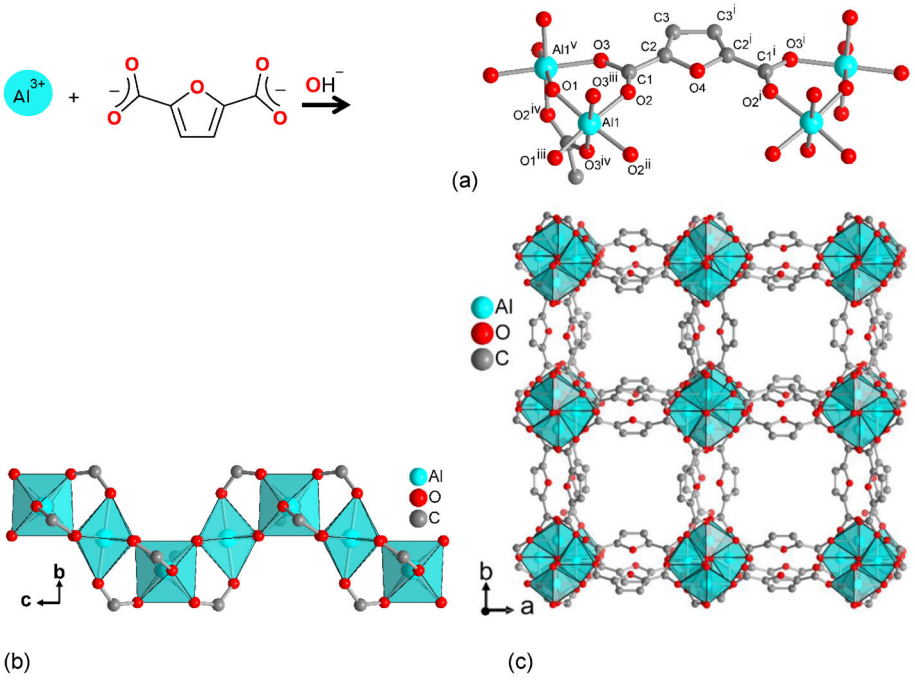

Figure S2: Structural elements in the framework of MIL-160: (a) Extended asymmetric unit with full Al coordination spheres and full ligand bridging mode. Symmetry transformations i = 1–x, y, z; ii = x, –y, –z; iii = 0.25+y, 0.25–x, –0.25+z; iv = 0.25+y, –0.25+x, 0.25–z; v = 0.25–y, –0.25+x, 0.25+z. (b) Helical chains of cis vertex-bridged {AlO_6}-polyhedra and (c) surrounded by the carboxylates ligands, to yield square-shaped one dimensional channels. Graphic produced by software Diamond [3] from cif-file for MIL-160 (CSD-Refcode PIBZOS) [6].

S2. MOF and Chitosan Synthesis

MIL-160 synthesis

Table S2: Overview MIL-160 synthesis.

Approach	Yield [%]	BET Surface [m^2 g^{-1}]
MIL-160	66	1186

Chitosan syntheses

Table S3: Overview of the crosslinked chitosan syntheses.

Chitosan concentration [g L^{-1}]	Chitosan [g]	2 wt-% acetic acid [mL]	BET surface [m^2 g^{-1}]
Crosslinked with $Na_5P_3O_{10}$			
6	0.3	50	144
20	0.4	20	230
30	0.6	20	220
40	0.4	10	202
Crosslinked with Glutaraldehyde			
6	0.04	6.66	233

Chitosan synthesis in glutaraldehyde

A chitosan solution with 6 g L^{-1} was prepared with 2 wt-%acetic acid. The solution was transferred to a truncated syringe (5 mL) and glutaraldehyde (25 % in water, 1 mL, 83 g L^{-1} final concentration) added under vigorous stirring. As soon as a slight gelation occurred, the stirrer was quickly removed. The syringe was closed and the gel aged (RT, 72 h). The resulting gel was gently pushed out of the syringe into Milli-Q water and washed (24 h). It was then dehydrated in ethanol (at least 6 d). The resulting monolith was dried by supercritical CO_2.

S3 Composite Synthesis

Table S4: Comparison of the composite materials and the educts. (d. s. = dried supercritically)

Educt/Composite materials	**Chitosan conc. [g L^{-1}]**	**BET-surface [m^2 g^{-1}]**	
		measured	**calculated**
Alfum	-	988	-
Alfum60@chitosan	6	20	650
Alfum60@chitosan	20	294	685
Alfum80@chitosan	6	474	819
Alfum80@chitosan	20	587	836
Alfum80@chitosan d. s.	6	844	819
Alfum80@chitosan d. s.	20	893	836
Alfum90@chitosan	6	964	904
Alfum90@chitosan	20	856	912
Alfum60@chitosan	30	202	681
Alfum60@chitosan	40	26	674
Alfum60@chitosan with glutaraldehyde	6	697	686
MIL-160	-	1186	-
MIL-160(60)@chitosan	6	32	769
MIL-160(60)@chitosan	20	138	804
MIL-160(80)@chitosan	6	720	978
MIL-160(80)@chitosan	20	610	995
MIL-160(80)@chitosan d. s.	6	858	978
MIL-160(80)@chitosan d. s.	20	918	995
MIL-160(90)@chitosan	6	1068	1082
MIL-160(90)@chitosan	20	964	1090
Alfum@PVA	-	716	-
MIL-160@PVA	-	925	-
Alfum pressed	-	759	988
Alfum pressed with Silikophen®	-	257	988
MIL-160 pressed	-	726	1126
MIL-160 pressed with Silikophen®	-	479	1126

MOF@Silikophen composites (pressure calculation)

$$Surface = \pi * r^2 = \pi * (0.0065\ m)^2 = 1.33 * 10^{-4} m^2 \quad \textbf{(S1)}$$

$$Force = mass * acceleration = 2000\ kg * 9.81 \frac{m}{s^2} = 19620 \frac{kg*m}{s^2} \quad \textbf{(S2)}$$

$$Pressure = \frac{force}{surface} = \frac{19620 \frac{k*m}{s^2}}{1.33*10^{-4} m^2} = 147518797\ Pa = 1475.2\ bar \quad \textbf{(S3)}$$

Alfum@chitosan synthesis in glutaraldehyde

A chitosan solution with 6 g L^{-1} was prepared with 2 wt-%acetic acid. Then 40 mg Alfum were added to 2 mL of the solution and stirred for 30 minutes. The suspension was transferred to a truncated syringe (5 mL) and glutaraldehyde (25 % in water, 1 mL, 83 g L^{-1} final concentration) was added under vigorous stirring. As soon as a slight gelation occurred, the stirrer was quickly removed. The syringe was closed and the gel aged (RT, 72 h). The resulting gel was gently pushed out of the syringe into Milli-Q water and washed (24 h). It was then dehydrated in ethanol (at least 6 d). The resulting monolith was dried by supercritical CO_2.

For PXRD see Fig. S7, for IR spectra see Fig. S12, for N_2 sorption Fig. S31, for H_2O sorption Fig. S39.

S4 Antifouling Tests

The amounts of the experiment antifouling tests are shown in the following Table S5.

Table S5: Composition of the nutrient medium in the fungi tests.

Chemical	**Amount**
Stock mineral salt solution 1.1	
$NaNO_3$	4.0 g
KH_2PO_4	1.4 g
K_2HPO_4	0.6 g
KCl	1.0 g
$MgSO_4$ * 7 H_2O	1.0 g
$FeSO_4$ · * 7 H_2O	0.02 g
Reinstwasser	2000 mL
Mineral salt solution with additive 1.2	
Tween80	0.05 g auf 500 mL *1.1*
Incomplete culture medium 1.4	
Agar	20.0 g auf 1000 mL *1.1*

Table S6: Results of the antifouling tests with Chaetomium globosum and Aspergillus falconensis.

Sample	**Fungi**		
	Chaetomium globosum	*Aspergillus falconensis*	
	1. Run	1. Run	2./3. Run
Chitosan (medium molecular weight)	-	3	5
Chitosan (20 g/L)	2	0	5
Alfum60@chitosan	-	0	0
Alfum80@chitosan	5	0	0
Alfum90@chitosan	5	2	0
MIL-160(60)@chitosan	5	2	0
MIL-160(80)@chitosan	5	1	0
MIL-160(90)@chitosan	5	2	0
Alfum (Basolite® A520)	5	3	5
MIL-160	5	1	1
Alfum@PVA	5	2	3
MIL-160@PVA	1	0	2
Alfum@Silikophen®	5	5	5
MIL-160@Silikophen®	5	1	2

The evaluation of the samples was based on Method A of DIN EN ISO 846 (10/1997) (testing for resistance to fungi) [7].

S5 PXRD Measurements

Powder X-ray diffractometry (PXRD) used a *Bruker D2 Phaser* diffractometer (unless noted otherwise) with a flat silicon, low background sample holder and Cu-Kα radiation (λ = 1.54184 Å) at 30 kV and 0.0125° s^{-1} in the 2θ = 5-50 ° range, exposure time: 1 s, stepsize: 0.15 or 0.05° giving typically a total measurement time of 6 for a diffractogram.
In Figure S3 and S4, the PXRDs of the neat MOFs were also measured with a Rigaku Miniflex 600 (Rigaku, Tokio;Japan) using Cu-Kα radiation (λ = 1.54182 Å) between 5° < 2θ < 50° with a scan rate of 0.083 ° s^{-1} (600 W, 40 kV, 15 mA) and a step size of 0.01 °per step giving a total measurement time of 10 min for a diffractogram.
Figure S3 - Figure S9 depict PXRD patterns of all obtained samples.

Alfum

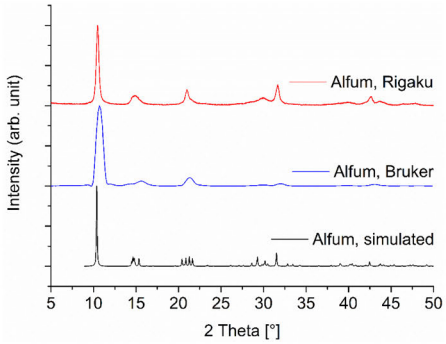

Figure S3: PXRD patterns of Alfum samples obtained by measurements of the Basolite® A520, in comparison with simulatd pattern (CSD-Refcode DOYBEA) [4]. Bruker D2 diffractometer (blue), Rigaku Miniflex diffractometer (red). The PXRD of Alfum was obtained from the purchased MOF from BASF which is less crystalline than MIL-160 (cf. Figure S4), due to the industrial scale of its synthesis.

MIL-160

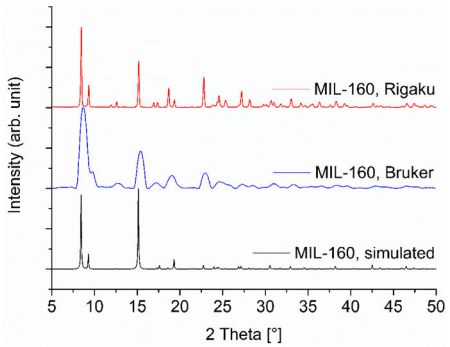

Figure S4: PXRD pattern of MIL-160 obtained by synthesis in comparison with simulated pattern (CSD-Refcode PIBZOS) [6]. Bruker D2 diffractometer (blue), Rigaku Miniflex diffractometer (red).

Alfum@chitosan

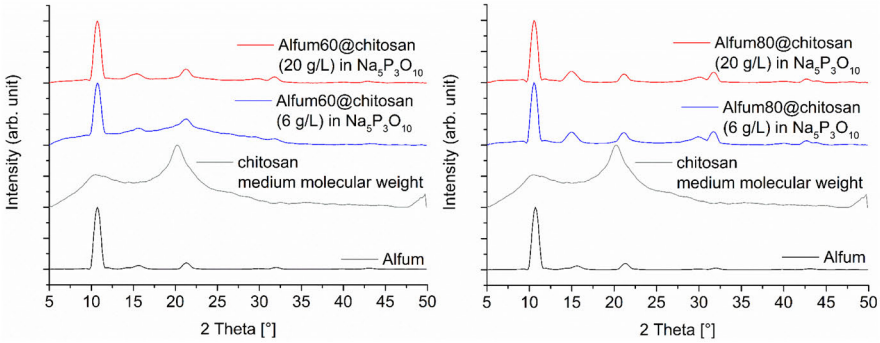

Figure S5: PXRD patterns of Alfum@chitosan composites for a MOF content of 60 wt-% (left) and 80 wt-% (right), prepared with different chitosan concentrations.

MIL-160@chitosan

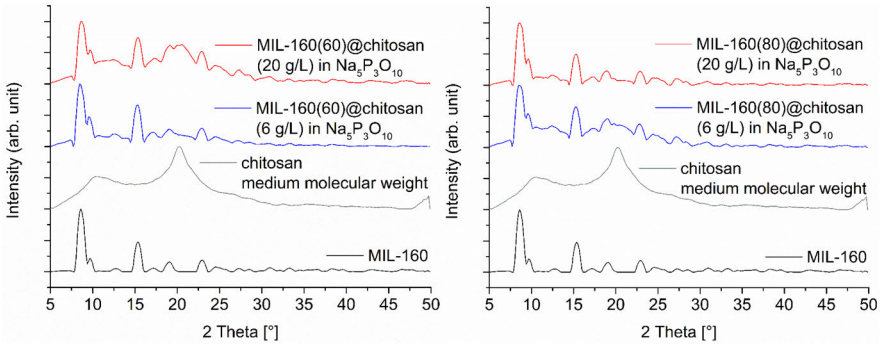

Figure S6: PXRD patterns of MIL-160@chitosan composites with different chitosan concentrations, in comparison with educts. Left: 60 wt-% MOF loading, right: 80 wt-% MOF loading.

Alfum@chitosan in glutaraldehyde

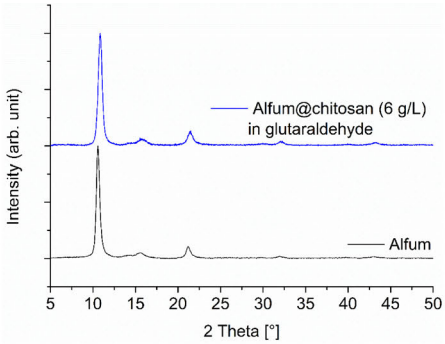

Figure S7: PXRD pattern of Alfum@chitosan in glutaraldehyde composites with chitosan, in comparison with the starting material. The diffractograms here were measured with a time of 30 min, thereby giving narrower reflections than in the other 6-minute diffractograms.

MOF@PVA

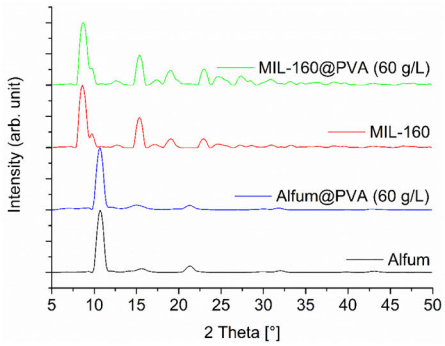

Figure S8: PXRD patterns of MOF@PVA composites, in comparison with the starting materials.

MOF@Silikophen®

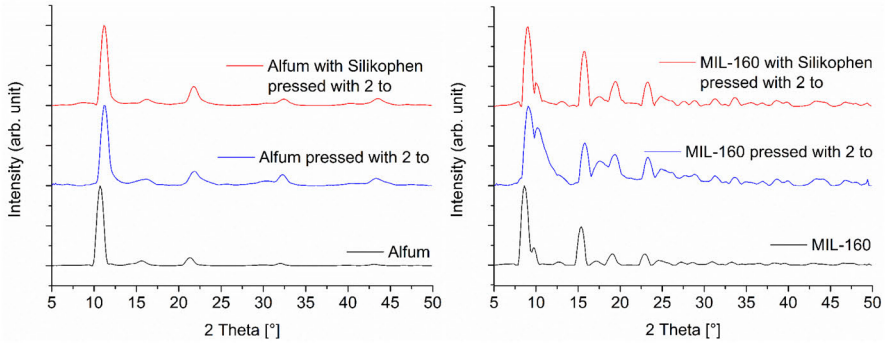

Figure S9: PXRD patterns of MOF@Silikophen® composites in comparison with starting materials and pressed starting materials. Left: Alfum, right: MIL-160 (to = tons of pressure). It can be seen, that the preparation of the pellets with a pressure of 2 tons results in a visible peak broadening which correlates with a loss of crystallinity. It is known that (porous) MOF structures are not very stable at high pressures. The preparation of pellets was necessary to perform the antifouling tests.

S6 Infrared spectra

FT-IR spectra were measured in KBr-mode on a BRUKER TENSOR 37 IR spectrometer in the range of 4000−400 cm^{-1}.

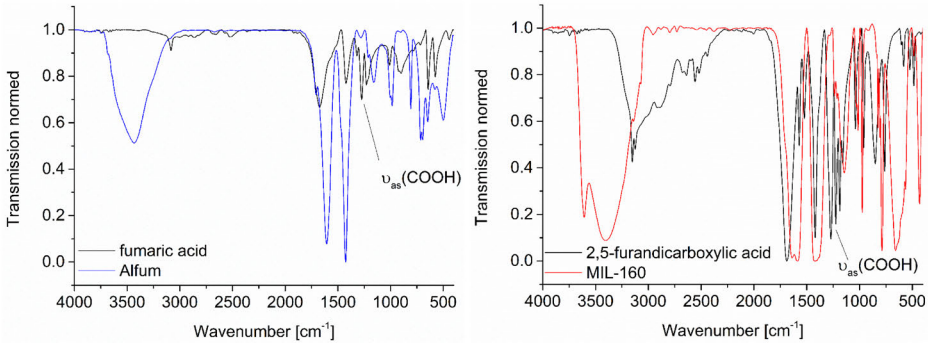

Figure S10: IR-spectra of MOFs in comparison with linker. Left: Alfum and fumaric acid, right: MIL-160 and 2,5-furandicarboxylic acid.

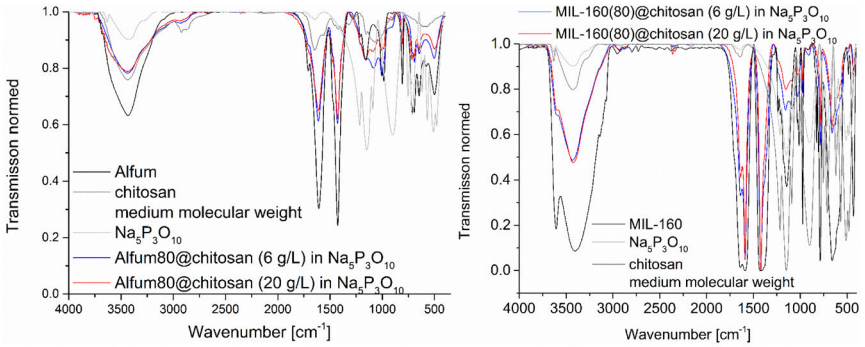

Figure S11: IR-spectra of MOF@chitosan composites with different chitosan concentrations, in comparison with educts. Left: Comppsites, Alfum, Chitosan, $Na_5P_3O_{10}$ and fumaric acid, right: Composites, MIL-160, Chitosan, $Na_5P_3O_{10}$ and 2,5-furandicarboxylic acid.

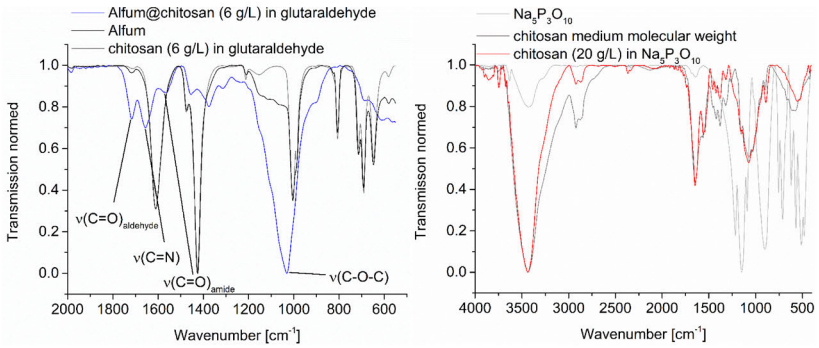

Figure S12: IR-spectra of MOF@chitosan in glutaraldehyde (left) and crosslinked Chitosan, in comparison with chitosan and $Na_5P_3O_{10}$ (right).

S7 Thermogravimetric Analysis (TGA)

Exemplarily, we performed thermogravimetric analyses (TGA) of some samples.

Figure S13 - Figure S16: TG curve of MOF@PVA composites, compared with educts.

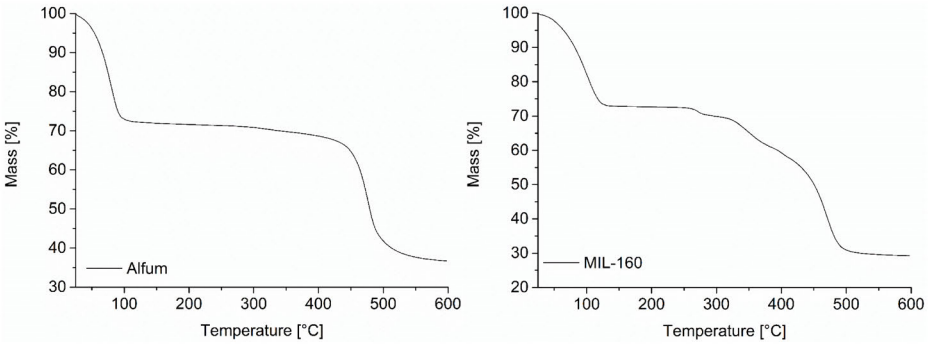

Figure S13: TG curve of Alfum (Basolite® A520) (left) and MIL-160 (right).

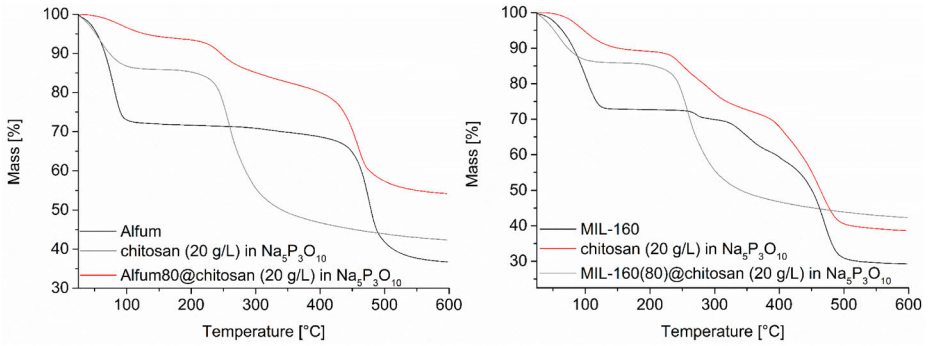

Figure S14: TG curves of MOF@chitosan curves, in comparison with MOF and crosslinked chitosan. Left: Alfum, right: MIL-160.

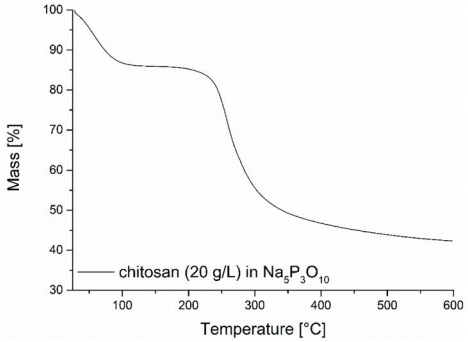

Figure S15: TG curve of crosslinked chitosan.

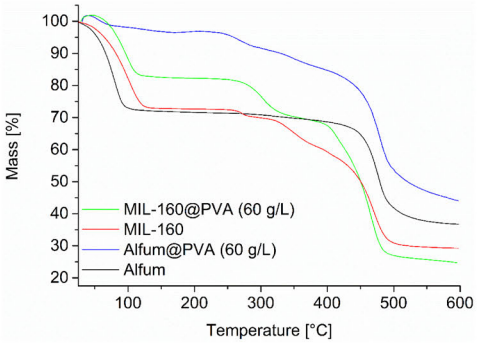

Figure S16: TG curve of MOF@PVA composites, compared with educts.

S8 Scanning electron microscopy (SEM)

For control of morphology we recorded SEM images using a *JEOL JSM-6510 advanced electron microscope* with a LaB_6 cathode at 20 keV. The microscope was equipped with a *Bruker Xflash 410 silicon drift detector* and the *Bruker ESPRIT* software for EDX analysis.
Figure S17 – Figure S25 exemplarily depict SEM images and EDX measurements of selected samples of the MOFs and MOF@Polymer composites.

Alfum

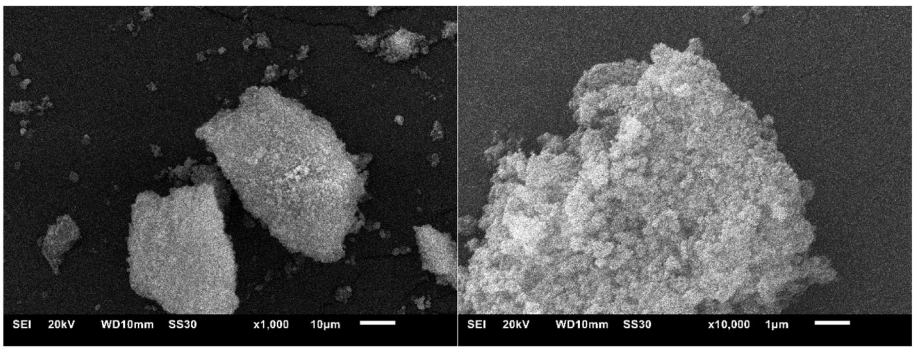

Figure S17: SEM images of Alfum at different magnifications (left: overview, right: close-up).

MIL-160

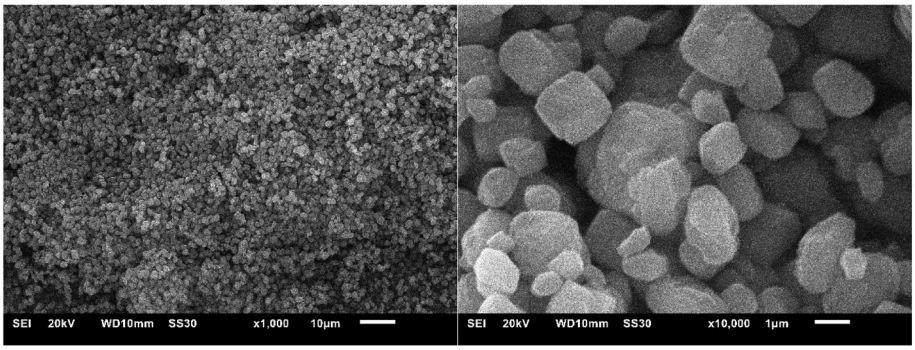

Figure S18: SEM images of MIL-160 at different magnifications (left: overview, right: close-up).

Chitosan

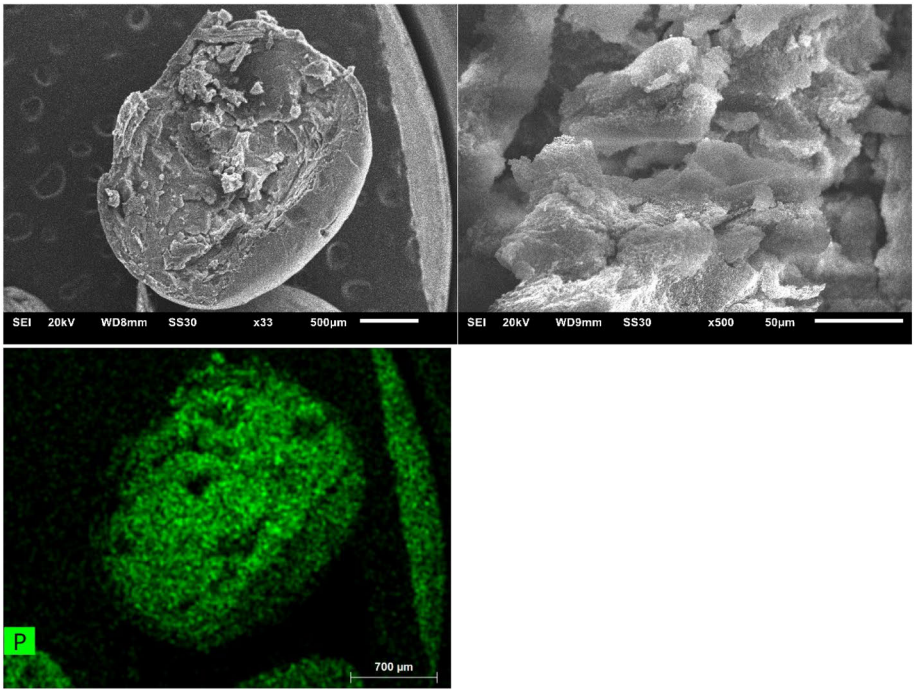

Figure S19: SEM images of chitosan at different magnifications (top left: overview, top right: close-up). EDX-element mapping for phosphorus (bottom) for the particle in the overview at top left.

Alfum@chitosan

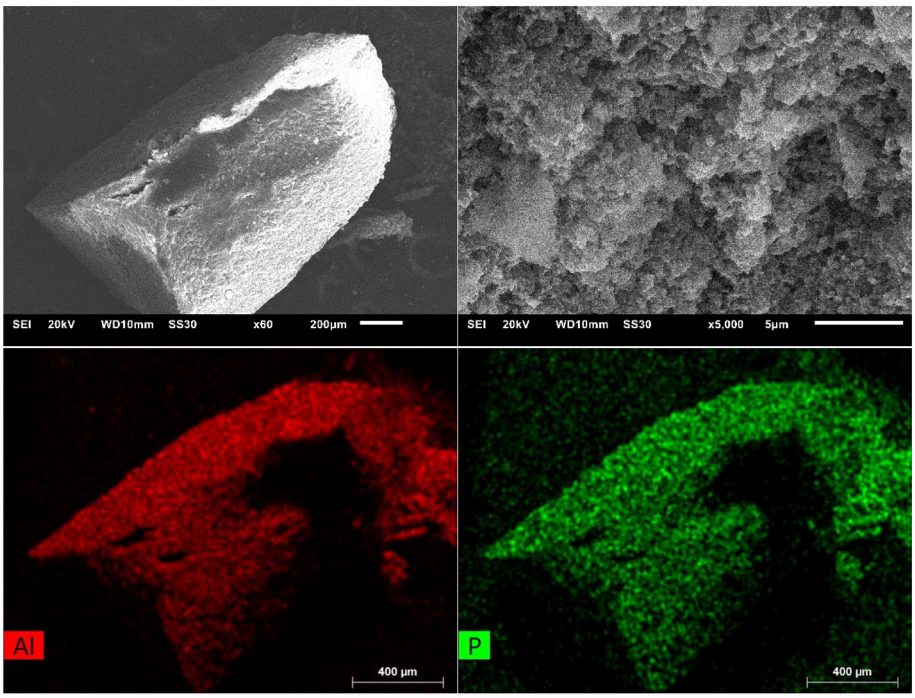

Figure S20: SEM images of Alfum90@chitosan at different magnifications (top left: overview, top right: close-up). EDX-element mapping for aluminum and phosphorus (bottom) for the particle in the overview at top left. The dark areas, that is lower amount of Al and P in the center-right of the element mapping is due to the particle geometry. The hollow in the middle of the particle causes a blocking of the emerging X-rays from the sample which then cannot be detected.

MIL-160@chitosan

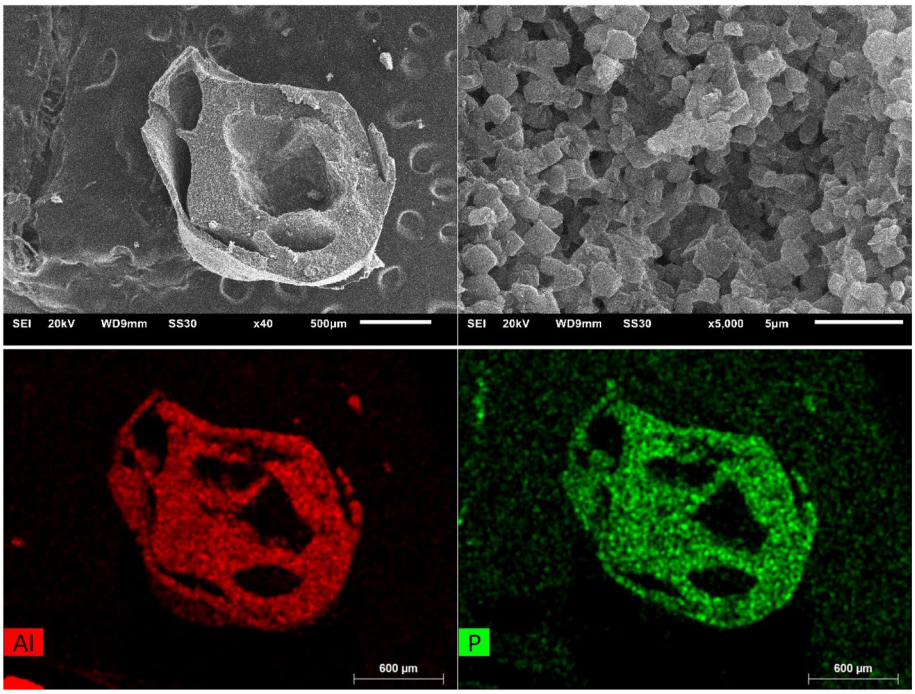

Figure S21: SEM images of MIL-160(80)@chitosan at different magnifications (top left: overview, top right: close-up). EDX-element mapping for aluminum and phosphorus (bottom) for the particle in the overview at top left. The dark features in the element maps are and artefact due to blocking of the emerging element-specific X-rays from the sample by the grooves in the bead surface so that these X-rays cannot be detected.

MOF@PVA

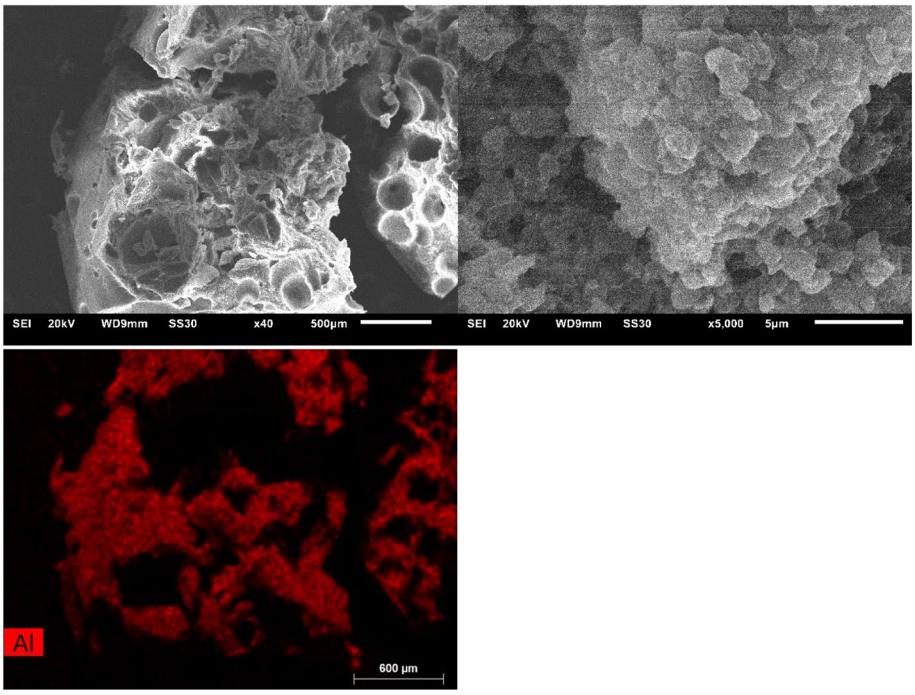

Figure S22: SEM images of Alfum80@PVA at different magnifications (top left: overview, top right: close-up). EDX-element mapping for aluminum (bottom). The dark features in the element maps are and artefact due to blocking of the emerging element-specific X-rays from the sample by the grooves in the bead surface so that these X-rays cannot be detected.

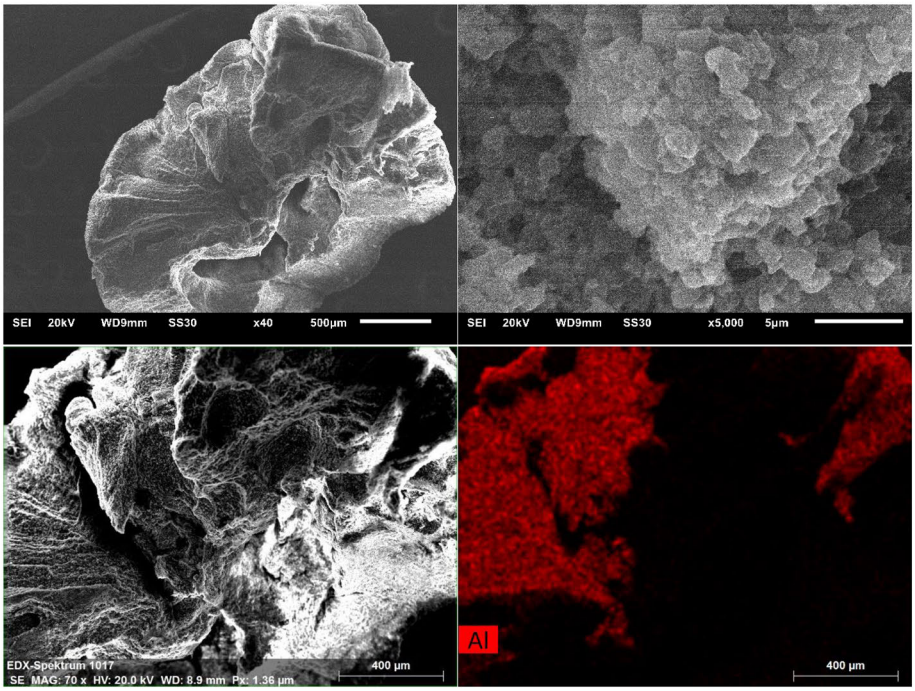

Figure S23: SEM images of MIL-160(80)@PVA at different magnifications (top left: overview, top right: close-up, bottom left: cutout from the overview). EDX-element mapping for aluminum (bottom right). The dark features in the element maps are and artefact due to blocking of the emerging element-specific X-rays from the sample by the grooves in the bead surface so that these X-rays cannot be detected.

MOF@Silikophen®

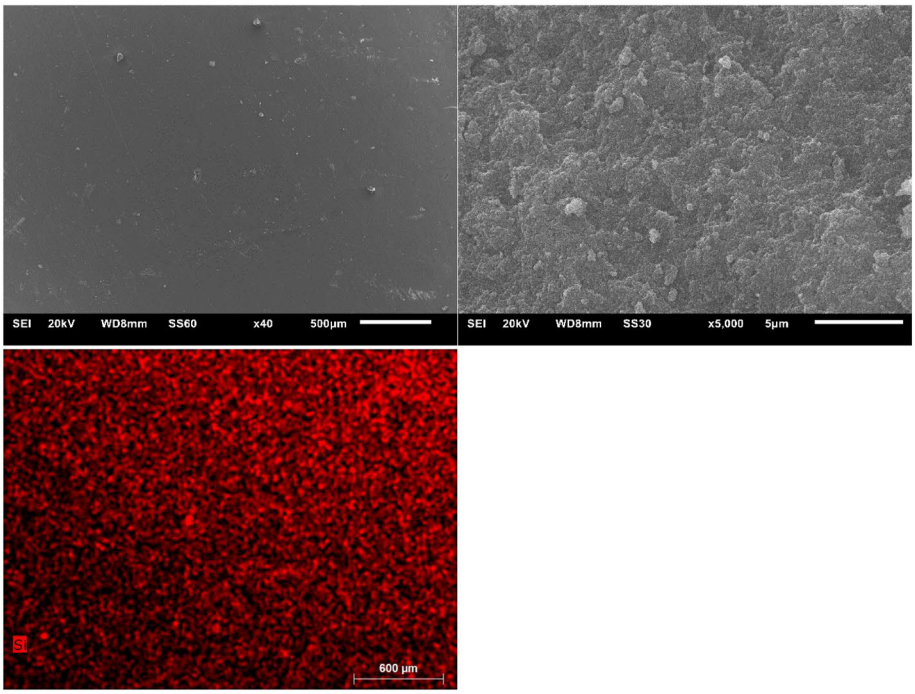

Figure S24: SEM images of Alfum80@Silikophen® at different magnifications (top left: overview, top right: close-up). EDX measurement for aluminum (bottom).

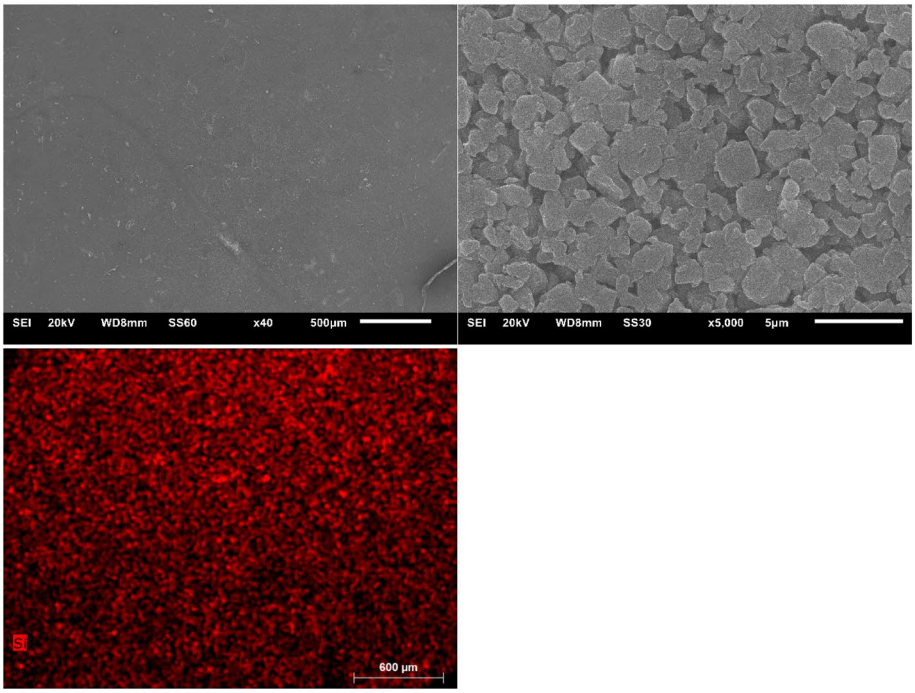

Figure S25: SEM images of MIL-160(80)@Silikophen® at different magnifications (top left: overview, top right: close-up). EDX measurement for aluminum (bottom).

S9 Nitrogen sorption experiments (T = 77 K)

Surface areas (BET) were determined by nitrogen (purity 99.999%) sorption experiments at 77.35 K using a *Quantachrome Autosorb6* instrument within a partial pressure range of p p_0^{-1} = 10–3^{-1} bar. Each sample was degassed under vacuum (< 10^{-2} mbar) at 120 °C for *ca.* 3 h, prior to measurement. All surface areas (BET) were calculated from five adsorption points in the pressure range pp_0^{-1} = 0.009 -0.041 bar for all samples. This range is indeed not recommended by IUPAC (International Union of Pure and Applied Chemistry) for BET surface determination, but rather suitable for microporous materials [8]. Figure S26 - Figure S33 depict the N_2 sorption isotherms of all samples.

Alfum

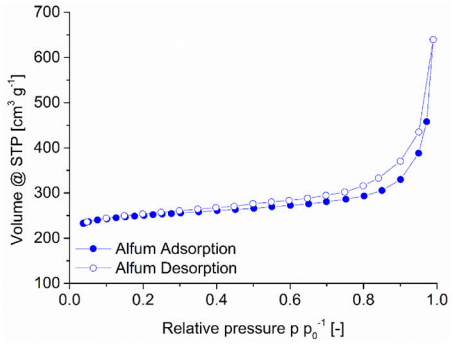

Figure S26: Nitrogen sorption (77 K) isotherm of Alfum.

MIL-160

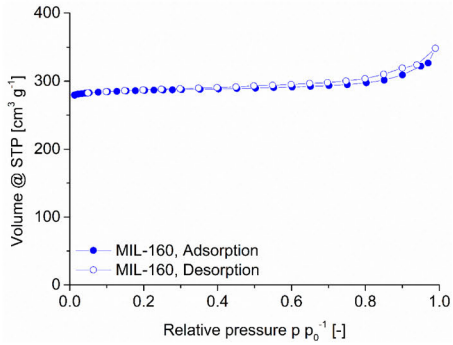

Figure S27: Nitrogen sorption (77 K) isotherms of MIL-160.

Chitosan

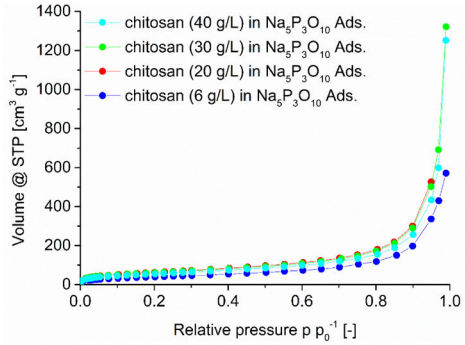

Figure S28: Nitrogen sorption (77 K) isotherm of chitosan beads with different concentrations.

Alfum@chitosan

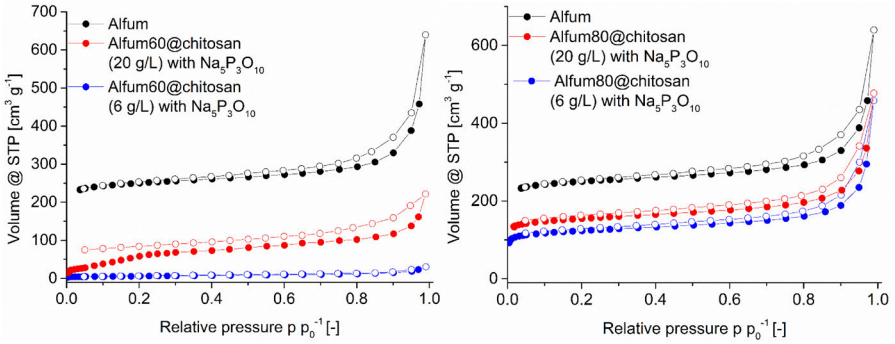

Figure S29: Nitrogen sorption (77 K) isotherm of Alfum@chitosan composites with different chitosan concentrations, in comparison with Alfum. Left: 60 wt-% MOF loading, right: 80 wt-% MOF loading.

MIL-160@chitosan

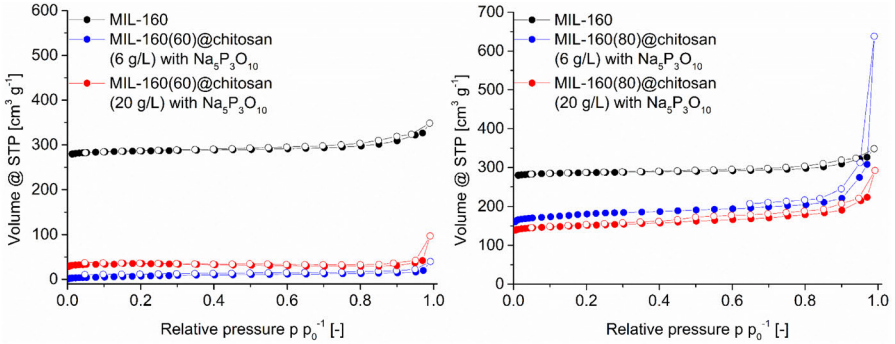

Figure S30: Nitrogen sorption (77 K) isotherm of MIL-160@chitosan composites with different chitosan concentrations, in comparison with MIL-160. Left: 60 wt-% MOF loading, right: 80 wt-% MOF loading.

Alfum@chitosan in glutaraldehyde

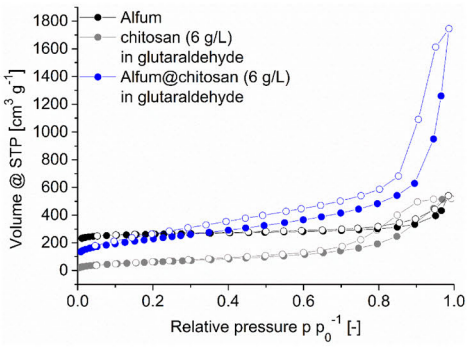

Figure S31: Nitrogen sorption (77 K) isotherm of Alfum@chitosan in glutaraldehyde composites with chitosan, in comparison with Alfum.

MOF@PVA

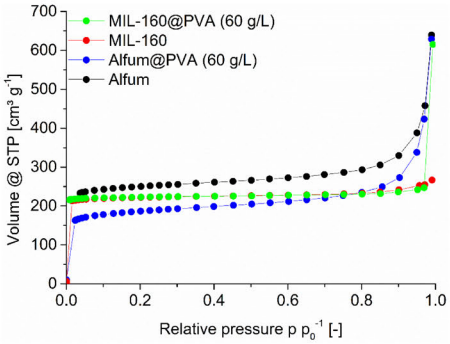

Figure S32: Nitrogen sorption (77 K) isotherms of MOF@PVA composites, in comparison with MOFs. Only adsorption is shown.

MOF@Silikophen®

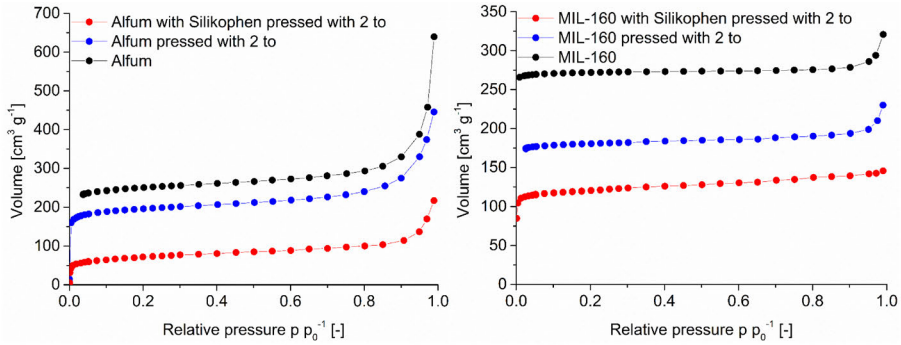

Figure S33: Nitrogen sorption (77 K) isotherms of MOF@Silikophen® composites, in comparison with MOFs and pressed MOFs. Only adsorption is shown.

S10 Water sorption experiments (T = 293 K)

Water sorption experiments were carried out on a *Quantachrome VStar4* (QUANTACHROME, Odelzhausen, Germany) instrument within a partial pressure range of $pp0^{-1}$ = 10–3^{-1} bar. Each sample was degassed under vacuum (< 10^{-3} mbar) at 120 °C for *ca.* 3 h prior to measurement, using a *FloVac* (QUANTACHROME, Odelzhausen, Germany) degasser.
Figure S34 - Figure S40 depict water sorption isotherms of all obtained samples.

Alfum

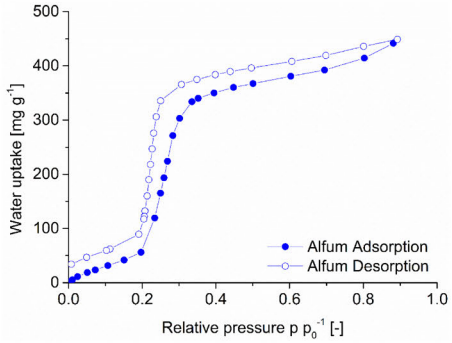

Figure S34: Water sorption (293 K) isotherm of Alfum.

MIL-160

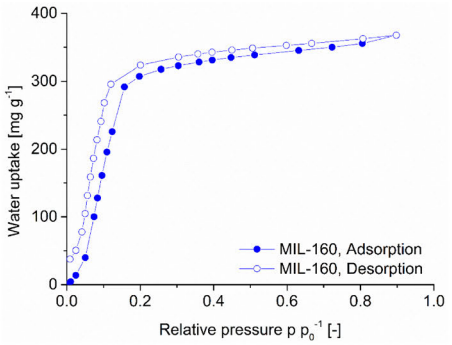

Figure S35: Water sorption (293 K) isotherms of MIL-160.

Chitosan

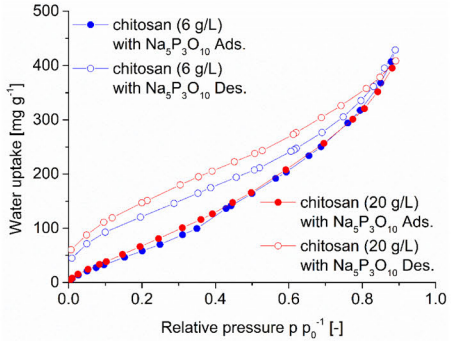

Figure S36: Water sorption (293 K) isotherms of chitosan beads with different concentrations.

Alfum@chitosan

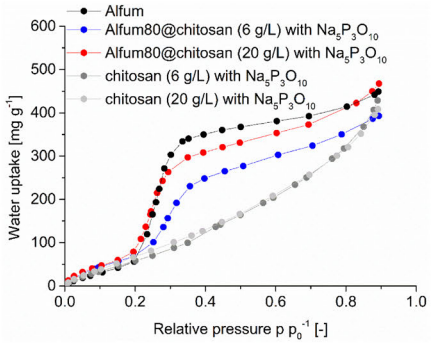

Figure S37: Water sorption (293 K) isotherms of Alfum80@chitosan composites with different chitosan concentrations, in comparison with Alfum and crosslinked chitosan.

MIL-160@chitosan

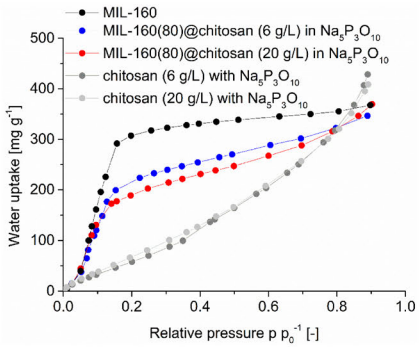

Figure S38: Water sorption (293 K) isotherms of MIL-160(80)@chitosan composites with different chitosan concentrations, in comparison with MIL-160 and crosslinked chitosan.

Alfum@chitosan in glutaraldehyde

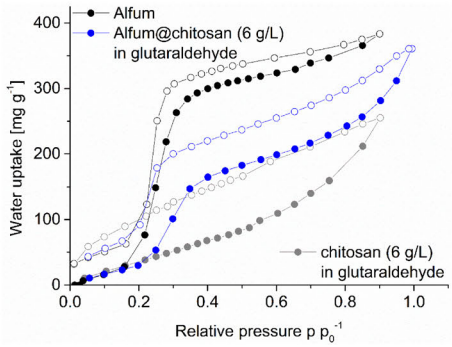

Figure S39: Water sorption (293 K) isotherms of Alfum@chitosan in glutaraldehyde with chitosan in comparison with Alfum.

MOF@PVA

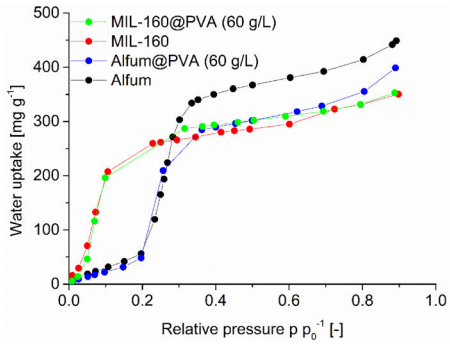

Figure S40: Water sorption (293 K) isotherms of MOF@PVA composites, in comparison with MOFs. Only adsorption is shown.

S11 Antifouling tests series (images)

Method A: *Chaetomium globosum*

Sample / Day	Chitosan	Alfum	Alfum80 @chitosan	Alfum90 @chitosan
0			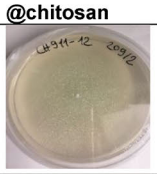	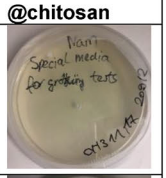
1		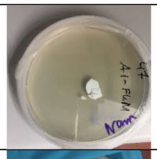	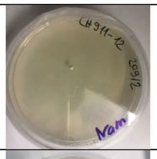	
2				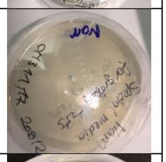
3		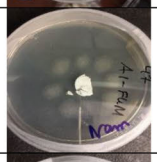	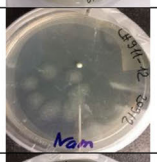	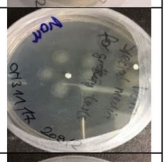
5	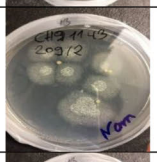	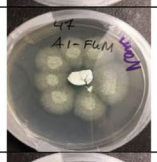		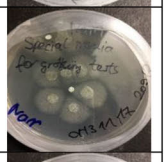
7	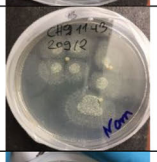	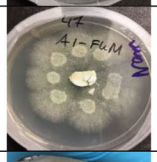	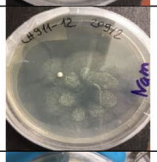	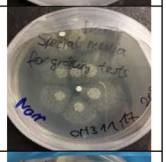
8	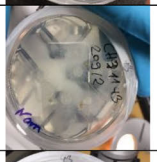		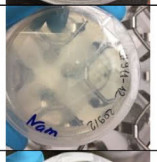	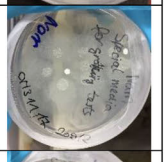
9	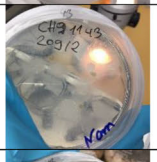			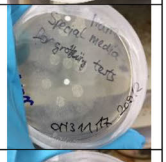
15	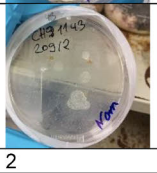	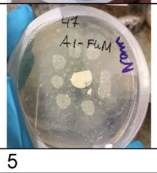	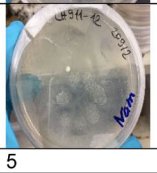	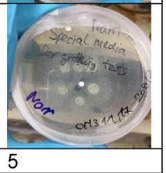
category	2	5	5	5

Sample / Day	Chitosan	MIL-160	MIL-160(60) @chitosan	MIL-160(80) @chitosan	MIL-160(90) @chitosan
0			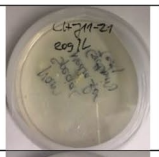		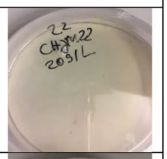
1					
2	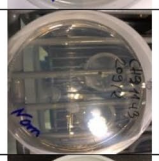	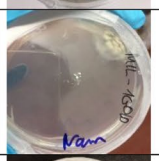	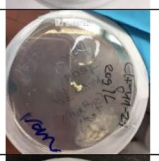		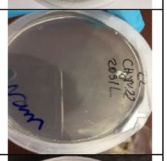
3					
5			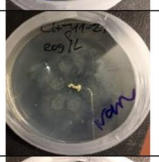		
7				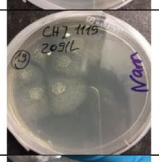	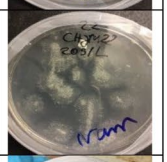
8	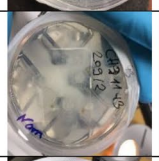	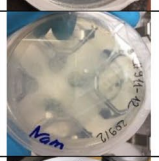	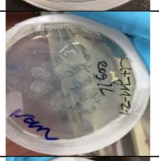		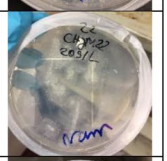
9	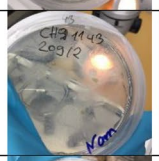				
15	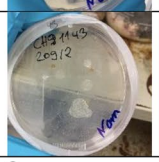	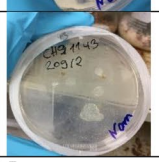	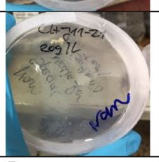	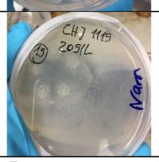	
category	2	5	5	5	5

S29

Sample / Day	Alfum@PVA	MIL-160@PVA	Alfum@ Silikophen®	MIL-160@ Silikophen®
0				
1	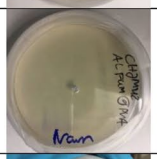			
2	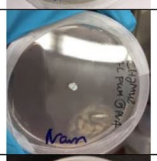			
3				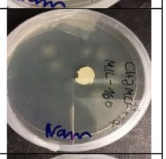
5				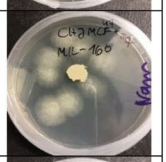
7	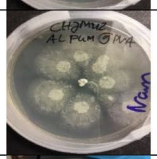			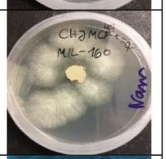
8	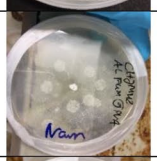	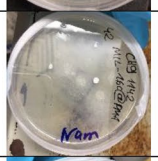		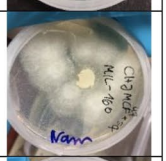
9	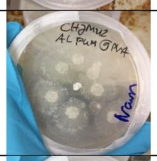			
15			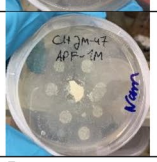	
category	5	(1)	5	5

S30

Method A: *Aspergillus falconensis* (1st Run)

Sample / Day	Chitosan	Alfum	Alfum60 @chitosan	Alfum80 @chitosan	Alfum90 @chitosan
0	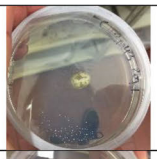				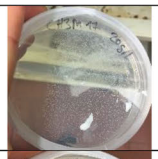
2					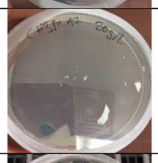
3					
4					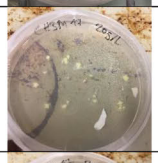
5			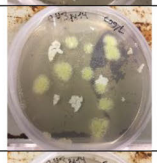		
6					
11	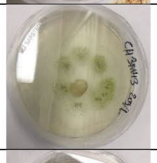	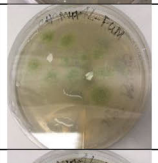	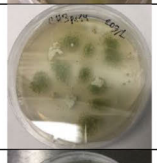	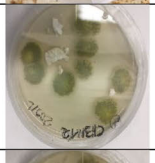	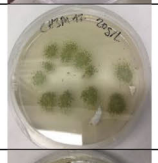
27		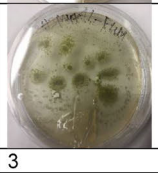	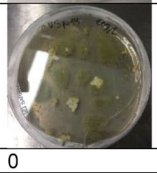		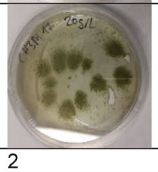
category	3	3	0	0	2

Sample / Day	Chitosan	MIL-160	MIL-160(60) @chitosan	MIL-160(80) @chitosan	MIL-160(90) @chitosan
0					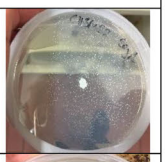
2					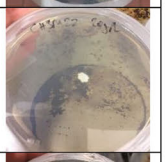
3			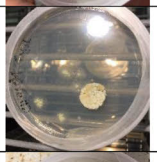	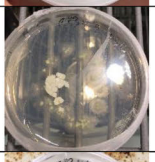	
4		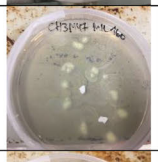			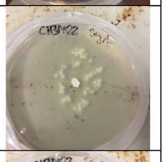
5			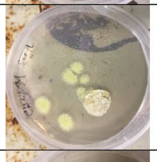		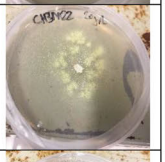
6					
11	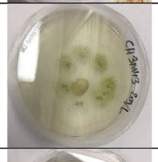	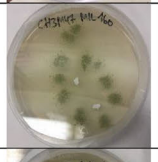	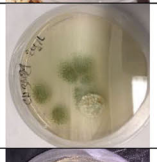	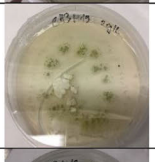	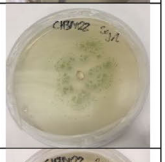
27	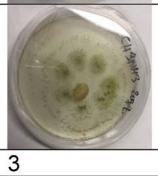	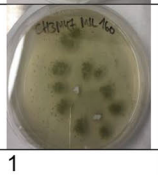	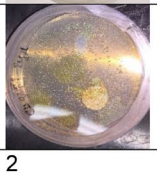	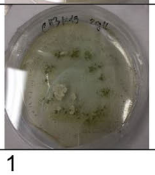	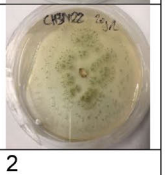
category	3	1	2	1	2

Sample / Day	Alfum@PVA	MIL-160@PVA	Alfum@ Silikophen®	MIL-160@ Silikophen®
0	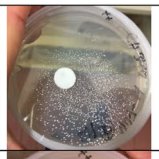	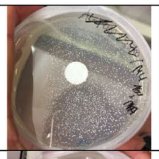	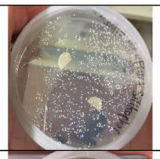	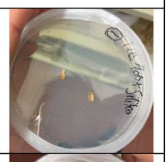
2			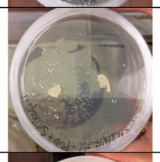	
3		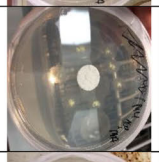		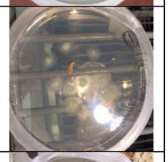
4	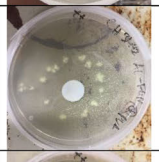		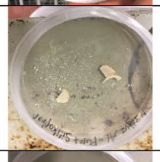	
5	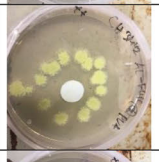	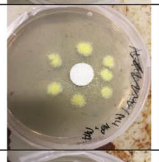		
6			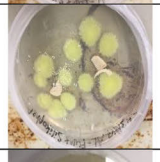	
11	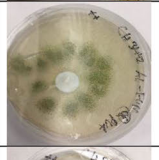	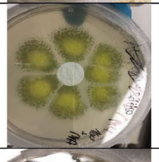	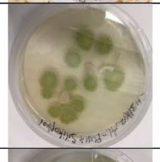	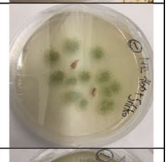
27	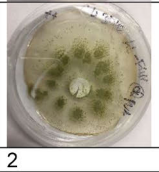	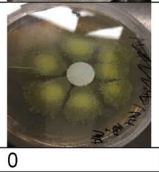	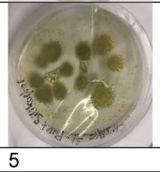	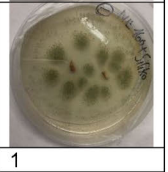
category	2	0	5	1

Method A: ***Aspergillus falconensis*** **(2./3. run, only final image after 30 days depicted)**

Sample / Day	Chitosan crosslinked	Alfum	Alfum60 @chitosan	Alfum80 @chitosan	Alfum90 @chitosan
30					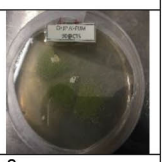
category	5	5	0	0	0

Sample / Day	Chitosan crosslinked	MIL-160	MIL-160(60) @chitosan	MIL-160(80) @chitosan	MIL-160(90) @chitosan
30		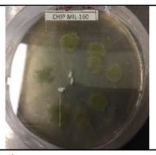		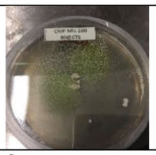	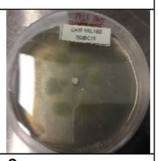
category	5	1	0	0	0

Sample / Day	Alfum@PVA	MIL-160@ PVA	Alfum@ Silikophen®	MIL-160@ Silikophen®
30		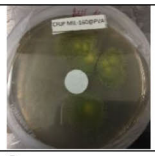		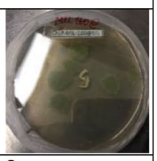
category	3	2	5	2

S12 Images of the MOF@chitosan composites

Images of the Alfum@Chitosan composites. Four exemplary selected beads.

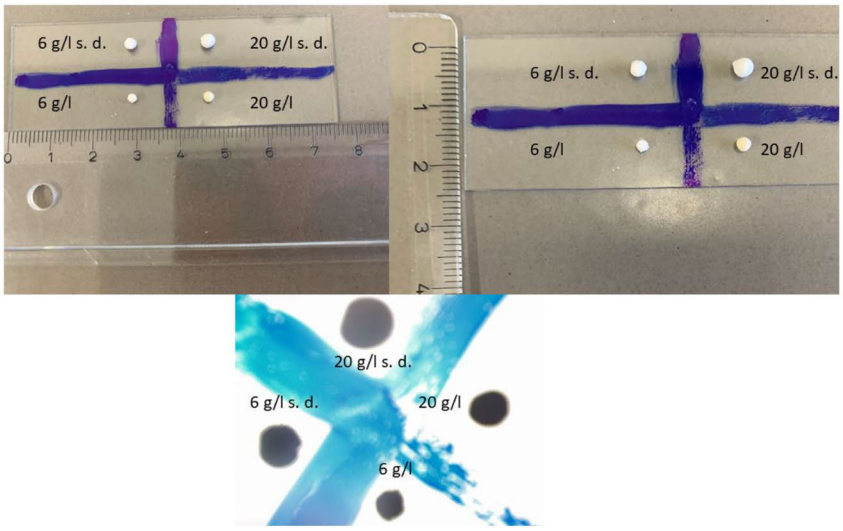

Figure S41: Images of the MOF@chitosan composites with camera (both images on top) and by a light microscope (below).

S13 Reaction scheme of chitosan and glutaraldehyde

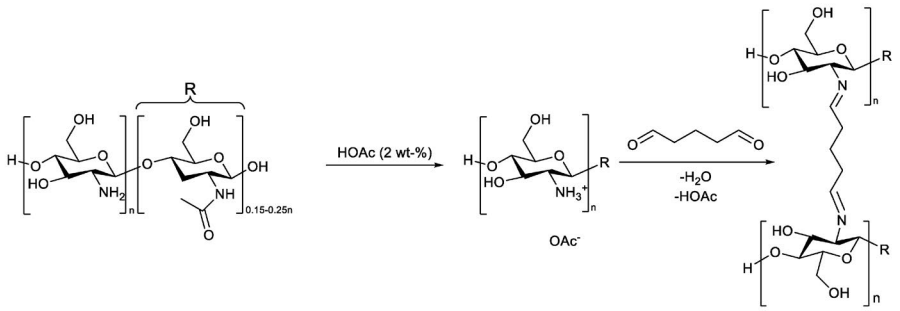

Figure S42: Reaction scheme of chitosan and glutaraldehyde.

S14 Graphics

S15 References

1 E. Leung, U. Müller, N. Trukhan, H. Mattenheimer, G. Cox and S. Blei, *Process for preparing porous metal-organic frameworks based on aluminum fumarate*, U.S. Patent No. 8,524,932, BASF SE, 3 Sep. 2013.

2 C. Kiener, U. Müller, and M. Schubert, *Method of using a metal organic frameworks based on aluminum fumarate*, U.S. Patent No. 8,518,264, BASF SE, 27 Aug. 2013.

3 K. Brandenburg, Diamond 4.6.6, Crystal and Molecular Structure Visualization, Crystal Impact - K. Brandenburg GbR, Bonn, Germany, 1997-2021.

4 Alvarez, E.; Guillou, N.; Martineau, C.; Bueken, B.; Van de Voorde, B.; Le Guillouzer, C.; Fabry, P.; Nouar, F.; Taulelle, F.; Vos, D. de; Chang, J.-S.; Cho, K.H.; Ramsahye, N.; Devic, T.; Daturi, M.; Maurin, G.; Serre, C. The structure of the aluminum fumarate metal-organic framework A520. *Angew. Chem.* **2015**, *54*, 3664–3668, doi:10.1002/anie.201410459.

5 Cadiau, A.; Lee, J.S.; Damasceno Borges, D.; Fabry, P.; Devic, T.; Wharmby, M.T.; Martineau, C.; Foucher, D.; Taulelle, F.; Jun, C.-H.; Hwang, Y.K.; Stock, N.; Lange, M.F. de; Kapteijn, F.; Gascon, J.; Maurin, G.; Chang, J.-S.; Serre, C. Design of hydrophilic metal organic framework water adsorbents for heat reallocation. *Adv. Mater.* **2015**, *27*, 4775–4780, doi:10.1002/adma.201502418.

6 Wahiduzzaman, M.; Lenzen, D.; Maurin, G.; Stock, N.; Wharmby, M.T. Rietveld Refinement of MIL-160 and Its Structural Flexibility Upon H_2O and N_2 Adsorption. *Eur. J. Inorg. Chem.* **2018**, 3626–3632, doi:10.1002/ejic.201800323.

7 Deutsches Institut für Normung. *DIN EN ISO 846 Plastics - Evaluation of the action of microorganisms;* Beuth: Berlin, 2018 (846:2018).

8 Thommes, M.; Kaneko, K.; Neimark, A.V.; Olivier, J.P.; Rodriguez-Reinoso, F.; Rouquerol, J.; Sing, K.S.W. Physisorption of gases, with special reference to the evaluation of surface area and pore size distribution (IUPAC Technical Report). *Pure Appl. Chem.* **2015**, *87*, 1051–1069, doi:10.1515/pac-2014-1117.

3.3 Metal organic framework/polyelectrolyte composites for water vapor sorption applications

Tatsiana Shutava, Christian Jansen, Kanstantsin Livanovich, Vladimir Pankov, Christoph Janiak

Dalton Trans. **2022**, *51*, 7053-7067

DOI: 10.1039/d2dt00518b

Impact-Faktor: 4.569 (2021)

Kurzzusammenfassung:

Die verschiedenen MOFs MIL-101(Cr), Aluminiumfumarat, MIL-53-TDC, Zirconiumfumarat und UiO-66 wurden modifiziert, indem dünne polyelektrolytbasierende Hüllen über die MOFs gezogen wurden, ohne die Kristallstruktur dieser MOFs zu verändern. Bei Variation der Polyelektrolyte und Anzahl der Hüllenschichten (1 oder 3) wurde der Massenanteil der Hüllen zwischen 0.6-2.5 (für eine Schicht) bis hin zu 50 % (für drei Schichten) verändert. Die Wassersorptionseigenschaften in einem relativen Druckbereich, ähneln mit ihren S-förmigen Adsorptionsisothermen denen der reinen MOFs. Die relevanten Abweichungen der Wassersorptionen, also die Verschiebung hinzu höheren oder niedrigeren relativen Druckbereichen oder die Steigerung oder die Reduzierung der Wasseraufnahme in bestimmten Regionen, sind somit auf die Kern-Hülle-Struktur der Komposite zurückzuführen. Ebenso spielt auch die Änderung der Morphologie des MOF-Pulvers hierbei eine entscheidende Rolle. Die Komposite können somit hin zu einer höheren oder schwächeren Hydrophilie verändert werden, was auch in der Interaktion mit Wasser gezeigt werden kann.

Anteile an der Publikation:

- Konzept, experimentelle Arbeiten und Analytik im Bereich des Wassersorptionen und der MOF-Synthesen und der Charakterisierung der MOFs
- Aufarbeitung der Ergebnisse, Verfassen des Manuskripts und das Erstellen der Abbildungen und Tabellen im Zusammenhang mit den MOFs und den Ergebnissen der Charakterisierung und der Wassersorption

Volume 51
Number 18
14 May 2022
Pages 6981-7364

Dalton Transactions

An international journal of inorganic chemistry

rsc.li/dalton

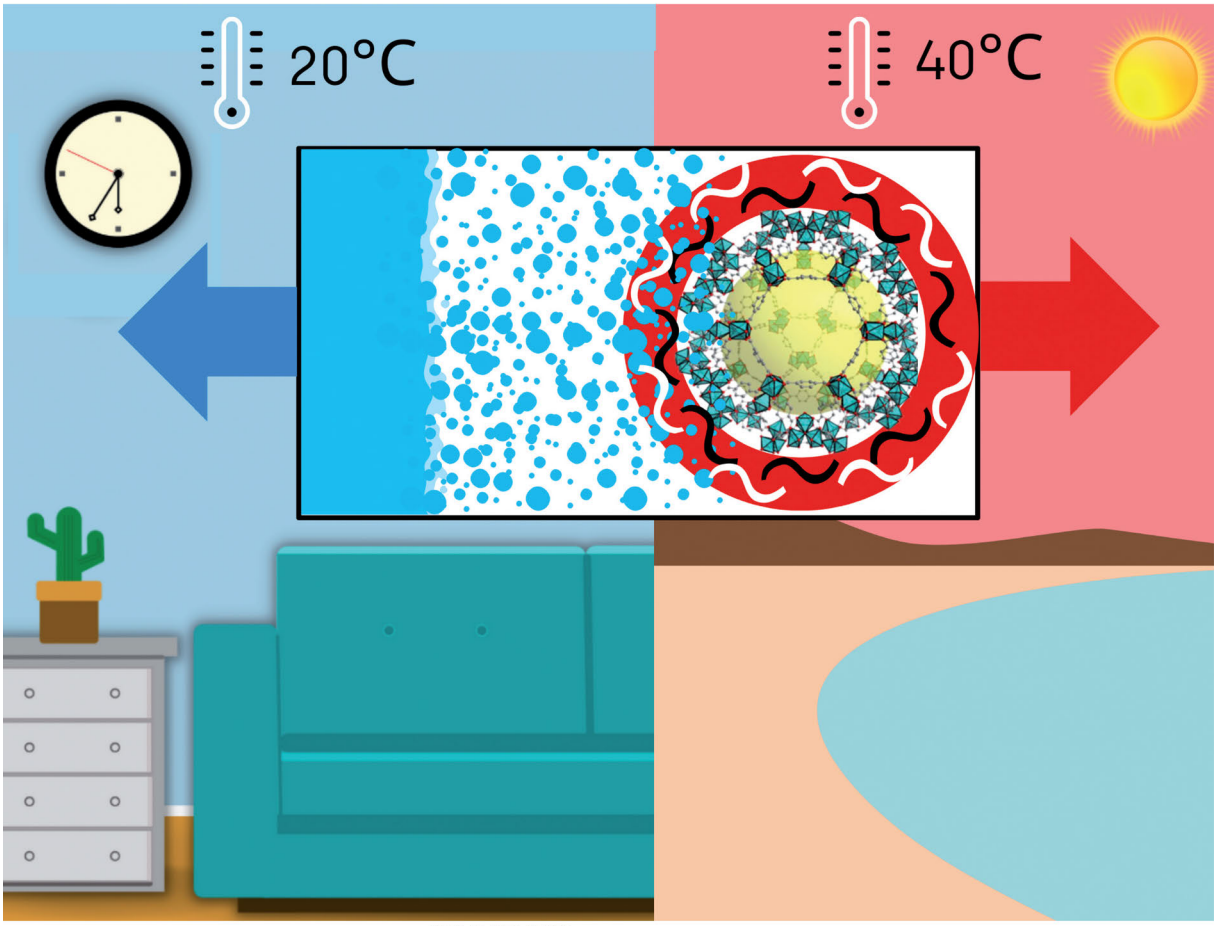

ISSN 1477-9226

ROYAL SOCIETY OF CHEMISTRY

PAPER
Tatsiana Shutava, Christoph Janiak *et al.*
Metal organic framework/polyelectrolyte composites for water vapor sorption applications

Dalton Transactions

ROYAL SOCIETY OF CHEMISTRY

PAPER

View Article Online
View Journal | View Issue

Cite this: *Dalton Trans.*, 2022, **51**, 7053

Metal organic framework/polyelectrolyte composites for water vapor sorption applications†

Tatsiana Shutava, *‡[a] Christian Jansen,‡[b] Kanstantsin Livanovich,[a] Vladimir Pankov[c] and Christoph Janiak*[b]

Received 18th February 2022,
Accepted 27th March 2022

DOI: 10.1039/d2dt00518b

rsc.li/dalton

Metal–organic framework (MOF) core particles of MIL-101(Cr), aluminum fumarate (Basolite® A520), MIL-53-TDC, zirconium fumarate, and UiO-66 were modified by adsorption of thin polyelectrolyte (PE)-based shells without deterioration of their crystal structure. By applying different PEs and depositing a single layer (MOF/PE) or one to three layer-by-layer assembled bilayers (MOF/LbL), the mass percent of shell material in the composite was varied from 0.6–2.5% to 50%. Under a constant relative pressure of water vapor, the moisture uptake by a MOF/PE and a MOF/LbL is rather comparable with its S-shaped curvature to that of pristine MOFs. The relevant differences, such as a shift of the ascending adsorption part to lower/higher relative pressure or an increase/decrease in water uptake in selected regions, are associated with the core–shell structure and related to the morphological changes of the MOF powders. The hydrophilic surface promotes the formation of liquid menisci at the points of contact between particles and accelerates the moisture uptake and loss. A decrease in water sorption under an atmosphere with high humidity by some composites can be associated with the inhibition of liquid water condensation by the more hydrophobic shells.

1. Introduction

Since the first metal–organic frameworks (MOFs) were synthesized, the interest in these porous crystalline materials has been steadily increasing.[1–6] MOFs are 3D coordination networks built of metal ions or metal clusters (nodes) linked by rigid polydentate organic ligands in such a way that a homogeneous one-, two- or three-dimensional spatial structure containing voids–potential pores is formed.[7–9] Due to their structure, MOFs have a tremendous specific surface area and can exchange small guest molecules with the surrounding. Until now, MOFs are being investigated as catalysts[2,4] and materials for storage and separation of gases,[5,6,10] humidity sorbents in harvesters of atmospheric water, air-conditioners, environmentally friendly heating and cooling technologies based on the sorption–desorption cycle of water vapor,[1,3,11–14] and humidity sensors.[15] The devices based on MOF utilizing sorbents can effectively capture water at low (below 30%) atmospheric humidity and further use solar energy or other secondary heat sources to regenerate the sorbent. Model units operating in arid climates (10–30% humidity, dew point below zero) can produce 0.25 L of water per 1 kg of MOF in one daily cycle.[16,17]

For practical applications, finely dispersed and microcrystalline MOF powders have to be mixed with polymeric or inorganic binders and molded into pellets, pressed into tablets or granules with a high percentage of the porous material, aiming to facilitate material handling and avoid the formation of dust particles.[18–21] Various approaches have been used to obtain MOF/polymer composites, for example, the inclusion of 35–75 wt% MOF into the macroporous matrices of polyacrylonitrile and poly-*N*-isopropyl acrylamide or resorcinol-formaldehyde xerogels.[18–20] Despite the achieved high mechanical stability, the incasing of MOF in polymer matrices often leads to a significant loss of its porosity and loading capacity, as well as an increase in the time period required to complete one adsorption/desorption cycle.[18–23] The reasons are the hydrophobicity and prolonged swelling of the polymer matrix material, its low water sorption capacity, and limited diffusion of water molecules through the polymer. Recent work in the shaping of MOFs has tried to develop procedures, such as freeze-casting or phase-separation techniques to prevent such loss of porosity.[24–26]

A distinctive feature of this work is the combination of MOF nano/microparticles and hydrophilic polymers bearing charged groups, that is polyelectrolytes. Those are polycations containing quaternary or protonated primary amino groups,

[a]*Institute of Chemistry of New Materials, National Academy of Sciences of Belarus, 36 F. Skaryna St., Minsk 220141, Belarus. E-mail: shutova@ichnm.by*
[b]*Institut für Anorganische Chemie und Strukturchemie, Heinrich-Heine-Universität Düsseldorf, 40204 Düsseldorf, Germany*
[c]*Belarusian State University, 4 Nezavisimosti Av., Minsk 220030, Belarus*
† Electronic supplementary information (ESI) available. See DOI: https://doi.org/10.1039/d2dt00518b
‡ Both authors contributed equally.

such as poly(diallyldimethylammonium chloride) (PDDA), polyallylamine hydrochloride (PAH), polyethyleneimine (PEI), and chitosan (CH), and polyanions containing carboxy or sulfo groups, for example polyacrylic (PAA), carboxymethyl cellulose (CMC), polystyrene sulfonic acid sodium salt (PSS), dextran sulfate (DexS) (ESI, Fig. S1†). Typical polyelectrolytes are soluble in aqueous solutions and readily adsorb the surfaces of substrates with different geometries, including micro/nanoparticles and porous membranes. If the sequential adsorption of pairs of oppositely charged polyelectrolytes is repeated multiple times using the layer-by-layer (LbL) assembly method, a thin continuous film is formed on the surface of macroobjects, while each nano/microparticle envelops individually in a thin semipermeable shell.[27–29] The electrostatic interaction of adsorbing components of the coating is the main driving force of layer-by-layer assembly; however, in some cases, hydrogen bonds and other types of interactions contribute considerably.[30–33]

The thickness of the LbL film or shell is controlled with nanometer accuracy by simply changing the number of polycation/polyanion bilayers (n) and the conditions of their formation. It can be varied from 1–2 nm to several hundreds of nanometers by performing the required number of adsorption cycles.[30,35–44] By changing the pH, ionic strength, concentration of solutions and molecular weight of polyelectrolytes, the structure and surface properties of a coating are manipulated to achieve its linear or exponential growth.[29,41]

An important aspect of the preparation and application of polyelectrolyte films is their tendency to be saturated with water in both the liquid and gas phases. The mass fraction of water in polyelectrolyte layers in contact with an aqueous solution can reach 90% and depends on the polymers used and preliminary drying.[41,42] The average pore diameter of wet $(PAH/PSS)_n$, n = 7–10 multilayer films experimentally determined by NMR cryoporometry is 1.2–1.5 nm. The inner layers adsorbed on the substrate are tightly packed, while larger pores appear as a result of the loose packing of polymer outer layers with increasing n.[45] LbL-based shells in solution are permeable for water, ions, and small molecules; the diffusion coefficient of sucrose, glucose, methanol, and glycerin in multilayers is in the range of $(0.52–1.56) \times 10^{-9}$ m^2 s^{-1}.[44] The permeability of polyelectrolyte films for macromolecules with a molecular weight of more than 5 kDa depends on pH, temperature, and other factors.[29,41]

At the same time, the swelling of dry multilayer coatings in contact with the gas phase with a given partial pressure of water vapor (p/p_0), or relative humidity (RH), and its effect on the characteristics of the films are of practical importance.[46–51] The degree of LbL film swelling depends on the nature of the polyelectrolytes used, the conditions of layer preparation, and other factors. For example, for $(PAH/PAA)_n$ films, the relative increase in mass ranges from 1.1 to 1.35 at 80% humidity, depending on the pH value used upon film adsorption.[46] For $(PAH/PSS)_n$, n = 6–12, the percentage of water in the film reaches 30–50% and depends on the number of bilayers.[48] The swelling coefficient of thin multilayer films of poly(methacrylic acid) and poly-2-(dimethylamino) ethyl methacrylate chloride increases from 1.65 to 1.87 with an increase in the adsorption time of each layer from 3 to 25 min.[49] The water uptake by $(PDDA/PSS)_n$ and $(chitosan/dextran\ sulfate)_n$, n = 3 films at ambient temperature from gas phase with p/p_0 = 0.97 is 220 ± 10 and 380 ± 10 mg g^{-1} with ~a 15 min saturation time.[52]

The data on the effect of surface charge on LbL film swelling are contradictory. In ref. 46, it was shown that the positive electrostatic charge of the outer layer promotes swelling of the film, while in ref. 48 the degree of swelling of negatively charged films with the outer layer of PSS was 5–10% higher. A characteristic feature of multilayers $(PAH/PAA)_n$ prepared at two different pH values is a small hysteresis of the water sorption/desorption cycle,[46] while it is completely absent for common interpolyelectrolyte complexes. The diffusion coefficients of water from the gas phase into individual polyelectrolyte films (PSS and PAA), interpolyelectrolyte complex membranes and LbL films are within the range of 10^{-14}–10^{-6} cm^2 s^{-1} and affected by the thickness of the layer and temperature.[47,52–54]

Among the important features of LbL films that are relevant to the topic discussed here are the high water sorption capacity comparable to that of most MOF powders, the almost linear dependence of it on p/p_0, and the short saturation period.

In recent years, some attempts have been made to combine the advantages of MOFs and polyelectrolyte LbL films in one material. One of these approaches is the preparation of composites with high ion-exchange capacity *in situ* by polymerization of the corresponding monomers in MOF.[55,56] MOFs of the zeolite-imidazole type (ZIF) have been used as water-soluble cores for LbL microcapsules with pronounced edges.[57,58] Small molecules with therapeutic activity and contrast agents are effectively incorporated into nanosized MOFs coated with a polyelectrolyte shell.[59] However, the effect of polyelectrolyte shells on the water sorption characteristics of MOF/polyelectrolyte composites has not been investigated yet.

We report a new approach to control the water vapor sorption properties of MOF powders, namely by adsorption of a hydrophilic polyelectrolyte layer (MOF/PE) or a multilayer shell (MOF/LbL) on the surface of the MOF (Fig. 1). Due to the double compartment porous structure, the composite powders consisting of a MOF core and a polyelectrolyte shell are envisioned to have improved water sorption capacity and fast sorption/desorption cycle kinetics.

2. Experimental section

2.1 Materials and methods

Polycations [chitosan (ChH, 450 kDa, degree of deacetylation (DD) 75%, poly(diallyldimethylammonium chloride) (PDDA, 100–200 kDa), polyallylamine hydrochloride (PAH, 58 kDa), polyethyleneimine (PEI, 60 kDa)] and polyanions [polystyrene sulfonate sodium salts (PSS, 70 kDa), polyacrylic acid (PAA, 2.5 kDa), carboxymethyl cellulose (CMC, 250 kDa), dextran sulfate (DexS, 6.5–10.0 kDa and DexH, >500 kDa), and

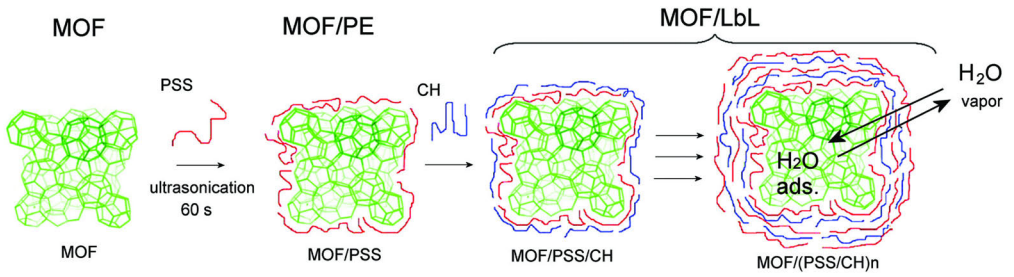

Fig. 1 Scheme of the formation of a shell on the surface of a MOF powder using adsorption of single polyelectrolyte layer (MOF/PE) or layer-by-layer shell (MOF/LbL) with the exemplifying polymers, polystyrene sulfonic acid (PSS) and chitosan (CH).

κ-carrageenan (CAR, 5–25 mPa s, 0.3% in H_2O, 25 °C)] were obtained from Sigma-Aldrich and used to form mono- and multilayer polyelectrolyte shells on MOF particles. Chitosan of low molecular weight (CH, 18 kDa, DD 75%) and two hydrophilic graft-copolymers of CH with 5 kDa polyethylene glycol (CH-PEG) and 6 kDa dextran (CH-DEX) were synthesized.[60] Polyallylamine hydrochloride labeled with fluorescein isothiocyanate (PAH-FITC) was synthesized from PAH of 18 kDa and FITC as described.[60]

All chemicals for MOFs syntheses were used as received from suppliers.

A Zetasizer NanoZS (Malvern) analyzer was used for measuring the ζ-potential and the hydrodynamic diameter of MOF particles. The value of the number average hydrodynamic diameter (d_N) and polydispersity index (PDI) of each sample was obtained from three independent measurements using the instrument software. To obtain the porosity of the MOF powders, nitrogen (purity 99.9990%) physisorption isotherms were measured with *ca.* 20–50 mg of the MOF sample using an Autosorb-6 from Quantachrome at 77 K, thermostated with liquid nitrogen. Before each nitrogen or water sorption measurement, the samples were activated under vacuum (1×10^{-3} mbar) at 373 K for 3 h. Water vapor sorption isotherms were measured volumetrically using a Quantachrome VSTAR vapor sorption analyzer (model number Vstar4-0000-1000-XS) at 293 K. For water uptake as a function of relative pressure of water vapor *V-Star*, a Quantachrome analyzer was used.

The apparent Brunauer–Emmett–Teller (BET) surface areas were calculated from the nitrogen physisorption isotherms. All surface areas (BET) were calculated from five adsorption points by applying Roquerol plots ($r > 0.998$). We note that the microporous MOF surface areas derived from type I isotherms should be regarded as "apparent S (BET) values" since "the BET-area derived from a type I isotherm must not be treated as a realistic probe accessible surface area" but it "represents an apparent surface area, which may be regarded as a useful adsorbent fingerprint".[61] The density functional theory (DFT) calculations for the pore size distribution curves were done with the native NovaWin 11.03 software using the "N_2 at 77 K on carbon, slit pore, non-local density functional theory (NLDFT) equilibrium" model for nitrogen. In addition, none of the present DFT kernels for "N_2 on carbon" reflect the surface properties of a MOF material. The numbers can be used for the comparison of similar materials but must not be taken as exact values for the pore sizes or surface areas of MOFs. In the absence of MOF-specific kernels, the N_2 on carbon kernels with different pore types is frequently used to study the surface properties of the MOFs.[62]

Powder X-ray diffractometry (PXRD) was performed at ambient temperature using a *D2 Phaser* (Bruker AXS, Karlsruhe, Germany) using Cu-K_α radiation (λ = 1.54182 Å) between $5° < 2\theta < 50°$ with a scan rate of 0.0125 s^{-1} (300 W, 30 kV, 10 mA). Analyses of the diffractograms were carried out with the Match 3.11 software.

2.2 QCM measurements of water vapor uptake by MOF/LbL powders

The time-related parameters of water uptake by MOFs were determined by the quartz crystal microbalance technique using a QCM200 Stanford Research System instrument equipped with quartz resonators with a gold working surface and a nominal frequency of 5 MHz. Before the experiment, the resonators were cleaned for 5 min at 75 °C with a mixture of water, 25% NH_3 solution, and 30% H_2O_2 solution taken in a volume ratio of 3 : 1 : 1, washed 4–5 times with distilled water and dried in an argon flow. The unloaded resonator was placed in an open cell of the device, which allowed the resonator surface to contact the environment, and its resonant frequency (F_0) and dynamic resistance (R_0) were determined at a given temperature and relative humidity over dry KOH (RH 6–10%). The temperature and humidity near the resonator surface were determined using a TKA-PKM thermohygrometer.

The temperature dependence of the frequency and the dynamic resistance of an unloaded resonator are due to the fundamental properties of quartz and depend on the shape of the quartz crystal or the type of its cut.[63] When the temperature increases from 23 to 34 °C, the F_0 value of the resonator decreased by 10–15 Hz, and the dynamic resistance R_0 by no more than 0.5 Ohm. At constant temperature, humidity does not affect the oscillation frequency of the unloaded resonator

(the change does not exceed 1 Hz), while the resistance changes less than 1.5 Ohm when RH changes from 6 to 90%.

The MOF under investigation (~10 μg) was applied on the planar surface of the resonator in the form of a diluted suspension in water, pretreated with ultrasound for 2 min, and dried over KOH at room temperature for 1 h. The cell with the resonator was placed in a chamber with controlled RH and temperature and kept over KOH until a constant value of frequency (F_{KOH}) was established.

The mass of dry deposit on the surface of the resonator (m_f) was calculated using the Sauerbrey equation:[63]

$$m_f = -\Delta F/C, \quad (1)$$

where $\Delta F = F_{KOH} - F_0$ is the change in frequency, Hz; m_f is the deposit weight per unit area, μg cm^{-2}; C is the sensitivity factor equal to 56.6 Hz cm^2 μg^{-1} for a quartz resonator with a frequency of 5 MHz. The sample mass on the resonator surface was 2.4–5.2 μg cm^{-2}.

The specified RH of the medium in the thermostat was maintained by using a saturated solution of the corresponding salt.[64] At a constant temperature, the cell with the resonator was sequentially placed over saturated salt solutions (LiCl, $MgCl_2$, NaBr, NaCl, KCl, and K_2SO_4) in the order of increasing partial pressure of water vapor, after which the relative humidity was successively decreased, ending with a medium over dry KOH. After reaching the constant temperature and relative humidity, as well as the equilibrium values of the frequency and dynamic resistance of the resonator, they were determined with one decimal point accuracy. When calculating the saturation of MOF powders at different humidity (q_e), the resonator with the deposit was sequentially placed over dry KOH (F_0^{RH}) and saturated salt solutions, and after establishing a constant value, the oscillation frequency of the resonator with the MOF deposit at a given humidity (F_e^{RH}) was determined.

The kinetics of water sorption by the MOF deposit was investigated by rapidly moving the resonator from the atmosphere over dry KOH (RH < 10%), which corresponds to the initial values of frequency and resistance F_{to} and R_{to}, into a chamber saturated with water vapor (RH = 90%) and recording the F_t and R_t values of the resonator in time. The water content of MOF at time t (q_t) was used for the calculation of the kinetic parameters of the process. Desorption of water vapor was studied in a similar way.

The water content in the powder $q_{e,t}$ (in g/g) was calculated using the formula:

$$q_{e,t} = -\Delta F_{e,t}/(C \cdot m_f), \quad (2)$$

where $\Delta F_e = F_e^{RH} - F_0^{RH}$ and $\Delta F_t = F_t - F_{to}$.

The changes in the resonant frequency and resistance due to water absorption by a deposit are recalculated relative to the values of the semi-dry deposit above KOH (RH is equal to or less than 10%). As a result, despite the amount being relatively small, water that is already present in the deposit at the lowest experimental humidity is not taken into account.

2.3 Synthesis

2.3.1 Metal–organic frameworks. Metal–organic frameworks (MOF) were synthesized as described in detail elsewhere.[65–69] MIL-101(Cr) was synthesized according to Chang *et al.* by microwave-assisted synthesis. The reaction mixture was loaded in a Teflon autoclave, sealed and placed in a lab microwave oven. Purification and drying were done using the reported method.[65] Aluminum fumarate (Al-fum) was synthesized according to the BASF patent at 60 °C and was also purchased from BASF as Basolite® A520.[66] MIL-53-TDC was synthesized according to Tannert *et al.*[67] The aluminum source was $NaAlO_2$ and the synthesis was carried out under reflux at 135 °C for 24 h. Zirconium fumarate (Zr-fum) was synthesized according to Zahn *et al.*[68] The used modulator was acetic acid and the synthesis was achieved at 120 °C for 24 h. UiO-66 was synthesized according to Shearer *et al.*[69] The used modulators were hydrochloric acid and HCl/H_2O and the synthesis conditions were 100 °C for 24 h.

2.3.2 Preparation of MOF powders modified with polyelectrolyte single layer or shell. The MOF powder was dispersed in water at a concentration of 2 mg mL^{-1} using a *Sapphire* ultrasonic bath for 20 s, then 0.25 mg of polyelectrolyte per 1 mg of MOF was added as an aliquot of 10 mg mL^{-1} polyelectrolyte solution and the suspension was additionally sonicated for 60 s and left for 10 min at room temperature. The particles coated with the polyelectrolyte layer were separated by centrifugation (a *ZH36, Hermle* centrifuge, 1000*g*, 10 min), washed once with water to remove unadsorbed polyelectrolyte, and redispersed in water. In a similar way, shells were formed on the surface of the particles, consisting of 1–6 layers of polyelectrolyte (0.5–3.0 bilayers). The dispersions of MOFs modified with a single polyelectrolyte and a shell of required number of layers in water were frozen at −20 °C and lyophilized.

In an additional series of experiments, 20 mg of selected MOF powder was suspended in 9 mL of water and 0.1 mg mL^{-1} PSS solution was added dropwise as 150 μL aliquots to obtain a low ratio of m_{PSS} and m_{MOF}. The mixture was carefully shaken. After 10 min, 25 μL of it was withdrawn with a pipette, resuspended in 2 mL of water, and used for the measurements of the hydrodynamic diameter and ζ-potential of MOF particles.

Polyelectrolyte shells consisting of three bilayers of PSS/PDDA or DexH/ChH were formed on Al-fum in a 0.2 M sodium chloride solution. A 4 mg mL^{-1} suspension of Al fumarate was mixed with an equal volume of 2 mg mL^{-1} of PSS or DexH solution, sonicated for 1–2 min, and left at room temperature for 30 min. The resulting particles with a polymer layer adsorbed on them were separated by centrifugation, washed 2 times, and dispersed in 0.5 mL of a 0.2 M NaCl solution. The chitosan or PDDA layer was formed in a similar way.

2.3.3 Preparation of MOF/thick LbL composite. A thick shell consisting of two PSS/PDDA bilayers was formed on the particles of Al fumarate powder using excessive amounts of polyelectrolytes: a MOF sample weighing ~0.08 g was dispersed in 1 mL of water, 0.02 g of PSS was added as a 10 mg

mL^{-1} solution, and the mixture was treated by ultrasound for 60 s. Without intermediate washing, 0.02 g of PDDA was added to the mixture as a concentrated aqueous solution. The procedure of PSS/PDDA deposition was repeated. The MOF particles with a thick polyelectrolyte shell were separated by centrifugation and dried at 110 °C in air. The calculated ratio of the mass of polyelectrolyte shell to the mass of MOF is 1 : 1. The composite sample was stored at RH = 97% in a sealed desiccator overnight and the water content of the sample was characterized using a MAX 50 Radwag moisture analyzer by heating to 80 °C to evaporate water adsorbed by the composite. The kinetics of water sorption by the composite powder was measured at 23 °C and an ambient relative humidity of 70%.

3. Results and discussion

The criteria for the selection of MOF powders for modification with a polyelectrolyte shell were high chemical stability and hydrolytic resistance, large values of specific surface area (above 400 $m^2\ g^{-1}$) and water vapor capacity (at least 500 mg g^{-1} or higher), as well as an S-shaped water sorption isotherm with an inflection point of water uptake lower than $p/p_0 = 0.5$. The chosen MOFs MIL-101(Cr), aluminum fumarate (Basolite® A520), MIL-53-TDC, zirconium fumarate, and UiO-66 were all well-investigated for their water sorption behavior before as noted in the given references.[34,67,70–74] A brief structure description of these MOFs is given in the ESI, Table S2.† In the selected MOFs, the diameter of windows through which small molecules can penetrate the framework does not exceed 0.8–1.6 nm.

3.1 Quantification of PE adsorption on MOF

By quantitative analysis of polyelectrolyte adsorption on porous MOF particles, we selected PSS as a strong polyelectrolyte that is fully charged in a wide range of pH.[75–78] Among the MOFs, UiO-66 and MIL-53-TDC are samples with high ζ-potential values; the two aluminum fumarate samples differ in particle size, Al-fum (2.3 μm) and Basolite® A520 (270 nm), with a moderate positive ζ-potential in the range of 5 to 15 mV, while Zr-fum has ζ ≈ 0. Fig. 2 shows the changes in the ζ-potential and hydrodynamic diameter of the MOF UiO-66 during a step-wise addition of negatively charged PSS. Upon increasing the m_{PSS}/m_{MOF} ratio, the negative charge of the particles increases. We assumed that PSS adsorbs quantitatively on MOF particles until a saturated polyelectrolyte layer is formed and a constant negative ζ-potential value is attained. PSS added over that amount remains dissolved in solution but does not cause an additional decrease of the ζ-potential. In the subsequent washing stage, this excessive PSS is removed but the adsorbed polyelectrolyte macromolecules remain on the surface electrostatically bound to it at numerous points.

As one can see from Table 1, the amount of PSS required to fully recharge the MOFs depends on the powder under investigation. The value is definitely related to the difference in their structure; however, for all studied MOFs, the recharge values

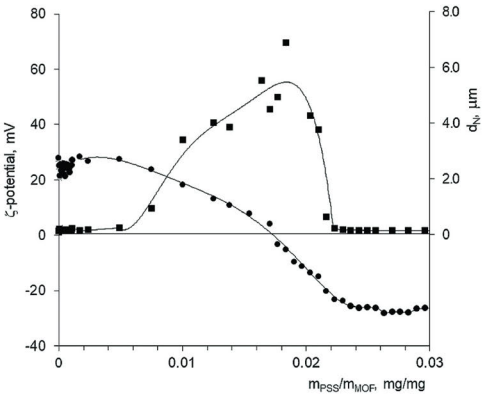

Fig. 2 Dependence of the ζ-potential and the hydrodynamic diameter (d_N) of particles of the MOF UiO-66 on m_{PSS}/m_{MOF}.

Table 1 ζ-Potential and the PSS-based neutralization and recharge points of MOFs

		m_{PSS}/m_{MOF}, mg g^{-1}	
MOF	ζ-Potential, mV	Zero charge	Recharge
UiO-66	27.9 ± 0.1	17.5	25.5
MIL-53-TDC	23.4 ± 1.1	4.0	13.6
Al fumarate	13.6 ± 0.1	2.4	6.2
Basolite®A520	7.4 ± 0.2	9.2	15.6
Zr fumarate	1.1 ± 0.1	—	4.3

do not exceed 25–26 mg g^{-1} MOF, or 2.5 wt%. At the same time, the water uptake by the MOF powders reaches usually a 20-fold higher value. The results obtained prove that the adsorption of polyelectrolytes on MOFs is not associated with their penetration into micropores but apparently occurs on the surface of particles. A higher recharge value for Basolite® A520 that has smaller particles as compared with the larger ones for Al fumarate confirms the outer surface–related adsorption of PSS.

To coat the MOFs, all polyelectrolytes were taken in excess (~0.25 mg per 1 mg MOF) and the unadsorbed polymer was removed after deposition of each layer by rinsing with DI water. Taking the PSS-based recharge value for different MOFs as an approximate mass of a single polyelectrolyte layer, one can estimate that the mass of an LbL shell that consists of 3 bilayers is less than 150 mg per 1 g of MOF, or 13 wt%.

Another value obtained in this series is the zero charge m_{PSS}/m_{MOF} ratio needed to neutralize the positive charge of the pristine MOF particles. It is reasonably smaller than the recharge PSS/MOF ratio. Obviously, in the vicinity of the zero-charge ratio, the MOF particles are most agglomerated in a dispersion due to the disappearance of electrostatic repulsion (Fig. 2). However, at such small polyelectrolyte-to-MOF ratios,

it is difficult to uniformly modify concentrated MOF dispersions.

A composite consisting of Al-fum particles coated with a thick $(PSS/PDDA)_2$ shell was also obtained by using LbL assembly without intermediate washing.[79,80] This technique precisely controls the weight fraction of the shell material by adding a predetermined, excessive in the given case, amount of polyelectrolyte in each step without separating it after adsorption. In the obtained MOF/thick LbL shell composite, the mass of the LbL shell is 50 wt%, or equal to the mass of the MOF cores.

3.2 Morphology of the MOF/PE and MOF/LbL powders

The SEM microphotographs of the selected MOFs modified with a single polyelectrolyte layer or an LbL shell are shown in Fig. 3. The shape and size of the particles of the different MOFs vary but all of them are faceted; those are typical of crystalline substances. The SEM images of pristine MOFs are given in the ESI, Fig. S3† for comparison. A single polyelectrolyte layer does not change the morphology of any other MOFs as illustrated in the ESI, Fig. S4† on the example of MIL-53-TDC coated with PAA, CMC, DexS, and CAR.

Due to high hydrophilicity, all MOF powders are easily dispersed in water, while the sedimentation of their suspensions depends on the size of the particles. The average hydrodynamic particle diameter of the pristine MOFs as determined by dynamic laser light scattering (DLS) ranges from 0.2 to 2.3 μm with a PDI value exceeding 0.3 (ESI, Fig. S5†), which is typical of polydispersed particles. In the process of sonication-assisted polyelectrolyte adsorption, MOFs with an average hydrodynamic diameter of less than 700 nm (such as MIL-101(Cr), MIL-53-TDC and Basolite®A520) tend to aggregate at varying degrees through the added PE shell; the polydispersity values of the PE-coated samples remain high. For the MOF Al fumarate, diameters of 2.3 and 2.0 μm and polydispersity values of 0.33 and 0.43 were found before and after single adsorption of polystyrene sulfonate on the MOF, indicating the negligible influence of the ultrasound-assisted PSS adsorption on the powder morphology.

The SEM images of the prepared Al-fum and commercial Basolite® A520 powders with LbL shells of different numbers of bilayers are shown in Fig. 3c and d (the additional SEM images are given in the ESI, Fig. S6†) and ESI, Fig. S7,† respectively. The effect of a shell consisting of one (polycation/polyanion) bilayer on the morphology of both powders is insignificant. For Al-fum powders with a three bilayer shell, the microparticles in dry powder have well-defined boundaries and fairly close sizes. According to the DLS data (ESI, Fig. S5†), the diameter of Al fumarate microparticles with a shell based on chitosan and its copolymers with polyethylene glycol and dextran decreases.

The thickness of a single adsorbed polyelectrolyte layer usually does not exceed 1–2 nm, while for a 3 bilayer shell it is typically less than 20 nm.[30,31,41–43,45] Due to the minimal dimensions and the absence of any staining, the adsorbed PE or LbL shells do not appear in the SEM images of the MOF powders. The presence of an LbL shell on the surface of the MOF particles was confirmed by using a dye-labeled polyelec-

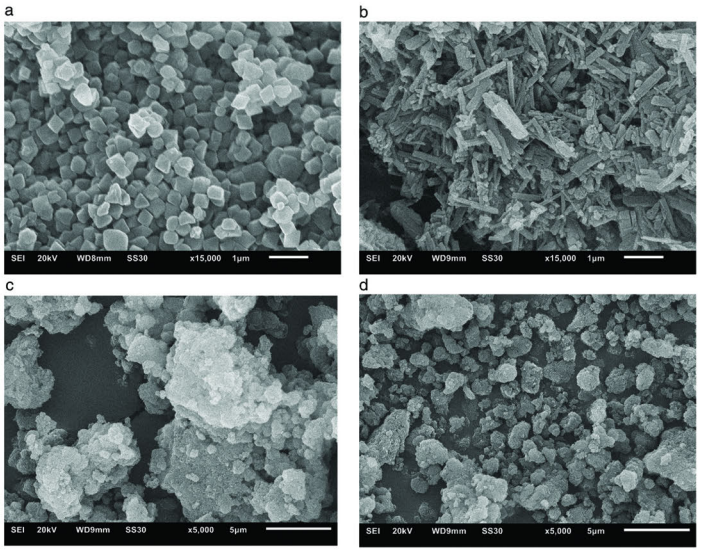

Fig. 3 SEM micrographs of MIL-101 (Cr) modified by PSS (a) MIL-53-TDC with PAA (b), Al fumarate modified with an LbL shell: PSS/CH (c) and $(PSS/CH)_3$ (d).

trolyte as one of the shell components. The images in transmitted and reflected light showing agglomerated Al-fum powder coated with a shell of PSS and FITC-labeled PAH are presented in the ESI,† Fig. 8. The location of the yellowish regions coincides with the spatial arrangement of the MOF particles confirming the inclusion of FITC-labeled polymer into a shell.

Most importantly, the MOFs have to retain their phase and crystallinity together with their porosity in the MOF/PE composites as assessed by PXRD and nitrogen porosimetry, respectively. The positions of the reflections in the PXRDs of the MOF/PE and MOF/LbL composites are in good agreement with the pristine MOF powders and their simulation (ESI, Fig. S9†) proving the unchanged phase and crystallinity. The diffractograms are not affected by the nature of the polyelectrolyte layer on the MOF surface. Since the adsorption of polyelectrolytes occurs under mild conditions (aqueous solutions of polymers with close to neutral pH, 25 ± 1 °C), the chosen MOFs do not degrade during the adsorption of polyelectrolytes in aqueous solutions.

The BET surface area of most PE or LbL modified MOF powders as evaluated by nitrogen sorption (Fig. 4) remains comparable to that of the unmodified MOF, and only in few cases decreases significantly. On the other hand, the surface area of MIL-101(Cr) treated with polycations (PDDA, PAH, and CH) and UiO-66 modified with PAA, as well as some aluminum fumarates with an LbL shell (PSS/CH and $(PSS/CH\text{-}DEX)_3$ for Al-fum; and PSS/PDDA and PAA/PDDA for Basolite®A520) were found to increase. Such an increase can occur through the formation of the added interface volume.

Two cases showing a significant decrease in the surface area were MIL-101(Cr)/PAA and MIL-53-TDC with PSS or DexS. Among the used polyelectrolytes, PAA and DexS were of low molecular weight (2.5 and <10 kDa, respectively). Since no aggregation of MIL-101(Cr) in solution was found after treatment with various polymers as confirmed by DLS measurements (ESI, Fig. S5†), the low BET surface area of MIL-101(Cr)/PAA reflects the filling of mesopores with oligomeric PAA molecules; for the PAA-modified MOF, the volume and surface of mesopores available for nitrogen adsorption decrease (ESI, Fig. S10†).

For MIL 53-TDC, there is a more complex situation. The BET surface area of the powders declines to various degrees after their modification with any negative polyelectrolyte (Fig. 4). The decrease is accompanied by both aggregation of nanoparticles (appearing as an increasing d_N and PDI in ESI Fig. S5†) and reduction of micropore volume (ESI, Fig. S10†). For the MIL 53-TDC/DexS powder, both these effects are intense and lead to a pronounced decrease in the BET surface. The SEM images of these modified MOFs (ESI, Fig. S4†) also show large agglomerates of MIL 53-TDC/DexS particles.

Nevertheless, for the overwhelming number of MOFs, single adsorption of the polyelectrolyte does not lead to a significant decrease in the specific surface area of the powders. A size comparison shows that the radius of gyration (R_g) of most polyelectrolytes with molecular weights above 20–30 kDa in water is several times larger than the half diameter of the micropore cage window and the interior space in most MOFs.[81–86] Thus, the micropores are inaccessible for penetration and localization in the polyelectrolytes in a random coil conformation. At the same time, they can adsorb on the inner surface of mesopores with a diameter of up to 50 nm and macropores forming a complete or partially filled layer of the adsorbate. Consistently, the higher the molecular weight and the corresponding value of R_g of the used polyelectrolyte, the less likely it adsorbs on the inner mesopore voids and affects

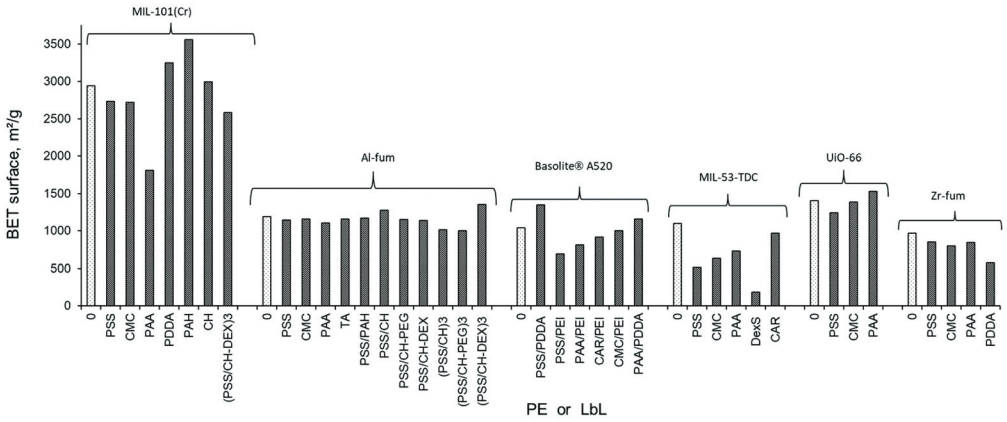

Fig. 4 Specific surface area of MOF powders modified by the adsorption of a single polyelectrolyte layer or LbL shell. At a surface area of 1000 m^2 g^{-1}, the error is assumed to be ±50 m^2 g^{-1}.

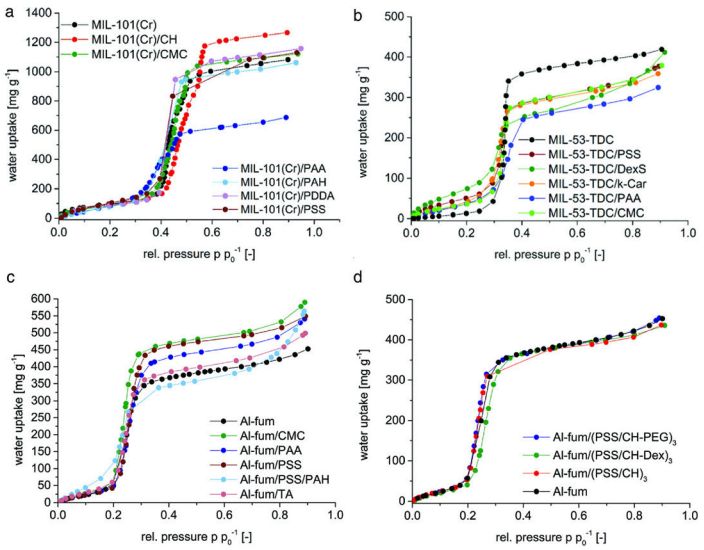

Fig. 5 Sorption isotherms of MOF/PE and MOF/LbL powders: (a) MIL-101(Cr), (b) MIL-53-TDC; and (c and d) Al fumarate.

the porosity-related properties of the powders. Therefore, unchanged sorption characteristics of modified MOFs can be expected.

3.3 Water uptake

The isotherms of water uptake by MOF, MOF/PE, and MOF/LbL powders against the relative pressure of water vapor are all S-shaped (Fig. 5 and ESI, Fig. S11†). Similar to the pristine MOFs, all modified powders retain the main sorption profile of the parent powders while there are some specific features brought upon by the adsorption of polyelectrolytes.

At first sight, the PE-modified MOFs of MIL-101(Cr), Al-fum and MIL-53-TDC seem to have the same low adsorption of water in the low relative pressure regions before the sharp incline and a sharp increase in water uptake, which is characteristic of the pristine MOF. A closer inspection shows the relevant differences, such as a shift in the ascending part to the lower/higher relative pressure (Fig. 6a) or an increase/decrease in water uptake in the selected regions (Fig. 6b).

A shift to 'earlier' uptake, that is to lower relative pressure, means that the composite has become more hydrophilic compared to the neat MOF. Such an earlier uptake is seen for MIL-101(Cr)/(PSS, CMC, PAA, PAH), all Al-fum/PE, and all MIL-53-TDC/PE composites.

A shift to 'later' uptake, that is to higher relative pressure, means that the composite has become more hydrophobic compared to the neat MOF. Such a shift to later uptake is brought about by chitosan to MIL-101, along with an increase in the uptake capacity after the inflection point. For UiO-66 also, a shift to later uptake upon composite formation takes place, together with an increase in the uptake capacity under a humid atmosphere. The synthesized UiO-66 is a hydrophilic MOF with most of its uptake below p/p_0 = 0.2. Relative to UiO-66, the used polymers are more hydrophobic and therefore shift the uptake to higher p/p_0. An interesting case is Zr-fum (MOF-801) which has the same structure as UiO-66 and is even more hydrophilic since a significant part of the water uptake is concluded at p/p_0 = 0.1.[74] Yet, the uptake pressure in Zr-fum is essentially slightly shifted with relatively more hydrophobic PE shells. The effect of the increased uptake capacity is noticeable only for Zr-fum modified with PSS, which is usually considered as more hydrophobic PE than CMC or PAA. Due to the high water uptake under an arid atmosphere, even as a composite, the MOF Zr-fum can be an excellent desiccant for high-precision optical and electronic equipment.

For MIL-101(Cr) with the $(PSS/CH\text{-}Dex)_3$ LbL coating, there is also a light shift to 'earlier' water uptake as compared to the unmodified MOF. LbL-coated Al-fum and Basolite®A520 experience a light hydrophilic shift similar to the parent Al-fum/PE powders. A decrease in water uptake after the steep increase for MIL-101(Cr)/(PSS/CH-Dex) and for all Basolite/LbL composites is quite noticeable, while all Al-fum/LbL composites show little, but also negative, change in uptake capacity.

The effect of modifications on water uptake by MOF/PE and MOF/LbL at low partial water pressure is associated, first of all, with the high water sorption capacity of the individual polyelectrolytes and based on the LbL shells. For example, for $(PDDA/PSS)_n$ and $(CH/DexS)_n$ layers, it can be as high as ~50 mg g^{-1} at p/p_0 = 0.2; the value is comparable with that for some MOFs under an arid atmosphere.[52] The MOFs with high

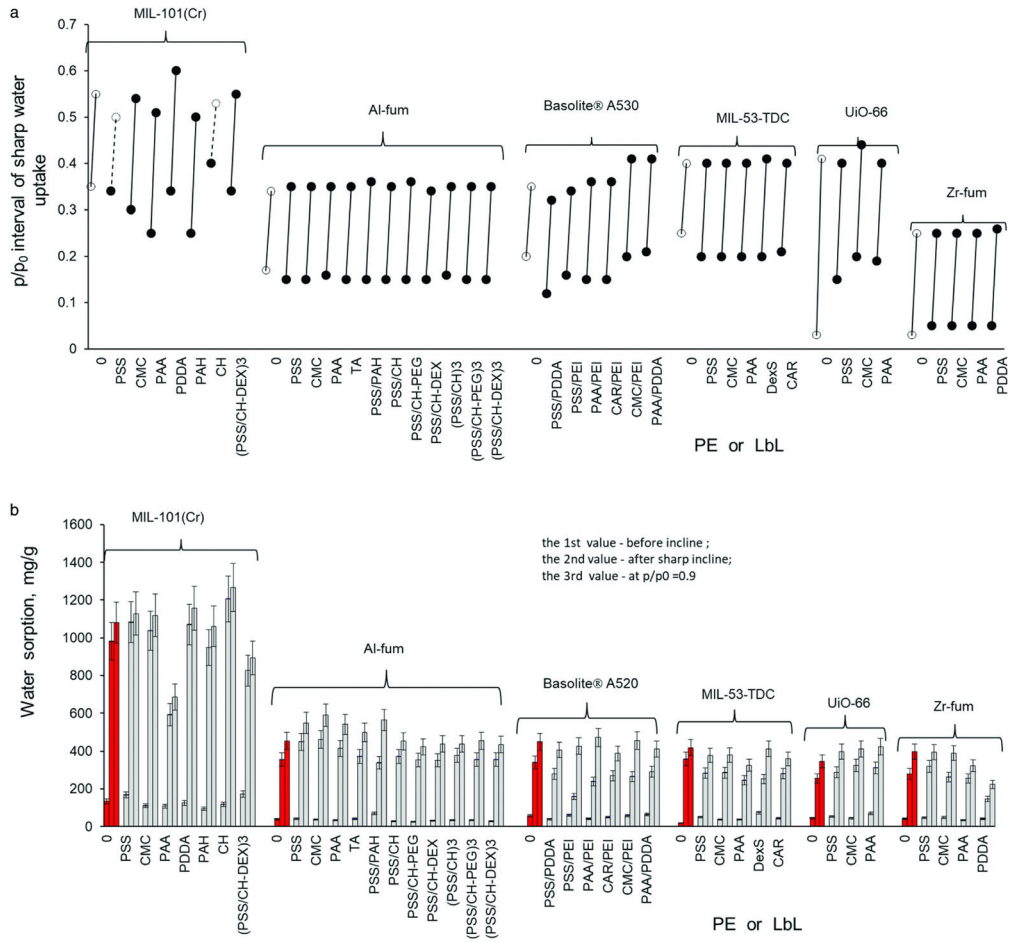

Fig. 6 Steep rise in the p/p_0 interval of the S-shaped water uptake curve (a) and the corresponding water uptake. (b) The values are given in the following order: before and after the sharp incline and at p/p_0 = 0.9 for MOF/PE and MOF/LbL powders.

polyelectrolyte adsorption per layer, such as UiO-66, Basolite® A520, and MIL-53-TDC (Table 1), are expected to be more prone to increased uptake below their inflection point than Zr-fum and Al-Fum.

At the same time, a light or reverse effect of chitosan-based shells is apparently related to the small water adsorption capacity of chitosan at low partial water pressure[87,88] as compared with other polyelectrolytes; moreover, its replacement with a copolymer or complexation with PSS does not improve the water vapor adsorption.

For the discussion of water uptake capacity by different MOFs, the technologically important value lies at the end of the steep rise of the S-shaped water uptake curve, which is at $p/p_0 \approx 0.55$ for MIL-101(Cr), ≈0.35 for Al-fum, ≈0.4 for MIL-53-TDC and UiO-66 and ≈0.25 for Zr-fum. The corresponding water uptake values are given in the middle columns of the diagram for each composite in Fig. 6b.

The changes in the water uptake capacity and BET surface area of the modified MOFs do not always correlate (compare Fig. 4 and 6b). The significant decrease in surface area which was seen for MIL-101(Cr)/PAA is also followed by a decrease in water uptake. Not just MIL-53-TDC with PSS or DexS shows a noticeable decrease in surface area but all other MIL-53-TDC/PE composites and Zr-fum/PDDA also exhibit a sizable decrease in water uptake, albeit the decrease in their surface area is minor. On the other hand, Al-fum/PE and UiO-66/PE,

in which the surface areas vary slightly around one of the pristine MOFs, exhibit a remarkable increase in water uptake. Most likely this is due to the MOF–PE interaction at the nanoscale and the added MOF–PE interface volume. An indication of the latter is the strong increase in the slope of the water sorption isotherm above $p/p_0 > 0.6$, that is, with an even steeper slope than that of the neat MOF (Fig. 5c and ESI, Fig. S11c†).

For LbL-coated samples, the strong increase in the slope of the water sorption isotherm under a humid and fog atmosphere (above $p/p_0 > 0.6$) is more typical than that for the neat MOFs or MOF/PE composites (see the isotherm for Al-fum/(PSS/PAH) in Fig. 5c and those for Basolite® A520/LbL in ESI, Fig. S11b†). In several cases, it compensates for the decrease in adsorption under mild humidity and sometimes increases the water uptake value above that of neat MOFs. For example, the composite with a thick LbL shell also shows increased water sorption characteristics (420 and 440 mg g^{-1} in the first and second sorption cycles at 23 °C, $p/p_0 = 0.7$, respectively) as compared with pristine Al-fum (415 mg g^{-1}). At the same time, the water sorption capacity of planar $(PSS/PDDA)_n$ films under these conditions does not exceed 100 mg g^{-1}.[52] This also proves the non-additive effect of the polyelectrolyte shell on water uptake by the composite.

3.4 Water vapor uptake kinetics

The kinetics of water vapor uptake by two MOFs, Al-fum and MIL-53-TDC, and two Al-fum/LbL composites were followed by the QCM technique. Typical changes in frequency F_t and motional resistance R_t of a resonator with a thin deposit of MOF composite particles on its surface while it is in the chamber with alternately changing from 10 to 90% humidity are shown in ESI, Fig. S12.† A decrease in F_t (directly proportional to adsorbed mass) and an increase in R_t (characterizing viscoelastic properties of deposit) of the resonator at RH 90% correspond to the sorption of water vapor by immobilized MOF particles. At RH 10%, an increase in F_t and a decrease in R_t are observed due to water desorption. The process of water sorption at temperatures of 25–47 °C is reversible for both unmodified and modified MOFs at least within four consecutive adsorption–desorption cycles.

Calculated on the basis of ΔF_t, the values of apparent water uptake and loss by MOF Al-fum and Al-fum/LbL composite as a function of time are shown in Fig. 7. Regardless of temperature, the kinetic curves of water adsorption by MOF-based powders consist of two sections: a short initial stage, where up to 90% of the mass change occurs due to fast water sorption, and a long smoothly sloping section which can be apparently associated with the slow relaxation of the deposited structure (Fig. 7a). The shape of the water vapor desorption curves (Fig. 7b) indicates that the process proceeds in several stages, more pronounced at 25 °C.

The experimental values of water uptake (q_e) obtained after the exposure of arid MOFs to $p/p_0 = 0.9$ for 15 min are summarized in Table 2. For both unmodified MOFs, Al-fum and MIL-53-TDC, the q_e values are lower than the water vapor uptake value measured previously by the volumetric method (Fig. 6) or calculated from the static humidity QCM measurements (ESI, Fig. S13†). The design of the QCM-based experiment does not allow us to take into account the moisture already trapped in the deposit at RH = 10% and the water that can be additionally adsorbed by a sample under a fog atmosphere if the equilibrium capacity is reached after a much longer exposure. Although the research on this topic is limited, the response of particulates to humid air (mass change, kinetics, hysteresis effect) is extremely sensitive to the sequence and the ratio of wet/dry relative humidity changes and the duration of each stage in a cyclic process.[89]

As one can see from Table 2, there is a 2–3 fold increase in the q_e value of Al fumarate/LbL powders as compared with the pristine MOF, although the mass fraction of polyelectrolytes in the composites is obviously less than 15% and the water absorption capacity of the LbL film material itself on planar surfaces is lower than the value for Al fumarate. Those are 220 ± 10 and 380 ± 10 mg g^{-1} for $(PSS/PDDA)_n$ and $(DexH/ChH)_n$ films, respectively,[52] against 450 ± 10 mg g^{-1} for the MOF. The enhanced water

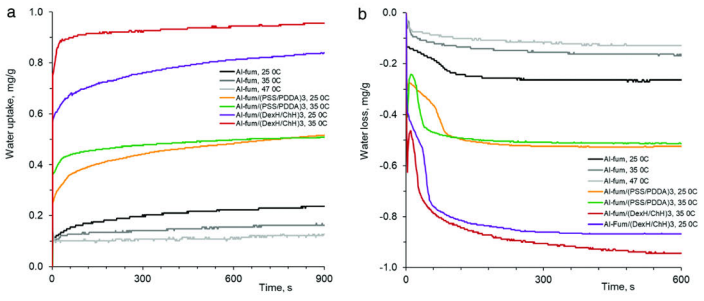

Fig. 7 Water uptake (a) and loss (b) *vs.* time curves of pristine Al-fum and modified with a $(PSS/PDDA)_3$ and $(DexH/ChH)_3$ shell as evaluated by QCM. In (b): the sharp drop of the curves within the first 20 s is due to the mechanical disturbance of the resonator after a rapid change of humid air in the measurement chamber.

Table 2 Parameters of water vapor adsorption/desorption by MOFs and MOF/LbL composites

			q_e, mg g^{-1}				$t_{90\%}$, s		
MOF	Shell	T, °C	Sorption	Desorption	q^a, mg g^{-1}	k^a, mg (g s)$^{-1}$	Sorption	Desorption	ΔR, Ohm
MIL-53-TDC	—	25	220 ± 20	200 ± 30	214 ± 29	199 ± 21	371 ± 18	71 ± 39	7–20
		35	110 ± 20	100 ± 10	110 ± 28	379 ± 85	231 ± 123	345 ± 95	0–1
		45	70 ± 10	60 ± 10	~55	>460	834 ± 191	618 ± 41	0–1
Al-fum	—	25	260 ± 20	280 ± 20	279 ± 15	49 ± 8	578 ± 99	105 ± 6	3–7
		35	170 ± 10	160 ± 10	173 ± 3	137 ± 51	409 ± 77	199 ± 22	0–1
		47	160 ± 20	160 ± 20	~141	>143	465 ± 62	294 ± 42	0–1
	$(PSS/PDDA)_3$	25	520 ± 20	550 ± 10	578 ± 33	47 ± 14	417 ± 72	89 ± 5	21–27
		35	500 ± 10	500 ± 10	514 ± 12	113 ± 24	100 ± 55	52 ± 2	9–11
	$(DexH/ChH)_3$	25	810 ± 40	880 ± 20	939 ± 99	36 ± 11	261 ± 22	61 ± 16	30–60
		35	980 ± 30	980 ± 30	986 ± 37	94 ± 22	23 ± 2	164 ± 13	25–30

[a] – calculated using the PSO model.

uptake by LbL coated powders is not completely due to the additive sorption by the shell material but is apparently caused by the changes introduced into the shape of the corresponding adsorption isotherm, namely, into the adsorption values before and after sharp incline at the inflection point and extra fast growth of adsorption in humid and fog atmosphere, similar to those found for other MOF/LbL composites (Fig. 6). It is assumed that the presence of the LbL shell changed the conditions of water vapor condensation at the particle–gas interface.

Moreover, for both investigated LbL shell compositions, the time period needed to reach 90% of the q_e value decreases as compared to that needed by Al fumarate; the drop is more pronounced at 35 °C than at lower temperatures (Table 2). In contrast to the unmodified sample, for which q_e decreases by ~35% when the temperature increases from 25 to 35 °C, water uptake by Al-fum/$(PSS/PDDA)_3$ is not affected by this temperature increase. However, for the Al-fum/$(DexH/ChH)_3$ powder, a 11% increase in the q_e value is observed as the temperature increases from 25 to 35 °C.

At 25 and 35 °C, water vapor sorption by both the neat Al-fum and MOF-53-TDC as well as their LbL composites can be approximated by a kinetic equation of the pseudo-second order (PSO) in its linear form:[52,90]

$$\frac{t}{q_t} = \frac{1}{k^* q^{*2}} + \frac{t}{q^*}$$

where t is time, s; q_t is the amount of adsorbed water at time t, mg g^{-1}; q^* is the amount of adsorbed water in equilibrium, mg g^{-1}, and k^* is the PSO constant, g (mg s)$^{-1}$. In the coordinates $\left(\frac{t}{q_t} - t\right)$, the kinetic curves are fitted by a linear function with a correlation coefficient higher than 0.995. The calculated values of q^* are in good agreement with the experimental q_e (Table 2). The calculated k^* reasonably rises with temperature.

As the temperature increases to 45–47 °C, water vapor adsorption accelerates as shown for Al fumarate (Fig. 7a) and is complete within a short time period that is shorter than the interval required for equilibrating the QCM resonator after injecting water vapor into the system. In this instance, only a lower limit of the constant was evaluated. Moreover, a weakly ascending part appears near the saturation point on the kinetic curves of both the MOFs that apparently reflects the changes in the nature of the adsorption sites.

The kinetics of water uptake by the bulk Al fumarate unmodified powder and the Al-fum/thick LbL composite with 50 wt% $(PSS/PDDA)_2$ shell evaluated on the basis of gravimetric measurements under real indoor conditions (23 °C, RH 70%) are shown in ESI, Fig. S14.† The saturation time of the composite also decreases similar to that for Al-fum/LbL deposits as found by QCM. The time changes from approximately 25 min for unmodified MOF to 15 min and 18 min in the 1st and 2nd humidity sorption cycles on the composite.

3.5 Apparent mechanism of LbL shell influence based on $\Delta F_t - \Delta R_t$ changes in the process of water uptake by MOF/LbL

A comparative analysis of water sorption and desorption by different MOF deposits on a quartz resonator in the (ΔR_t, ΔF_t) coordinates provides additional information on their structural transformations caused by alternately changing humidity. In the timeless coordinates, the process of water sorption by pristine Al fumarate is characterized by a linear dependence with a large negative $\Delta F_t/\Delta R_t$ slope (Fig. 8a), which is typical of rigid deposits.[60,91–98] A similar sharp decrease of the line in the (ΔR_t, ΔF_t) coordinates was obtained for MIL-53-TDC. The water desorption for pristine MOFs follows the same linear dependences as for adsorption just in the reversed direction.

At the same time, for LbL-coated Al fumarate powders, there are two pronounced sections on the ΔF_t *vs.* ΔR_t curves both for water uptake and desorption (Fig. 8b and c). The actual shapes of the curves depend on the temperature and structure of the shell but were observed for all the investigated Al-fum/LbL powders. We presume that the first section with a large negative $\Delta F_t/\Delta R_t$ slope corresponds to fast water suction into the MOF/LbL powder with a double-porous compartment structure. Due to the high rate and close sorption characteristics of the MOF and LbL shell materials, their individual contribution to the process remains indistinguishable. Previously, a large negative ΔF_t accompanied by almost zero ΔR_t has been observed in the process of the water vapor sorption into planar

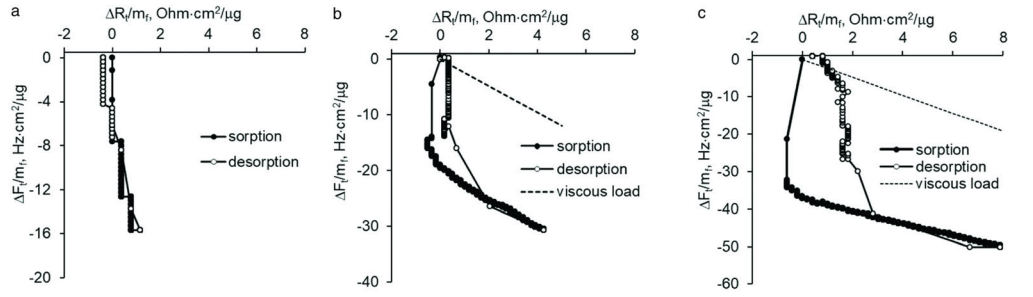

Fig. 8 ΔF_t *vs.* ΔR_t for water sorption (at RH 90%) and desorption (at RH 10%) by Al fumarate: unmodified (a); $(PSS/PDDA)_3$ (b), and $(DexH/ChH)_3$ (c). The 3rd cycle of humidity alternation. T = 25 °C.

$(PSS/PDDA)_n$ and $(ChH/DexH)_n$ films assembled on the surface of a QCM resonator.[52]

In the second stage of water uptake by Al-fum/LbL samples, ΔR_t increases considerably, while the $\Delta F_t/\Delta R_t$ slope declines. Ranging from −4.5 to −1.7 Hz Ohm^{-1}, the slope of the second stage fluctuates around the $\Delta F_t/\Delta R_t$ value for a typical viscous load (−2.4 Hz Ohm^{-1}).[97] The slow changes can be attributed to the rearrangement of the structure of fast wetted deposit accompanied by the formation of the meniscus of liquid water between the contacting particles and at the point of their contact with the resonator surface, and the involvement of repulsive forces between identically charged particles, resulting in a decrease in the strength of the deposit contact with the resonator surface and an increase in its porosity or viscosity. Based on the analysis of the $\Delta F_t - \Delta R_t$ curves within this stage, it is reasonable to assume some additional condensation of water in the stretched structure (for the MOF/LbL with $\Delta F_t/\Delta R_t < -2.4$ Hz Ohm^{-1}) but not the formation of massive liquid film or droplets. In that case, the changes in the resonant frequency would be much larger and unlimited. The two-stage reversed process apparently involves flash evaporation of liquid water from menisci followed by water desorption from porous MOF/LbL microparticles.

The amplitude of R_t changes seems to diminish gradually with the increase in the number of water adsorption/desorption cycles (ESI, Fig. S12b†). This effect was observed for both uncoated MOFs, Al-fum and MIL-53-TDC, and MOF/LbL deposits. The changes can be explained in terms of the rearrangement of MOF particles in each wetting/dewetting cycle and a step-wise increase in the packing density of the deposit on the resonator surface.[98,99]

4. Conclusions

Water-stable metal–organic frameworks can be modified with a single polyelectrolyte layer or LbL shell without deterioration of their crystal structure which is responsible for the developed BET surface and high water uptake. Besides that, with the correct selection of shell composition and architecture, one can expect enhanced water sorption properties from the composite MOF/PE and MOF/LbL powders.

The selected hydrophilic MOFs are easily dispersed in water and their chemical structure does not deteriorate during the process of LbL assembly based on the adsorption of polyelectrolytes from their aqueous solutions. The PXRD analysis confirms that the crystal lattice parameters of the polyelectrolyte-coated MOF particles are identical to those of the unmodified powders. For the majority of MOFs coated with a single polyelectrolyte layer or one bilayer (two single layers) shell of negative and positive polyelectrolytes, no visual changes in the microparticle shape and size are found in the SEM microphotographs. If the LbL shell consists of 2 or 3 bilayers, the particles in the SEM images of the dry powder have well-defined boundaries and fairly close sizes. Simultaneously analyzing the MOF/PE suspensions by DLS, we found that during the process of sonication-assisted polyelectrolyte adsorption, MOFs with an average hydrodynamic diameter less than 700 nm tend to aggregate to varying degrees, while MOF bulk particles are slightly disintegrated or retain their size and polydispersity. The average diameter of original MOF powders varies from ~250 nm to 2.5 μm, while samples with only few coats show a diameter higher than 3.5 μm, which is associated with the aggregation of the dispersed phase by the polyelectrolyte.

By evaluating the ζ-potential changes upon step-wise addition of PSS, it was shown that the amount of polyelectrolyte needed to complete the layer of polymeric adsorbate on different MOFs is as low as 25 mg g^{-1}, it is 20 times lower than water typically absorbed by MOFs. Judging by the retention of high BET surface, overall water uptake parameters, and low shift of isotherm inflection, the adsorption of polyelectrolyte takes place predominantly on the surface of MOF particles regardless of their chemical and crystal structure. The only exceptions are polyelectrolytes with extremely low molecular weight, such as PAA and DexS. The mass percent of the polyelectrolyte material, therefore the thickness of the shell, was controlled by depositing the only polyelectrolyte layer as in MOF/PE (0.6–2.5 wt%), up to 3 bilayers as in MOF/LbL (<15 wt%) using the conventional LbL technique and applying the LbL technique without intermediate washing steps to accelerate the formation of a thick shell (50 wt%).

The core–shell structure and the related morphological changes of the MOF powders (aggregation of MOF particles by polyelectrolyte, partial disintegration by applied ultrasound, and the thin hydrophilic polymeric shell that uniformly enveloped each particle) make the water uptake characteristics of the MOF/PE and MOF/LbL powders unique. Under a constant relative pressure of water vapor, the moisture uptake by composite MOF/PE and MOF/LbL is rather comparable to that of pristine MOFs; this favorably distinguishes the core/shell composites from the matrix composites with conventional polymers, even highly hydrophilic ones.

The changes in the hydrophilicity/hydrophobicity of the surface by the adsorbed polyelectrolyte layers are well known. The hydrophilic surface promotes the formation of liquid menisci at the points of contact between particles.[100,101] The effect can apparently explain the higher values of water sorption than that of pristine MOFs by some MOF/PE at $0.3 < p/p_0 < 0.9$ on isotherms (Fig. 5), the increase in the water uptake by the Al-fum/$(PSS/PDDA)_3$ and Al-fum/$(DexH/ChH)_3$ powders under alternately changing humidity, and the slightly higher water moisture content of the MOF/LbL composite with a high mass percentage (~50 wt%) of the shell material. In the terms of changes in polyelectrolyte adsorption surfaces properties, a decrease in water sorption under an atmosphere with high humidity by some composites can be associated with an inhibition of liquid water condensation by more hydrophobic layers. Another advantage of the hydrophilic LbL shell coating on MOFs is that it accelerates moisture uptake and loss (Table 2).

Author contributions

Tatsiana Shutava: Conceptualization, investigation, methodology, visualization, writing – original draft, and review & editing. Christian Jansen: Investigation, data curation, formal analysis, visualization, and writing – original draft. Kanstantsin Livanovich: Investigation, methodology, and data curation. Vladimir Pankov: Conceptualization, funding acquisition, project administration, supervision, and writing – review & editing. Christoph Janiak: Conceptualization, funding acquisition, project administration, resources, supervision, validation, and writing – review & editing.

Conflicts of interest

There are no conflicts to declare.

Acknowledgements

This work was supported by grants 8.3.1.5 and 8.1.3.6 from the SPSR "Materials science, new materials and technologies" for 2021–2025, the Republic of Belarus.

References

1 D. M. Steinert, S.-J. Ernst, S. Henninger and C. Janiak, *Eur. J. Inorg. Chem.*, 2020, **2020**, 4502.
2 G. Maurin, C. Serre, A. Cooper and G. Férey, *Chem. Soc. Rev.*, 2017, **46**, 3104.
3 E. Hastürk, S.-J. Ernst and C. Janiak, *Curr. Opin. Chem. Eng.*, 2019, **24**, 26.
4 Q. Wang and D. Astruc, *Chem. Rev.*, 2020, **120**, 1438.
5 A. E. Baumann, D. A. Burns, B. Liu and V. S. Thoi, *Commun. Chem.*, 2019, **2**, 86.
6 K. Adil, Y. Belmabkhout, R. S. Pillai, A. Cadiau, P. M. Bhatt, A. H. Assen, G. Maurin and M. Eddaoudi, *Chem. Soc. Rev.*, 2017, **46**, 3402.
7 N. Stock and S. Biswas, *Chem. Rev.*, 2012, **112**, 933.
8 S.-T. Zheng, T. Wu, C. Chou, A. Fuhr, P. Feng and X. Bu, *J. Am. Chem. Soc.*, 2012, **134**, 4517.
9 M. Rubio-Martinez, C. Avci-Camur, A. W. Thornton, I. Imaz, D. Maspoch and M. R. Hill, *Chem. Soc. Rev.*, 2017, **46**, 3453.
10 B. J. Bucior, N.S. Bobbitt, T. Islamoglu, S. Goswami, A. Gopalan, T. Yildirim, O.K. Farha, N. Bagheri and R. Q. Snurr, *Mol. Syst. Des. Eng.*, 2019, **4**, 162.
11 D. Farrusseng, C. Daniel, C. Hamill, J. Casaban, T. Didriksen, R. Blom, A. Velte, G. Füldner, P. Gantenbein, P. Persdorf, X. Daguenet-Frick and F. Meunier, *Faraday Discuss.*, 2021, **225**, 384.
12 D. Lenzen, J. Zhao, S.-J. Ernst, M. Wahiduzzaman, A. K. Inge, D. Fröhlich, H. Xu, H.-J. Bart, C. Janiak, S. Henninger, G. Maurin, X. Zou and N. Stock, *Nat. Commun.*, 2019, **10**, 3025.
13 X. Liu, X. Wang and F. Kapteijn, *Chem. Rev.*, 2020, **120**, 8303.
14 M. P. Silva, A. M. Ribeiro, C. G. Silva, K. H. Cho, U.-H. Lee, J. L. Faria, J. M. Loureiro, J.-S. Chang, A. E. Rodrigues and A. Ferreira, *Sep. Purif. Technol.*, 2022, **290**, 120803.
15 D. Zhang, N. Luo, Z. Xue, Y.-L. Bai and J. Xu, *ACS Appl. Nano Mater.*, 2022, **5**, 2147.
16 H. Kim, S. R. Rao, E. A. Kapustin, L. Zhao, S. Yang, O. M. Yaghi and E. N. Wang, *Nat. Commun.*, 2018, 1191.
17 Y. Tu, R. Wang, Y. Zhang and J. Wang, *Joule*, 2018, **2**, 1452.
18 M. Wickenheisser and C. Janiak, *Microporous Mesoporous Mater.*, 2015, **204**, 242.
19 M. Wickenheisser, A. Herbst, R. Tannert and B. Milow, *Microporous Mesoporous Mater.*, 2015, **215**, 143.
20 M. Wickenheisser, T. Paul and C. Janiak, *Microporous Mesoporous Mater.*, 2016, **220**, 258.
21 V. Finsy, L. Ma, L. Alaerts, D. De Vos, G. Baron and J. Denayer, *Microporous Mesoporous Mater.*, 2009, **120**, 221.
22 D. Bradshaw, A. Garai and J. Huo, *Chem. Soc. Rev.*, 2012, **41**, 2344.
23 O.-L. Zhu and Q. Xu, *Chem. Soc. Rev.*, 2014, **43**, 5468.
24 E. Hastürk, S.-P. Höfert, B. Topalli, C. Schlüsener and C. Janiak, *Microporous Mesoporous Mater.*, 2020, **295**, 1909907.

25 E. Hastürk, C. Schlüsener, J. Quodbach, A. Schmitz and C. Janiak, *Microporous Mesoporous Mater.*, 2019, **280**, 277.
26 S. Gökpinar, S.-J. Ernst, E. Hastürk, M. Möllers, I. El Aita, R. Wiedey, N. Tannert, S. Nießing, S. Abdpour, A. Schmitz, J. Quodbach, G. Füldner, S. K. Henninger and C. Janiak, *Ind. Eng. Chem. Res.*, 2019, **58**, 2149.
27 R. G. Chaudhuri and S. Paria, *Chem. Rev.*, 2012, **112**, 2373.
28 J. Borges and J. F. Mano, *Chem. Rev.*, 2014, **114**, 8883.
29 M. Bruening and M. Adusumilli, *Mater. Matters*, 2011, **6**, 76.
30 G. Sukhorukov, in *Dendrimers, Assemblies, Nanocomposite, MML Series 5*, ed. R. Arshady and A. Guyot, Citus Books, London, 2002, ch. 4, pp. 111–147.
31 Y. Lvov, P. Pattekari and T. Shutava, in *Multilayer Thin Films: Sequential Assembly of Nanocomposite Materials*, ed. G. Decher and J. Schlenoff, Wiley-VCH, NY, London, 2012, ch. 8, pp. 151–170.
32 J. Sun, J. Li, D. Liu, Y. Ma and S. Yang, *Langmuir*, 2018, **34**, 6653.
33 R. Hlushko, J. F. Ankner and S. Sukhishvili, *Macromolecules*, 2021, **54**, 7469.
34 J. Ehrenmann, S. K. Henninger and C. Janiak, *Eur. J. Inorg. Chem.*, 2011, 471.
35 J. J. Richardson, J. Cui, M. Björnmalm, J. A. Braunger, H. Ejima and F. Caruso, *Chem. Rev.*, 2016, **116**, 14828.
36 J. Borges and J. F. Mano, *Chem. Rev.*, 2014, **114**, 8883.
37 Z. Zhang, J. Nong and Y. Zhong, *J. Neural Eng.*, 2015, **12**, 046015.
38 G. Cheng, C. Yin, H. Tu, S. Jiang, Q. Wang, X. Zhou, X. Xing, C. Xie, X. Shi, Y. Du, H. Deng and Z. Li, *ACS Nano*, 2019, **13**, 6372.
39 T. G. Shutava, K. S. Livanovich and V. V. Pankov, *Colloid. Surf. A.*, 2018, **539**, 69.
40 J. Lipton, G.-M. Weng, J. A. Röhr, H. Wang and A. D. Taylor, *Matter*, 2020, **2**, 1148.
41 C. Picart, *Curr. Med. Chem.*, 2008, **15**, 685.
42 S. B. Abbott, W. M. de Vos, L. L. E. Mears, R. Barker, R. M. Richardson and S. W. Prescott, *Macromolecules*, 2014, **47**, 3263.
43 V. Kozlovskaya, S. Harbaugh, I. Drachuk, O. Shchepelina, N. Kelly-Loughnane, M. Stone and V. V. Tsukruk, *Soft Matter*, 2011, **7**, 2364.
44 X. Liu and M. L. Bruening, *Chem. Mater.*, 2004, **16**, 351.
45 F. Vaca Chávez and M. Schönhoff, *J. Chem. Phys.*, 2007, **126**, 104705.
46 S.-W. Lee and D. Lee, *Macromolecules*, 2013, **46**, 2793.
47 C. Peniche-Covas, W. Argüelles-Monal and J. San Roman, *Polym. Int.*, 1995, **38**, 45.
48 J. E. Wong, F. Rehfeldt, P. Hänni, M. Tanaka and R. von Klitzing, *Macromolecules*, 2004, **37**, 7285.
49 M. Schönhoff, V. Ball, A. R. Bausch, C. Dejugnat, N. Delorme, K. Glinel, R. von Klitzing and R. Steitz, *Colloids Surf., A*, 2007, **303**, 14.
50 S. Dodoo, B. N. Balzer, T. Hugel, A. Laschewsky and R. von Klitzing, *Soft Matter*, 2013, **11**, 157.
51 V. Selin, J. F. Ankner and S. A. Sukhishvili, *Gels*, 2018, **4**, 7.
52 K. S. Livanovich, A.A. Bautramovich, V. V. Pankov and T. G. Shutava, *Polymer materials and technologies (Gomel)*, 2021, vol. 7, p. 50 (in russian).
53 B. D. Vogt, C. L. Soles, H.-J. Lee, E. K. Lin and W.-L. Wu, *Langmuir*, 2004, **20**, 1453.
54 A. Arce, F. Fornasiero, O. Rodriguez, C. J. Radke and J. M. Prausnitz, *Phys. Chem. Chem. Phys.*, 2004, **6**, 103.
55 L. Gao, C. Y. V. Li and K. Y. Chan, *Chem. Mater.*, 2015, **27**, 3601.
56 L. Gao, C. Y. V. Li, K. Y. Chan and Z. N. Chen, *J. Am. Chem. Soc.*, 2014, **136**, 7209.
57 H. Ejima, N. Yanai, J. P. Best, M. Sindoro, S. Granik and F. Caruso, *Adv. Mater.*, 2013, **25**, 5767.
58 S. Beyer, R. Schürmann, I. Feldmann, A. Blocki, I. Bald, R. J. Schneider and F. Emmerling, *Colloid Interface Sci. Commun.*, 2018, **22**, 14.
59 S. Liu, J. Chen, X. Bao, T. Li, Y. Ling, C. Li, C. Wu and Y. Zhao, *Chem. – Asian J.*, 2016, **11**, 1811.
60 T. G. Shutava, K. S. Livanovich and A. A. Sharamet, *Colloids Surf., B*, 2019, **173**, 412.
61 M. Thommes, K. Kaneko, A. V. Neimark, J. P. Olivier, F. Rodriguez-Reinoso, J. Rouquerol and K. S. W. Sing, *Pure Appl. Chem.*, 2015, **87**, 1051.
62 J. Landers, G. Y. Gor and A. V. Neimark, *Colloids Surf., A*, 2013, **437**, 3.
63 G. Sauerbrey, *Z. Phys.*, 1959, **155**, 206.
64 State Standard (GOST) 28237-89, *Test enclosures of non-injection type for constant relative humidity*, Standartinform Publ., Moscow, 2006.
65 S. H. Jhung, J.-H. Lee, J. W. Yoon, C. Serre, G. Férey and J.-S. Chang, *Adv. Mater.*, 2007, **19**, 121.
66 E. Leung, U. Müller, N. Trukhan, H. Mattenheimer, G. Cox and S. Blei, *US Pat*, 20120082864A1, 2011.
67 N. Tannert, S.-J. Ernst, C. Jansen, H.-J. Bart, S. K. Henninger and C. Janiak, *J. Mater. Chem. A*, 2018, **6**, 17706.
68 G. Zahn, H. A. Schulze, J. Lippke, S. König, U. Sazama, M. Fröba and P. Behrens, *Microporous Mesoporous Mater.*, 2015, **203**, 186.
69 G. C. Shearer, S. Chavan, J. Ethiraj, J. G. Vitillo, S. Svelle, U. Olsbye, C. Lamberti, S. Bordiga and K. P. Lillerud, *Chem. Mater.*, 2014, **26**, 4068.
70 F. Jeremias, D. Fröhlich, C. Janiak and S. K. Henninger, *RSC Adv.*, 2014, **4**, 24073.
71 K. H. Cho, P. G. M. Mileo, J. S. Lee, U.-H. Lee, J. Park, S. J. Cho, S. K. Chitale, G. Maurin and J.-S. Chang, *ACS Appl. Mater. Interfaces*, 2021, **13**, 1723.
72 P. Ghosh, Y. J. Colón and R. Q. Snurr, *Chem. Commun.*, 2014, **50**, 11329.
73 Y. Sun, A. Spieß, C. Jansen, A. Nuhnen, S. Gökpinar, R. Wiedey, S.-J. Ernst and C. Janiak, *J. Mater. Chem. A*, 2020, **8**, 13364.
74 T. J. M. M. Ntep, H. Reinsch, B. Moll, E. Hastürk, S. Gökpinar, H. Breitzke, C. Schlüsener, L. Schmolke, G. Buntkowsky and C. Janiak, *Chem. – Eur. J.*, 2018, **24**, 14048.

75 B. N. Dickhaus and R. Priefer, *Colloids Surf., A*, 2016, **488**, 15.
76 F. Hua, J. Shi, Y. Lvov and T. Cui, *Nanotechnology*, 2003, **14**, 453.
77 E. Kharlampieva, T. Tsukruk, J. M. Slocik, H. Ko, N. Poulsen, R. R. Naik, N. Kröger and V. V. Tsukruk, *Adv. Mater.*, 2008, **20**, 3274.
78 Z. Mao, L. Ma, C. Gao and J. Shen, *J. Controlled Release*, 2005, **104**, 193.
79 T. G. Shutava, P. P. Pattekari, K. A. Arapov, V. P. Torchilin and Y. M. Lvov, *Soft Matter*, 2012, **8**, 9418.
80 G. Bantchev, Z. Lu and Y. Lvov, *J. Nanosci. Nanotechnol.*, 2009, **9**, 396.
81 I. Teraoka, *Polymer Solutions: An Introduction to Physical Properties*, John Wiley & Sons, Inc., 2002.
82 A. Chatterjee and B. Das, *Carbohydr. Polym.*, 2013, **98**, 1297.
83 V. M. Prabhu, M. Muthukumara, G. D. Wignall and Y. B. Melnichenko, *Polymer*, 2001, **42**, 8935.
84 M. Nierlich, F. Boué, A. Lapp and R. Oberthur, *J. Phys. I*, 1985, **46**, 649.
85 H. M. Fares, Y. E. Ghoussoub, J. D. Delgado, J. Fu, V. S. Urban and J. B. Schlenoff, *Macromolecules*, 2018, **51**, 4945.
86 V. M. Prabhu, M. Muthukumara, G. D. Wignall and Y. B. Melnichenko, *J. Chem. Phys.*, 2003, **119**, 4085.
87 S. Despond, E. Espuche and A. Domard, *J. Polym. Sci., Part B: Polym. Phys.*, 2001, **39**, 3114.
88 R. Y. Aguiree-Loredo, A. I. Rodrigues-Hernandez and G. Velasquez, *Food Sci. Technol.*, 2017, **37**, 112.
89 R. Demir, S. Okur, M. Seker and M. Zor, *Ind. Eng. Chem. Res.*, 2011, **50**, 5606.
90 G. W. Kajjumba, S. Emik, A. Öngen, H. K. Özcan and S. Aydin, in *Advanced Sorption Process Applications*, ed. S. Edebali, IntechOpen, London, 2019.
91 K. A. Marx, T. Zhou, A. Montrone, H. Schulze and S. J. Braunhut, *Biosens. Bioelectron.*, 2001, **16**, 773.
92 M. C. Dixon, *J. Biomol. Tech.*, 2008, **19**, 151.
93 R. Lucklum and P. Hauptmann, *Electrochim. Acta*, 2000, **45**, 3907.
94 K. M. M. Aung, X. Ho and X. Su, *Sens. Actuators, B*, 2008, **131**, 371.
95 J. Iturri, A. C. Vianna, A. Moreno-Cencerrado, D. Pum, U. B. Sleytr and J. L. Toca-Herrera, *Beilstein J. Nanotechnol.*, 2017, **8**, 91.
96 R. Lucklum, *Electrochim. Acta*, 2000, **45**, 3907.
97 S. J. Martin, V. E. Granstaff and G. C. Frye, *Anal. Chem.*, 1991, **63**, 2272.
98 B. Acharya, C. M. Seed, D. W. Brenner, A. I. Smirnov and J. Krim, *Sci. Rep.*, 2019, **9**, 18584.
99 B. Du, A. M. König and D. Johannsmann, *New J. Phys.*, 2008, **10**, 053014.
100 S. D. N. Lourenço, D. Gallipoli, C. E. Augarde, D. G. Toll, P. C. Fisher and A. Congreve, *Géotechnique*, 2012, **62**, 193.
101 B. Torun, C. Kunze, C. Zhang, T. D. Kühne and G. Grundmeier, *Phys. Chem. Chem. Phys.*, 2014, **16**, 7377.

Electronic Supplementary Material (ESI) for Dalton Transactions.

Supporting Information

Metal organic framework/Polyelectrolyte composites for water vapor sorption applications

Tatsiana Shutava[1†]*, Christian Jansen[2†], Kanstantsin Livanovich[1], Vladimir Pankov[3], Christoph Janiak[2]*

[1]Institute of Chemistry of New Materials, National Academy of Sciences of Belarus, 36 F. Skaryna St., Minsk 220141, Belarus

[2]Institut für Anorganische Chemie und Strukturchemie, Heinrich-Heine-Universität Düsseldorf, 40204 Düsseldorf, Germany

[3] Belarusian State University, 4 Nezavisimosti Av., Minsk 220030, Belarus

E-mails:
shutova@ichnm.by, christian.jansen@hhu.de, kslivonovich@ichnm.by, pankov@bsu.by, janiak@hhu.de

[†] Both authors contributed equally.

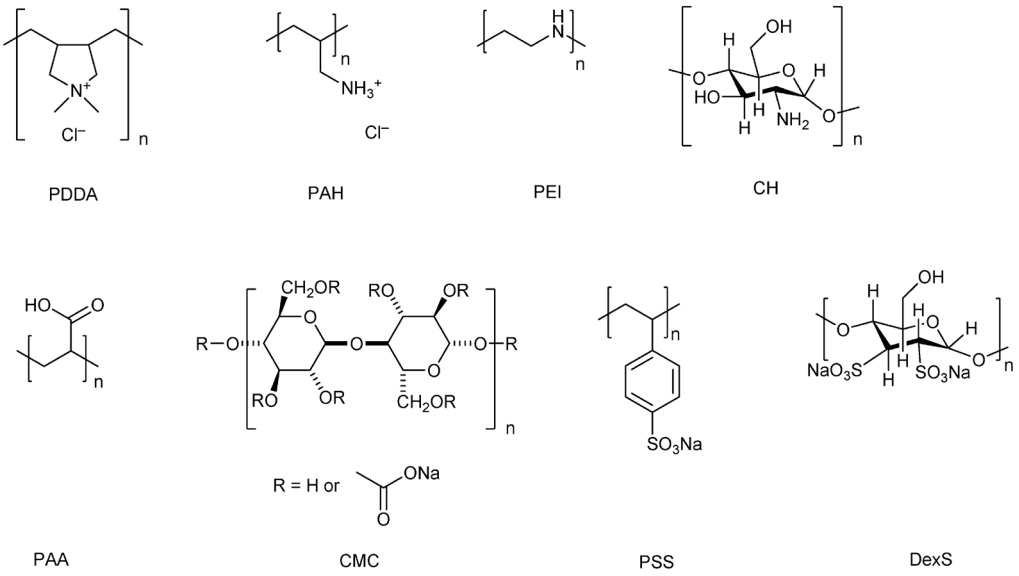

Fig. S1. Structure of the used polyelectrolytes :.poly(diallyldimethylammonium chloride) (PDDA), polyallylamine hydrochloride (PAH), polyethyleneimine (PEI), and chitosan (CH), polyacrylic (PAA), carboxymethyl cellulose (CMC), polystyrene sulfonic acid sodium salt (PSS), dextran sulfate (DexS).

Table S2. Structure of used MOFs

MOF	MIL-101(Cr)	Basolite®A520; Al fumarate	MIL-53 (Al)-TDC	UiO-66	Zr fumarate (MIL-801)
Metal ion	Cr	Al	Al	Zr	Zr
Ligand	1,4-benzene dicarboxylic (terephthalic) acid	Fumaric acid	2,5-thiophene dicarboxylic acid (TDC)	1,4-benzene dicarboxylic (terephthalic) acid	Fumaric acid
Pore structure	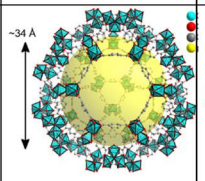	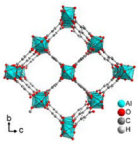	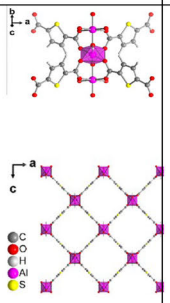	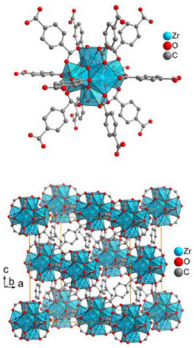	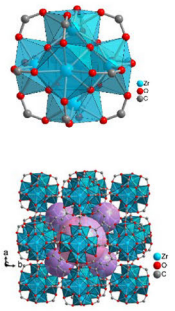

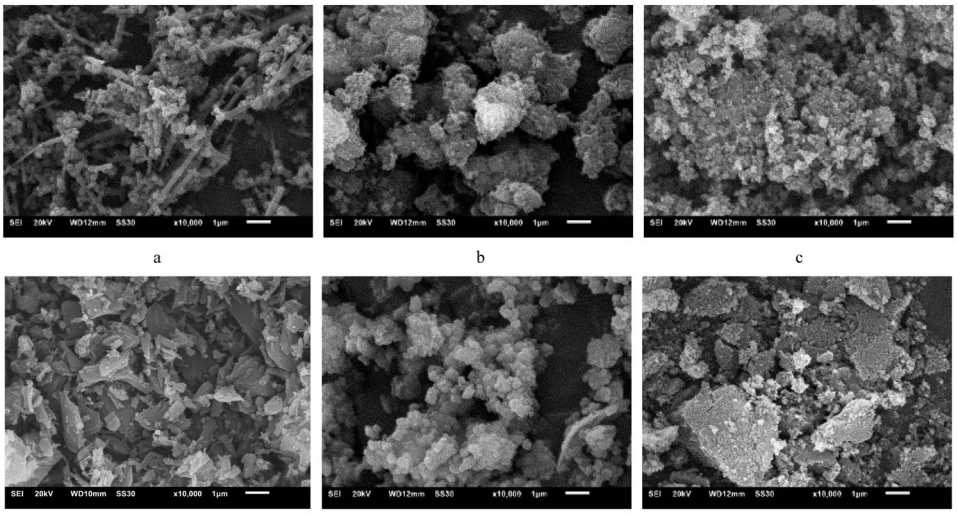

Fig. S3. SEM images of the neat MOFs: MIL-101(Cr) (a), Al-fum (b), Basolite® A520 (c), MIL-53-TDC (d), UiO-66 (e), Zr-fum (fe).

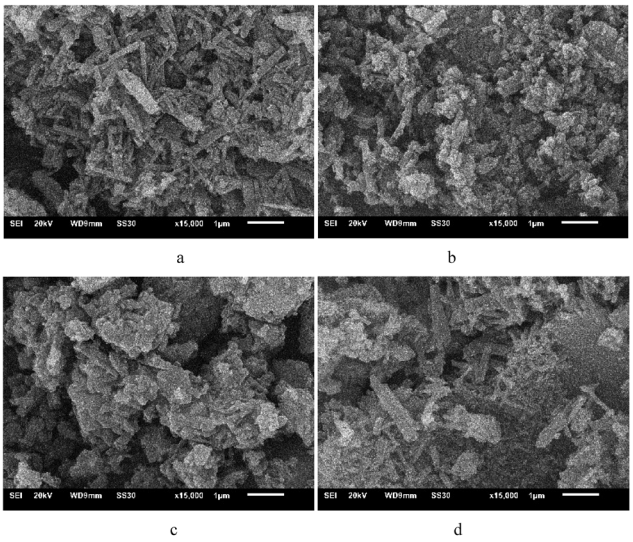

Fig. S4. SEM images of MOF MIL-53-TDC modified with PE: PAA (a), CMC (b), DexS (c), CAR (d).

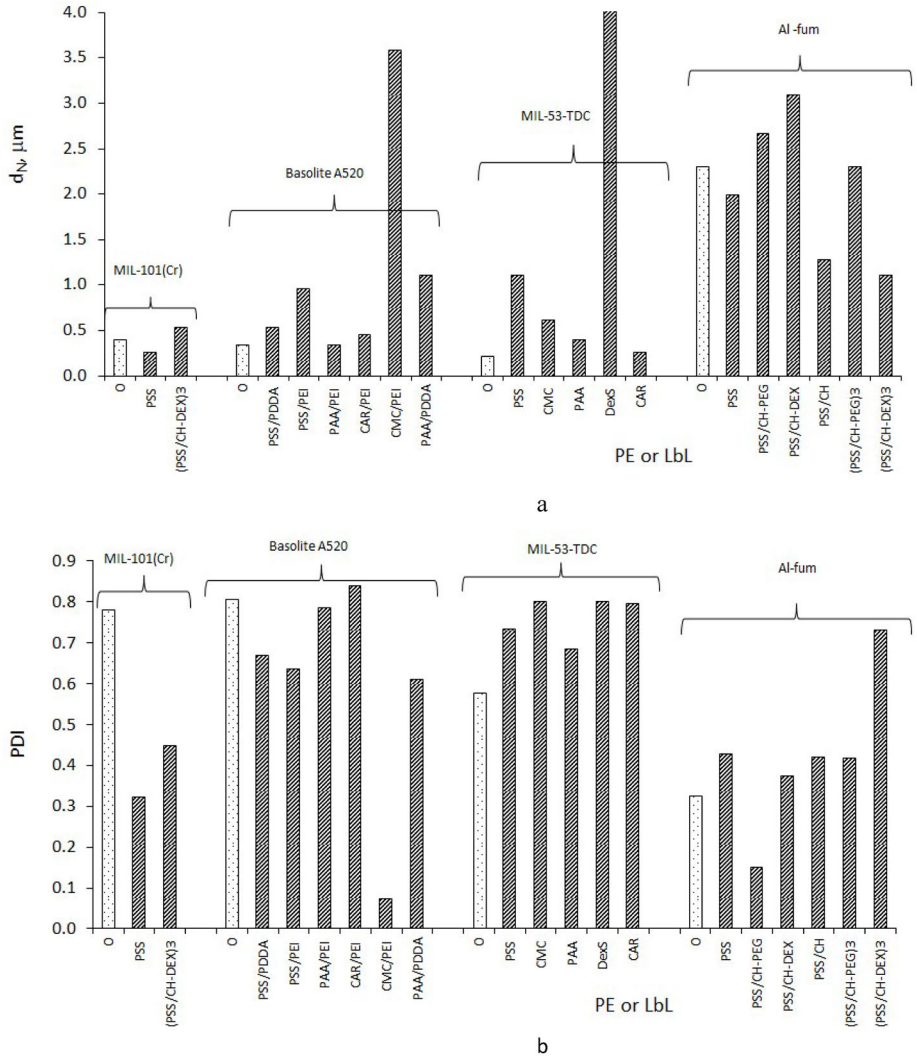

Fig. S5. Hydrodynamic diameter (d_N) (a) and polydispersity index (PDI) (b) of MOF powders coated with a single polyelectrolyte layer or a LbL shell as indicated on the X-axis, determined by DLS in a water dispersion.

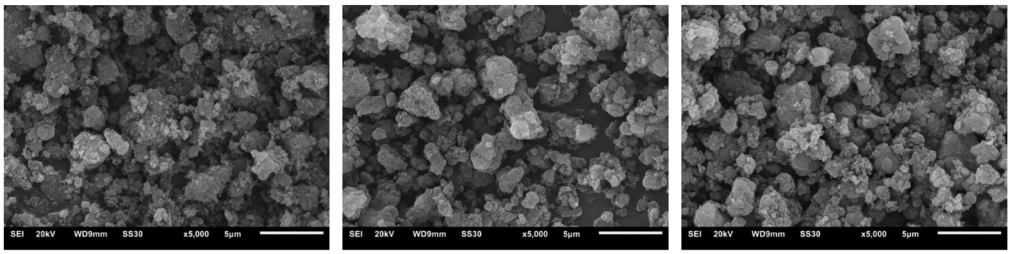

Fig. S6. SEM microphotographs of Al fumarate modified with a LbL shell: PSS (a), $(PSS/CH\text{-}DEX)_3$ (b), $(PSS/CH\text{-}PEG)_3$ (c).

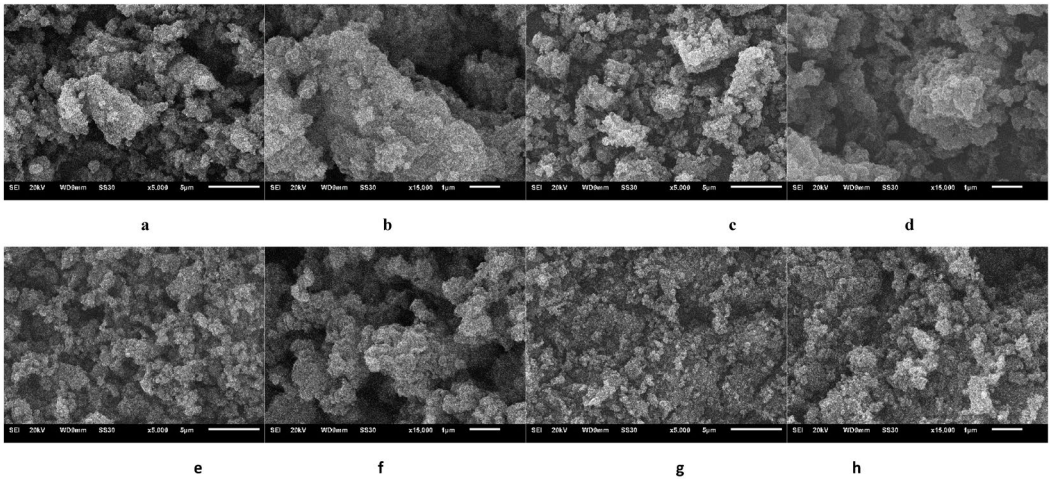

Fig. S7. SEM images of MOF Basolite® A520 modified with a LbL shell of PSS/PDDA (a,b), CMC/PEI (c,d), PAA/PDDA (e,f), PAA/PEI (g,h).

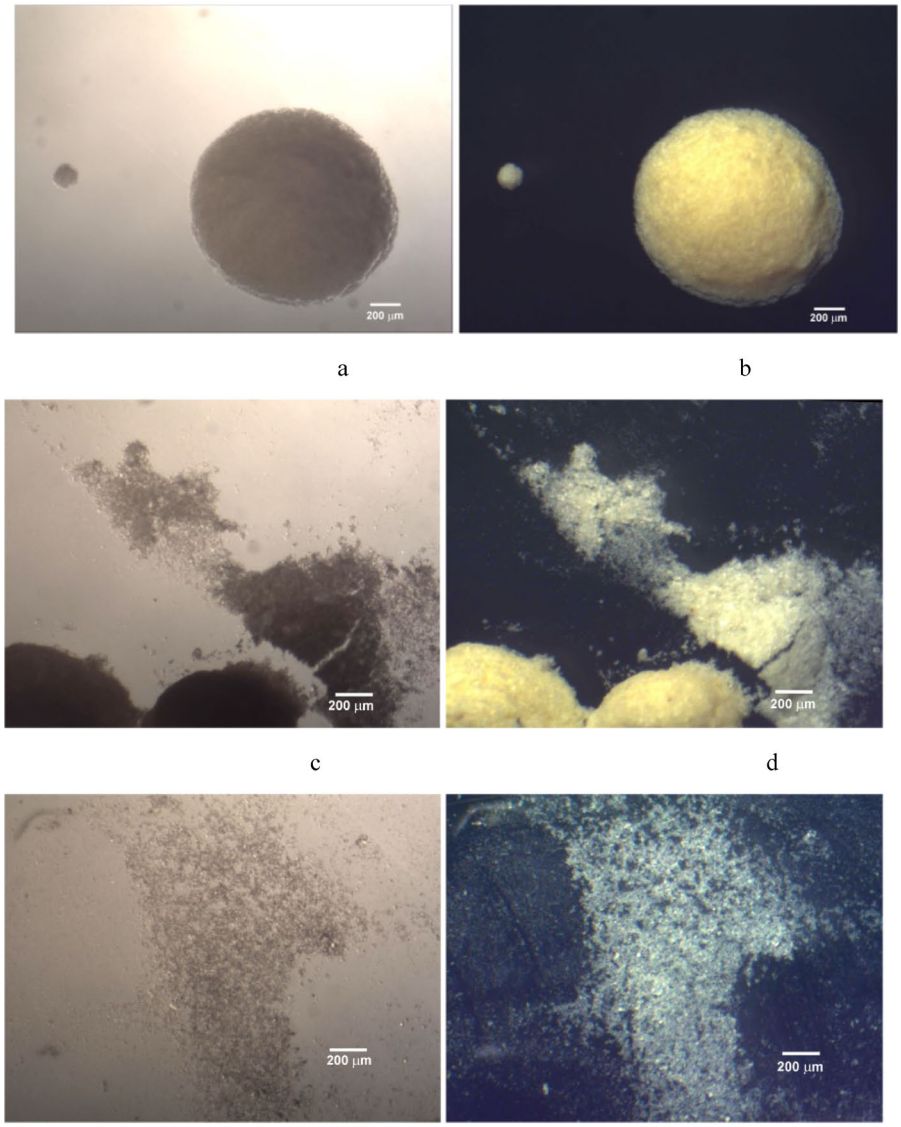

Fig. S8. Micrographs of dry Al fumarate microparticles coated with a $(PSS/PAH\text{-}FITC)_2$ shell of different degree of aglomeration obtained in transmitted (a,c,e) and reflected (b,d,f) light. Yellow color shows the distribution of LbL shell containing FITC-labled PAH 15 kDa. T=25 ^{0}C. The images were taken using a LOMO MSP-1 option 5 stereoscopic microscope equipped with a TCA-5.0C camera.

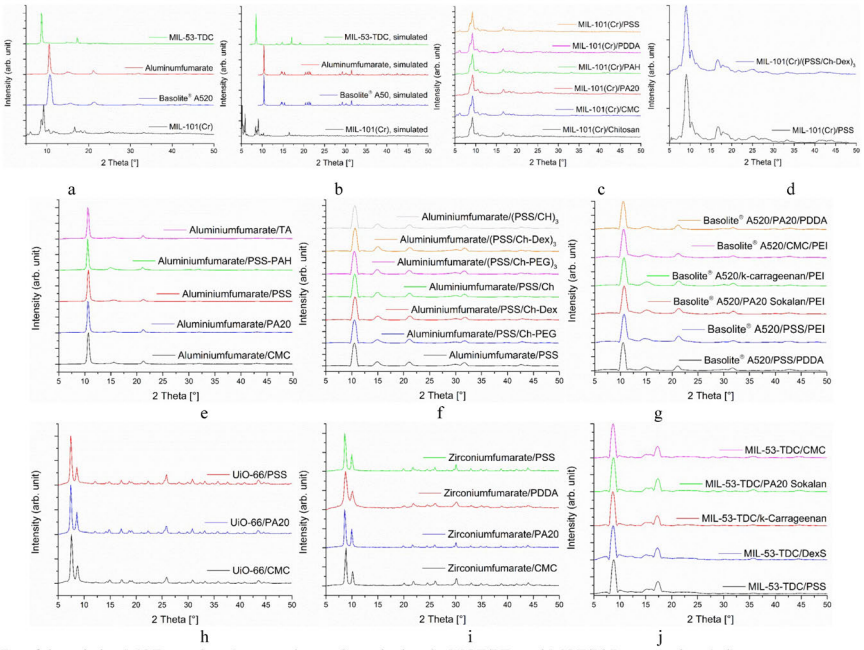

Fig. S9. PXRDs of the pristine MOF powders (a –experiment, b - calculated), MOF/PE, and MOF/LbL composites (c-j).

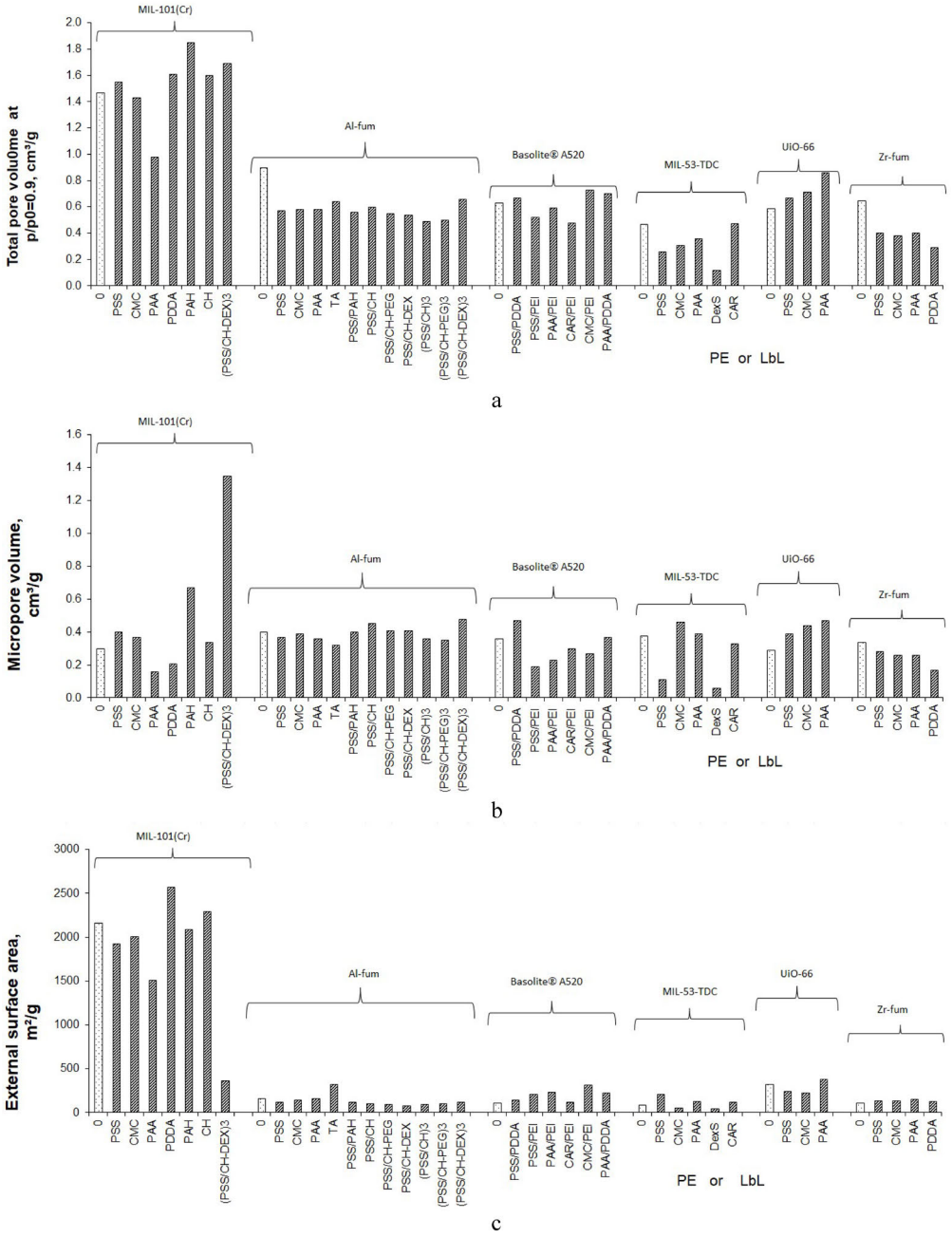

Fig. S10. Total pore volume (a), micropore volume (b), and external surface area (c) of the MOFs after single polyelectrolyte modification as evaluated by nitrogen sorption.

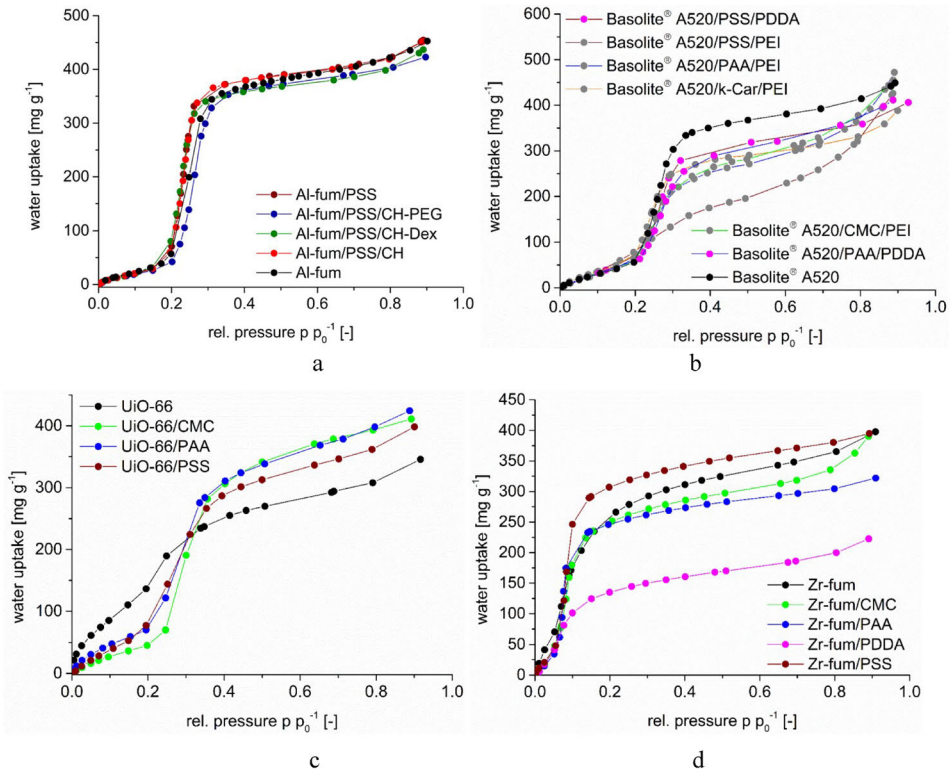

Fig. S11. Isotherms of water vapor sorption by MOF/PE and MOF/LbL composites: a) Al-fum, b), Basolite®A520, c) UiO-66, d) Zr-fum.

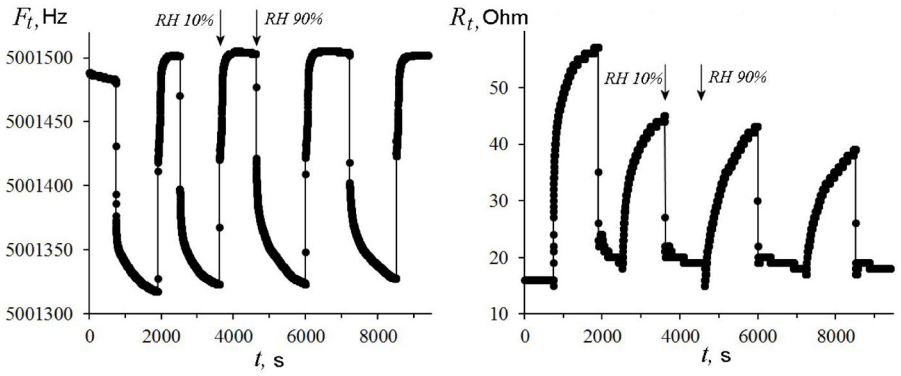

a b

F ig. S12. Changes of F_t (a) and R_t (b) of a 5 MHz resonator with Al-fum/$(PSS/PDDA)_3$ deposit in the process of alternately changing humidity. T = 25.4 °C.

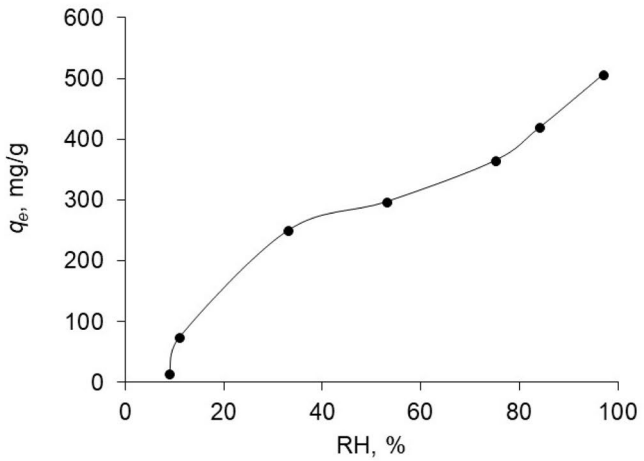

Fig. S13. Water uptake by Al-Fum at 26.4 ^{0}C.

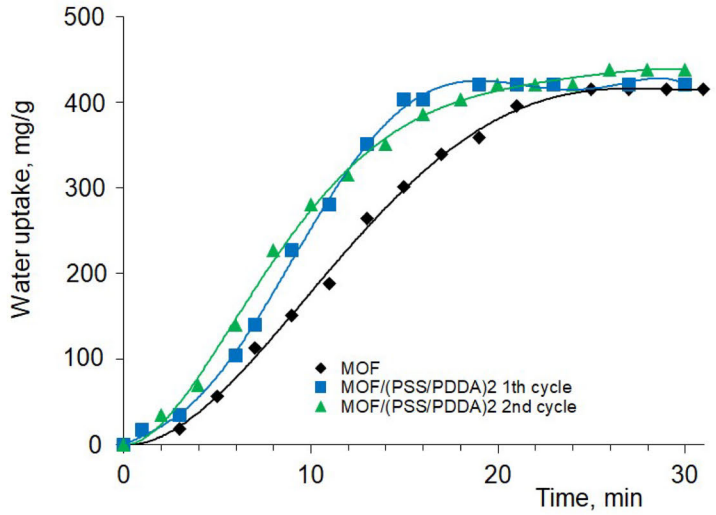

Fig. S14. Water vapor uptake by Al fumarate and Al fumarate / thick $(PSS/PDDA)_2$ shell composite (23 ^{0}C, RH 70%).

3.4 Unravelling gas sorption in the aluminum metal-organic framework CAU-23: CO_2, H_2, CH_4, SO_2 sorption isotherms, enthalpy of adsorption and mixed-adsorptive calculations

Christian Jansen, Niels Tannert, Dirk Lenzen, Marco Bengsch, Simon Millan, Anna Goldman, Dustin Nils Jordan, Linda Sondermann, Norbert Stock, Christoph Janiak

Z. Anorg. Allg. Chem. **2022**, *648*, e202200170

DOI: 10.1002/zaac.202200170

Impact-Faktor: 1.414 (2021)

Kurzzusammenfassung:

Diese Veröffentlichung ist die erste breitere Einordnung der Eigenschaften von CAU-23 für die Gassorption, mit den Adsorptiven CO_2, H_2, CH_4 und SO_2. CAU-23 ist ein aluminiumbasiertes MOF mit einer mittleren Oberfläche. Die Reihung der spezifischen BET-Oberflächen der Al-MOFs, die in dieser Veröffentlichung betrachtet werden, sind MIL-100 > MIL-53 > CAU-23 > MIL-160 > MIL-53-TDC > Aluminiumfumarat > CAU-10-H und beim absoluten Porenvolumen MIL-100 > MIL-53 > CAU-23 > Aluminiumfumarat = MIL-160 > MIL-53-TDC > CAU-10-H. Die CO_2-Aufnahme (3.97 mmol g^{-1}, 293 K) und die H_2-Aufnahme (10.25 mmol g^{-1}, 77 K) von CAU-23 sind die Zweitbesten und nur minimal geringer als die Aufnahmen von MIL-160. Die CH_4-Aufnahme von CAU-23 (0.89 mmol g^{-1}, 293 K) ist unerheblich, im Vergleich zu den anderen Al-MOFs. Die SO_2-Aufnahme (8.4 mmol g^{-1}, 293 K) folgt der Porosität der MOFs und höhere SO_2 Aufnahmen konnten nur für MIL-53 and MIL-100 beobachtet werden. CAU-23 ist eines der besten Al-MOFs für die Hochdrucksorption von CO_2, mit einer Aufnahme von 33 wt.-% bei 20 bar und einer Temperatur von 293 K. Gassorptionsmessungen mit zwei Isothermen gaben Adsorptionsenthalpien ΔH_{ads}^0 für CO_2 von –22 kJ mol^{-1} und bei SO_2 von –38 kJ mol^{-1} und sind somit am unteren Ende für die Al-MOFs (–22 to –39 kJ mol^{-1} für CO_2; –41 to –51 kJ mol^{-1} für SO_2).Die Adsorptionsenthalpie Δ_{Hads} erhöht sich bei CAU-23 für CO_2 und SO_2 bis hin zu –25 und –57 kJ mol^{-1}. Für die CO_2/CH_4- und SO_2/CO_2-Trennung ergeben sich mit der „ideal adsorbed solution theory" Selektivitäten von 5 und 27-50 (in Abhängigkeit von den molaren Verhältnissen und dem gewählten Modell). Diese stimmen überein mit Selektivitäten von 4.5-6.3 und 17-50, für die anderen Al-MOFs, wobei nur MIL-53-TDC mit 83 und MIL-160 mit 126 höhere SO_2/CO_2 Selektivitäten zeigen bei einem molaren Verhältnis von 0.5.

Anteile an der Publikation:

- Idee der Publikation in Zusammenarbeit mit Herrn Niels Tannert

- Konzept, experimentelle Arbeiten und Analytik (bis auf unten gelistete Ausnahmen) in Zusammenarbeit mit Herrn Niels Tannert
- Experimentelle Vorarbeiten durch Herr Marco Bengsch
- Aufarbeitung der Ergebnisse, Verfassen des Manuskripts und das Erstellen der Abbildungen und Tabellen
- Anfertigung der theoretischen Rechnungen
- Korrekturen und Verschriftlichung und Revision durch Herr Prof. Dr. Christoph Janiak
- Korrekturen durch Herr Prof. Dr. Norbert Stock
- Erstmalige Produktsynthese durch Herr Dirk Lenzen
- Sorptionsaufnahmen durch Herr Simon Millan, Frau Anna Goldman, Frau Linda Sondermann
- Hochdrucksorptionsaufnahmen durch Herr Dustin Nils Jordan

Journal of Inorganic and General Chemistry
ZAAC
Zeitschrift für anorganische und allgemeine Chemie
www.zaac.wiley-vch.de
RESEARCH ARTICLE

DOI: 10.1002/zaac.202200170

Unravelling gas sorption in the aluminum metal-organic framework CAU-23: CO_2, H_2, CH_4, SO_2 sorption isotherms, enthalpy of adsorption and mixed-adsorptive calculations

Christian Jansen,[a] Niels Tannert,[a] Dirk Lenzen,[b] Marco Bengsch,[a] Simon Millan,[a] Anna Goldman,[a] Dustin Nils Jordan,[a] Linda Sondermann,[a] Norbert Stock,[b] and Christoph Janiak*[a]

The report is the first broader evaluation of the gas sorption properties of CAU-23 for the adsorptives CO_2, H_2, CH_4, and SO_2. CAU-23 is of intermediate porosity among Al-MOFs with specific BET surface areas of the order of MIL-100 > MIL-53 > CAU-23 > MIL-160 > MIL-53-TDC > Alfum > CAU-10-H and total pore volumes of the order of MIL-100 > MIL-53 > CAU-23 > Alfum = MIL-160 > MIL-53-TDC > CAU-10-H. CO_2 uptake (3.97 mmol g^{-1}, 293 K) and H_2 uptake (10.25 mmol g^{-1}, 77 K) of CAU-23 are second in the series and only slightly smaller than for MIL-160. The CH_4 uptake of CAU-23 (0.89 mmol g^{-1}, 293 K) is unremarkable in comparison with the other Al-MOFs. The SO_2 uptake (8.4 mmol g^{-1}, 293 K) follows the porosity and higher SO_2 uptakes were only observed for MIL-53 and MIL-100. CAU-23 is one of the best Al-MOFs for high-pressure sorption of CO_2, with an uptake of 33 wt.-% at 20 bar, 293 K. Gas sorption measurements at two different temperatures gave near zero-coverage enthalpy of adsorptions, $\triangle H_{ads}^0$ for CO_2 of −22 kJ mol^{-1} and of SO_2 for −38 kJ mol^{-1} which is at the low end of the other Al-MOFs (−22 to −39 kJ mol^{-1} for CO_2; −41 to −51 kJ mol^{-1} for SO_2), yet $\triangle H_{ads}$ increases for CAU-23 with CO_2 and SO_2 to −25 and −57 kJ mol^{-1}, respectively. For CO_2/CH_4 and SO_2/CO_2 separation, ideal adsorbed solution theory (IAST) predicted gas selectivities of 5 and 27–50 (depending on molar ratio and model), respectively, in line with 4.5–6.3 and 17–50, respectively, with most of the other Al-MOFs, where only MIL-53-TDC with 83 and MIL-160 with 126 gave a higher SO_2/CO_2 selectivity at a molar ratio of 0.5.

Introduction

Metal-organic frameworks (MOFs) are coordination networks, that consist of metal nodes and bridging organic linkers with a wide structural diversity.[1–3] MOFs are mainly interesting due to their porosity for a variety of potential applications and properties, e.g. gas sorption and separation,[4–9] catalysis,[10,11] luminescence,[12–14] conductivity.[15] MOFs can be obtained through various synthesis routes,[16] for example under solvothermal,[17] or reflux conditions using microwave-assisted heating,[18] electrochemical,[19] or mechanochemical energy input, with variation of metal precursor, solvent, concentration or the presence of modulators.[20,21]

An important aspect in MOF chemistry and utilization is their kinetic stability towards ligand exchange, especially hydrolysis.[22] The inertness or lability of a metal ion towards hydrolysis can be estimated from the Merbach series of rate constants for the exchange of aqua ligands in metal-aqua complexes according to $[M(H_2O)_n]^{c+} + H_2O^* \rightarrow [M(H_2O)_{n-1}(H_2O^*)]^{c+} + H_2O$.[23–25] The most inert main-group metal ion is Al^{3+} with a rate constant for the water exchange in $[Al(H_2O)_6]^{3+}$ of $k(H_2O) = 1.3\ s^{-1}$. Al^{3+} is much more inert than divalent transition-metal cations from Mn^{2+} to Cu^{2+} which have large rate constants $k(H_2O)$ of over $10^{-6}\ s^{-1}$. Among the trivalent metal ions Al^{3+} has an intermediate rate constant and is more labile than for example Cr^{3+} ($k(H_2O) = 2.4 \cdot 10^{-6}\ s^{-1}$) but less labile than Fe^{3+} ($k(H_2O) = 180\ s^{-1}$) and much less labile than Ti^{3+} ($k(H_2O) = 1.8 \cdot 10^{-5}\ s^{-1}$).

Further, aluminum salts are inexpensive and exhibit low toxicity.[26–29] Therefore, aluminum-based MOFs such as MIL-53,[30] Al-fumarate (Basolite® A520; short: Alfum),[31–33] CAU-10,[34] or MIL-160[35] are frequently investigated in application-oriented MOF studies (MIL=Matériaux de l'Institute Lavoisier, CAU=Christian-Albrechts-University).[26,27,36–38] In 2017, Tschense *et al.* published the Al-based MOF [Al(OH)(TDC)] containing the linker 2,5-thiophenedicarboxylate (TDC^{2-}) (Figure 1a) and crystallizing in the MIL-53 type structure topology.[40] This compound was named MIL-53-TDC and subsequently investigated for water

[a] C. Jansen, Dr. N. Tannert, M. Bengsch, Dr. S. Millan, Dr. A. Goldman, D. N. Jordan, L. Sondermann, Prof. C. Janiak
Institut für Anorganische Chemie und Strukturchemie
Heinrich-Heine-Universität Düsseldorf
40204 Düsseldorf, Germany
E-mail: janiak@uni-duesseldorf.de
[b] Dr. D. Lenzen, Prof. N. Stock
Institut für Anorganische Chemie,
Christian-Albrechts-Universität Kiel, Max-Eyth-Straße 2, 24118 Kiel, Germany
E-mail: stock@ac.uni-kiel.de

Supporting information for this article is available on the WWW under https://doi.org/10.1002/zaac.202200170

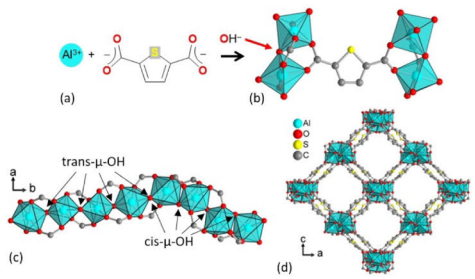

Figure 1. Crystal structure of CAU-23: (a) Al^{3+}, 2,5-thiophenedicarboxylate (TDC^{2-}) and hydroxide ions as building blocks, (b) TDC^{2-} linker coordination to {AlO_6} octahedra, (c) chains composed of alternating segments of four helical cis- and four trans-corner sharing {AlO_6} octahedra, (d) section of the packing diagram with the {AlO_6} chains connected by the TDC^{2-} linkers to yield square-shaped channels. The graphics were produced by the software Diamond[39] from the cif-file with CSD-Refcode ZOVHUQ (CAU-23).[44]

sorption in connection with heat transformation applications,[41] for CO_2 capture,[42] and SO_2 sorption.[43]

A MOF synthesized with the same starting materials and having the same composition as MIL-53-TDC, is the polymorph CAU-23 [Al(OH)(TDC)], which was reported by Lenzen *et al.* in 2019.[44] CAU-23 and many structurally similar Al-MOFs are built from chains of μ-OH^- and carboxylate bridged {AlO_6} octahedra which share vertices through the μ-OH bridge (Figure 1b). The dicarboxylate linkers connect these parallel chains to 3D-framework with square to rhombic channels along the chain directions (Figure 1d). Different to the other Al-MOFs the chains in CAU-23 have both cis- and trans μ-OH-corner-sharing {AlO_6} octahedra (Figure 1c), while MIL-160,[35] and CAU-10-H[34] have only cis- and MIL-53-TDC[40] and MIL-53 have only trans-μ-OH-connectivity.[30,45] CAU-23 was found as an ideal compound for ultra-low temperature driven adsorption heat pumps (AHPs) with impressive stability. CAU-23 could operate at the low regeneration or driving temperature of 60 °C with a low cooling temperature of 10 °C and it has a high uptake capacity of 0.37 g(H_2O)/g(sorbent).[44]

Up to now only the sorption properties of CAU-23 to N_2 at 77 K and H_2O at 298 K[44] and the C_2H_2/CO_2 separation have been studied.[46] The reported specific surface area (S_{BET}), micropore volume ($V_{micropore}$) and water capacity (H_2O_{uptake}) are S_{BET} = 1250 $m^2 g^{-1}$,[44] S_{BET} = 1320 $m^2 g^{-1}$,[46] $V_{micropore}$ = 0.48 $cm^3 g^{-1}$ (at p p_0^{-1} = 0.5) and H_2O_{uptake} = 0.40 g g^{-1}.[44] In addition to neat CAU-23, mixed-linker materials of the MOFs CAU-23 and MIL-160 have been investigated.[45] In order to further characterize CAU-23, we report here gas sorption data of Ar, CO_2, H_2, CH_4, SO_2 up to a relative pressure p p_0^{-1} of 1, and high-pressure CO_2 sorption experiments up to 20 bar.

Results and Discussion

The synthesis of CAU-23 was carried out as described by Lenzen *et al.*[44] The starting materials were $AlCl_3 \cdot 6\ H_2O$, $NaAlO_2$ and sodium 2,5-thiophenedicarboxylate. The CAU-23 material used in this gas sorption study has a specific surface area of S_{BET} = 1176 $m^2 g^{-1}$ and a total pore volume of $V_{total\ pore}$ = 0.51 $cm^3 g^{-1}$ (at p p_0^{-1} = 0.90) as from N_2 sorption at 77 K (Table S4). Ar sorption at 87 K gave a surface area of 1097 $m^2 g^{-1}$ (Table S7).

The CO_2 sorption isotherms at three different temperatures (195, 273 and 293 K) are presented in Figure 2. Uptakes of 3.97 mmol g^{-1} (293 K), 6.02 mmol g^{-1} (273 K) are observed. It increases to 10.89 mmol g^{-1} at 195 K, which is the condensation/sublimation point of CO_2. The isotherm shows a large hysteresis, which is probably due to a structural change of the framework,[47] or related to kinetic effects of the desorption of CO_2 from the narrow micropores of CAU-23.

Figure 3 compares the CO_2 uptake of CAU-23 with data of other Al-MOFs, which were taken from the literature.[38] CAU-23 shows a high CO_2 uptake among Al-MOFs, just somewhat less than MIL-160 which contains 2,5-furandicarboxylate linker molecules with S_{BET} = 1106 $m^2 g^{-1}$, V_{pore} = 0.44 $cm^3 g^{-1}$ (at p p_0^{-1} = 0.90) (this work, Table S6). Furthermore, CAU-23 has a higher CO_2 uptake than Al-MOFs with higher specific surface areas, like MIL-53 (S_{BET} = 1338 $m^2 g^{-1}$) or MIL-100 (S_{BET} = 1368 $m^2 g^{-1}$) (this, work, Table S6).

The flexible structure of MIL-53 does not present an advantage for CO_2 capture properties. Comparison of the polymorphs MIL-53-TDC and CAU-23, which contain the same 2,5-thiophenedicarboxylate linker shows a significant increase in the uptake by CAU-23 which may be due to the different connectivities of the {AlO_6} polyhedra in the two MOFs.

The H_2 isotherms at 77, 87 and 100 K, (Figure 4) show uptakes of 10.25, 10.46 and 5.71 mmol g^{-1} at around 720 Torr with no hysteresis upon desorption. At all three temperatures the H_2 adsorption isotherms still have a high positive slope at 700 Torr and are not levelling off, which indicates an adsorption curve far from saturation, which will be reached only at higher

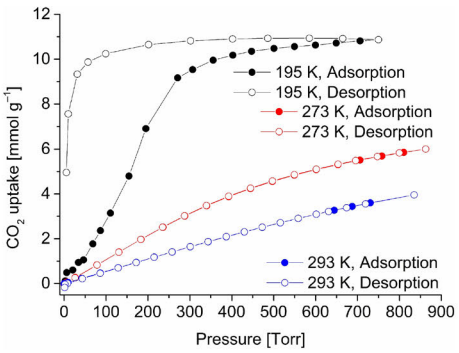

Figure 2. CO_2 sorption isotherms of CAU-23 recorded at different temperatures.

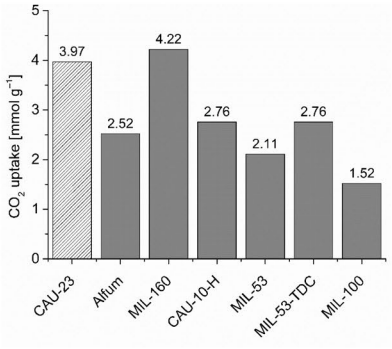

Figure 3. Comparison of CO_2 uptake of CAU-23 (shaded area) with selected Al-MOFs (grey) at 293 K and 1 bar (Alfum,[38] MIL-160,[38] CAU-10-H,[38] MIL-53,[38] MIL-53-TDC,[38] and MIL-100[38]). For uptake data at other temperatures and the uptake in $cm^3 g^{-1}$ or wt-% see Table S8 in SI.[46,48–52]

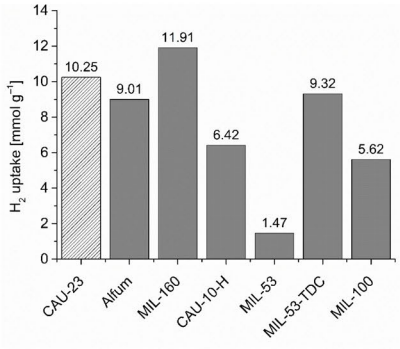

Figure 5. Comparison of H_2 uptake of CAU-23 (shaded area) with selected Al-MOFs (grey) at 77 K and 1 bar (data for Alfum, MIL-160, CAU-10-H, MIL-53, MIL-53-TDC, and MIL-100 measured by us). For uptake in $cm^3 g^{-1}$ or wt-% see Table S10 in SI.[53]

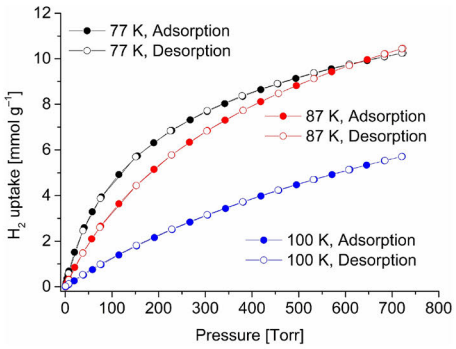

Figure 4. H_2 sorption isotherms of CAU-23 for different temperatures.

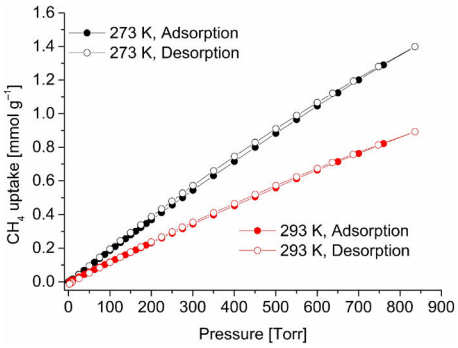

Figure 6. CH_4 sorption isotherms of CAU-23 for different temperatures.

pressures. This is an interesting fact for the use of CAU-23 in possible hydrogen storage applications under high pressure conditions.

In Figure 5 the hydrogen sorption capacity of CAU-23 at 77 K is compared with values which we measured for the other Al-MOFs (Table S10, SI). Due to the fact that H_2 storage is typically investigated under higher pressure, to the best of our knowledge no data is available in the literature for H_2 sorption of Al-MOFs up to 1 bar, except for Alfum (Table S10). Only MIL-160 has a higher H_2 uptake capacity at 1 bar than CAU-23 at 77 K.

The CH_4 uptake capacity of CAU-23 ranges between 0.89 and 1.38 mmol g^{-1} at 293 and 273 K, respectively (Figure 6, Table S11 in SI). The CH_4 adsorption isotherms also did not reach saturation at 1 bar as seen by their still large positive slope, far from levelling off. Saturation will require a pressure above 800 Torr. CAU-23 has no significant hysteresis for the methane sorption.

The comparison to literature values of other Al-MOFs shows that CAU-23 has no particular affinity for methane. The uptake is in the range of other Al-MOFs at similar temperatures (293 and 298 K, Table S11). The effect of the surface area is not so important and there is also no correlation between the pore limiting diameter and the uptake. The highest methane uptake of an Al-MOF near 298 K is observed for Alfum (Figure 7) which has a lower specific surface area (S_{BET} = 898 $m^2 g^{-1}$) than CAU-23, MIL-160, MIL-53 and MIL-53-TDC (S_{BET} = 973 to 1338 $m^2 g^{-1}$, Table S6).

SO_2 sorption of CAU-23 at 273 and 293 K (Figure 8) gave highly reversible Type I isotherms,[56] which almost levelled-off at 760 Torr, a feature which is not always seen for the SO_2 uptake in Al-MOFs where saturation is not necessarily reached at this pressure.[38,57] MIL-53 and Alfum have a still positive

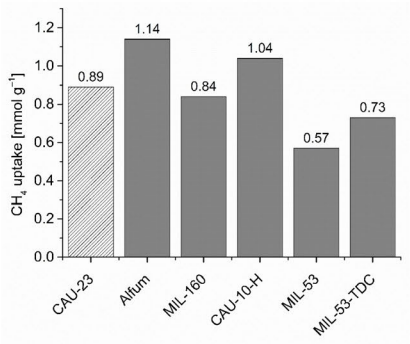

Figure 7. Comparison of CH_4 uptake of CAU-23 (shaded area) with selected Al-MOFs (grey) at 293 or 298 K and 1 bar (Alfum,[54] MIL-160,[49] CAU-10-H,[49] MIL-53,[54] and MIL-53-TDC[49]). For uptake data at other temperatures and the uptake in $cm^3 g^{-1}$ or wt-% see Table S11 in SI.[55,54,51]

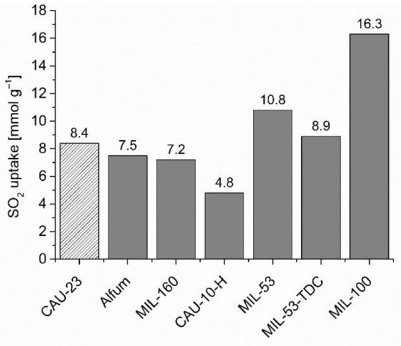

Figure 9. Comparison of SO_2 uptake of CAU-23 (shaded area) with selected Al-MOFs (grey) at 293 K and 1 bar (Alfum,[38] MIL-160,[59] CAU-10-H,[38] MIL-53,[60] MIL-53-TDC,[60] and MIL-100[38]). For uptake data at other temperatures and the uptake in $cm^3 g^{-1}$ or wt-% see Table S12 in SI.[38]

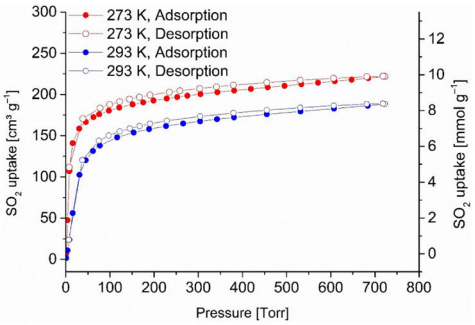

Figure 8. SO_2 sorption isotherms of CAU-23 at different temperatures.

slope, signaling unsaturation.[38] For MIL-53-TDC and CAU-10-H the slope near 760 Torr (1 bar) is only slightly positive. Only MIL-160 exhibits a fully levelled-off Type I isotherm. CAU-23 and MIL-160 also show a similar isotherm shape with a high uptake already at low pressure (below 50 Torr, 0.07 bar) and a small hysteresis. CAU-23 gives SO_2 uptakes of 8.4 mmol g^{-1} at 293 K, 9.9 mmol g^{-1} at 273 K and 760 Torr and 15.5 mmol g^{-1} at 263 K and 610 Torr, before a strong uptake increase due to condensation (Figure S17, boiling point of SO_2 is 263 K).

Figure 9 compares the SO_2 uptake data of CAU-23 with other Al-MOFs at 1 bar and 293 K.[38,58–60] A similar uptake is found for MIL-53-TDC. The MOFs MIL-53 and MIL-100, both having a higher specific surface area and pore volume (Table S6), have significantly higher SO_2 uptakes. The large uptake of MIL-53 can be related to the structural flexibility of the MOF with a breathing effect between 0.4 to 0.5 bar, after which the SO_2 uptake at 1 bar becomes about twice as high as at 0.4 bar.[38] The SO_2 uptake in MIL-53 follows a Type F–I isotherm.[38,58] The high SO_2 uptake of MIL-100 with 365.3 $cm^3 g^{-1}$/16.3 mmol g^{-1} at 293 K is due to its high surface area and total pore volume (Table S6).

Finally, the CO_2 adsorption of CAU-23 was also studied up to 20 bar. The MOF has a CO_2 uptake of 493 mg g^{-1} at 20 bar (33 wt.–%), which is at the high end of the other Al-MOFs (Figure 11). MIL-53 appears to be the Al-MOF with the highest uptake of 31 or 37.8 wt.–% at 30 bar/304 K or 20 bar/298 K.[52,61] The S-shape of the high-pressure CO_2 isotherm (Figure 10 and Figure S18) is typical for a small group of Al-MOFs and was also observed for MIL-53,[52] and MIL-53-TDC (this work). Al-MOFs, like Alfum,[48] MIL-160,[62] CAU-10-H[63] or MIL-100[63] have more a Type I shape for the high-pressure isotherm with an immediate and high uptake already in the 1–2 bar range (Table S13), which

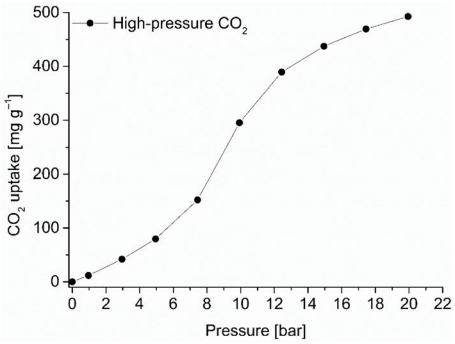

Figure 10. High pressure CO_2 adsorption isotherms of CAU-23 recorded at 293 K.

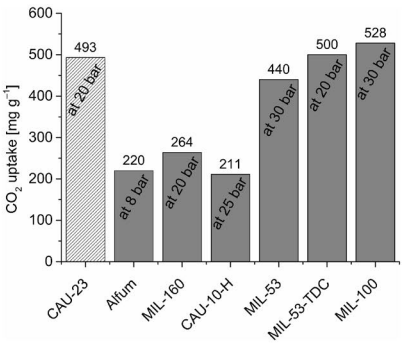

Figure 11. Comparison of high-pressure CO_2 uptake of CAU-23 (shaded area) with selected Al-MOFs (grey) at different temperatures and pressures (Alfum,[48] MIL-160,[62] CAU-10-H,[63] MIL-53,[52] MIL-53-TDC (this work), and MIL-100[63]). For uptake data in wt-% and further details (pressure and temperature) see Table S13 in SI.[61]

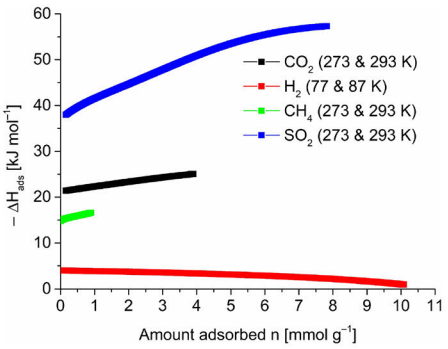

Figure 12. Isosteric enthalpy of adsorption $\Delta H_{ads}(n)$ of CO_2, H_2, CH_4 and SO_2 as a function of uptake from the adsorption isotherms at the given two temperatures.

is also seen for UiO-66-type Zr-MOFs.[64] CAU-23 has a similar uptake capacity and isotherm shape at 20 bar/293 K as its polymorph MIL-53-TDC. The steep rise of the S-shaped CO_2 isotherm of CAU-23 between 6 to 12 bar is shifted to lower pressures, that is, between 5 to 10 bar in MIL-53-TDC. As both CAU-23 and MIL-53-TDC have the same 2,5-thiophenedicarboxylate ligand, this shift is due to the different crystal structures.[30,40,45]

Enthalpy of Adsorption for CAU-23. The isosteric enthalpy of adsorption (ΔH_{ads}) of CO_2, H_2, CH_4 and SO_2 was determined from two adsorption isotherms at different but still close temperatures ($\Delta T = 10$ or 20 K) by applying the isosteric method based on the Clausius-Clapeyron equation or the virial analysis of adsorption isotherms.[65] CO_2, H_2 and CH_4 isotherms could be well fitted with the Freundlich-Langmuir model for the Clausius-Clapeyron approach (Figure S13, S14, and S16). For the SO_2 adsorption isotherms a virial fit was used as preferred in the literature (Figure S17).[65] The virial fit was also used for the CO_2 adsorption data (Figure S13) in the higher pressure range.

CAU-23 shows varying degrees of affinity for the four measured gases, as quantified by the affinity constants K from the isotherm fits (Table S14). Among the four gases the affinity towards CO_2, H_2 and CH_4 is rather low at zero coverage, while SO_2 has the highest affinity, due to its dipole moment. Thus, it can interact with the μ-OH bridge, the thiophene S atom and π-system as well as the thiophene carboxylate and C–H groups. DFT calculations on MIL-160, Zr-fumarate and the nickel DMOF-TM have identified these groups as higher-energy binding sites.[38,59,66]

Figure 12 shows the isosteric enthalpies of adsorption as a function of uptake of CO_2, H_2, CH_4 and SO_2. For $\Delta H_{ads}(n)$ of H_2 a steady decrease is observed which is expected upon initial interaction with the highest-energy binding sites and saturation of the binding sites with sequentially lower energy upon increasing uptake. The isosteric enthalpy of adsorption for CH_4 stays rather invariant with coverage in the overall low uptake regime (up to 1 mmol g^{-1}). For CO_2 and SO_2 a somewhat unexpected increase in ΔH_{ads} with the uptake is seen, which is different from the behavior of Alfum, Zr-fumarate, NH_2-MIL-53(Al),[38] but was also observed for MIL-160.[59] As just noted, more typical is a decrease in the enthalpy of adsorption with increased loading as the higher-energy sites are occupied first. A rationalization may be that a phase transition takes place where higher-energy binding sites become available. In MIL-160 such a phase transition was invoked from an activated, empty phase I to a SO_2-loaded phase II which was also seen in water sorption studies.[59,67]

The isosteric enthalpy of adsorption near zero coverage for CO_2 was calculated to -22 kJ mol^{-1} for CAU-23 (Figure 12), which in comparison with the literature for other Al-MOFs is at the low end (cf. -37 kJ mol^{-1} for MIL-160,[59] -39 kJ mol^{-1} for MIL-53,[69] Table 1). Noteworthy, $\triangle H_{ads}$ for CAU-23 and CO_2 increases to -25 kJ mol^{-1} at the uptake of 1 bar. This is related to the sigmoidal shape of the isotherm (Figure 2, Figure S13b), that is, the at first slowly increasing uptake. Yet, the calculated value of ~ -22 kJ mol^{-1} (Figure S19, virial fit) is in good comparison with the literature data (Table 1).[46] When ΔH_{ads}^0 for CO_2 and CAU-23 was calculated from a Freundlich-Langmuir fit (Figure S13b), then a value of only -2 kJ mol^{-1} was obtained (Figure S19). The virial analysis should be superior over the Freundlich-Langmuir fit/Clausius-Clapeyron fit in order to obtain rational $\triangle H_{ads}^0$ values, as the Freundlich-Langmuir fit can deviate more at low-uptake data.[65]

ΔH_{ads}^0 for H_2 was calculated to -4 kJ mol^{-1} for CAU-23. Due to lack of data in the literature, values for the other Al-MOFs are not available for comparison. Usually only H_2 adsorption studies at high-pressure are reported for MOFs which are typically measured only at one temperature. The isosteric enthalpy of adsorption near zero coverage for CH_4 was -14.8 kJ mol^{-1} for CAU-23 and is only slightly lower than -17.3 kJ mol^{-1} for MIL-160, or -18.3 kJ mol^{-1} for MIL-53 (Table 1). ΔH_{ads}^0 for SO_2 is

Table 1. Isosteric enthalpy of adsorption (near zero coverage) of aluminum MOFs for CO_2, H_2, CH_4 and SO_2.

MOF	$\Delta H_{ads}^0(CO_2)$ [kJ mol^{-1}]	Ref.	$\Delta H_{ads}^0(H_2)$ [kJ mol^{-1}]	Ref.	$\Delta H_{ads}^0(CH_4)$ [kJ mol^{-1}]	Ref.	$\Delta H_{ads}^0(SO_2)$ [kJ mol^{-1}]	Ref.
CAU-23	~−22[a,c] (−2[b,c])	our work	−4	our work	−14.8[c]	our work	−38[c]	our work
	−20.0[e]	[46]						
Alfum	−22[c]	[53]	–		–		−42[f]	[38]
MIL-160	−37[c]	[59]	–		−17.26[g]	[68]	−42[c]	[59]
	−28.03[g]	[68]	–		–		–	
CAU-10-H	~−25*	[50]	–		–		–	
MIL-53	−26.4[h]	[51]	-		−18.3[h]	[51]	−50.6[i]	[60]
	−39[j]	[69]	–		–		-	
MIL-53-TDC	–		–		–		−41.0 [i]	[60]
MIL-100	–		–		–		–	

[a] Virial fit, see Figure S19, [b] Freundlich Langmuir fit, see Figure S19; [c–i] calculation temperatures: [c] 273/293 K, [d] 77/87 K, [e] 273/298 K, [f] 293/303 K, [g] 273/295 K, [h] 288/303 K, [i] 303/308 K, [j] 273/296 K. * Visually read from a figure in the referenced literature (273/296 K).

−38 kJ mol^{-1} for CAU-23, only somewhat lower than −42 kJ mol^{-1} for MIL-160 or −51 kJ mol^{-1} for MIL-53 (Table 1). Again, H_{ads} increases for CAU-23 with SO_2 and reaches −57 kJ mol^{-1} at the uptake of 1 bar.

IAST (Ideal Adsorbed Solution Theory) for CAU-23. If one envisions the use of MOFs in adsorptive gas separation, CO_2/CH_4 separation for natural gas sweetening,[70,71] and SO_2/CO_2 separation for flue gas desulfurization[72,73] are possible areas of application. CO_2 can be regarded as the main competitor to SO_2 for a potential adsorptive separation during flue gas desulfurization. Therefore, the ideal adsorbed solution theory (IAST) selectivity of CO_2/CH_4 and SO_2/CO_2 was evaluated (Figure 13). The IAST model estimates on the mixed-gas adsorption behavior of an adsorbent based on data determined from single-gas adsorption experiments at the same temperatures. IAST-based estimations are most suitable when the following conditions are fulfilled: (i) the same accessible surface area is available to all adsorbates, (ii) low pressures (≤1 bar), and (iii) similar polarity of adsorbates.[74] IAST selectivities in this work were calculated with the "3P sim" software (see Supporting Information) by fitting the adsorption isotherm data points with the Toth or dual-site Langmuir Sips model (DSLAI Sips).[75] Parameters are listed in Table S15. IAST selectivities for SO_2 and CO_2 gas mixtures for CAU-23 are displayed in Figure 13. CAU-23 shows a low IAST selectivity for CO_2 and CH_4 with the Toth model, simulated in a pressure range up to 1 bar. The IAST selectivity of ~5 is in the range of values reported for other Al-MOFs (Table 2).

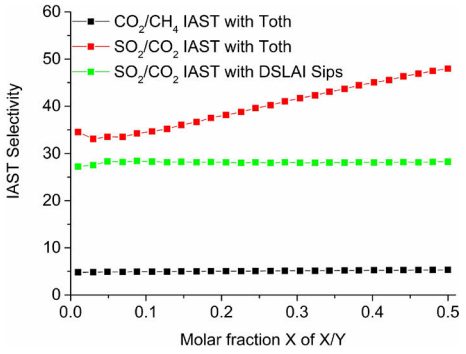

Figure 13. IAST selectivity for CAU-23 between CO_2/CH_4 and SO_2/CO_2 with Toth and DSLAI Sips model.

Al-MOFs in general have a low selectivity towards CO_2 and CH_4 separation. The common channel structure of most Al-MOFs with the lack of open metal sites[76] prevents targeted adsorption of gases, especially of gases with low dipole moments. It is probably mostly the difference in kinetic diameter between CO_2 (3.30 Å) and CH_4 (3.80 Å) which yields to a size-dependent separation.

The IAST selectivity of SO_2 and CO_2 was calculated with two different models, to investigate also the influence of the model. The Toth and Dual-Site Langmuir Sips model was chosen. The IAST selectivity difference between the two models varies between 34 (Toth) and 27 (DSLAI Sips) at 0.01 molar ratio and

Table 2. CO_2/CH_4 IAST selectivities at 293 K of aluminum MOFs.

MOF	CO_2/CH_4 IAST selectivity at CO_2/CH_4 molar ratio of 0.5	Ref.
CAU-23 (Toth)	5.3 (293 K)	our work
Alfum	4.5 (273 K)	[53]
MIL-160	6 (295 K)[a]	[68]
CAU-10-H	–	–
MIL-53	6.3 (298 K)	[77]
MIL-53-TDC	–	–
MIL-100	–	–

[a] Visually read from a figure in the referenced literature.

Table 3. SO_2/CO_2 IAST selectivities at 293 K of aluminum MOFs.

MOF	IAST selectivity at SO_2/CO_2 molar ratio			Ref.
	0.01	0.1	0.5	
CAU-23 (Toth)	34	34	48	our work
CAU-23 (DSLAI Sips)	27	28	28	our work
Alfum	34	35	36	[38]
MIL-160	–	–	126	[59]
CAU-10-H	29	27	25	[38]
MIL-53	17	22	43	[38]
MIL-53-TDC	24	48	83	[38]
MIL-100	17	18	38	[38]

48 and 28 at 0.5. Especially the values at a molar ratio of 0.5 are quite different, which could be related to the low R^2 value of 0.989625 for the Toth fitting of SO_2 (cf. Table S15).

The increase in IAST selectivity, simulated with the Toth model, is also observed for comparable, other structurally similar Al-MOFs in the literature.[38] MIL-53 is a MOF with an even steeper increase of the SO_2/CO_2 IAST selectivity. The calculated IAST selectivity with the DSLAI Sips model has no significant variation over the whole molar fraction range and remains steady around 27–28. Depending on the used model, CAU-23 is in the middle or the higher range of IAST selectivities for Al-MOFs, but compared to MIL-53 or MIL-100 it has a higher selectivity at low molar ratios or low SO_2 pressures (Table 3). This is an important aspect in considering to use MOFs in a possible technical adsorptive desulfurization application, because they may probably be aimed to remove low SO_2 concentrations from $N_2/CO_2/SO_2$ gas mixtures, that is the selective adsorption of SO_2 traces below 500 ppm (low partial pressure, $p < 0.01$ bar).

In comparison with zirconium MOFs CAU-23 has similar selectivity values to, for example, DUT-67 and NU-1000, but lower than Zrfum and MOF-808.[38] Zr-MOFs are frequently investigated for applications due to their high hydrothermal stabilities.

Conclusions

CAU-23 is one of the least studied Al-MOFs. Within this study, different gas sorption properties of CAU-23 were examined and the isosteric enthalpy of adsorption and IAST selectivites were calculated from the single-gas adsorption isotherms. The gas uptake of CAU-23 was compared with literature data. Furthermore high-pressure CO_2 sorption was performed up to 20 bar and compared with the polymorph MIL-53-TDC. CAU-23 shows promising properties in gas separation of SO_2 and CO_2, as well as in high pressure CO_2 sorption. With its high water stability, CAU-23 is an interesting MOF for possible technical applications.

Experimental Section

Materials and Methods

All chemicals were used as received from the suppliers (see section S1, Table S1 in the SI†).

Powder X-ray diffraction (PXRD) patterns were obtained at ambient temperature on a Bruker D2 phaser (Bruker AXS, Karlsruhe, Germany) using Cu–Kα radiation ($\lambda = 1.54182$ Å) between $5° < 2\Theta < 50°$ with a scanning rate of 0.0125°/s (300 W, 30 kV, 10 mA). The diffractograms were obtained on a flat "low background sample holder", where at low angle the beam spot is strongly broadened so that only a fraction of the reflected radiation reaches the detector, hence the relative intensities measured at $2\Theta < 7°$ are low. Analyses of the diffractograms were carried out with Match 3.1.0 software.

Karl-Fischer-titrations were carried out on an ECH AQUA 40.00 (ECH, Halle (Saale), Germany) with repeated determinations. Elemental analysis was acquired on a vario MICRO cube (Elementar Analysensysteme, Langenselbold, Germany). Thermogravimetric analyses (TGA) were carried out on a Netzsch TG209 F3 Tarsus (Netzsch, Selb, Germany) device under nitrogen atmosphere with a heating rate of 5 $Kmin^{-1}$ to the target temperature of 600 °C. Infrared (IR) spectra were acquired on a Bruker Tensor 37 FT-IR device (Bruker AXS, Karlsruhe, Germany) as KBr pellets in the range of 4000–400 cm^{-1}. Scanning electron microscopy (SEM) images were recorded on a JEOL JSM-6510 Advanced electron microscope (Jeol, Akishima, Japan) with a LaB_6 cathode at 5–20 keV. The microscope was equipped with an Xflash 410 (Bruker AXS, Karlsruhe, Germany) silicon drift detector for energy dispersive X-ray spectroscopy (EDX).

Brunauer-Emmett-Teller surface areas (S_{BET}) were determined by nitrogen (purity 99.999 %, 5.0) sorption experiments at 77 K using liquid nitrogen cooling on a Quantachrome NOVA-4200e instrument (Quantachrome, Odelzhausen, Germany) within a partial pressure range of $10^{-3} < p/p_0^{-1} < 1$ and also on a Quantachrome Autosorb iQ MP instrument (Quantachrome, Odelzhausen, Germany) within a partial pressure range of $10^{-7} < p/p_0^{-1} < 1$. The samples were degassed under vacuum ($p < 10^{-2}$ mbar) at 150 °C for ca. 3 h, prior to measurement. The gas uptake values are given @STP, that is at a standard temperature of 0 °C (although the manifold is maintained well above this temperature) and a pressure of 760 Torr (1 atm) with the associated molar volume for an ideal gas of 22.414 L.[78]

Argon (purity 99.999 %, 5.0) sorption experiments were performed at 87 K using a Quantachrome CryoCooler (Quantachrome, Odelzhausen, Germany) for appropriate adjustment of 87 K on a Quantachrome Autosorb iQ MP instrument (Quantachrome, Odelzhausen, Germany) within a partial pressure range of $10^{-7} < p/p_0^{-1} < 1$. Activation was achieved under vacuum ($p < 10^{-5}$ mbar) at 150 °C for ca. 3 h. Carbon dioxide (purity 99.995 %, 4.5) sorption isotherms were collected using an ASAP 2020 automatic gas sorption analyzer (Micromeritics, Aachen, Germany) with oil-free vacuum pumps (ultimate pressure $p/p_0^{-1} = 10^{-8}$). The temperatures were set with dry ice/acetone (195 K), water/ice (273 K) and water (293 K). Samples were activated under vacuum ($p < 10^{-3}$ mbar) at 150 °C for ca. 3 h before the measurement. Hydrogen (purity 99.999 %, 5.0) sorption experiments were carried on the Quantachrome Autosorb iQ MP using the CryoCooler for thermostating, except for 77 K where liquid nitrogen was used. H_2 sorption was performed within the partial pressure range of $10^{-7} < p/p_0^{-1} < 1$. Sample were degassed under vacuum ($p < 10^{-5}$ mbar) at 150 °C for ca. 3 h. Methane (purity 99.995 %, 4.5) isotherms were collected using the ASAP 2020. Sample were activated under vacuum ($p/p_0^{-1} < 10^{-3}$ mbar) at 150 °C for ca. 3 h.

Sulfur dioxide (purity 99.999%, 5.0) sorption experiments were performed at 263 K (boiling point of SO_2, set with the CryoCooler), at 273 K (water/ice bath) and at 293 K (water bath) on the Autosorb iQ MP within the partial pressure range of $10^{-5} < pp_0^{-1} < 1$. Activation was done under vacuum ($p < 10^{-5}$ mbar) at 150 °C for ca. 3 h. SO_2-sorption experiments were prone to limitations from the corrosive nature of SO_2. The uninterrupted measurement time on the device was limited to 10 h for safety precautions to prevent damage to the seals.[38,59,66] At 263 K (boiling/condensation point of SO_2 at 1 bar) and above 600 Torr condensation of SO_2 in the sample tube takes place. For the Viton® gaskets in the Autosorb iQ MP device, each SO_2-sorption run had to be completed within a maximum time of 10 h after which the system had to be flushed with N_2 for regeneration (see ref. [79] for the chemical compatibility of Viton® gaskets). The time limit was recommended by Quantachrome to prevent damage to the gaskets due to irreversible swelling, which could cause leaks in the system. Then, after flushing the gas line with N_2 several times the line remained under N_2 atmosphere for at least 12 h to regenerate the gaskets. For long equilibration times during adsorption and desorption the adsorption data points were still collected as complete as possible with long-enough equilibration times but for desorption fewer data points could then be measured. This compromise then led to incomplete, i.e. not-closed desorption branches, due to the safety precautions.

The device for high pressure CO_2 uptake (HP-CO_2) studies was an IsoSORB Static (G-HP) (Rubotherm, Bochum – Germany). The measurements were performed at 293 K and up to 20 bar. The measurements were done gravimetrically and the blank measurements were made with helium. The mass change was measured with a magnetic suspension balance (resolution 0.01 mg; reproducibility, i.e. standard deviation 0.03 mg) between 0–20 bar.

Acknowledgements

The authors gratefully acknowledge the financial support of the Federal German Ministry of Education and Research (BMBF) in the project Optimat under grant no. 03SF0492C. The authors thank Marcus Fetzer and Alex Spieß for providing the MOF materials (MIL-100 and CAU-10-H) for the comparative hydrogen sorption measurements. Open Access funding enabled and organized by Projekt DEAL.

Conflict of Interest

The authors declare no conflict of interest.

Data Availability Statement

The data that support the findings of this study are available from the corresponding author upon reasonable request.

Keywords: Aluminum MOFs · CAU-23 · Gas sorption · Enthalpy of adsorption · Gas separation

[1] S. R. Batten, N. R. Champness, X.-M. Chen, J. Garcia-Martinez, S. Kitagawa, L. Öhrström, M. O'Keeffe, M. Paik Suh, J. Reedijk, *Pure Appl. Chem.* **2013**, *85*, 1715–1724.
[2] C. Janiak, J. K. Vieth, *New J. Chem.* **2010**, *34*, 2366–2388.
[3] Z. Chen, M. C. Wasson, R. J. Drout, L. Robison, K. B. Idrees, J. G. Knapp, F. A. Son, X. Zhang, W. Hierse, C. Kühn, S. Marx, B. Hernandez, O. K. Farha, *Faraday Discuss.* **2021**, *225*, 9–69.
[4] H. Wu, Q. Gong, D. H. Olson, J. Li, *Chem. Rev.* **2012**, *112*, 836–868.
[5] J. Li, P. M. Bhatt, J. Li, M. Eddaoudi, Y. Liu, *Adv. Mater.* **2020**, *32*, 1–18.
[6] T. Xu, L. Fan, Z. Jiang, P. Zhou, Z. Li, H. Lu, Y. He, *Dalton Trans.* **2020**, *49*, 7174–7181.
[7] H. Chen, X. Li, M. Liu, Y. Zhang, Y. Liu, H.-M. Wen, *Z. Anorg. Allg. Chem.* **2021**, *647*, 1250–1253.
[8] X.-W. Gu, J.-X. Wang, E. Wu, H. Wu, W. Zhou, G. Qian, B. Chen, B. Li, *J. Am. Chem. Soc.* **2022**, *144*, 2614–2623.
[9] L. Zhang, K. Jiang, L. Yang, L. Li, E. Hu, L. Yang, K. Shao, H. Xing, Y. Cui, Y. Yang, B. Li, B. Chen, G. Qian, *Angew. Chem. Int. Ed.* **2021**, *60*, 15995–16002.
[10] F. N. Al-Rowaili, A. Jamal, M. S. Ba Shammakh, A. Rana, *ACS Sustainable Chem. Eng.* **2018**, *6*, 15895–15914.
[11] R.-J. Li, Y.-F. Qi, Q. Wang, J.-J. Wang, Z.-Y. Liu, X.-G. Wang, X.-J. Zhao, E.-C. Yang, *Z. Anorg. Allg. Chem.* **2020**, *646*, 1412–1418.
[12] Y. Liu, X.-Y. Xie, C. Cheng, Z.-S. Shao, H.-S. Wang, *J. Mater. Chem. C* **2019**, *7*, 10743–10763.
[13] J. Chen, T. Chen, S. Xiang, J. Zhang, Z. Zhang, *Z. Anorg. Allg. Chem.* **2021**, *647*, 1301–1304.
[14] Y. Li, Y. Zhao, W. Zhang, K. Shao, H. Zhou, *Z. Anorg. Allg. Chem.* **2021**, *647*, 1091–1095.
[15] L. Sun, M. G. Campbell, M. Dincă, *Angew. Chem. Int. Ed.* **2016**, *55*, 3566–3579; *Angew. Chem.* **2016**, *128*, 3628–3642.
[16] M. Rubio-Martinez, C. Avci-Camur, A. W. Thornton, I. Imaz, D. Maspoch, M. R. Hill, *Chem. Soc. Rev.* **2017**, *46*, 3453–3480.
[17] S. Leubner, H. Zhao, N. van Velthoven, M. Henrion, H. Reinsch, D. E. de Vos, U. Kolb, N. Stock, *Angew. Chem. Int. Ed.* **2019**, *58*, 10995–11000; *Angew. Chem.* **2019**, *131*, 11111–11116.
[18] N. Tannert, S. Gökpinar, E. Hastürk, S. Nießing, C. Janiak, *Dalton Trans.* **2018**, *47*, 9850–9860.
[19] A. Martinez Joaristi, J. Juan-Alcañiz, P. Serra-Crespo, F. Kapteijn, J. Gascon, *Cryst. Growth Des.* **2012**, *12*, 3489–3498.
[20] Y.-R. Lee, J. Kim, W.-S. Ahn, *Korean J. Chem. Eng.* **2013**, *30*, 1667–1680.
[21] N. Stock, S. Biswas, *Chem. Rev.* **2012**, *112*, 933–969.
[22] A. J. Rieth, A. M. Wright, M. Dincă, *Nat. Rev. Mater.* **2019**, *4*, 708–725.
[23] L. Helm, A. E. Merbach, *Coord. Chem. Rev.* **1999**, *187*, 151–181.
[24] L. Helm, G. M. Nicolle, A. E. Merbach, *Adv. Inorg. Chem.* **2005**, *57*, 327–379.
[25] S. E. Lincoln, *Helv. Chim. Acta* **2005**, *88*, 523–545.
[26] F. Jeremias, D. Fröhlich, C. Janiak, S. K. Henninger, *RSC Adv.* **2014**, *4*, 24073–24082.
[27] D. Fröhlich, S. K. Henninger, C. Janiak, *Dalton Trans.* **2014**, *43*, 15300–15304.
[28] F. Jeremias, A. Khutia, S. K. Henninger, C. Janiak, *J. Mater. Chem.* **2012**, *22*, 10148–10151.
[29] A. Samokhvalov, *Coord. Chem. Rev.* **2018**, *374*, 236–253.
[30] T. Loiseau, C. Serre, C. Huguenard, G. Fink, F. Taulelle, M. Henry, T. Bataille, G. Férey, *Chem. Eur. J.* **2004**, *10*, 1373–1382.
[31] C. Kiener, U. Müller, M. Schubert, Germany Pat. WO2007/118841 A2, BASF SE, **2007**.
[32] C. Kiener, U. Müller, M. Schubert, US Pat. 12/297,666, BASF SE, **2012**.
[33] E. Leung, U. Müller, N. Trukhan, H. Mattenheimer, G. Cox, US Pat. 13/249,943, BASF SE, **2012**.
[34] H. Reinsch, M. A. van der Veen, B. Gil, B. Marszalek, T. Verbiest, D. de Vos, N. Stock, *Chem. Mater.* **2013**, *25*, 17–26.
[35] A. Cadiau, J. S. Lee, D. D. Borges, P. Fabry, T. Devic, M. T. Wharmby, C. Martineau, D. Foucher, F. Taulelle, C.-H. Jun, Y. K.

Hwang, N. Stock, M. F. De Lange, F. Kapteijn, J. Gascon, G. Maurin, J.-S. Chang, C. Serre, *Adv. Mater.* **2015**, *27*, 4775–4780.
[36] M. Gaab, N. Trukhan, S. Maurer, R. Gummaraju, U. Müller, *Microporous Mesoporous Mater.* **2012**, *157*, 131–136.
[37] D. Fröhlich, E. Pantatosaki, P. D. Kolokathis, K. Markey, H. Reinsch, M. Baumgartner, M. A. van der Veen, D. E. de Vos, N. Stock, G. K. Papadopoulos, S. K. Henninger, C. Janiak, *J. Mater. Chem. A* **2016**, *4*, 11859–11869.
[38] P. Brandt, S.-H. Xing, J. Liang, G. Kurt, A. Nuhnen, O. Weingart, C. Janiak, *ACS Appl. Mater. Interfaces* **2021**, *13*, 29137–29149.
[39] K. Brandenburg, Diamond 4.6.6, Crystal and Molecular Structure Visualization, Crystal Impact – K. Brandenburg GbR, Bonn, Germany, 1997–2021.
[40] C. B. L. Tschense, N. Reimer, C.-W. Hsu, H. Reinsch, R. Siegel, W.-J. Chen, C.-H. Lin, A. Cadiau, C. Serre, J. Senker, N. Stock, *Z. Anorg. Allg. Chem.* **2017**, *643*, 1600–1608.
[41] N. Tannert, C. Jansen, S. Nießing, C. Janiak, *Dalton Trans.* **2019**, *48*, 2967–2976.
[42] G. A. González-Martínez, T. Jurado-Vázquez, D. Solís-Ibarra, B. Vargas, E. Sánchez-González, A. Martínez, R. Vargas, E. González-Zamora, I. A. Ibarra, *Dalton Trans.* **2018**, *47*, 9459–9465.
[43] A. López-Olvera, J. A. Zárate, E. Martínez-Ahumada, D. Fan, M. L. Díaz-Ramírez, P. A. Sáenz-Cavazos, V. Martis, D. R. Williams, E. Sánchez-González, G. Maurin, I. A. Ibarra, *ACS Appl. Mater. Interfaces* **2021**, *13*, 39363–39370.
[44] D. Lenzen, J. Zhao, S.-J. Ernst, M. Wahiduzzaman, A. Ken Inge, D. Fröhlich, H. Xu, H.-J. Bart, C. Janiak, S. Henninger, G. Maurin, X. Zou, N. Stock, *Nat. Commun.* **2019**, *10*, 3025.
[45] C. Schlüsener, D. N. Jordan, M. Xhinovci, T. J. Matemb Ma Ntep, A. Schmitz, B. Giesen, C. Janiak, *Dalton Trans.* **2020**, *49*, 7373–7383.
[46] Y. Ye, S. Xian, H. Cui, K. Tan, L. Gong, B. Liang, T. Pham, H. Pandey, R. Krishna, P. C. Lan, K. A. Forrest, B. Space, T. Thonhauser, J. Li, S. Ma, *J. Am. Chem. Soc.* **2022**, *144*, 1681–1689.
[47] P. Kanoo, S. K. Reddy, G. Kumari, R. Haldar, C. Narayana, S. Balasubramanian, T. K. Maji, *Chem. Commun.* **2012**, *48*, 8487–8489.
[48] J. A. Coelho, A. M. Ribeiro, A. F. P. Ferreira, S. M. P. Lucena, A. E. Rodrigues, D. C. S. D. Azevedo, *Ind. Eng. Chem. Res.* **2016**, *55*, 2134–2143.
[49] D. Shade, B. Marszalek, K. S. Walton, *Adsorption* **2021**, *27*, 227–236.
[50] J. Pei, H.-M. Wen, X.-W. Gu, Q.-L. Qian, Y. Yang, Y. Cui, B. Li, B. Chen, G. Qian, *Angew. Chem. Int. Ed.* **2021**, *60*, 25068–25074.
[51] P. Rallapalli, K. P. Prasanth, D. Patil, R. S. Somani, R. V. Jasra, H. C. Bajaj, *J. Porous Mater.* **2011**, *18*, 205–210.
[52] S. Bourrelly, P. L. Llewellyn, C. Serre, F. Millange, T. Loiseau, G. Férey, *J. Am. Chem. Soc.* **2005**, *127*, 13519–13521.
[53] T. J. Matemb Ma Ntep, W. Wu, H. Breitzke, C. Schlüsener, B. Moll, L. Schmolke, G. Buntkowsky, C. Janiak, *Aust. J. Chem.* **2019**, *72*, 835.
[54] Z. Huang, P. Hu, J. Liu, F. Shen, Y. Zhang, K. Chai, Y. Ying, C. Kang, Z. Zhang, H. Ji, *Sep. Purif. Technol.* **2022**, *286*, 120446.
[55] M. M. Sadiq, M. Rubio-Martinez, F. Zadehahmadi, K. Suzuki, M. R. Hill, *Ind. Eng. Chem. Res.* **2018**, *57*, 6040–6047.
[56] M. Thommes, K. Kaneko, A. V. Neimark, J. P. Olivier, F. Rodriguez-Reinoso, J. Rouquerol, S. W. Sing, *Pure Appl. Chem.* **2015**, *87*, 1051–1069.
[57] P. Brandt, A. Nuhnen, S. Öztürk, G. Kurt, J. Liang, C. Janiak, *Adv. Sustainable Syst.* **2021**, *5*, 2000285.
[58] Q.-Y. Yang, P. Lama, S. Sen, M. Lusi, K.-J. Chen, W.-Y. Gao, M. Shivanna, T. Pham, N. Hosono, S. Kusaka, J. J. Perry, S. Ma, B. Space, L. J. Barbour, S. Kitagawa, M. J. Zaworotko, *Angew. Chem. Int. Ed.* **2018**, *57*, 5684–5689; *Angew. Chem.* **2018**, *130*, 5786–5791.
[59] P. Brandt, A. Nuhnen, M. Lange, J. Möllmer, O. Weingart, C. Janiak, *ACS Appl. Mater. Interfaces* **2019**, *11*, 17350–17358.
[60] A. López-Olvera, J. A. Zárate, E. Martínez-Ahumada, D. Fan, M. L. Díaz-Ramírez, P. A. Sáenz-Cavazos, V. Martis, D. R. Williams, E. Sánchez-González, G. Maurin, I. A. Ibarra, *ACS Appl. Mater. Interfaces* **2021**, *13*, 39363–39370.
[61] D. Liu, L. Yan, L. Li, X. Gu, P. Dai, L. Yang, Y. Liu, C. Liu, G. Zhao, X. Zhao, *CrystEngComm.* **2018**, *20*, 2102–2111.
[62] D. Damasceno Borges, P. Normand, A. Permiakova, R. Babarao, N. Heymans, D. S. Galvao, C. Serre, G. de Weireld, G. Maurin, *J. Phys. Chem. C* **2017**, *121*, 26822–26832.
[63] A. D. Wiersum, C. Giovannangeli, D. Vincent, E. Bloch, H. Reinsch, N. Stock, J. S. Lee, J.-S. Chang, P. L. Llewellyn, *ACS Comb. Sci.* **2013**, *15*, 111–119.
[64] J. H. Cavka, C. A. Grande, G. Mondino, R. Blom, *Ind. Eng. Chem. Res.* **2014**, *53*, 15500–15507.
[65] A. Nuhnen, C. Janiak, *Dalton Trans.* **2020**, *49*, 10295–10307.
[66] S. Xing, J. Liang, P. Brandt, F. Schäfer, A. Nuhnen, T. Heinen, I. Boldog, J. Möllmer, M. Lange, O. Weingart, C. Janiak, *Angew. Chem. Int. Ed.* **2021**, *60*, 17998–18005.
[67] M. Wahiduzzaman, D. Lenzen, G. Maurin, N. Stock, M. T. Wharmby, *Eur. J. Inorg. Chem.* **2018**, 3626–3632.
[68] W. Fan, Y. Ying, S. B. Peh, H. Yuan, Z. Yang, Y. D. Yuan, D. Shi, X. Yu, C. Kang, D. Zhao, *J. Am. Chem. Soc.* **2021**, *143*, 17716–17723.
[69] H. R. Abid, Z. H. Rada, J. Shang, S. Wang, *Polyhedron* **2016**, *120*, 103–111.
[70] F. M. Baena-Moreno, E. le Saché, L. Pastor-Pérez, T. R. Reina, *Environ. Chem. Lett.* **2020**, *18*, 1649–1658.
[71] Y. Zhang, J. Sunarso, S. Liu, R. Wang, *Int. J. Greenhouse Gas Control* **2013**, *12*, 84–107.
[72] L. Zhang, L. Xiao, Y. Zhang, L. J. France, Y. Yu, J. Long, D. Guo, X. Li, *Energy Fuels* **2018**, *32*, 678–687.
[73] M. A. Hanif, N. Ibrahim, A. Abdul Jalil, *Environ. Sci. Pollut. Res. Int.* **2020**, *27*, 27515–27540.
[74] N. F. Cessford, N. A. Seaton, T. Düren, *Ind. Eng. Chem. Res.* **2012**, *51*, 4911–4921.
[75] J. Tóth, *Adv. Colloid Interface Sci.* **1995**, *55*, 1–239.
[76] Ü. Kökçam-Demir, A. Goldman, L. Esrafili, M. Gharib, A. Morsali, O. Weingart, C. Janiak, *Chem. Soc. Rev.* **2020**, *49*, 2751–2798.
[77] S. Kavak, H. M. Polat, H. Kulak, S. Keskin, A. Uzun, *Chem. Asian J.* **2019**, *14*, 3655–3667.
[78] K. D. Hammond, W. C. Conner Jr., *Adv. Catal.* **2013**, *56*, 1–101.
[79] https://www.coleparmer.com/masterflex-tubing-chemical-compatibility, retrieved July 20rd **2022**. Select "Material Compatibility", 1. Material: Select "Viton", 2. Chemical: Select "Sulfurous acid", then click "view compatibility"..

Manuscript received: May 10, 2022
Revised manuscript received: June 30, 2022
Accepted manuscript online: July 10, 2022

Zeitschrift für anorganische und allgemeine Chemie

Supporting Information

Unravelling gas sorption in the aluminum metal-organic framework CAU-23: CO_2, H_2, CH_4, SO_2 sorption isotherms, enthalpy of adsorption and mixed-adsorptive calculations

Christian Jansen, Niels Tannert, Dirk Lenzen, Marco Bengsch, Simon Millan, Anna Goldman, Dustin Nils Jordan, Linda Sondermann, Norbert Stock, and Christoph Janiak*

Supporting Information (SI)

Unravelling gas sorption in the aluminum metal-organic framework CAU-23: CO_2, H_2, CH_4, SO_2 sorption isotherms, enthalpy of adsorption and mixed-adsorptive calculations

Christian Jansen[a], Niels Tannert[a], Dirk Lenzen[b], Marco Bengsch[a], Simon Millan[a], Anna Goldmann[a], Dustin Nils Jordan[a], Linda Sondermann[a], Norbert Stock[b] and Christoph Janiak*[a]

[a] *Institut für Anorganische Chemie und Strukturchemie, Heinrich-Heine-Universität Düsseldorf, Universitätsstraße 1, 40225 Düsseldorf, Germany. *E-mail: Janiak@uni-duesseldorf.de*

[b] *Institut für Anorganische Chemie, Christian-Albrechts-Universität Kiel, Max-Eyth-Straße 2, 24118 Kiel, Germany. *E-mail: stock@ac.uni-kiel.de*

Emails: Christian.Jansen@hhu.de, tannert@hhu.de, dirk_lenzen@web.de, marco.bengsch@hhu.de, simon.millan@mail.com, Anna.Goldman@uni-duesseldorf.de, Dustin.Jordan@uni-duesseldorf.de, linda.sondermann@hhu.de, stock@ac.uni-kiel.de, Janiak@uni-duesseldorf.de

Table of Contents

S1 Materials and equipment

All chemicals were used as received from the supplier (Table S1).

Table S1. *Used chemicals, supplier and purities.*

Chemical	Supplier	Purity
Acetone	Sigma Aldrich	>99.5%
$AlCl_3 \cdot 6\ H_2O$	Janssen Chimica	99%
$Al(OH)(acetate)_2 \cdot x\ H_2O$	AlfaAesar	not specified
$Al(SO)_4 \cdot 18H_2O$	AppliChem	not specified
Diethylether	Riedel de Haën	99.8%
Dimethylformamide	Fischer Chemicals	99.99%
Ethanol	Chem Solute	99.9%
Hydrochloric acid, 37%	Sigma Aldrich	37%
$NaAlO_2$	VWR Chemicals	not specified
NaOH (microgranulate)	Chem Solute	not specified
Tetrahydrofuran	Riedel de Haën	p.a.
2,5-thiophenedicarboxylic acid, H_2TDC	TCI	>98%

The used water was de-ionized *via* ion exchange.

Synthesis

CAU-23

CAU-23 was synthesized identically as reported by Lenzen *et al.* in 2019.[1]
The amount of 4.30 g H_2TDC (25 mmol) was mixed with 2.0 g (50 mmol) sodium hydroxide in 100 mL of deionized water until a clear solution of Na_2TDC was obtained. After adding 18.75 mL of aqueous aluminum chloride solution (1 mol L^{-1}, 18.75 mmol), and 12.5 mL of aqueous sodium aluminate solution (0.5 mol L^{-1}, 6.25 mmol), the slurry was stirred under reflux conditions for 6 h, and then filtered off and dried at 100 °C for 4 h. After an additional washing step with 200 mL of water under stirring and reflux, filtration and drying, 4.5 g of a white powder was obtained (84 % yield based on H_2TDC).

Using identical synthesis conditions, Schlüsener observed the occurrence of a non-porous phase.[2] This phase occurs after longer reaction times (> 24 h) or prolonged washing (under reflux). It appears that CAU-23 is the kinetic product and the non-porous phase is the thermodynamic reaction product.

To achieve a better understanding of the formation of CAU-23 we carried out these synthesis variations:

- the aluminum source was varied (Table S2, Table S4),

- the synthesis time was varied (24 h instead of 6 h, Table S5),

- the washing time and solvent was varied and second and third step was added, due two the RT conditions for the washing, instead of the reflux conditions (Table S5).

Synthesis variations were done with the following procedure:
Amounts in the range of 3.0 - 5.0 mmol of H_2TDC and 3.0 - 5.7 mmol of either $AlCl_3 \cdot 6\ H_2O$, $Al_2(SO_4)_3 \cdot 18\ H_2O$, $Al(OH)(ac)_2 \cdot x\ H_2O$ or $AlCl_3/NaAlO_2$ were refluxed (100 °C) with 15 - 40 mL of water for 24 h, instead of 6 h. The stoichiometric addition of NaOH (2 eq) for the deprotonation of H_2TDC was omitted in the case of $Al(OH)(ac)_2$. The precipitate was recovered by centrifugation, consecutively washed and re-dispersed in water (two times, 50 mL each, RT). A third (instead of one one additional) washing step was applied by stirring in water (50 mL, 24 h, RT). After final

centrifugation and decantation, the product was dried under reduced pressure (24 h, 80 °C, 50 mbar). All products were obtained as white powders. Table S2 summarizes the aluminum reactand amounts, the yields and concomitant BET surface areas.

Variation of the aluminum starting material together with the increase of synthesis time and a third washing step did not improve the porosity. Only the basic aluminum acetate $Al(OH)(ac)_2 \cdot x\ H_2O$ came close in the BET surface area to $AlCl_3/NaAlO_2$ used by Lenzen *et al.* (Table S2, Table S4)

PXRD and sorption studies suggest the formation of a non-porous phase as side product (Figure S2, Table S5) upon variation of the reaction conditions.

Table S2. *Synthesis results of CAU-23 syntheses using different aluminum sources.*

Al-source (reaction time)	**Reactant [g][a]**	**Yield [g]**	**Yield [%]**	**BET [m^2g^{-1}][b]**
$Al(OH)(ac)_2 \cdot x\ H_2O$ (24 h)	1.0344	1.053	88	1027
$AlCl_3/NaAlO_2$ (24 h)	0.4830/0.0819	0.557	78	686
$AlCl_3 \cdot 6\ H_2O$ (24 h)	0.7216	0.417	58	201
$Al_2(SO_4)_3 \cdot 18H_2O$ (24 h)	2.0003	0.732	102*	19
$AlCl_3/NaAlO_2$ (6 h)[1]	4.527/0.512	4.5	84	1176

[a] The amounts of $Al(OH)(ac)_2 \cdot x\ H_2O$ and $NaAlO_2$ were adjusted for the water content which was determined by Karl-Fischer titrations. [b] Determined from five points of the nitrogen sorption isotherms. * Yield > 100%, based on theoretical yield and sum formula of CAU-23. As PXRD shows, the phase is not (only) CAU-23 but a non-porous product.

MIL-53-TDC

MIL-53-TDC was synthesized, according to Tannert *et al.*[3] Approximately 5.0 mmol (0.8608 g) of 2,5-thiophenedicarboxylic acid (H2TDC) and 5.7 mmol (3.7984 g) of $Al_2(SO4)_3 \cdot 18\ H2O$ were refluxed (24 h, 135 °C) with 32 mL of water and 8 mL of dimethylformamide (DMF). The precipitate was recovered by centrifugation, consecutively washed and re-dispersed in water (three times, 100 mL each). A fourth washing step was applied by further stirring in water (100 mL, 24 h). After final centrifugation and decantation, the product was dried under reduced pressure (24 h, 80 °C, 50 mbar).

other Al-MOFs

The other Al-MOFs, which where used for gas sorption studies were synthesized according to the following literature procedures. Only if the literature syntheses have been modified, it is briefly stated below. Otherwise, the synthesis routes and the batch sizes were taken exactly from the literature.

Alfum was received from BASF, known as Basolite® A520.[4]
MIL-160 was synthesized according to the literature of Cadiau *et al.* with twice the amount of NaOH, compared to the ligand.[5]
CAU-10-H was synthesized according to Fröhlich *et al.*[6]
MIL-53 was synthesized according to Zi *et al.*[7]
MIL-53-TDC was synthesized like above described.[3]
MIL-100 was synthesized according to Qiu *et al.*[8]

Powder X-ray diffraction (PXRD)

PXRD of CAU-23 and the simulation and all PXRDs from CAU-23 of varying Al-sources.

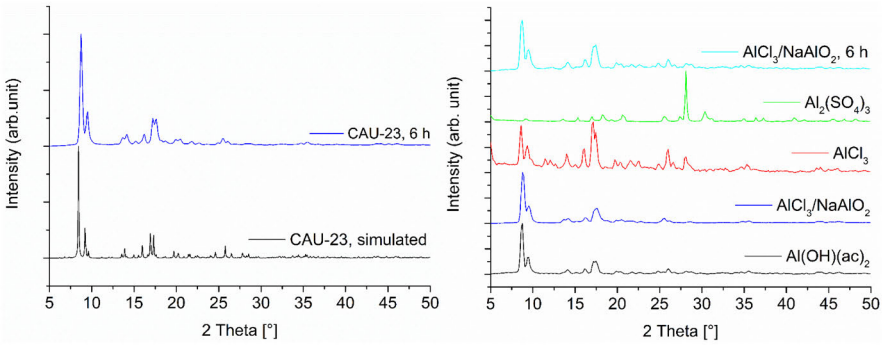

Figure S1. *PXRD of CAU-23 synthesized via Lenzen et al. in comparison with the simulated powder pattern (CSD-Refcode SUFVOH)(left) and PXRDs of CAU-23 synthesized with different Al-sources (right).*[1]

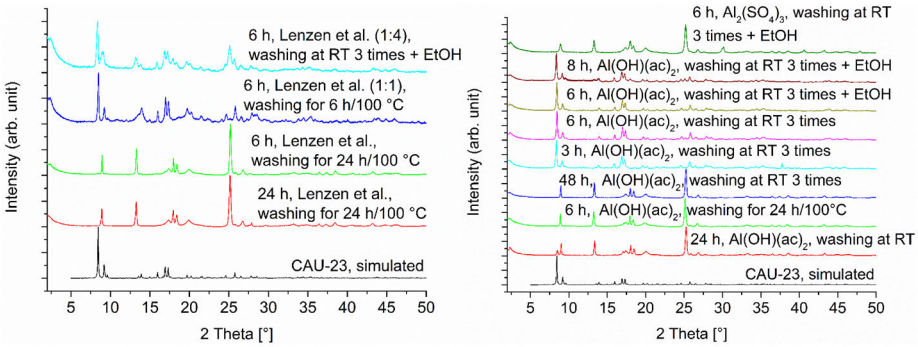

Figure S2. *PXRDs of CAU-23 syntheses according Lenzen et al. using different washing processes or reaction time (24 h instead of 6 h) (left) or with basic aluminum acetate, $Al(OH)(ac)_2$ or aluminum sulfate, $Al_2(SO_4)_3$ (right). The stated time is the reaction time. The simulated CAU-23 pattern is based on CSD-Refcode SUFVOH.*[1]

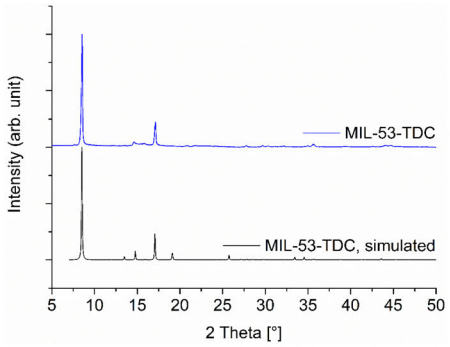

Figure S3. *PXRD of MIL-53-TDC synthesized via Tannert et al.,*[3] *in comparison with the simulated powder pattern (CSD-Refcode LIQWEQ).*[9]

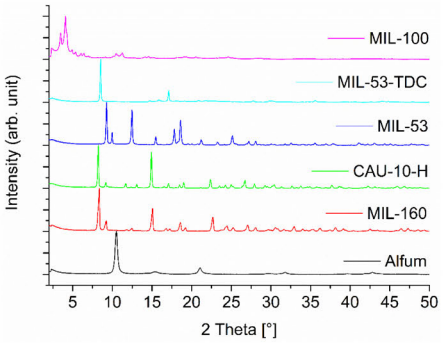

Figure S4. *PXRDs of the different Al-MOFs, which were used for comparison reason (hydrogen sorptions).*

Chemical stability *via* PXRD

In order to check the chemical stability of CAU-23 towards different solvents and pH 1/pH 12 solutions, approximately 10 mg of CAU-23 was suspended in 3 mL solvent each. After 24 h of stirring, the solid was recovered by centrifugation and dried (80 °C, 50 mbar). Subsequent PXRD analyses are illustrated in the Figure S5.
For CAU-23 after pH 12 no PXRD is available, because the MOF was dissolved at this pH.

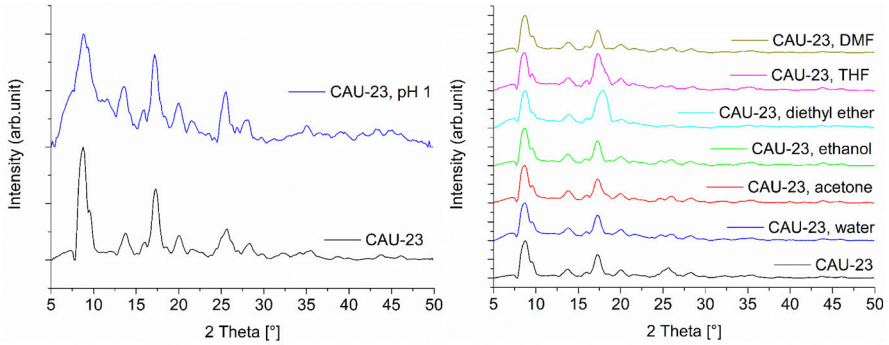

Figure S5. *Chemical stability test of CAU-23 against pH (left) and different solvents (right).*

Figure S6 illustrates the chemical stability of CAU-23 towards the different solvents after checking the remaining BET surface area.

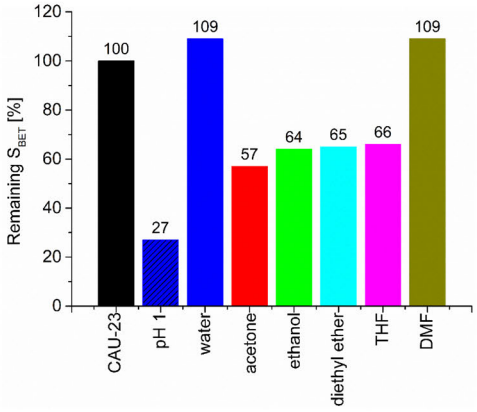

***Figure S6**. Remaining surface area of CAU-23 after treatment with different solvents.*

Karl-Fischer titrations

In order to weigh out the proper stoichiometric amounts of $Al(OH)(ac)_2 \cdot x\ H_2O$ and $NaAlO_2$, which was suspected to contain water too, we carried out Karl-Fischer-titrations. Therefore, $Al(OH)(ac)_2 \cdot x\ H_2O$ (12.90 mg) and $NaAlO_2$ (11.00 mg) were analyzed. The water contents were determined to be 9.82% for $Al(OH)(ac)_2 \cdot x\ H_2O$ and 3.21% for $NaAlO_2$, correlating to formulas of approximately $Al(OH)(ac)_2 \cdot 1\ H_2O$ and $NaAlO_2 \cdot 0.2\ H_2O$. Hence, both molar weights were adjusted and taken into account for calculation of reactant ratios during synthesis optimizations.

Elemental analysis

***Table S3.** Elemental analysis of CAU-23 [$Al(OH)(C_6SO_4H_2)$] obtained from $Al(OH)(ac)_2 \cdot x\ H_2O$.*

Element	Calclulated (+ 1 H_2O) [wt-%]	Found [wt-%]
C	33.65 (31.04)	31.08
H	1.41 (2.17)	1.67
N	0 (0)	0
S	14.97 (13.81)	13.97

The results are in good agreement with the thermogravimetric analysis.

Thermogravimetric analysis (TGA)

Figure S7 shows the TGA curve of CAU-23 synthesized with $Al(OH)(ac)_2 \cdot x\ H_2O$ as metal source and the as synthesized (a. s.) product without purification .

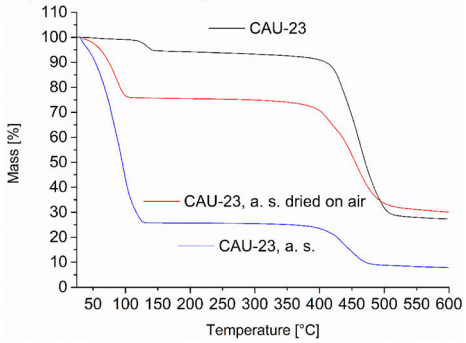

Figure S7. *TGA curve of CAU-23 obtained from $Al(OH)(ac)_2 \cdot x\ H_2O$ and the as-synthesized a. s. product.*

Infrared (IR) spectral analysis

Figure S8 depict the IR spectra of CAU-23 obtained from $Al(OH)(ac)_2 \cdot x\ H_2O$ and the linker H_2TDC. The C-OH bending vibration at 928 cm^{-1} cannot be seen in the MOF (black line), this also speaks for the successful bonding of the carboxylate linker with the aluminum.

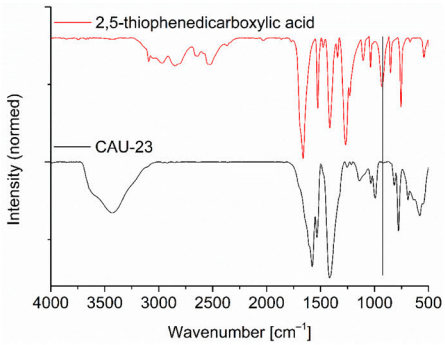

Figure S8. *IR spectra of CAU-23 obtained from $Al(OH)(ac)_2 \cdot x\ H_2O$ (black) and linker H_2TDC (red).*

Scanning electron microscopy (SEM)

SEM images of CAU-23 at different maggnifications.

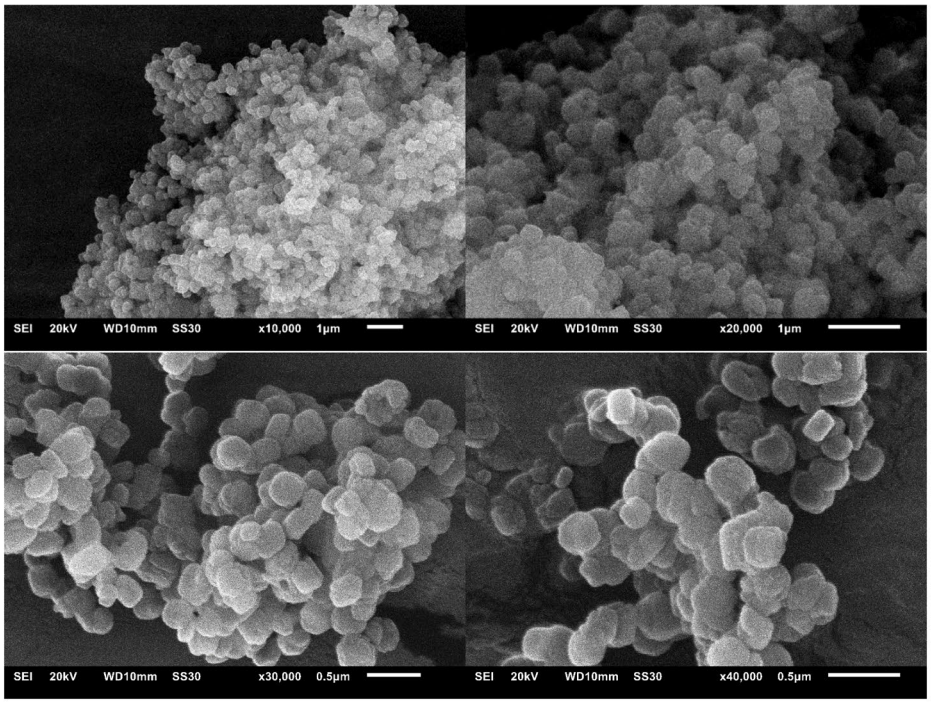

Figure S9. *SEM images of CAU-23 at different magnifications.*

Gas sorption analysis

- **Nitrogen (77 K)**

All surface areas (BET) were calculated from five adsorption points in the pressure range $10^{-4} < pp_0^{-1} < 10^{-2}$, applying Roquerol plots ($r > 0.998$). This range is indeed not recommended by IUPAC (*International Union of Pure and Applied Chemistry*) for BET surface determination, but rather suitable for microporous materials.[10,11,12]

Total pore volumes were calculated from the N_2-sorption isotherm at $p/p_0 = 0.90$ for pore sizes ≤ 20 nm. NLDFT calculations were done with the native *NovaWin 11.03* software using the 'N_2 at 77 K on carbon, slit pore, NLDFT equilibrium' model. Thickness model for calculation of micropore volumes and micropore areas was set to 'De Boer'.

Table S4 sums up the porosity parameters of CAU-23 samples synthesized out of different Al-sources.

Table S4. *Porosity parameters of different CAU-23 samples obtained out of varying Al-sources, determined with nitrogen sorption (77 K) and stated calculation methods.*

Al-source (reaction time)	**S_{BET} [m^2g^{-1}]**[a]	**$S_{BET\ (micro)}$ [m^2g^{-1}]**[b]	**V_{total} [cm^3g^{-1}]**[c]	**V_{micro} [cm^3g^{-1}]**[d]
$Al(OH)(ac)_2 \cdot x\ H_2O$ (24 h)	1027	894	0.46	0.35
$AlCl_3/NaAlO_2$ (24 h)	686	568	0.32	0.22
$AlCl_3 \cdot 6\ H_2O$ (24 h)	201	103	0.18	0.04
$Al_2(SO_4)_3 \cdot 18H_2O$ (24 h)	19	0	0.02	0.00
$AlCl_3/NaAlO_2$ (6 h)	1176	1050	0.51	0.40

[a] Specific surface areas (S_{BET}) were determined by five adsorption points of nitrogen sorption isotherms in the range $10^{-4} < pp_0^{-1} < 10^{-2}$.

[b] Micropore areas were determined by t-plot method with 'De Boer' model in the range $0.2 < pp_0^{-1} < 0.6$.

[c] Total pore volumes (V_{total}) were calculated at $pp_0^{-1} = 0.90$.

[d] Micropore volumes (V_{micro}) were calculated by t-plot method ('De Boer' model).

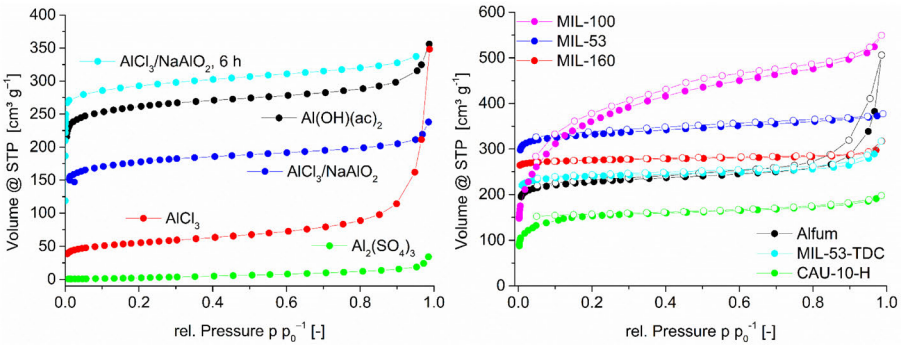

Figure S10. *Nitrogen sorption isotherms for CAU-23 from different Al-sources (left) and the nitrogen sorption isotherms of the comparative Al-MOFs (right).*

Figure S11 presents the different nitrogen sorption isotherms (surface areas Table S5), which are the result of different synthesis time, washing procedures and metal-sources. The formation of a nonporous side phase is promoted by long reaction or washing times.

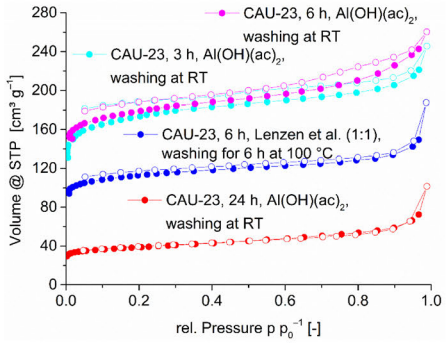

Figure S11. *Nitrogen sorption isotherms of CAU-23 from different syntheses by the route of Lenzen et al.*[1] *or with varying Al-sources for a better understanding of the non-porous side product.*

Table S5. *Surface areas of the different synthesis and washing procedures for CAU-23 and the non-porous side phase.*

Synthesis and washing procedure (synthesis time; route; washing procedure)	**S_{BET} [m^2g^{-1}]**
24 h; $Al(OH)(ac)_2$; washing at RT	145
6 h; Lenzen *et al.* (1:1); washing for 6 h at 100 °C	437
3 h; $Al(OH)(ac)_2$; washing at RT	668
6 h; $Al(OH)(ac)_2$; washing at RT	692

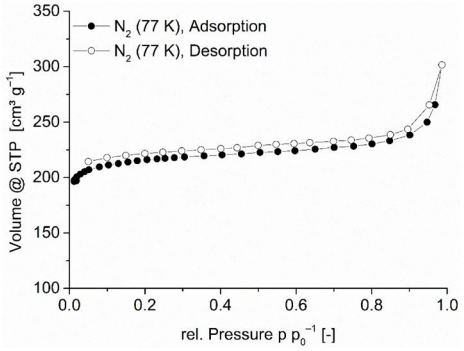

Figure S12. *Nitrogen (77 K) isotherm of MIL-53-TDC.*

Table S6. *Surface area, pore volume and micropore volume determined in this work for the compared Al-MOFs.*

MOF	**S_{BET} [m^2g^{-1}][a]**	**$S_{BET\ (micro)}$ [m^2g^{-1}][b]**	**V_{total} [cm^3g^{-1}][c]**	**V_{micro} [cm^3g^{-1}][d]**
CAU-23	1176	1050	0.51	0.40
Alfum	898	775	0.44	0.30
MIL-160	1106	1061	0.44	0.41
CAU-10-H	575	484	0.28	0.20
MIL-53	1338	1209	0.57	0.52
MIL-53-TDC	973	917	0.41	0.35
MIL-100	1368	613	0.77	0.23

[a] Specific surface areas (S_{BET}) were determined by five adsorption points of nitrogen sorption isotherms in the range $10^{-4} < pp_0^{-1} < 10^{-2}$.

[b] Micropore areas were determined by t-plot method with 'De Boer' model in the range $0.2 < pp_0^{-1} < 0.6$.

[c] Total pore volumes (V_{total}) were calculated at $pp_0^{-1} = 0.90$.

[d] Micropore volumes (V_{micro}) were calculated by t-plot method ('De Boer' model).

- **Argon (87 K)**

All surface areas (BET) were calculated from five adsorption points in the pressure range $0.005 < pp_0^{-1} < 0.01$.

Total pore volumes for pore sizes ≤ 20 nm were calculated from the Ar-sorption isotherm at $p/p_0 = 0.95$. NLDFT calculations were done with the native *NovaWin 11.03* software using the 'Ar at 87 K on carbon, slit pore, NLDFT equilibrium' model. Thickness model for calculation of micropore volumes and micropore areas was set to 'De Boer'.

While nitrogen sorption often overestimates BET areas of (especially micro- to mesoporous) MOFs,[13,14] it determined for the product obtained from the synthesis route with $AlCl_3/NaAlO_2$ (6 h) a specific surface area of $S_{BET} = 1176\ m^2g^{-1}$ and a total pore volume of $V_{total} = 0.51\ cm^3g^{-1}$ at $pp_0^{-1} = 0.90$. Argon sorption revealed a surface area of $S_{BET} = 1097\ m^2g^{-1}$ (1012 m^2g^{-1} by NLDFT), a total pore volume of $V_{total} = 0.44\ cm^3g^{-1}$ at $pp_0^{-1} = 0.95$ and even higher value at $pp_0^{-1} = 0.995$, that is $V_{total} = 0.60\ cm^3g^{-1}$ (0.28 cm^3g^{-1} by NLDFT, carbon, slit pore, argon, 87 K). The micropore volume was calculated to $V_{micro} = 0.38\ cm^3g^{-1}$ (t-plot), correlating to a micropore area of $S_{BET\ (micro)} = 1066\ m^2g^{-1}$. It has to be noted that BET calculation is usually performed in a pressure range $0.05 < pp_0^{-1} < 0.3$, but its applicability also works for microporous materials in a lower range (here: $0.005 < pp_0^{-1} < 0.05$).[10]

Figure S13 depicts nitrogen (77 K) and argon (87 K) sorption isotherms in comparison and nitrogen sorption isotherms for different metal sources.

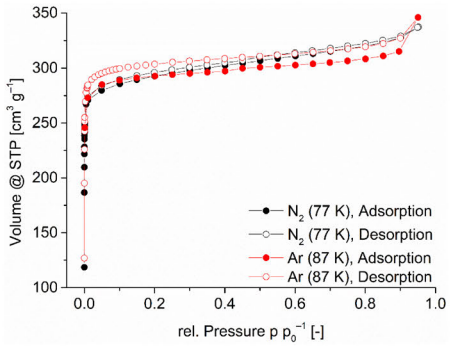

Figure S13. *Nitrogen (77 K) and argon (87 K) isotherms of CAU-23 obtained according to Lenzen et al.*[1]

Table S7 concludes the porosity parameters obtained from nitrogen (77 K) and argon (87 K) sorption data.

Table S7. *Porosity parameters of CAU-23 obtained via the synthesis route with $AlCl_3/NaAlO_2$ (6 h), determined by nitrogen (77 K) and argon (87 K) sorption data.*

Adsorptive	S_{BET} [m^2g^{-1}]	$S_{BET\ (micro)}$ [m^2g^{-1}]	V_{total} [cm^3g^{-1}]	$V_{total\ (NLDFT)}$ [cm^3g^{-1}]	V_{micro} [cm^3g^{-1}]
Nitrogen (77 K)	1176	1050	0.51	0.47	0.40
Argon (87 K)	1097	1066	0.44	0.28	0.38

- **Carbon dioxide (195 K, 273 K, 293 K)**

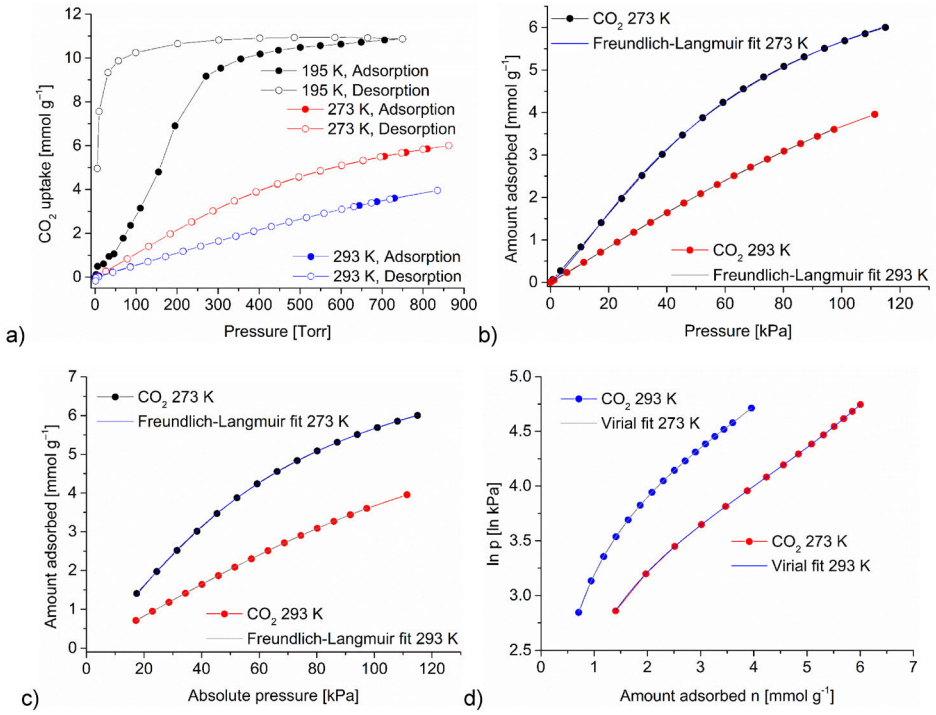

Figure S14. *CO_2 sorption isotherms of CAU-23 obtained via the synthesis route with $AlCl_3$/$NaAlO_2$ (6 h) (a) and the fitted isotherms starting near 0 kPa (b). (c,d) Fitted isotherms starting at 17 kPa: Freundlich-Langmuir (c) and virial (d).*

Table S8 shows carbon dioxide sorption data of CAU-23 from the synthesis route with $AlCl_3$/$NaAlO_2$ (6 h) at different temperatures. The CO_2 capacity of CAU-23 appears to be remarkably high, as it adsorbs 26.4 wt.-% (6 mmol g^{-1}) at moderate temperatures of 273 K and even 32.36 wt.-% at the CO_2 condensation point of 195 K.

The isosteric enthalpy of adsorption was determined multiple times from two isotherms (273/293 K) using *OriginPro 9.0 OG* software to fit the isotherms. [15] The corresponding graph is depicted in Figure 12 in the main article. The isosteric enthalpy of adsorption at zero-coverage was determined to be –2 kJ mol^{-1} from a Freundlich-Langmuir fit from the isotherms starting near 0 kPa, but as –22 kJ mol^{-1} from a virial fit starting at 17 kPa (0.17 bar).

Table S8. *CO_2 adsorption capacity of aluminum MOFs.*

MOF	**Maximum uptake@STP[a]**			**Temp. [K]**	**Ref.**
	[cm^3 g^{-1}]	**[mmol g^{-1}]**	**[wt-%]**		
CAU-23	244	10.89	32.40	195	our work
	135	6.02	20.94	273	our work
	89	3.97	14.87	293	our work
	72	3.21	12.38	298	[16]
Alfum	47.1	2.10 (pellets)	8.46	303	[17]
	56.4	2.52	9.98	293	[18]
MIL-160	94.7	4.22	15.66	293	[18]
	88.3	3.94	14.78	298	[19]
CAU-10-H	60.0	2.68	10.55	296	[20]
	78.5	3.50	13.35	298	[19]
	61.9	2.76	10.83	293	[18]
MIL-53	56.5	2.52	9.98	288	[21]
	51.3	2.29	9.16	303	
	58.3	2.60	10.27	304	[22]
	47.3	2.11	8.50	293	[18]
MIL-53-TDC	61.8	2.76	10.83	293	[18]
	77.1	3.44	13.15	298	[19]
MIL-100	34.1	1.52	6.27	293	[18]

[a] From value in cm^3 g^{-1} or mmol g^{-1} divided or multiplied by X L mol^{-1} (= cm^3 $mmol^{-1}$) with X = 22.414 L as the molar volume of an ideal gas at 1 atm ($1.01325 \cdot 10^5$ Pa) and 273.15 K. The measurement accuracy does not support decimal digits in cm^3 g^{-1}, yet the literature values in cm^3 g^{-1} with often two decimal digits were rounded to just one decimal digit to match the conversion into mmol g^{-1}. Multiplication of the value in mmol g^{-1} with 44.01 g mol^{-1} for the molar mass of CO_2 yields the uptake in Y g(CO_2)/g(MOF) and Y/(1+Y)·100% then gives the uptake in wt-% CO_2.

- **Hydrogen (100 K, 87 K, 77 K)**

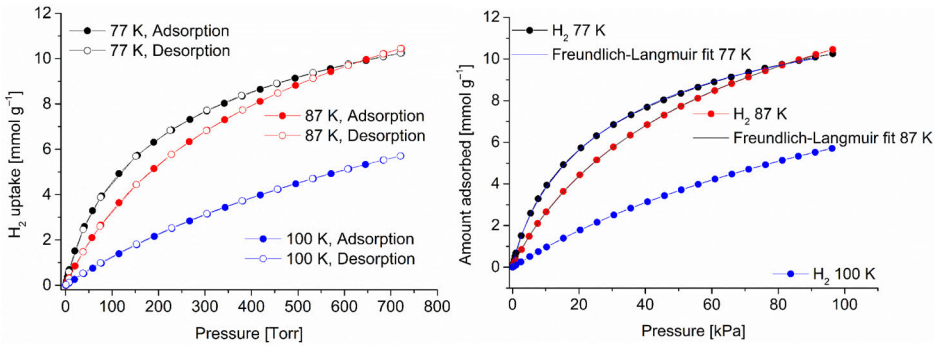

Figure S15. *Hydrogen sorption isotherms of CAU-23 obtained via the synthesis route with $AlCl_3$/$NaAlO_2$ (6 h) (left) and the fitted isotherms (right).*

Table S9 shows hydrogen sorption data of CAU-23 from the synthesis route with $AlCl_3$/$NaAlO_2$ (6 h) at different temperatures. The H_2 capacity of CAU-23 is 2.02 wt-% (10.25 mmol g^{-1}) at 77 K.

Table S9. *Hydrogen sorption data of CAU-23 at different temperatures.*

Temperature	Adsorbed quantity		
	[cm^3g^{-1}]	[$mmolg^{-1}$]	[wt.-%]
77 K	230	10.25	2.02
87 K	235	10.46	2.06
100 K	128	5.71	1.14

The isosteric enthalpy of adsorption was determined multiple times from either two isotherms (77/87 K) using the *3P sim* software to fit the isotherms. [23] The corresponding graph is depicted in Figure 12 in the main article. The isosteric enthalpy of adsorption at zero-coverage was determined to be –4 kJ mol^{-1}.

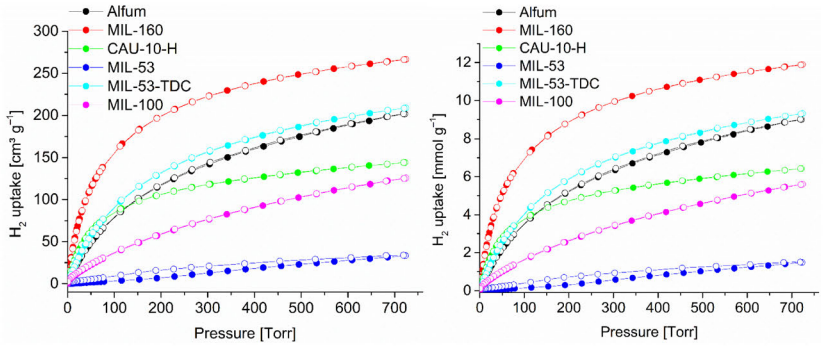

Figure S16. *Hydrogen sorption isotherms at 77 Kof the compared Al-MOFs, uptake in $cm^3\ g^{-1}$(left) and in mmol g^{-1} (right).*

Table S10. *H_2 adsorption capacity of aluminum MOFs.*

MOF	Maximum uptake@STP[a]			Temp. [K]	Ref.
	[$cm^3\ g^{-1}$]	[mmol g^{-1}]	[wt-%]		
CAU-23	230	10.25	2.02	77	our work
Alfum	202	9.01	1.78	77	our work
	201	8.97	1.78	77	[24]
MIL-160	267	11.91	2.34	77	our work
CAU-10-H	144	6.42	1.28	77	our work
MIL-53	33	1.47	0.30	77	our work
MIL-53-TDC	209	9.32	1.84	77	our work
MIL-100	126	5.62	1.12	77	our work

[a] From value in $cm^3\ g^{-1}$ or mmol g^{-1} divided or multiplied by X L mol^{-1} (= cm^3 $mmol^{-1}$) with X = 22.414 L as the molar volume of an ideal gas at 1 atm ($1.01325 \cdot 10^5$ Pa) and 273.15 K. The values were rounded to a reasonable accuracy with no decimal digits in $cm^3\ g^{-1}$ or two decimal digits in mmol g^{-1}. Multiplication of the value in mmol g^{-1} with 2.016 g mol^{-1} for the molar mass of H_2 yields the uptake in Y g(H_2)/g(MOF) and Y/(1+Y)·100% then gives the uptake in wt-% H_2.

- **Methane (273 K, 279 K, 293 K)**

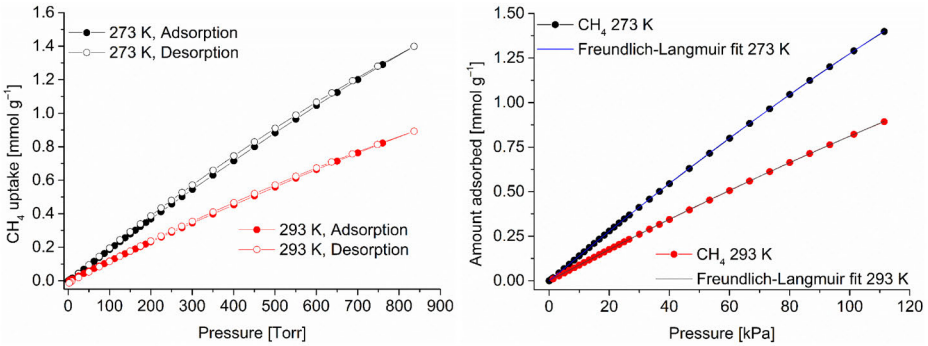

Figure S17. *Methane sorption isotherms of CAU-23 obtained via the synthesis route with $AlCl_3$/$NaAlO_2$ (6 h) (left) and the fitted isotherms (right).*

Table S11 shows methane sorption data of CAU-23 from the synthesis route with $AlCl_3$/$NaAlO_2$ (6 h)path at different temperatures. The CH_4 capacity of CAU-23 appears to be 2.2 wt-% (1.40 mmol g^{-1}) at 273 K.

The isosteric enthalpy of adsorption was determined multiple times from two isotherms (273/293 K) using *OriginPro 9.0 OG* software to fit the isotherms.[15] The corresponding graph is depicted in Figure 12 in the main article. The isosteric enthalpy of adsorption at zero-coverage was determined to be –15 kJ mol^{-1}.

Table S11. *CH_4 adsorption capacity of aluminum MOFs.*

MOF	**Maximum uptake@STP[a]**			**Temp. [K]**	**Ref.**
	[cm^3 g^{-1}]	**[mmol g^{-1}]**	**[wt-%]**		
CAU-23	31	1.38	2.17	273	our work
	20	0.89	1.41	293	our work
Alfum	24.5	1.09[a]	1.72	300	[25]
	25.6	1.14	1.80	298	[26]
MIL-160	10.5	0.47	0.75	298	[26]
	18.8	0.84	1.33	298	[19]
CAU-10-H	23.3	1.04	1.64	298	[19]
	16.6	0.74	1.17	298	[26]
MIL-53	19.9	0.89	1.41	288	[21]
	13.5	0.60	0.95	303	
	12.8	0.57	0.91	298	[26]
MIL-53-TDC	16.4	0.73	1.16	298	[19]
MIL-100	-	-		-	-

[a] From value in cm^3 g^{-1} or mmol g^{-1} divided or multiplied by X L mol^{-1} (= cm^3 $mmol^{-1}$) with X = 22.414 L as the molar volume of an ideal gas at 1 atm ($1.01325 \cdot 10^5$ Pa) and 273.15 K. The measurement accuracy does not support decimal digits in cm^3 g^{-1}, yet the literature values in cm^3 g^{-1} with often two decimal digits were rounded to just one decimal digit to follow the conversion into mmol g^{-1}. Multiplication of the value in mmol g^{-1} with 16.04 g mol^{-1} for the molar mass of CH_4 yields the uptake in Y g(CH_4)/g(MOF) and Y/(1+Y)·100% then gives the uptake in wt-% CH_4.

- **Sulfur dioxide (263 K, 273 K, 293 K)**

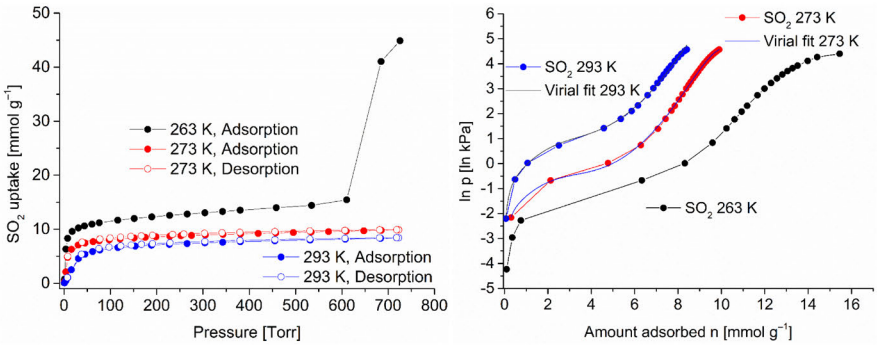

Figure S18. *SO_2 sorption isotherms of CAU-23 obtained via the synthesis route with $AlCl_3$/$NaAlO_2$ (6 h) (left) and the fitted isotherms (right). The desorption branch at 263 K was unfinished, due to equilibration times and measurement running time reaching the SO_2 durability time of the sealings inside the iQ MP device. The increased uptake at higher relative pressures (263 K) corresponds to condensation (the condensation point of SO_2 is 263 K at 1 bar).*

We used eight parameters (a_0 and $a_{1\text{-}7}$) of the virial fit to describe the adsorption isotherm (cf.: Table S14).

Table S12 shows SO_2 sorption data of CAU-23 from the synthesis route with $AlCl_3$/$NaAlO_2$ (6 h) at different temperatures. CAU-23 displays a significant uptake of 38.81 wt-% (9.90 mmol g^{-1}) SO_2 at 273 K.

The isosteric enthalpy of adsorption was determined from two isotherms (273/293 K) using the *OriginPro 9.0 OG* software to fit the isotherms.[15] The corresponding graph is depicted in Figure 12. The isosteric enthalpy of adsorption at zero-coverage was determined to be –38 kJ mol^{-1}.

Table S12. *SO_2 adsorption capacity of aluminum MOFs.*

MOF	**Maximum uptake@STP[a]**			**Temp. [K]**	**Ref.**
	[$cm^3\ g^{-1}$]	**[mmol g^{-1}]**	**[wt-%]**		
CAU-23	346 (pre condens.)	15.5	49.82	263	our work
	222	9.9	38.81	273	our work
	189	8.4	34.99	293	our work
Alfum	168.1	7.5	32.46	293	[18]
MIL-160	161.4	7.2	31.57	293	[27]
CAU-10-H	107.6	4.8	23.52	293	[18]
MIL-53	242.1	10.8	40.90	298	[28]
	235.4	10.5	40.22	293	[18]
MIL-53-TDC	199.5	8.9	36.31	298	[28]
	154.7	6.9	30.65	293	[18]
MIL-100	365.4	16.3	51.08	293	[18]

[a] From value in $cm^3\ g^{-1}$ or mmol g^{-1} divided or multiplied by X L mol^{-1} (= $cm^3\ mmol^{-1}$) with X = 22.414 L as the molar volume of an ideal gas at 1 atm ($1.01325 \cdot 10^5$ Pa) and 273.15 K. The measurement accuracy does not support decimal digits in $cm^3\ g^{-1}$, yet the literature values in $cm^3\ g^{-1}$ with often two decimal digits were rounded to just one decimal digit to follow the conversion into mmol g^{-1}. Multiplication of the value in mmol g^{-1} with 64.066 g mol^{-1} for the molar mass of SO_2 yields the uptake in Y g(SO_2)/g(MOF) and Y/(1+Y)·100% then gives the uptake in wt-% SO_2.

- **High-pressure CO_2 (293 K)**

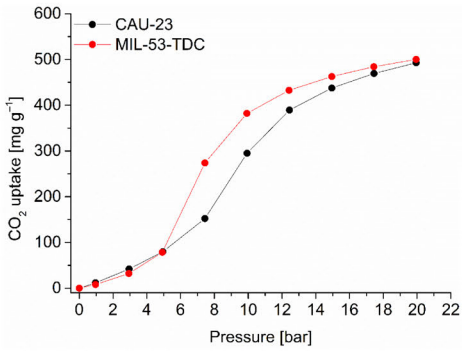

Figure S19. *High-pressure CO_2 sorption of CAU-23 obtained via the synthesis route with $AlCl_3$/$NaAlO_2$ (6 h).*

The material CAU-23 takes up 33 wt.-% of CO_2 at 20 bar.

Table S13. *High-pressure CO_2 adsorption capacity of aluminum MOFs.*

MOF	**Maximum uptake**		**Pressure**	**Temp. [K]**	**Ref.**
	[mg g^{-1}]	**[wt-%]**	**[bar]**		
CAU-23	492.7 (11.2 mmol g^{-1})	33	20	293	our work
Alfum	~220 (~5 mmol g^{-1})[a]	18	8	303	[17]
MIL-160	~264 (~6 mmol g^{-1})[a]	21	20	303	[29]
CAU-10-H	~211 (~4.8 mmol g^{-1})[a]	17	25	303	[30]
MIL-53	~440 (~10 mmol g^{-1})	31	30	304	[22]
	-	37.8	20	298	[31]
MIL-53-TDC	499.9 (11.4 mmol g^{-1})	33	20	293	our work
MIL-100	~528 (~12 mmol g^{-1})	35	30	303	[30]

[a] Visually read from a figure in the referenced literature.

- **Gas sorption cycles (CO_2 and SO_2)**

Three adsorption/desorption cycles were performed with CO_2 and SO_2 and then the stability of the samples was checked with PXRD and nitrogen sorption. These two gases are the most relevant and interesting candidates for a possible industrial application and are also most relevant for possibly inducing degradation in the MOF.

The uptake of the gas sorption cycles of CO_2 and SO_2 at 273 K are illustrated in Figure S20, as well as the surface area before and after the cycles.

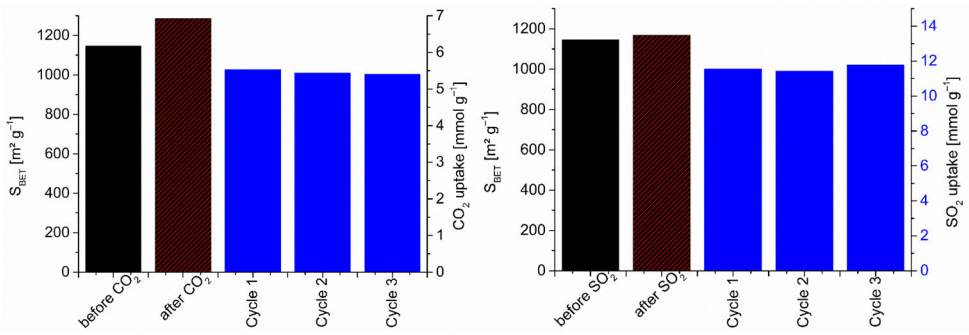

Figure S20. *Gas sorption cycles of CO_2 (left) and SO_2 (right) with the surface areas before and after the cycles.*

The following Figure S21 confirms the stability of the CAU-23 material via PXRD.

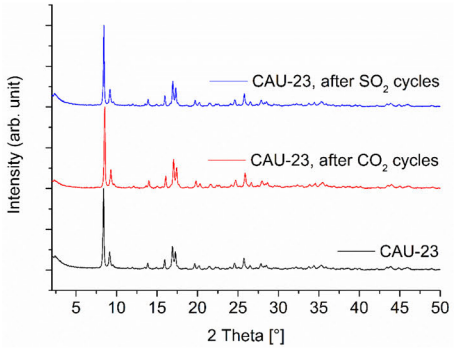

Figure S21. *PXRD of the CAU-23 after the CO_2 or SO_2 gas sorption cycles compared with the CAU-23 PXRD before the tests.*

S2 Enthalpy of adsorption - isotherm fitting

OriginPro 9.0 OG software (OriginLab) or *3P Sim* software was used to fit the experimental adsorption isotherms.[15,23] Possible models for isotherms are: Freundlich-Langmuir or Virial fit, with the following equations:

Freundlich-Langmuir: $n = \frac{a*b*p^c}{1+b*p^c}$ or $q_{eq} = q_{max}\frac{(K*p)^t}{1+(K*p)^t}$ (1)

n or q_{eq} = amount adsorbed (the loading) [mmol g^{-1}]
p = pressure [kPa]
a or q_{max} = maximal loading [mmol g^{-1}]
b = affinity constant (1/kPa^c)
K = afiinity constant (1/kPa)
c or t = heterogeneity exponent
(the product of $b*p^c$ must be dimension-less)

Virial fit: $\ln\ p = \ln\ n + \frac{1}{T}\sum_{i=0}^{m} a_i n^i + \sum_{i=0}^{m} b_j m^j$ (2)

p = pressure [kPa]
n = total amount adsorbed [mmol g^{-1}]
T = temperature [K]
a_i and b_j a= virial coefficients
m = number of coefficients required to adequately fit the isotherms

To calculate the isosteric enthalpy of adsorption (ΔH_{ads}) for CO_2, H_2 and CH_4 two or three isotherms at different temperatures were fitted according to the Freundlich-Langmuir equation (1), to be able to calculate gas loadings for different temperatures at the same pressure.

By applying the Clausius-Clapeyron equation we can now calculate the isosteric enthalpy of adsorption at any loading (eq. 3)

$$\Delta H_{ads} = -R \ln\ (\frac{p_2}{p_1})\frac{T_1 T_2}{(T_2 - T_1)} \quad (3)$$

R = ideal gas constant

To calculate the isosteric heat of adsorption (Q_{st}) or isosteric enthalpy of adsorption (ΔH_{ads}) for SO_2 isotherm data virial method was used. Equation (eq. 2) was used to fit the adsorption data simultaneously at 273 K and 293 K in Origin

Then Q_{st} or ΔH_{ads} can be calculated from eq. 4, where R is the universal gas constant:

$Q_{st} = -R\sum_{i=0}^{n} a_i n^i$ or $\Delta H_{ads} = R\sum_{i=0}^{n} a_i n^i$ (4)

Note that eqn. (4) will yield a negative value for ΔH_{ads}(n) from the most important coefficient a_0 being negative. (Furthermore, with the unit of the ideal gas constant R of J K^{-1} mol^{-1} and n with the unit mol, the virial coefficients a_i must have the unit K mol^{-1} in order to derive at the unit of (k)J mol^{-1} for ΔH_{ads}.)

Table S14. *Fitting parameters of the single adsorption isotherms for enthalpy of adsorption calculations.*

Adsorbate	Freundlich-Langmuir parameters	
H_2 (77 K)	qmax	14.4938
	K	0.0290
	t	0.8324
	R^2	0.9999
H_2 (87 K)	qmax	18.2095
	K	0.0142
	t	0.9150
	R^2	1.0000
CO_2 (273 K)	a	8.8422
	b	1.7863
	c	1.2836
	R^2	0.9999
CO_2 (293 K)	a	11.82515
	b	0.45031
	c	1.11631
	R^2	0.99993
CH_4 (273 K)	a	9.6800
	b	0.0014
	c	1.0167
	R^2	1.0000
CH_4 (293 K)	a	7.19065
	b	0.00120
	c	1.01275
	R^2	1.00000

Adsorbate	Virial fit parameters	
SO_2	a_0	-4452.58069
	a_1	-774.14582
	a_2	354.72097
	a_3	-155.03932
	a_4	35.91792
	a_5	-4.47992
	a_6	0.29239
	a_7	-0.00789
	b_0	15.74625
	b_1	1.24465
Adsorbate	**Virial fit parameters**	
CO_2	a_0	-2549.61421
	a_1	-144.47092
	a_2	20.35281
	a_3	-12.96767
	a_4	5.12427
	a_5	-1.06172
	a_6	0.11304
	a_7	-0.00481
	b_0	11.90848
	b_1	0.33473

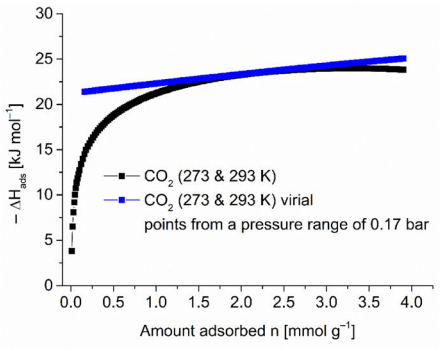

Figure S22. *Different isosteric enthalpy of adsorption calculations depending on the model and the points used in the calculation. Effect is based on the sigmoidal adsorption isotherm shape in the lower pressure regions.*

S3 Ideal adsorbed solution theory (IAST) – isotherm fitting

3P sim software was used to fit the experimental adsorption isotherms.[23] Possible models for isotherms are: Henry, Langmuir, Toth, Sips, Freundlich, Dual-Site Langmuir or Dual-Site Langmuir Sips. We applied several commonly used models on our isotherm data. The best fits for our isotherms were given with isotherm models Toth (CO_2/CH_4 and SO_2/CO_2) and Dual-Site Langmuir Sips (SO_2/CO_2).

We applied the described two models on our isotherm data, with the following equations (5 and 6):

Toth: $$q_{eq} = \frac{q_{max} * K * p}{(1+(K*p)^t)^{1/t}} \quad (5)$$

Dual-Site Langmuir Sips: $$q_{eq} = q_{max}\left(\frac{K_1 * p}{1+K_1 * p} + \frac{(K_2 * p)^t}{(1+K_2 * p)^t}\right) \quad (6)$$

q_{eq} = amount adsorbed [mmol g^{-1}]
q_{max} = maximum adsorption capacity [mmol g^{-1}]
K = affinity constant for adsorption [1 bar^{-1}]
p = pressure [kPa]
t = index of heterogeneity

3P sim software was used to simulate mixed-gas adsorption behavior of CAU-23. Applying binary mixtures of CO_2/CH_4 and SO_2/CO_2.

IAST selectivities *S* of binary gas mixtures were calculated using the following equation (eq. 7), where x_i represents the absorbed gas amount and y_i the mole fraction of each adsorptive.

$$S = \frac{x_1/x_2}{y_1/y_2} \quad (7)$$

The mixture SO_2/CO_2 we performed is useful in flue gas purification, as well. For this reason we tried two different adsorption isotherm models.

Table S15. *Fitting parameters of the single adsorption isotherms for IAST selectivites with two different models.*

Adsorbate (X_1 and X_2)	**Model**	**R^2(X1)=**	**R^2(X2)=**	**Simulated pressure range up to bar**	**Parameters**			
					Affinity const. [1/bar]	**Max. loading [mmol/g]**	**Heterogenity exponent**	
CO_2 (293 K) and CH_4 (293 K)	Toth	0.999999	-	1	0.700301	5.902492	2.7164	
	Toth	-	0.999989	1	0.152631	5.806995	1.1811	
SO_2 (293 K) and CO_2 (293 K)	Toth	0.989625	-	1	20.654741	8.222994	1.1603	
	Toth	-	0.999999	1	0.704736	5.863839	2.7387	
					Affinity const. 1 [1/bar]	**Max. loading [mmol/g]**	**Affinity const. 2 [1/bar]**	**Heterogenity exponent**
SO_2 (293 K) and CO_2 (293 K)	DSLAI Sips	0.999755	-	1	0.396236	6.601317	36.280702	1.678748
	DSLAI Sips	-	0.999999	1	1.062186	3.84404	0.878153	1.841302

S4 References

1 D. Lenzen, J. Zhao, S.-J. Ernst, M. Wahiduzzaman, A. Ken Inge, D. Fröhlich, H. Xu, H.-J. Bart, C. Janiak, S. Henninger G. Maurin, X. Zou, N. Stock, *Nat. Commun.* **2019**, *10*, 3025.

[2] C. Schlüsener, "Mixed-Linker-Synthesen von Aluminium-basierten Metall-Organischen Gerüstverbindungen und deren Anwendung in der Wassersorption", Dissertation, Heinrich-Heine-University, **June/2020**.

3 N. Tannert, S.-J. Ernst, C. Jansen, H.-J. Bart, S. K. Henninger, C. Janiak, *J. Mater. Chem. A* **2018**, *6*, 17706–17712.

4 Leung, E.; Müller, U.; Trukhan, N.; Mattenheimer, H.; Cox, G.; Blei, S. Process for Preparing Porous Metal-Organic Framework Based on Aluminium Fumarate. U.S. Patent 2012/0082864 A1, 30 September 2011.

5 A. Cadiau, J. S. Lee, D. Damasceno Borges, P. Fabry, T. Devic, M. T. Wharmby, C. Martineau, D. Foucher, F. Taulelle, C.-H. Jun, Y. K. Hwang, N. Stock, M. F. de Lange, F. Kapteijn, J. Gascon, G. Maurin, J.-S. Chang, C. Serre, *Adv. Mater.* **2015**, *27*, 4775–4780.

6 D. Fröhlich, E. Pantatosaki, P. D. Kolokathis, K. Markey, H. Reinsch, M. Baumgartner, M. A. van der Veen, D. E. de Vos, N. Stock, G. K. Papadopoulos, S. K. Henninger, C. Janiak, *J. Mater. Chem. A* **2016**, *4*, 11859–11869.

7 G. Zi, Z. Yan, Y. Wang, Y. Chen, Y. Guo, F. Yuan, W. Gao, Y. Wang, J. Wang, *Carbohydr. Polym.* **2015**, *115*, 146–151.

8 M. Qiu, Q. Guan, W. Li, *Cryst. Growth. Des.* **2016**, *16*, 3639–3646.

9 M. Wahiduzzaman, N. Reimer, J.-P. Itié, N. Stock, G. Maurin, P. G. Yot, *Polyhedron* **2018**, *155*, 144–148.

10 K. S. Walton, R. Q. Snurr, *J. Am. Chem. Soc.* **2007**, *129*, 8552–8556.

11 Z. Jiang, Y. Zou, T. Xu, L. Fan, P. Zhou, Y. He, *Dalton Trans.* **2020**, *49*, 3553–3561.

12 T. Xu, Z. Jiang, P. Liu, H. Chen, X. Lan, D. Chen, L. Li, Y. He, *ACS Appl. Nano Mater.* **2020**, *3*, 2911–2919.

13 J. Zou, C. Fan, X. Liu, *Langmuir* **2020**, *36*, 14656–14665.

14 M. Thommes, K. Kaneko, A. V. Neimark, J. P. Olivier, F. Rodriguez-Reinoso, J. Rouquerol, K. S.W. Sing, *Pure Appl. Chem.* **2015**, *87*, 1051-1069.

15 OriginLab Corporation, OriginPro, Version 9.0.0G., OriginLab Corporation 1991-2012.

16 Y. Ye, S. Xian, H. Cui, K. Tan, L. Gong, B. Liang, T. Pham, H. Pandey, R. Krishna, P. C. Lan, K. A. Forrest, B. Space, T. Thonhauser, J. Li, S. Ma, *J. Am. Chem. Soc.* **2022**, *144*, 1681–1689.

17 J. A. Coelho, A. M. Ribeiro, A. F. P. Ferreira, S. M. P. Lucena, A. E. Rodrigues, D. C. S. d. Azevedo, *Ind. Eng. Chem. Res.* **2016**, *55*, 2134–2143.

18 P. Brandt, S.-H. Xing, J. Liang, G. Kurt, A. Nuhnen, O. Weingart, C. Janiak, *ACS Appl. Mater. Interfaces* **2021**, *13*, 29137-29149.

19 D. Shade, B. Marszalek, K. S. Walton, *Adsorption* **2021**, *27*, 227–236.

20 J. Pei, H.-M. Wen, X.-W. Gu, Q.-L. Qian, Y. Yang, Y. Cui, B. Li, B. Chen, G. Qian, *Angew. Chem. Int. Ed.* **2021**, *60*, 25068–25074.

21 P. Rallapalli, K. P. Prasanth, D. Patil, R. S. Somani, R. V. Jasra, H. C. Bajaj, *J. Porous Mater.* **2011**, *18*, 205–210.

22 S. Bourrelly, P. L. Llewellyn, C. Serre, F. Millange, T. Loiseau, G. Férey, *J. Am. Chem. Soc.* **2005**, *127*, 13519–13521.

23 3P INSTRUMENTS, 3P sim, Version 1.1.0.7, Simulation and Evaluation Tool for mixSorb, 3P INSTRUMENTS 2018.

24 T. J. Matemb Ma Ntep, W. Wu, H. Breitzke, C. Schlüsener, B. Moll, L. Schmolke, G. Buntkowsky, C. Janiak, *Aust. J. Chem.* **2019**, *72*, 835.

25 M. M. Sadiq, M. Rubio-Martinez, F. Zadehahmadi, K. Suzuki, M. R. Hill, *Ind. Eng. Chem. Res.* **2018**, *57*, 6040–6047.

26 Z. Huang, P. Hu, J. Liu, F. Shen, Y. Zhang, K. Chai, Y. Ying, C. Kang, Z. Zhang, H. Ji, *Sep. Purif. Technol.* **2022**, *286*, 120446.

27 P. Brandt, A. Nuhnen, M. Lange, J. Möllmer, O. Weingart, C. Janiak, *ACS Appl. Mater. Interfaces* **2019**, *11*, 17350-17358.

28 A. López-Olvera, J. A. Zárate, E. Martínez-Ahumada, D. Fan, M. L. Díaz-Ramírez, P. A. Sáenz-Cavazos, V. Martis, D. R. Williams, E. Sánchez-González, G. Maurin, I. A. Ibarra, *ACS Appl. Mater. Interfaces* **2021**, *13*, 39363–39370.

29 D. Damasceno Borges, P. Normand, A. Permiakova, R. Babarao, N. Heymans, D. S. Galvao, C. Serre, G. de Weireld, G. Maurin, *J. Phys. Chem. C* **2017**, *121*, 26822–26832.

30 A. D. Wiersum, C. Giovannangeli, D. Vincent, E. Bloch, H. Reinsch, N. Stock, J. S. Lee, J.-S. Chang, P. L. Llewellyn, *ACS Comb. Sci.* **2013**, *15*, 111–119.

31 D. Liu, L. Yan, L. Li, X. Gu, P. Dai, L. Yang, Y. Liu, C. Liu, G. Zhao, X. Zhao, *CrystEngComm* **2018**, *20*, 2102–2111.

3.5 The Complexity of Comparative Adsorption of C_6 Hydrocarbons (Benzene, Cyclohexane, *n*-Hexane) at Metal-Organic Frameworks

Christian Jansen, Nabil Assahub, Alex Spieß, Jun Liang, Alexa Schmitz, Shanghua Xing, Serkan Gökpinar, Christoph Janiak

Nanomaterials **2022**, *12*, 3614

DOI: 10.3390/nano12203614

Impact-Faktor: 5.719 (2021)

Kurzzusammenfassung:

Die stabilen MOFs Aluminiumfumarat, MIL-160, DUT-4, DUT-5, MIL-53-TDC, MIL-53, UiO-66, UiO-66-NH_2, UiO-66(F)$_4$, UiO-67, DUT-67, NH_2-MIL-125, MIL-125, MIL-101(Cr), ZIF-8, ZIF-11 und ZIF-7 wurden ausgewählt, um ihre C_6-Sorptionseigenschaften zu untersuchen. Hierbei kann das Verhalten bei der Sorption der größeren C_6-Moleküle nicht allein durch die Oberfläche und das Porenvolumen erklärt werden, sondern ist in Zusammenhang mit der komplexen Mikroporenstruktur der MOFs zu sehen. Die maximale Aufnahme bei p p_0^{-1} = 0.9 wurde von DUT-4 für Benzol, von MIL-101(Cr) für Cyclohexan und von DUT-5 für *n*-Hexan erreicht. Im niedrigen Druckbereich von p p_0^{-1} = 0.1 bis hinunter zu 0.05 ist die maximale Benzol-Aufnahme durch DUT-5, DUT-67/UiO-67 und MIL-101(Cr), für Cyclohexan und *n*-Hexan durch DUT-5, UiO-67 und MIL-101(Cr) gegeben. Die höchsten Aufnahmen bei p p_0^{-1} = 0.02 zeigten MIL-53 für Benzol, MIL-125 für Cyclohexan und DUT-5 für *n*-Hexan. DUT-5 und MIL-101(Cr) sind die MOFs mit den größten Porenfenstern, jedoch scheint die Aufnahme im niedrigen Druckbereich eine komplexe Kombination aus dem jeweiligen Liganden und der Porengröße zu sein. IAST Selektivitäten zwischen den drei binären Gemischen zeigen eine sehr spezielle und schwierig vorherzusagende Wechselwirkung zwischen den Porengrößen und der kritischen Adsorptiv-Größe und der möglichen Rolle einer elektrostatischen Wechselwirkung einer funktionellen Gruppe wie NH_2.

Anteile an der Publikation:

- Idee der Publikation
- Konzept, experimentelle Arbeiten und Analytik (bis auf unten gelistete Ausnahmen)
- Experimentelle Vorarbeiten und Produktsynthesen durch Herrn Nabil Assahub
- Aufarbeitung der Ergebnisse, Verfassen des Manuskripts und das Erstellen der Abbildungen und Tabellen
- Dampfsorptionsmessungen

- Anfertigung der theoretischen Rechnungen
- Korrekturen und Verschriftlichung und Revision durch Herr Prof. Dr. Christoph Janiak
- REM-Aufnahmen durch Alex Spieß
- TGAs durch Frau Alexa Schmitz
- Gassorptionsaufnahmen durch Herr Jun Liang und Frau Shanghua Xing

nanomaterials

MDPI

Article

The Complexity of Comparative Adsorption of C_6 Hydrocarbons (Benzene, Cyclohexane, *n*-Hexane) at Metal–Organic Frameworks

Christian Jansen [1], Nabil Assahub [1], Alex Spieß [1], Jun Liang [1], Alexa Schmitz [1], Shanghua Xing [1], Serkan Gökpinar [2] and Christoph Janiak [1,*]

[1] Institut für Anorganische Chemie und Strukturchemie, Heinrich-Heine-Universität, D-40225 Düsseldorf, Germany
[2] Microtrac Retsch GmbH, Retsch-Allee 1-5, D-42781 Haan, Germany
* Correspondence: janiak@hhu.de

Abstract: The relatively stable MOFs Alfum, MIL-160, DUT-4, DUT-5, MIL-53-TDC, MIL-53, UiO-66, UiO-66-NH_2, UiO-66$(F)_4$, UiO-67, DUT-67, NH_2-MIL-125, MIL-125, MIL-101(Cr), ZIF-8, ZIF-11 and ZIF-7 were studied for their C_6 sorption properties. An understanding of the uptake of the larger C_6 molecules cannot simply be achieved with surface area and pore volume (from N_2 sorption) but involves the complex micropore structure of the MOF. The maximum adsorption capacity at p p_0^{-1} = 0.9 was shown by DUT-4 for benzene, MIL-101(Cr) for cyclohexane and DUT-5 for *n*-hexane. In the low-pressure range from p p_0^{-1} = 0.1 down to 0.05 the highest benzene uptake is given by DUT-5, DUT-67/UiO-67 and MIL-101(Cr), for cyclohexane and *n*-hexane by DUT-5, UiO-67 and MIL-101(Cr). The highest uptake capacity at p p_0^{-1} = 0.02 was seen with MIL-53 for benzene, MIL-125 for cyclohexane and DUT-5 for *n*-hexane. DUT-5 and MIL-101(Cr) are the MOFs with the widest pore window openings/cross sections but the low-pressure uptake seems to be controlled by a complex combination of ligand and pore-size effect. IAST selectivities between the three binary mixtures show a finely tuned and difficult to predict interplay of pore window size with (critical) adsorptive size and possibly a role of electrostatics through functional groups such as NH_2.

Keywords: metal–organic frameworks (MOFs); zeolitic imidazolate frameworks (ZIFs); vapor adsorption; C_6 volatile organic compounds (VOCs); benzene adsorption; cyclohexane adsorption; *n*-hexane adsorption; IAST selectivity

Citation: Jansen, C.; Assahub, N.; Spieß, A.; Liang, J.; Schmitz, A.; Xing, S.; Gökpinar, S.; Janiak, C. The Complexity of Comparative Adsorption of C_6 Hydrocarbons (Benzene, Cyclohexane, *n*-Hexane) at Metal–Organic Frameworks. *Nanomaterials* **2022**, *12*, 3614. https://doi.org/10.3390/nano12203614

Academic Editors: Bin Li and Hui-Min Wen

Received: 2 September 2022
Accepted: 10 October 2022
Published: 15 October 2022

Publisher's Note: MDPI stays neutral with regard to jurisdictional claims in published maps and institutional affiliations.

1. Introduction

Toxic volatile organic compounds (VOCs) in the atmosphere are of general concern and their removal, prevention of emission, and the separation of organic molecules in industrial processes [1] is technologically important [2–12]. A specific group of VOCs are hydrocarbons [11], which can be classified by the number of their carbon atoms. VOCs can be selectively adsorbed by specific materials. State of the art of VOC-removal by adsorption is the use of activated carbon [13], or zeolites [1]. However, the selectivity of activated carbon or zeolites for different VOCs is low, hence, components from a mixture of similar VOCs are difficult to separate by these standard adsorption materials. On the other hand, the design possibilities of metal-organic framework (MOF) adsorbents should allow for the separation of chemically similar VOC mixtures. MOFs are typically three-dimensional coordination networks with potential voids from the combination of metal clusters (secondary building units, SBUs) and organic ligands (called linkers) [14]. MOFs have already been investigated for the adsorption of VOCs such as *n*-hexane, xylene, toluene, acetaldehyde in vapor [7,15], liquid phase [16,17], or under humid conditions [18]. MOFs offer advantages [19] for VOC removal over materials [20] like

zeolites [21], activated carbon [22], or silica gel [23]. A large variation of linkers and metal-atoms in MOFs [24] allows to adapt the pore size to the VOC to be adsorbed and separated [25]. The MOF linker can contain functional groups [26] for specific interactions to the VOC. The adsorptive selectivity of benzene over cyclohexane was improved with a nitro-decorated MOF which stabilized the interactions between the framework and benzene through a smaller window diameter with increased $\pi\cdots\pi$-stacking and C-H···O (nitro) hydrogen bonding [27]. The presence of open-metal sites [28] could give an added high selectivity towards adsorptives. In the example of MOF-74 the adsorbate benzene can be arranged more structured at the open-metal sites than in bulk liquid benzene [29]. Such effects can be used to achieve a high affinity for benzene towards its separation from other VOCs. The flexibility of the framework in MOFs such as in MIL-53 with its breathing-effect [30], or in ZIF-7 with its gate-opening-effect is another opportunity to achieve a selective adsorption of a specific VOC [31–34]. By introducing defects in MOFs such as UiO-66, which is one of the most common defective MOFs [35], the maximum toluene adsorption capacity could be increased [36].

While the adsorption capacity and selectivity of MOFs for different VOCs has been widely tested, the stability of the MOF towards a VOC has been less examined. An important topic in VOC adsorption and separation deals with C_6 hydrocarbons, e.g., benzene, cyclohexane and *n*-hexane. These three VOCs are among the ones found in indoor environments [37]. Benzene adsorption on MOFs is partly well examined [38,39]. In industry, the separation of benzene and cyclohexane by distillation is one of the most difficult cases due to their similar boiling point and vapor pressure [40,41]. The adsorption of *n*-hexane is particularly important with regard to its metabolization to nerve-damaging toxic 2,5-hexanedione [42]. The adsorption and separation of benzene , cyclohexane and *n*-hexane with MOFs has been examined with single vapor adsorption isotherms [43–46], in liquid phases [47] and with breakthrough experiments [48]. The recyclability and long-term stability of MOFs towards C_6 vapor sorption has been seldom addressed and the focus is only on individual MOFs and no comparative investigations of a comprehensive series of MOFs [27,49].

Furthermore, only for some MOFs the ideal adsorbed solution theory (IAST) is used to simulate the separation properties of the MOF from single gas adsorption isotherms for a selective sorption of benzene over cyclohexane or different hexane isomers [50–52]. This method is a useful first approximation to study the separation properties and to obtain an overview of many different MOFs.

In this work, for the first time a broad series of MOFs with different metals were comparatively investigated for their adsorption of the C_6-VOCs benzene, cyclohexane and *n*-hexane by volumetric sorption analysis, not so much for their maximum uptake capacity but especially for their uptake at low pressure down to $p\,p_0^{-1} = 0.02$, to find MOFs for the removal of C_6 traces. Furthermore, the stability after VOC adsorption and their IAST selectivities were taken into account. The stability of the MOFs was tested in liquid and vapor phase over a few days to simulate a potential long-term application.

2. Materials and Methods

All commercial chemicals were used as received (see Section S1 in the Supplementary Materials). The MOFs were synthesized according to literature reported procedures or optimized syntheses which are given in the Supplementary Materials.

Powder X-ray diffractometry (PXRD) was performed at ambient temperature on a D2 phaser (Bruker AXS, Karlsruhe, Germany) using Cu-K_α radiation (λ = 1.54182 Å) between $5° < 2\theta < 50°$ with a scan rate of $0.0125° \, s^{-1}$ (300 W, 30 kV, 10 mA) and on a Miniflex 600 (Rigaku, Tokyo, Japan) using Cu-K_α radiation (λ = 1.54182 Å) between $2° < 2\theta < 50°$ with a scan rate of $0.083° \, s^{-1}$ (600 W, 40 kV, 15 mA) and a D/teX ultra detector. Analyses of the diffractograms were carried out with Match 3.1.0 software. All PXRD patterns are collected in Sections S3 and S12.

Thermogravimetric analysis (TGA) was measured on a Netzsch TG209 F3 Tarsus (Netzsch, Selb, Germany) device under nitrogen atmosphere, ramping 10 K min^{-1} to 600 °C. TGA curves are given in Section S7.

Scanning electron microscopy (SEM) images were acquired on a JEOL JSM-6510 Advanced electron microscope (Jeol, Akishima, Japan) with a LaB_6 cathode at 5–20 keV. The microscope was equipped with a Xflash 410 (Bruker, Billerica, US) silicon drift detector for energy-dispersive X-ray spectroscopy. SEM images are collected in Section S8.

Nitrogen sorption isotherms for the determination of Brunauer-Emmett-Teller [53] BET surface areas were obtained at 77 K within a pressure range of p = 10^{-3}-1 bar on a Quantachrome NOVA (Quantachrome, Odelzhausen, Germany) instrument using ca. 20–50 mg of sample (nitrogen with purity of 99.999%, 5.0). Each sample was degassed under vacuum (<10^{-2} mbar) at 393 K for ca. 3 h prior to measurement using a FloVac (Quantachrome, Odelzhausen, Germany) degasser. All BET surface areas were calculated from five adsorption points applying Rouquerol plots (r > 0.998). All N_2-sorption isotherms are shown in Section S4. Total pore volumes were calculated from the N_2-sorption isotherm at p p_0^{-1} = 0.9 for pore sizes ≤20 nm. NLDFT calculations were carried out with the native NovaWin 11.03 software using the 'N_2 at 77 K on carbon, slit pore, NLDFT equilibrium' model. Thickness model for calculation of micropore volumes and micropore areas was set to 'De Boer'. Micropore volumes were calculated from the N_2 adsorption isotherm at p p_0^{-1} = 0.1 for pores with d ≤2 nm (20 Å). Micropore volumes (V_{micro}) were calculated by the t-plot method ('De Boer' model).

Vapor sorption experiments were carried out on a Quantachrome VStar4 (Quantachrome, Odelzhausen, Germany) instrument. Each sample was degassed under vacuum (<10^{-3} mbar) at 393 K for ca. 3 h prior to measurement, using a FloVac (Quantachrome, Odelzhausen, Germany) degasser. The detailed experimental equilibrium settings and all vapor sorption isotherms are given in Section S6. The measurement conditions had been set to achieve thermodynamic equilibrium with longer equilibrium times at low pressures and faster equilibration times in the saturated plateau region at higher relative pressures (Section S6). On average the time for the adsorption isotherm branch was 48 h, for the desorption branch 24 h. The vapor isotherms were recorded to only p p_0^{-1} = 0.9 to avoid the vapor condensation when approaching p p_0^{-1} = 1. The absolute pressures at 293 K were 75.26 Torr for benzene, 77.51 Torr for cyclohexane and 121.53 Torr for *n*-hexane.

The cyclic benzene adsorption experiment was performed at 298 K on a BELSORP-max II (HP model) (Microtrac MRB, Haan, Germany). The sample was pretreated under vacuum at 373 K for 3 h for a full adsorption cycle and evacuated at 298 K for 0.5 h for a short adsorption cycle. Adsorption points are measured at a relative pressure of about p p_0^{-1} 0.3 with high dosing rates to reduce the measurement time (fluctuations in relative pressure possible).

Carbon dioxide sorption was measured with a Quantachrome Autosorb iQ MP (Quantachrome, Odelzhausen, Germany) at 273 K (ice/deionized water bath) (Section S13). The Autosorb iQ MP is equipped with oil-free vacuum pumps (ultimate vacuum <10^{-8} mbar) and valves, which guaranteed contamination free measurements. The sample was connected to the preparation port of the sorption analyzer and degassed under vacuum. After weighing, the sample tube was then transferred to the analysis port of the sorption analyzer. The samples were degassed before each measurement for a minimum of 3 h at 393 K under vacuum. The gas for the sorption measurements was of ultrapure grades (99.999%, 5.0) and the STP volumes are given at 273.15 K, 1 atm (1.013 bar). All carbon dioxide sorption isotherms are depicted in Section S5.

3. Results and Discussion

The seven aluminum-MOFs Basolite A520 [54] or Aflum [55], MIL-160 [56], DUT-4 [57], DUT-5 [58], MIL-53-TDC [59], MIL-53 [60], five zirconium-MOFs UiO-66, UiO-66-NH_2 [61], UiO-66$(F)_4$ [62], UiO-67 [63], DUT-67 [64], two titanium-MOFs MIL-125 [65] and MIL-125-NH_2 [66], the chromium-MOF MIL-101(Cr) [67] and the three (Zn-)ZIFs ZIF-8 [68], ZIF-11 [69] and ZIF-7 [70,71], which are used for comparative C_6 adsorption are depicted in Figure 1 with their secondary building unit, the linker, the acronym and their formula (MIL = Materials of Institute Lavoisier, DUT = Dresden University of Technology, TDC = thiophenedicarboxylate, UiO = Universitet i Oslo, ZIF = zeolitic imidazolate framework).

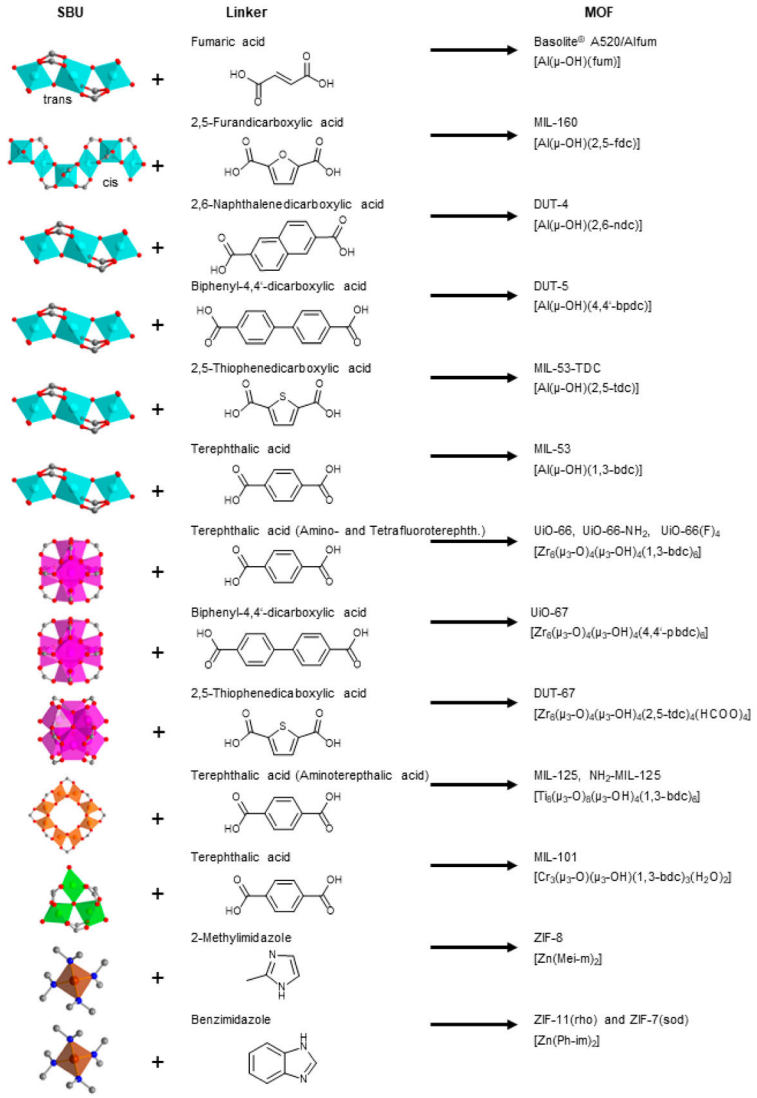

Figure 1. MOFs investigated here for C_6-VOC adsorption. Secondary building units (SBUs) depict the metal atoms and their coordination polyhedra (Al cyan, Zr magenta, Ti orange, Cr green and Zn brown), which are connected via the linker (acid or imidazole form in the middle column) to form the respective MOFs (right column) (carbon gray, oxygen red, nitrogen blue). For further details to the MOFs see Section S2.

The MOFs can be considered as typical representatives which are frequently encountered in many studies. Powder X-ray diffractograms of the synthesized samples positively match with the simulations from the deposited structure files and thereby authenticate the crystalline phase (Figures S14–S24). The BET surface area and pore volumes from nitrogen sorption isotherms are in the range found in the literature (Table S2).

The three VOCs benzene, cyclohexane and *n*-hexane have six carbon atoms and no dipole moment, but different structures and electronic properties. In the gaseous phase the adsorptive benzene has a kinetic diameter of 5.85 Å, cyclohexane of 6 Å, and linear *n*-hexane of 4.3 Å [37]. The more specific van-der-Waals dimensions along the x, y and z axis of the molecule are for benzene x = 6.628 (MIN2), y = 7.337, z = 3.277 Å, cyclohexane x = 7.168, y = 6.580 (MIN2), z = 4.982 Å, *n*-hexane x = 10.344, y = 4.536 (MIN2), z = 4.014 Å with the value which is denoted as MIN2 being the critical dimension for a diffusion through cylindrical pore cross sections [72].

3.1. C_6 Sorption Isotherms

Most MOFs have adsorption isotherms towards the C_6-VOCs which are a composite of Type-I and -II or have a Type-IV [53] or F-I adsorption isotherm [73]. The Type-I-II composite follows a Type-Ia, -Ib in the lower pressure section ($p\ p_0^{-1} < \sim 0.5$) and a Type-II branch at higher relative pressure (Table S4, Figures S36–S46, for further details on the isotherm categorization). Most MOF-adsorbate pairs reach at least half of their maximum uptake at $p\ p_0^{-1} = 0.9$ already at $p\ p_0^{-1} = 0.1$, following Type-I, -F-I or -IV isotherms (Tables S4–S7, Figures 2–4). There are only few MOF-adsorbate pairs with rather little adsorption at $p\ p_0^{-1} = 0.1$ followed with a much larger uptake at higher pressure as evidenced by Type -II, -F-III or -V isotherms or in Type-F-I or -IV isotherms with much less uptake in the low versus the higher-pressure region. These few MOFs are ZIF-8 and ZIF-7 for benzene, ZIF-8, ZIF-11 and ZIF-7 for cyclohexane. Noteworthy, also UiO-66 and UiO-66(F)$_4$ feature Type-I-II isotherms with only 1/3 of the cyclohexane uptake at $p\ p_0^{-1}$ 0.1 versus 0.9 and for UiO-66(F)$_4$ also towards *n*-hexane (Tables S5–S7). This feature of a low uptake at $p\ p_0^{-1} = 0.1$ is mostly accompanied by a wide hysteresis. For the ZIFs the low uptake at $p\ p_0^{-1} = 0.1$ is due to a gate-opening effect in these materials with their narrow pore windows (cf. Section S12. For the UiO-66 compounds with their cluster or linker defects the guest may induce a distortion of the framework which then allows the accommodation of further adsorbates. Several isotherms exhibit a second gradual uptake step above ~0.4 $p\ p_0^{-1}$ followed by a saturation plateau such that the isotherm resembles an F-I or a Type-IV isotherm (Table S4, Figures S36–S46).

In the desorption branch the MOFs with the Type-II, Type-IV of F-I isotherm feature a wide or very wide hysteresis. Out of the 18 MOFs investigated here, 15 gave desorption isotherms with a wide or very wide hysteresis to the adsorption branch, at least for one of the vapors. Eight MOFs had a wide to very wide hysteresis to all three vapors. The visual appearance of the sorption isotherms differs also with the vapor for some MOFs. Upon further analysis (vide infra) there does not appear to be a unifying correlation of the isotherm shape with the MOF structure or vapor. In the literature benzene adsorptions in MOFs with a discernible hysteresis are interpreted with guest-host C-H···π or π···π interactions (Figure S128c) [74]. When no hysteresis is found this is seen to indicate that the molecules can move unrestricted in and out of the pores, as can be expected if the critical dimensions of the adsorptive molecule (for benzene x = 6.6 Å, for cyclohexane y = 6.6 Å, for *n*-hexane y = 4.5 Å) are smaller than the pore window cross sectional diameter [72].

It was beyond the scope of this work to theoretically study the adsorbate-adsorbent interactions in our MOFs. For example, the adsorption of benzene in MOF-74 at different pressure points was studied by Liu et al. [29]. The adsorption starts at 0.01 Pa with single molecules which lie flat on the adsorbent surface in separate pores. At 0.1 Pa, additional adsorbed benzene molecules begin to form a monolayer while other pores are still empty. At 0.2 Pa, benzene molecules are adsorbed in most pores. From 0.3 to 0.5 Pa the monolayers in each pore are almost complete. From 0.5 Pa multilayer adsorption with pore filling takes place which according to the calculations is completed at 20 Pa [29]. Macreadie et al. present the DFT-optimized location of one benzene or cyclohexane guest molecule in MOF-5, CUB-5 and 3DL-MOF-1 where the single molecule is located at the metal cluster nodes. The authors also note that aromatic MOFs favor aliphatic VOCs and vice versa due to the importance of aliphatic/aromatic C-H··· π interactions [43]. Yu et al. report the crystal structures of the MOF Al-tbbotb (tbbotb = 4,4′,4′′-(benzene-1,3,5-triyltris(oxy))tribenzoate) loaded with *n*-hexane or 3-methylpentane which are adsorbed in pairs along the adsorbent surface. There are close H···H contacts from the guests of 2.19 Å for *n*-hexane and 2.27 Å for 3-methylpentane to the bridging OH groups in the metal SBU [75]

We note that in the literature often only the adsorption branches are given and discussed while the desorption branch is not shown. It has been noted that desorption isotherms for vapors may be unreliable because the desorption process is accompanied by a transition from a saturated vapor or liquid state of the adsorbate to the gaseous adsorptive state [52].

Concerning the Type-II or Type-IV isotherm appearance and the presence of uptake steps in the adsorption branch at higher relative pressure this may be due to inter-particle condensation. From the cif files of the X-ray structures the solvent accessible void volume (in $Å^3$/unit cell) was obtained, from which the theoretical specific pore volume could be calculated (Table S3). There is in most cases a reasonable match between the experimental pore volume and the calculated specific void volume. At the same time the vapor uptake in mg g^{-1} at p p_0^{-1} = 0.9 can be transformed into the volume the adsorbate would use in a liquid state [cm^3(liquid adsorbate) g^{-1}(MOF)] by dividing the vapor uptake in mg g^{-1} through the density of the respective liquid at 293 K to approximate the volume of benzene, cyclohexane or *n*-hexane in the MOF (Table S3a–c). Further dividing this liquid adsorbate volume by either the experimental pore volume or the calculated specific void volume gives the degree of pore filling (Table S3). Remarkably, often a pore filling substantially above 100% is derived this way especially for those MOFs where the noted uptake steps are seen in the adsorption isotherm. Hence, we conclude that these uptake steps and concomitant larger-than-100% pore fillings are due to inter-particle condensation. The SEM images in Figures S67–S84 indicate the presence of fine powders with particle sizes below 5 μm and for the UiOs even below 0.5 μm.

3.2. C_6 Uptake

The benzene adsorption capacity at p p_0^{-1} = 0.9 and 293 K ranges between 262 to 1043 mg g^{-1} for the MOFs, with ZIF-7 (83 mg g^{-1}) being a clear low-uptake outlier (Figure 2, Table S5). For cyclohexane the uptake at p p_0^{-1} = 0.9 and 293 K extends from 227 to 1007 mg g^{-1} again with ZIF-7 (59 mg g^{-1}) being significant lower (Figure 3, Table S6). For *n*-hexane under these conditions, the uptake lies between 207 to 997 mg g^{-1} (ZIF-7 at 96 mg g^{-1}) (Figure 4, Table S7).

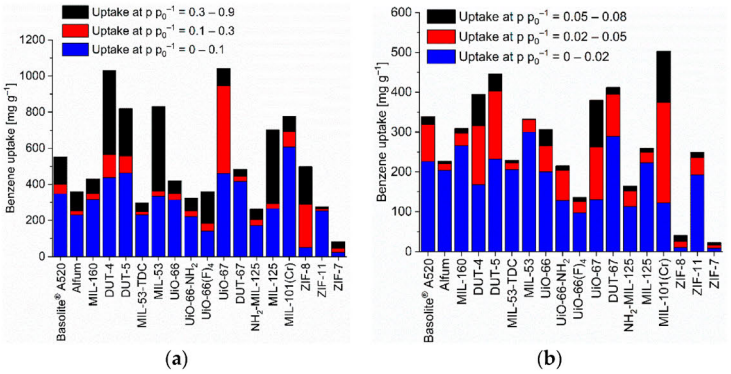

Figure 2. Benzene uptake capacity (at 293 K) of the different MOFs at different relative pressures. (**a**) At relative pressures of 0.1, 0.3 and 0.9; (**b**) at relative pressures of 0.02, 0.05 and 0.08 (specific values in Table S5). For the surface-specific uptake at p p_0^{-1} = 0.1 see Figure S88a.

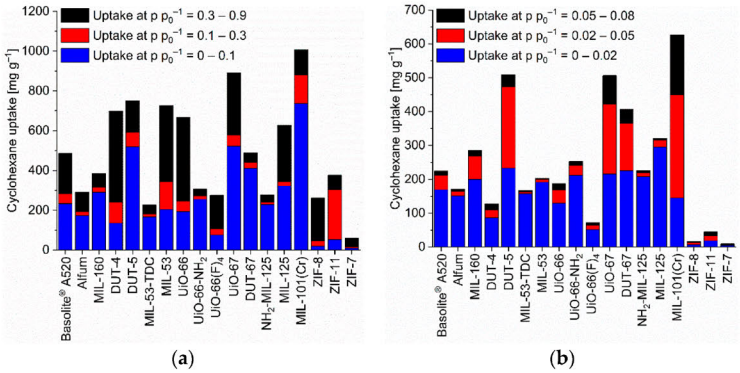

Figure 3. Cyclohexane uptake capacity (at 293 K) of the different MOFs at different relative pressures. (**a**) At relative pressures of 0.1, 0.3 and 0.9; (**b**) at relative pressures of 0.02, 0.05 and 0.08 (specific values in Table S6). For the surface-specific uptake at p p_0^{-1} = 0.1 see Figure S88b.

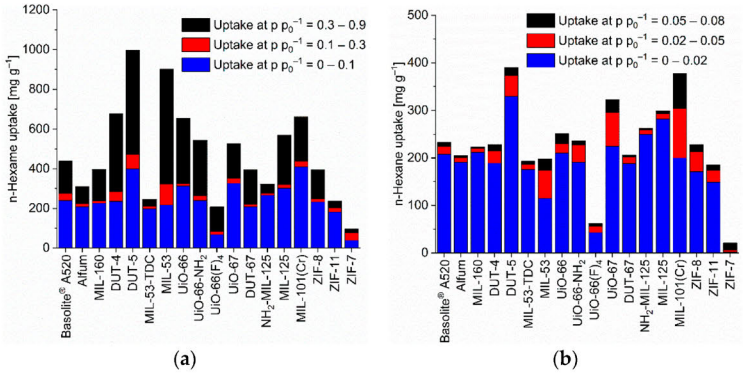

Figure 4. *n*-Hexane uptake capacity (at 293 K) of the different MOFs at different relative pressures. (**a**) At relative pressures of 0.1, 0.3 and 0.9; (**b**) at relative pressures of 0.02, 0.05 and 0.08 (specific values in Table S7). For the surface-specific uptake at p p_0^{-1} = 0.1 see Figure S88c.

The uptake of benzene, cyclohexane and *n*-hexane at p p_0^{-1} = 0.9 follows roughly the experimental pore volume (Figure 5), BET surface area (Figure S85), pore window size (Figure S86) and micropore volume (Figure S87). The (total) pore volumes (Table S2) were obtained from NLDFT calculations using the 'N_2 at 77 K on carbon, slit pore, equilibrium' model. This is noted above, when comparing the volume which the adsorbate would use in a liquid state to the available pore volume deviations to higher uptakes than expected from the pore volume are seen. These can be explained by inter-particle condensation and a slightly higher than expected uptake can also be due to framework transformations, adapting to the guest molecules and giving larger pores. MIL-53 with its known breathing effect is the best studied example [30]. Deviation to lower uptake can be due to solvent inaccessible pore regions which are smaller than the size of the adsorptive or where the access is prevented by gate-opening effects as in the ZIFs [31,76]. Thereby we note that the surface area and experimental pore volume have been determined from nitrogen sorption, with N_2 having a kinetic diameter of (only) 3.64 Å. Adsorptives which are larger than N_2 can be excluded from small pore regions which were included in the nitrogen measurements. The Connolly surface or probe accessible surface, as well as the accessible pore volume should be significantly smaller for larger adsorptives, either because pore windows become too small or pore regions with acute angles become inaccessible for bulkier molecules [53]. A simple correlation of C_6 uptake with surface area and pore volume (from N_2 sorption) cannot reflect this (in)accessibility of pores for larger adsorbates.

As noted in the introduction, for the adsorptive removal of C_6 traces it is not so much the maximum uptake capacity but the uptake at low pressures which is important. Hence, Figures 2–4 (cf. Tables S5–S7) also show the uptake in relative pressure regions down to p p_0^{-1} = 0.02, in order to indicate the MOFs for the removal of C_6 traces.

We have singled out three MOFs from Figures 2–4 for each C_6 vapor at each relative pressure of p p_0^{-1} = 0.1, 0.08, 0.05 and 0.02 which gave the highest uptake values and collected them in Figure 6. For the C_6 vapors a relative pressure of p p_0^{-1} = 0.02 corresponds to an absolute pressure of 1.5 Torr (0.20 kPa) for benzene, 1.55 Torr (0.21 kPa) for cyclohexane and 2.43 Torr (0.32 kPa) for *n*-hexane (Table S8). Remarkably, in the pressure range from p p_0^{-1} = 0.1 down to 0.05 it is pretty much the same three MOFs for each vapor. For benzene, these are DUT-5, DUT-67/UiO-67 and MIL-101(Cr), for cyclohexane and *n*-hexane it is DUT-5, UiO-67 and MIL-101(Cr). DUT-5 and MIL-101(Cr) are always among the top-3 in the range from p p_0^{-1} = 0.1 to 0.05. The third MOF is then either DUT-67 or UiO-67.

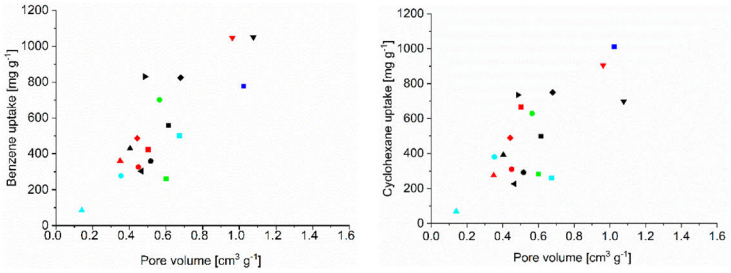

(**a**) (**b**)

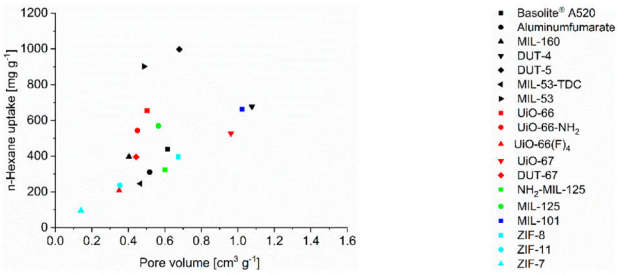

Figure 5. C_6-VOC uptake at p p_0^{-1} = 0.9 (293 K) versus pore volume (NLDFT and total pore volume, Table S2) for (**a**) benzene, (**b**) cyclohexane and (**c**) *n*-hexane with (**d**) legend to the figures.

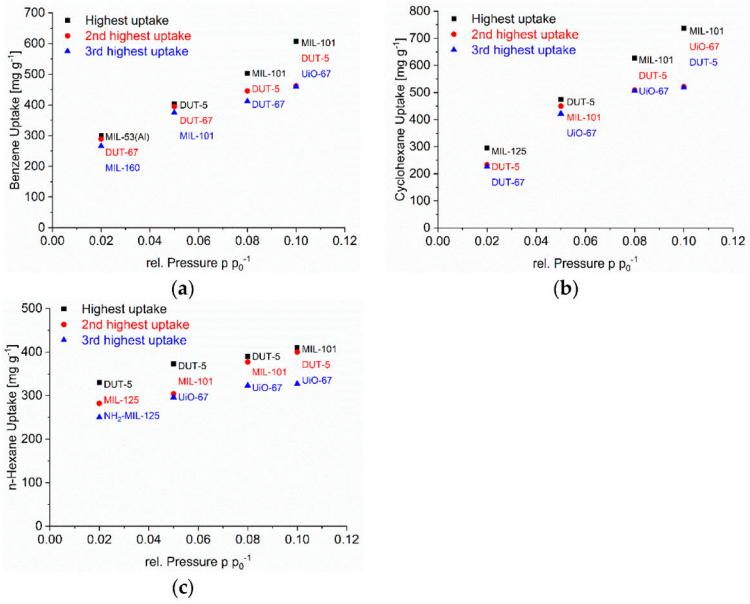

Figure 6. Top three MOFs with the highest C_6 vapor at each relative pressure of p p_0^{-1} = 0.1, 0.08, 0.05 and 0.02 for (**a**) benzene, (**b**) cyclohexane, and (**c**) *n*-hexane.

The MOFs DUT-5 and UiO-67 have the same long biphenyl-4,4′-dicarboxylate linker (Figure 1). At the same time DUT-4 with its also long naphthalene-2,6-dicarboxylate linker does not feature a high uptake at low pressure. MIL-101(Cr) contains the common terephthalate linker which is also part of other MOFs without high uptake. DUT-5 and MIL-101(Cr) are the MOFs with the widest pore window openings/cross sections (Table S2). Notably DUT-67 (with the TDC = thiophenedicarboxylate linker) and UiO-67 already have smaller pore windows which are in the range of DUT-4, MIL-53-TDC and MIL-53 with the latter having lower uptakes in this pressure region. This comparison illustrates that the low-pressure uptake seems to be controlled by a complex combination of ligand and pore-size effect.

The interpretation of the uptake at low pressure is further complicated by the observation that at the lowest pressure of p p_0^{-1} = 0.02 one or two other MOFs come in which were not among the top three above p p_0^{-1} = 0.02. For benzene MIL-160, MIL-53 and

DUT-67, for cyclohexane DUT-5, DUT-67 and MIL-125, for *n*-hexane DUT-5, MIL-125 and NH_2-MIL-125 performed best at p p_0^{-1} = 0.02. Hence, only DUT-5 and/or DUT-67 still remain in the top-3 lists at p p_0^{-1} = 0.02. The other top three MOFs now have smaller pore cross sections of 5-6 Å (MIL-160, MIL-53 edge-edge distance, MIL-125 and NH_2-MIL-125). This cross-section diameter corresponds to the intermediate (critical) van-der-Waals dimensions for benzene of x = 6.628 Å, cyclohexane y = 6.580 Å and *n*-hexane y = 4.536 Å (vide supra) [72]. At this cross-section range, one can assume the C_6 molecules to have dispersive interactions with multiple sides of the molecule to the surface. Such local optima exist for adsorbent structures where the opposite Connolly surfaces are separated by the dimension of the adsorbed molecule which can then simultaneously interact with the surface at its opposite sides [53]. For the long *n*-hexane molecule this multiple-side interaction will probably involve different sections of the chain.

The low-pressure benzene sorption capacity of the top-3 MOFs here is lower than the top literature examples with the MOFs BUT-53 to BUT-58 with 193–256 mg g^{-1} (2.47–3.28 mmol g^{-1}) at 298 K, <10 Pa (p p_0^{-1} < 0.001) (Type-Ia isotherm) [77] or the benchmark materials MOF-5 with 802 mg g^{-1} at 295 K [78] or $[Zn_4O(bdc)(bpz)_2]$ with 561 mg g^{-1} at 298 K and p p_0^{-1} = 0.1 [74] to which only MIL-101(Cr) with 607 mg g^{-1} at 293 K and p p_0^{-1} = 0.1 comes close (Table S2, Figure 2).

Absolute cyclohexane uptakes are difficult to compare to literature data, as most studies aim to achieve benzene/cyclohexane selectivities as high as possible, and thus the reported MOFs feature often very low cyclohexane uptakes as in the work of Mukherjee et al. where the M-MOF-74 analogues have nearly no cyclohexane uptake at all [51]. On the other hand, Eddaoudi et al. tested MOF-5 for cyclohexane and benzene sorption and reached values between 600 and 800 mg g^{-1} at p p_0^{-1} = 1 for both VOCs at 295 K [79]. A cyclohexane uptake above 600 mg g^{-1} at p p_0^{-1} = 0.9 (293 K) is reached with DUT-4, DUT-5, MIL-53, UiO-66, UiO-67, MIL-125 and MIL-101(Cr) (Table S2, Figure 3).

In the literature uptake values for *n*-hexane near p p_0^{-1} = 1 were noted as high for MOF-5 (249 mg g^{-1} at 298 K), MIL-101(Cr) (504 mg g^{-1} at 298 K), or Cu-BTC (175 mg g^{-1} at 303 K) [80]. Here, an *n*-hexane uptake above 500 mg g^{-1} at p p_0^{-1} = 0.9 (293 K) is seen with DUT-4, DUT-5, MIL-53, UiO-66, UiO-66-NH_2, UiO-67, MIL-125 and MIL-101(Cr) (Table S2, Figure 4). We emphasize again that the uptake at p p_0^{-1} = 0.9 may involve condensation in inter-particle mesopores (vide supra).

3.3. Comparative C_6 Uptake

With respect to the three VOCs the comparative adsorption capacity and uptake order at, for example, p p_0^{-1} = 0.1 is depending on the individual MOF and follows no unifying trend (Table S9, because of the possible inter-particle condensation we refrain from comparing the uptake at p p_0^{-1} = 0.9). For the surface-specific vapor uptake at p p_0^{-1} = 0.1 see Figure S88 and discussion in Section S9. Out of the 18 MOFs investigated here (at p p_0^{-1} = 0.1), 10 have benzene, 5 cyclohexane and 3 *n*-hexane as VOC with the highest uptake (Tables S5–S7). Furthermore, benzene being lowest in uptake is only seen for 3 MOFs at p p_0^{-1} = 0.1. At p p_0^{-1} = 0.1 the most frequent order with seven MOFs is benzene > *n*-hexane > cyclohexane; for another three each it is benzene > cyclohexane > *n*-hexane and cyclohexane > benzene > *n*-hexane. In the liquid phase the densities are 0.876 g cm^{-3} for benzene, 0.779 g cm^{-3} for cyclohexane and 0.655 g cm^{-3} for *n*-hexane (at 293 K). Thus, if an available porosity is filled with the adsorbate in a liquid-like state, the specific uptake in g(adsorbate)/g(adsorbent) should be highest for benzene because of its highest density, followed by cyclohexane. Hence, only in four MOFs the uptake follows the reciprocal kinetic diameter (*n*-hexane < benzene < cyclohexane), that is, the smallest adsorbate is preferentially adsorbed only in a few materials. This confirms that the diffusion of the adsorptives in the MOF pore system is not influencing the data and that our measurement conditions ensured thermodynamic equilibrium.

The preferentially higher adsorption of benzene over cyclohexane and *n*-hexane is rationalized through the π···π or C-H···π interactions of benzene (Figure S128c) with the

framework and its higher density in a liquid-like adsorbate state for a given pore volume. When *n*-hexane shows higher adsorption capacity at p p_0^{-1} = 0.1 as in NH_2-MIL-125, ZIF-8 and ZIF-7 (Table S7) it may be tempting to invoke its linear structure and a more favorable packing of adsorbed molecules [37]. However, the liquid state density for *n*-hexane is significantly lower than that for cyclohexane and benzene (vide supra). Thus, higher *n*-hexane adsorption can in our opinion and in the absence of special adsorbate-adsorbent interaction only be explained from its small critical diameter in the series (vide supra). Hence, *n*-hexane can enter (slit) pores and pore window regions which are inaccessible for larger cyclohexane and benzene molecules. The surface area and pore volume from nitrogen sorption will not be fully accessible for larger molecules [53]. However, while one may indeed have such small pore regions together with gate-opening effects in ZIF-8 and ZIF-7 with pore windows near 3 Å (Table S2, unnumbered images in Section S15) this is difficult to see in NH_2-MIL-125 which has pore windows of 6 Å as many other MOFs (Table S2). Additionally, ZIF-11 has a 3 Å pore window and the same benzimidazole ligand as ZIF-7, but gives a higher amount of benzene than *n*-hexane uptake at p p_0^{-1} = 0.1. Thus, an understanding of the C_6 uptake cannot simply be achieved with surface area and pore volume (from N_2 sorption or CO_2 sorption) but involves the complex micropore structure of the MOF.

3.4. Separation–IAST Selectivity

The ideal adsorbed solution theory (IAST) model simulates mixed gas/vapor adsorption behavior and selectivity from single adsorption isotherms (see Sections S10 and S11, for details). Benzene/cyclohexane separation can be regarded as the industrially most interesting process as their separation by distillation is one of the most difficult cases due to similar boiling points and vapor pressures. For comparison equimolar mixtures are investigated of all three C_6-VOC combinations.

In the pairs benzene/cyclohexane, benzene/*n*-hexane and *n*-hexane/cyclohexane the first given adsorptive is the preferred one for most MOFs (Figure 7, black bars). The opposite selectivity, that is a preference for cyclohexane over benzene etc. is seen in fewer MOFs. At the same time, the selectivity value of most investigated MOFs is below 6, although selectivity values higher than 3 would already be sufficient for an adsorbent to be applicable in an industrial separation process [37,81].

The selectivity changes with pressure (Figures S102–S112). Figure 7 plots only the highest selectivity value from three chosen points at 0.01, 0.05 and 0.09 bar (Table S12). We note that selectivities could be much higher for some MOFs, especially for the ZIFs below 0.01 bar, but in this very low pressure range the selectivity can also be strongly influenced from isotherm fitting errors. Relative maxima in the IAST selectivity between the three pressure points were in the error range of the calculation.

When we look at selectivities larger than 10, we find NH_2-MIL-125 with a value of 12 for cyclohexane/benzene and with a value of 14 for *n*-hexane/benzene. Obviously, this MOF discriminates well against benzene. NH_2-MIL-125 is also the only MOF with a high preference of the alkanes over benzene. The next best candidate is ZIF-8 which however significantly (value of 8) prefers *n*-hexane over benzene only at 0.01 bar. We trace the high alkane selectivity of MIL-125-NH_2 to the presence of the amino group in combination with the pore size. The other amino-MOF UiO-66-NH_2 also favors the alkanes over benzene, albeit only slightly. The pore window of UiO-66-NH_2 (7.0 × 7.0 $Å^2$) is slightly larger than in NH_2-MIL-125 (5.9 × 5.9 $Å^2$) so that the effect of NH_2 could be less pronounced. At the same time, also MIL-125 without the NH_2 group still slightly favors the alkanes over benzene with an only somewhat larger pore window of 6.1 × 6.1 $Å^2$. UiO-66 with the same pore size as NH_2-MIL-125 favors either benzene over cyclohexane or has little to no separation effect on the *n*-hexane/benzene mixture.

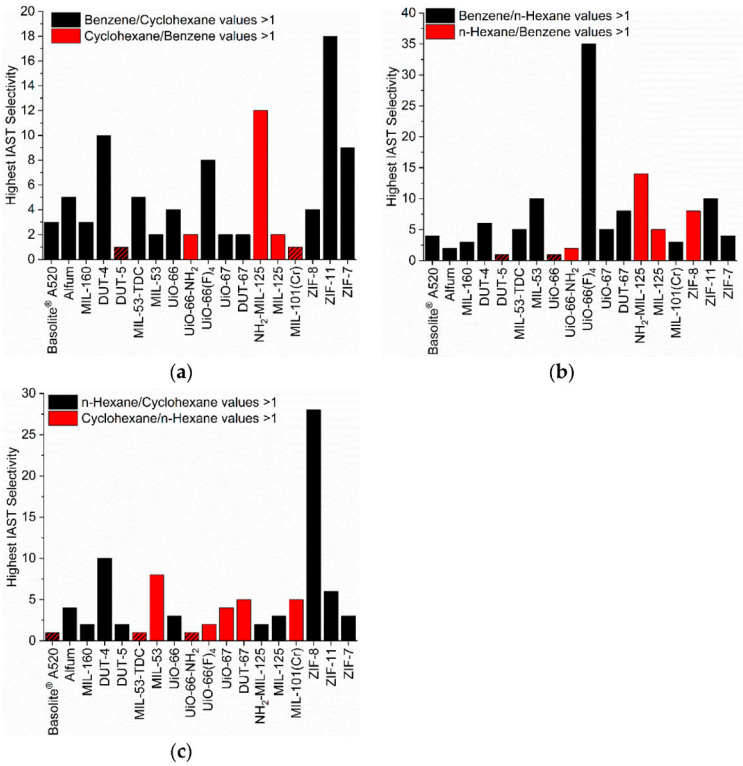

Figure 7. Highest values of the IAST selectivities from the three points at 0.01, 0.05 and 0.09 bar of each MOF for the different VOC pairs (50/50 molar ratio (**a**) benzene/cyclohexane, (**b**) benzene/*n*-hexane and (**c**) cyclohexane/*n*-hexane). The IAST selectivities of 1 are visualized via cross-hatched bars. For the IAST-calculated selectivity dependence with pressure, see Figures S102–S112.

Further, ZIF-11 has a selectivity of 18 for benzene/cyclohexane and UiO-66(F)$_4$ of 13–35 for benzene/*n*-hexane which may be traced to the small pore window cross-sections of 3.0 × 3.0 Å^2 and 2.4 × 4.6 Å^2 respectively (Table S2). In view of the several times noted critical dimensions (for benzene x = 6.628 Å, for cyclohexane y = 6.580 Å, for *n*-hexane y = 4.536 Å) it is difficult to see why benzene can pass and cyclohexane or *n*-hexane are excluded. At the same time, the only slightly smaller window size in ZIF-7 of 2.9 × 2.9 Å^2 still leads to a selectivity of 9 for benzene/cyclohexane but appears to already hinder the entry of benzene when compared to ZIF-11 (cf. Figure 2).

For a benzene/cyclohexane mixture, the MOF DUT-4 and for a benzene/*n*-hexane mixture the MOFs MIL-53 and ZIF-11 give selectivities around 10. The square-channel MOFs DUT-4 and MIL-53 have similar pore windows of 8.5 × 8.5 Å^2. The dimensions obviously allow for the energetically favorable C-H···π arrangement of the benzene adsorbate with the aromatic walls of the adsorbent (Figure S128c). We note that for a benzene dimer the energy of the π···π stacking interaction is 2.73 kcal mol^{-1}, whereas the C-H···π T-shape is more stable with an interaction energy of 2.84 kcal mol^{-1} [82]. Additionally, the crystal structures of benzene all show the herringbone packing with C-H···π interactions (Section S14, Figure S128).

The role of the benzimidazole linker in ZIF-11 and ZIF-7 towards possibly engaging in π···π or C-H···π interactions with the benzene adsorbate (Figure S128c) cannot be very

significant as the selectivity of both ZIFs for benzene/*n*-hexane is much lower (10 and 4, respectively) than for benzene/cyclohexane.

A selectivity of *n*-hexane over cyclohexane is most pronounced for ZIF-8 and is at the same time also the second highest calculated selectivity in the chosen pressure region. The *n*-hexane/cyclohexane selectivity of ZIF-8 can be correlated to the small pore window size and its gate-opening effects. For DUT-4 a pronounced *n*-hexane/cyclohexane selectivity is only present in the low-pressure range.

The separation of benzene/cyclohexane, benzene/*n*-hexane etc. with selectivities of 10 and above (Figure 7 and Section S11) show again a finely tuned and difficult to predict interplay of pore window size with (critical) adsorptive size and possibly a role of electrostatics through functional groups such as NH_2.

3.5. Cycling Adsorption Runs

The MOFs were found stable towards the liquid and gaseous C_6-VOCs from PXRD and nitrogen sorption analysis after 5 days of contact with the VOC and re-activation (see Section S12 for details). For ZIF-11 we also performed a cycling adsorption tests for benzene to check for the cycling stability and uptake consistency. (Figure 8).

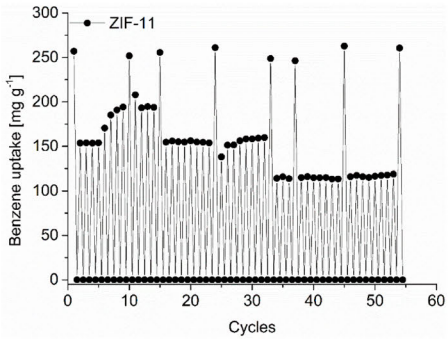

Figure 8. Benzene cycling test of ZIF-11 with 55 ad/desorption cycles up to a relative pressure of p p_0^{-1} = 0.3 and a full adsorption measured every few cycles and at the end of the 55 cycles.

To increase the rate of the cycling process the measurements were mostly performed only up to a relative pressure of p p_0^{-1} 0.3. Within the in total 54 cycles depicted in Figure 8 we also did eight full adsorption cycles. The full adsorption measurements did not show a decrease in the initial benzene uptake of about 250 mg g^{-1}. However, the more rapid short adsorption cycles with evacuation at 298 K for only 0.5 h and high dosing rates upon adsorption show a fluctuation. The short-time cycling starts with a benzene uptake of 150 mg g^{-1} under these conditions. This uptake value started to increase after 5 cycles to near 200 mg g^{-1} which could be due to an enhanced activation through residual solvent removal from the repeated activation. However, after 15 total cycles the benzene uptake returned to 150 mg g^{-1} at which value it stayed until cycle 32 (Figure 8). From cycle 34 onwards, the uptake dropped to 120 mg g^{-1} where it stayed rather constant until cycle 53. However, a subsequent full adsorption run gave the initial 250 mg g^{-1} uptake.

4. Conclusions

The C_6 volatile organic compounds (VOCs) benzene, cyclohexane and *n*-hexane are important industrial products, but toxic for humans or the environment and need to be removed from water and air. This removal is an important part of industrial processes as well. Benzene is classified as a carcinogen, whereas cyclohexane causes dermatitis and *n*-hexane nerve damage. Metal–organic frameworks (MOFs) are promising candidates for toxic gas and vapor removal. In this work, for 18 different MOFs and ZIFs (15 MOFs and

3 ZIFs) the maximum VOC uptake capacity and the long-term stability were tested and correlated with the properties of the different MOFs. The analyzed properties were metal-source, linker, pore volume, micropore volume, pore window and BET surface area. The uptake capacity was tested via volumetric adsorption measurements at 293 K and the long-term stability was tested under liquid and vapor conditions at room temperature. All investigated MOFs proved stable against the C_6-VOCs. Out of the 18 MOFs investigated here, 15 gave desorption isotherms with a wide or very wide hysteresis to the adsorption branch, at least for one of the vapors. Most MOF-adsorbate pairs reach at least half of their maximum uptake at p p_0^{-1} = 0.9 already at p p_0^{-1} = 0.1 which is the upper end for the uptake of vapor traces. Already above a relative pressure (p p_0^{-1}) of about 0.45 interparticle condensation takes place. Even at lower relative pressure—which is important for trace vapor removal—there is no single parameter, such as surface area, pore volume or pore dimensions, which correlates with the uptake or selectivity. From the 18 MOFs, 10 have benzene, 5 have cyclohexane and 3 have *n*-hexane as VOC with the highest uptake (at p p_0^{-1} = 0.1). The VOC uptake correlates only roughly with pore volume, BET surface area or pore window and micropore volume (obtained from N_2 sorption). From a comparison of the MOF pore volume with the approximated volume of the adsorbate in a liquid state, a pore filling substantially above 100% is seen, which is explained by inter-particle condensation. The best correlation is between the benzene uptake and pore volume. The widest spread is the correlation between VOC uptake and BET surface area. Another interesting correlation is between the pore window and the uptake. While it could be expected that large pore cross sections and large pore volumes generate a high uptake, it was remarkable to see that even MOFs with pore window sizes smaller than the diameter of the adsorbent molecules can give a sizeable uptake. For a good selectivity, MOFs in particular with such a small pore window cross section feature prominently.

To a surprise, MOF with an amino group on the ligand was also highly discriminating against benzene, that is, it gave higher cyclohexane and *n*-hexane uptakes. No uptake is seen in ZIF-7 for benzene and cyclohexane; only the smaller *n*-hexane has access to the pore. The influence of the metal does not affect the sorption properties, as was to be expected and was not further investigated. The simulated IAST selectivities of the MOFs show a necessity towards small pore windows or diameters for high selectivity values, as found for ZIFs (ZIF-8, ZIF-11 and ZIF-7). However, the interplay between pore window size and (critical) size of the adsorbate and possibly the role of functional groups such as NH_2 require more in-depth investigations for a more complete understanding.

Supplementary Materials: The following supporting information can be downloaded at: https://www.mdpi.com/article/10.3390/nano12203614/s1. S1 Materials and equipment; S2 MOF syntheses, crystal structures and MOF parameters; S3 Powder X-ray diffraction (PXRD) measurements; S4 Nitrogen sorption experiments (T = 77 K); S5 Carbon dioxide experiments (T = 273 K); S6 Vapor sorption experiments (T = 293 K); S7 Thermogravimetric analysis (TGA); S8 Scanning electron microscopy (SEM); S9 VOC uptake versus BET surface, pore window size, micropore volume; S10 VOC sorption studies; S11 Ideal Adsorbed Solution Theory, IAST-Selectivity; S12 Stability tests; S13 Gas Sorption at 293 K; S14 Crystal structures of benzene; S15 Images from 'Mercury' – Display Voids' calculation; S16 References. References [83–110] are cited in the Supplementary Materials.

Author Contributions: Conceptualization: C.J. (Christian Jansen) and C.J. (Christoph Janiak); methodology: C.J. (Christian Jansen); validation: C.J. (Christian Jansen); formal analysis: C.J. (Christian Jansen), N.A., A.S. (Alex Spieß), J.L., A.S. (Alexa Schmitz), S.X., S.G.; investigation: C.J. (Christian Jansen), N.A., A.S. (Alex Spieß), J.L., A.S. (Alexa Schmitz), S.X., S.G.; resources: C.J. (Christoph Janiak); data curation: C.J (Christian Jansen); writing—original draft preparation: C.J. (Christian Jansen); writing—review and editing: C.J. (Christian Jansen) and C.J. (Christoph Janiak); visualization: C.J. (Christian Jansen); supervision: C.J. (Christoph Janiak); project administration: C.J. (Christoph Janiak); funding acquisition: C.J. (Christoph Janiak). All authors have read and agreed to the published version of the manuscript.

Funding: C.J. (Christoph Janiak) is indebted to the DFG for funding within the priority program SPP 1928 "COORNET" (grant Ja466–43/1).

Data Availability Statement: The data presented in this study are available on request from the corresponding author.

Conflicts of Interest: The authors declare no conflict of interest.

References

1. Mukherjee, S.; Desai, A.V.; Ghosh, S.K. Potential of metal–organic frameworks for adsorptive separation of industrially and environmentally relevant liquid mixtures. *Coord. Chem. Rev.* **2018**, *367*, 82–126. https://doi.org/10.1016/j.ccr.2018.04.001.
2. Barea, E.; Montoro, C.; Navarro, J.A.R. Toxic gas removal–metal-organic frameworks for the capture and degradation of toxic gases and vapours. *Chem. Soc. Rev.* **2014**, *43*, 5419–5430. https://doi.org/10.1039/c3cs60475f.
3. Woellner, M.; Hausdorf, S.; Klein, N.; Mueller, P.; Smith, M.W.; Kaskel, S. Adsorption and Detection of Hazardous Trace Gases by Metal-Organic Frameworks. *Adv. Mater.* **2018**, *30*, 1704679. https://doi.org/10.1002/adma.201704679.
4. Brandt, P.; Nuhnen, A.; Lange, M.; Möllmer, J.; Weingart, O.; Janiak, C. Metal-Organic Frameworks with Potential Application for SO_2 Separation and Flue Gas Desulfurization. *ACS Appl. Mater. Interfaces* **2019**, *11*, 17350–17358. https://doi.org/10.1021/acsami.9b00029.
5. Mukherjee, S.; He, Y.; Franz, D.; Wang, S.-Q.; Xian, W.-R.; Bezrukov, A.A.; Space, B.; Xu, Z.; He, J.; Zaworotko, M.J. Halogen-C_2H_2 Binding in Ultramicroporous Metal-Organic Frameworks (MOFs) for Benchmark C_2H_2/CO_2 Separation Selectivity. *Chem. Eur. J.* **2020**, *26*, 4923–4929. https://doi.org/10.1002/chem.202000008.
6. Agrawal, M.; Sava Gallis, D.F.; Greathouse, J.A.; Sholl, D.S. How Useful Are Common Simulants of Chemical Warfare Agents at Predicting Adsorption Behavior? *J. Phys. Chem. C* **2018**, *122*, 26061–26069. https://doi.org/10.1021/acs.jpcc.8b08856.
7. Sun, X.; Wu, T.; Yan, Z.; Chen, W.-J.; Lian, X.-B.; Xia, Q.; Chen, S.; Wu, Q.-H. Novel MOF-5 derived porous carbons as excellent adsorption materials for n-hexane. *J. Solid State Chem.* **2019**, *271*, 354–360. https://doi.org/10.1016/j.jssc.2019.01.002.
8. Zhang, X.; Yang, Y.; Lv, X.; Wang, Y.; Liu, N.; Chen, D.; Cui, L. Adsorption/desorption kinetics and breakthrough of gaseous toluene for modified microporous-mesoporous UiO-66 metal organic framework. *J. Hazard. Mater.* **2019**, *366*, 140–150. https://doi.org/10.1016/j.jhazmat.2018.11.099.
9. Duan, C.; Li, F.; Yang, M.; Zhang, H.; Wu, Y.; Xi, H. Rapid Synthesis of Hierarchically Structured Multifunctional Metal–Organic Zeolites with Enhanced Volatile Organic Compounds Adsorption Capacity. *Ind. Eng. Chem. Res.* **2018**, *57*, 15385–15394. https://doi.org/10.1021/acs.iecr.8b04028.
10. Kim, B.; Lee, Y.-R.; Kim, H.-Y.; Ahn, W.-S. Adsorption of volatile organic compounds over MIL-125-NH_2. *Polyhedron* **2018**, *154*, 343–349. https://doi.org/10.1016/j.poly.2018.08.010.
11. Yang, C.; Miao, G.; Pi, Y.; Xia, Q.; Wu, J.; Li, Z.; Xiao, J. Abatement of various types of VOCs by adsorption/catalytic oxidation: A review. *Chem. Eng. Technol.* **2019**, *370*, 1128–1153. https://doi.org/10.1016/j.cej.2019.03.232.
12. Li, X.; Zhang, L.; Yang, Z.; Wang, P.; Yan, Y.; Ran, J. Adsorption materials for volatile organic compounds (VOCs) and the key factors for VOCs adsorption process: A review. *Sep. Purif. Technol.* **2020**, *235*, 116213. https://doi.org/10.1016/j.seppur.2019.116213.
13. Gelles, T.; Krishnamurthy, A.; Adebayo, B.; Rownaghi, A.; Rezaei, F. Abatement of gaseous volatile organic compounds: A material perspective. *Catal. Today* **2020**, *350*, 3–18. https://doi.org/10.1016/j.cattod.2019.06.017.
14. Batten, S.R.; Champness, N.R.; Chen, X.-M.; Garcia-Martinez, J.; Kitagawa, S.; Öhrström, L.; O'Keeffe, M.; Paik Suh, M.; Reedijk, J. Terminology of metal–organic frameworks and coordination polymers (IUPAC Recommendations 2013). *Pure Appl. Chem.* **2013**, *85*, 1715–1724. https://doi.org/10.1351/PAC-REC-12-11-20.
15. Bhattarai, D.P.; Pant, B.; Acharya, J.; Park, M.; Ojha, G.P. Recent Progress in Metal-Organic Framework-Derived Nanostructures in the Removal of Volatile Organic Compounds. *Molecules* **2021**, *26*, 4948. https://doi.org/10.3390/molecules26164948.
16. Agrawal, M.; Bhattacharyya, S.; Huang, Y.; Jayachandrababu, K.C.; Murdock, C.R.; Bentley, J.A.; Rivas-Cardona, A.; Mertens, M.M.; Walton, K.S.; Sholl, D.S.; et al. Liquid-Phase Multicomponent Adsorption and Separation of Xylene Mixtures by Flexible MIL-53 Adsorbents. *J. Phys. Chem. C* **2018**, *122*, 386–397. https://doi.org/10.1021/acs.jpcc.7b09105.
17. Sini, K.; Bourgeois, D.; Idouhar, M.; Carboni, M.; Meyer, D. Metal–organic framework sorbents for the removal of perfluorinated compounds in an aqueous environment. *New J. Chem.* **2018**, *42*, 17889–17894. https://doi.org/10.1039/C8NJ03312A.
18. Chevalier, V.; Martin, J.; Peralta, D.; Roussey, A.; Tardif, F. Performance of HKUST-1 Metal-Organic Framework for a VOCs mixture adsorption at realistic concentrations ranging from 0.5 to 2.5 ppmv under different humidity conditions. *J. Environ. Chem. Eng.* **2019**, *7*, 103131. https://doi.org/10.1016/j.jece.2019.103131.
19. Wang, H.; Liu, Y.; Li, J. Designer Metal-Organic Frameworks for Size-Exclusion-Based Hydrocarbon Separations: Progress and Challenges. *Adv. Mater.* **2020**, *32*, 2002603. https://doi.org/10.1002/adma.202002603.
20. Li, J.-R.; Kuppler, R.J.; Zhou, H.-C. Selective gas adsorption and separation in metal-organic frameworks. *Chem. Soc. Rev.* **2009**, *38*, 1477–1504. https://doi.org/10.1039/b802426j.
21. Monneyron, P.; Manero, M.-H.; Foussard, J.-N. Measurement and modeling of single- and multi-component adsorption equilibria of VOC on high-silica zeolites. *Environ. Sci. Technol.* **2003**, *37*, 2410–2414. https://doi.org/10.1021/es026206c.
22. Ouzzine, M.; Romero-Anaya, A.J.; Lillo-Ródenas, M.A.; Linares-Solano, A. Spherical activated carbons for the adsorption of a real multicomponent VOC mixture. *Carbon* **2019**, *148*, 214–223. https://doi.org/10.1016/j.carbon.2019.03.075.
23. Sui, H.; Liu, J.; He, L.; Li, X.; Jani, A. Adsorption and desorption of binary mixture of acetone and ethyl acetate on silica gel. *Chem. Eng. Sci.* **2019**, *197*, 185–194. https://doi.org/10.1016/j.ces.2018.12.010.

24. Eddaoudi, M.; Kim, J.; Rosi, N.; Vodak, D.; Wachter, J.; O'Keeffe, M.; Yaghi, O.M. Systematic design of pore size and functionality in isoreticular MOFs and their application in methane storage. *Science* **2002**, *295*, 469–472. https://doi.org/10.1126/science.1067208.
25. Wang, H.; Dong, X.; Lin, J.; Teat, S.J.; Jensen, S.; Cure, J.; Alexandrov, E.V.; Xia, Q.; Tan, K.; Wang, Q.; et al. Topologically guided tuning of Zr-MOF pore structures for highly selective separation of C6 alkane isomers. *Nat. Commun.* **2018**, *9*, 1745. https://doi.org/10.1038/s41467-018-04152-5.
26. Wu, Y.; Chen, H.; Liu, D.; Xiao, J.; Qian, Y.; Xi, H. Effective ligand functionalization of zirconium-based metal-organic frameworks for the adsorption and separation of benzene and toluene: A multiscale computational study. *ACS Appl. Energy Mater.* **2015**, *7*, 5775–5787. https://doi.org/10.1021/am508570d.
27. Sapianik, A.A.; Kovalenko, K.A.; Samsonenko, D.G.; Barsukova, M.O.; Dybtsev, D.N.; Fedin, V.P. Exceptionally effective benzene/cyclohexane separation on a nitro-decorated metal-organic framework. *Chem. Commun.* **2020**, *56*, 8241–8244. https://doi.org/10.1039/D0CC03227A.
28. Kökçam-Demir, Ü.; Goldman, A.; Esrafili, L.; Gharib, M.; Morsali, A.; Weingart, O.; Janiak, C. Coordinatively unsaturated metal sites (open metal sites) in metal-organic frameworks: Design and applications. *Chem. Soc. Rev.* **2020**, *49*, 2751–2798. https://doi.org/10.1039/c9cs00609e.
29. Liu, A.; Peng, X.; Jin, Q.; Jain, S.K.; Vicent-Luna, J.M.; Calero, S.; Zhao, D. Adsorption and Diffusion of Benzene in Mg-MOF-74 with Open Metal Sites. *ACS Appl. Mater. Interfaces* **2019**, *11*, 4686–4700. https://doi.org/10.1021/acsami.8b20447.
30. Loiseau, T.; Serre, C.; Huguenard, C.; Fink, G.; Taulelle, F.; Henry, M.; Bataille, T.; Férey, G. A rationale for the large breathing of the porous aluminum terephthalate (MIL-53) upon hydration. *Chem. Eur. J.* **2004**, *10*, 1373–1382. https://doi.org/10.1002/chem.200305413.
31. Chen, D.-L.; Wang, N.; Wang, F.-F.; Xie, J.; Zhong, Y.; Zhu, W.; Johnson, J.K.; Krishna, R. Utilizing the Gate-Opening Mechanism in ZIF-7 for Adsorption Discrimination between N_2O and CO_2. *J. Phys. Chem. C* **2014**, *118*, 17831–17837. https://doi.org/10.1021/jp5056733.
32. Cuadrado-Collados, C.; Fernández-Català, J.; Fauth, F.; Cheng, Y.Q.; Daemen, L.L.; Ramirez-Cuesta, A.J.; Silvestre-Albero, J. Understanding the breathing phenomena in nano-ZIF-7 upon gas adsorption. *J. Mater. Chem. A* **2017**, *5*, 20938–20946. https://doi.org/10.1039/C7TA05922A.
33. Gücüyener, C.; van den Bergh, J.; Gascon, J.; Kapteijn, F. Ethane/ethene separation turned on its head: Selective ethane adsorption on the metal-organic framework ZIF-7 through a gate-opening mechanism. *J. Am. Chem. Soc.* **2010**, *132*, 17704–17706. https://doi.org/10.1021/ja1089765.
34. van den Bergh, J.; Gücüyener, C.; Pidko, E.A.; Hensen, E.J.M.; Gascon, J.; Kapteijn, F. Understanding the anomalous alkane selectivity of ZIF-7 in the separation of light alkane/alkene mixtures. *Chem. Eur. J.* **2011**, *17*, 8832–8840. https://doi.org/10.1002/chem.201100958.
35. Shearer, G.C.; Chavan, S.; Ethiraj, J.; Vitillo, J.G.; Svelle, S.; Olsbye, U.; Lamberti, C.; Bordiga, S.; Lillerud, K.P. Tuned to Perfection: Ironing Out the Defects in Metal–Organic Framework UiO-66. *Chem. Mater.* **2014**, *26*, 4068–4071. https://doi.org/10.1021/cm501859p.
36. Zhang, X.; Shi, X.; Chen, J.; Yang, Y.; Lu, G. The preparation of defective UiO-66 metal organic framework using MOF-5 as structural modifier with high sorption capacity for gaseous toluene. *J. Environ. Chem. Eng.* **2019**, *7*, 103405. https://doi.org/10.1016/j.jece.2019.103405.
37. Saini, V.K.; Pires, J. Development of metal organic fromwork-199 immobilized zeolite foam for adsorption of common indoor VOCs. *J. Environ. Sci.* **2017**, *55*, 321–330. https://doi.org/10.1016/j.jes.2016.09.017.
38. Belarbi, H.; Gonzales, P.; Basta, A.; Trens, P. Comparison of the benzene sorption properties of metal organic frameworks: Influence of the textural properties. *Environ. Sci. Process. Impacts* **2019**, *21*, 407–412. https://doi.org/10.1039/c8em00481a.
39. Gwardiak, S.; Szczęśniak, B.; Choma, J.; Jaroniec, M. Benzene adsorption on synthesized and commercial metal–organic frameworks. *J. Porous Mater.* **2019**, *26*, 775–783. https://doi.org/10.1007/s10934-018-0678-0.
40. Dörfelt, C.; Kolvenbach, R.; Wirth, A.S.; Albert, M.; Köhler, K. Catalytic Properties of a Novel Raney-Nickel Foam in the Hydrogenation of Benzene. *Catal. Lett.* **2016**, *146*, 2425–2429. https://doi.org/10.1007/s10562-016-1879-2.
41. Villaluenga, J.P.G.; Tabe-Mohammadi, A. A review on the separation of benzene/cyclohexane mixtures by pervaporation processes. *J. Membr. Sci.* **2000**, *169*, 159–174.
42. Krasavage, W.J.; O´Donoghue, J.L.; Di Vincenzo, G.D.; Terhaar, C.J. The relative neurotoxicity of methyl-n-butyl ketone, n-hexane and their metabolites. *Toxicol. Appl. Pharmacol.* **1980**, *52*, 433–441. https://doi.org/10.1016/0041-008X(80)90338-5.
43. Macreadie, L.K.; Qazvini, O.T.; Babarao, R. Reversing Benzene/Cyclohexane Selectivity through Varying Supramolecular Interactions Using Aliphatic, Isoreticular MOFs. *ACS Appl. Mater. Interfaces* **2021**, *26*, 30885–30890. https://doi.org/10.1021/acsami.1c08823.
44. Jiao, Y.; Liu, Y.; Zhu, G.; Hungerford, J.T.; Bhattacharyya, S.; Lively, R.P.; Sholl, D.S.; Walton, K.S. Heat-Treatment of Defective UiO-66 from Modulated Synthesis: Adsorption and Stability Studies. *J. Phys. Chem. C* **2017**, *121*, 23471–23479. https://doi.org/10.1021/acs.jpcc.7b07772.
45. Kondo, A.; Suzuki, T.; Kotani, R.; Maeda, K. Liquid/vapor-induced reversible dynamic structural transformation of a three-dimensional Cu-based MOF to a one-dimensional MOF showing gate adsorption. *Dalton Trans.* **2017**, *46*, 6762–6768. https://doi.org/10.1039/c7dt01126a.

46. Santra, A.; Francis, M.; Parshamoni, S.; Konar, S. Nanoporous Cu(I) Metal-Organic Framework: Selective Adsorption of Benzene and Luminescence Sensing of Nitroaromatics. *ChemistrySelect* **2017**, 2, 3200–3206. https://doi.org/10.1002/slct.201700416.
47. Lysova, A.A.; Samsonenko, D.G.; Dorovatovskii, P.V.; Lazarenko, V.A.; Khrustalev, V.N.; Kovalenko, K.A.; Dybtsev, D.N.; Fedin, V.P. Tuning the Molecular and Cationic Affinity in a Series of Multifunctional Metal-Organic Frameworks Based on Dodecanuclear Zn(II) Carboxylate Wheels. *J. Am. Chem. Soc.* **2019**, *141*, 17260–17269. https://doi.org/10.1021/jacs.9b08322.
48. Zhou, L.; Wang, S.; Chen, Y.; Serre, C. Direct synthesis of robust hcp UiO-66(Zr) MOF using poly(ethylene terephthalate) waste as ligand source. *Microporous Mesoporous Mater.* **2019**, *290*, 109674. https://doi.org/10.1016/j.micromeso.2019.109674.
49. Sapianik, A.A.; Dudko, E.R.; Kovalenko, K.A.; Barsukova, M.O.; Samsonenko, D.G.; Dybtsev, D.N.; Fedin, V.P. Metal-Organic Frameworks for Highly Selective Separation of Xylene Isomers and Single-Crystal X-ray Study of Aromatic Guest-Host Inclusion Compounds. *ACS Appl. Mater. Interfaces* **2021**, *13*, 14768–14777. https://doi.org/10.1021/acsami.1c02812.
50. Manna, B.; Mukherjee, S.; Desai, A.V.; Sharma, S.; Krishna, R.; Ghosh, S.K. A π-electron deficient diaminotriazine functionalized MOF for selective sorption of benzene over cyclohexane. *Chem. Commun.* **2015**, *51*, 15386–15389. https://doi.org/10.1039/c5cc06128h.
51. Mukherjee, S.; Manna, B.; Desai, A.V.; Yin, Y.; Krishna, R.; Babarao, R.; Ghosh, S.K. Harnessing Lewis acidic open metal sites of metal-organic frameworks: The foremost route to achieve highly selective benzene sorption over cyclohexane. *Chem. Commun.* **2016**, *52*, 8215–8218. https://doi.org/10.1039/c6cc03015g.
52. Macreadie, L.K.; Babarao, R.; Setter, C.J.; Lee, S.J.; Qazvini, O.T.; Seeber, A.J.; Tsanaktsidis, J.; Telfer, S.G.; Batten, S.R.; Hill, M.R. Enhancing Multicomponent Metal-Organic Frameworks for Low Pressure Liquid Organic Hydrogen Carrier Separations. *Angew. Chem. Int. Ed.* **2020**, *59*, 6090–6098. https://doi.org/10.1002/anie.201916159.
53. Thommes, M.; Kaneko, K.; Neimark, A.V.; Olivier, J.P.; Rodriguez-Reinoso, F.; Rouquerol, J.; Sing, K.S. Physisorption of gases, with special reference to the evaluation of surface area and pore size distribution (IUPAC Technical Report). *Pure Appl. Chem.* **2015**, *87*, 1051–1069. https://doi.org/10.1515/pac-2014-1117.
54. Leung, E.; Müller, U.; Trukhan, N.; Mattenheimer, H.; Cox, G.; Blei, S. Process for Preparing Porous Metal-Organic Frameworks Based On Aluminum Fumarate. US 2012/0082864 A1, 5 April 2012.
55. Alvarez, E.; Guillou, N.; Martineau, C.; Bueken, B.; Van de Voorde, B.; Le Guillouzer, C.; Fabry, P.; Nouar, F.; Taulelle, F.; de Vos, D.; et al. The structure of the aluminum fumarate metal-organic framework A520. *Angew. Chem. Int. Ed.* **2015**, *54*, 3664–3668. https://doi.org/10.1002/anie.201410459.
56. Cadiau, A.; Lee, J.S.; Damasceno Borges, D.; Fabry, P.; Devic, T.; Wharmby, M.T.; Martineau, C.; Foucher, D.; Taulelle, F.; Jun, C.-H.; et al. Design of hydrophilic metal organic framework water adsorbents for heat reallocation. *Adv. Mater.* **2015**, *27*, 4775–4780. https://doi.org/10.1002/adma.201502418.
57. Senkovska, I.; Hoffmann, F.; Fröba, M.; Getzschmann, J.; Böhlmann, W.; Kaskel, S. New highly porous aluminium based metal-organic frameworks: Al(OH)(ndc) (ndc=2,6-naphthalene dicarboxylate) and Al(OH)(bpdc) (bpdc=4,4′-biphenyl dicarboxylate). *Microporous Mesoporous Mater.* **2009**, *122*, 93–98. https://doi.org/10.1016/j.micromeso.2009.02.020.
58. Gotthardt, M.A.; Grosjean, S.; Brunner, T.S.; Kotzel, J.; Gänzler, A.M.; Wolf, S.; Bräse, S.; Kleist, W. Synthesis and post-synthetic modification of amine-, alkyne-, azide- and nitro-functionalized metal-organic frameworks based on DUT-5. *Dalton Trans.* **2015**, *44*, 16802–16809. https://doi.org/10.1039/c5dt02276b.
59. Tannert, N.; Ernst, S.-J.; Jansen, C.; Bart, H.-J.; Henninger, S.K.; Janiak, C. Evaluation of the highly stable metal–organic framework MIL-53(Al)-TDC (TDC = 2,5-thiophenedicarboxylate) as a new and promising adsorbent for heat transformation applications. *J. Mater. Chem. A* **2018**, *6*, 17706–17712. https://doi.org/10.1039/C8TA04407D.
60. Zi, G.; Yan, Z.; Wang, Y.; Chen, Y.; Guo, Y.; Yuan, F.; Gao, W.; Wang, Y.; Wang, J. Catalytic hydrothermal conversion of carboxymethyl cellulose to value-added chemicals over metal-organic framework MIL-53(Al). *Carbohydr. Polym.* **2015**, *115*, 146–151. https://doi.org/10.1016/j.carbpol.2014.08.065.
61. Aguilera-Sigalat, J.; Bradshaw, D. A colloidal water-stable MOF as a broad-range fluorescent pH sensor via post-synthetic modification. *Chem. Commun.* **2014**, *50*, 4711–4713. https://doi.org/10.1039/c4cc00659c.
62. Hu, Z.; Peng, Y.; Kang, Z.; Qian, Y.; Zhao, D. A Modulated Hydrothermal (MHT) Approach for the Facile Synthesis of UiO-66-Type MOFs. *Inorg. Chem.* **2015**, *54*, 4862–4868. https://doi.org/10.1021/acs.inorgchem.5b00435.
63. Katz, M.J.; Brown, Z.J.; Colón, Y.J.; Siu, P.W.; Scheidt, K.A.; Snurr, R.Q.; Hupp, J.T.; Farha, O.K. A facile synthesis of UiO-66, UiO-67 and their derivatives. *Chem. Commun.* **2013**, *49*, 9449–9451. https://doi.org/10.1039/c3cc46105j.
64. Drache, F.; Bon, V.; Senkovska, I.; Marschelke, C.; Synytska, A.; Kaskel, S. Postsynthetic Inner-Surface Functionalization of the Highly Stable Zirconium-Based Metal-Organic Framework DUT-67. *Inorg. Chem.* **2016**, *55*, 7206–7213. https://doi.org/10.1021/acs.inorgchem.6b00829.
65. Sohail, M.; Yun, Y.-N.; Lee, E.; Kim, S.K.; Cho, K.; Kim, J.-N.; Kim, T.W.; Moon, J.-H.; Kim, H. Synthesis of Highly Crystalline NH_2-MIL-125 (Ti) with S-Shaped Water Isotherms for Adsorption Heat Transformation. *Cryst. Growth Des.* **2017**, *17*, 1208–1213. https://doi.org/10.1021/acs.cgd.6b01597.
66. Santaclara, J.G.; Nasalevich, M.A.; Castellanos, S.; Evers, W.H.; Spoor, F.C.M.; Rock, K.; Siebbeles, L.D.A.; Kapteijn, F.; Grozema, F.; Houtepen, A.; et al. Organic Linker Defines the Excited-State Decay of Photocatalytic MIL-125(Ti)-Type Materials. *ChemSusChem.* **2016**, *9*, 388–395. https://doi.org/10.1002/cssc.201501353.
67. Zhao, T.; Jeremias, F.; Boldog, I.; Nguyen, B.; Henninger, S.K.; Janiak, C. High-yield, fluoride-free and large-scale synthesis of MIL-101(Cr). *Dalton Trans.* **2015**, *44*, 16791–16801. https://doi.org/10.1039/c5dt02625c.

68. Kida, K.; Okita, M.; Fujita, K.; Tanaka, S.; Miyake, Y. Formation of high crystalline ZIF-8 in an aqueous solution. *CrystEngComm.* **2013**, *15*, 1794–1801. https://doi.org/10.1039/c2ce26847g.
69. He, M.; Yao, J.; Liu, Q.; Zhong, Z.; Wang, H. Toluene-assisted synthesis of RHO-type zeolitic imidazolate frameworks: Synthesis and formation mechanism of ZIF-11 and ZIF-12. *Dalton Trans.* **2013**, *42*, 16608–16613. https://doi.org/10.1039/c3dt52103f.
70. Kang, C.-H.; Lin, Y.-F.; Huang, Y.-S.; Tung, K.-L.; Chang, K.-S.; Chen, J.-T.; Hung, W.-S.; Lee, K.-R.; Lai, J.-Y. Synthesis of ZIF-7/chitosan mixed-matrix membranes with improved separation performance of water/ethanol mixtures. *J. Membr. Sci.* **2013**, *438*, 105–111. https://doi.org/10.1016/j.memsci.2013.03.028.
71. Li, Y.; Liang, F.; Bux, H.; Yang, W.; Caro, J. Zeolitic imidazolate framework ZIF-7 based molecular sieve membrane for hydrogen separation. *J. Membr. Sci.* **2010**, *354*, 48–54. https://doi.org/10.1016/j.memsci.2010.02.074.
72. Webster, C.E.; Drago, R.S.; Zerner, M.C. Molecular Dimensions for Adsorptives. *J. Am. Chem. Soc.* **1998**, *1998*, 5509–5516. https://doi.org/10.1021/ja973906m.
73. Yang, Q.-Y.; Lama, P.; Sen, S.; Lusi, M.; Chen, K.-J.; Gao, W.-Y.; Shivanna, M.; Pham, T.; Hosono, N.; Kusaka, S.; et al. Reversible Switching between Highly Porous and Nonporous Phases of an Interpenetrated Diamondoid Coordination Network That Exhibits Gate-Opening at Methane Storage Pressures. *Angew. Chem. Int. Ed.* **2018**, *57*, 5684–5689. https://doi.org/10.1002/anie.201800820.
74. Hou, L.; Lin, Y.-Y.; Chen, X.-M. Porous metal-organic framework based on mu4-oxo tetrazinc clusters: Sorption and guest-dependent luminescent properties. *Inorg. Chem.* **2008**, *47*, 1346–1351. https://doi.org/10.1021/ic702085x.
75. Yu, L.; Dong, X.; Gong, Q.; Acharya, S.R.; Lin, Y.; Wang, H.; Han, Y.; Thonhauser, T.; Li, J. Splitting Mono- and Dibranched Alkane Isomers by a Robust Aluminum-Based Metal-Organic Framework Material with Optimal Pore Dimensions. *J. Am. Chem. Soc.* **2020**, *142*, 6925–6929. https://doi.org/10.1021/jacs.0c01769.
76. Novaković, S.B.; Bogdanović, G.A.; Heering, C.; Makhloufi, G.; Francuski, D.; Janiak, C. Charge-density distribution and electrostatic flexibility of ZIF-8 based on high-resolution X-ray diffraction data and periodic calculations. *Inorg. Chem.* **2015**, *54*, 2660–2670. https://doi.org/10.1021/ic5028256.
77. He, T.; Kong, X.-J.; Bian, Z.-X.; Zhang, Y.-Z.; Si, G.-R.; Xie, L.-H.; Wu, X.-Q.; Huang, H.; Chang, Z.; Bu, X.-H.; et al. Trace removal of benzene vapour using double-walled metal–dipyrazolate frameworks. *Nat. Mater.* **2022**, *119*, 4471. https://doi.org/10.1038/s41563-022-01237-x.
78. Eddaoudi, M.; Moler, D.B.; Li, H.; Chen, B.; Reineke, T.M.; O'Keeffe, M.; Yaghi, O.M. Modular Chemistry: Secondary Building Units as a Basis for the Design of Highly Porous and Robust Metal−Organic Carboxylate Frameworks. *Acc. Chem. Res.* **2001**, *34*, 319–330. https://doi.org/10.1021/ar000034b.
79. Eddaoudi, M.; Li, H.; Yaghi, O.M. Highly Porous and Stable Metal–Organic Frameworks: Structure Design and Sorption Properties. *J. Am. Chem. Soc.* **2000**, *122*, 1391–1397. https://doi.org/10.1021/ja9933386.
80. Li, M.; Huang, W.; Tang, B.; Fang, Q.; Ling, X.; Lv, A. Characterizations and n -Hexane Vapor Adsorption of a Series of MOF/Alginates. *Ind. Eng. Chem. Res.* **2020**, *59*, 18835–18843. https://doi.org/10.1021/acs.iecr.9b06744.
81. Yang, R.T. *Adsorbents: Fundamentals and Applications*; John Wiley & Sons: Hoboken, NJ, USA, 2003.
82. Lee, E.C.; Kim, D.; Jurecka, P.; Tarakeshwar, P.; Hobza, P.; Kim, K.S. Understanding of Assembly Phenomena by Aromatic-Aromatic Interactions: Benzene Dimer and the Substituted Systems. *J. Phys. Chem. A* **2007**, *111*, 3446–3457. https://doi.org/10.1021/jp068635t.
83. Brandenburg, K. Diamond 4.6, Crystal and Molecular Structure Visualization. Copyright 1997-2022 Crystal Impact GbR, Bon, Germany. Available online: https://www.crystalimpact.com/diamond/ (accessed on 10 August 2022).
84. Wahiduzzaman, M.; Lenzen, D.; Maurin, G.; Stock, N.; Wharmby, M.T. Rietveld Refinement of MIL-160 and Its Structural Flexibility Upon H_2O and N_2 Adsorption. *Eur. J. Inorg. Chem.* **2018**, 3626–3632. https://doi.org/10.1002/ejic.201800323.
85. Rallapalli, P.; Patil, D.; Prasanth, K.P.; Somani, R.S.; Jasra, R.V.; Bajaj, H.C. An alternative activation method for the enhancement of methane storage capacity of nanoporous aluminium terephthalate, MIL-53(Al). *J. Porous Mater.* **2010**, *17*, 523–528. https://doi.org/10.1007/s10934-009-9320-5.
86. Ortiz, G.; Chaplais, G.; Paillaud, J.-L.; Nouali, H.; Patarin, J.; Raya, J.; Marichal, C. New Insights into the Hydrogen Bond Network in Al-MIL-53 and Ga-MIL-53. *J. Phys. Chem. C* **2014**, *118*, 22021–22029. https://doi.org/10.1021/jp505893s.
87. Cavka, J.H.; Jakobsen, S.; Olsbye, U.; Guillou, N.; Lamberti, C.; Bordiga, S.; Lillerud, K.P. A new zirconium inorganic building brick forming metal organic frameworks with exceptional stability. *J. Am. Chem. Soc.* **2008**, *130*, 13850–13851. https://doi.org/10.1021/ja8057953.
88. Bon, V.; Senkovska, I.; Baburin, I.A.; Kaskel, S. Zr- and Hf-Based Metal–Organic Frameworks: Tracking Down the Polymorphism. *Cryst. Growth Des.* **2013**, *13*, 1231–1237. https://doi.org/10.1021/cg301691d.
89. Dan-Hardi, M.; Serre, C.; Frot, T.; Rozes, L.; Maurin, G.; Sanchez, C.; Férey, G. A new photoactive crystalline highly porous titanium(IV) dicarboxylate. *J. Am. Chem. Soc.* **2009**, *131*, 10857–10859. https://doi.org/10.1021/ja903726m.
90. Férey, G.; Mellot-Draznieks, C.; Serre, C.; Millange, F.; Dutour, J.; Surblé, S.; Margiolaki, I. A chromium terephthalate-based solid with unusually large pore volumes and surface area. *Science* **2005**, *309*, 2040–2042. https://doi.org/10.1126/science.1116275.
91. Morris, W.; Stevens, C.J.; Taylor, R.E.; Dybowski, C.; Yaghi, O.M.; Garcia-Garibay, M.A. NMR and X-ray Study Revealing the Rigidity of Zeolitic Imidazolate Frameworks. *J. Phys. Chem. C* **2012**, *116*, 13307–13312. https://doi.org/10.1021/jp303907p.
92. Park, K.S.; Ni, Z.; Côté, A.P.; Choi, J.Y.; Huang, R.; Uribe-Romo, F.J.; Chae, H.K.; O'Keeffe, M.; Yaghi, O.M. Exceptional chemical and thermal stability of zeolitic imidazolate frameworks. *Proc. Natl. Acad. Sci. USA* **2006**, *103*, 10186–10191. https://doi.org/10.1073/pnas.0602439103.

93. Tschense, C.B.L.; Reimer, N.; Hsu, C.-W.; Reinsch, H.; Siegel, R.; Chen, W.-J.; Lin, C.-H.; Cadiau, A.; Serre, C.; Senker, J.; et al. New Group 13 MIL-53 Derivates based on 2,5-Thiophenedicarboxylic Acid. *Z. Anorg. Allg. Chem.* **2017**, *643*, 1600–1608. https://doi.org/10.1002/zaac.201700260.
94. Lin, Z.-J.; Zheng, H.-Q.; Zeng, Y.-N.; Wang, Y.-L.; Chen, J.; Cao, G.-J.; Gu, J.-F.; Chen, B. Effective and selective adsorption of organoarsenic acids from water over a Zr-based metal-organic framework. *Chem. Eng. J.* **2019**, *378*, 122196. https://doi.org/10.1016/j.cej.2019.122196.
95. Chen, D.-L.; Wu, S.; Yang, P.; He, S.; Dou, L.; Wang, F.-F. Ab Initio Molecular Dynamic Simulations on Pd Clusters Confined in UiO-66-NH_2. *J. Phys. Chem. C* **2017**, *121*, 8857–8863. https://doi.org/10.1021/acs.jpcc.7b00957.
96. Reinsch, H.; Bueken, B.; Vermoortele, F.; Stassen, I.; Lieb, A.; Lillerud, K.-P.; de Vos, D. Green synthesis of zirconium-MOFs. *CrystEngComm.* **2015**, *17*, 4070–4074. https://doi.org/10.1039/C5CE00618J.
97. Kim, S.-N.; Kim, J.; Kim, H.-Y.; Cho, H.-Y.; Ahn, W.-S. Adsorption/catalytic properties of MIL-125 and NH_2-MIL-125. *Catal. Today* **2013**, *204*, 85–93. https://doi.org/10.1016/j.cattod.2012.08.014.
98. Mercury 2021.2.0, Program for Crystal Structure Visualisation, Exploration and Analysis from the Cambridge Crystallographic Data Center, Copyright CCDC 2001–2021. Available online: http://www.ccdc.cam.ac.uk/mercury/ (accessed on 10 July 2022).
99. Macrae, C.F.; Sovago, I.; Cottrell, S.J.; Galek, P.T.A.; McCabe, P.; Pidcock, E.; Platings, M.; Shields, G.P.; Stevens, J.S.; Towler, M.; Wood, P.A. Mercury 4.0: From visualization to analysis, design and prediction. *J. Appl. Cryst.* **2020**, *53*, 226–235.
100. Trickett, C.A.; Gagnon, K.J.; Lee, S.; Gándara, F.; Bürgi, H.-B.; Yaghi, O.M. Definitive molecular level characterization of defects in UiO-66 crystals. *Angew. Chem. Int. Ed.* **2015**, *54*, 11162–11167. https://doi.org/10.1002/anie.201505461.
101. Øien, S.; Wragg, D.; Reinsch, H.; Svelle, S.; Bordiga, S.; Lamberti, C.; Lillerud, K.P. Detailed Structure Analysis of Atomic Positions and Defects in Zirconium Metal–Organic Frameworks. *Cryst. Growth. Des.* **2014**, *14*, 5370–5372. https://doi.org/10.1021/cg501386j.
102. Zhao, P.; Bennett, T.D.; Casati, N.P.M.; Lampronti, G.I.; Moggach, S.A.; Redfern, S.A.T. Pressure-induced oversaturation and phase transition in zeolitic imidazolate frameworks with remarkable mechanical stability. *Dalton Trans.* **2015**, *44*, 4498–4503. https://doi.org/10.1039/c4dt02680b.
103. Lin, X.; Blake, A.J.; Wilson, C.; Sun, X.Z.; Champness, N.R.; George, M.W.; Hubberstey, P.; Mokaya, R.; Schröder, M. A porous framework polymer based on a zinc(II) 4,4'-bipyridine-2,6,2',6'-tetracarboxylate: Synthesis, structure, and "zeolite-like" behaviors. *J. Am. Chem. Soc.* **2006**, *128*, 10745–10753. https://doi.org/10.1021/ja060946u.
104. Brandt, P.; Xing, S.-H.; Liang, J.; Kurt, G.; Nuhnen, A.; Weingart, O.; Janiak, C. Zirconium and Aluminum MOFs for Low-Pressure SO_2 Adsorption and Potential Separation: Elucidating the Effect of Small Pores and NH_2 Groups. *ACS Appl. Mater. Interfaces* **2021**, *13*, 29137–29149. https://doi.org/10.1021/acsami.1c06003.
105. Brandt, P.; Nuhnen, A.; Öztürk, S.; Kurt, G.; Liang, J.; Janiak, C. Comparative Evaluation of Different MOF and Non-MOF Porous Materials for SO_2 Adsorption and Separation Showing the Importance of Small Pore Diameters for Low-Pressure Uptake. *Adv. Sustain. Syst.* **2021**, *122*, 2000285. https://doi.org/10.1002/adsu.202000285.
106. 3P INSTRUMENTS, 3P sim, Version 1.1.0.7, Simulation and Evaluation Tool for mixSorb, 3P INSTRUMENTS 2018.
107. Cessford, N.F.; Seaton, N.A.; Düren, T. Evaluation of Ideal Adsorbed Solution Theory as a Tool for the Design of Metal–Organic Framework Materials. *Ind. Eng. Chem. Res.* **2012**, *51*, 4911–4921. https://doi.org/10.1021/ie202219w.
108. Zhao, P.; Lampronti, G.I.; Lloyd, G.O.; Wharmby, M.T.; Facq, S.; Cheetham, A.K.; Redfern, S.A.T. Phase Transitions in Zeolitic Imidazolate Framework 7: The Importance of Framework Flexibility and Guest-Induced Instability. *Chem. Mater.* **2014**, *26*, 1767–1769. https://doi.org/10.1021/cm500407f.
109. Budzianowski, A.; Katrusiak, A. Pressure-frozen benzene I revisited. *Acta Crystallogr. Sect. B* **2006**, *62*, 94–101.
110. Katrusiak, A.; Podsiadzo, M.; Budzianowski, A. Association CH···π and No van der Waals Contacts at the Lowest Limits of Crystalline Benzene I and II Stability Regions. *Cryst. Growth Des.* **2010**, *10*, 3461–3465.

Electronic Supporting Information (ESI)

The Complexity of Comparative Adsorption of C_6 Hydrocarbons (Benzene, Cyclohexane, *n*-Hexane) at Metal–Organic Frameworks

Christian Jansen [1], Nabil Assahub [1], Alex Spieß [1], Jun Liang [1], Alexa Schmitz [1], Shanghua Xing [1], Serkan Gökpinar [2] and Christoph Janiak [1,*]

[1] Institut für Anorganische Chemie und Strukturchemie, Heinrich-Heine-Universität, D-40225 Düsseldorf, Germany
[2] Microtrac Retsch GmbH, Retsch-Allee 1-5, D-42781 Haan, Germany
* Correspondence: janiak@hhu.de

Keywords

Metal-organic frameworks (MOFs), zeolitic imidazolate frameworks (ZIFs), vapor adsorption, C_6 volatile organic compounds (VOCs), adsorption, stability, IAST selectivity

Table of Contents

Citation: Jansen, C.; Assahub, N.; Spieß, A.; Liang, J.; Schmitz, A.; Xing, S.; Gökpinar, S.; Janiak, C. The Complexity of Comparative Adsorption of C_6 Hydrocarbons (Benzene, Cyclohexane, *n*-Hexane) at Metal–Organic Frameworks. *Nanomaterials* **2022**, *12*, 3614. https://doi.org/10.3390/nano12203614

Academic Editors: Bin Li and Hui-Min Wen

Received: 2 September 2022
Accepted: 10 October 2022
Published: 15 October 2022

Publisher's Note: MDPI stays neutral with regard to jurisdictional claims in published maps and institutional affiliations.

S1. Materials and equipment

All chemicals were used as received by the supplier (*cf.* Table S1*)*.

Table S1 *Used chemicals, supplier and purities.*

Chemical	**CAS-Nr.:**	**Supplier**	**Purity [%]**
Acetic acid	64-19-7	Sigma Aldrich	≥ 99.8
Aluminum chloride hexahydrate	7784-13-6	Alfa Aesar	99
Aluminumfumarate (Basolite® A520)	not specified	BASF	not specified
Aluminum nitrate nonahydrate	7784-27-2	Carl-Roth	≥ 98
Aluminum sulfate octadecahydrate	7784-31-8	Sigma Aldrich	≥ 98
Ammonia hydroxide	7664-41-7	VWR Chemicals	25
Benzene	71-43-2	AppliChem	p.a.
Benzimidazole	51-17-2	Sigma Aldrich	98
Biphenyl-4,4´-dicarboxylic acid	787-70-2	Abcr GmbH	98
Chromium nitrate nonahydrate	7789-02-8	Acros Organics	99
Cyclohexane	110-82-7	AppliChem	p.a.
Dichloromethane	75-09-2	Fischer Chemicals	≥ 99.8
Ethanol	64-17-5	Merck	p.a.
Fumaric acid	110-17-8	TCI	≥ 99
n-Hexane	110-54-3	VWR Chemicals	98
Hydrochloric acid	7647-01-0	Sigma Aldrich	≥ 37
Methanol	67-56-1	Sigma Aldrich	≥ 99.8
Nitric acid	7697-37-2	Fischer Chemicals	65
N-Methyl-2-pyrrolidione	872-50-4	Carl-Roth	≥ 99.8
N,N-Dimethylformamide	68-12-2	Honeywell	≥ 99.8
Sodium hydroxide microgranulate	1310-73-2	Chemsolute	99.5
Terephthalic acid	100-21-0	Alfa Aesar	98+
Toluene	108-88-3	Sigma Aldrich	99.8
Titanium(IV)isopropoxide	546-68-9	Sigma Aldrich	97
Zinc acetate dihydrate	5970-45-6	Carl-Roth	98+
Zinc nitrate hexahydrate	10196-18-6	Acros Organics	98
Zirconium chloride	10026-11-6	Chempur	98
2-Aminoterephthalic acid	10312-55-7	Acros Organics	99
2-Methylimidazole	693-98-1	Acros Organics	99
2,3,5,6-Tetrafluoroterephthalic acid	652-36-8	BLDpharm	97
2,5-Furandicarboxylic acid	3238-40-2	BLDpharm	99.25
2,5-Thiophenedicarboxylic acid	4282-31-9	BLDpharm	98.14
2,6-Naphthalenedicarboxylic acid	1141-38-4	Alfa Aesar	98+

S2. MOF syntheses, crystal structures and MOF parameters

Al-MOFs

Aluminum-MOFs show in general a good thermal and chemical stability against water and other chemicals, which makes them suitable candidates for sorption applications.

Basolite® A520 (commercial Aluminumfumarate) was purchased by BASF (BET = 988 $m^2 g^{-1}$).

The synthesis of **Aluminumfumarate** was carried out according to the procedure of Alvarez *et al.*[1] $Al_2(SO_4)_3$ $18H_2O$ (7.00 g, 10.50 mmol, 1 eq), sodium hydroxide (2.52 g, 63 mmol, 6 eq) and fumaric acid (3.36 g, 28.95 mmol, 3 eq) were educts. In a first step, the $Al_2(SO_4)_3$ $18H_2O$ was dissolved in 30 mL deionized water at 60 °C. while stirring. The fumaric acid and sodium hydroxide were dissolved in 36 mL of deionized water. In a further step, the fumaric acid-NaOH solution was added dropwise to the $Al_2(SO_4)_3$ $18H_2O$ solution over the period of 30 minutes. The reaction mixture was stirred for a further two hours at 60 °C. After that the temperature was turned off and the solution was cooled while stirring. The solid was washed three times with 60 mL deionized water (one time overnight). The product was centrifuged (10000 U min^{-1}, 15 min), decanted and placed in the vacuum oven (60 ° C, 1-10 mbar) to dry overnight. Yielding a white powder (3.38 g yield, BET = 1035 $m^2 g^{-1}$).

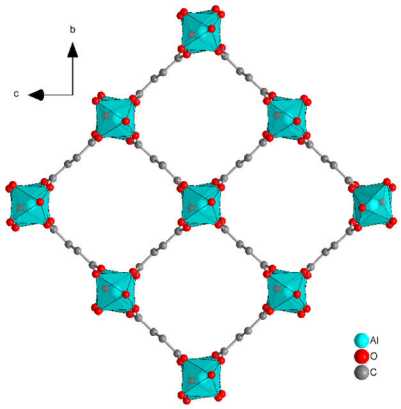

Figure S1 *The 3D framework structure of Alfum exhibits square shaped one-dimensional channels. Graphic produced by software Diamond[2] from cif-file for Aluminumfumarate (CSD-Number: 1051975).[1]*

The synthesis of **MIL-160** was carried out following a modified protocol of Cadiau *et al.*[3] who used 1 eq NaOH, whereas we used 2 eq NaOH to deprotonate the linker fully: 2,5-furandicarboxylic acid (4.6814 g, 30.0 mmol, 1 eq) and sodium hydroxide (2.4032 g, 60.08 mmol, 2 eq) were converted in water (150 mL, 1.5 h). $AlCl_3 \cdot 6H_2O$ (7.2457 g, 30.01 mmol, 1 eq) was added and reflux (24 h, 100 °C) was initiated. After decantation, the product was washed with water three times (160 mL each), centrifuged (10000 U min^{-1}, 30 min), decanted and re-dispersed each time. Subsequently, the product was dried overnight (80 °C, 1 – 10 mbar), yielding a white powder (3.7861 g yield, BET = 1161 $m^2 g^{-1}$).

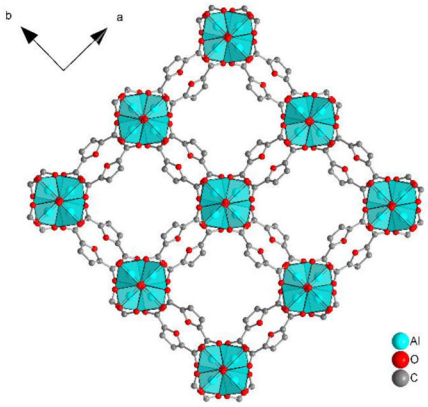

Figure S2 *The 3D framework structure of MIL-160 exhibits square shaped one-dimensional channels. Graphic produced by software Diamond[2] from cif-file for MIL-160 (CSD-Number: 1828694).[4]*

The synthesis of **DUT-4** was carried out in accordance with a report by Senkovska *et al.*[5] 2,6-naphthalenedicarboxylic acid (0.2603 g, 1.2 mmol, 1 eq) was dissolved in 30 ml *N,N*-dimethylformamide DMF. $Al(NO_3)_3 \cdot 9H_2O$ (0.5235 g, 1.4 mmol, 1.167 eq) was added and the mixture was filled in a 40 ml Teflon liner, placed in an autoclave, heated to 120 °C for 24 h and cooled to room temperature. After the product was separated by centrifugation, the sediment was washed with DMF (30 ml, each) for three times. Subsequently, the product was dried overnight (80 °C, 1 – 10 mbar), yielding a white powder (0.3505 g yield, BET = 1764 $m^2 g^{-1}$).

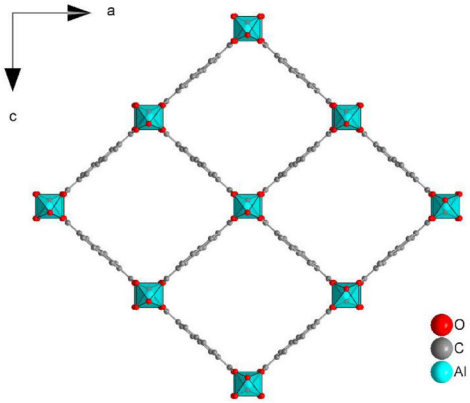

Figure S3 *The 3D framework structure of DUT-4 exhibits square shaped one-dimensional channels. Graphic produced by software Diamond[2] from cif-file for DUT-4 (CSD-Number: 691978).[5]*

The synthesis of **DUT-5** was carried out following a modified protocol of Gotthardt *et al.*[6] Biphenyl-4,4'-dicarboxylic acid (0.36058 g, 1.5 mmol, 1 eq) was dissolved in 40 mL DMF at 120 °C. A solution of $Al(NO_3)_3 \cdot 9H_2O$ (0.7620 g, 3 mmol, 2 eq) in 20 mL DMF was added over a period of 1.5 h. The reaction mixture was stirred for 24 h under reflux at 120 °C After the product was separated by centrifugation, the sediment was washed with DMF (60 ml, each) for three times. Subsequently, the product was dried overnight (80 °C, 1 – 10 mbar), yielding a white powder (0.6447 g yield, BET = 1323 $m^2 g^{-1}$).

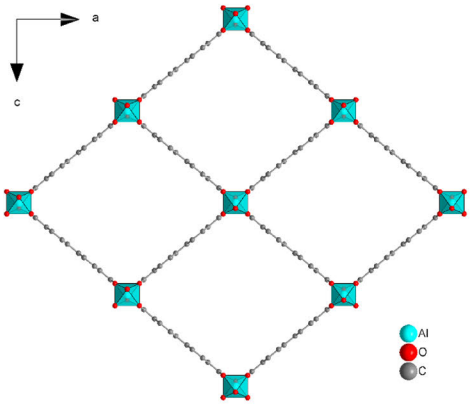

Figure S4 *The 3D framework structure of DUT-5 exhibits square shaped one-dimensional channels. Graphic produced by software Diamond[2] from cif-file for DUT-5 (CSD-Number: 691979).[5]*

The synthesis of **MIL-53-TDC** was carried out following a protocol of Tannert *et al.*[7] For the batch, $Al_2(SO_4)_3$ $18H_2O$ (3.79 g, 5.69 mmol, 1 eq), 2,5-thiophenedicarboxylic acid (0.86 g, 5 mmol, 1 eq) were dissolved in a mixture of *N,N*-dimethylformamide (8 mL) and deionized water (32 mL) and refluxed at 135 °C for 24 hours. The solid was centrifuged off (10000 U min^{-1}, 15 min) and the solvent was decanted off. The product was washed three times with 100 mL deionized water. Another fourth wash was carried out overnight. In contrast to the literature, the product was also refluxed in 100 mL ethanol for 24 hours at 80 °C. The end product was centrifuged off (10000 U min^{-1}, 15 min) and dried overnight in a vacuum oven (60 °C, 1-10 mbar), yielding a white powder (1.11 g yield, BET = 1015 $m^2 g^{-1}$).

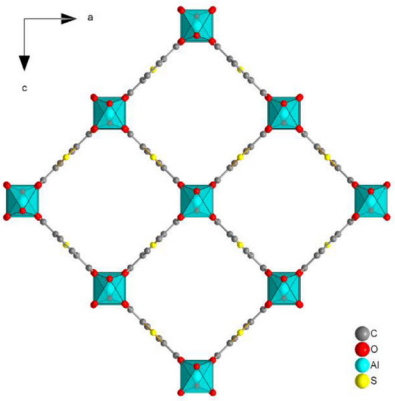

Figure S5 *The 3D framework structure exhibits of MIL-53-TDC square shaped one-dimensional channels. Graphic produced by software Diamond[2] from cif-file for MIL-53-TDC (The graphics were produced from a cif-filethat was generously provided by Serre and co-workers.).*

The synthesis of **MIL-53** was carried out following a protocol of Zi *et al.*[8] First, terephthalic acid (1.15 g, 6.92 mmol, 0.5 eq) was dissolved in deionized water (30 mL) and then the $Al(NO_3)_3 \cdot 9H_2O$ (5.21 g, 13.89 mmol, 1 eq) was added and dissolved with stirring. The reaction mixture was transferred to a steel autoclave with a Teflon inlay and placed in the oven at 200 °C for 24 h. The solid was centrifuged off (10000 U min^{-1}, 15 min). The washing and activation of the MOF was carried out according to Rallapalli et al.[9] The product was washed four times with deionized water (4x50 mL) until the filtrate reached a pH value of 7. The product was washed once at RT overnight in DMF (50 ml) with stirring and twice overnight under reflux (155 °C) in DMF (2 × 50 ml). After the product was centrifuged off, it was washed with methanol (50 mL), centrifuged again and placed in

the vacuum oven (60 °C, 1-10 mbar) for two hours. Finally, it was washed twice again with methanol (2 × 50 mL), centrifuged off and dried in a vacuum oven (60 °C, 1-10 mbar), yielding a white powder (0.72 g yield, BET = 1325 $m^2 g^{-1}$)

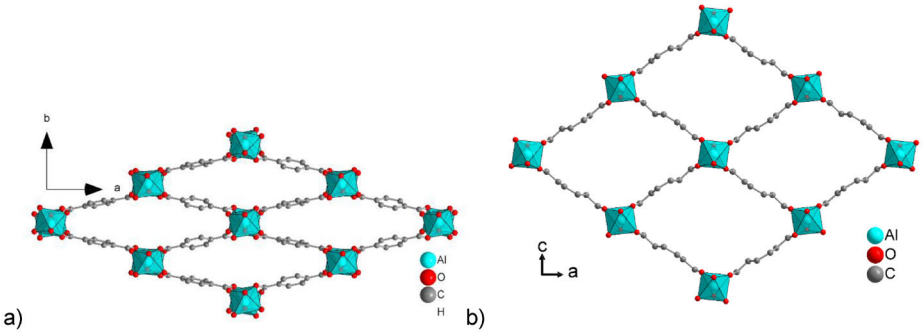

Figure S6 *The 3D framework structure of MIL-53 exhibits one-dimensional channels, with the dimensions depending on the breathing-effect. (a) Narrow-pore form, (b) Wide-pre form.Graphic produced by software Diamond[2] from cif-file for MIL-53 (a) CSD-Number: 1007172[10], (b) CSD-Number 220475, CSD-Refcode SABVOH[11]).*

Zr-MOFs

Zirconium-MOFs also show extremely high chemical stability, especially the UiO-series, which follows the isoreticular principle and allows the use of functionalized linkers. Thereby, the influence of linker functionalization on a gas or vapor uptake can be assessed. The zirconium MOF DUT-67 does not belongs to the UiO-series, but has the same thiophenedicarboxylate (TDC) linker as the aluminum-MOF MIL-53-TDC.

The synthesis of **UiO-66** was carried out following a modified protocol of Aguilera-Sigalat *et al.*[12] $ZrCl_4$ (0.2027 g, 0.87 mmol, 1 eq) and terephthalic acid (0.1145 g, 0.87 mmol, 1 eq) were dissolved in DMF (50 ml) with acetic acid (1.5 ml) and the mixture was sonicated for 10 min. The mixture was filled in a 100 ml Schott glas, heated to 120 °C for 24 h and cooled to room temperature. After the product was separated by centrifugation, the sediment was washed with DMF (50 ml, each) for three times and with ethanol (50 ml, each) for three times. Subsequently, the product was dried overnight (80 °C, 1 – 10 mbar), yielding a white powder (0.1007 g yield, BET = 1178 $m^2 g^{-1}$).

The synthesis of **UiO-66-NH_2** was carried out in accordance with a report by Aguilera-Sigalat *et al.*[12] $ZrCl_4$ (0.2023 g, 0.87 mmol, 1 eq) and 2-aminoterephthalic acid (0.1574 g, 0.87 mmol, 1 eq) were dissolved in DMF (50 ml) with acetic acid (1.5 ml) and the mixture was sonicated for 10 min. The mixture was filled in a 100 ml Schott glas, heated to 120 °C for 24 h and cooled to room temperature. After the product was separated by centrifugation, the sediment was washed with DMF (50 ml, each) for three times and with ethanol (50 ml, each) for three times. Subsequently, the product was dried overnight (80 °C, 1 – 10 mbar), yielding a yellow powder (0.2121 g yield, BET = 1127 $m^2 g^{-1}$).

The synthesis of **UiO-66(F)$_4$** was carried out in accordance with a report by Hu *et al.*[13] $ZrCl_4$ (1.653 g, 5 mmol, 1 eq) and tetrafluoroterephthalic acid (1.1907 g, 5 mmol, 1 eq) were dissolved in DMF (30 ml) with acetic acid (20 ml) and the mixture was heated to reflux for 24 h and cooled to room temperature. After the product was separated by centrifugation, the sediment was washed with methanol and dichloromethane for three days. Subsequently, the product was dried overnight (80 °C, 1 – 10 mbar), yielding a white powder (1.1639 g yield, BET = 346 $m^2 g^{-1}$).

The synthesis of **UiO-67** was carried out in accordance with a report by Katz *et al.*[14] $ZrCl_4$ (0.2517 g, 1.08 mmol, 1 eq) was dissolved in DMF (20 ml) with HCl (2 ml) and the mixture was sonicated for 10 min. Then biphenyl-4,4'-dicarboxylic acid (0.3682 g, 1.52 mmol, 1.41 eq) and DMF (40 ml) were added and sonicated for another 20 min. The mixture was filled in a 100 ml Schott glas, heated to 80 °C for 24 h and cooled to room temperature. After the product was separated by centrifugation, the sediment was washed with DMF (60 ml, each) for three times and with ethanol (60 ml, each) for

three times. Subsequently, the product was dried overnight (80 °C, 1 – 10 mbar), yielding a white powder (0.3596 g yield, BET = 2317 $m^2 g^{-1}$).

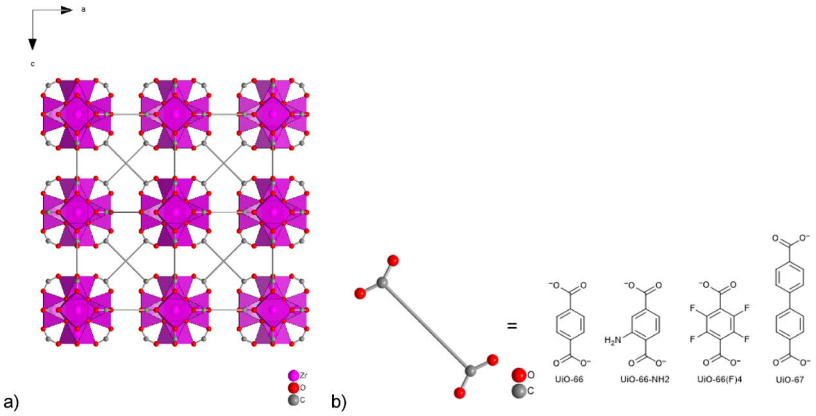

Figure S7 *The 3D framework structure simulated for UiO-type materials (a) and their linker (b). Graphic produced by software Diamond² from cif-file for UiO-66 (CSD-Number: 733458).*[15]

The synthesis of **DUT-67** was carried out in accordance with a report by Drache *et al.*[16] $ZrCl_4$ (1.3822 g, 6 mmol, 1.5 eq) was dissolved in DMF (75 ml) and *N*-methyl-2-pyrrolidione (NMP) (75 ml) and the mixture was sonicated for 10 min. Then 2,5-thiophendicarboxylic acid (0.6651 g, 4 mmol, 1 eq) was added and sonicated for another 5 min and finally formic acid (26 ml) was added. The mixture was filled in a 250 ml Schott glas, heated to 120 °C for 48 h and cooled to room temperature. After the product was separated by centrifugation, the sediment was washed with DMF (120 ml, each) for three times and with (120 ml, each) for three times. Subsequently, the product was dried overnight (80 °C, 1 – 10 mbar), yielding a yellow powder (0.9432 g yield, BET = 1178 $m^2 g^{-1}$).

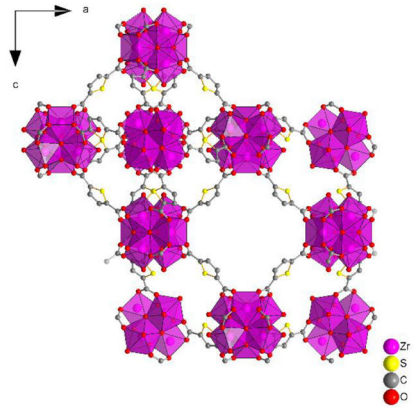

Figure S8 *The 3D framework structure simulated for DUT-67 with both pore types. Graphic produced by software Diamond² from cif-file for DUT-67 (CSD-Number: 921644).*[17]

Ti-MOFs

NH_2-MIL-125 has a higher chemical stability than unfunctionalized MIL-125 and the aminoterephthalate linker is the same as in UiO-66-NH_2. MIL-125 has the same terephthalate or benzene-1,4-dicarboxylate linker, as MIL-53, UiO-66 and MIL-101(Cr).

The synthesis of **NH_2-MIL-125** was carried out following a modified protocol of Sohail *et al.*[18] 2-aminoterphthalic acid (1.0856 g, 5.99 mmol, 4.02 eq) was dissolved in DMF (3.5 ml) and methanol (3.5 ml) *via* sonication for 5 min and stirred for 20 h. $Ti[OCH(CH_3)_2]_4$ (0.44 ml, 0.4224 g, 1.49 mmol, 1 eq) was added to the solution and transferred to aTeflon liner, placed in an autoclave, heated to 150 °C for 16 h and cooled to room temperature. After the product was separated by centrifugation, the sediment was washed with DMF (30 ml, each) for three times and with ethanol (30 ml, each) for three times. Subsequently, the product was dried overnight (80 °C, 1 – 10 mbar), yielding a yellow powder (0.3503 g yield, BET = 1570 $m^2 g^{-1}$).

The synthesis of **MIL-125** was carried out according to the procedure in Santaclara *et al.*[19] For the batch, $Ti[OCH(CH_3)_2]_4$ (4.2 mL, 14.19 mmol, 1 eq) and terephthalic acid (3.53 g, 21.25 mmol, 1.5 eq) were reacted in DMF (56 mL) and methanol (14 mL). In a first step, the terephthalic acid was dissolved in DMF under reflux (105 °C, 1 h). Then methanol was added. After a further hour under reflux, the titanium isopropoxide was added and the mixture was stirred under reflux (100 °C, 72 h). After the mixture had cooled to RT, the solid was centrifuged off (10000 U min^{-1}, 15 min). For washing, the product was refluxed in 60 mL DMF (155 °C, 24 h) and then in methanol (100 °C, 24 h). The product was dried overnight in a vacuum oven (60 °C., 1-10 mbar), yielding a white powder (3.72 g yield, BET = 1425 $m^2 g^{-1}$).

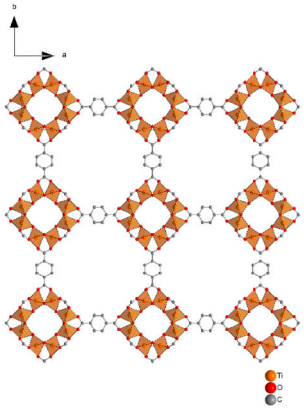

Figure S9 *The 3D framework structure simulated for MIL-125, structure is simular to NH_2-MIL-125. Graphic produced by software Diamond² from cif-file for MIL-125 (CSD-Number: 751157).*[20]

Cr-MOF

MIL-101(Cr) was chosen because of the high surface area and pore volume together with unsurpassed hydrothermal and chemical stability. MIL-101(Cr) often gives a maximum absorption capacity through its large pores and is a benchmark material, which is often noted in the literature.

The synthesis of **MIL-101(Cr)** was carried out in accordance with a report by Zhao *et al.*[21] $Cr(NO_3)_3 \cdot 9H_2O$ (0.4038 g, 1 mmol, 1 eq) and terephthalic acid (0.1645 g, 1 mmol, 1 eq) were solved in water (5 ml) and nitric acid (69.7 µl, 1 mmol). The mixture was transferred to a Teflon liner, placed in an autoclave, heated to 220 °C for 8 h and cooled to room temperature. After the product was separated by centrifugation, the sediment was washed with DMF (30 ml) and with water (30 ml) and ethanol (30 ml). Subsequently, the product was dried overnight (80 °C, 1 – 10 mbar), yielding a green powder (0.2447 g yield, BET = 2002 $m^2 g^{-1}$).

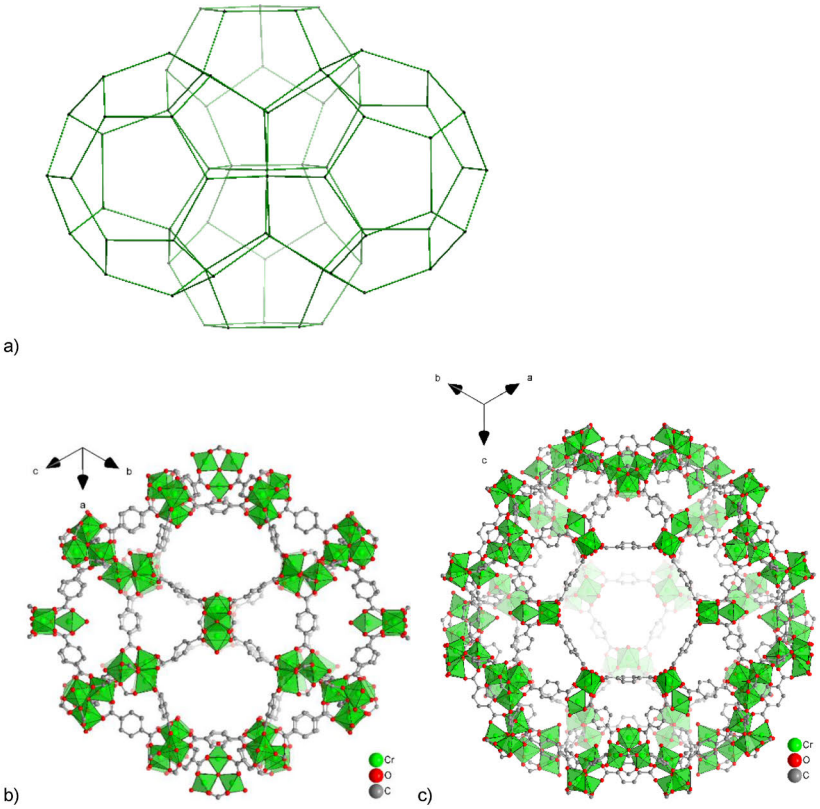

Figure S10 *(a) The 3D zeotypic framework structure for MIL-101(Cr) with (b) small (pentagonal windows only) and (c) large cages (pentagonal and hexagonal windows). Graphic produced by software Diamond[2] from cif-file for MIL-101(Cr) (CSD-Number: 605510).*[22]

ZIFs

ZIF-8 is a hydrophobic MOF with the 2-methylimidazolate linker, which is well investigated and easy to synthesize and has a high thermal and chemical stability, which makes it interesting for industrial applications. ZIF-11 and ZIF-7 have the same benzimidazolate linker but different topologies and therefore different pore sizes and surface area, with ZIF-11 being a **rho** and ZIF-7 a **sod** network.

The synthesis of **ZIF-8** was carried out in accordance with a report by Kida *et al.*[23] $Zn(NO_3)_3 \cdot 6H_2O$ (0.7520, 2.5 mmol, 1 eq) was dissolved in water (10 ml) and 2-methylimidazole (12.3033 g, 150 mmol, 60 eq) was dissolved in water (90 ml). The mixture was stirred for 24 h at room temperature. After the product was separated by centrifugation, the sediment was washed with ethanol (100 ml, each) for three times. Subsequently, the product was dried overnight (80 °C, 1 – 10 mbar), yielding a white powder (0.5198 g yield, BET = 1615 $m^2 g^{-1}$).

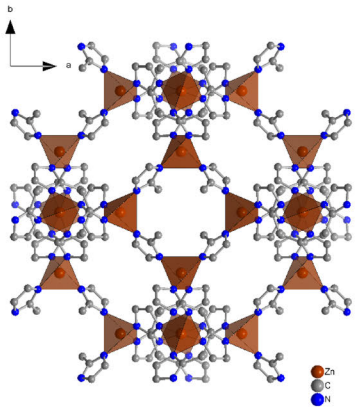

Figure S11 *The 3D framework structure simulated for ZIF-8. Graphic produced by software Diamond² from cif-file for ZIF-8 (CSD-Number: 864309).*[24]

The synthesis of **ZIF-11** was carried out in accordance with a report by He *et al.*[25] Benzimidazole (0.4723 g, 4 mmol, 2 eq) was dissolved in methanol (24.33 ml), and then toluene (21.18 ml) and ammonia hydroxide (0.3 ml) were added under stirring at room temperature. $Zn(CH_3COO)_2 \cdot 2H_2O$ (0.4394 g, 2 mmol, 1 eq) were added to this mixture and stirred for 3 h at room temperature. After the product was separated by centrifugation, the sediment was washed with methanol (60 ml, each) for three times. Subsequently, the product was dried overnight (80 °C, 1 – 10 mbar), yielding a white powder (0.5609 g yield, BET = 448 $m^2 g^{-1}$).

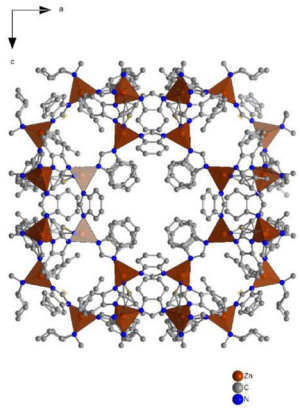

Figure S12 *The 3D building block structure simulated for ZIF-11. Graphic produced by software Diamond² from cif-file for ZIF-11 (CSD-Number: 602545).*[26]

The synthesis of **ZIF-7** was carried out following a modified protocol of Kang *et al.*[27] and Li *et al.*[28] DMF (20 ml) was added to a solid mixture of $Zn(NO_3)_2 \cdot 6H_2O$ (0.3813 g, 1.27 mmol, 1 eq) and benzimidazole (0.2002 g, 1.69 mmol, 1.33 eq) and stirred till a clear solution was made. The mixture was transferred to a Teflon liner, placed in an autoclave, heated to 160 °C for 24 h and cooled to room temperature. After the product was separated by centrifugation, the sediment was washed with methanol (30 ml, each) for six times. Subsequently, the product was dried overnight (80 °C, 1 – 10 mbar), yielding a white powder (0.1712 g yield, BET = 275 $m^2 g^{-1}$).

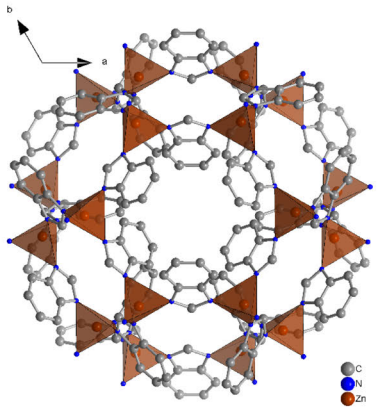

Figure S13 *The 3D framework structure simulated for ZIF-7. Graphic produced by software Diamond[2] from cif-file for ZIF-7 (CSD-Number:602541).*[26]

MOF parameters

Table S2 *MOF parameters (BET-surface area, (total) pore volume (DFT), micropore volume, pore window).*[a]

MOF	BET-Surface area [$m^2\ g^{-1}$]	Pore volume (DFT) [$cm^3\ g^{-1}$] [c]	Micropore volume [$cm^3\ g^{-1}$] [d]		Pore window [Å^2]	Literature (with respect to Pore Window)
Basolite® A520 (Aluminumfumarate)	988	0.615	0.33		5.7 x 6.0	Alvarez *et al.*[1]
Aluminumfumarate	1035	0.517	0.354		5.7 x 6.0	Alvarez *et al.*[1]
MIL-160	1161	0.404	0.426		5.5 x 5.5	Wahiduzzaman *et al.*[4]
DUT-4	1764	1.077	0.92		8.5 x 8.5	Senkovska *et al.*[5]
DUT-5	1323	0.68	0.409		11.1 x 11.1	Senkovska *et al.*[5]
MIL-53-TDC	1015	0.466	0.33		8 x 8.2	Tschense *et al.*[29]
MIL-53(Al)	1325	0.486	0.462		8.5 x 8.5	Loiseau *et al.*[11]
UiO-66	1178	0.503	0.414		5.9 x 5.9	Lin *et al.*[30]
UiO-66-NH_2	1127	0.45	0.384		7.0 x 7.0	Chen *et al.*[31]
UiO-66$(F)_4$	346	0.35	0.091		2.4 x 4.6	Reinsch *et al.*[32]
UiO-67	2317	0.962	0.858		8.3 x .8.3	Lin *et al.*[30]
DUT-67	1178	0.443	0.403		6.7 x 6.7	Lin *et al.*[30]
NH_2-MIL-125	1570	0.601	0.559		5.9 x 5.9	Kim *et al.*[33]
MIL-125	1425	0.565	0.493		6.1 x 6.1	Kim *et al.*[33]
MIL-101(Cr)	2002	1.024	0.604		12 x 12	Ferey *et al.*[22]
ZIF-8	1615	0.673	0.632		3.4 x 3.4	Novakovic *et al.*[34]
ZIF-11	491	0.354	0.014		3.0 x 3.0	He *et al.*[25]
ZIF-7	275 (from CO_2)[b]	0.1405[e]	0		2.9 x 2.9	He *et al.*[25]

[a] BET surface area, pore volume and micropore volume were derived from our N_2 sorption isotherm measurements at 77 K of the synthesized samples.

[b] ZIF-7 does not show an N_2 adsorption at 77 K, hence the BET surface area was derived from CO_2 adsorption (3.03 mmol CO_2) at 273 K.

[c] Total pore volumes were calculated from the N_2-sorption isotherm at p p_0^{-1} = 0.90 for pore sizes ≤ 20 nm. NLDFT calculations were done with the native *NovaWin 11.03* software using the 'N_2 at 77 K on carbon, slit pore, NLDFT equilibrium' model. Thickness model for calculation of micropore volumes and micropore areas was set to 'De Boer'.

[d] Micropore volumes were calculated from the N_2 adsorption isotherm at p p_0^{-1} = 0.2-0.3 for pores with d ≤ 2 nm (20 Å). Micropore volumes (V_{micro}) were calculated by the t-plot method ('De Boer' model).

[e] Total pore volume was calculated from the CO_2 adsorption isotherm at p p_0^{-1}.

Table S3 *MOF parameters exp. pore volume (DFT), calculated void volume and specific void volume, and percent of pore filling with the C_6-VOCs.* [a]

MOF	Exp. pore volume (DFT) [$cm^3\ g^{-1}$] [b]	Calc. void volume, $V_{unit\ cell}$ [$Å^3$] [c]	calc. Specific void volume [$cm^3\ g^{-1}$] [d]	Pore filling C_6H_6 [%] [i]	Pore filling C_6H_{12} [%] [i]	Pore filling C_6H_{14} [%] [i]	Z, $M_{asym\ unit}$ [--], [g mol^{-1}]
Basolite® A520 (commercial Alfum)	0.615	481	0.46	-	-	-	Z = 4, M = 158
Aluminumfumarate, Alfum	0.517	481	0.46	79 89	71 80	91 102	Z = 4, M = 158
MIL-160	0.404	2217	0.42	121 116	121 116	151 145	Z = 16, $C_6H_3O_6Al$, M = 198
DUT-4	1.077	1320	0.77	110 153	84 117	96 134	Z = 4, $C_{12}H_7O_5Al$, M = 258
DUT-5	0.68	1917	1.02	138 92	141 94	224 149	Z = 4, $C_{14}H_9O_5Al$, M = 284
MIL-53-TDC	0.466	746	0.52	73 65	62 56	82 73	Z = 4, C6H3O5S-Al, M = 214
MIL-53(Al)	0.486	678	0.49	195 194	191 190	283 282	Z = 4, $C_8H_5O_5Al$, M = 208
UiO-66	0.503	4807	0.43	95 112	169 198	199 233	Z = 4 $Zr_6O_4(OH)_4(C_8H_4O4)_6$ = $C_{48}H_{28}O_{32}Zr_6$, M = 1664
UiO-66-NH_2 [e]	0.45	3671	0.32	82 116	87 122	184 259	Z = 4 $Zr_6O_4(OH)_4(C_8H_5NO_4)_6$ = $C_{48}H_{34}N_6O_{32}Zr_6$, M = 1754
UiO-66$(F)_4$ [f]	0.35	3671	0.26	117 158	100 135	91 123	--
UiO-67	0.962	12442	0.83	124 143	119 137	83 96	Z = 4, $Zr_6O_4(OH)_4(C_{14}H_8O_4)_6$ = $C_{96}H_{52}O_{32}Zr_6$, M = 2265
DUT-67	0.443	39628	0.66	124 83	142 96	135 91	Z = 24, $Zr_6O_4(OH)_4(OH)_4(H_2O)_4$-$(C_6H_2O_4S)_4$ = $C_{24}H_{24}O_{32}S_4Zr_6$, M = 1500
NH_2-MIL-125 [g]	0.601	4157	0.80	50 38	60 45	82 61	--
MIL-125	0.565	4157	0.80	141 100	142 100	154 109	Z = 2, $Ti_8(OH)_{12}$-$(C_8H_4O_4)_6$ $C_{48}H_{36}O_{36}Ti_8$, M = 1572
MIL-101(Cr)	1.024	n.a.	n.a.	n.a.	n.a	n.a.	too large for calculation
ZIF-8	0.673	2329	0.51	85 112	51 67	89 118	Z = 4, $C_{24}H_{30}N_{12}Zn_3$ M = 683
ZIF-11 [h]	0.354	10391	0.43	90 74	136 112	102 84	Z = 12, $C_{56}H_{40}N_{16}Zn_4$, M = 1199
ZIF-7	0.1405	1819	0.20	64 45	57 40	107 75	Z = 18, $C_{14}H_{10}N_4Zn$, M = 308

[a] BET surface area, pore volume and micropore volume were derived from our N_2 sorption isotherm measurements at 77 K of the synthesized samples.

[b] Total pore volumes were calculated from the N_2-sorption isotherm at p/p_0 = 0.90 for pore sizes ≤ 20 nm. NLDFT calculations were done with the native *NovaWin 11.03* software using the 'N_2 at 77 K on carbon, slit pore, NLDFT equilibrium' model. Thickness model for calculation of micropore volumes and micropore areas was set to 'De Boer'.

[c] Void volume in Å^3 calculated by a 'Void' calculation with Mercury[35,36] using a probe radius of 1.5 Å for the contact surface. Any solvent of crystallization was removed from the cif file. Not given H atoms were added. If possible, a disorder was removed (e.g. in ZIF-11).

[d] Specific pore volume in cm^3 g^{-1} calculated according to $(V_{unit\ cell} \times N_A)/(Z \times M_{asym\ unit})$; N_A = Avogadro's constant, $6.022 \cdot 10^{23}$ mol^{-1}, Z = number of asymmetric formula units, $M_{asym\ unit}$ = molecular weight of asymmetric formula unit (in g mol^{-1}). As a help to reproduce the specific number the values for *Z* and $M_{asym\ unit}$ from the X-ray structures are given in the last column. Note that the given values were obtained from Checkcif (checkcif.iucr.org) with the deposited or from a drawing of the unit cell with the program Diamond.[2] In case no H atoms were included in the cif, these were added to give $M_{asym\ unit}$. The Z and related molecular weight in the cif could differ due to crystal solvent or due to non-corrected unit cell content from the structure solution and refinement.

[e] In UiO-66-NH_2 there is an N atom at each C atom of the benzene ring, induced by the crystallographic symmetry. This crystallographically-induced disorder cannot be removed. Thus, the actual available void volume of UiO-66-NH_2 will be somewhat larger and lie in-between the given calculated value and the value for UiO-66.

[f] No X-ray structure available, but isostructural to UiO-66 and UiO-66-NH_2 and UiO-66-$(F)_4$ should be close in the calculated void volume of UiO-66-NH_2 due to the crystallographically-induced N atom (in place of F) at each C atom.

[g] No X-ray structure available, but isostructural to MIL-125 with values taken from there.

[h] Disorder (part A) in the linker was removed.

[i] Pore filling calculated from vapor uptake in [mg g^{-1}] (293 K) at $p\ p_0^{-1}$ = 0.9 divided by the density ρ of the liquid (at 293 K) to approximate the volume of liquid benzene, cyclohexane or *n*-hexane adsorbed in the MOFs at $p\ p_0^{-1}$ = 0.9 ($\rho_{benzene}$ = 0.876 g cm^{-3}; $\rho_{cyclohexane}$ = 0.779 g cm^{-3}; ρ_{hexane} = 0.655 g cm^{-3}) (the respective values are summarized in Table S3a-c on the next page) and further divided by the experimental pore volume (lower line) and calculated specific void volume (upper line) and multiplied by 100%.

Interpretation to Table S3:

There is in most cases a reasonable match between the experimental pore volume and the calculated specific void volume. Substantial discrepancies are only seen for DUT-4 and DUT-5 which are explained by the low surface area of DUT-5, due to the synthesis.

In cases where the calculated specific void volume is larger than the experimental pore volume a larger probe radius would give a smaller void volume. The largest possible probe radius in Mercury is 2.0 Å (cf. Table S3), the standard probe radius is normally 1.2 Å. A larger calculated specific void volume than experimental pore volume can signal either incomplete activation or inaccessible pore regions for the N_2 adsorbate (kinetic diameter 3.64 Å).

In cases where the calculated specific void volume is smaller than the experimental pore volume, as for UiO-66, UiO-66-NH_2 and UiO-67, this can be traced to the known defect formation in UiOs.[37] For the larger experimental pore volume in ZIF-8 the known gate effect can be operating which does not work in the static theoretical void volume calculation.[34]

Table S3a *Experimental benzene vapor uptake in [mg g^{-1}] and [cm^3 g^{-1}].*

MOF	benzene uptake p p_0^{-1} = 0.9 (293 K)	
	[mg g^{-1}]	cm^3 liq. benzene/gMOF [a]
Alfum (Basolite® A520)	551	0.63
Aluminumfumarate	358	0.41
MIL-160	429	0.49
DUT-4	1031	1.18
DUT-5	820	0.94
MIL-53-TDC	298	0.34
MIL-53(Al)	830	0.95
UiO-66	419	0.48
UiO-66-NH_2	323	0.37
UiO-66$(F)_4$	359	0.41
UiO-67	1043	1.19
DUT-67	483	0.55
NH_2-MIL-125	262	0.30
MIL-125	701	0.80
MIL-101(Cr)	776	0.89
ZIF-8	498	0.57
ZIF-11	277	0.32
ZIF-7	83	0.09

[a] benzene uptake / $\rho_{benzene}$ = cm^3 liq. benzene/gMOF with density $\rho_{benzene}$ = 0.876 g cm^{-3} of liquid C_6H_6 at 293 K to approximate the volume of benzene adsorbed in the MOFs at p p_0^{-1} = 0.9 and 293 K

Table S3b *Experimental cyclohexane vapor uptake in [mg g^{-1}] and [cm^3 g^{-1}].*

MOF	cyclohexane uptake p p_0^{-1} = 0.9 (293 K)	
	[mg g^{-1}]	cm^3 liq. cyclo-hexane/gMOF [a]
Alfum (Basolite® A520)	485	0.62
Aluminumfumarate	291	0.37
MIL-160	385	0.49
DUT-4	698	0.90
DUT-5	750	0.96
MIL-53-TDC	227	0.29
MIL-53(Al)	726	0.93
UiO-66	666	0.85
UiO-66-NH_2	307	0.39
UiO-66$(F)_4$	276	0.35
UiO-67	890	1.14
DUT-67	487	0.63
NH_2-MIL-125	279	0.36
MIL-125	627	0.80
MIL-101(Cr)	1007	1.29
ZIF-8	262	0.34
ZIF-11	376	0.48
ZIF-7	59	0.08

[a] cyclohexane uptake / $\rho_{cyclohexane}$ = cm^3 liq. cyclohexane/gMOF with density $\rho_{cyclohexane}$ = 0.779 g cm^{-3} of liquid cyclohexane at 293 K to approximate the volume of cyclohexane adsorbed in the MOFs at p p_0^{-1} = 0.9 and 293 K

Table S3c *Experimental n-hexane vapor uptake in [mg g^{-1}] and [cm^3 g^{-1}].*

MOF	***n*-Hexane uptake p p_0^{-1} = 0.9 (293 K)**	
	[mg g^{-1}]	cm^3 liq. hexane/gMOF [a]
Alfum (Basolite® A520)	438	0.67
Aluminiumfumarate	310	0.47
MIL-160	397	0.61
DUT-4	677	1.03
DUT-5	997	1.52
MIL-53-TDC	246	0.38
MIL-53(Al)	901	1.38
UiO-66	654	1.00
UiO-66-NH_2	543	0.83
UiO-66$(F)_4$	207	0.32
UiO-67	527	0.80
DUT-67	395	0.60
NH_2-MIL-125	323	0.49
MIL-125	569	0.87
MIL-101(Cr)	663	1.01
ZIF-8	395	0.60
ZIF-11	236	0.36
ZIF-7	96	0.15

[a] hexane uptake / ρ_{hexane} = cm^3 liq. hexane/gMOF with density ρ_{hexane} = 0.655 g cm^{-3} of liquid cyclohexane at 293 K to approximate the volume of hexane adsorbed in the MOFs at p p_0^{-1} = 0.9 and 293 K

S3 Powder X-ray diffraction (PXRD) measurements

Al-MOFs

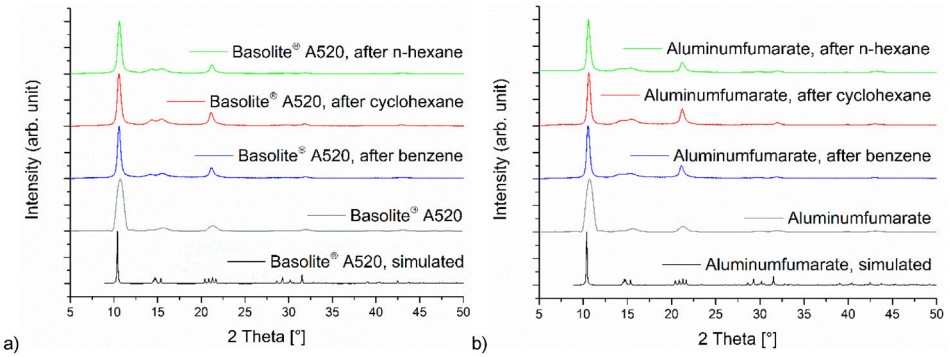

Figure S14 *(a) PXRDs of Basolite® A520 after VOC-sorption, compared with MOF before sorption and with simulated pattern (CSD-Number: 1051975).[1] (b) PXRDs of Aluminumfumarate after VOC-sorption, compared with MOF before sorption and with simulated pattern (CSD-Number: 1051975).[1]*

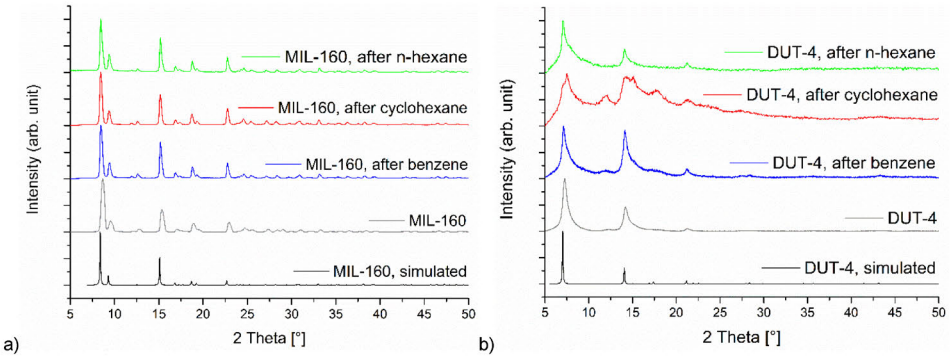

Figure S15 *(a) PXRDs of MIL-160 after VOC-sorption, compared with MOF before sorption and with simulated pattern (CSD-Number: 1828696).[4] (b) PXRDs of DUT-4 after VOC-sorption, compared with MOF before sorption and with simulated pattern (CSD-Number: 691978).[5]*

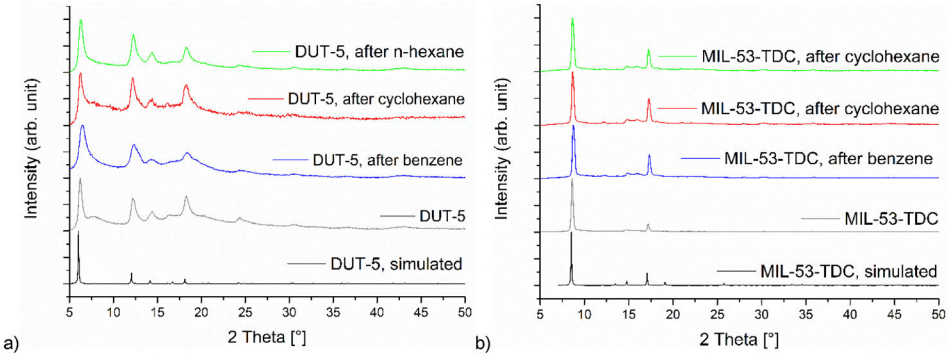

Figure S16 *(a) PXRDs of DUT-5 after VOC-sorption, compared with MOF before sorption and with simulated pattern (CSD-Number: 691979).[5] (b) PXRDs of MIL-53-TDC after VOC-sorption, compared with MOF before sorption and with simulated pattern (CSD-Number: Serre and Co-Workers).*

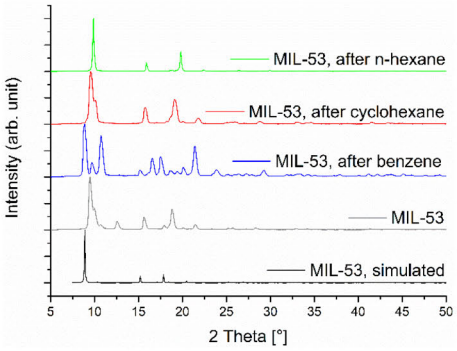

Figure S17 *PXRDs of MIL-53 after VOC-sorption, compared with MOF before sorption and with simulated pattern (CSD-Number: 1007172).*[10]

Zr-MOFs

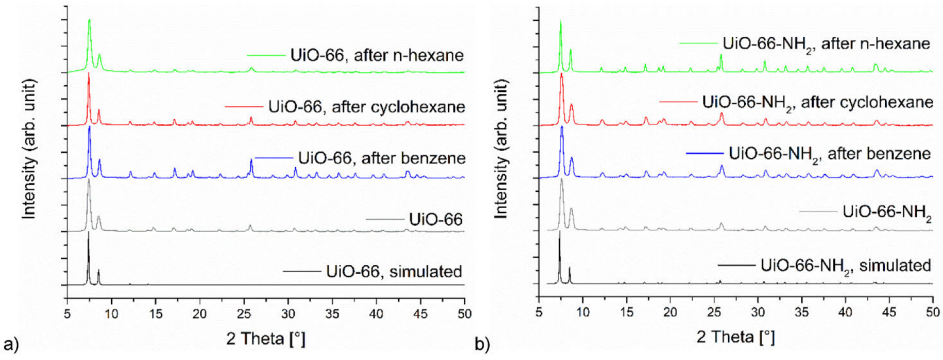

Figure S18 *(a) PXRDs of UiO-66 after VOC-sorption, compared with MOF before sorption and with simulated pattern (CSD-Number: 733458).*[15] *(b) PXRDs of UiO-66-NH₂ after VOC-sorption, compared with MOF before sorption and with simulated pattern (CSD-Number: 1405751).*[38]

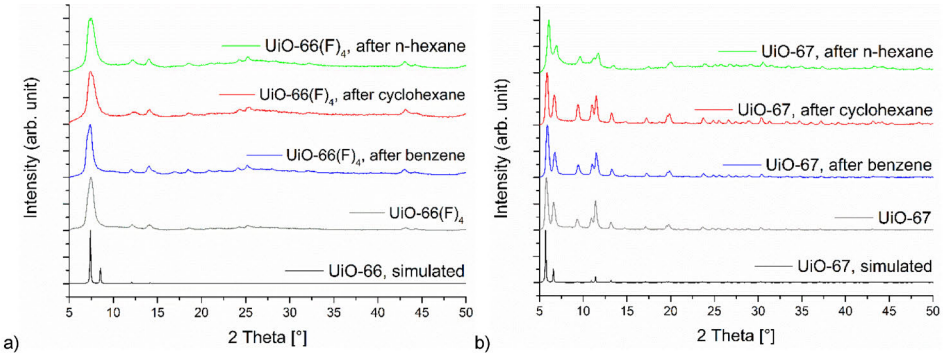

Figure S19 *(a) PXRDs of UiO-66(F)₄ after VOC-sorption, compared with MOF before sorption and with simulated pattern (CSD-Number: 733458).*[15] *(b) PXRDs of UiO-67 after VOC-sorption, compared with MOF before sorption and with simulated pattern (CSD-Number: 1018032).*[39]

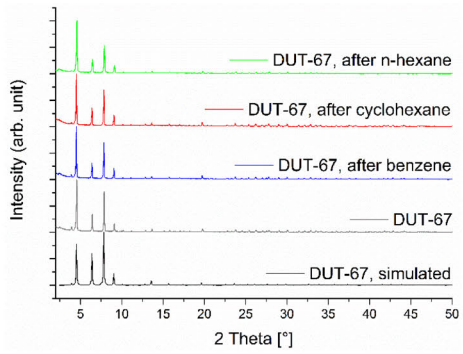

Figure S20 *PXRDs of DUT-67 after VOC-sorption, compared with MOF before sorption and with simulated pattern (CSD-Number: 921644).*[17]

Ti-MOFs

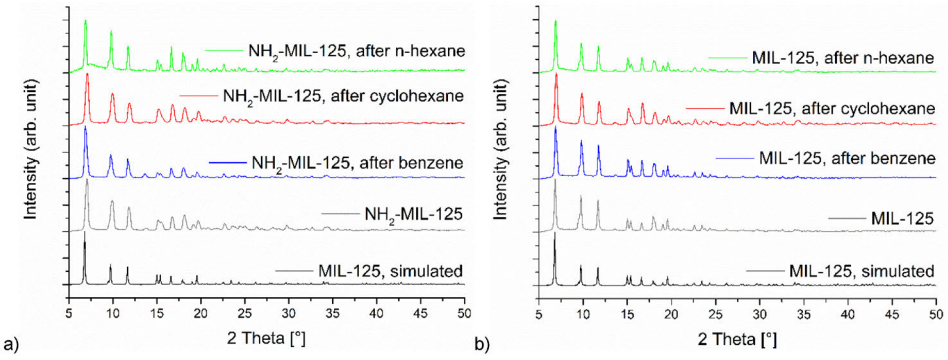

Figure S21 *(a) PXRDs of NH_2-MIL-125 after VOC-sorption, compared with MOF before sorption and with simulated pattern (CSD-Number: 751157).*[20] *(b) PXRDs of MIL-125 after VOC-sorption, compared with MOF before sorption and with simulated pattern (CSD-Number: 751157).*[20]

Cr-MOF

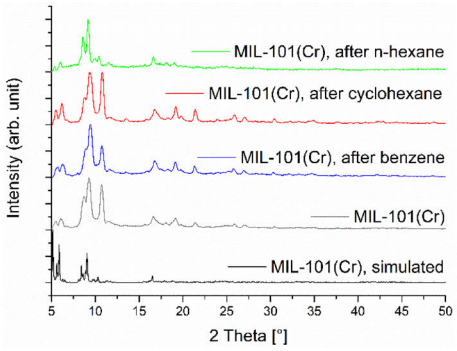

Figure S22 *PXRDs of MIL-101(Cr) after VOC-sorption, compared with MOF before sorption and with simulated pattern (CSD-Number: 605510).*[22]

ZIFs

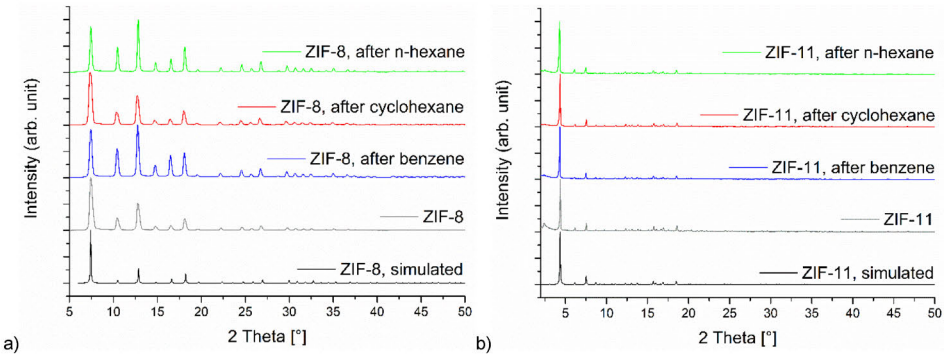

Figure S23 *(a) PXRDs of ZIF-8 after VOC-sorption, compared with MOF before sorption and with simulated pattern (CSD-Number: 864309).[24] (b) PXRDs of ZIF-11 after VOC-sorption, compared with MOF before sorption and with simulated pattern (CSD-Number: 602545).[26]*

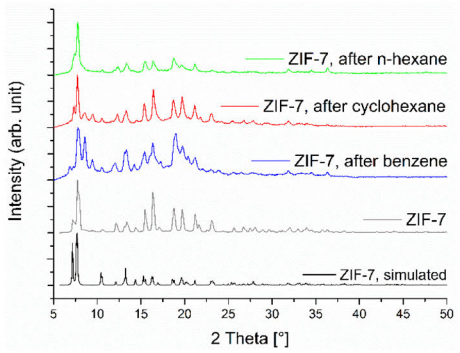

Figure S24 *PXRDs of ZIF-7 after VOC-sorption, compared with MOF before sorption and with simulated pattern (CSD-Number: 1036075).[40]*

S4 Nitrogen sorption experiments (T = 77 K)

Al-MOFs

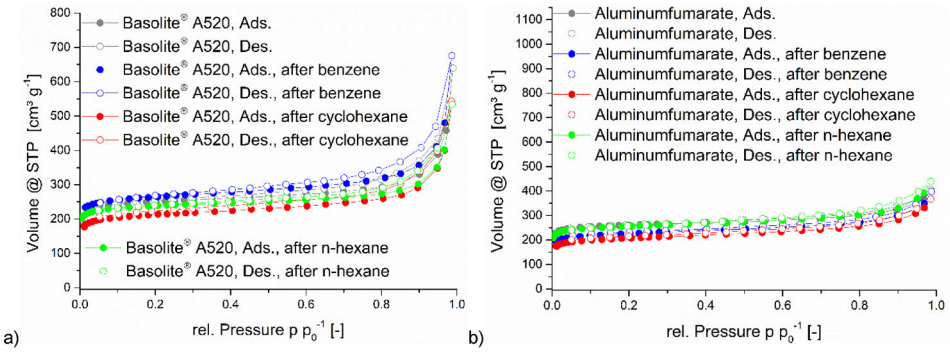

Figure S25 *(a) Nitrogen sorption of Basolite® A520 after VOC-sorption, compared with MOF before sorption. (b) Nitrogen sorption of Aluminumfumarate after VOC-sorption, compared with MOF before sorption.*

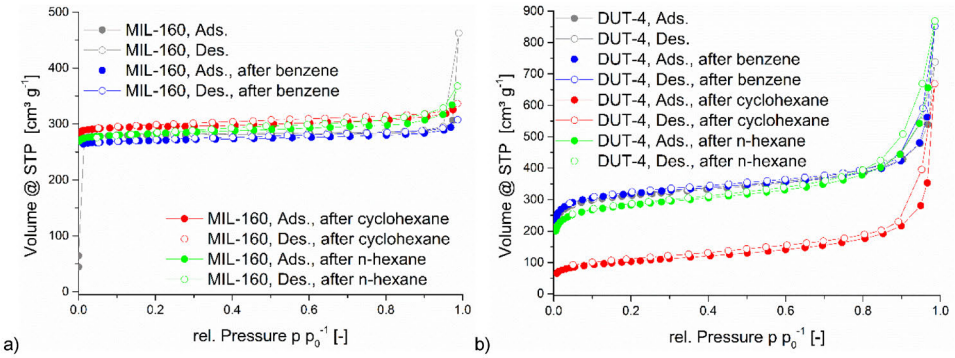

Figure S26 *(a) Nitrogen sorption of MIL-160 after VOC-sorption, compared with MOF before sorption. (b) Nitrogen sorption of DUT-4 after VOC-sorption, compared with MOF before sorption.*

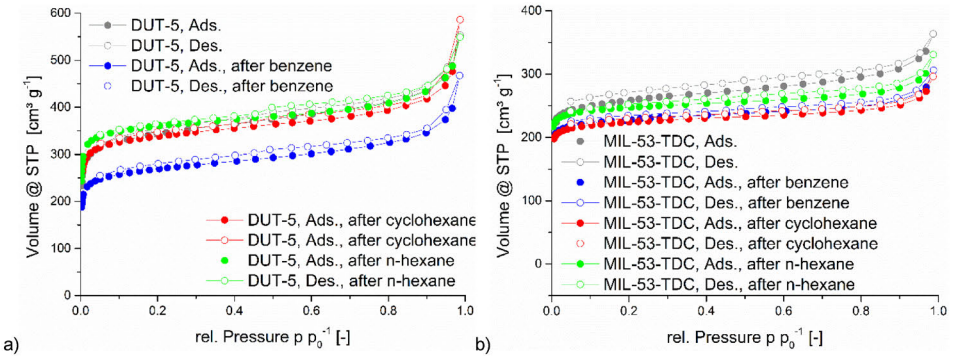

Figure S27 *(a) Nitrogen sorption of DUT-5 after VOC-sorption, compared with MOF before sorption. (b) Nitrogen sorption of MIL-53-TDC after VOC-sorption, compared with MOF before sorption.*

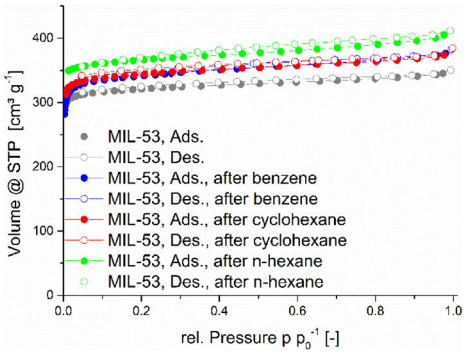

Figure S28 *Nitrogen sorption of MIL-53 after VOC-sorption, compared with MOF before sorption.*

Zr-MOFs

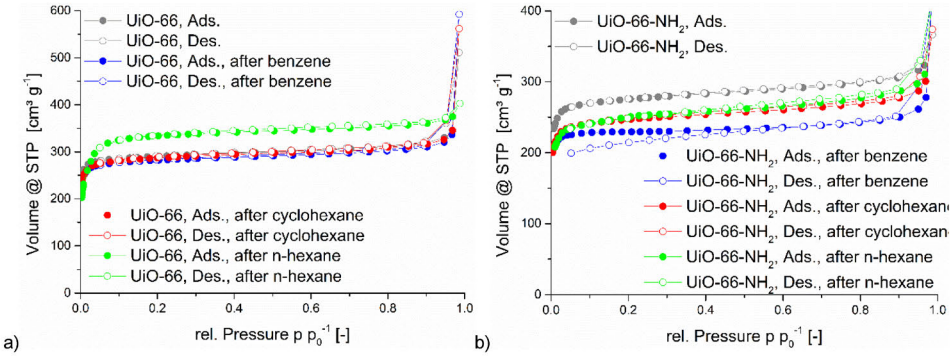

Figure S29 *(a) Nitrogen sorption of UiO-66 after VOC-sorption, compared with MOF before sorption. (b) Nitrogen sorption of UiO-66-NH₂ after VOC-sorption, compared with MOF before sorption.*

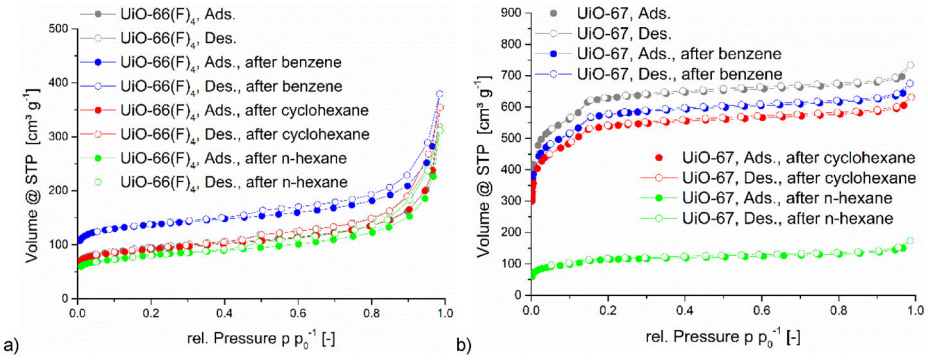

Figure S30 *(a) Nitrogen sorption of UiO-66(F)₄ after VOC-sorption, compared with MOF before sorption. (b) Nitrogen sorption of UiO-67 after VOC-sorption, compared with MOF before sorption.*

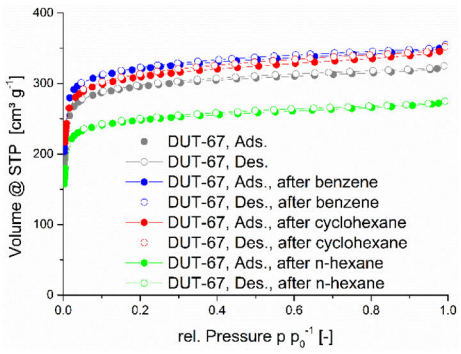

Figure S31 *Nitrogen sorption of DUT-67 after VOC-sorption, compared with MOF before sorption.*

Ti-MOFs

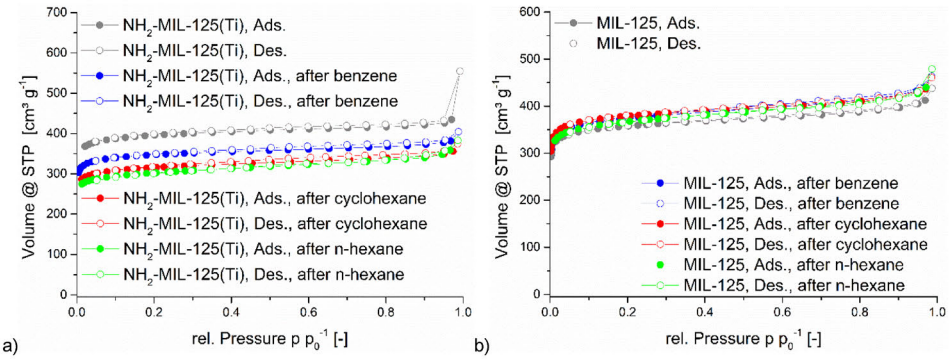

Figure S32 *(a) Nitrogen sorption of NH_2-MIL-125 after VOC-sorption, compared with MOF before sorption. (b) Nitrogen sorption of MIL-125 after VOC-sorption, compared with MOF before sorption.*

Cr-MOF

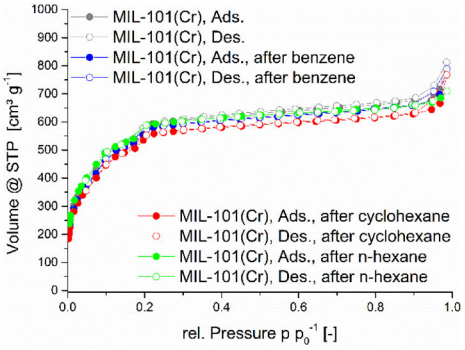

Figure S33 *Nitrogen sorption of MIL-101(Cr) after VOC-sorption, compared with MOF before sorption.*

ZIFs

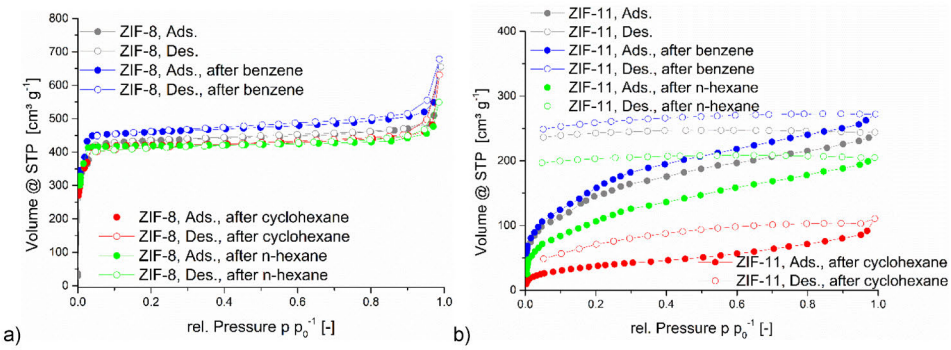

Figure S34 *(a) Nitrogen sorption of ZIF-8 after VOC-sorption, compared with MOF before sorption. (b) Nitrogen sorption of ZIF-11 after VOC-sorption, compared with MOF before sorption.*

S5 Carbon dioxide sorption experiments (T = 273 K)

ZIF-7

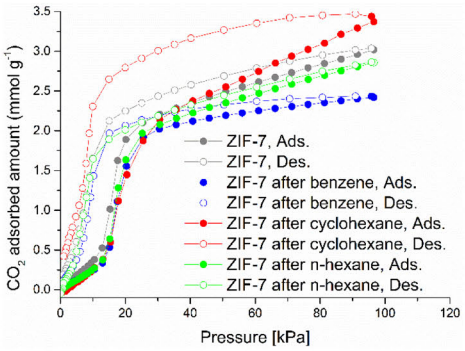

Figure S35 *Carbon dioxide sorption of ZIF-7 after VOC-sorption, compared with MOF before sorption.*

S6 Vapor sorption experiments (T = 293 K)

Equilibrium settings:

For each VOC measurement point the equilibrium is determined by three settings: maximum equilibrium points number (*P*), maximum equilibrium points interval time (*Int* in seconds) and maximum pressure-change rate limit (in *Torr min*$^{-1}$).
The equilibrium point numbers are the maximum numbers of individual points, which are used to measure the change of pressure. In our case these criteria were set to 10 points. The equilibrium points interval time describes the maximum time in seconds between the relevant points and was adapted due to the different pressure ranges. The last of the three settings is the pressure-change rate limit and it determines the maximum rate of pressure change per minute (Torr min^{-1}). Only values below this criterion will be considered as points in equilibrium.
These are the following conditions for the different VOCs due to their different relative pressure range:

Benzene

$p\ p_0^{-1}$ 0.001-0.4: *P:* 10, *Int:* 120, *Torr min*$^{-1}$*:* 0.001

$p\ p_0^{-1}$ 0.45-0.7: *P:* 10, *Int:* 180, *Torr min*$^{-1}$*:* 0.005

$p\ p_0^{-1}$ 0.8-0.9: *P:* 10, *Int:* 120, *Torr min*$^{-1}$*:* 0.01

$p\ p_0^{-1}$ 0.9-0.6: *P:* 10, *Int:* 90, *Torr min*$^{-1}$*:* 0.01

$p\ p_0^{-1}$ 0.5-0.01: *P:* 10, *Int:* 120, *Torr min*$^{-1}$*:* 0.005

Cyclohexane

$p\ p_0^{-1}$ 0.001-0.4: *P:* 10, *Int:* 120, *Torr min*$^{-1}$*:* 0.001

$p\ p_0^{-1}$ 0.45: *P:* 10, *Int:* 180, *Torr min*$^{-1}$*:* 0.001

$p\ p_0^{-1}$ 0.5-0.7: *P:* 10, *Int:* 180, *Torr min*$^{-1}$*:* 0.005

$p\ p_0^{-1}$ 0.8-0.9: *P:* 10, *Int:* 120, *Torr min*$^{-1}$*:* 0.01

$p\ p_0^{-1}$ 0.9-0.6: *P:* 10, *Int:* 90, *Torr min*$^{-1}$*:* 0.01

$p\ p_0^{-1}$ 0.5-0.01: *P:* 10, *Int:* 120, *Torr min*$^{-1}$*:* 0.005

n-Hexane

$p\ p_0^{-1}$ 0.001-0.45: *P:* 10, *Int:* 120, *Torr min*$^{-1}$*:* 0.01

$p\ p_0^{-1}$ 0.5-0.9: *P:* 10, *Int:* 180, *Torr min*$^{-1}$*:* 0.02

$p\ p_0^{-1}$ 0.9-0.6: *P:* 10, *Int:* 90, *Torr min*$^{-1}$*:* 0.01

$p\ p_0^{-1}$*:* 0.06-0.01: *P:* 10, *Int:* 120, *Torr min*$^{-1}$*:* 0.01

For each measured pressure point, the program performs a linear fit over a maximum of 10 points (to make it comparable), where each point is apart the maximum number of seconds as determined by the equilibrium points interval time.
If the slope of the fitted internal curve is below the pressure-change rate limit, the measurement will be defined to be in equilibrium. Due to the huge amount of data, these data were not given in the Supplementary Information.
The VOC *n*-hexane has the highest absolute pressure, compared to benzene and cyclohexane and therefore the measurement settings were adapted, by shortened equilibrium range.

Al-MOFs

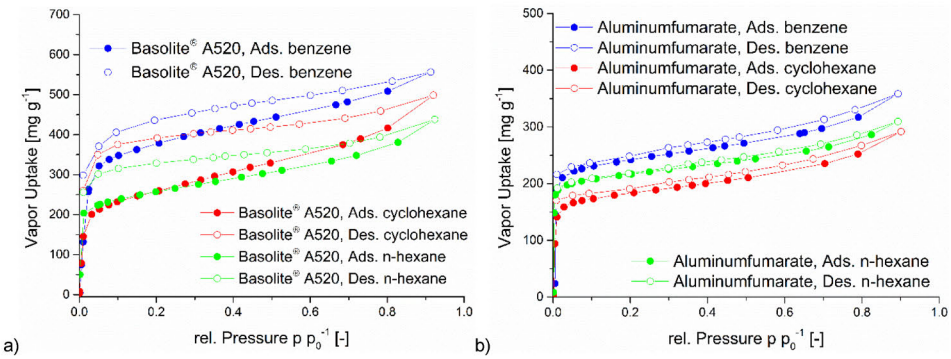

Figure S36 *(a) VOC sorption of Basolite® A520 for benzene/cyclohexane/n-hexane. (b) VOC sorption of Aluminumfumarate for benzene/cyclohexane/n-hexane.*

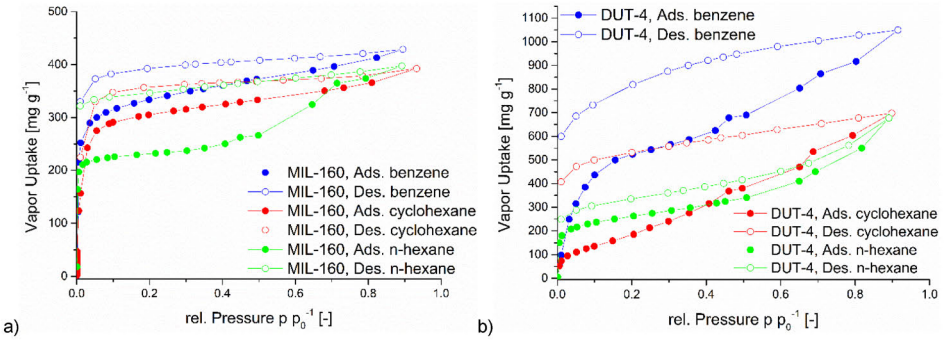

Figure S37 *(a) VOC sorption of MIL-160 for benzene/cyclohexane/n-hexane. (b) VOC sorption of DUT-4 for benzene/cyclohexane/n-hexane.*

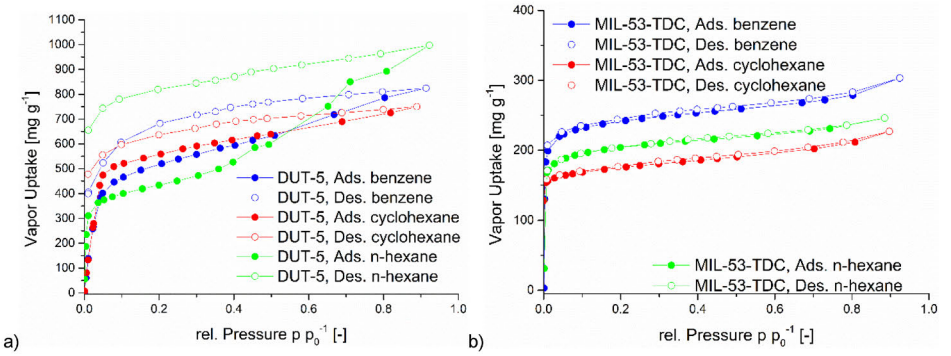

Figure S38 *(a) VOC sorption of DUT-5 for benzene/cyclohexane/n-hexane. (b) VOC sorption of MIL-53-TDC for benzene/cyclohexane/n-hexane.*

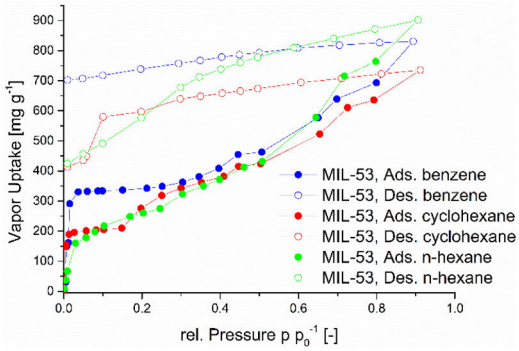

Figure S39 *VOC sorption of MIL-53 for benzene/cyclohexane/n-hexane.*

The aluminum-MOFs all show an early uptake in the low relative pressure range and uptakes between 303 mg g^{-1} and 1050 mg g^{-1} for benzene, 227 mg g^{-1} to 750 mg g^{-1} for cyclohexane and 246 mg g^{-1} and 997 mg g^{-1} for *n*-hexane. For all Al-MOFs, the first uptake step is completed in a pressure range below 0.1 p p_0^{-1}. For DUT-4 and MIL-53 a further additional continuous uptake takes place over the entire pressure range. MIL-160 and DUT-5 show only minor differences in the adsorption of benzene and cyclohexane, both, in the maximum uptake and over the entire relative pressure range. In the case of Basolite® A520 and Aluminumfumarate, the benzene uptake is higher over the entire pressure ranger than for cyclohexane and *n*-hexane. Interesting is the difference between Aluminumfumarate and Basolite® A520 in their adsorption capacity and hysteresis, because both materials are chemically the same MOF and the only difference is that Basolite® A520 is the industrial product, albeit with different surface area and porosity characteristics. Only for DUT-4 is the amount of benzene which is absorbed significantly higher than for cyclohexane and *n*-hexane over the entire measuring range and the maximum absorption capacity is over 350 mg g^{-1} more for benzene. The MOFs all show a very large hysteresis for benzene, cyclohexane and *n*-hexane, except for Aluminumfumarate and MIL-53-TDC.

Zr-MOFs

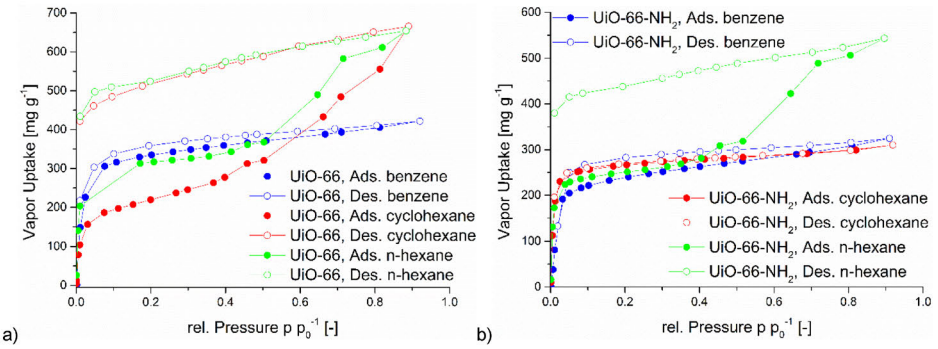

Figure S40 *(a) VOC sorption of UiO-66 for benzene/cyclohexane/n-hexane. (b) VOC sorption of UiO-66-NH_2 for benzene/cyclohexane/n-hexane.*

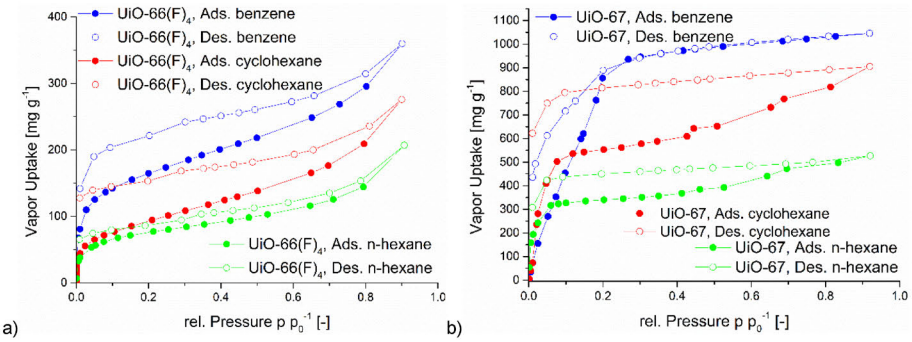

Figure S41 *(a) VOC sorption of UiO-66(F)$_4$ for benzene/cyclohexane/n-hexane. (b) VOC sorption of UiO-67 for benzene/cyclohexane/n-hexane.*

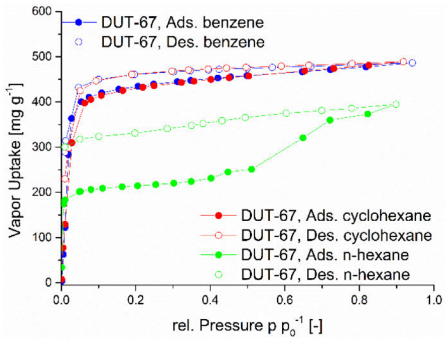

Figure S42 *VOC sorption of DUT-67 for benzene/cyclohexane/n-hexane.*

The zirconium MOFs show a high uptake in the low-pressure range and uptakes between 325 mg g^{-1} and 1046 mg g^{-1} for benzene, 276 mg g^{-1} to 905 mg g^{-1} for cyclohexane and 207 mg g^{-1} and 654 mg g^{-1} for *n*-hexane. The isotherm shape differs considerably, as well, as the occurrence of a hysteresis. A large hysteresis is significantly more common in the adsorption of cyclohexane compared to benzene and way more common for *n*-hexane. For example, only UiO-66-NH_2, UiO-66(F)$_4$ and UiO-67 show a hysteresis in the low-pressure range for benzene, but still small compared to cyclohexane and *n*-hexane sorption isotherms. Only with UiO-66-NH_2 cyclohexane shows no hysteresis. For the *n*-hexane sorptions only UiO-66(F)$_4$ has no significant hysteresis, but at the same time a low uptake. The absolute VOC uptakes for benzene and cyclohexane do not differ that much for the zirconium MOFs, except for UiO-66 where there is a difference of over 240 mg g^{-1} in favor of cyclohexane. The uptake of *n*-hexane and the shape of the isotherms are different compared to benzene and cyclohexane, but it is no clear trend recognizable. For UiO-66 and UiO-66-NH_2 the uptake for *n*-hexane is the same (UiO-66) or higher (UiO-66-NH_2) than the other VOCs. The other three zirconium MOFs have a lower *n*-hexane uptake.
All MOFs show a high affinity for *n*-hexane, too, but the shape of the isotherm is different to benzene and cyclohexane for the most MOFs, as mentioned before. For cyclohexane and *n*-hexane is a additional uptake recognizable for UiO-66 and UiO-66-NH_2. Benzene and cyclohexane show almost identical uptakes in UiO-66-NH_2 and in DUT-67. For the other Zr-MOFs the difference is in a small range, except for UiO-66.

The desorption process for *n*-hexane is only for UiO-66(F)$_4$ completed, all other four MOFs show an open, non-closed hysteresis. Due to this fact *n*-hexane still remains in the pores. This phenomenon exists as well for cyclohexane in UiO-66 and UiO-67 in an extended way.

Ti-MOFs

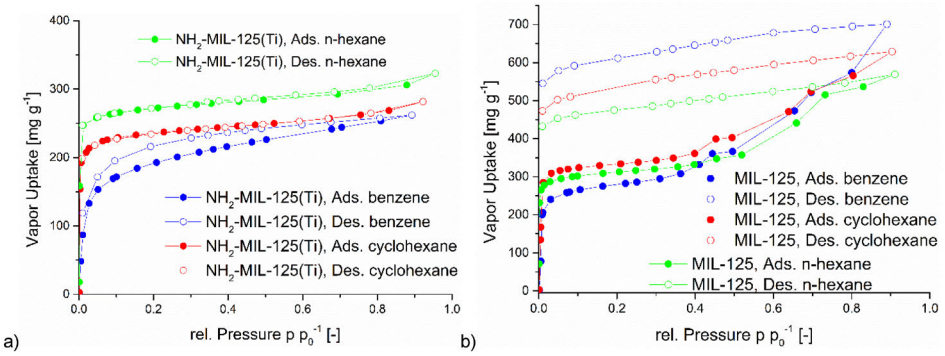

Figure S43 *(a) VOC sorption of NH_2-MIL-125 for benzene/cyclohexane/n-hexane. (b) VOC sorption of MIL-125 for benzene/cyclohexane/n-hexane.*

Like the zirconium MOFs, NH_2-MIL-125 shows no major difference in the final uptake of benzene, cyclohexane or *n*-hexane, albeit the uptake values are smaller than for UiO-66-NH_2. Analogous to UiO-66-NH_2, the hysteresis is larger for benzene than for cyclohexane or *n-hexane*. The initial uptake also takes place at a lower pressure for cyclohexane and *n*-hexane, compared to benzene. Between NH_2-MIL-125 and MIL-125 the isotherm shape, hysteresis and uptakes differ considerably. In MIL-125 all three VOC isotherms have a similar shape and a second uptake step after a relative pressure of 0.5 p p_0^{-1}. Furthermore, all VOCs have a large non-closen hysteresis. MIL-125 has an opposite maximum uptake order (benzene > cyclohexane > *n*-hexane) compared to NH_2-MIL-125 (*n*-hexane > cyclohexane > benzene).

Cr-MOF

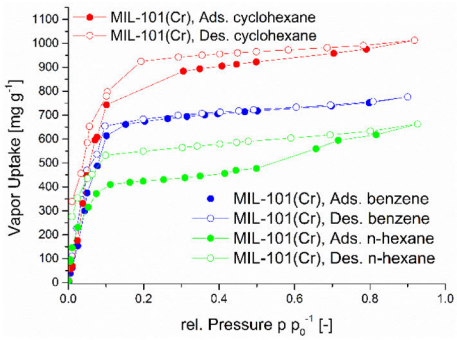

Figure S44 *VOC sorption of MIL-101(Cr) for benzene/cyclohexane/n-hexane.*

MIL-101(Cr) has the same terephthalate or benzene-1,4-dicarboxylate linker as MIL-53, UiO-66, MIL-125. MIL-101(Cr) it is no longer an only microporous MOF but also has mesopores (Figure S10). The uptake occurs in the low-pressure range, nearly the same as with the microporous MOFs. There is also a hysteresis with cyclohexane, compared to the MOF with the same linker UiO-66 and a larger hysteresis for *n*-hexane. Whereas there is almost no hysteresis for the benzene sorption. The maximum adsorption for cyclohexane is 236 mg g^{-1} more than the adsorption capacity for benzene. *n*-Hexane has the lowest amount with 663 mg g^{-1}. The large pores of MIL-101(Cr) are suitable for a high capacity.

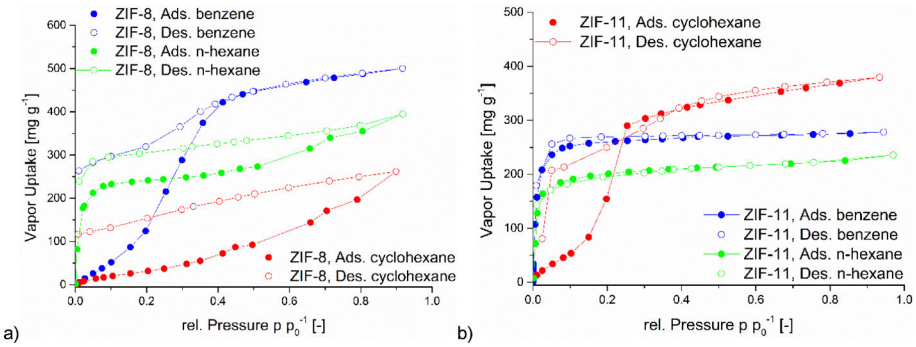

Figure S45 *(a) VOC sorption of ZIF-8 for benzene/cyclohexane/n-hexane. (b) VOC sorption of ZIF-11 for benzene/cyclohexane/n-hexane. The drop in the desorption curve below the adsorption branch for cyclohexane represent a measurement error.*

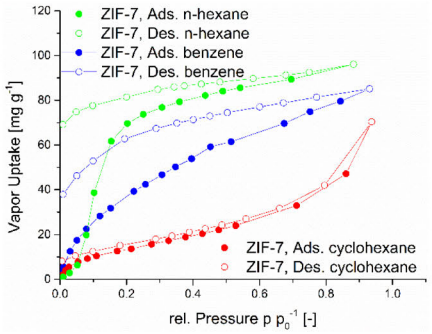

Figure S46 *VOC sorption of ZIF-7 for benzene/cyclohexane/n-hexane.*

ZIF-8 shows a clear difference in the maximum uptake of benzene, cyclohexane and *n*-hexane and the relative pressure range, where the uptake takes place. The benzene uptake occurs with an S-shaped uptake step between 0.1 and 0.5 p p_0^{-1} and increases to almost 500 mg g^{-1}. The uptake of cyclohexane is significantly lower and takes place constantly over the entire relative pressure range. The *n*-hexane uptake starts immediately at the beginning at a relative pressure below 0.04 p p_0^{-1}. All three adsorbates show a large hysteresis, the hysteresis with benzene only occurring at a relative pressure below 0.5 p p_0^{-1}.

The sorption isotherms of ZIF-11 and ZIF-7 differ significantly, not only between the adsorbates, but also between both ZIFs, despite the same metal and linker. In the case of ZIF-11, all three adsorbates show a pronounced uptake step, but in different relative pressure ranges. The uptake of benzene and *n*-hexane is in a low-pressure range of less than 0.1 p p_0^{-1} and has no additional uptake thereafter, as with type-I isotherms. [41] The increase in cyclohexane adsorption is from a relative pressure range of 0.1 to 0.3 p p_0^{-1} and then flattens off significantly with a small increase of less than 100 mg g^{-1} up to 0.9 p p_0^{-1}.

For ZIF-7, an S-shaped uptake is seen for *n*-hexane which above 0.1 p p_0^{-1} also exceeds the benzene and cyclohexane uptake. Yet, the maximum *n*-hexane uptake compared with the other MOFs is still low (Table S7). For cyclohexane ZIF-7 gives only a low constant uptake. Compared to cyclohexane, the benzene uptake is already significantly higher. Compared to ZIF-11, all VOC uptake values in ZIF-7 are significantly lower. The pores of ZIF-11 are larger than those of ZIF-7. The inner pore diameter of ZIF-11 is 14.6 Å and of ZIF-7 only 4.3 Å.[25]

Table S4 *Adsorption isotherm and hysteresis type for C_6 vapor adsorption in MOFs.*[a]

MOF	**Adsorption isotherm type (desorption hysteresis at 293 K)** [b]			**Comment**
	benzene	**cyclohexane**	***n*-hexane**	
Basolite® A520 (commercial Alfum)	Ib+II (H4 wide)	Ib+II (H4 wide)	Ia+II (H4 wide)	
Alfum (own synthesis)	Ia+II (H4 narrow)	Ia+II (H4 narrow)	Ia+II (H4 narrow)	
MIL-160	Ib+II (H4 wide)	Ib+II (H4 wide)	IVa (H2a very wide)	steps in *n*-hexane ads. at p p_0^{-1} ~0.5 and ~0.7
DUT-4	F-I (H2a or H4 very wide	II (H3 very wide)	Ia+II (H4 wide)	two small steps in benzene and cyclohexane ads. at p p_0^{-1} ~0.45 and ~0.7
DUT-5	Ib+II (H4 wide)	Ib+II (H4 wide)	Ia+II (H4 very wide)	two small steps in *n*-hexane ads. at p p_0^{-1} ~0.45 and ~0.7
MIL-53-TDC	Ia(+II) (H4 very narrow)	Ia(+II) (H4 very narrow)	Ia(+II) (no hysteresis)	only very slight increase of uptake with p p_0^{-1}, very small hystereses
MIL-53(Al)	F-I (H2a very wide)	F-I (H2a very wide)	F-I (H2a very wide)	F-I based on the known flexible character; steps in ads. of all vapors, for cyclohexane already at p p_0^{-1} ~0.2; hysteresis steps for *n*-hexane and cyclohexane; step in hysteresis for cyclohexane and *n*-hexane at low p p_0^{-1}
UiO-66	Ib (H4, narrow)	Ib+II (H2b very wide)	F-I or IV (H2b very wide)	only very slight increase of benzene uptake with p p_0^{-1}, very small benzene hysteresis; steps in cyclohex. and *n*-hexane ads. after p p_0^{-1} ~0.45
UiO-66-NH_2	Ia+II (H4 narrow)	Ia (no hysteresis)	F-I or IV (very wide)	steps in *n*-hexane ads. after p p_0^{-1} ~0.45
UiO-66$(F)_4$	Ib+II (H4 wide)	Ia+II (H4 wide)	Ia+II (H4 narrow)	
UiO-67	Ib (wide hyst. <0.3 p p_0^{-1})	F-I or Ib+II (H2b very wide)	F-I or IV (H2b wide)	no hysteresis for benzene >0.3 p p_0^{-1}; steps in cyclohex. and *n*-hexane ads. at p p_0^{-1} ~0.45
DUT-67	Ib(+II) (H4 narrow)	Ib(+II) (H4 narrow)	F-I or IV (H2b wide)	isotherms of cyclohex. and benzene almost super-imposible); steps in *n*-hexane ads. after p p_0^{-1} ~0.45
NH_2-MIL-125	Ib+II (H4 narrow)	Ia(+II) (no hysteresis)	Ia(+II) (almost no hyst.)	
MIL-125	Ia+II (H2b very wide)	F-I or IV (H2b very wide)	F-I or IV (H2b very wide)	steps in ads. of all vapors, most prominently for benzene and cyclohex. at p p_0^{-1} ~0.45
MIL-101(Cr)	Ib (narrow hyst. <0.2 p p_0^{-1})	Ib+II (H2 narrow)	F-I or IV (H2b wide)	hysteresis for benzene only below 0.2 p p_0^{-1}
ZIF-8	F-I (wide hyst. <0.4 p p_0^{-1})	F-III or III (H2b wide)	F-I or IV (H2b wide)	hysteresis for benzene only below 0.5 p p_0^{-1} with step in

				hysteresis for benzene at low p p_0^{-1}; S-shaped benzene ads. with inflection point at p p_0^{-1} ~0.3
ZIF-11	Ib (hyst. <0.4 p p_0^{-1})	F-I or IV (H2a wide)	Ib (no hysteresis)	S-shaped cyclohex. ads. with inflection point at p p_0^{-1} ~0.25
ZIF-7	Ib (H2b wide)	II (H3 narrow)	F-III or V (H2b wide)	S-shaped hexane ads. with inflection point at p p_0^{-1} ~0.1

[a] The type was chosen according to the classifications given in ref. 41 and 42 to represent visually the best approximation.
[b] wide and narrow with respect to the hysteresis describe a large and small, respectively, separation between the ad- and desorption branch.

Classification of adsorption isotherms

Type I isotherms are reversible and have a steep uptake at very low-pressure after which almost no further uptake takes place. Thus, the maximum uptake is reached before p p_0^{-1} = 1. A steep uptake at very low p p_0^{-1} is due to strong adsorbate-adsorbent interactions. Type Ia has sharp knee (the point where the isotherm turns from almost vertical to horizontal line). Type Ib has a more gradual, less distinctive knee.

Type II isotherms derive from the adsorption on non- to macroporous adsorbents with multilayer formation at high p p_0^{-1}. The increasing uptake in a Type II branch towards p p_0^{-1} = 1 can come from the adsorption on the outer surface of a fine powder and from the filling of interparticle voids.

Standard Type IV isotherms are seen with mesoporous adsorbents where initially (at low p p_0^{-1}) the adsorbate-adsorbent interaction on the pore walls and at higher p p_0^{-1} the pore condensation with multilayer formation determines the isotherm shape. An important aspect of Type IV isotherms is the saturation plateau at high p p_0^{-1}.[41]

A Type F-I isotherm reflects the uptake in a flexible microporous material with a structure transformation through a gradual opening of a small pore to a large pore.[42] It can be noted that from the isotherm shape alone Type F-I and Type IV appear identical. The F-I or IV isotherms have a similar uptake in the low and higher pressure regions.

Origin of hysteresis

Hysteresis in physisorption originates from kinetic effects of adsorption metastability, network effects and pore blocking, such that wide pores are only accessible through narrow pore windows. An H4 hysteresis is seen for adsorption isotherms which are a composite of Type I and II. If the isotherm is fully in equilibrium its shape only reflects the thermodynamics of the ad- and desorption. Thus, a gradual uptake or release cannot be descibed as 'slow'. As noted above, a hysteresis is, however, indicative of kinetic effects. Such a kinetic effect can be observed for larger adsorbates and relative smaller pore (window or neck) diameters. Only when the adsorption is driven by larger adsorption energies at the border of physisorption towards chemisorption the hysteresis will be due to thermodynamic effects of strong adsorbate-adsorbent interactions. Strong hydrogen-bonding and strong $\pi\cdots\pi$ or C-H$\cdots\pi$ interactions or adsorbate interactions with open-metal sites,[43] then allow the guest only to be removed at the end of the desorption branch, that is at very low p p_0^{-1} and possibly even under additional heating.[44] In this respect we note that all of the desorption branches with a wide and very wide hysteresis did not close until until very low p p_0^{-1}. While for benzene this non-closure could have been due to strong $\pi\cdots\pi$ interactions, any strong supramolecular interactions can be ruled out for *n*-hexane and cyclohexane. This leaves then only kinetic effects based on the relative guest-pore size for the latter and, in turn, also suggests the same for benzene. In general it can be envisioned that the pore structures of frameworks limit the diffusion of molecules of the size of benzene, cyclohexane and *n*-hexane more strongly than that of small gas molecules such as N_2, CO_2 etc.[44]

Description of C_6-VOC isotherms

The categorization in Table S4 may not reflect all small features of the isotherms.

In general, the thermodynamics of the physisorption of gases and solvent vapors depend on absorbate-absorbate and absorbate-absorbent interactions with the kinetics being determined mainly by the molecular size of the adsorptive and the pore size of the adsorbent. (In physisorption the host network is the adsorbent. The guest in the fluid phase is the adsorptive; the guest in the adsorbed state is the adsorbate. Often the terms adsorptive and adsorbate seem to be used indiscriminately.[41]) The magnitude of guest-host (absorbate-absorbent) interactions in physisorption depends on the possible supramolecular interactions between the guest molecules and the pore walls of the framework, giving rise to the different isotherm types of adsorption processes.[44] Benzene adsorption in MOFs may be expected to follow a Type-I isotherm, since in the low p p_0^{-1} region benzene adsorption can reach saturation due to $\pi \cdots \pi$-interactions with the often aromatic core of the linker in the MOF. Cyclohexane and *n*-hexane can only enter into weaker van-der-Waals interactions with the framework so that a gradually increasing adsorption with the increase in p p_0^{-1} of the absorbate could be foreseen.[44]

UiO-66, MIL-53 and MIL-125 show the same isotherm shape and a large hysteresis and all of them have the same linker (terephthalate). MIL-101(Cr) shows a different isotherm shape, without the additional step already mentioned above, but with the same linker. This may be attributed to the large pores (mesoporous) and thus lower interaction. The additional uptake in the three MOFs can be explained by VOC-VOC interaction, which can be better formed in a smaller pore or pore condensation. In addition, MIL-53 may still have a breathing effect in the pore and promote additional uptake.

This additional uptake step (MIL-53, UiO-66, MIL-125) may also be a reason for the poor desorption and the associated large hysteresis. Both, the amine functionalization and complete fluorination of the linker result in lower total uptake, as the pores and the pore window of the MOFs are smaller, but favor better desorption and the formation of a smaller hysteresis. When the π-system and thus the pores become larger, as in DUT-4, DUT-5 and UiO-67, the isotherms also show further steps and larger hysteresis. These MOFs have larger pores than the terephthalate MOFs, but are still microporous, in contrast to MIL-101(Cr). DUT-5 is an exception here with a lower second uptake step and smaller hysteresis, although this can also be explained by the BET surface area, which is lower than the literature values and lower than the surface area of DUT-4.

The functionalization of the MOFs like in UiO-66-NH_2, UiO-66$(F)_4$ and NH_2-MIL-125 reduces the pore window and the pore size/diameter. This has an influence on the sorption capacity and the isotherm shape of the MOFs, in comparison with their unfunctionalized derivatives UiO-66 and MIL-125. This reduction of the MOF pores leads to a no longer existing second uptake step for most of the MOF-VOC combinations and a smaller to nearly non-existing hysteresis. The reduced pore size could lead to a different arrangement of VOC molecules in the pore and less VOC-VOC interactions, which would lead to a second uptake step and to a strong hysteresis.

The MOFs MIL-160, MIL-53-TDC and DUT-67 have all a heteroatom inside their ligand, but different pore windows (cf. Table S2). MIL-160 and DUT-67 have a smaller pore than MIL-53-TDC, but DUT-67 and MIL-53-TDC have the same thiophenedicarboxylate ligand (cf. Figure 1 in the main text). All three MOFs show no second uptake step and a very small hysteresis for benzene and cyclohexane. The sorption isotherms for *n*-hexane are different than for benzene and cyclohexane. The two MOFs with the smaller pore window (MIL-160 and DUT-67) have a second uptake step and a huge hysteresis for the *n*-hexane sorption. The different structure and linker of the two MOFs suggests that this sorption effect may be related to the pore window. Possibly this window size is a bottleneck, both in adsorption and desorption, and prevents uniform uptake, as in MIL-53-TDC, which has a much larger pore window. MIL-53-TDC has the same isotherm shape for all three VOCs and a small closed hysteresis. The difference between the two ligands furandicarboxylate and thiophenedicarboxylate is the heteroatom and furandicarboxylate is the ligand with the weaker aromatic system. This can be seen in the slightly different isotherm shape, as MIL-53-TDC has an even earlier and more linear uptake step (more type Ia) than MIL-160 for the VOCs.

The ZIFs with their very small pore windows and gate-opening effects related to the linkers methylimidazolate and benzimidazolate show a different phenomenon, which is much more dependent on the particular VOC. The bulkiest VOC of these three is cyclohexane and the gate-opening effect blocks the adsorption in ZIF-8 and ZIF-7. In particular, uptake in ZIF-7 is extremely hindered or only occurs at high relative pressures around 0.8 p p_0^{-1}, and could be attributed to condensation of VOCs on the surface. For ZIF-8, the cyclohexane uptake rises over the entire pressure range, but remains very low relative to the other two VOCs. For benzene and *n*-hexane, isotherms with a clear uptake step are observed, but in different relative pressure ranges and an affinity of the ZIFs towards the different VOCs is clearly visible. Especially the clearly different isotherm curves for ZIF-11 and ZIF-7 are very interesting, since these are two MOFs with identical metal-linker composition and only a different 3D crystal packing. It can be seen that not only the metal and the linker have a significant influence, as in the case of the MOFs mentioned above, but also the structural composition of the porous compounds plays a major role.

Tabular summary of C_6-VOC uptake at different relative pressures, including BET-surface areas before and after VOC sorption.

Table S5 *Benzene sorption results at different relative pressures, including BET-surface areas before and after benzene sorption.*

MOF	BET-surface [m^2 g^{-1}]		benzene uptake [mg g^{-1}] (293 K)		
	before benzene sorption	after benzene sorption	p p_0^{-1} = 0.1	p p_0^{-1} = 0.3	p p_0^{-1} = 0.9
Alfum (Basolite® A520)	988	1034	347	401	551
Aluminumfumarate	1035	879	230	252	358
MIL-160	1161	1120	315	348	429
DUT-4	1764	1233	436	564	1031
DUT-5	1323	1038	462	557	820
MIL-53-TDC	1015	912	231	248	298
MIL-53(Al)	1325	1375	334	362	830
UiO-66	1178	1150	314	348	419
UiO-66-NH_2	1127	940	221	252	323
UiO-66$(F)_4$	346	521	142	183	359
UiO-67	2317	2046	460	946	1043
DUT-67	1178	1271	417	444	483
NH_2-MIL-125	1570	1390	172	205	262
MIL-125	1425	1471	265	293	701
MIL-101(Cr)	2002	2117	607	692	776
ZIF-8	1615	1785	52	290	498
ZIF-11	491	408	253	264	277
ZIF-7	3.03 mmol CO2 (275)	2.43 mmol CO2 (223)	25	47	83

MOF	benzene uptake [mg g^{-1}] (293 K)		
	p p_0^{-1} = 0.02	p p_0^{-1} = 0.05	p p_0^{-1} = 0.08
Alfum (Basolite® A520)	226	319	339

Aluminumfumarate	204	220	227
MIL-160	266	297	309
DUT-4	168	315	395
DUT-5	232	403	446
MIL-53-TDC	206	222	229
MIL-53(Al)	300	331	333
UiO-66	200	265	307
UiO-66-NH_2	128	204	215
UiO-66$(F)_4$	97	125	136
UiO-67	130	263	380
DUT-67	289	395	412
NH_2-MIL-125	113	152	165
MIL-125	223	249	260
MIL-101(Cr)	122	375	503
ZIF-8	11	26	41
ZIF-11	193	235	249
ZIF-7	9	17	23

Table S6 *Cyclohexane sorption results at different relative pressures, including BET-surface areas before and after cyclohexane sorption.*

MOF	**BET-surface [$m^2\ g^{-1}$]**		**cyclohexane uptake [mg g^{-1}] (293 K)**		
	before cyclohexane sorption	**after cyclohexane sorption**	**p p_0^{-1} = 0.1**	**p p_0^{-1} = 0.3**	**p p_0^{-1} = 0.9**
Alfum (Basolite® A520)	988	825	233	283	485
Aluminumfumarate	1035	802	173	192	291
MIL-160	1161	1201	291	316	385
DUT-4	1764	372	136	241	698
DUT-5	1323	1301	518	591	750
MIL-53-TDC	1015	888	168	181	227
MIL-53(Al)	1325	1371	205	343	726
UiO-66	1178	1158	193	246	666
UiO-66-NH_2	1127	994	256	273	307
UiO-66$(F)_4$	346	339	76	108	276
UiO-67	2317	1928	521	577	890
DUT-67	1178	1238	412	441	487
NH_2-MIL-125	1570	1259	229	241	279
MIL-125	1425	1510	323	343	627
MIL-101(Cr)	2002	2054	737	880	1007

ZIF-8	1615	1650	20	46	262
ZIF-11	491	140	53	303	376
ZIF-7	3.03 mmol CO2 (275)	3.47 mmol CO2 (326)	10	16	59

MOF	**cyclohexane uptake [mg g^{-1}] (293 K)**		
	p p_0^{-1} = 0.02	**p p_0^{-1} = 0.05**	**p p_0^{-1} = 0.08**
Alfum (Basolite® A520)	170	212	225
Aluminumfumarate	151	165	171
MIL-160	200	269	285
DUT-4	86	110	127
DUT-5	233	474	509
MIL-53-TDC	158	163	167
MIL-53(Al)	192	200	203
UiO-66	130	169	188
UiO-66-NH_2	212	241	253
UiO-66$(F)_4$	52	65	72
UiO-67	216	422	506
DUT-67	226	365	406
NH_2-MIL-125	208	220	226
MIL-125	295	315	321
MIL-101(Cr)	145	450	627
ZIF-8	7	13	17
ZIF-11	19	33	45
ZIF-7	5	7	9

Table S7 *n-Hexane sorption results at different relative pressures, including BET-surface areas before and after n-hexane sorption.*

MOF	**BET-Surface [m^2 g^{-1}]**		***n*-Hexane uptake [mg g^{-1}] (293 K)**		
	before *n*-hexane sorption	**after *n*-hexane sorption**	**p p_0^{-1} = 0.1**	**p p_0^{-1} = 0.3**	**p p_0^{-1} = 0.9**
Alfum (Basolite® A520)	988	944	240	276	438
Aluminumfumarate	1035	1010	209	225	310
MIL-160	1161	1178	226	237	397
DUT-4	1764	1076	236	286	677
DUT-5	1323	1418	400	472	997
MIL-53-TDC	1015	997	197	210	246
MIL-53(Al)	1325	958	217	323	901
UiO-66	1178	1355	313	326	654
UiO-66-NH_2	1127	1010	240	263	543

UiO-66(F)$_4$	346	290	68	84	207
UiO-67	2317	396	327	351	527
DUT-67	1178	992	209	220	395
NH_2-MIL-125	1570	1204	266	277	323
MIL-125	1425	1455	302	320	569
MIL-101(Cr)	2002	2159	410	438	663
ZIF-8	1615	2340	233	249	395
ZIF-11	491	418	182	203	236
ZIF-7	3.03 mmol CO2 (275)	2.85 mmol CO2 (215)	39	77	96

MOF	***n*-Hexane uptake [mg g^{-1}] (293 K)**		
	p p_0^{-1} = 0.02	**p p_0^{-1} = 0.05**	**p p_0^{-1} = 0.08**
Alfum (Basolite® A520)	208	224	233
Aluminumfumarate	191	200	205
MIL-160	212	220	223
DUT-4	189	215	228
DUT-5	330	373	390
MIL-53-TDC	176	187	193
MIL-53(Al)	115	174	198
UiO-66	210	230	251
UiO-66-NH_2	191	228	236
UiO-66(F)$_4$	43	56	62
UiO-67	225	296	323
DUT-67	188	202	206
NH_2-MIL-125	250	259	263
MIL-125	282	293	299
MIL-101(Cr)	200	304	377
ZIF-8	171	213	228
ZIF-11	149	174	186
ZIF-7	2	6	21

Table S8 *Relative pressure calculated into absolute pressure in torr and kPa with the different saturation pressures of the VOCs.*

	benzene		**cyclohexane**		***n*-hexane**	
	p_0= 75.26 Torr	**p_0= 10.03 kPa**	**p_0= 77.51 Torr**	**p_0= 10.33 kPa**	**p_0= 121.53 Torr**	**p_0= 16.20 kPa**
p p_0^{-1}	**p [Torr]**	**p [kPa]**	**p [Torr]**	**p [kPa]**	**p [Torr]**	**p [kPa]**
0.02	1.50	0.20	1.55	0.21	2.43	0.32
0.05	3.76	0.50	3.88	0.52	6.08	0.81
0.08	6.02	0.80	6.20	0.83	9.72	1.30
0.1	7.53	1.00	7.75	1.03	12.15	1.62

0.3	22.58	3.00	23.25	3.10	36.46	4.86
0.9	67.73	9.00	69.76	9.30	109.38	14.58

Order of the VOC affinity of each MOF at different relative pressures.

Table S9 *Order of the volatile organic compounds at two different relative pressures (0.1 and 0.9) (293 K).*

MOF	**VOC-Order @ 0.1 p p_0^{-1}**	**VOC-Order @ 0.9 p p_0^{-1}**
Alfum (Basolite® A520)	**B > n-H ≈ C**	**B > C > n-H**
Aluminumfumarate	**B > n-H > C**	**B > n-H > C**
MIL-160	**B > C > n-H**	**B > n-H ≈ C**
DUT-4	**B > n-H > C**	**B > C ≈ n-H**
DUT-5	**C > B > n-H**	**n-H > B > C**
MIL-53-TDC	**B > n-H > C**	**B > n-H > C**
MIL-53(Al)	**B > n-H ≈ C**	**n-H > B > C**
UiO-66	**B > n-H > C**	**C ≈ n-H > B**
UiO-66-NH_2	**C > n-H > B**	**n-H > B ≈ C**
UiO-66$(F)_4$	**B > C ≈ n-H**	**B > C > n-H**
UiO-67	**C > B > n-H**	**B > C > n-H**
DUT-67	**B ≈ C > n-H**	**C ≈ B > n-H**
NH_2-MIL-125	**n-H > C > B**	**n-H > C > B**
MIL-125	**C > n-H > B**	**B > C > n-H**
MIL-101(Cr)	**C > B > n-H**	**C > B > n-H**
ZIF-8	**n-H > B > C**	**B > n-H > C**
ZIF-11	**B > n-H > C**	**C > B > n-H**
ZIF-7	**n-H > B > C**	**n-H > B > C**

Different orders are highlighted by color code for clarity:

B > n-H > C **B > C > n-H**

C > B > n-H **C > n-H > B**

n-H > B > C **n-H > C > B**

Vapor sorption isotherms divided by metals: full isotherms and low relative pressure

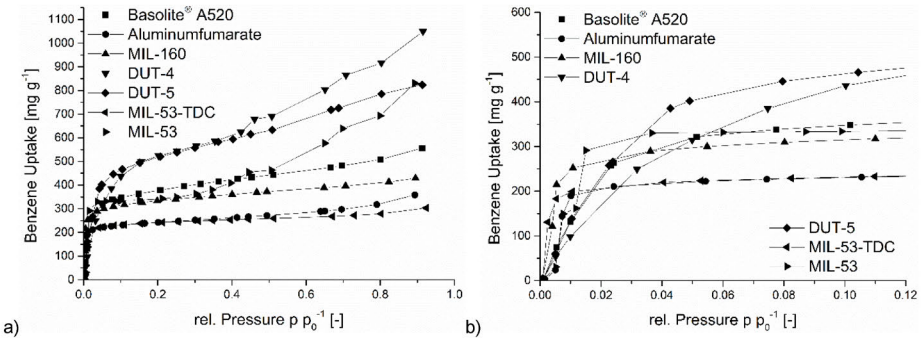

Figure S47 *Al-MOFs with benzene vapor isotherms 0-1 p p_0^{-1} (a) and 0-0.12 p p_0^{-1} (b) (293 K).*

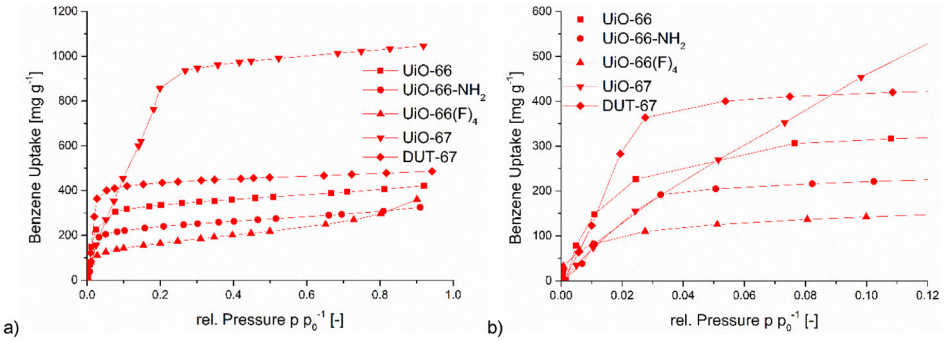

Figure S48 *Zr-MOFs with benzene vapor isotherms 0-1 p p_0^{-1} (a) and 0-0.12 p p_0^{-1} (b) (293 K).*

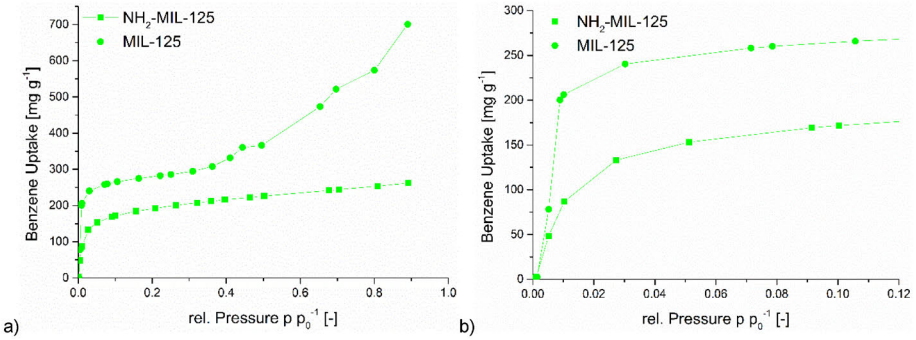

Figure S49 *Ti-MOFs with benzene vapor isotherms 0-1 p p_0^{-1} (a) and 0-0.12 p p_0^{-1} (b) (293 K).*

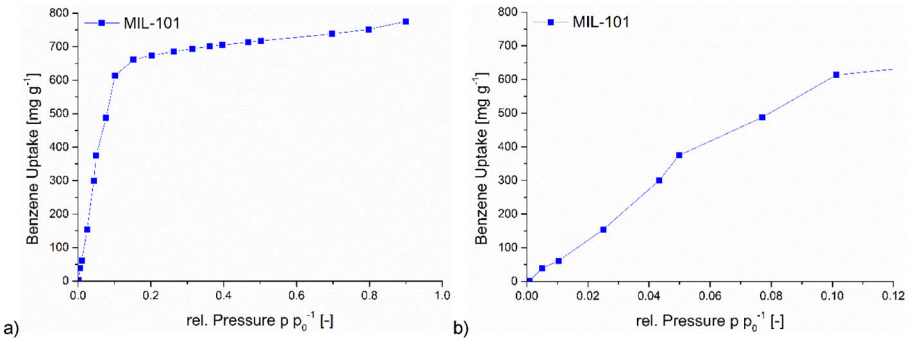

Figure S50 *Cr-MOF with benzene vapor isotherms 0-1 p p_0^{-1} (a) and 0-0.12 p p_0^{-1} (b) (293 K).*

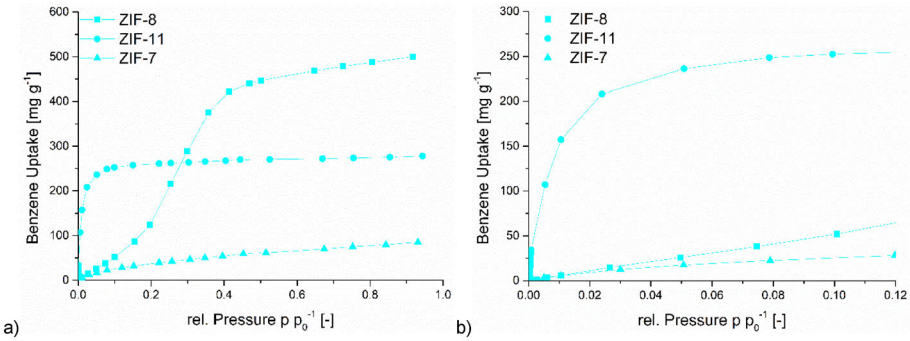

Figure S51 *ZIFs with benzene vapor isotherms 0-1 p p_0^{-1} (a) and 0-0.12 p p_0^{-1} (b) (293 K).*

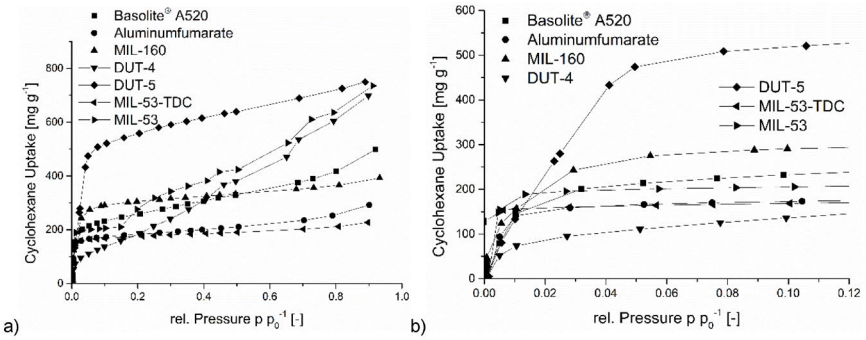

Figure S52 *Al-MOFs with cyclohexane vapor isotherms 0-1 p p_0^{-1} (a) and 0-0.12 p p_0^{-1} (b) (293 K).*

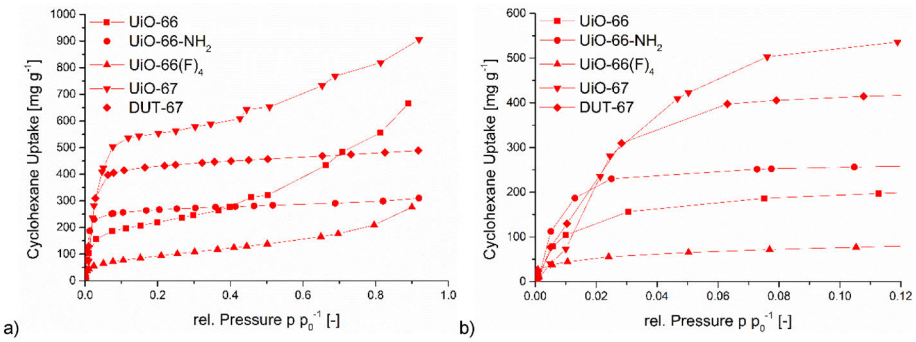

Figure S53 *Zr-MOFs with cyclohexane vapor isotherms 0-1 p p_0^{-1} (a) and 0-0.12 p p_0^{-1} (b) (293 K).*

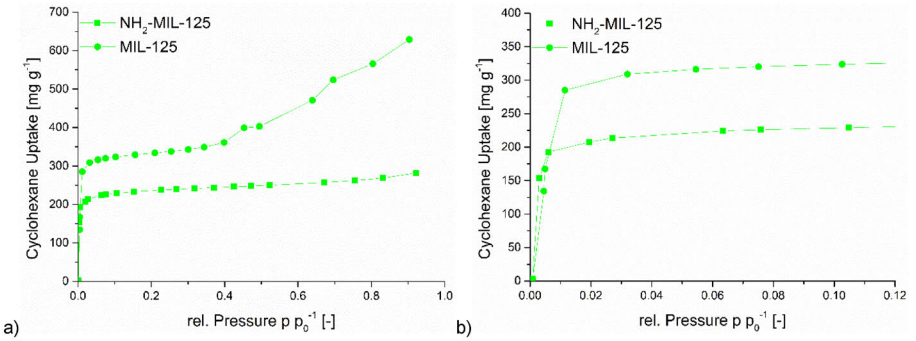

Figure S54 *Ti-MOFs with cyclohexane vapor isotherms 0-1 p p_0^{-1} (a) and 0-0.12 p p_0^{-1} (b) (293 K).*

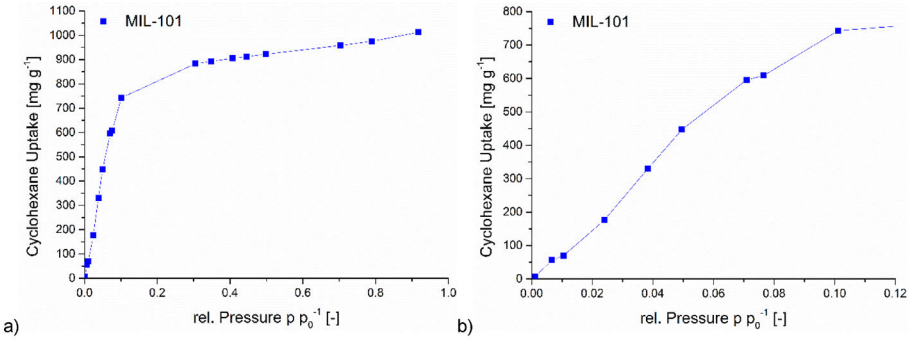

Figure S55 *Cr-MOF with cyclohexane vapor isotherms 0-1 p p_0^{-1} (a) and 0-0.12 p p_0^{-1} (b) (293 K).*

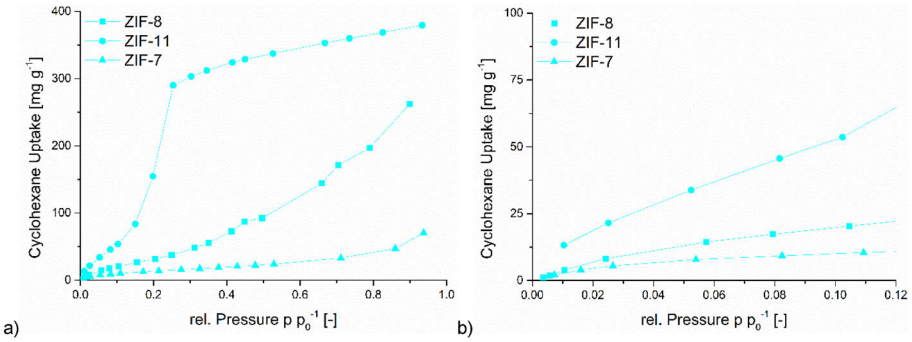

Figure S56 *ZIFs with cyclohexane vapor isotherms 0-1 p p_0^{-1} (a) and 0-0.12 p p_0^{-1} (b) (293 K).*

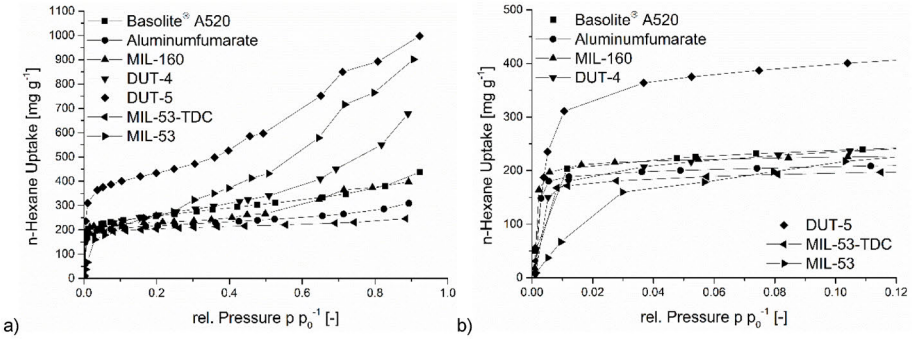

Figure S57 *Al-MOFs with n-hexane vapor isotherms 0-1 p p_0^{-1} (a) and 0-0.12 p p_0^{-1} (b) (293 K).*

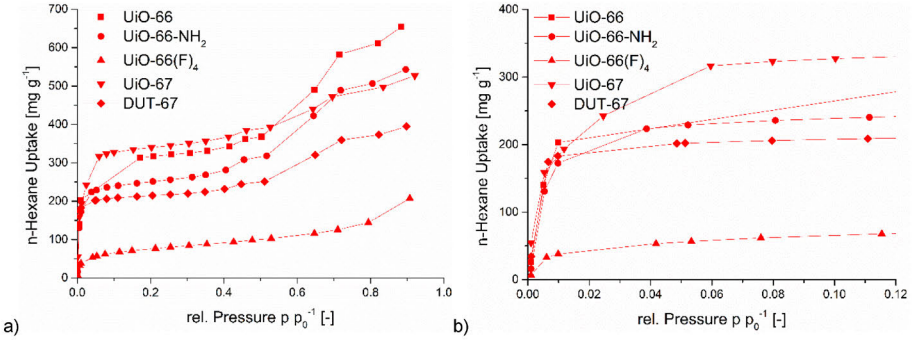

Figure S58 *Zr-MOFs with n-hexane vapor isotherms 0-1 p p_0^{-1} (a) and 0-0.12 p p_0^{-1} (b) (293 K).*

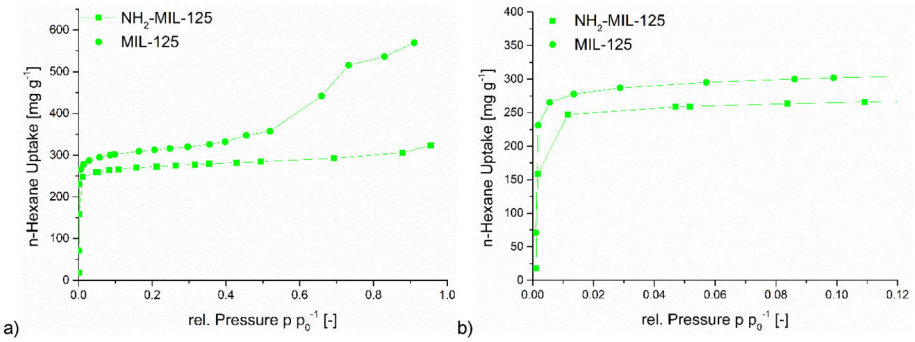

Figure S59 *Ti-MOFs with n-hexane vapor isotherms 0-1 p p_0^{-1} (a) and 0-0.12 p p_0^{-1} (b) (293 K).*

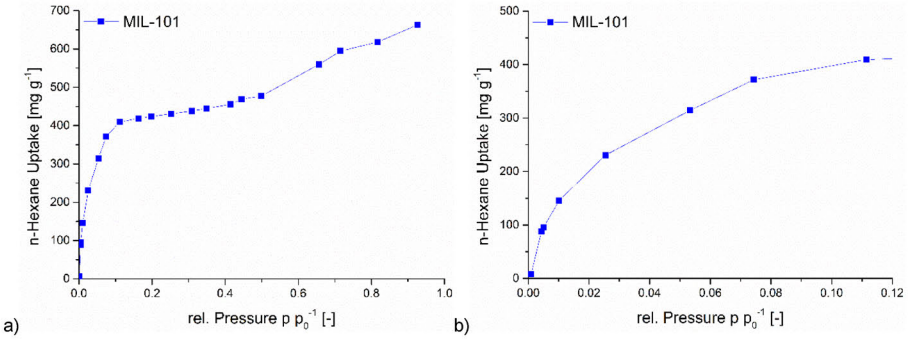

Figure S60 *Cr-MOF with n-hexane vapor isotherms 0-1 p p_0^{-1} (a) and 0-0.12 p p_0^{-1} (b) (293 K).*

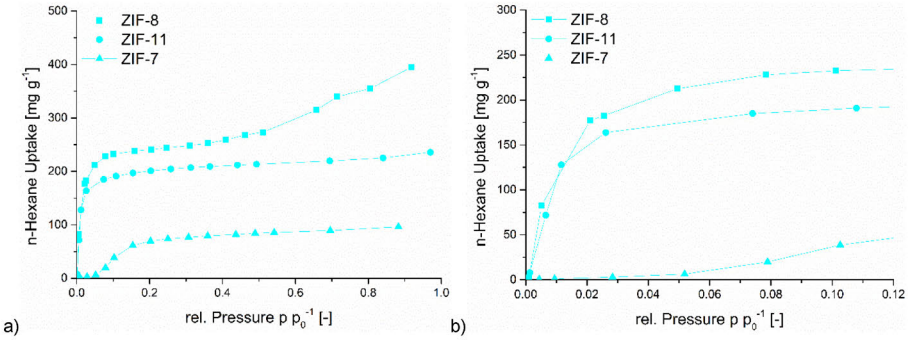

Figure S61 *ZIFs with n-hexane vapor isotherms 0-1 p p_0^{-1} (a) and 0-0.12 p p_0^{-1} (b) (293 K).*

S7 Thermogravimetric analysis (TGA)

Al-MOFs

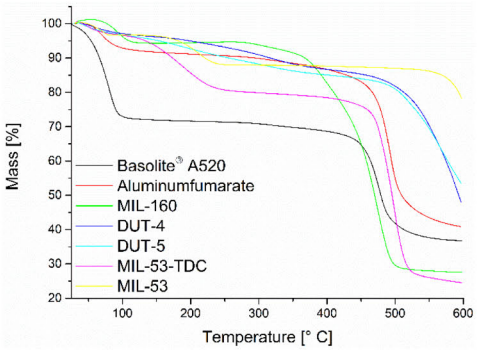

Figure S62 *TGA curves for the Al-MOFs under nitrogen atmosphere.*

Zr-MOFs

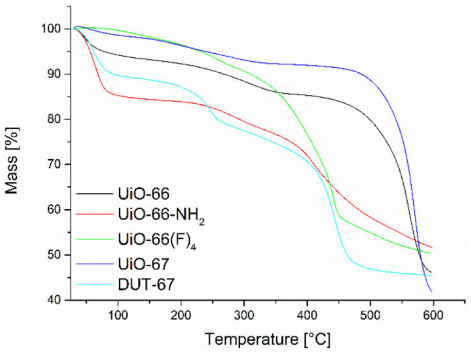

Figure S63 *TGA curves for the Zr-MOFs under nitrogen atmosphere.*

Ti-MOFs

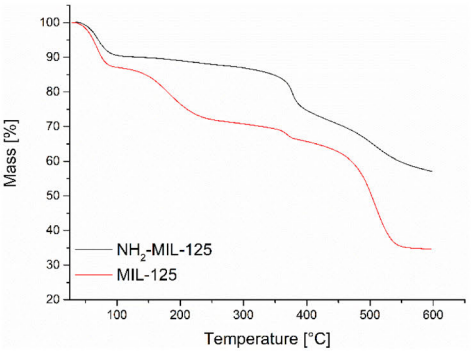

Figure S64 *TGA curves for the Ti-MOFs under nitrogen atmosphere.*

Cr-MOF

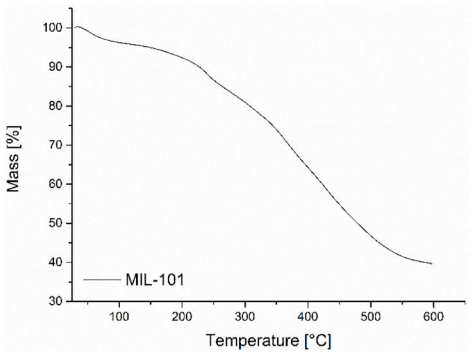

Figure S65 *TGA curve for the Cr-MOF under nitrogen atmosphere.*

ZIFs

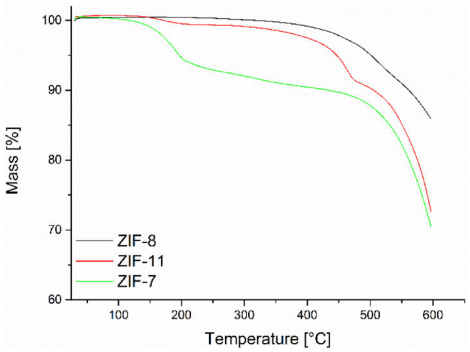

Figure S66 *TGA curves for the ZIFs under nitrogen atmosphere.*

S8 Scanning electron microscopy (SEM)

Al-MOFs

Basolite® A520

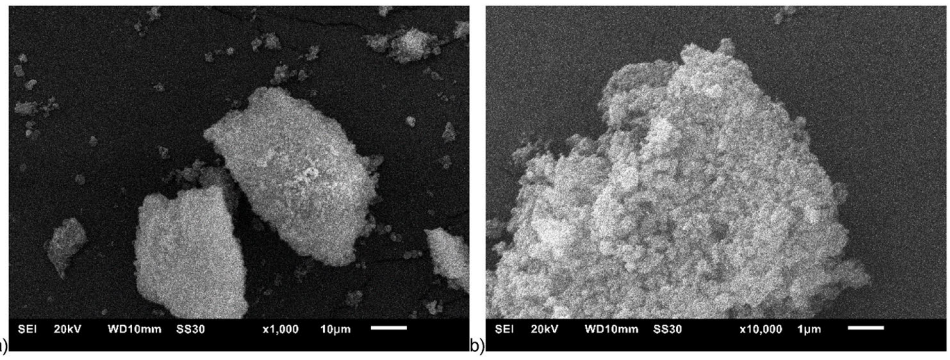

a) b)

Figure S67 *SEM images of Basolite® A520 at different magnifications ((a) overview, (b) close-up).*

Aluminumfumarate

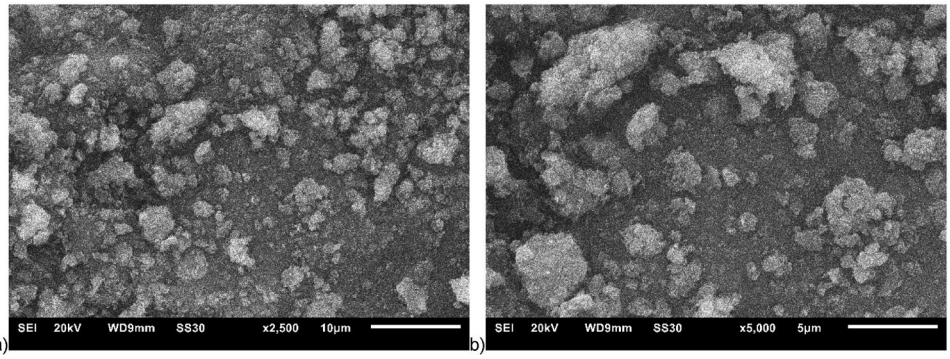

a) b)

Figure S68 *SEM images of Aluminumfumarate at different magnifications ((a) overview, (b) close-up).*

MIL-160

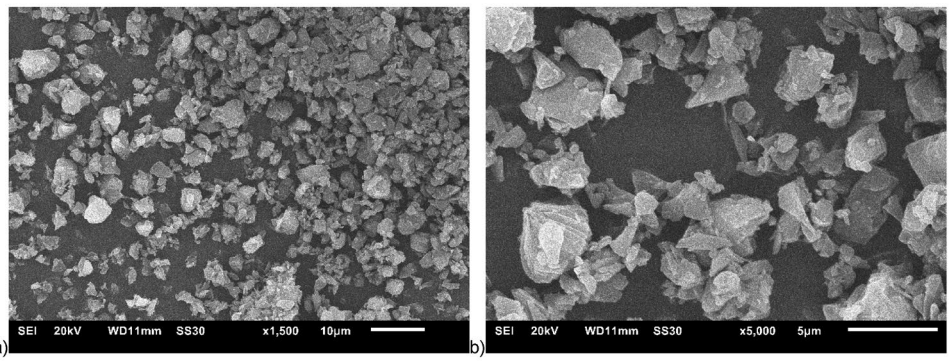

a) b)

Figure S69 *SEM images of MIL-160 at different magnifications ((a) overview, (b) close-up).*

DUT-4

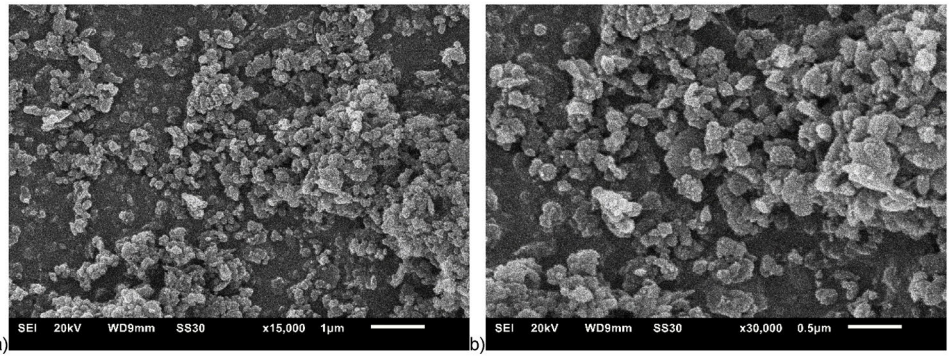

Figure S70 *SEM images of DUT-4 at different magnifications ((a) overview, (b) close-up).*

DUT-5

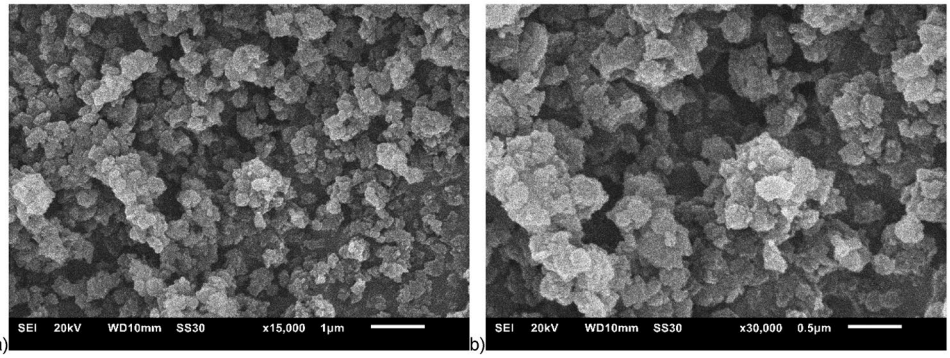

Figure S71 *SEM images of DUT-5 at different magnifications ((a) overview, (b) close-up).*

MIL-53-TDC

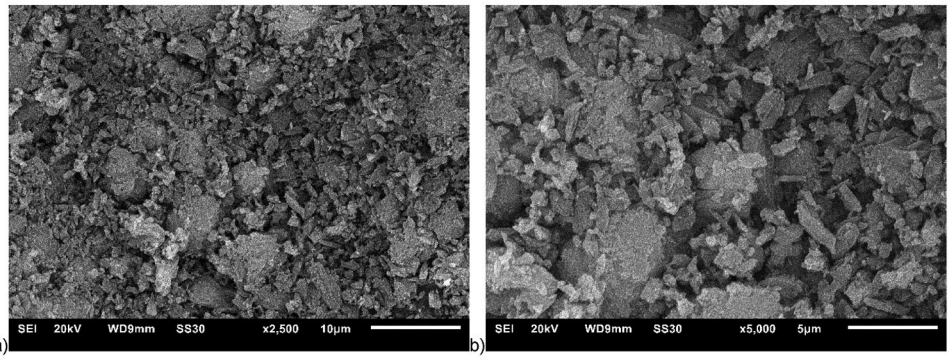

Figure S72 *SEM images of MIL-53-TDC at different magnifications ((a) overview, (b) close-up).*

MIL-53

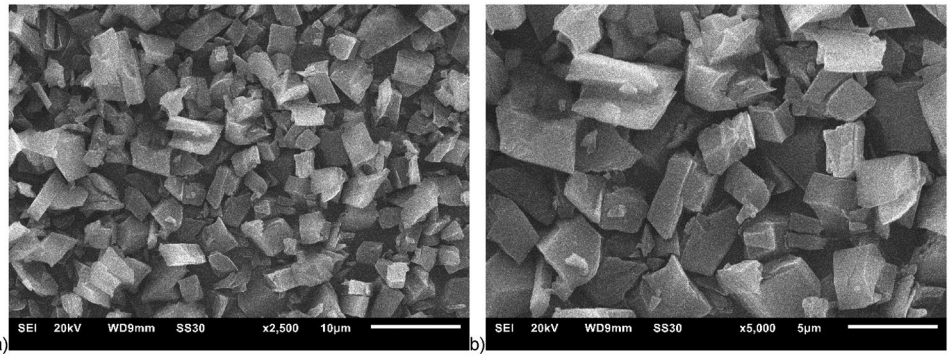

Figure S73 *SEM images of MIL-53 at different magnifications ((a) overview, (b) close-up).*

Zr-MOFs

UiO-66

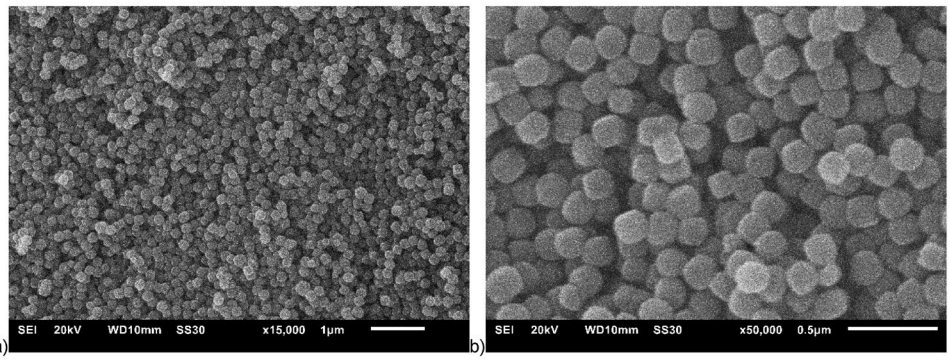

Figure S74 *SEM images of UiO-66 at different magnifications ((a) overview, (b) close-up).*

UiO-66-NH_2

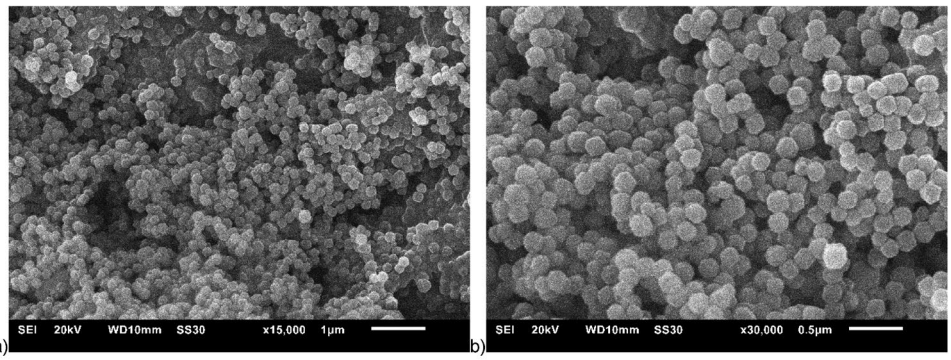

Figure S75 *SEM images of UiO-66-NH_2 at different magnifications ((a) overview, (b) close-up).*

UiO-66(F)$_4$

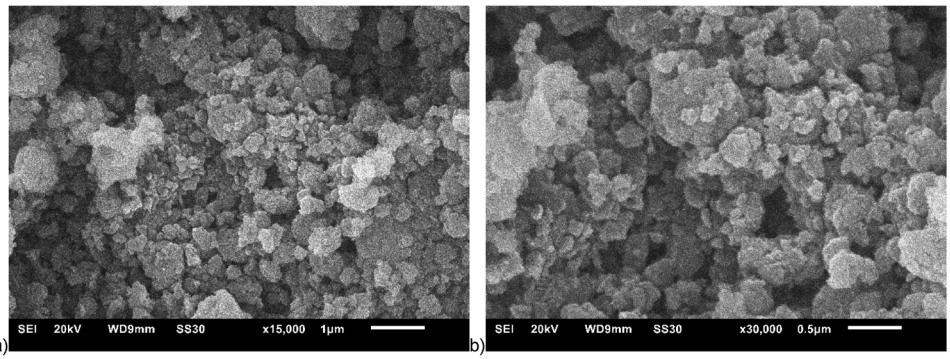

a) b)

Figure S76 *SEM images of UiO-66(F)$_4$ at different magnifications ((a) overview, (b) close-up).*

UiO-67

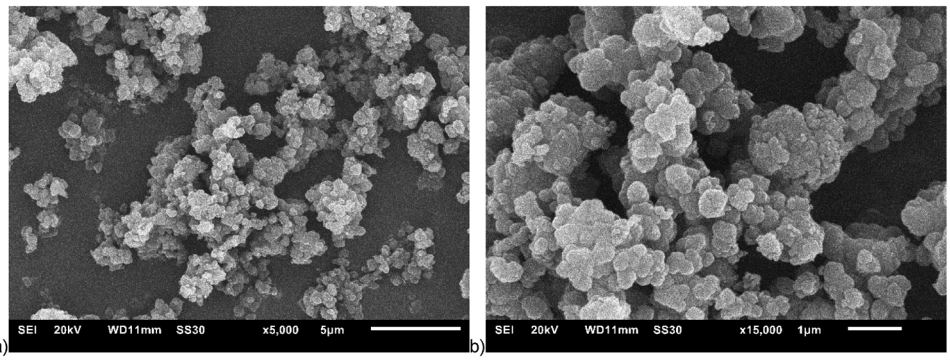

a) b)

Figure S77 *SEM images of UiO-67 at different magnifications ((a) overview, (b) close-up).*

DUT-67

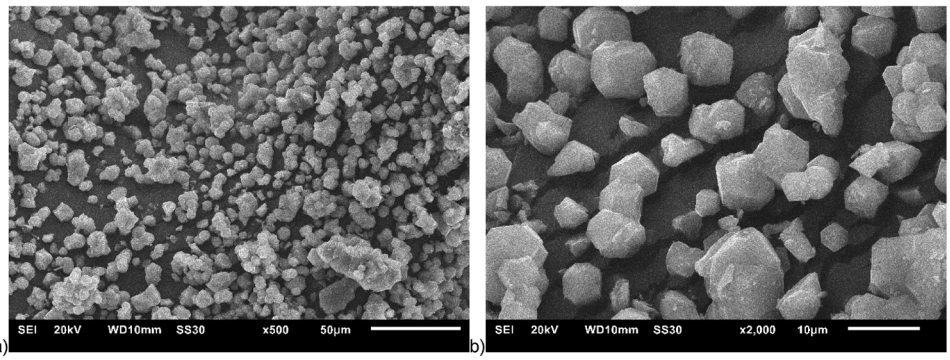

a) b)

Figure S78 *SEM images of DUT-67 at different magnifications ((a) overview, (b) close-up).*

Ti-MOFs

NH_2-MIL-125

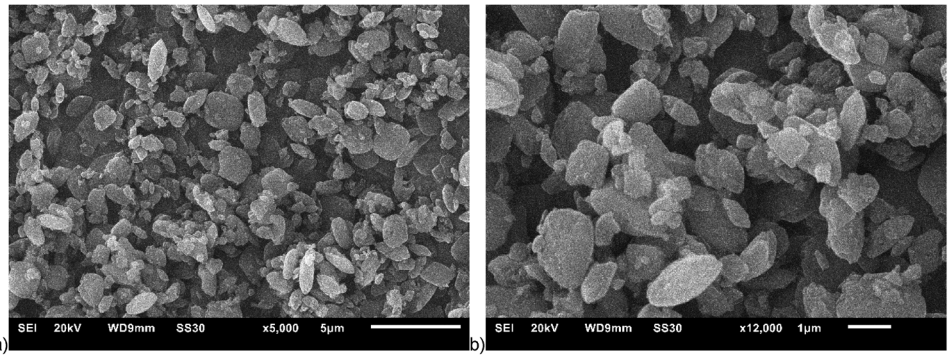

a) b)

Figure S79 *SEM images of NH_2-MIL-125 at different magnifications ((a) overview, (b) close-up).*

MIL-125

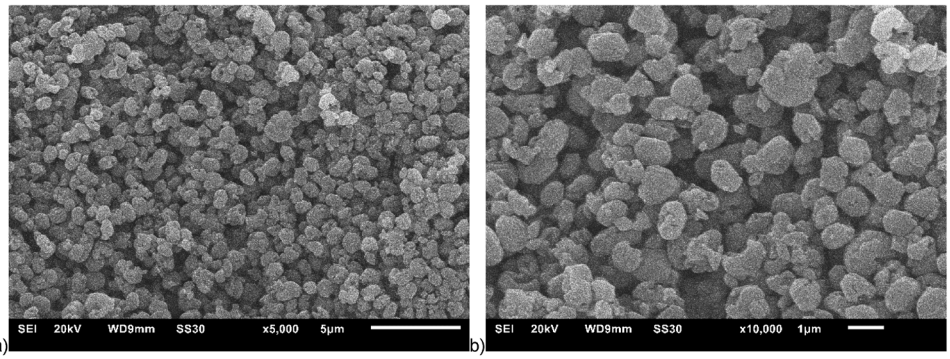

a) b)

Figure S80 *SEM images of MIL-125 at different magnifications ((a) overview, (b) close-up).*

Cr-MOF

MIL-101(Cr)

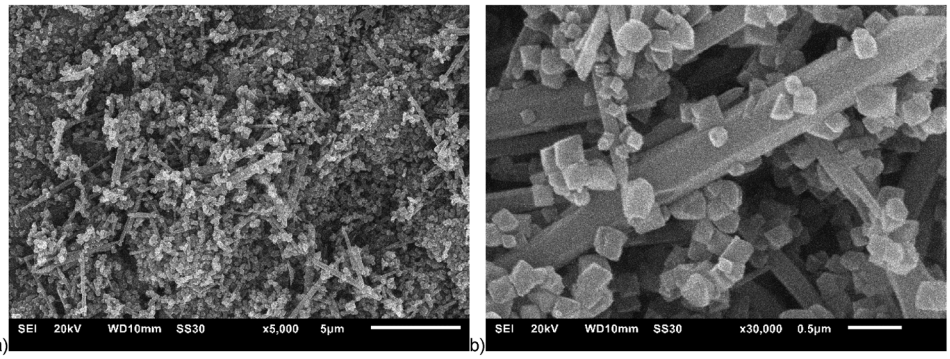

a) b)

Figure S81 *SEM images of MIL-101(Cr) at different magnifications ((a) overview, (b) close-up).*

ZIFs

ZIF-8

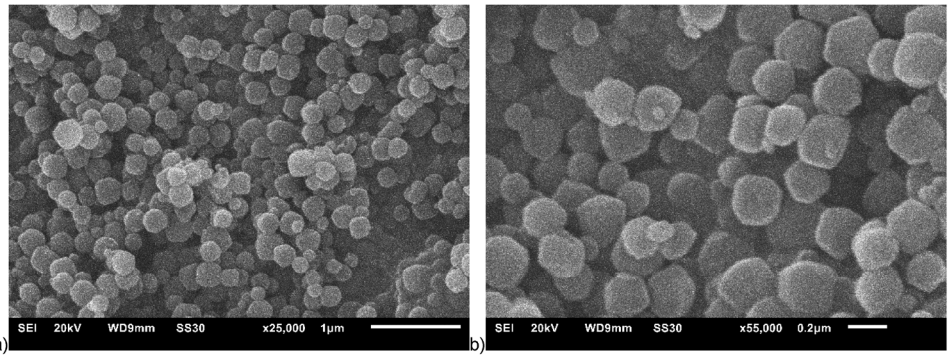

a) b)

Figure S82 *SEM images of ZIF-8 at different magnifications ((a) overview, (b) close-up).*

ZIF-11

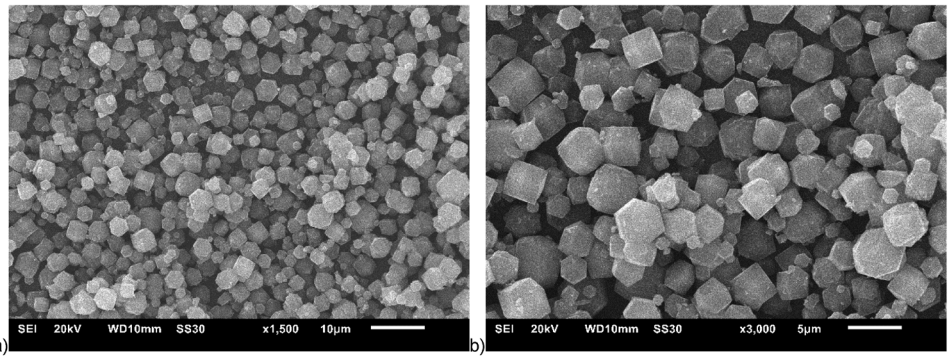

a) b)

Figure S83 *SEM images of ZIF-11 at different magnifications ((a) overview, (b) close-up).*

ZIF-7

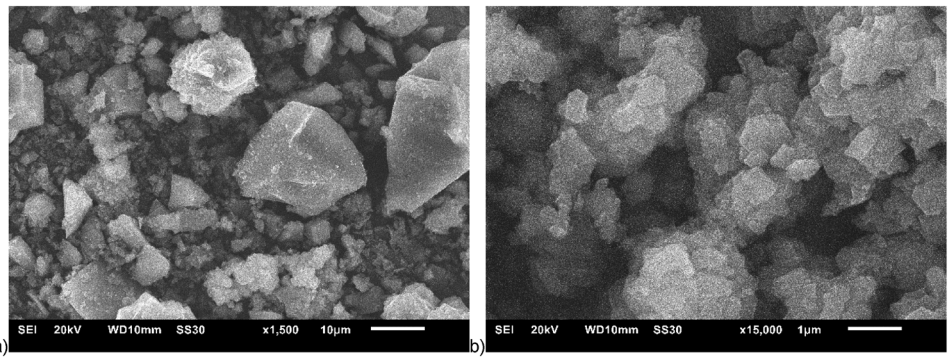

a) b)

Figure S84 *SEM images of ZIF-7 at different magnifications ((a) overview, (b) close-up).*

S9 VOC uptake versus BET surface, pore window size, micropore volume

To analyze the influence of the MOF microstructure on the sorption capacity different correlations were used. The uptake vs. pore volume correlation is given in Figure 5 in the main text. Here additional correlations of uptake vs. surface area, pore window size and micropore volume are depicted.

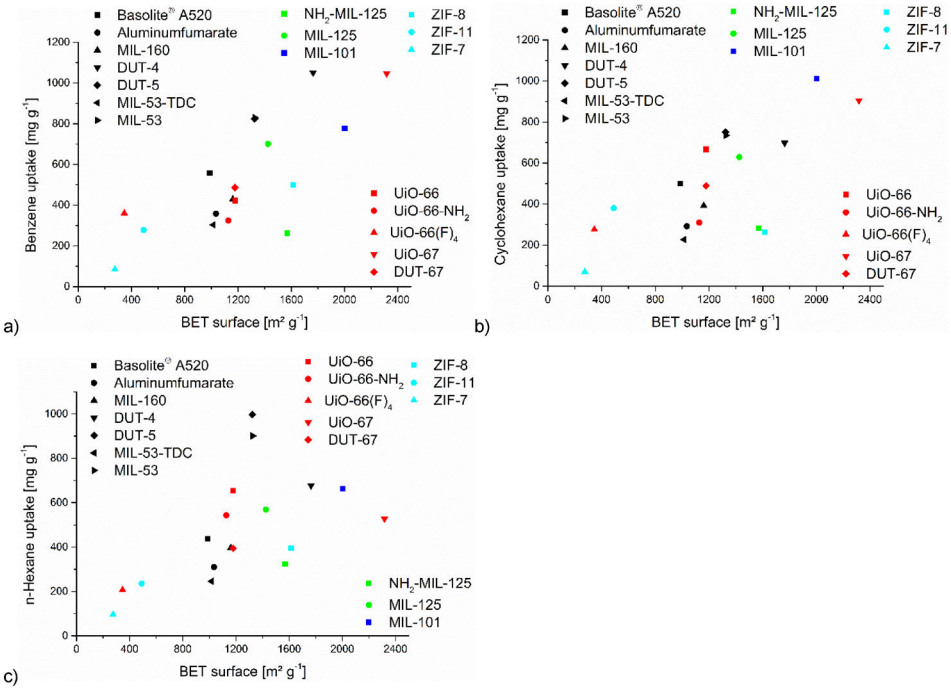

Figure S85 *C_6-VOC uptake at p p_0^{-1} = 0.9, 293 K versus BET surface area for (a) benzene, (b) cyclohexane and (c) n-hexane.*

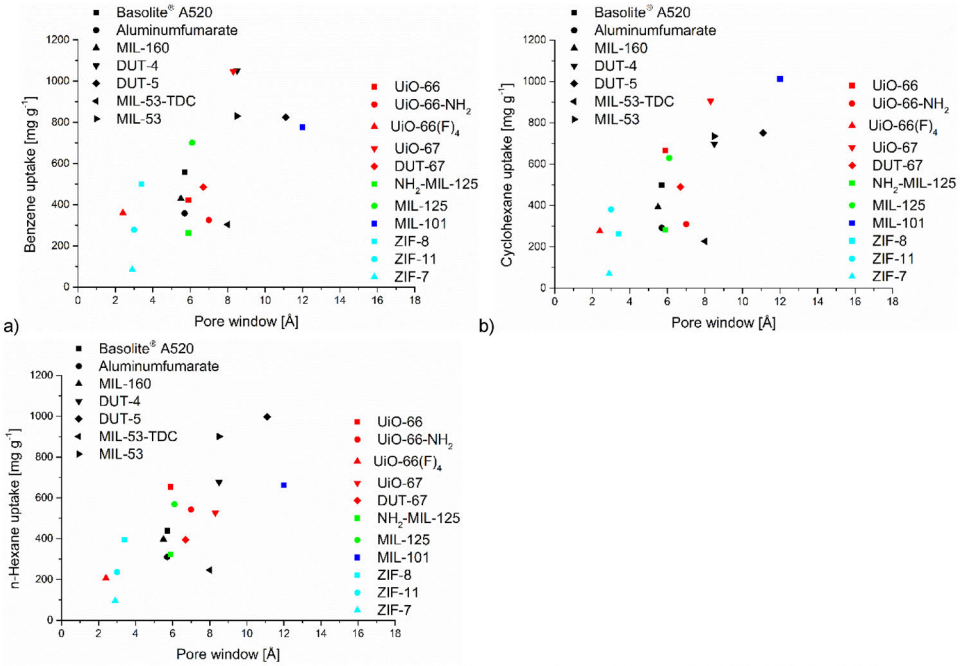

Figure S86 *C_6-VOC uptake at p p_0^{-1} = 0.9, 293 K versus Pore window (cf. Table S2) for (a) benzene, (b) cyclohexane, (c) n-hexane.*

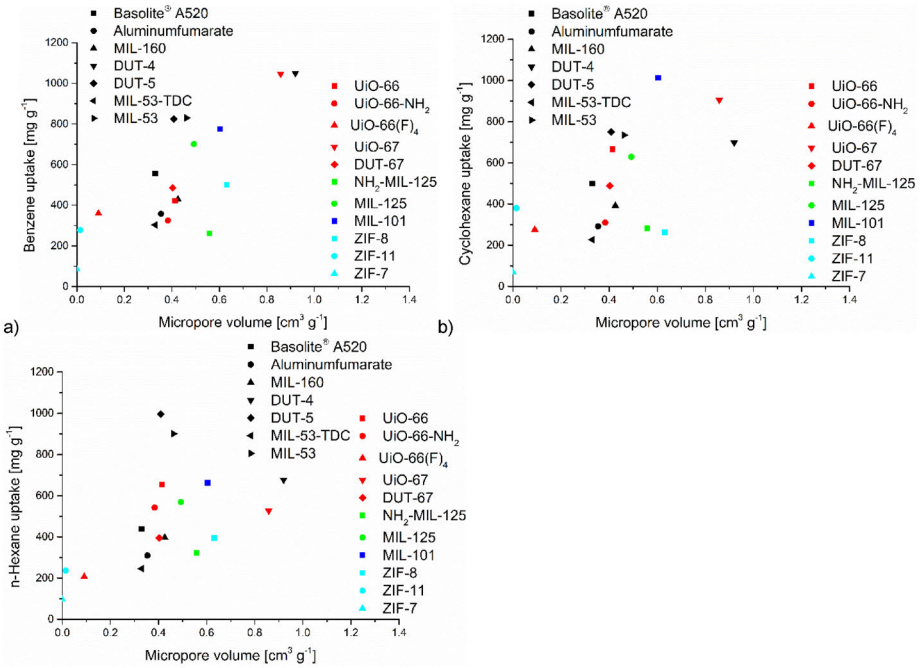

Figure S87 *C_6-VOC uptake at p p_0^{-1} = 0.9, 293 K versus Micropore volume (cf. Table S2) for (a) benzene, (b) cyclohexane, (c) n-hexane.*

Surface-specific uptake and pore limiting diameter

Often the adsorption capacity is normalized to the amount adsorbed on per unit area of the MOF adsorbent (see Table S2 for BET surface area).[45,46] This can give useful information regarding the adsorption affinity or a pore limiting diameter (PLD), for example the pore window as the limiting diameter (Table S2). In order to elucidate the adsorption affinity of relevant MOFs for C_6 trace adsorption, we used the uptake at p p_0^{-1} = 0.1 for the normalization (Figure S88).

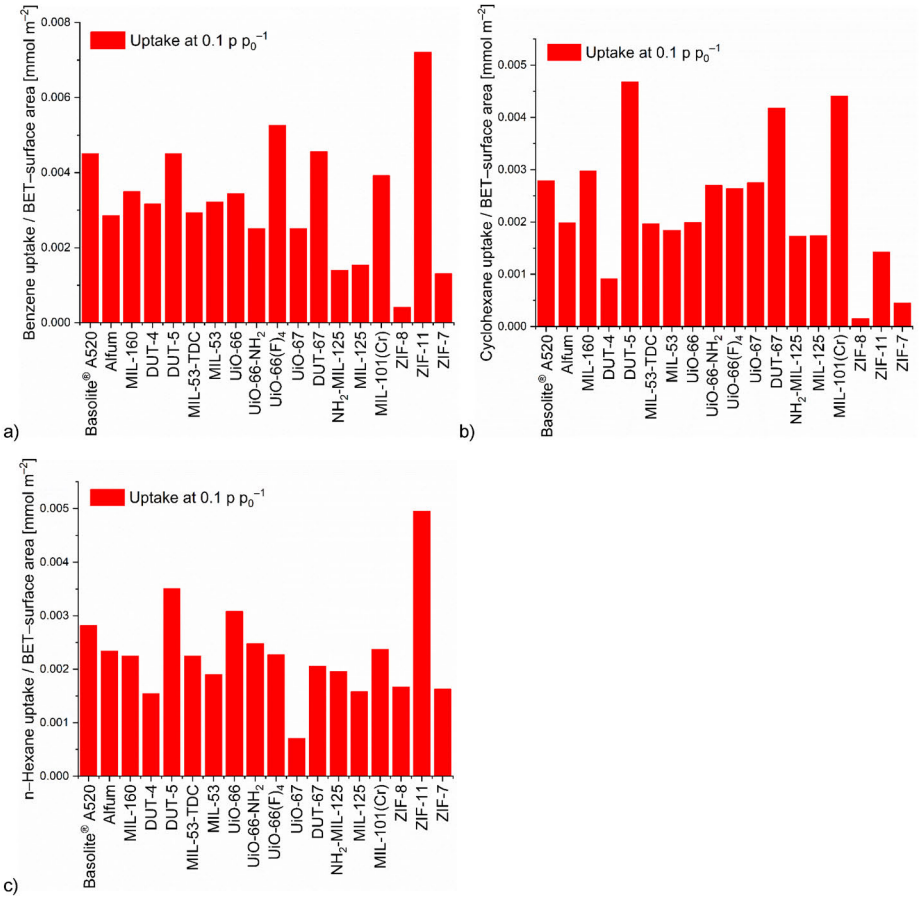

Figure S88 *Surface-specific benzene (a), cyclohexane (b) and n-hexane (c) uptake at p p_0^{-1} = 0.1 (293 K), which is the uptake in mmol g^{-1} at this pressure divided by the BET surface area.*

The surface-normalized, i.e. surface-specific benzene adsorption capacity at p p_0^{-1} = 0.1 (Figure S88) is highest for ZIF-11 and still higher than average for Basolite A520, DUT-5, UiO-66(F)$_4$, DUT-67 and MIL-101(Cr). For cyclohexane the highest surface normalized adsorption is reached by DUT-5, DUT-67 and MIL-101(Cr). For *n*-hexane, ZIF-11 has again and by far the highest surface-specific adsorption, with DUT-5 and UiO-66 still somewhat higher than average.

The high surface-specific uptake values originate from a substantial early uptake *together* with a relatively low surface area. High values for the surface-normalized uptake at p p_0^{-1} = 0.1 may contrast with low absolute specific C_6 uptakes, as is the case for ZIF-11 due to its overall small pore volume, size and surface area. Also, it has to be kept in mind that the surface normalization will not reflect if low uptake is due to inaccessible regions.

A plot of the surface-specific uptake *vs* pore limiting diameter (PLD) at 0.01 and 0.1 p p_0^{-1} shows invariance and does not give a clear maximum (Figure S89). The PLD is the smallest pore (window) diameter in a framework, as *e. g.* Brandt *et al.* described in 2021 and correlated the optimum SO_2 sorption capacity of their MOFs with the molecular size of SO_2.[47] At an optimal PLD the adsorptive would have dispersive interactions with several positions ("both ends, both sides") of the molecule to the surface. Local PLD optima exist for adsorbent structures where the distance between its Connolly surfaces corresponds to the length of the adsorbed molecule. The latter can then simultaneously interact with different atoms with the accessible surface. [41] The high surface-specific uptake values for benzene for UiO-66(F)$_4$ and ZIF-11 (at p p_0^{-1} 0.1) *vs.* a PLD of 2.4x4.6 and 3.0x3.0 Å (Table S2) may correlate with the 'thickness' of benzene. Yet, this contrasts with the below-average uptake values for ZIF-7 and ZIF-8, having similar PLDs or 2.9x2.9 and 3.0x3.0 Å (Table S2). Also, the PLD of MIL-160 with 5.5x5.5 Å is not much higher, yet the surface-specific uptake is average. This does not suggest an optimal pore diameter for benzene adsorption. For cyclohexane and for hexane (Figure S89) a first maximum is discernible from 5-7 Å, which could correlate with the dimensions of cyclohexane but not really with those of *n*-hexane. The surface-specific uptake at 0.9 p p_0^{-1} (Figure S90) shows a high value around 4 Å for UiO-66(F$_4$) for benzene, 3-4 Å for ZIF-11 and UiO-66(F$_4$) for cyclohexane and at 3 Å for ZIF-7 for *n*-hexane. Yet, MOFs with similar PLDs have at the same time much lower surface-specific uptakes. This rules out a significant correlation and suggests that the C_6 uptake is controlled by interactions of the individual VOCs other than a simple physisorption at opposite pore walls.

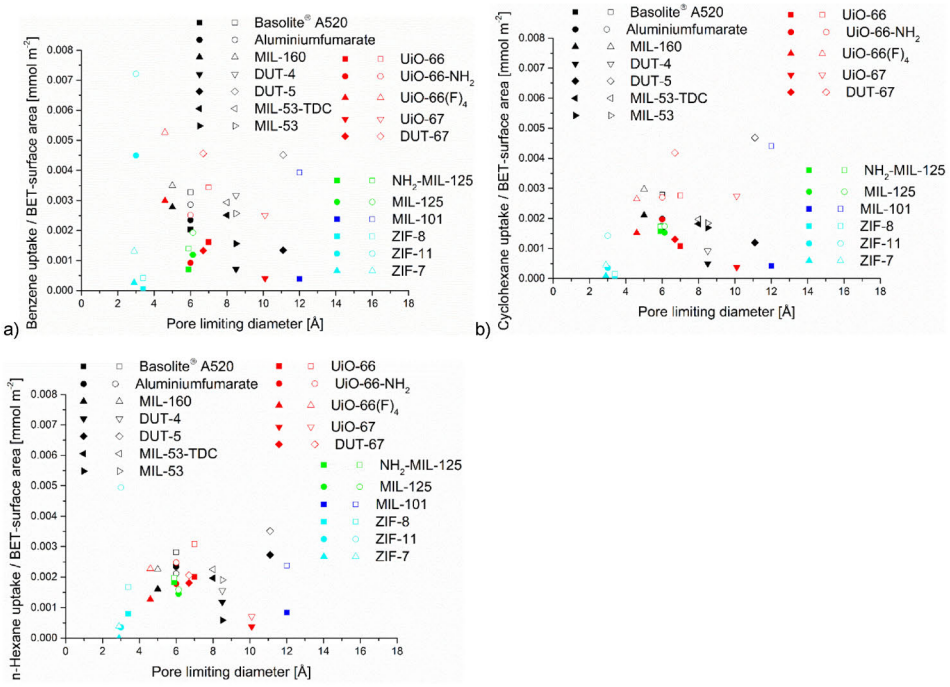

Figure S89 *Surface-specific uptake vs. pore limiting diameter (PLD) at 0.1 (blank) and 0.01(filled) p p_0^{-1} for (a) benzene, (b) cyclohexane, and (c) n-hexane.*

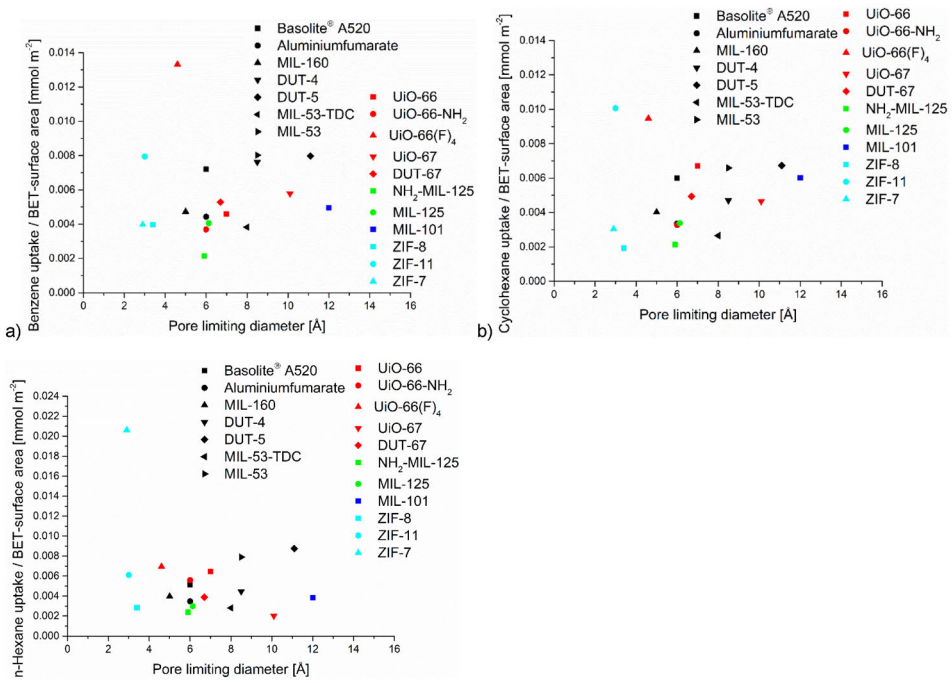

Figure S90 *Surface-specific uptake vs. pore limiting diameter (PLD) at 0.9 p p_0^{-1} for (a) benzene, (b) cyclohexane, and (c) n-hexane.*

S10 VOC sorption studies

Method of isotherm fitting

The measurement of adsorption isotherms of benezene, cyclohexane and *n*-hexane under the same conditions are used to examine sorption capacity and affinity and are further used to calculate the IAST-selectivity (S11). Fitting-simulations were calculated using 3P sim software.[48] We applied several commonly used models on our isotherm data. The best comparability for all three adsorption isotherms is obtained by applying the same model on all isotherm data and Dual-site Langmuir Sips was used. Fitting parameters are shown in Table S10 and Table S11.

DSLAISips

$$q_{eq} = q_{max} * \left(\frac{K_1 * p}{1 + K_1 * p} + \frac{(K_2 * p)^t}{(1 + K_2 * p)^t} \right)$$

q_{eq}= amount adsorbed [mmol g^{-1}]
q_{max} = maximum adsorption capacity [mmol g^{-1}]
K = affinity constant for adsorption [1 bar^{-1}]
p = pressure [bar]
t = index of heterogeneity

Table S10 *Model and R² of the fitted isotherms and simulated pressure range.*

MOF	VOC (X_1 and X_2)	Model	R²(X1)=	R²(X2)=	Simulated pressure range up to xx bar
Basolite® A520	Benzene and Cyclohexane	DSLAISips	0.994	0.984	0.09
	Benzene and *n*-Hexane	DSLAISips	0.994	0.991	0.09
	n-Hexane and Cyclohexane	DSLAISips	0.984	0.991	0.09
Aluminumfumarate	Benzene and Cyclohexane	DSLAISips	0.977	0.990	0.08
	Benzene and *n*-Hexane	DSLAISips	0.977	0.991	0.09
	n-Hexane and Cyclohexane	DSLAISips	0.990	0.991	0.08
MIL-160	Benzene and Cyclohexane	DSLAISips	0.979	0.997	0.09
	Benzene and *n*-Hexane	DSLAISips	0.979	0.995	0.09
	n-Hexane and Cyclohexane	DSLAISips	0.997	0.995	0.09
DUT-4	Benzene and Cyclohexane	DSLAISips	0.991	0.986	0.09
	Benzene and *n*-Hexane	DSLAISips	0.991	0.997	0.08
	n-Hexane and Cyclohexane	DSLAISips	0.986	0.997	0.08
DUT-5	Benzene and Cyclohexane	DSLAISips	0.996	0.992	0.09
	Benzene and *n*-Hexane	DSLAISips	0.996	0.993	0.09
	n-Hexane and Cyclohexane	DSLAISips	0.992	0.993	0.09
MIL-53-TDC	Benzene and Cyclohexane	DSLAISips	0.986	0.978	0.08
	Benzene and *n*-Hexane	DSLAISips	0.986	0.997	0.09
	n-Hexane and Cyclohexane	DSLAISips	0.978	0.997	0.08

MIL-53(Al)	Benzene and Cyclohexane	DSLAISips	0.961	0.965	0.05
	Benzene and *n*-Hexane	DSLAISips	0.961	0.990	0.09
	Cyclohexane and *n*-Hexane	DSLAISips	0.965	0.990	0.05
UiO-66	Benzene and Cyclohexane	DSLAISips	0.995	0.985	0.08
	Benzene and *n*-Hexane	DSLAISips	0.995	0.997	0.09
	n-Hexane and Cyclohexane	DSLAISips	0.985	0.997	0.08
UiO-66-NH_2	Cyclohexane and Benzene	DSLAISips	0.983	0.987	0.09
	n-Hexane and Benzene	DSLAISips	0.983	0.992	0.09
	Cyclohexane and *n*-Hexane	DSLAISips	0.987	0.992	0.09
UiO-66($F)_4$	Benzene and Cyclohexane	DSLAISips	0.978	0.960	0.09
	Benzene and *n*-Hexane	DSLAISips	0.978	0.993	0.09
	Cyclohexane and *n*-Hexane	DSLAISips	0.960	0.993	0.09
UiO-67	Benzene and Cyclohexane	DSLAISips	0.998	0.987	0.09
	Benzene and *n*-Hexane	DSLAISips	0.998	0.993	0.09
	Cyclohexane and *n*-Hexane	DSLAISips	0.987	0.993	0.09
DUT-67	Benzene and Cyclohexane	DSLAISips	0.995	0.994	0.09
	Benzene and *n*-Hexane	DSLAISips	0.995	0.984	0.09
	Cyclohexane and *n*-Hexane	DSLAISips	0.994	0.984	0.09
NH_2-MIL-125	Cyclohexane and Benzene	DSLAISips	0.998	0.987	0.09
	n-Hexane and Benzene	DSLAISips	0.998	0.992	0.09
	n-Hexane and Cyclohexane	DSLAISips	0.987	0.992	0.09
MIL-125	Cyclohexane and Benzene	DSLAISips	0.971	0.982	0.08
	n-Hexane and Benzene	DSLAISips	0.971	0.989	0.08
	n-Hexane and Cyclohexane	DSLAISips	0.982	0.989	0.09
MIL-101(Cr)	Cyclohexane and Benzene	DSLAISips	0.997	0.998	0.09
	Benzene and *n*-Hexane	DSLAISips	0.997	0.996	0.09
	Cyclohexane and *n*-Hexane	DSLAISips	0.998	0.996	0.09
ZIF-8	Benzene and Cyclohexane	DSLAISips	1.000	0.998	0.09
	n-Hexane and Benzene	DSLAISips	1.000	0.996	0.09
	n-Hexane and Cyclohexane	DSLAISips	0.998	0.996	0.09

ZIF-11	Benzene and Cyclohexane	DSLAISips	0.999	0.998	0.09
	Benzene and *n*-Hexane	DSLAISips	0.999	0.998	0.09
	n-Hexane and Cyclohexane	DSLAISips	0.998	0.998	0.09
ZIF-7	Benzene and Cyclohexane	DSLAISips	0.999	0.986	0.09
	Benzene and *n*-Hexane	DSLAISips	0.999	0.999	0.09
	n-Hexane and Cyclohexane	DSLAISips	0.986	0.999	0.09

Table S11 *Dual-site Langmuir Sips fitting parameters used for the calculation of VOC IAST-selectivities.*

Model		**Dual Site Langmuir Sips**			
		Parameters			
MOF	**VOC**	**Affinity const. 1 [1 bar^{-1}]**	**Max. loading [mmol g^{-1}]**	**Affinity const. 2 [1 bar^{-1}]**	**Heterogenity exponent**
Basolite® A520	Benzene	565.165	5.344	8.662	2.885
	Cyclohexane	771.935	3.288	13.069	3.435
	n-Hexane	1767.028	2.815	7.009	1.739
Aluminumfumarate	Benzene	2359.052	3.156	10.041	3.231
	Cyclohexane	2398.896	2.157	9.814	2.295
	n-Hexane	6101.405	2.368	4.330	1.392
MIL-160	Benzene	1906.082	4.293	6.525	1.799
	Cyclohexane	978.990	3.814	6.450	2.648
	n-Hexane	6633.506	2.641	8.982	4.255
DUT-4	Benzene	292.982	7.013	16.782	3.358
	Cyclohexane	44.246	5.147	13.667	4.803
	n-Hexane	2203.091	2.606	11.936	1.691
DUT-5	Benzene	353.543	7.596	10.008	2.845
	Cyclohexane	8.351	5.938	489.205	1.770
	n-Hexane	1255.007	4.958	11.869	4.222
MIL-53-TDC	Benzene	5487.091	2.999	5.519	1.606
	Cyclohexane	9999.000	2.010	5.779	1.553
	n-Hexane	7597.648	2.087	1.946	0.675
MIL-53(Al)	Benzene	713.604	5.153	15.410	6.910
	Cyclohexane	2956.745	2.572	36.003	3.872
	n-Hexane	135.134	3.820	11.820	5.110
UiO-66	Benzene	606.109	4.662	5.829	2.467

	Cyclohexane	404.155	3.189	16.820	7.457
	n-Hexane	859.966	3.885	9.506	8.077
UiO-66-NH_2	Benzene	472.539	3.455	7.372	3.049
	Cyclohexane	338.817	1.738	2180.625	3.405
	n-Hexane	920.661	3.111	10.140	7.879
UiO-66$(F)_4$	Benzene	586.254	2.365	14.568	4.585
	Cyclohexane	145.389	1.688	12.989	9.852
	n-Hexane	793.770	0.783	12.819	2.181
UiO-67	Benzene	188.863	6.759	67.131	3.929
	Cyclohexane	287.584	7.801	9.688	4.009
	n-Hexane	778.205	4.033	6.937	3.084
DUT-67	Benzene	414.857	3.009	731.498	3.872
	Cyclohexane	300.064	2.822	700.796	2.082
	n-Hexane	2261.157	2.517	9.264	5.215
NH_2-MIL-125	Benzene	708.042	2.479	7.690	1.489
	Cyclohexane	7062.105	2.707	4.008	1.378
	n-Hexane	5258.730	3.109	2.698	1.736
MIL-125	Benzene	1331.255	3.797	17.309	5.896
	Cyclohexane	1773.340	4.140	13.836	4.820
	n-Hexane	8831.719	3.567	9.143	5.437
MIL-101(Cr)	Benzene	167.326	4.916	197.208	3.087
	Cyclohexane	92.542	6.096	210.578	2.661
	n-Hexane	279.271	5.383	6.399	3.434
ZIF-8	Benzene	21.671	3.836	35.711	5.987
	Cyclohexane	2.183	8.673	7.140	3.566
	n-Hexane	596.021	2.950	7.099	4.050
ZIF-11	Benzene	1293.041	3.475	2.769	2.530
	Cyclohexane	33.274	2.471	46.363	11.594
	n-Hexane	2.039	2.176	745.968	1.773
ZIF-7	Benzene	4.708	1.330	10.418	0.623
	Cyclohexane	16.907	0.615	10.842	20.426
	n-Hexane	9.769	0.678	59.865	4.525

Fitted isotherms

Al-MOFs

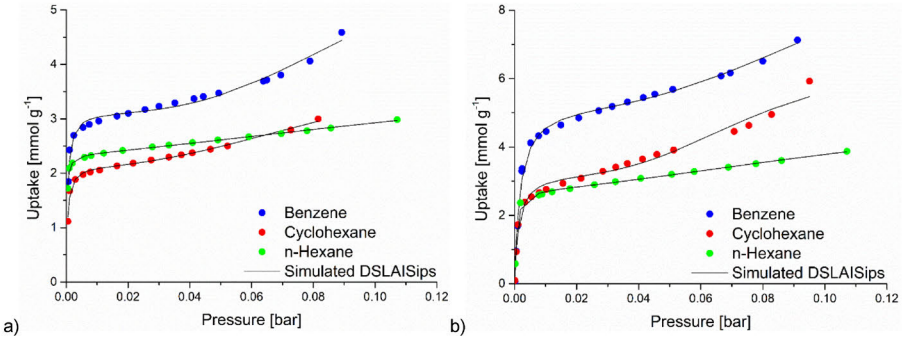

Figure S91 *Experimental sorption isotherms (circles) and fitted VOC adsorption isotherms (line) of Basolite® A520 (a) and Aluminumfumarate (b).*

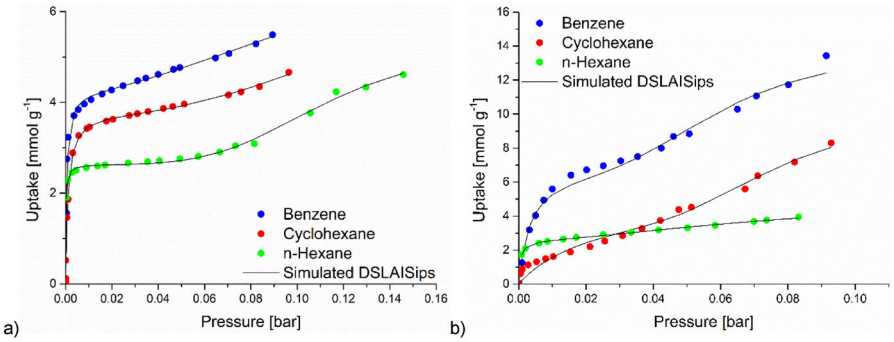

Figure S92 *Experimental sorption isotherms (circles) and fitted VOC adsorption isotherms (line) of MIL-160 (a) and DUT-4 (b).*

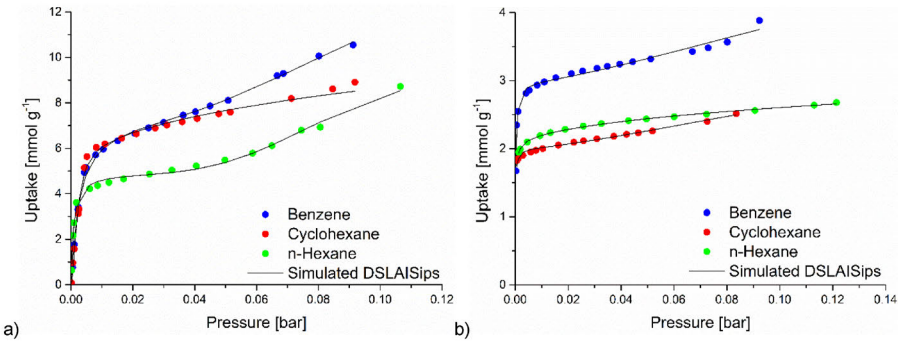

Figure S93 *Experimental sorption isotherms (circles) and fitted VOC adsorption isotherms (line) of DUT-5 (a) and MIL-53-TDC (b).*

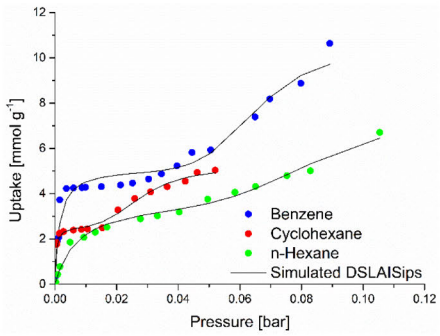

Figure S94 *Experimental sorption isotherms (circles) and fitted VOC adsorption isotherms (line) of MIL-53.*

Zr-MOFs

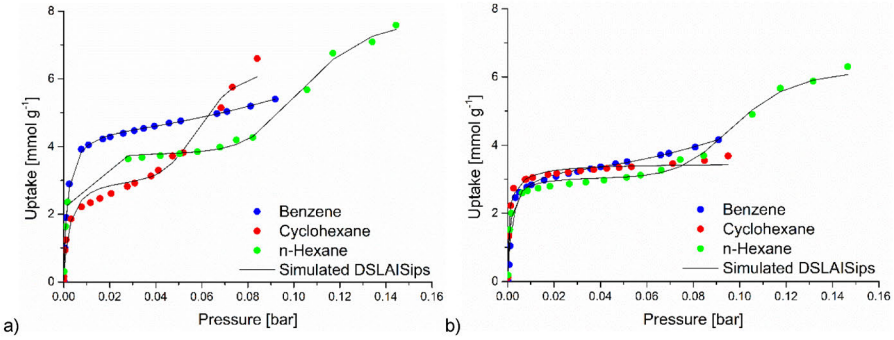

Figure S95 *Experimental sorption isotherms (circles) and fitted VOC adsorption isotherms (line) of UiO-66 (a) and UiO-66-NH_2 (b).*

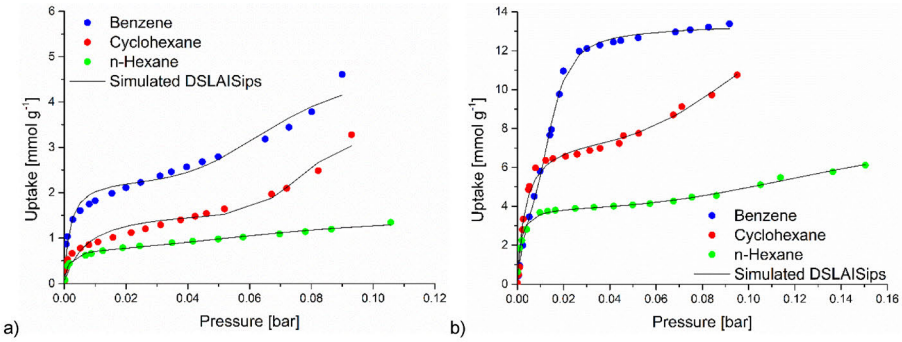

Figure S96 *Experimental sorption isotherms (circles) and fitted VOC adsorption isotherms (line) of UiO-66(F)$_4$ (a) and UiO-67 (b).*

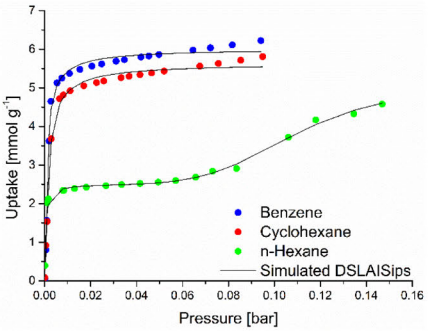

Figure S97 *Experimental sorption isotherms (circles) and fitted VOC adsorption isotherms (line) of DUT-67.*

Ti-MOFs

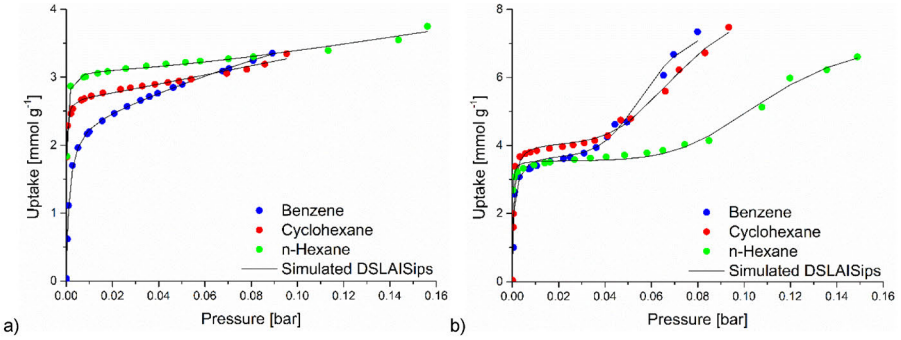

Figure S98 *Experimental sorption isotherms (circles) and fitted VOC adsorption isotherms (line) of NH_2-MIL-125 (a) and MIL-125 (b).*

Cr-MOF

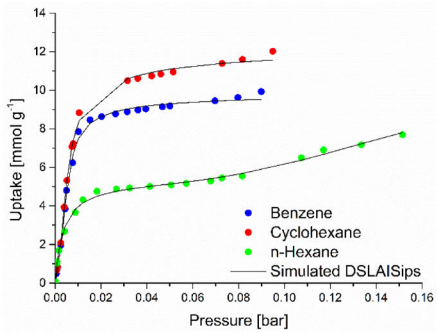

Figure S99 *Experimental sorption isotherms (circles) and fitted VOC adsorption isotherms (line) of MIL-101(Cr).*

ZIFs

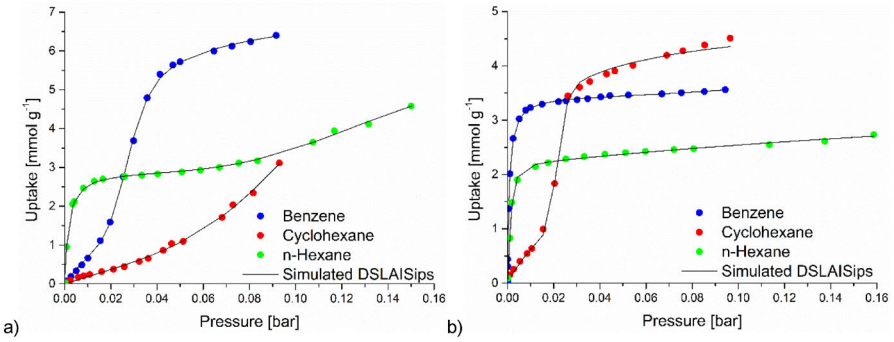

Figure S100 *Experimental sorption isotherms (circles) and fitted VOC adsorption isotherms (line) of ZIF-8 (a) and ZIF-11 (b).*

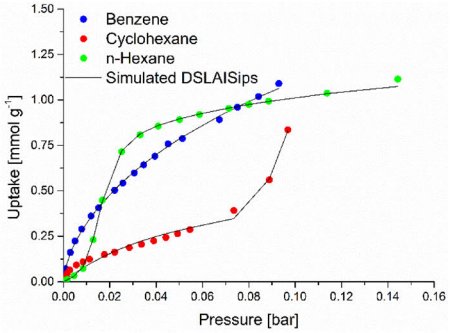

Figure S101 *Experimental sorption isotherms (circles) and fitted VOC adsorption isotherms (line) of ZIF-7.*

S11 Ideal Adsorbed Solution Theory, IAST-Selectivity

Method

Selectivities of VOCs in Figure 7 in the main article and

Table **S12** were calculated from fitted isotherm data (Section S10, Table S10 and Table S11) of the experimentally measured isotherms at 293 K. Here the VOC sorption isotherms are fitted with the dual-site Langmuir Sips model with the "3P sim" software (see above in section S10, Supplementary Information). The 3P sim software (3P Instruments, Germany, version 1.1.0.7) calculates the maximal loadings of each vapor depending on the given mole fraction. IAST selectivities S of binary vapor mixtures were calculated using the following equation, where x_i represents the absorbed gas amount and y_i the mole fraction of each adsorptive.

IAST-Selectivity

$$S = \frac{x_1/x_2}{y_1/y_2}$$

IAST selectivities were calculated over the pressure range of the fitted isotherms from 0.00 up to a maximum pressure of 0.09 bar. The pressure region below 0.01 was excluded from evaluation to avoid errors from the isotherm fitting in this region.

IAST-based estimations are most suitable when the following conditions are fulfilled: (i) the same accessible surface area is available to all adsorbates, (ii) low pressures (⩽1 bar), and (iii) similar polarity of adsorbates.[49]

Al-MOFs

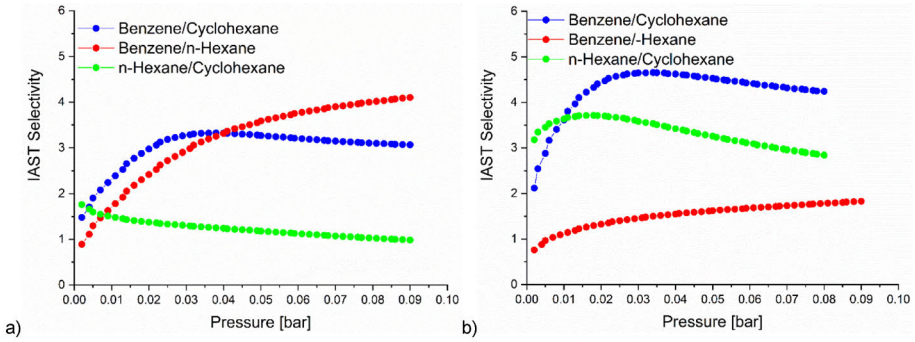

Figure S102 *The calculated VOC selectivity dependence on the pressure range [bar] for Basolite® A520 (a) and Aluminumfumarate (b).*

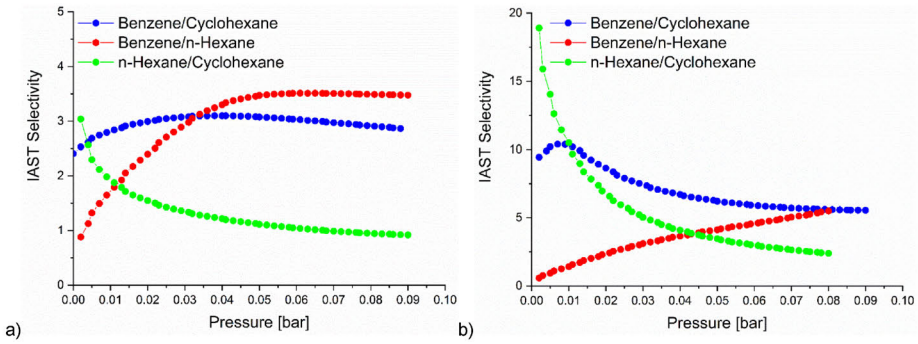

Figure S103 *The calculated VOC selectivity dependence on the pressure range [bar] for MIL-160 (a) and DUT-4 (b).*

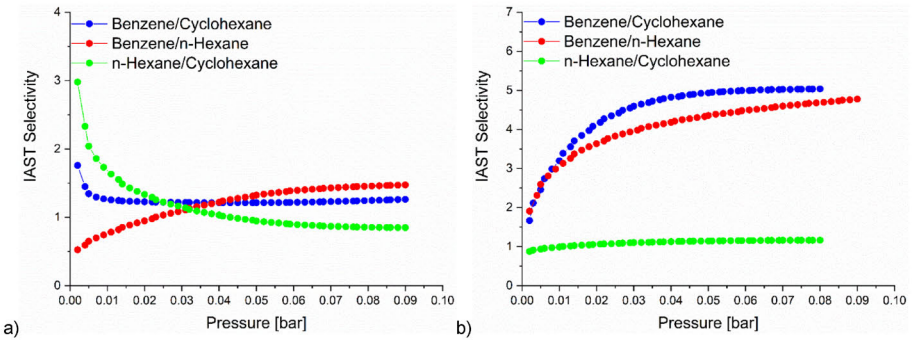

Figure S104 *The calculated VOC selectivity dependence on the pressure range [bar] for DUT-5 (a) and MIL-53-TDC (b).*

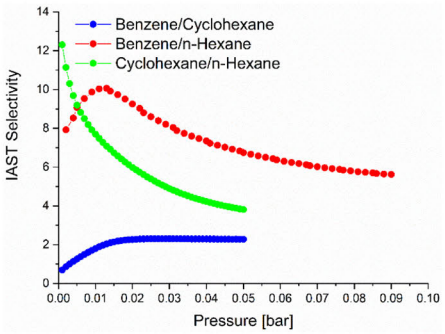

Figure S105 *The calculated VOC selectivity dependence on the pressure range [bar] for MIL-53.*

Zr-MOFs

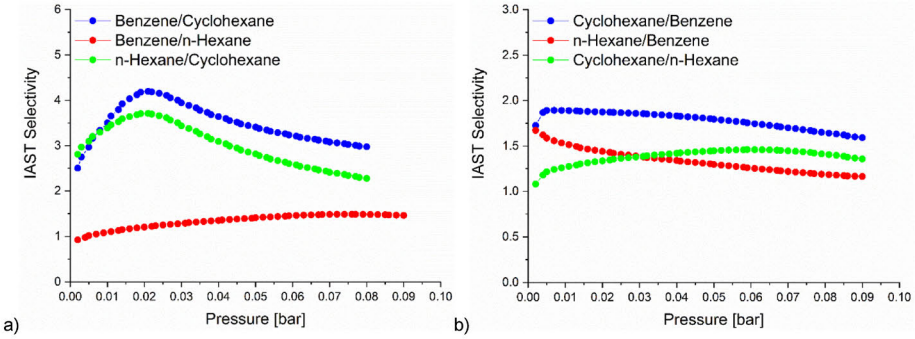

Figure S106 *The calculated VOC selectivity dependence on the pressure range [bar] for UiO-66 (a) and UiO-66-NH_2 (b).*

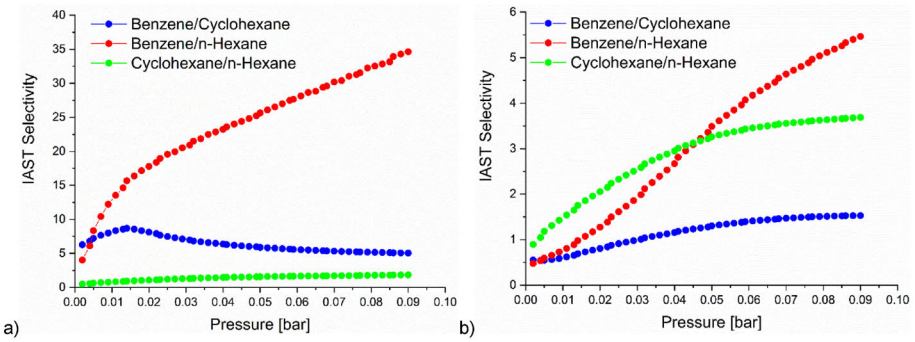

Figure S107 *The calculated VOC selectivity dependence on the pressure range [bar] for UiO-66(F)$_4$ (a) and UiO-67 (b).*

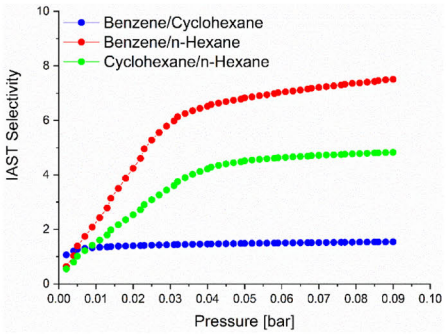

Figure S108 *The calculated VOC selectivity dependence on the pressure range [bar] for DUT-67*

Ti-MOFs

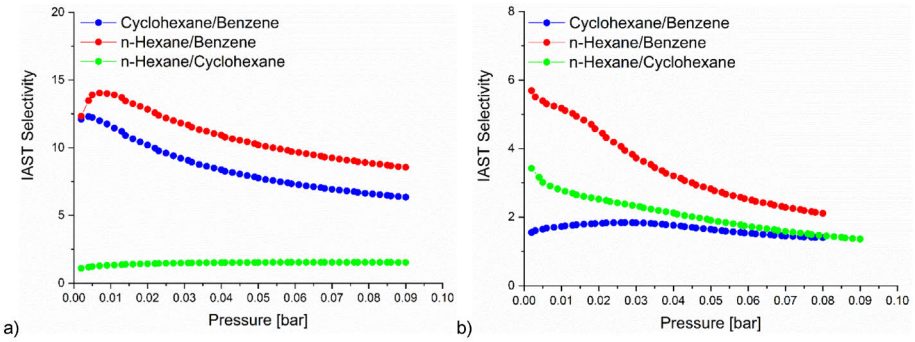

Figure S109 *The calculated VOC selectivity dependence on the pressure range [bar] for NH$_2$-MIL-125 (a) and MIL-125 (b).*

Cr-MOFs

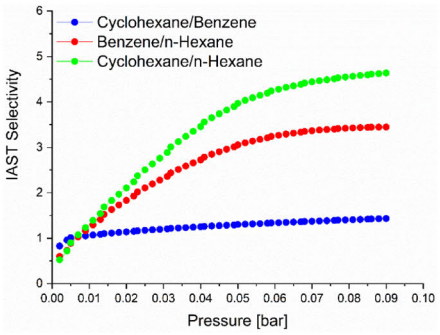

Figure S110 *The calculated VOC selectivity dependence on the pressure range [bar] for MIL-101(Cr).*

ZIFs

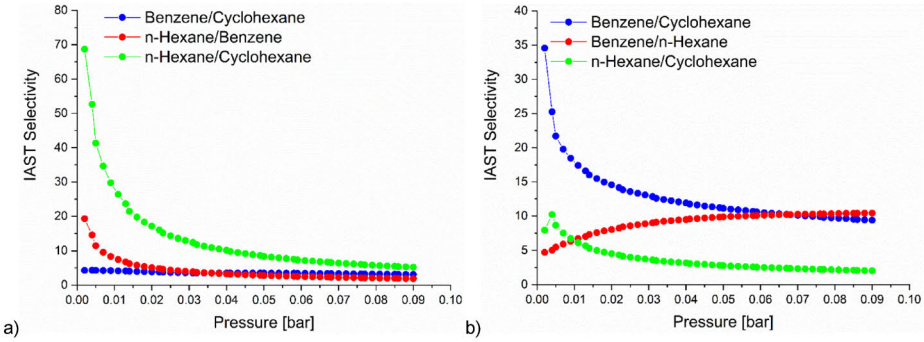

Figure S111 *The calculated VOC selectivity dependence on the pressure range [bar] for ZIF-8 (a) and ZIF-11 (b).*

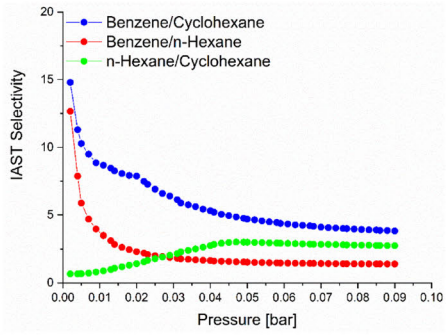

Figure S112 *The calculated VOC selectivity dependence on the pressure range [bar] for ZIF-7.*

All calculated binary IAST selectivities for all examined materials are presented in Figure 7 in the main article.

Table S12 *IAST selectivtiy of a 50/50 molar ratio of the different binary mixtures at different pressure for each MOF.*

MOF	**VOC (X_1 and X_2)**	**IAST Selectivity for X_1/X_2 (**rounded to the next integer value)		
		0.01 [bar]	**0.05 [bar]**	**0.09 [bar]**
Basolite® A520	Benzene and Cyclohexane	2	3	3
	Benzene and *n*-Hexane	2	4	4
	n-Hexane and Cyclohexane	1	1	1
Aluminumfumarate	Benzene and Cyclohexane	4	5	4
	Benzene and *n*-Hexane	1	2	2
	n-Hexane and Cyclohexane	4	3	3
MIL-160	Benzene and Cyclohexane	3	3	0
	Benzene and *n*-Hexane	2	3	3
	n-Hexane and Cyclohexane	2	1	1
DUT-4	Benzene and Cyclohexane	10	6	6
	Benzene and *n*-Hexane	1	4	6
	n-Hexane and Cyclohexane	10	3	2
DUT-5	Benzene and Cyclohexane	1	1	1
	Benzene and *n*-Hexane	1	1	1
	n-Hexane and Cyclohexane	2	1	1
MIL-53-TDC	Benzene and Cyclohexane	3	5	5
	Benzene and *n*-Hexane	3	4	5
	n-Hexane and Cyclohexane	1	1	1
MIL-53(Al)	Benzene and Cyclohexane	2	2	-
	Benzene and *n*-Hexane	10	7	6
	Cyclohexane and *n*-Hexane	8	4	-
UiO-66	Benzene and Cyclohexane	4	3	3
	Benzene and *n*-Hexane	1	1	1
	n-Hexane and Cyclohexane	3	3	2
UiO-66-NH_2	Cyclohexane and Benzene	2	2	2
	n-Hexane and Benzene	2	1	1
	Cyclohexane and *n*-Hexane	1	1	1
UiO-66$(F)_4$	Benzene and Cyclohexane	8	6	5
	Benzene and *n*-Hexane	13	26	35
	Cyclohexane and *n*-Hexane	1	2	2
UiO-67	Benzene and Cyclohexane	1	1	2

	Benzene and *n*-Hexane	1	3	5
	Cyclohexane and *n*-Hexane	1	3	4
DUT-67	Benzene and Cyclohexane	1	1	2
	Benzene and *n*-Hexane	2	7	8
	Cyclohexane and *n*-Hexane	2	5	5
NH_2-MIL-125	Cyclohexane and Benzene	12	8	6
	n-Hexane and Benzene	14	10	9
	n-Hexane and Cyclohexane	1	2	2
MIL-125	Cyclohexane and Benzene	2	2	1
	n-Hexane and Benzene	5	3	2
	n-Hexane and Cyclohexane	3	2	1
MIL-101(Cr)	Cyclohexane and Benzene	1	1	1
	Benzene and *n*-Hexane	1	3	3
	Cyclohexane and *n*-Hexane	1	4	5
ZIF-8	Benzene and Cyclohexane	4	3	3
	n-Hexane and Benzene	8	3	2
	n-Hexane and Cyclohexane	28	8	5
ZIF-11	Benzene and Cyclohexane	18	11	9
	Benzene and *n*-Hexane	6	10	10
	n-Hexane and Cyclohexane	6	3	2
ZIF-7	Benzene and Cyclohexane	9	5	4
	Benzene and *n*-Hexane	4	2	1
	n-Hexane and Cyclohexane	1	3	3

S12 Stability tests

All MOFs were tested under VOC-vapor conditions and in liquid VOCs for five days to simulate a long-term exposure towards benzene, cyclohexane and *n*-hexane. The stability of all 18 MOFs was tested with the following activation protocol. All MOF samples were activated overnight at 120 °C under vacuum and tested afterwards against benzene, cyclohexane and *n*-hexane.

Vapor stability

For the vapor stabilty tests 20 mg of each activated sample was used. Therfore the MOFs were put in an vacuum chamber and one of the three VOCs were let flow in the vacuum to create a VOC atmosphere. Each sample was left for five days under these VOC vapor conditions. Afterwards the samples were analyzed with the PXRD, to see if the crystallinity decreases. The experimental setup can be seen in the following Figure S113.

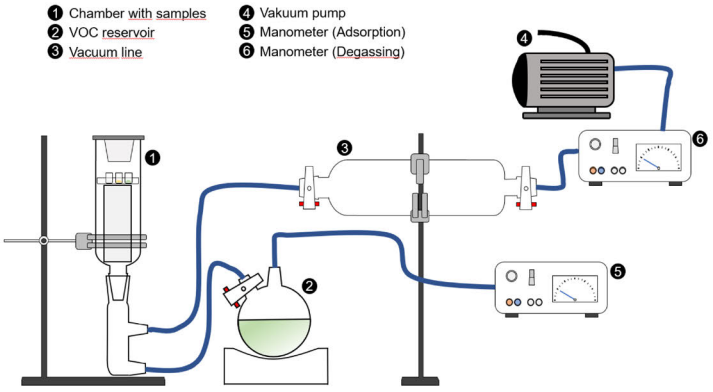

Figure S113 *Schematic graphic of the experimental set up for the vapor stability tests.*

Liquid stability

The stability of the MOFs was also examined against VOC solutions. For the implementation, 10 mg of each of the 18 MOFs were added to 10 mL of the benzene, cyclohexane and *n*-hexane solution, sealed airtight and left to stand for 5 days at room temperature. A large part of the solutions was then drawn off with the aid of a syringe and the remaining residue was dried at 60 °C overnight in a vacuum oven. The samples were then also measured with the PXRD.

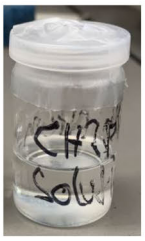

Figure S114 *Exemplary MOF sample in VOC solution.*

Vapor stability was tested with the set-up shown in Figure S114. Details about the experimental conditions and about the set-up are in the supporting information here in chapter S12. The activated MOFs were placed in a glass vial filled with VOC and stored for five days and afterwards PXRD were measured to analyze the samples for un/changed crystallinity. For this, the VOC were removed with a syringe and the MOFs were dried at 60 °C under vacuum and stored under a C_6 vapor. The PXRDs were measured directly, with the adsorbed VOC inside the pores.

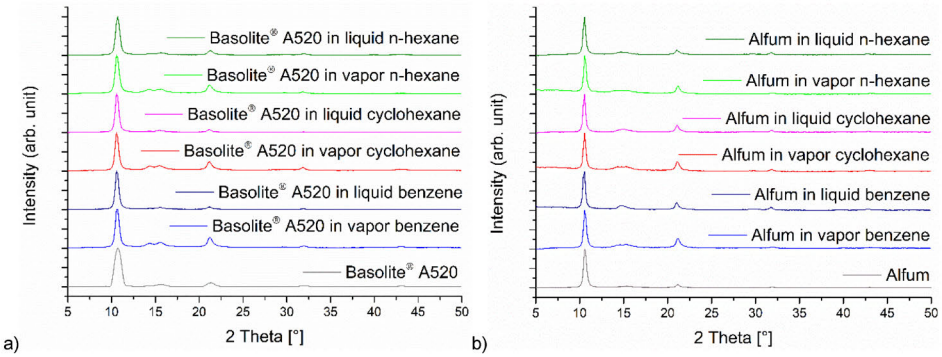

Figure S115 *(a) Stability tests of Basolite® A520 against benzene/cyclohexane/n-hexane in liquid and vapor phase. (b) Stability tests of Aluminumfumarate against benzene/cyclohexane/n-hexane in liquid and vapor phase.*

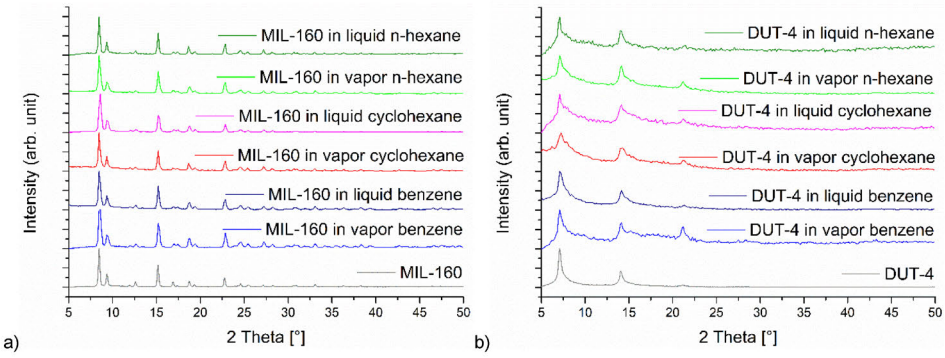

Figure S116 *(a) Stability tests of MIL-160 against benzene/cyclohexane/n-hexane in liquid and vapor phase. (b) Stability tests of DUT-4 against benzene/cyclohexane/n-hexane in liquid and vapor phase.*

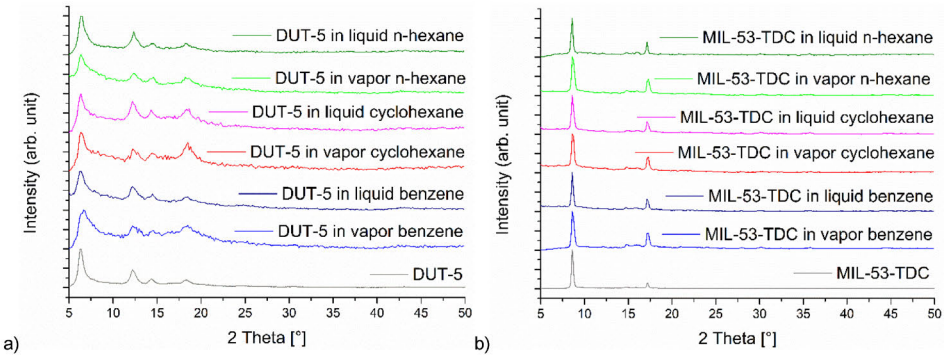

Figure S117 *(a) Stability tests of DUT-5 against benzene/cyclohexane/n-hexane in liquid and vapor phase. (b) Stability tests of MIL-53-TDC against benzene/cyclohexane/n-hexane in liquid and vapor phase.*

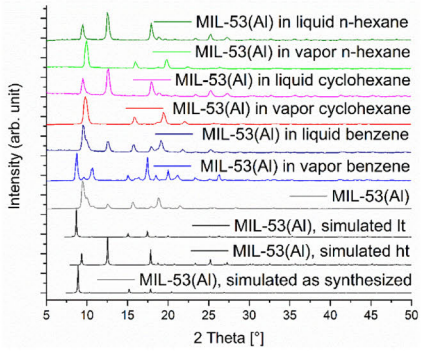

Figure S118 *Stability tests of MIL-53 against benzene/cyclohexane/n-hexane in liquid and vapor phase and with simulated pattern as synthesized, ht, lt (CSD-Number: 797261, 1007172, 220475).*[10,11]

Most of the aluminum-MOFs indicate a good stability against the VOCs, as shown in the PXRDs in Figure S115-Figure S118. There is no loss of crystallinity recognizable and the main peaks are still well resolved. DUT-4 and DUT-5 have a higher background after VOC adsorption, which is due to a lower stability against VOCs. This is supported by the N_2-sorption after the VOC-sorption for DUT-4 and DUT-5, which shows a decrease in the surface area for DUT-4 after cyclohexane-sorption to 372 $m^2 g^{-1}$. There is a clear difference for MIL-53, compared to the other Al-MOFs, because this MOF has three different phases (as = as synthesized; lt = low temperature/np = narrow pore; ht = high temperature/wp = wide pore), which are correlated with the breathing-effect of this MOF. It is interesting that the PXRD shows the ht-form for benzene (in liquid), cyclohexane (in liquid) and *n*-hexane (in liquid) (Figure S118), but for benzene there is also one diffraction peak of the lt-form at 17° 2θ. This means that drying at 60 ° C under vacuum is sufficient to reactivate the MOF for benzene, cyclohexane and *n*-hexane. The PXRDs which were measured for the samples in vapor show, that there are still molecules inside the pores, due to a measurement without drying.

Zr-MOFs

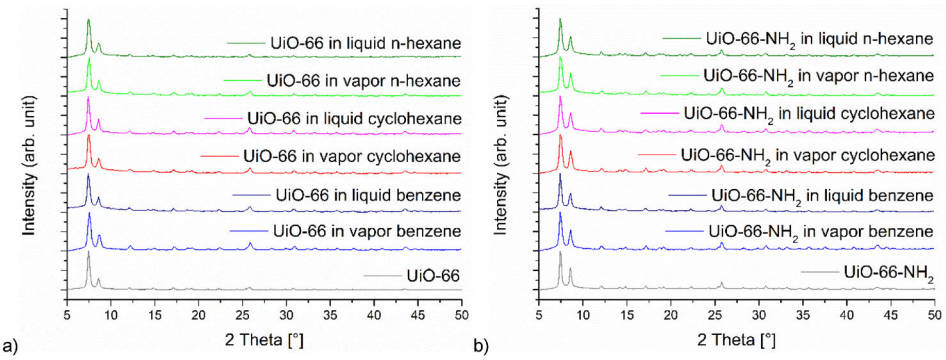

Figure S119 *(a) Stability tests of UiO-66 against benzene/cyclohexane/n-hexane in liquid and vapor phase. (b) Stability tests of UiO-66-NH_2 against benzene/cyclohexane/n-hexane in liquid and vapor phase.*

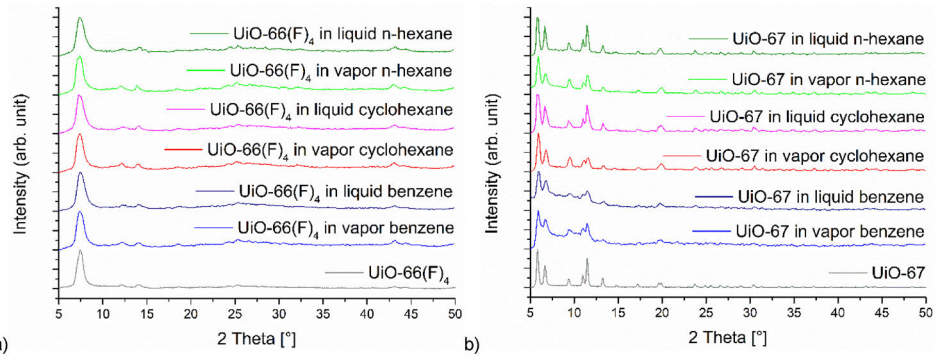

Figure S120 *(a) Stability tests of UiO-66(F)$_4$ against benzene/cyclohexane/n-hexane in liquid and vapor phase. (b) Stability tests of UiO-67 against benzene/cyclohexane/n-hexane in liquid and vapor phase.*

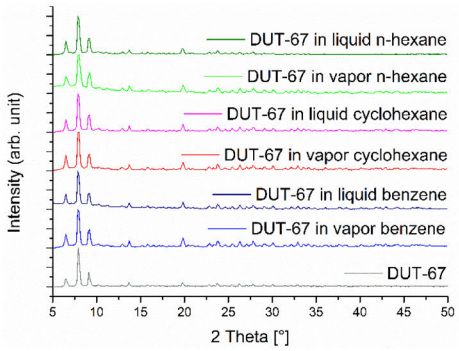

Figure S121 *Stability tests of DUT-67 against benzene/cyclohexane/n-hexane in liquid and vapor phase.*

All Zirconium-MOFs are stable against the C_6-VOCs, both in the liquid and the vapor phase. The diffraction peaks of all MOFs are still present (Figure S119-Figure S121). UiO-67 exhibits a broadening of the diffraction peaks and loss of intensity after the treatment with benzene (Figure S120 (b)).

Ti-MOFs

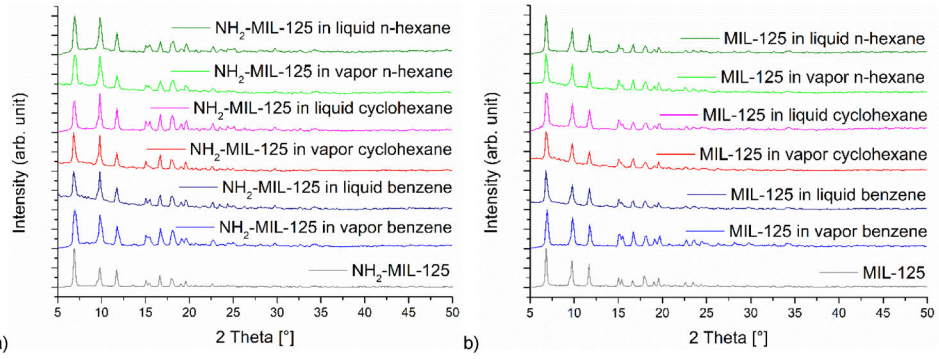

Figure S122 *(a) Stability tests of NH$_2$-MIL-125 against benzene/cyclohexane/n-hexane in liquid and vapor phase. (b) Stability tests of MIL-125 against benzene/cyclohexane/n-hexane in liquid and vapor phase.*

Cr-MOF

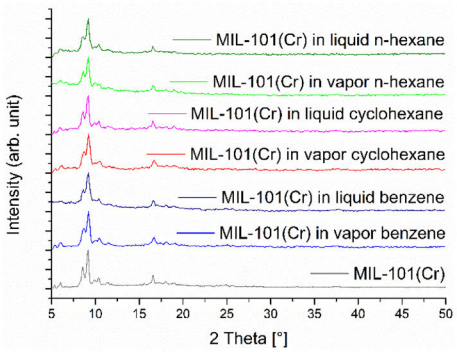

Figure S123 *Stability tests of MIL-101(Cr) against benzene/cyclohexane/n-hexane in liquid and vapor phase.*

Both Titanium-MOFs (MIL-125 and NH_2-MIL-125) and MIL-101(Cr) are stable against all three VOCs in liquid and in the vapor phase. No effect in the PXRD can be seen in Figure S122-Figure S123.

ZIFs

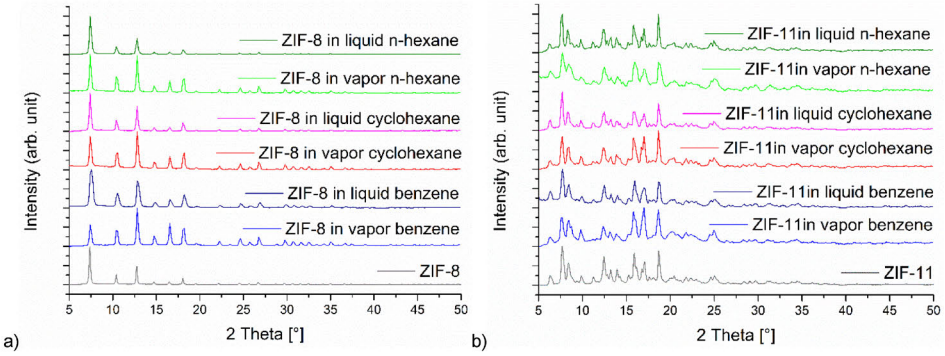

Figure S124 *(a) Stability tests of ZIF-8 against benzene/cyclohexane/n-hexane in liquid and vapor phase. (b) Stability tests of ZIF-11 against benzene/cyclohexane/n-hexane in liquid and vapor phase.*

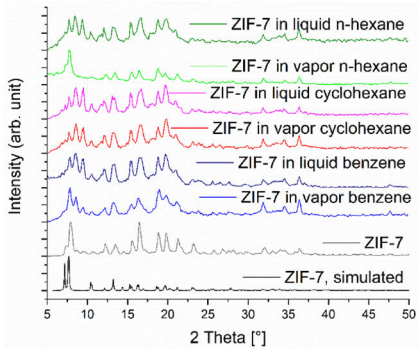

Figure S125 *Stability tests of ZIF-7 against benzene/cyclohexane/n-hexane in liquid and vapor phase and with simulated pattern (CSD-Number: 1036075).*[40]

ZIFs are known for their high stability and all three ZIFs are stable against the VOCs. There is no recognizable loss of crystallinity. For ZIF-7, however, it can be seen that a phase change has taken place, when the material was exposed to the vapor phase of *n*-hexane. The PXRD is shown in Figure S124-Figure S125 and the lower resolution is due to the shortened measurement time. The PXRD shows that a phase change has taken place between two of the three known phases of ZIF-7, namely phase I and II occur, because less diffraction peaks can be seen. The experimental PXRDs of ZIF-7 can be correlated to phase I. Phase III only occurs in connection with water and can be excluded in the absence of any polar solvents, as noted by Zhao et al.[50] The PXRDs of the MOFs with the other experimental conditions differ significantly and show a combination of phase I and II, therefore the simulated pattern of Phase I was shown again, to underline the phase change. I

S13 Gas Sorption at 293 K

The six best performing MOFs at low pressures were further investigated at 293 K with different gases (nitrogen, oxygen, carbon dioxide). The following Figure S126 and Figure S127 show the adsorption isotherms for all six MOFs.

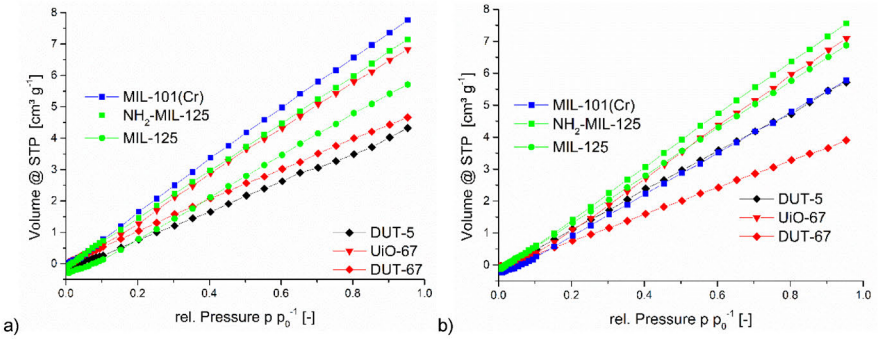

Figure S126 *Nitrogen (a) and oxygen (b) adsorption isotherms at 293 K for the six best performing MOFs at low pressures.*

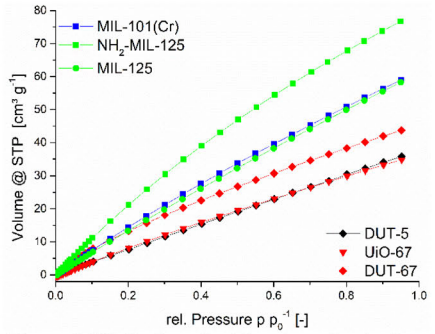

Figure S127 *Carbon dioxide adsorption isotherms at 293 K for the six best performing MOFs at low pressures.*

Due to the higher measurement temperature, in comparison to the standard experiment temperature (e. g. 77 K for nitrogen), the MOFs have no capacity for nitrogen and oxygen. Only the carbon dioxide adsorption is significant at 293 K and competes with the VOCs.

S14 Crystal structures of benzene

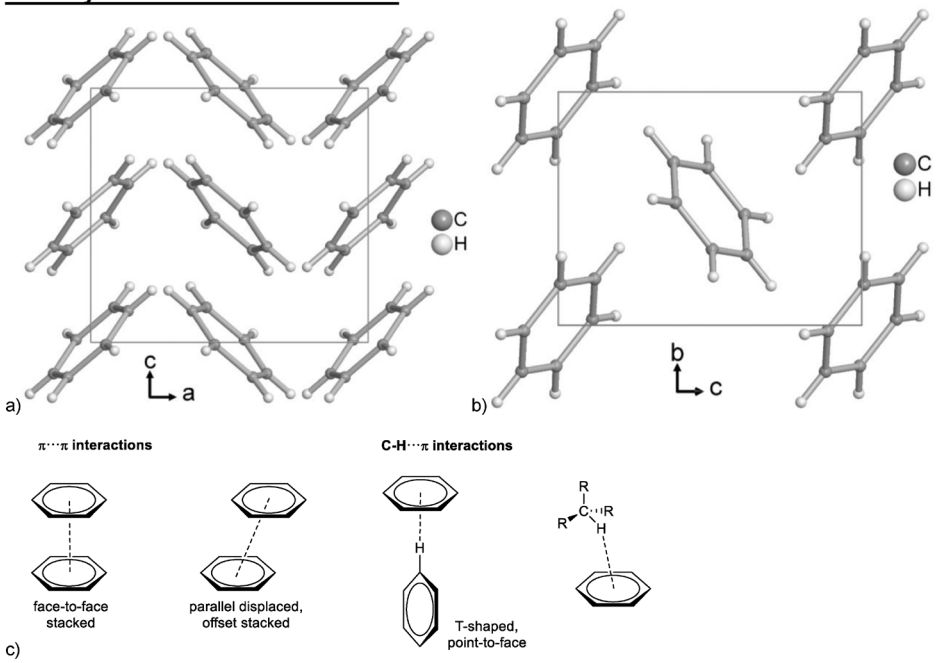

Figure S128 *Section of the packing diagrams in the crystal structure of benzene. (a) Orthorhombic polymorph I (CSD Refcode BENZEN11, CCDC 298305).*[51] *(b) Monoclinic polymorph II (CSD Refcode BENZEN16, CCDC 757060).*[52] *(c) Schematic representation of π···π and C-H···π interactions between benzene molecules.*

S15 Images from 'Mercury – Display Voids' calculation

The images picture the solvent accessible surface (outside color light yellow, inside color dark yellow) for a probe radius of 2 Å (the maximum to which the probe radius can be set in Mercury) unless noted otherwise, and an approximate grid spacing of 0.1.

In Mercury voids can be calculated using two different methods:
- Calculate voids using Solvent Accessible Surface gives the volume which can be occupied by the center of a probe of a given radius.
- Calculate voids using Contact Surface maps the volume that can be occupied by the full probe (including its radius) and thus gives a better estimate of the volume that could be filled by solvent or guest molecules.
- A full description of these two different surfaces and the ways in which they can be used is given in: L. J. Barbour, *Chem. Commun.* **2006**, 1163–1168.

The dimensions of the crystallograpic axes are given above the images to facilitate the estimate of the cross-sections of the pore apertures:

Aluminum fumarate, Alfum (CCDC 1051975) water removed, view along a, b to right, c down (a = 6.84 Å, b = 12.09 Å, c = 14.21 Å)

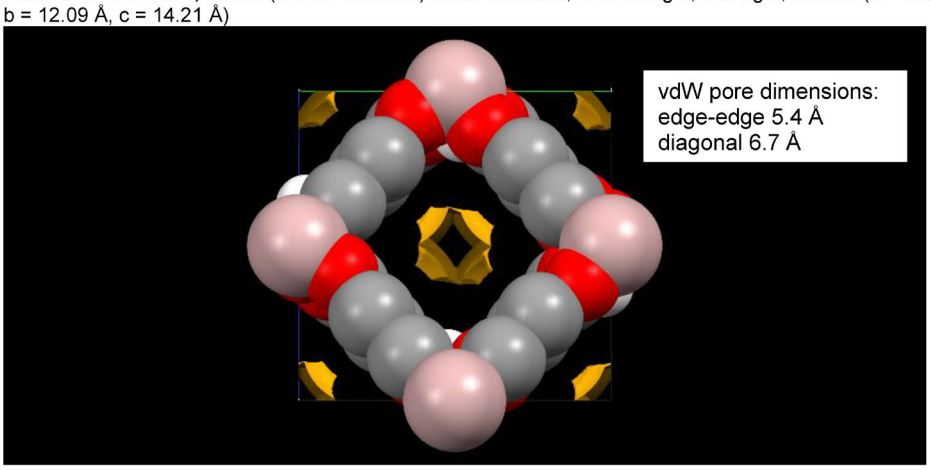

MIL-160 (CCDC 1828695), water removed, view along c, a right, b down (a = b = 21.07, c = 10.64 Å)

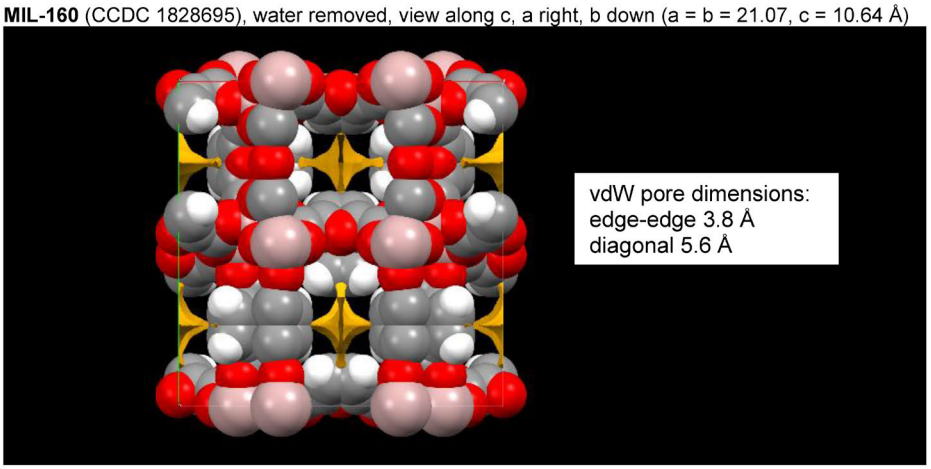

view along a, c right, b down (w. depth cuing)

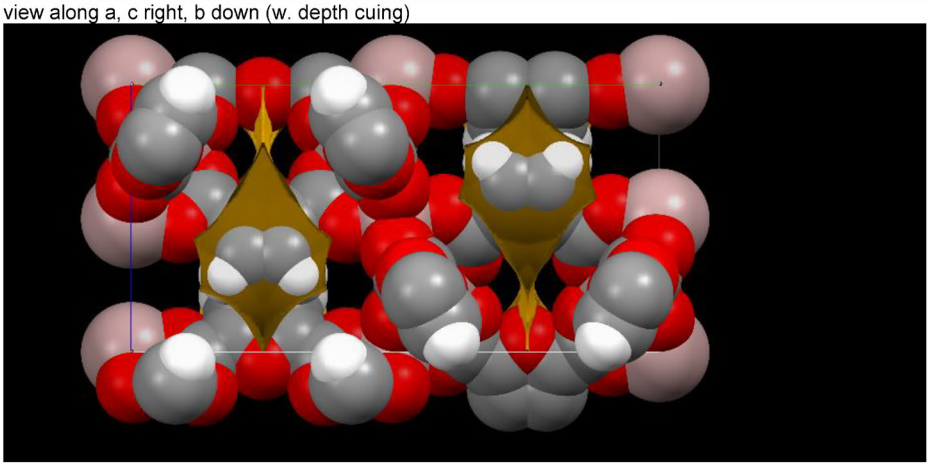

DUT-4 (CCDC 691978), view along b, c to right, a down: (a = 18.82, b = 6.7, c = 16.90 Å)

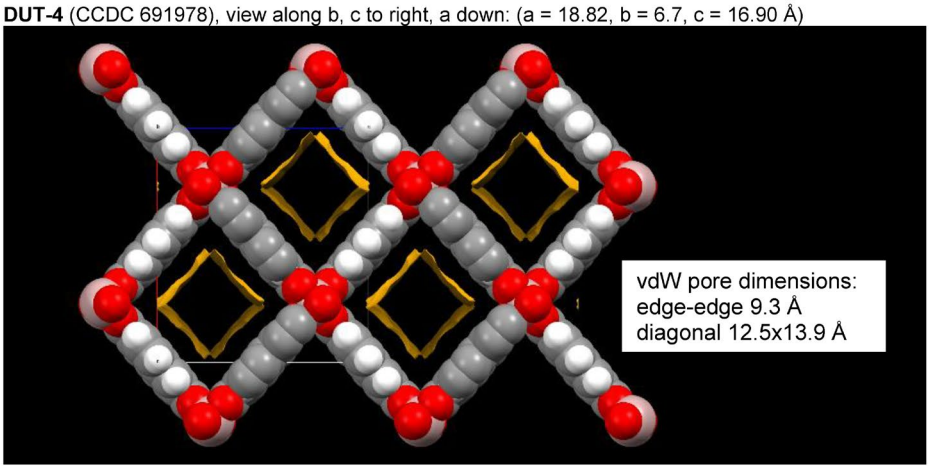

DUT-5 (CCDC 691979) along b, c to right, a down: (a = 22.70, b = 6.61, c = 19.24 Å)

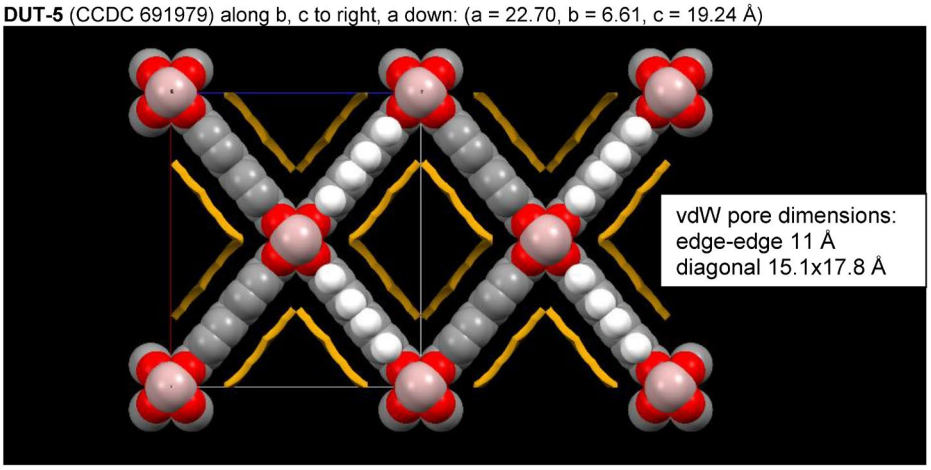

MIL-53-TDC, water removed, along b, c to right, a down: (a = 14.63, b = 6.56, c = 14.73 Å)

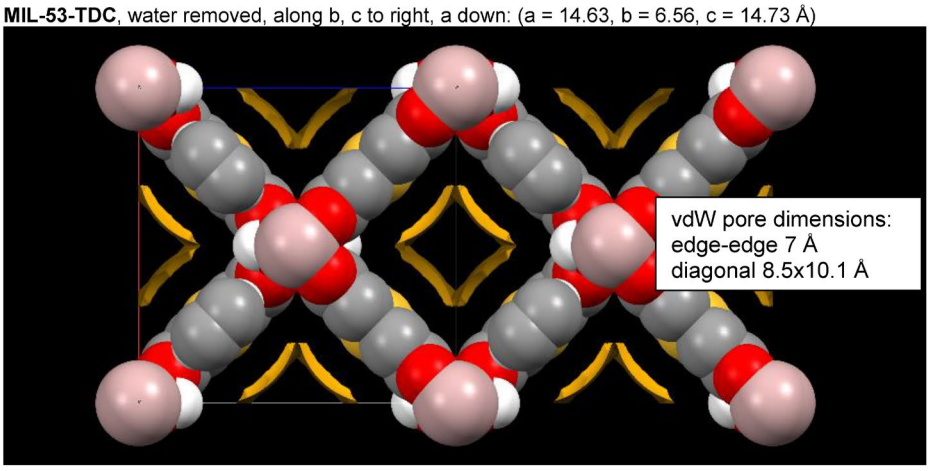

MIL-53(Al) as, (CCDC 220475), view along b, c up, a right (a = 17.13, b = 6.63, c = 12.18 Å)

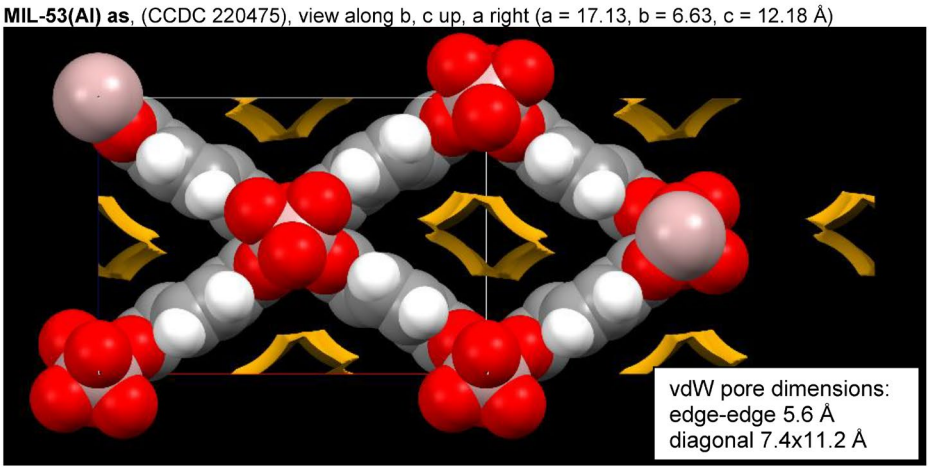

UiO-66 (CCDC 733458, view along b, a down, c right (a = b = c = 20.70 Å)
probe radius 2 Å:

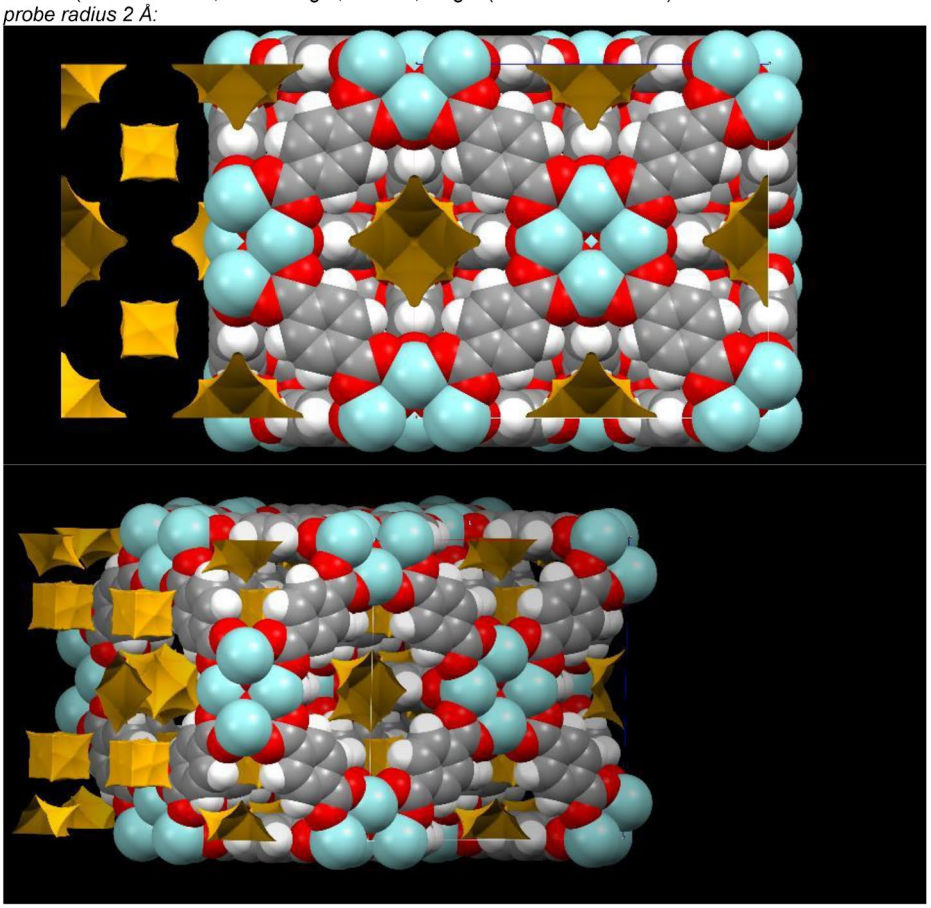

UiO-66 (CCDC 733458, view along b, a down, c right (a = b = c = 20.70 Å)
probe radius 1.5 Å:

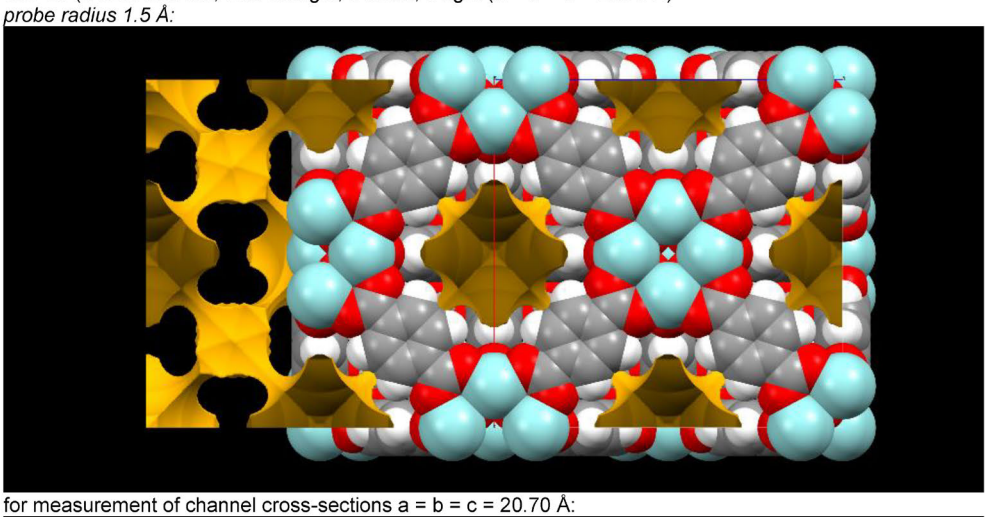

for measurement of channel cross-sections a = b = c = 20.70 Å:

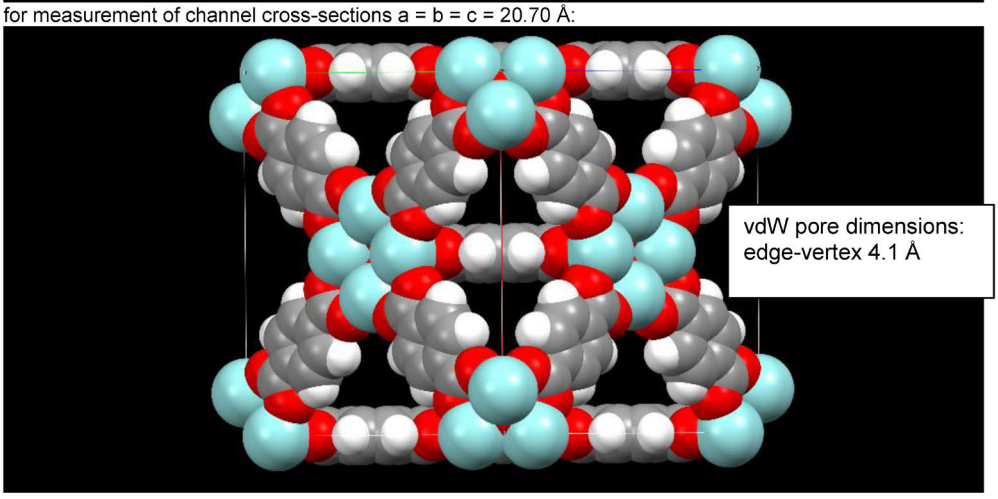

UiO-66-NH_2 (CCDC 1405751) (disordered O atom on Zr removed) view along b, a down, c right
(H atoms not added, because of N atom disorder, and thus, H atoms not shown)
probe radius 2 Å:

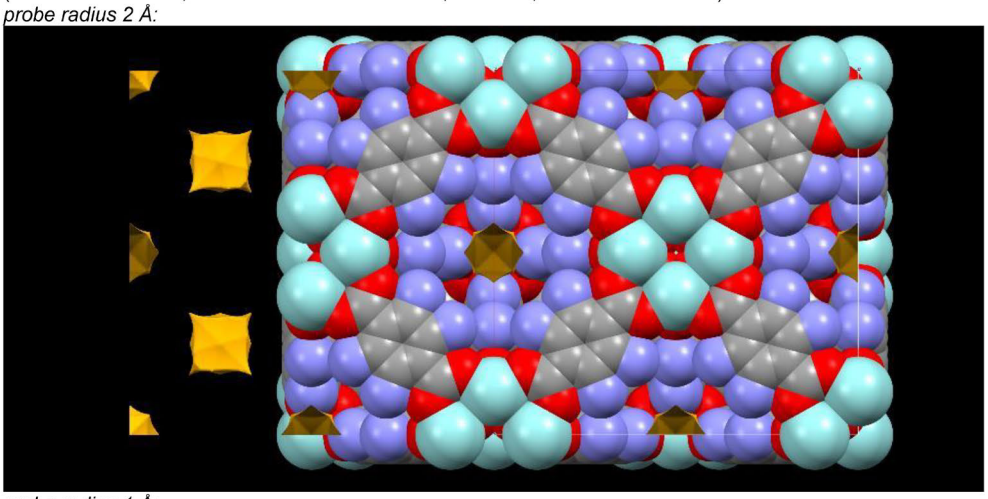

probe radius 1 Å:

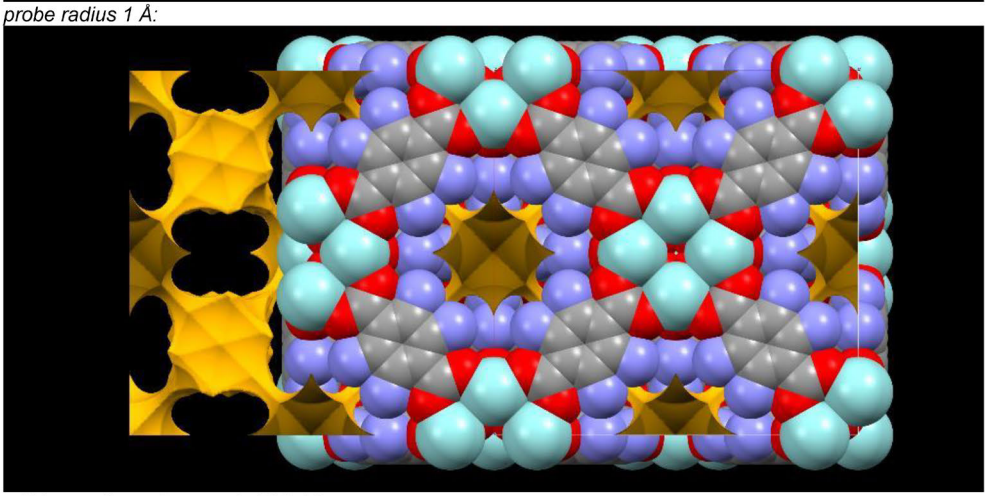

vdW pore dimensions: as in UiO-66
edge-vertex 4.1 Å
The N atoms are statistically oriented. Induced by the crystallographic symmetry, there is a ¼ N atom at each C atom. There will also be channel sections which are just lined by H atoms as in UiO-66.

UiO-66(F)$_4$ no X-ray structure, but isostructural to UiO-66-NH$_2$
The pore volume, pore aperture and images for the solvent accessible surface can be taken from the structure of UiO-66-"N" (above and below) with the crystallographically-induced N atom at each C atom of the benzene ring. (For measurement of channel cross-sections a = b = c = 20.80 Å).

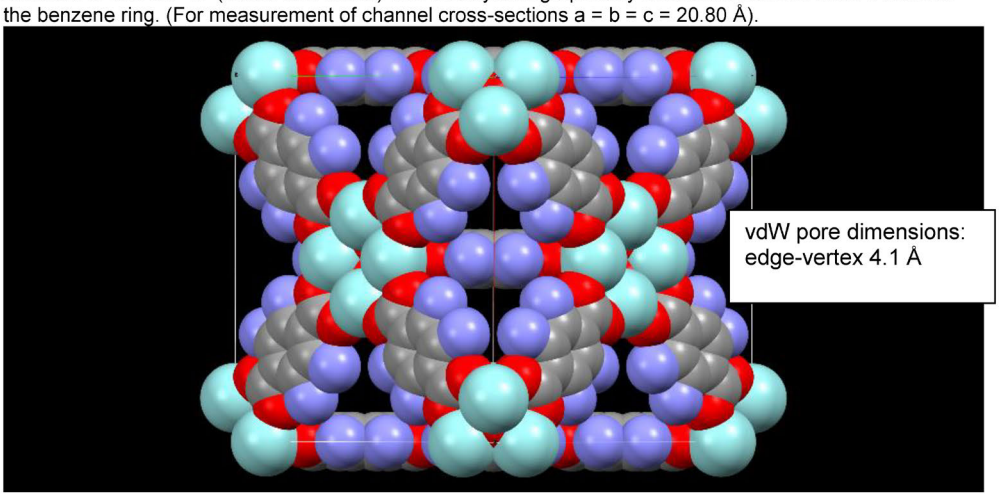

UiO-67 (CCDC 1018032) view along b, a down, c right (a = b = c = 26.9 Å)

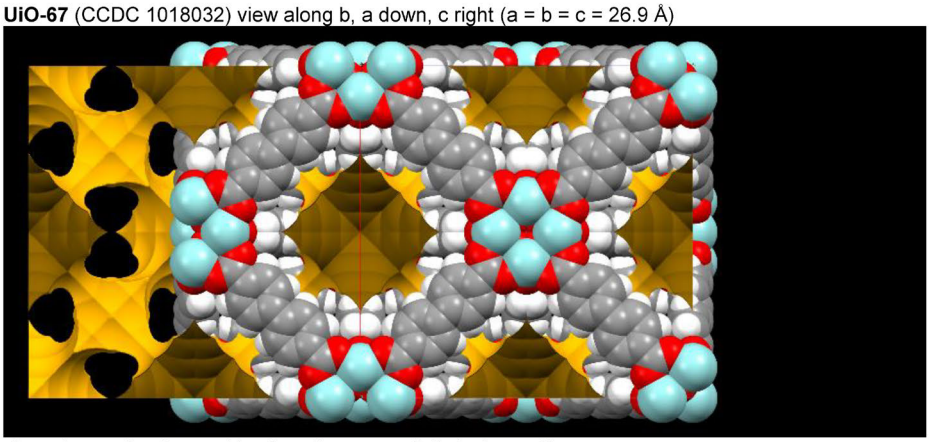

view along cube diagonal to show the connectivity between the pores:

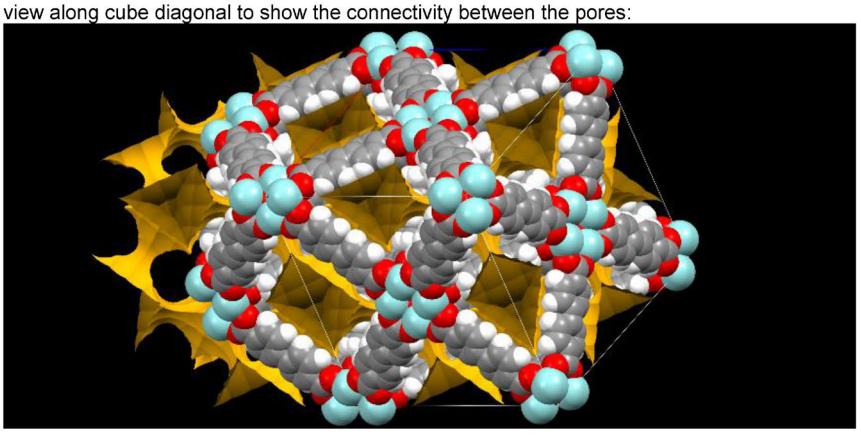

UiO-67 for measurement of channel cross-sections a = b = c = 26.9 Å

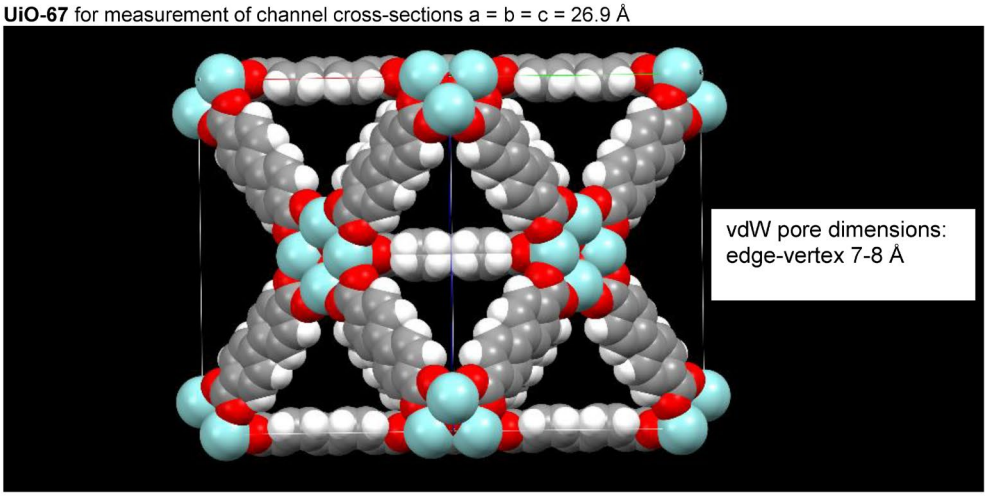

DUT-67 (CCDC 921644) along b, c to right, a down (a = b = c = 39.1 Å)

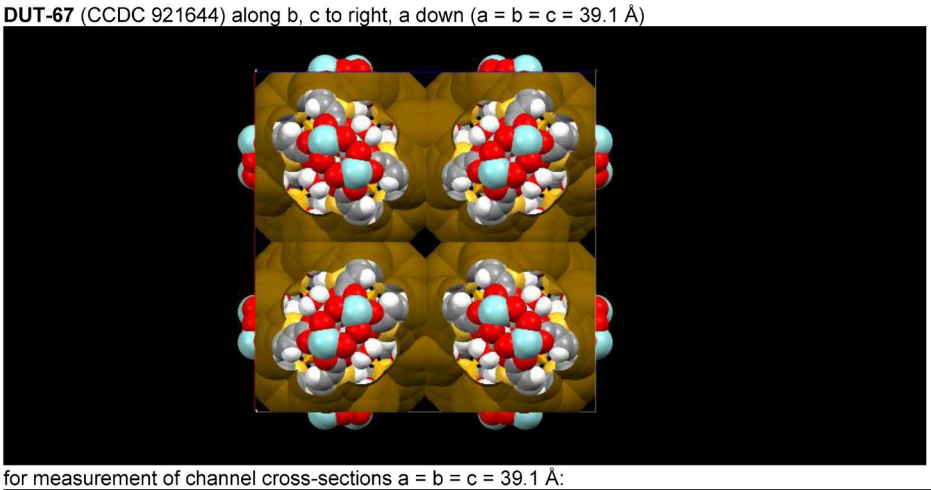

for measurement of channel cross-sections a = b = c = 39.1 Å:

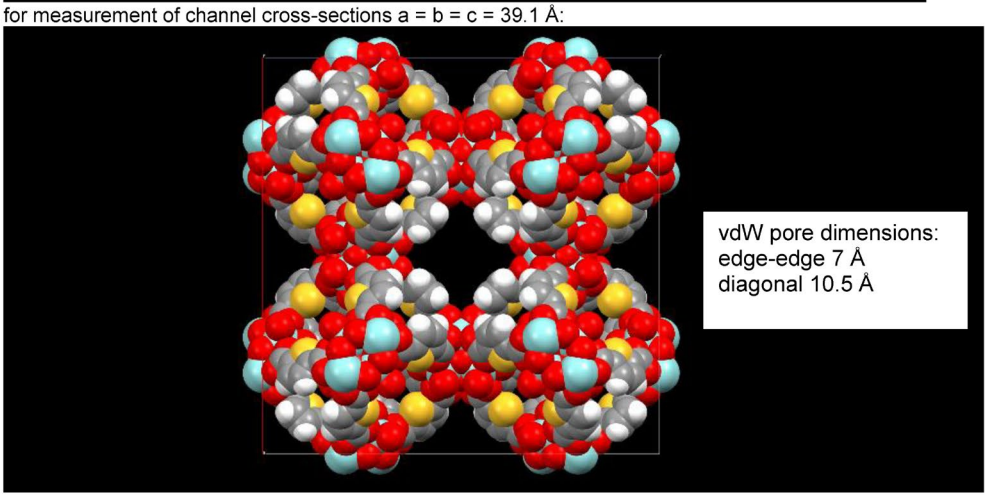

MIL-125 (CCDC 751157), along b, c to right, a down

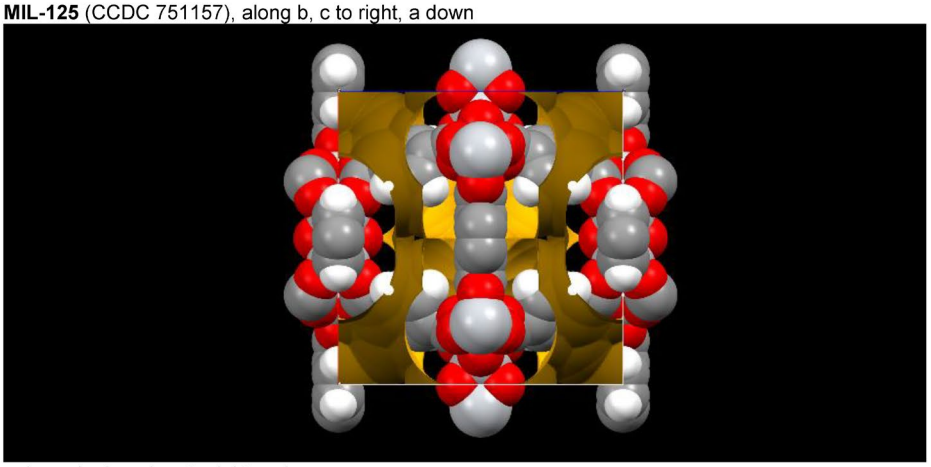

enlarged, along b, c to right, a down

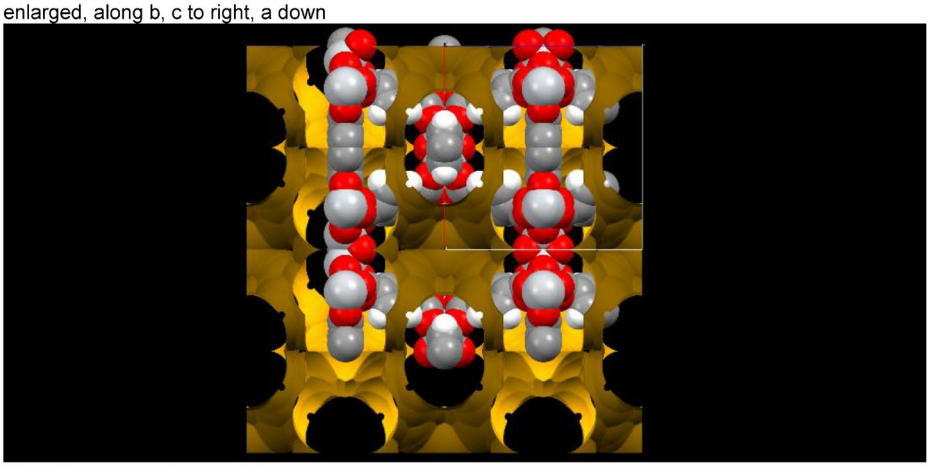

view along c, a to right, b down

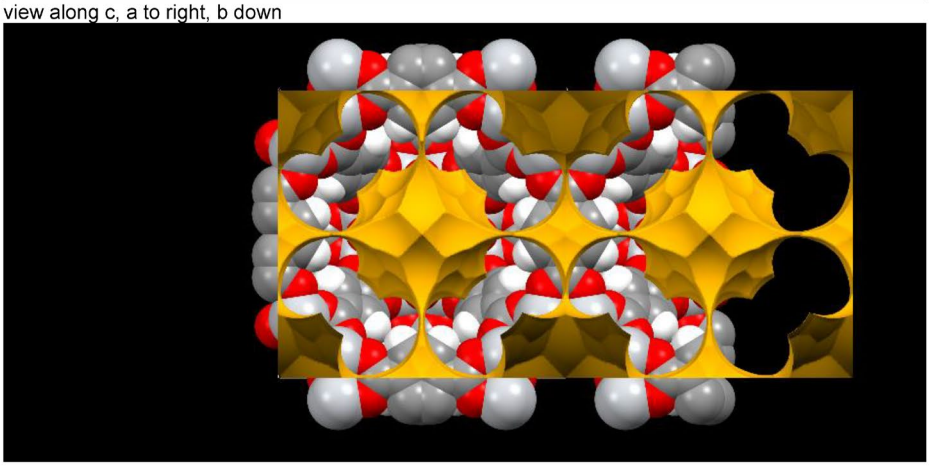

86

MIL-125 for measurement of channel cross-sections a = b = 18.65, c = 18.14 Å:

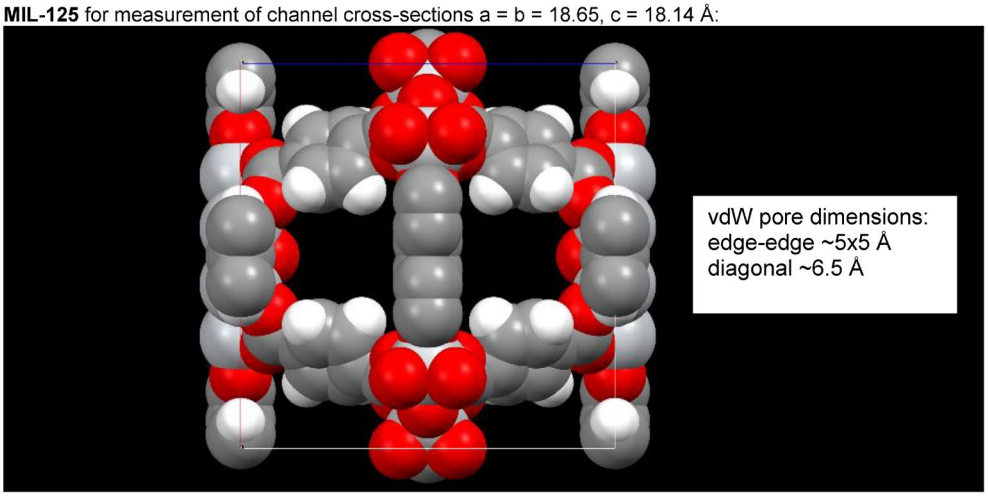

ZIF-8 (CCDC 864309), water removed, along b, c to right, a down (a = b = c = 16.85 Å)
probe radius 2 A:

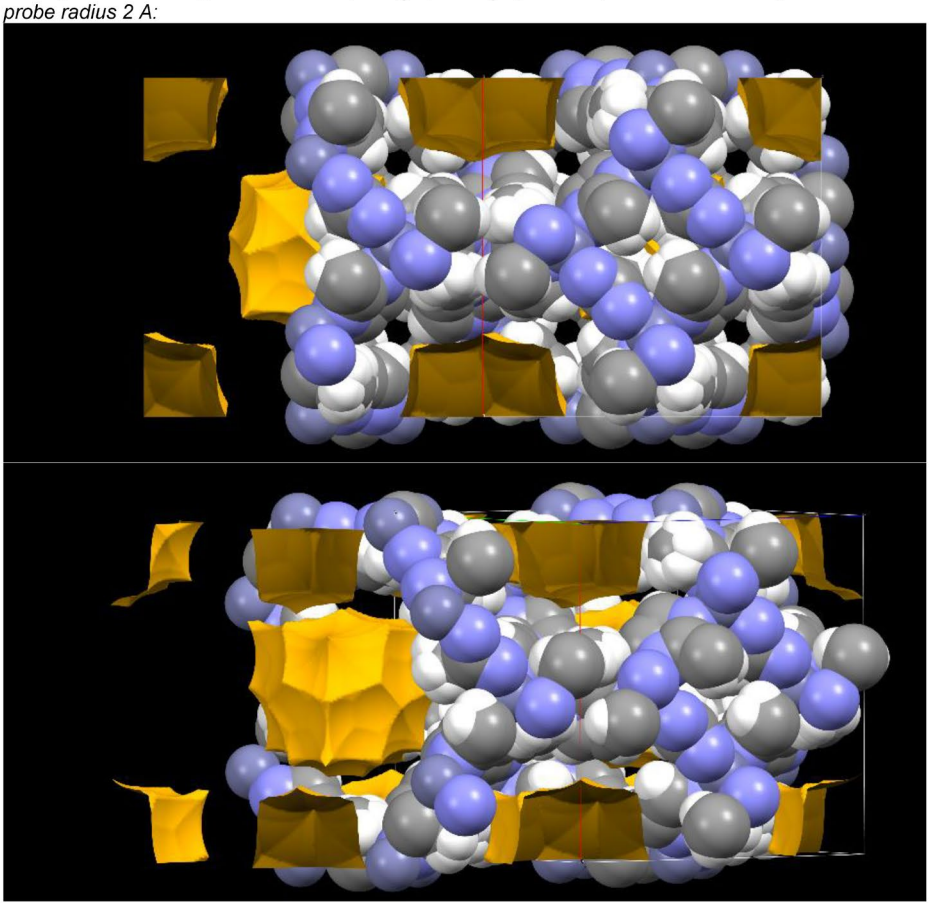

probe radius 1.5 Å – continuous channels:

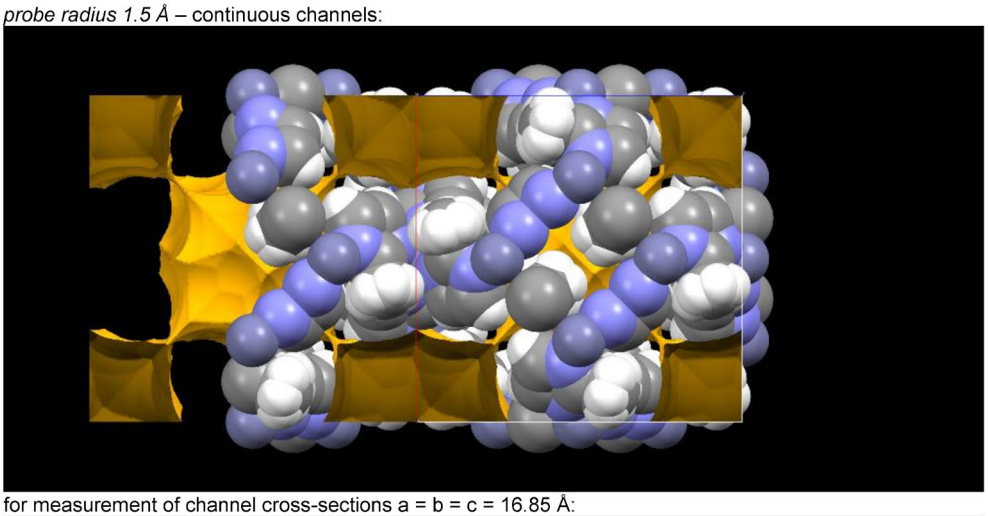

for measurement of channel cross-sections a = b = c = 16.85 Å:

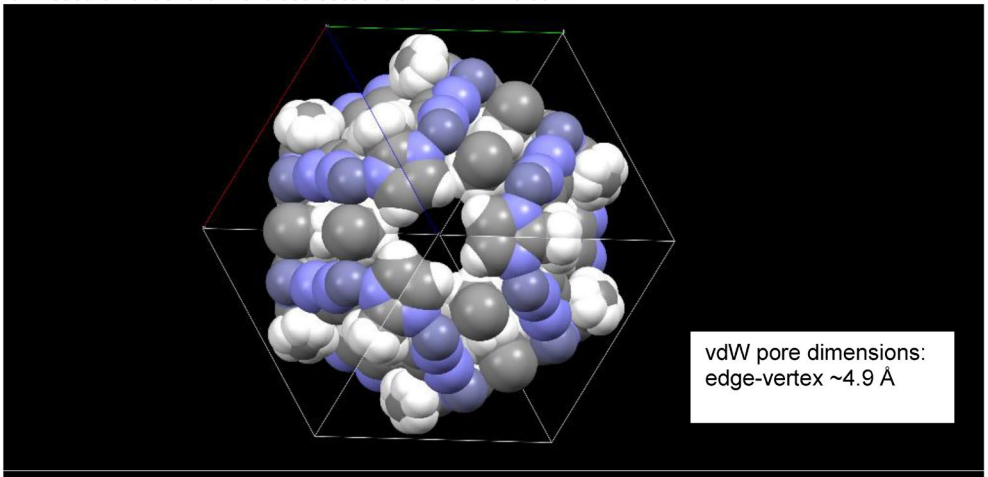

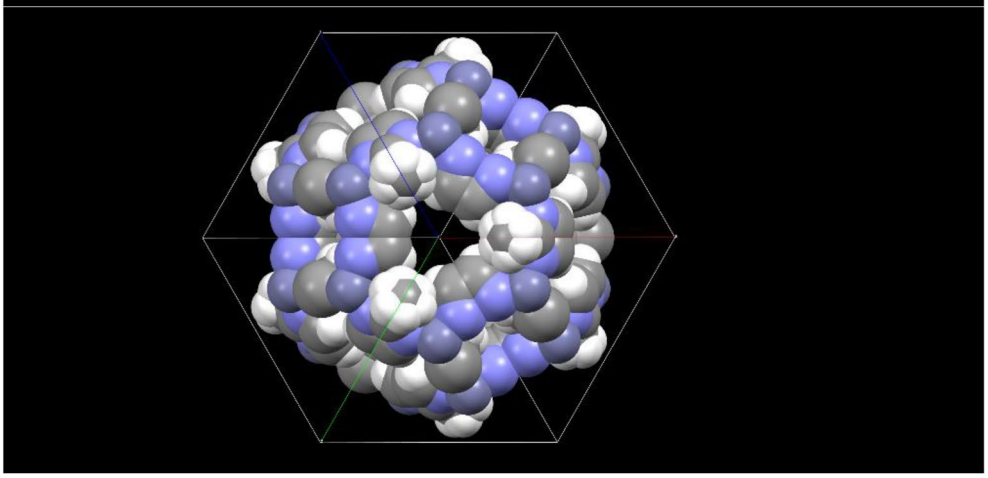

vdW pore dimensions:
edge-vertex ~4.9 Å

ZIF-11 (CCDC 602545), water removed, disorder removed, along b, c to right, a down (a = b = c = 28.76 Å)
probe radius 2 Å:

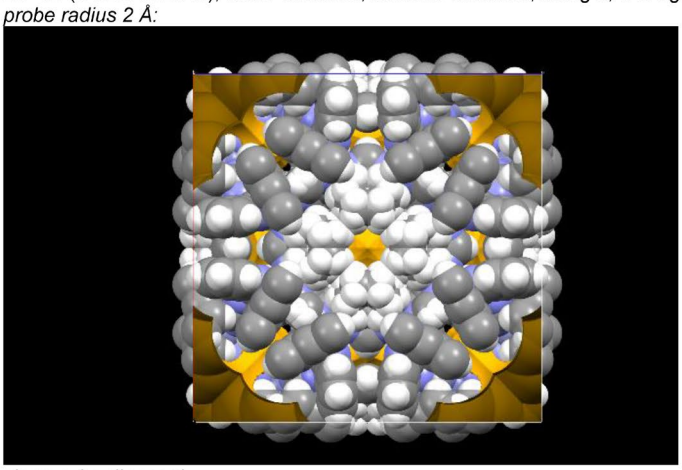

along cube diagonal:

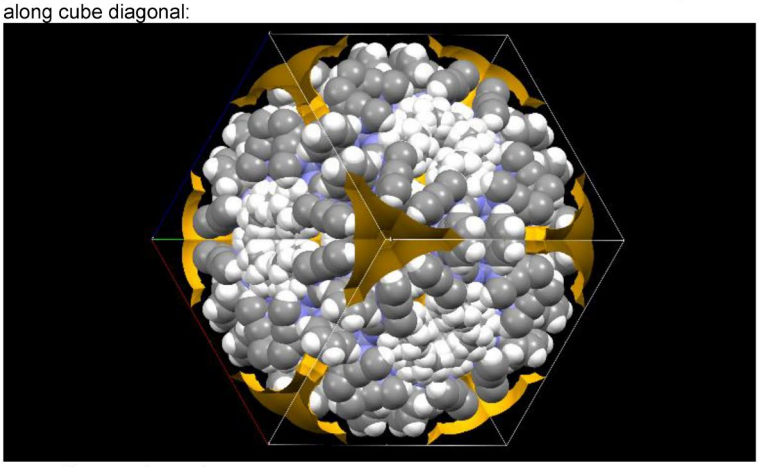

no continuous channels:

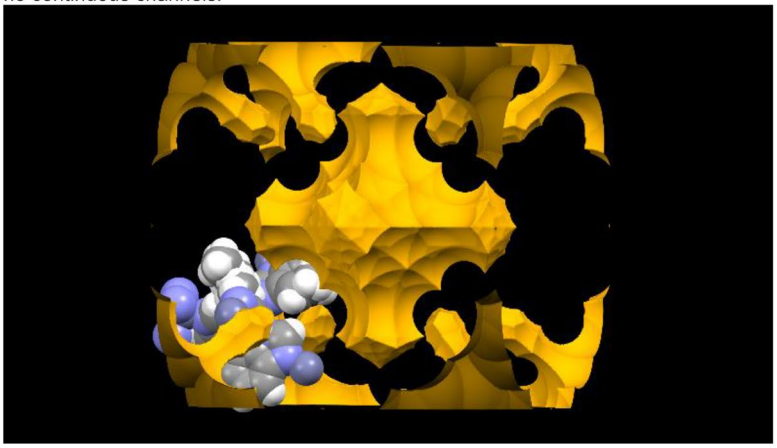

probe radius 1.5 Å, continuous channels:

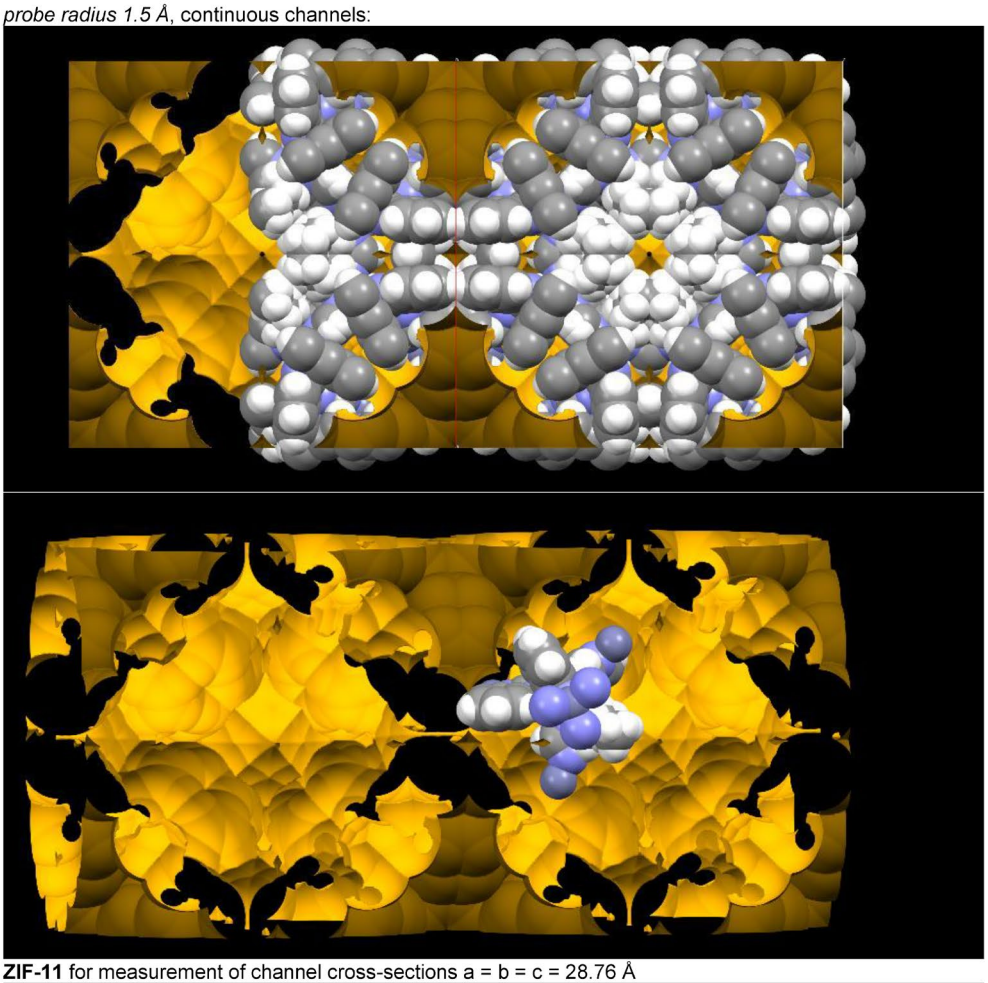

ZIF-11 for measurement of channel cross-sections a = b = c = 28.76 Å

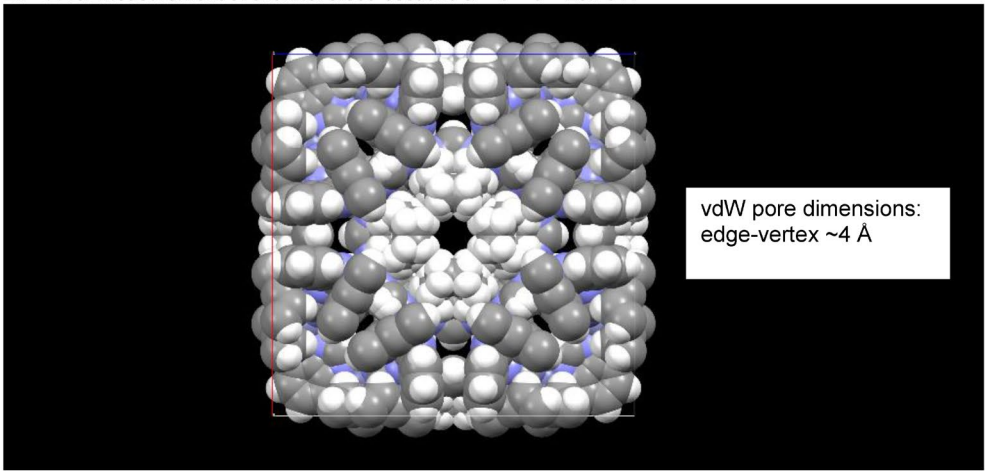

90

ZIF-7 (CCDC 973356), along b, c to right, a down (a = b = 22.94, c = 15.75 Å)
probe radius 2 Å:

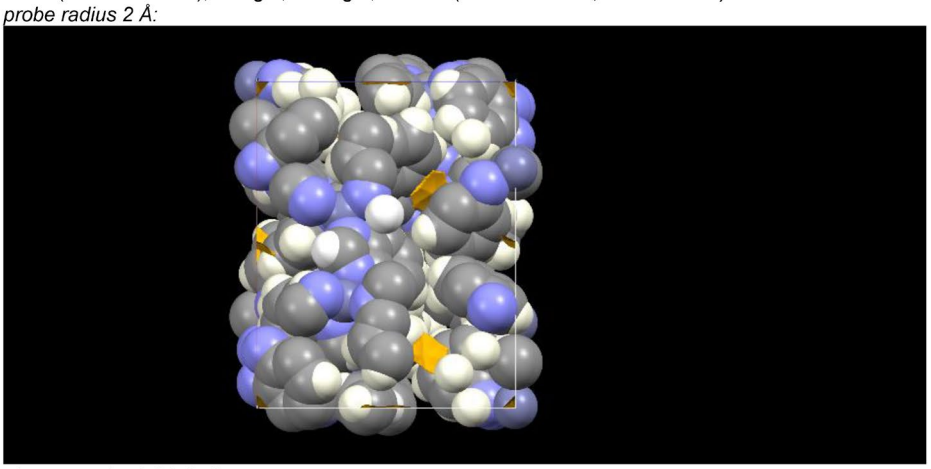

along c, a to right, b down:

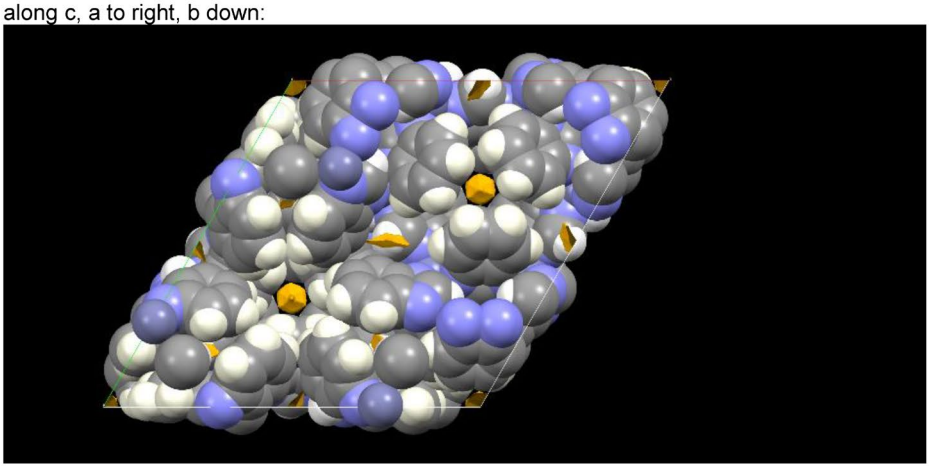

probe radius 1.5 Å, along b, c to right, a down:

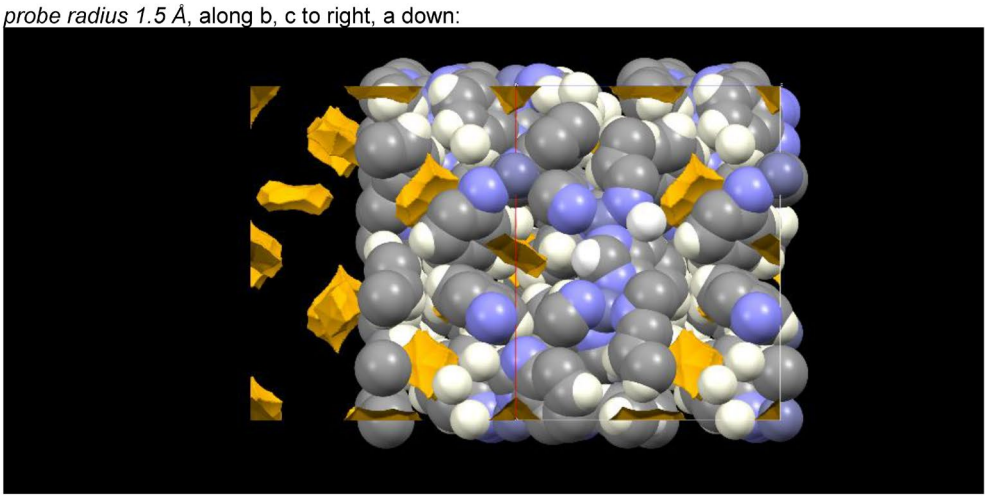

91

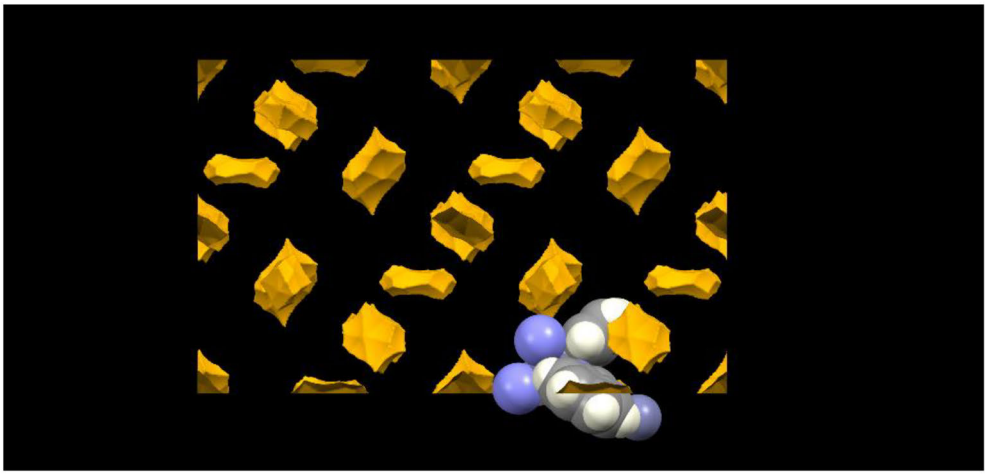

probe radius 1 Å, continuous channels:

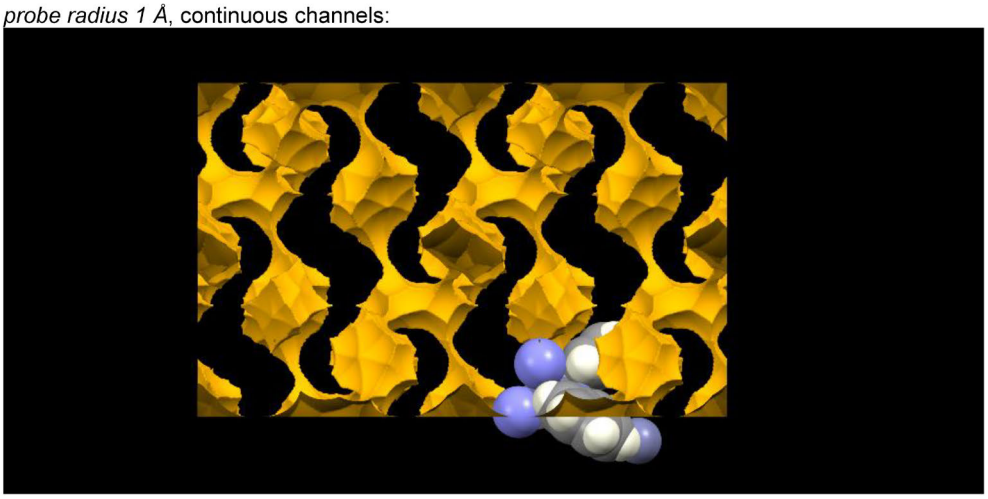

92

S16 References

[1] Alvarez, E.; Guillou, N.; Martineau, C.; Bueken, B.; Van de Voorde, B.; Le Guillouzer, C.; Fabry, P.; Nouar, F.; Taulelle, F.; Vos, D. de; Chang, J.-S.; Cho, K.H.; Ramsahye, N.; Devic, T.; Daturi, M.; Maurin, G.; Serre, C. The structure of the aluminum fumarate metal-organic framework A520. *Angew. Chem. Int. Ed.* **2015**, *54*, 3664–3668, doi:10.1002/anie.201410459.

[2] Brandenburg, K. Diamond 4.6, Crystal and Molecular Structure Visualization. Copyright 1997-2022 Crystal Impact GbR, Bon, Germany. Available online: https://www.crystalimpact.com/diamond/ (accessed on 10 August 2022).

[3] Cadiau, A.; Lee, J.S.; Damasceno Borges, D.; Fabry, P.; Devic, T.; Wharmby, M.T.; Martineau, C.; Foucher, D.; Taulelle, F.; Jun, C.-H.; Hwang, Y.K.; Stock, N.; Lange, M.F. de; Kapteijn, F.; Gascon, J.; Maurin, G.; Chang, J.-S.; Serre, C. Design of hydrophilic metal organic framework water adsorbents for heat reallocation. *Adv. Mater.* **2015**, *27*, 4775–4780, doi:10.1002/adma.201502418.

[4] Wahiduzzaman, M.; Lenzen, D.; Maurin, G.; Stock, N.; Wharmby, M.T. Rietveld Refinement of MIL-160 and Its Structural Flexibility Upon H_2O and N_2 Adsorption. *Eur. J. Inorg. Chem.* **2018**, 3626–3632, doi:10.1002/ejic.201800323.

[5] Senkovska, I.; Hoffmann, F.; Fröba, M.; Getzschmann, J.; Böhlmann, W.; Kaskel, S. New highly porous aluminium based metal-organic frameworks: Al(OH)(ndc) (ndc=2,6-naphthalene dicarboxylate) and Al(OH)(bpdc) (bpdc=4,4′-biphenyl dicarboxylate). *Microporous Mesoporous Mater.* **2009**, *122*, 93–98, doi:10.1016/j.micromeso.2009.02.020.

[6] Gotthardt, M.A.; Grosjean, S.; Brunner, T.S.; Kotzel, J.; Gänzler, A.M.; Wolf, S.; Bräse, S.; Kleist, W. Synthesis and post-synthetic modification of amine-, alkyne-, azide- and nitro-functionalized metal-organic frameworks based on DUT-5. *Dalton Trans.* **2015**, *44*, 16802–16809, doi:10.1039/c5dt02276b.

[7] Tannert, N.; Ernst, S.-J.; Jansen, C.; Bart, H.-J.; Henninger, S.K.; Janiak, C. Evaluation of the highly stable metal–organic framework MIL-53(Al)-TDC (TDC = 2,5-thiophenedicarboxylate) as a new and promising adsorbent for heat transformation applications. *J. Mater. Chem. A* **2018**, *6*, 17706–17712, doi:10.1039/C8TA04407D.

[8] Zi, G.; Yan, Z.; Wang, Y.; Chen, Y.; Guo, Y.; Yuan, F.; Gao, W.; Wang, Y.; Wang, J. Catalytic hydrothermal conversion of carboxymethyl cellulose to value-added chemicals over metal-organic framework MIL-53(Al). *Carbohydr. Polym.* **2015**, *115*, 146–151, doi:10.1016/j.carbpol.2014.08.065.

[9] Rallapalli, P.; Patil, D.; Prasanth, K.P.; Somani, R.S.; Jasra, R.V.; Bajaj, H.C. An alternative activation method for the enhancement of methane storage capacity of nanoporous aluminium terephthalate, MIL-53(Al). *J. Porous Mater.* **2010**, *17*, 523–528, doi:10.1007/s10934-009-9320-5.

[10] Ortiz, G.; Chaplais, G.; Paillaud, J.-L.; Nouali, H.; Patarin, J.; Raya, J.; Marichal, C. New Insights into the Hydrogen Bond Network in Al-MIL-53 and Ga-MIL-53. *J. Phys. Chem. C* **2014**, *118*, 22021–22029, doi:10.1021/jp505893s.

[11] Loiseau, T.; Serre, C.; Huguenard, C.; Fink, G.; Taulelle, F.; Henry, M.; Bataille, T.; Férey, G. A rationale for the large breathing of the porous aluminum terephthalate (MIL-53) upon hydration. *Chem. Eur. J.* **2004**, *10*, 1373–1382, doi:10.1002/chem.200305413.

[12] Aguilera-Sigalat, J.; Bradshaw, D. A colloidal water-stable MOF as a broad-range fluorescent pH sensor via post-synthetic modification. *Chem. Commun.* **2014**, *50*, 4711–4713, doi:10.1039/c4cc00659c.

[13] Hu, Z.; Peng, Y.; Kang, Z.; Qian, Y.; Zhao, D. A Modulated Hydrothermal (MHT) Approach for the Facile Synthesis of UiO-66-Type MOFs. *Inorg. Chem.* **2015**, *54*, 4862–4868, doi:10.1021/acs.inorgchem.5b00435.

[14] Katz, M.J.; Brown, Z.J.; Colón, Y.J.; Siu, P.W.; Scheidt, K.A.; Snurr, R.Q.; Hupp, J.T.; Farha, O.K. A facile synthesis of UiO-66, UiO-67 and their derivatives. *Chem. Commun.* **2013**, *49*, 9449–9451, doi:10.1039/c3cc46105j.

[15] Cavka, J.H.; Jakobsen, S.; Olsbye, U.; Guillou, N.; Lamberti, C.; Bordiga, S.; Lillerud, K.P. A new zirconium inorganic building brick forming metal organic frameworks with exceptional stability. *J. Am. Chem. Soc* **2008**, *130*, 13850–13851, doi:10.1021/ja8057953.

[16] Drache, F.; Bon, V.; Senkovska, I.; Marschelke, C.; Synytska, A.; Kaskel, S. Postsynthetic Inner-Surface Functionalization of the Highly Stable Zirconium-Based Metal-Organic Framework DUT-67. *Inorg. Chem.* **2016**, *55*, 7206–7213, doi:10.1021/acs.inorgchem.6b00829.

[17] Bon, V.; Senkovska, I.; Baburin, I.A.; Kaskel, S. Zr- and Hf-Based Metal–Organic Frameworks: Tracking Down the Polymorphism. *Cryst. Growth. Des.* **2013**, *13*, 1231–1237, doi:10.1021/cg301691d.

[18] Sohail, M.; Yun, Y.-N.; Lee, E.; Kim, S.K.; Cho, K.; Kim, J.-N.; Kim, T.W.; Moon, J.-H.; Kim, H. Synthesis of Highly Crystalline NH_2-MIL-125 (Ti) with S-Shaped Water Isotherms for Adsorption Heat Transformation. *Cryst. Growth. Des.* **2017**, *17*, 1208–1213, doi:10.1021/acs.cgd.6b01597.

[19] Santaclara, J.G.; Nasalevich, M.A.; Castellanos, S.; Evers, W.H.; Spoor, F.C.M.; Rock, K.; Siebbeles, L.D.A.; Kapteijn, F.; Grozema, F.; Houtepen, A.; Gascon, J.; Hunger, J.; van der Veen, M.A. Organic Linker Defines the Excited-State Decay of Photocatalytic MIL-125(Ti)-Type Materials. *ChemSusChem.* **2016**, *9*, 388–395, doi:10.1002/cssc.201501353.

[20] Dan-Hardi, M.; Serre, C.; Frot, T.; Rozes, L.; Maurin, G.; Sanchez, C.; Férey, G. A new photoactive crystalline highly porous titanium(IV) dicarboxylate. *J. Am. Chem. Soc* **2009**, *131*, 10857–10859, doi:10.1021/ja903726m.
[21] Zhao, T.; Jeremias, F.; Boldog, I.; Nguyen, B.; Henninger, S.K.; Janiak, C. High-yield, fluoride-free and large-scale synthesis of MIL-101(Cr). *Dalton Trans.* **2015**, *44*, 16791–16801, doi:10.1039/c5dt02625c.
[22] Férey, G.; Mellot-Draznieks, C.; Serre, C.; Millange, F.; Dutour, J.; Surblé, S.; Margiolaki, I. A chromium terephthalate-based solid with unusually large pore volumes and surface area. *Science* **2005**, *309*, 2040–2042, doi:10.1126/science.1116275.
[23] Kida, K.; Okita, M.; Fujita, K.; Tanaka, S.; Miyake, Y. Formation of high crystalline ZIF-8 in an aqueous solution. *CrystEngComm.* **2013**, *15*, 1794–1801, doi:10.1039/c2ce26847g.
[24] Morris, W.; Stevens, C.J.; Taylor, R.E.; Dybowski, C.; Yaghi, O.M.; Garcia-Garibay, M.A. NMR and X-ray Study Revealing the Rigidity of Zeolitic Imidazolate Frameworks. *J. Phys. Chem. C* **2012**, *116*, 13307–13312, doi:10.1021/jp303907p.
[25] He, M.; Yao, J.; Liu, Q.; Zhong, Z.; Wang, H. Toluene-assisted synthesis of RHO-type zeolitic imidazolate frameworks: synthesis and formation mechanism of ZIF-11 and ZIF-12. *Dalton Trans.* **2013**, *42*, 16608–16613, doi:10.1039/c3dt52103f.
[26] Park, K.S.; Ni, Z.; Côté, A.P.; Choi, J.Y.; Huang, R.; Uribe-Romo, F.J.; Chae, H.K.; O'Keeffe, M.; Yaghi, O.M. Exceptional chemical and thermal stability of zeolitic imidazolate frameworks. *Proc. Natl. Acad. Sci. USA* **2006**, *103*, 10186–10191, doi:10.1073/pnas.0602439103.
[27] Kang, C.-H.; Lin, Y.-F.; Huang, Y.-S.; Tung, K.-L.; Chang, K.-S.; Chen, J.-T.; Hung, W.-S.; Lee, K.-R.; Lai, J.-Y. Synthesis of ZIF-7/chitosan mixed-matrix membranes with improved separation performance of water/ethanol mixtures. *J. Membr. Sci.* **2013**, *438*, 105–111, doi:10.1016/j.memsci.2013.03.028.
[28] Li, Y.; Liang, F.; Bux, H.; Yang, W.; Caro, J. Zeolitic imidazolate framework ZIF-7 based molecular sieve membrane for hydrogen separation. *J. Membr. Sci.* **2010**, *354*, 48–54, doi:10.1016/j.memsci.2010.02.074.
[29] Tschense, C.B.L.; Reimer, N.; Hsu, C.-W.; Reinsch, H.; Siegel, R.; Chen, W.-J.; Lin, C.-H.; Cadiau, A.; Serre, C.; Senker, J.; Stock, N. New Group 13 MIL-53 Derivates based on 2,5-Thiophenedicarboxylic Acid. *Z. Anorg. Allg. Chem.* **2017**, *643*, 1600–1608, doi:10.1002/zaac.201700260.
[30] Lin, Z.-J.; Zheng, H.-Q.; Zeng, Y.-N.; Wang, Y.-L.; Chen, J.; Cao, G.-J.; Gu, J.-F.; Chen, B. Effective and selective adsorption of organoarsenic acids from water over a Zr-based metal-organic framework. *Chem. Eng. J.* **2019**, *378*, 122196, doi:10.1016/j.cej.2019.122196.
[31] Chen, D.-L.; Wu, S.; Yang, P.; He, S.; Dou, L.; Wang, F.-F. Ab Initio Molecular Dynamic Simulations on Pd Clusters Confined in UiO-66-NH_2. *J. Phys. Chem. C* **2017**, *121*, 8857–8863, doi:10.1021/acs.jpcc.7b00957.
[32] Reinsch, H.; Bueken, B.; Vermoortele, F.; Stassen, I.; Lieb, A.; Lillerud, K.-P.; Vos, D. de. Green synthesis of zirconium-MOFs. *CrystEngComm.* **2015**, *17*, 4070–4074, doi:10.1039/C5CE00618J.
[33] Kim, S.-N.; Kim, J.; Kim, H.-Y.; Cho, H.-Y.; Ahn, W.-S. Adsorption/catalytic properties of MIL-125 and NH_2-MIL-125. *Catal. Today* **2013**, *204*, 85–93, doi:10.1016/j.cattod.2012.08.014.
[34] Novaković, S.B.; Bogdanović, G.A.; Heering, C.; Makhloufi, G.; Francuski, D.; Janiak, C. Charge-density distribution and electrostatic flexibility of ZIF-8 based on high-resolution X-ray diffraction data and periodic calculations. *Inorg. Chem.* **2015**, *54*, 2660–2670, doi:10.1021/ic5028256.
[35] Mercury 2021.2.0, Program for Crystal Structure Visualisation, Exploration and Analysis from the Cambridge Crystallographic Data Center, Copyright CCDC 2001-2021, Available online: http://www.ccdc.cam.ac.uk/mercury/ (accessed on 10 July 2022)
[36] Macrae, C.F.; Sovago, I.; Cottrell, S.J.; Galek, P.T.A.; McCabe; P., Pidcock, E.; Platings, M.; Shields, G.P.; Stevens, J.S.; Towler, M.; Wood, P.A. Mercury 4.0: from visualization to analysis, design and prediction. *J. Appl. Cryst.* **2020**, *53*, 226–235.
[37] Shearer, G.C.; Chavan, S.; Ethiraj, J.; Vitillo, J.G.; Svelle, S.; Olsbye, U.; Lamberti, C.; Bordiga, S.; Lillerud, K.P. Tuned to Perfection: Ironing Out the Defects in Metal–Organic Framework UiO-66. *Chem. Mater.* **2014**, *26*, 4068–4071, doi:10.1021/cm501859p.
[38] Trickett, C.A.; Gagnon, K.J.; Lee, S.; Gándara, F.; Bürgi, H.-B.; Yaghi, O.M. Definitive molecular level characterization of defects in UiO-66 crystals. *Angew. Chem. Int. Ed.* **2015**, *54*, 11162–11167, doi:10.1002/anie.201505461.
[39] Øien, S.; Wragg, D.; Reinsch, H.; Svelle, S.; Bordiga, S.; Lamberti, C.; Lillerud, K.P. Detailed Structure Analysis of Atomic Positions and Defects in Zirconium Metal–Organic Frameworks. *Cryst. Growth. Des.* **2014**, *14*, 5370–5372, doi:10.1021/cg501386j.
[40] Zhao, P.; Bennett, T.D.; Casati, N.P.M.; Lampronti, G.I.; Moggach, S.A.; Redfern, S.A.T. Pressure-induced oversaturation and phase transition in zeolitic imidazolate frameworks with remarkable mechanical stability. *Dalton Trans.* **2015**, *44*, 4498–4503, doi:10.1039/c4dt02680b.
[41] Thommes, M.; Kaneko, K.; Neimark, A.V.; Olivier, J.P.; Rodriguez-Reinoso, F.; Rouquerol, J.; Sing, K.S. Physisorption of gases, with special reference to the evaluation of surface area and pore size distribution (IUPAC Technical Report). *Pure Appl. Chem.* **2015**, *87*, 160, doi:10.1515/pac-2014-1117.
[42] Yang, Q.-Y.; Lama, P.; Sen, S.; Lusi, M.; Chen, K.-J.; Gao, W.-Y.; Shivanna, M.; Pham, T.; Hosono, N.; Kusaka, S.; Perry, J.J.; Ma, S.; Space, B.; Barbour, L.J.; Kitagawa, S.; Zaworotko, M.J. Reversible Switching between Highly Porous and Nonporous Phases of an Interpenetrated Diamondoid Coordination

Network That Exhibits Gate-Opening at Methane Storage Pressures. *Angew. Chem. Int. Ed.* **2018**, *57*, 5684–5689, doi:10.1002/anie.201800820.

[43] Kökçam-Demir, Ü.; Goldman, A.; Esrafili, L.; Gharib, M.; Morsali, A.; Weingart, O.; Janiak, C. Coordinatively unsaturated metal sites (open metal sites) in metal-organic frameworks: design and applications. *Chem. Soc. Rev.* **2020**, *49*, 2751–2798, doi:10.1039/c9cs00609e.

[44] Lin, X.; Blake, A.J.; Wilson, C.; Sun, X.Z.; Champness, N.R.; George, M.W.; Hubberstey, P.; Mokaya, R.; Schröder, M. A porous framework polymer based on a zinc(II) 4,4'-bipyridine-2,6,2',6'-tetracarboxylate: synthesis, structure, and "zeolite-like" behaviors. *J. Am. Chem. Soc.* **2006**, *128*, 10745–10753, doi:10.1021/ja060946u.

[45] Saini, V.K.; Pires, J. Development of metal organic fromwork-199 immobilized zeolite foam for adsorption of common indoor VOCs. *J. Environ. Sci.* **2017**, *55*, 321–330, doi:10.1016/j.jes.2016.09.017.

[46] Brandt, P.; Xing, S.-H.; Liang, J.; Kurt, G.; Nuhnen, A.; Weingart, O.; Janiak, C. Zirconium and Aluminum MOFs for Low-Pressure SO_2 Adsorption and Potential Separation: Elucidating the Effect of Small Pores and NH2 Groups. *ACS Appl. Mater. Interfaces* **2021**, *13*, 29137–29149, doi:10.1021/acsami.1c06003.

[47] Brandt, P.; Nuhnen, A.; Öztürk, S.; Kurt, G.; Liang, J.; Janiak, C. Comparative Evaluation of Different MOF and Non-MOF Porous Materials for SO_2 Adsorption and Separation Showing the Importance of Small Pore Diameters for Low-Pressure Uptake. *Adv. Sustain. Syst.* **2021**, *122*, 2000285, doi:10.1002/adsu.202000285.

[48] 3P INSTRUMENTS, 3P sim, Version 1.1.0.7, Simulation and Evaluation Tool for mixSorb, 3P INSTRUMENTS 2018.

[49] Cessford, N.F.; Seaton, N.A.; Düren, T. Evaluation of Ideal Adsorbed Solution Theory as a Tool for the Design of Metal–Organic Framework Materials. *Ind. Eng. Chem. Res.* **2012**, *51*, 4911–4921, doi:10.1021/ie202219w.

[50] Zhao, P.; Lampronti, G.I.; Lloyd, G.O.; Wharmby, M.T.; Facq, S.; Cheetham, A.K.; Redfern, S.A.T. Phase Transitions in Zeolitic Imidazolate Framework 7: The Importance of Framework Flexibility and Guest-Induced Instability. *Chem. Mater.* **2014**, *26*, 1767–1769, doi:10.1021/cm500407f.

[51] Budzianowski, A.; Katrusiak, A. Pressure-frozen benzene I revisited. *Acta Crystallogr. Sect. B* **2006**, *B62*, 94-101.

[52] Katrusiak, A.; Podsiadzo, M.; Budzianowski, A. Association CH···π and No van der Waals Contacts at the Lowest Limits of Crystalline Benzene I and II Stability Regions. *Cryst. Growth Des.* **2010**, *10*, 3461-3465.

3.6 Co-Autorenschaften

Während der Promotion wurde an verschiedenen Publikationen als Co-Autor mitgewirkt, die im Folgenden kurz vorgestellt werden und der eigene Anteil an den Publikationen aufgeführt wird.

3.6.1 Evaluation of the highly stable metal-organic framework MIL-53(Al)-TDC (TDC = 2,5-thiophenedicarboxylate) as a new and promising adsorbent for heat transformation applications

Niels Tannert, Sebastian-Johannes Ernst, Christian Jansen, Hans-Jörg Bart, Stefan K. Henninger, Christoph Janiak

J. Mater. Chem. A **2018**, *6,* 17706-17712

DOI: 10.1039/c8ta04407d

Impact-Faktor: 14.511 (2022)

Kurzzusammenfassung:

Das aluminiumbasierte MOF MIL-53-TDC besitzt geeignete Wassersorptionseigenschaften bezüglich der adsorptionsgetriebenen Wärmetransformationsanwendungen, wie eine hohe thermale Stabilität und eine hohe Stabilität gegenüber Lösemitteln und verschiedenen pH-Werten. Des Weiteren konnte eine hydrothermale Stabilität gegenüber Wasser bei 40 Zyklen nachgewiesen werden. Ebenso wurde die Adsorptionsenthalpie berechnet und weitere Eigenschaften untersucht, die MIL-53-TDC besonders machen und einen entscheidenden Vorteil gegenüber kommerziell erhältlichen Adsorbenzien erzielen.

Eigenanteile an der Publikation:

- Entwicklung und Optimierung der Rückflusssynthese von MIL-53-TDC
- Revision des Manuskripts

3.6.2 Tunable LiCl@UiO-66 composites for water sorption-based heat transformation applications

Yangyang Sun, Alex Spieß, Christian Jansen, Alexander Nuhnen, Serkan Gökpinar, Raphael Wiedey, Sebastian-Johannes Ernst, Christoph Janiak

Tunable LiCl@UiO-66 composites for water sorption-based heat transformation applications

J. Mater. Chem. A **2020**, *8*, 13364-13375

DOI: 10.1039/d0ta03442h

Impact-Faktor: 14.511 (2022)

Kurzzusammenfassung:

Poröse Kompositmaterialien sind potenzielle Kandidaten für wasserbasierte Wärmetransformationsanwendungen. In dieser Veröffentlichung wurde LiCl@UiO-66 hergestellt, als Vertreter der Komposite bestehend aus einem Salz in einer porösen Matrix, durch die Nass-Imprägnierungsmethode. Hierbei wurde die Salzlösung nicht vollständig getrocknet, um ein Auskristallisieren des Salzes auf der Oberfläche zu verhindern. Durch diese Methode konnte die Wassersorption enorm gesteigert werden, durch den Salzgehalt. Das Kompositmaterial zeigt deutlich verbesserte Eigenschaften im Vergleich zu reinem Salz, da die Partikel besser verteilt sind. Ebenso konnte die Wasseraufnahme gegenüber reinem UiO-66 bis hin zum 3 bis 8-fachen gesteigert und eine maximale Aufnahme von 2.15 g g^{-1} bei der volumetrischen und der gravimetrischen Messung erzielt werden. Diese Aufnahme ist die höchste (Stand der Veröffentlichung) Wasseraufnahme eines UiO-66-Kompositmaterials. Zusätzlich wurden weitere für die Anwendung relevanten Daten ermittelt, wie die kinetischen Daten und auch der Performance-Koeffizient. Des Weiteren wurde die Wärmespeicherungskapazität bestimmt, die für Anwendungen einer thermischen Batterie relevant sind.

Eigenanteile an der Publikation:

- Atomabsorptionsspektroskopie-Messungen
- Revision des Manuskripts

3.6.3 Cucurbituril-Encapsulating Metal–Organic Framework via Mechanochemistry: Adsorbents with Enhanced Performance

Jun Liang, Vasily Gvilava, Christian Jansen, Secil Öztürk, Alex Spieß, Jingxiang Lin, Shanghua Xing, Yangyang Sun, Hao Wang, Christoph Janiak

Angew. Chem. Int. Ed. **2021**, *60*, 15365-15370

DOI: 10.1002/anie.202100675

Impact-Faktor: 16.823 (2021)

Kurzzusammenfassung:

Es werden die ersten Beispiele für monolithische kristalline Wirt-Gast-Hybridmaterialien beschrieben. Durch die Reaktion von 1,3,5-Benzoltricarbonsäure und Eisennitrat-Nonahydrat in Gegenwart von Decamethylcucurbit-[5]uril-Ammoniumchlorid entstehen *in situ* MC5@MIL-100(Fe)-Hybrid-Monolithe mit hierarchischen Mikro-, Meso- und Makroporen.

Diese „Flasche-um-Schiff“-Synthese und die Ein-Topf-Formgebung werden insbesondere durch ein neu entdecktes, mechanochemisch gebildetes Fe-MC5-Fließgel erleichtert. Das entworfene MC5@MIL-100(Fe)-Hybridmaterial mit MC5 als aktive Domänen hat eine verbesserte Methan- und Blei(II)-Aufnahmeleistung und eine selektive Aufnahme von Blei(II)-Kationen bei niedrigen Konzentrationen. Dies zeigt, dass Wirt-Gast-Hybridmaterialien synergetische Eigenschaften aufweisen können, die Materialien auf Basis von Einzelkomponenten übertreffen.

Eigenanteile an der Publikation:

- Atomabsorptionsspektroskopie-Messungen
- Aufnahme von Videos zum Herstellungsprozess des Komposits
- Hochdrucksorptionsmessungen von Methan
- Revision des Manuskripts

4. Unveröffentlichte Ergebnisse

In den folgenden Kapiteln werden die weiteren Ergebnisse diskutiert, die nicht in wissenschaftlichen Artikeln veröffentlicht wurden.

4.1 BTEX Adsorption mit MOFs

Im folgenden Kapitel 4.1 BTEX Adsorption mit MOFs und den zugehörigen Unterkapiteln soll die Adsorption von Benzol, Toluol, Ethylbenzol und den drei Xylol-Isomeren untersucht werden. Hierbei wird der Einsatz von verschiedenen UiO-MOFs untersucht, sowohl mit verschiedenen Defektstellen, aber auch verschieden funktionalisierte UiOs. Zusätzlich werden die MIL-140 MOFs verglichen, die ebenfalls aus einem Zirconiumsalz und Terephthalsäure, bzw. isoretikulär verlängerten Linker synthetisiert werden, jedoch hierbei keine Defektstrukturen besitzen.

4.1.1 Defektstellenberechnung der MOFs

Die Synthesen der unterschiedlichen MOFs und deren Analytik ist in den Kapiteln 5.4.1.1 Synthesen zu den UiO-MOFs, 5.4.2.1 Sorptionsisothermen und PXRDs der UiO-MOFs und in Kapitel 7. Anhang zu finden. Für diese MOFs wurden PXRDs, Stickstoffsorptionen und REM-Aufnahmen gemacht. Zusätzlich wurden zur Berechnung der Defektstellen thermogravimetrische Analysen unter Sauerstoffatmosphäre durchgeführt, um die Defektstellen mit der Methode von Shearer *et al.* Berechnen zu können.[58,59,60] Die Methode ist in der Literatur umfassend untersucht, weshalb an dieser Stelle auf eine ausführliche Vorstellung der Kalkulation verzichtet wird und lediglich die Ergebnisse gezeigt werden. Die Ergebnisübersicht erfolgt in Tabelle 2, die zur Vollständigkeit ebenfalls die zugehörigen BET-Oberflächen angibt.

Tabelle 2: *Übersichtstabelle über die verwendeten MOFs, inkl. der ermittelten Defektstellen und der zugehörigen BET-Oberflächen.*

MOFs	Defektstellenberechnung	BET-Oberfläche [$m^2\ g^{-1}$]
UiO-66 (wenige Defekte)	0	994
UiO-66 (viele Defekte)	1.6	1402
UiO-66 (mittlere Defekte)	1.1	1531
UiO-66-NH_2	0.3	1046
UiO-66-NO_2	-2.6	478
UiO-66-$(OH)_2$	-0.4	550
UiO-67	2	2152
MIL-140A (ohne Modulator)	0 (0.05)	375
MIL-140A (mit Modulator)	0 (0.003)	382
MIL-140B	0 (0.01)	388

MIL-140C	0 (0.01)	696

Es ist jedoch hierbei zu beachten, dass die Defektstellen für die funktionalisierten UiOs stark fehlerbehaftet sein können, da eine saubere Verbrennung des Materials zu ZrO_2 nicht gewährleistet werden kann, aufgrund des Stickstoffs. Dies ist an den Werten von UiO-66-NO_2 und UiO-66-$(OH)_2$ zu erkennen, die im negativen Bereich liegen. Generell entsprechen die Defekte den Erwartungen und die MIL-140 MOFs zeigen, wie gewünscht, keine Defekte. Zusätzlich zeigt UiO-66 (mittlere Defekte) eine höhere Oberfläche, als UiO-66 (viele Defekte) und ist auf das Auftreten von Cluster-Defekten zurückzuführen, die mit dieser Methode nicht erfasst werden können.

Dennoch repräsentieren die synthetisierten MOFs eine große Bandbreite mit unterschiedlichen Eigenschaften, die einen breiten Überblick über die BTEX-Extraktion geben sollten, die im nächsten Kapitel untersucht wird.

4.1.2 BTEX Adsorption mittels HPLC

Die BTEX-Adsorption bzw. -Extraktion aus Wasser erfolgte bei Raumtemperatur für eine Stunde, wobei vollständig unter Vakuum ausgeheizte MOFs verwendet wurden. Hierbei wurden 5 mg MOF und 25 ml BTEX/Wasser-Gemisch (verschiedene Konzentrationen) eingesetzt und die restliche überstehende Lösung mittels HPLC untersucht. Die detaillierten Versuchsangaben bzw. die Kalibriergeraden und die verwendeten Einstellungen für die HPLC sind in den Kapiteln 5.3 Geräte und Parameter und 7. Anhang zu finden.

Die nachfolgende Tabelle 3 zeigt in einer Übersicht die Extraktionswerte für die einzelnen VOCs und die maximale VOC-Kapazität der einzelnen MOFs. Die dargestellten Werte zeigen die maximale Aufnahme bei einer Konzentration von 100 mg ml^{-1} und repräsentieren im Optimalfall die Plateau-Werte der MOFs.

Hierzu wurden die MOFs und ihre Extraktionskapazitäten bei verschiedenen Konzentrationen untersucht (20, 40, 60 und 100 mg ml^{-1}) und gegen die aufgenommen Mengen (mg g^{-1}) aufgetragen, dies ist aufgrund der Übersichtlichkeit nicht gezeigt und nur tabellarisch angegeben. Generell ist der Trend für die Extraktion bzw. Adsorption der BTEX innerhalb der VOCs immer gleich. Ethylbenzol wird von allen MOFs bevorzugt aufgenommen und Benzol zeigt die geringsten Aufnahmen. Die Werte für Xylol sind gesondert zu betrachten, da hierbei das Isomerengemisch aufgenommen wird und nur zwei getrennte Peaks in der HPLC zu identifizieren sind, daher ist eine vollständige Auftrennung der *ortho*-, *meta*- und *para*-Verbindungen nicht möglich. So werden die *ortho*- und die *meta*- und die *para*-Verbindungen getrennt betrachtet und in der Tabelle aufgelistet. Die Verteilung der Xylole innerhalb des Isomerengemischs wurde mittels NMR untersucht und ist im Anhang abgebildet.

Im Nachfolgenden wird sich auf die max. VOC Kapazität bzw. die Gesamtaufnahme der einzelnen MOFs fokussiert und diese mit den Defektstellen bzw. den BET-Oberflächen korreliert.

Tabelle 3: *Ermittelte Extraktionswerte der einzelnen MOFs, mittels HPLC.*

MOF	Benzol	Toluol	Ethylbenzol	Xylol	max. VOC Kapazität
	Extraktion	Extraktion	Extraktion	Extraktion	Extraktion
	[mg g^{-1}]	[mg g^{-1}]	[mg g^{-1}]	[mg g^{-1}]	[mg g^{-1}]
UiO-66 (wenige Defekte)	68.62	102.95	112.58	67.37/ 53.41	404.93
UiO-66 (viele Defekte)	64.16	112.85	134.5	71.99/ 63.05	446.55
UiO-66 (mittlere Defekte)	60.05	119.98	151.76	82.52/ 71.72	486.03
UiO-66-NH_2	21.95	30.82	46.66	29.41/ 19.7	148.54
UiO-66-NO_2	22.14	32.26	44.01	32.05/ 18.03	148.49
UiO-66-$(OH)_2$	16.89	22.03	29.5	18.18/ 12.63	99.23
UiO-67	54.41	65.96	82.81	42.6/ 45.85	291.63
MIL-140A (ohne Modulator)	39.46	57.65	73.93	34.94/ 34.08	240.06
MIL-140A (mit Modulator)	30.03	50.72	62.72	29.04/ 29.25	201.76
MIL-140B	48.05	53.24	66.79	34.34/ 35.64	238.06
MIL-140C	59.17	67.44	81.54	39.4/ 42.57	290.12

Die aus den Daten abgeleiteten Trends für die reinen UiO-MOFs korrelieren mit den Oberflächen der MOFs und weichen somit von den Defektstellen ab. Dies kann mit dem Auftreten von Cluster-Defekten zusammenhängen, die eine BTEX-Adsorption im MOF begünstigen können. Dies würde sowohl die höhere Oberfläche, als auch die gesteigerte BTEX-Adsorption erklären.

Die funktionalisierten UiOs zeigen eine deutlich geringere BTEX-Aufnahme im Vergleich zu den reinen UiOs. Dies kann mit der kleineren Pore zusammenhängen, da die funktionelle Gruppe in diese hineinragt und unter Umständen auch die Diffusion in diese hemmen. Das isoretikulär vergrößerte MOF UiO-67 zeigt ebenfalls eine geringere Adsorptionskapazität im Vergleich zu dem kleineren UiO-66. Dies erscheint konträr zu den reinen UiO-66 Ergebnissen, jedoch kann die vergrößerte Pore einen negativen Einfluss auf die Sorption haben, da die Wechselwirkungen zwischen Linker und BTEX schwächer sein können.
Für die MIL-140 MOFs zeigt sich eine leichte Korrelation zwischen den BET-Oberflächen bzw. der Linkergröße und der BTEX-Extraktionskapazität, so steigt mit der Linkergröße auch die Extraktionskapazität. Der Einfluss eines Modulators ist für die Synthese von MIL-140A nicht entscheidend, wie die Ergebnisse zeigen, und stimmt mit der Aussage überein, dass diese MOFs nahezu defektfrei sind. So hat das MIL-140, welches ohne Modulator synthetisiert wurde, eine höhere BTEX-Adsorption.
Die Ergebnisse zeigen vielversprechende Ansätze für die Extraktion von VOCs aus wässriger Lösung, genauer gesagt der BTEX. Zusätzlich lassen sich die erhaltenen Ergebnisse auch mit den strukturellen Merkmalen der MOFs korrelieren und legen einen grundlegenden Unterschied zwischen den MOFs der UiO- und der MIL-140 Reihe dar.
Die durchgeführte Forschung kann als Basis für weitere Untersuchungen dienen und auch auf weitere VOCs ausgeweitet werden, die spezifischer mit den funktionalisierten MOFs wechselwirken können, oder auch eine höhere Affinität zu Defektstellen bzw. ungesättigten Koordinationsstellen besitzen.

4.2 Al-MOFs mit Tetrafluoroterephthalsäure

In diesem Kapitel wurde die Synthese einer potenziellen MIL-53-analogen Struktur untersucht unter der Verwendung des Linkers Tetrafluoroterephthalsäure. Hierbei ist zu beachten, dass der Linker mit vier Fluor-Atomen deutlich größer ist, als unfunktionalisierte Terephthalsäure. Dies kann bei der Synthese zu erheblichen Veränderungen bzw. zu großen Problemen führen, da Aluminium als Metallquelle kleiner ist, als zum Beispiel Zirconium. Für Zirconium ist eine zu UiO-66 analoge Struktur mit Tetrafluoroterephthalsäure bekannt UiO-66$(F)_4$, welche erstmals erfolgreich von Reinsch *et al.* Im Jahr 2015 synthetisiert wurde.[251] Auf Basis dieser Ergebnisse soll analog hierzu eine Aluminium-Verbindung synthetisiert werden, die einen hohen Fluor-Anteil besitzt, was für potenzielle Anwendungen interessant sein kann.

Die Details zu den Synthesen bzw. den Syntheseversuchen sind in Kapitel 5.4.1.2 Synthesen zu den Al-MOFs mit Tetrafluoroterephthalsäure zusammengefasst und die PXRDS im Kapitel 5.4.2.2 PXRDs zu den Al-MOFs mit Tetrafluoroterephthalsäure dargestellt. Es wurden zur Überprüfung der verschiedenen Synthesen sowohl PXRDs als auch Stickstoffsorptionen aufgenommen, um die Verbindungen zu charakterisieren.

Es wurden verschiedene Syntheseansätze durchgeführt und eine Vielzahl an Parametern variiert, wie die Syntheseroute. So wurden sowohl Autoklavensynthesen als auch Rückflusssynthesen durchgeführt, um die Bildung einer porösen Al-Tetrafluoroterephthalsäure zu gewährleisten. Zusätzlich wurde die Reaktionstemperatur und auch die Reaktionszeit stark variiert, um die Bildung eines kinetischen und eines thermodynamischen Produkts zu untersuchen. Ebenso wurde die doppelte Menge Natriumhydroxid (stöchiometrisch zum Linker) verwendet, um eine vollständige Deprotonierung des Liganden zu erreichen, was für einige Aluminium-MOFs begünstigend ist. Die folgende Tabelle 4 zeigt eine Übersicht über die Synthesebedingungen.

Tabelle 4: *Synthesebedingungen für die verschiedenen Al-Tetrafluoroterephthalsäure-MOF Ansätze.*

Versuch	Lösungsm.	Temp.	Zeit	Bemerkungen
1	Wasser	100 °C	24 h	doppelte Menge NaOH/ refluxiert
2	Wasser	220 °C	3 d	Autoklavensynthese
3	Wasser	100 °C	24 h	Tetrafluoroterephthal- und Terepthalsäure

Es wurden sowohl Synthesen mit gekaufter, wie auch selbst synthetisierter Tetrafluoroterephthalsäure (Pulver und Kristalle erhalten) durchgeführt. Hier wurden exemplarisch drei Ergebnisse vorgestellt, wobei einer der Ansätze ein Mixed-Linker-Ansatz ist, aus Terephthalsäure und Tetrafluoroterephthalsäure.

Keine der durchgeführten Synthesen führte zu einer porösen Struktur, dennoch konnten kristalline Verbindungen erhalten werden, welche als Ausgangsgrundlage für weitere

Forschung dienen könnten.
Die nicht vorhandene Porosität der Materialien kann verschiedene Ursachen haben, die sehr vielfältig sind. So könnten die Synthesebedingungen nicht ausreichend variiert worden sein und die Zeiten verlängert oder verkürzt werden müssen. Das Gleiche gilt für die Temperatur der Synthesen. Zusätzlich ist eine tiefergehende Analyse notwendig, um ein geeigneteres Lösemittel zu finden, anstelle von Wasser. Hier könnte zum Beispiel der Einsatz von Dimethylformamid oder auch Diethylformamid, welches besonders gut für Kristallisationsansätze geeignet ist, erfolgreich sein. Eine weitere Möglichkeit, um die Produkte in poröser Form zu erhalten, könnte der Einsatz von Modulatoren sein, wobei diese für Aluminium-MOFs weniger weit verbreitet sind.

Falls die Variationen der Synthesebedingungen bzw. der Einsatz der anderen Chemikalien nicht zum Erfolg führen sollte, könnte dies an dem Liganden liegen. Dies würde bedeuten, dass die Fluor-Atome zu groß sind und die Pore ausfüllen und für Stickstoff blockieren. Wenn dies untersucht werden sollte, wäre eine Synthesereihe von Vorteil bei der der Funktionalisierungsgrad der Terephthalsäure gesteigert wird, von einem hin zu vier Fluor-Atomen. Aufgrund der nicht vorhandenen Porosität wurde auf ein Abbilden der Stickstoffsorptionsisothermen in dieser Arbeit verzichtet.

5. Experimentalteil

5.1 Allgemeine Hinweise

Falls nicht anders angegeben, wurden alle Synthesen unter atmosphärischen Bedingungen durchgeführt. Glasgeräte wurden durch Aufbewahrung in einem KOH/Isopropanol-Bad für mindestens 24 h und anschließender Neutralisierung in einem Bad mit verd. HCl für einige Stunden gereinigt. Nach der Aufbewahrung in beiden Bädern wurden die Glasgeräte mit deion. H_2O gewaschen und bei 60 °C in einem Trockenschrank für mindestens 24 h getrocknet.

5.2 Verwendete Chemikalien

Alle kommerziell erworbenen Chemikalien wurden, sofern nicht anders angegeben, ohne weitere Aufreinigung eingesetzt (Tabelle 5).

Tabelle 5: *Übersicht über die für diese Arbeit verwendeten Chemikalien, bei kommerziell erhältlichen Chemikalien mit Angabe des Herstellers und der Reinheit.*

Chemikalie	Hersteller	Reinheit	CAS-Nr.:
Aceton	Sigma Aldrich	p.a.	67-64-1
Aluminiumsulfat · 18 H_2O	Sigma Aldrich	≥ 98 %	7784-31-8
2-Aminoterephthalsäure	Acros Organics	99 %	10312-55-7
Benzol	AppliChem	p.a.	71-43-2
4,4‘-Biphenyldicarbonsäure	abcr	98 %	787-70-2
2,5-Dihydroxyterephthalsäure	abcr	97 %	610-92-4
N,N-Dimethylformamid	Fisher Chemical	99.5 %	68-12-2
Ethanol	Sigma Aldrich	≥ 98.8 %	64-17-5
Ethylbenzol	Sigma Aldrich	p.a.	100-41-4
2,6-Naphtalendicarbonsäure	Alfa Aesar	98+	1141-38-4
2-Nitroterephthalsäure	Acros Organics	99 %	610-29-7
Terephthalsäure	Alfa Aeser	> 98 %	100-21-0
2,3,5,6-Tetrafluoroterephthalsäure	BLDpharm	97	652-36-8
Toluol	Sigma Aldrich	99.8	108-88-3
Trifluoressigsäure	Acros Organics	99.5 %	76-05-1
Salzsäure	Sigma Aldrich	37 %	7647-01-0
Xylol (Isomerengemisch)	Sigma Aldrich	≥ 98.5 %	1330-20-7
Zirkonium(IV)-chlorid	ChemPUR	98 %	10026-11-6

5.3 Geräte und Parameter

Gassorptionsmessungen

Die Gassorptionsmessungen wurden an einem NOVA 4000 Gassorptionsanalyser oder einem Autosorb-6 der Firma Quantachrome durchgeführt. Das für die Sorptionsmessung verwendete Gas besaß eine Reinheit von 99.999% (N_2; 5.0). Die Proben wurden vor den Messungen im Vakuum bei materialspezifischen Temperaturen entgast. Die N_2-Sorptionsmessungen wurden in einem mit Flüssigstickstoff gefüllten Dewar bei 77 K durchgeführt. Für die Berechnung der BET-Oberfläche (Brunauer-Emmett-Teller) wurde die Software NovaWin 11.03 verwendet.

Hochdruckflüssigkeitschromatographe (HPLC, high-pressure liquid chromatography)

Die Detektion und Quantifizierung von Benzol, Toluol, Ethylbenzol und Xylol aus wässriger Lösung erfolgte mit Hilfe einer HPLC des Typs LC 20AT der Firma Shimadzu mit einem SPD-M20A Detektor und einer Luna C18(2) (250 * 4.60 mm, 5 micron) Säule von Phenomenex. Das Injektionsvolumen betrug 10 µL. Die Detektion der BTEX erfolgte bei einer Wellenlänge von 201 nm. Als mobile Phase wurde ein Gemisch aus 50 % Wasser und 50 % Acetonitril mit einer Flussrate von 1.4 ml min^{-1} verwendet, bei 30 °C. Die Messdauer betrug 20 bzw. 30 Minuten für die Standards bzw. für die Proben. Die Gehaltsbestimmung der BTEX erfolgte durch Integration der Peakflächen. Zuvor wurden jeweils Kalibrierkurven erstellt.

NMR-Spektroskopie (Kernmagnetresonanzspektroskopie)

Das ^{1}H-NMR-Spektrum des Xylol-Isomerengemisches wurden an einem FT-NMR-Spektrometer Avance III – 300 gemessen. Die Messung wurde bei 298 K durchgeführt. Die chemischen Verschiebungen sind in ppm angegeben. Die Messung wurde in deuteriertem Benzol aufgenommen (das Restprotonensignal 1H-NMR 7.16 ppm).

Rasterelektronenmikroskop (REM)

Die REM-Aufnahmen wurden an einem JSM-6510 mit einer LaB6- oder einer Wolfram-Kathode der Firma Jeol durchgeführt. Die EDX-Messungen wurden an einem Jeol Q-SEM Paket der Firma Bruker mit einem Si(Li)-Halbleiter-Detektor durchgeführt.

Pulverröntgendiffraktometrie (PXRD)

Die Pulverröntgendiffraktogramme wurden an einem D2 Phaser der Firma Bruker (300 W, 30 kV, 10 mA) aufgenommen. Gemessen wurde bei Raumtemperatur im 2 Theta-Winkel bei einer Cu-Kα-Strahlung (λ = 1.54182 Å) zwischen 5°< 2θ <50°. Für weitere Aufnahmen wurde ein Miniflex 300 der Firma Rigaku (600 W, 40 kV, 15 mA) verwendet. Die Probe wurde auf flachen Si-Probenträgern aufgebracht. Als Messbereich wurde 5°< 2θ <50° gewählt. Verwendet wurde monochromatische Cu-Kα-Strahlung (λ = 1.54182 Å). Alle Proben wurden

bei Raumtemperatur gemessen und zuvor für mindestens 24 Stunden im Vakuumtrockenschrank getrocknet.

Die Auswertung erfolgte mithilfe der Software Match! der Firma Crystal Impact in der Version 3.5.3.

Syntheseöfen

Die Autoklavensynthesen erfolgten in einem programmierfähigen Ofen der Firma Memmert.

Thermogravimetrische Analyse

Die TGA wurde an einem TG Tarsus 209 F3 der Firma Netzsch durchgeführt. Die Proben für die Defektstellenberechnung wurden unter Sauerstoffatmosphäre durchgeführt. Die Analyse der Proben wurde zwischen 20 °C und 1000 °C mit einer Heizrate von 5 K min^{-1} durchgeführt.

Trocknung der Produkte

Im Vakuumofen des Typs VACUTHERM der Firma Heraeus wurden die einzelnen Proben bei 60-80 °C getrocknet.

5.4 Präparativer Teil

Die Synthesen zu den unveröffentlichten Ergebnissen werden in den folgenden Unterkapiteln aufgezeigt, ebenso die zu den synthetisierten MOFs gehörenden PXRDs und Sorptionsisothermen und weitergehende Analytik, die nicht im Anhang (Kapitel 7) abgebildet und zusammengefasst ist.

5.4.1 Synthesen

Das Kapitel 5.4.1 Synthesen ist ebenso untergliedert, wie die zugehörigen Kapitel 4.1 BTEX Adsorption mit MOFs und 4.2 Al-MOFs mit Tetrafluoroterephthalsäure mit den zugehörigen aufbereiteten Ergebnissen.

5.4.1.1 Synthesen zu den UiO-MOFs

UiO-66 (wenige Defekte)

UiO-66 mit einer geringen Anzahl an Defekten wurde nach den Methoden von Shearer *et al.* synthetisiert.[58,59,60] Hierzu wurden die Edukte mit einem Modulator (Zirconiumchlorid: 1.8907 g, 8.11 mmol / Terephthalsäure 2.6950 g, 16.22 mmol / Salzsäure konz. 1.42 ml / DMF 48 ml) unter Rühren zusammengegeben und bei 220 °C für 20 h in den Ofen gestellt in einem Stahl-Autoklaven mit Teflon-Inlay. Anschließend wurde das Produkt jeweils zweimal mit DMF und Methanol gewaschen und bei 60 °C unter Vakuum getrocknet. Die Ausbeute betrug 2.3828 g und konnte mittels PXRD als UiO-66 identifiziert werden.

UiO-66 (viele Defekte)

UiO-66 mit einer großen Anzahl an Defekten wurde nach den Methoden von Shearer *et al.* synthetisiert.[58,59,60] Hierzu wurden die Edukte mit einem Modulator (Zirconiumchlorid: 0.8626 g, 3.699 mmol / Terephthalsäure 0.6147 g, 3.702 mmol / Trifluoressigsäure 10 ml / DMF 100 ml / Wasser 0.2 ml) unter Rühren zusammengegeben und bei 120 °C für 72 h in den Ofen gestellt in einer Glasflasche mit Schraubverschluss. Anschließend wurde das Produkt jeweils zweimal mit DMF und Methanol gewaschen und bei 60 °C unter Vakuum getrocknet. Die Ausbeute betrug 0.963 g und konnte mittels PXRD als UiO-66 identifiziert werden.

UiO-66 (mittlere Defekte)

UiO-66 mit einer mittleren Anzahl an Defekten wurde nach den Methoden von Shearer *et al.* synthetisiert.[58,59,60] Hierzu wurden die Edukte mit einem Modulator (Zirconiumchlorid: 1.8914 g, 8.11 mmol / Terephthalsäure 2.6950 g, 16.22 mmol / Salzsäure konz. 1.42 ml / DMF 49 ml) unter Rühren zusammengegeben und bei 100 °C für 24 h in den Ofen gestellt in einer Glasflasche mit Schraubverschluss. Anschließend wurde das Produkt jeweils zweimal mit DMF und Methanol gewaschen und bei 60 °C unter Vakuum getrocknet. Die Ausbeute betrug 2.4277 g und konnte mittels PXRD als UiO-66 identifiziert werden.

UiO-66-NH_2

UiO-66-NH_2 wurde nach den Methoden von Aguilera-Sigalat *et al.* synthetisiert.[117] Hierzu wurden die Edukte mit einem Modulator (Zirconiumchlorid: 0.2510 g, 1.07 mmol / Aminoterephthalsäure 0.2682 g, 1.48 mmol / Salzsäure konz. 2 ml / DMF 30 ml) unter Ultraschall (vorher bereits im Ultraschall getrennt gelöst) zusammengegeben und bei 80 °C für 12 h in den Ofen gestellt in einer Glasflasche mit Schraubverschluss. Anschließend wurde das Produkt jeweils dreimal mit DMF und Ethanol gewaschen und bei 60 °C unter Vakuum getrocknet. Die Ausbeute betrug 0.3465 g und konnte mittels PXRD als UiO-66-NH_2 identifiziert werden.

UiO-66-NO_2

UiO-66-NO_2 wurde nach der Methode von Rada *et al.* synthetisiert.[252] Hierzu wurden die Edukte ohne Modulator (Zirconiumchlorid: 1.4687 g, 6.3 mmol / Nitroterephthalsäure 1.2248 g, 5.8 mmol / DMF 86 ml) unter Ultraschall für 25 Minuten zusammengegeben und bei 120 °C für 24 h in den Ofen gestellt in einer Glasflasche mit Schraubverschluss. Anschließend wurde das Produkt dreimal mit DMF gewaschen und bei 60 °C unter Vakuum getrocknet. Die Ausbeute betrug 1.8829 g und konnte mittels PXRD als UiO-66 identifiziert werden.

UiO-66-$(OH)_2$

UiO-66-$(OH)_2$ wurde nach der Methode von Katz *et al.* synthetisiert.[253] Hierzu wurden die Edukte mit einem Modulator (Zirconiumchlorid: 0.2503 g, 1.08 mmol / 2,5-Dihydroxyterephthalsäure 0.2939 g, 1.50 mmol / Salzsäure konz. 2 ml / DMF 30 ml) unter Ultraschall (vorher bereits im Ultraschall getrennt gelöst) zusammengegeben und bei 80 °C für 12 h in den Ofen gestellt in einer Glasflasche mit Schraubverschluss. Anschließend wurde das Produkt jeweils dreimal mit DMF und Ethanol gewaschen und bei 60 °C unter Vakuum getrocknet. Die Ausbeute betrug 0.3259 g und konnte mittels PXRD als UiO-66-$(OH)_2$ identifiziert werden.

UiO-67

UiO-67 wurde nach der Methode von Katz *et al.* synthetisiert.[253] Hierzu wurden die Edukte mit einem Modulator (Zirconiumchlorid: 0.2517 g, 1.08 mmol / Biphenyldicarbonsäure 0.3688 g, 1.52 mmol / Salzsäure konz. 2 ml / DMF 60 ml) unter Ultraschall (vorher bereits im Ultraschall getrennt gelöst) zusammengegeben und bei 80 °C für 24 h in den Ofen gestellt in einer Glasflasche mit Schraubverschluss. Anschließend wurde das Produkt jeweils dreimal mit DMF und Ethanol gewaschen und bei 60 °C unter Vakuum getrocknet. Die Ausbeute betrug 0.3065 g und konnte mittels PXRD als UiO-67 identifiziert werden.

MIL-140A (ohne Modulator)

MIL-140A (ohne Modulator) wurde nach der Methode von Schulz *et al.* synthetisiert.[254] Hierzu wurden die Edukte ohne Modulator (Zirconiumchlorid: 2.2654 g, 9.72 mmol / Terephthalsäure 1.6148 g, 9.72 mmol / DMF 30 ml) unter Rühren zusammengegeben und bei 150 °C für 24 h in den Ofen gestellt in einer Glasflasche mit Schraubverschluss. Anschließend wurde das Produkt jeweils einmal mit DMF und Aceton gewaschen und bei 60 °C unter Vakuum getrocknet. Die Ausbeute betrug 1.9632 g und konnte mittels PXRD als MIL-140A identifiziert werden.

MIL-140A (mit Modulator)

MIL-140A (mit Modulator) wurde nach den Methoden von Schulz *et al.* synthetisiert.[254] Hierzu wurden die Edukte mit Modulator (Zirconiumchlorid: 2.2655 g, 9.72 mmol / Terephthalsäure 1.6143 g, 9.72 mmol / Essigsäure 0.929 ml / DMF 30 ml) unter Rühren zusammengegeben und bei 150 °C für 24 h in den Ofen gestellt in einer Glasflasche mit Schraubverschluss. Anschließend wurde das Produkt jeweils einmal mit DMF und Aceton gewaschen und bei 60 °C unter Vakuum getrocknet. Die Ausbeute betrug 2.4248 g und konnte mittels PXRD als MIL-140A identifiziert werden.

MIL-140B

MIL-140B wurde nach der Methode von Guillerm *et al.* synthetisiert.[255] Hierzu wurden die Edukte mit Modulator (Zirconiumchlorid: 0.5250 g, 2.25 mmol / Naphthalendicarbonsäure 0.9750 g, 4.5 mmol / Essigsäure 0.257 ml / DMF 11.25 ml) unter Rühren zusammengegeben und bei 220 °C für 6 h in den Ofen gestellt in einem Stahl-Autoklaven mit Teflon-Inlay. Anschließend wurde das Produkt jeweils einmal mit DMF und Aceton gewaschen und bei 60 °C unter Vakuum getrocknet. Die Ausbeute betrug 0.6653 g und konnte mittels PXRD als MIL-140B identifiziert werden.

MIL-140C

MIL-140C wurde nach der Methode von Guillerm *et al.* synthetisiert.[255] Hierzu wurden die Edukte mit Modulator (Zirconiumchlorid: 0.8739 g, 3.75 mmol / Biphenyldicarbonsäure 1.8155 g, 7.5 mmol / Essigsäure 1.073 ml / DMF 19 ml) unter Rühren zusammengegeben und bei 220 °C für 12 h in den Ofen gestellt in einem Stahl-Autoklaven mit Teflon-Inlay. Anschließend wurde das Produkt jeweils einmal mit DMF und Aceton gewaschen und bei 60 °C unter Vakuum getrocknet. Die Ausbeute betrug 1.1198 g und konnte mittels PXRD als MIL-140C identifiziert werden.

5.4.1.2 Synthesen zu den Al-MOFs mit Tetrafluoroterephthalsäure

Synthesevariationen mit Tetrafluoroterephthalsäure

Die Synthesen mit Tetrafluoroterephthalsäure wurden sowohl unter Rückflussbedingungen als auch unter solvothermalen Bedingungen durchgeführt. Hierzu wurden die Edukte im Zweihalskolben oder im Autoklaven zusammengegeben und die Synthese gestartet.
Bei der Synthese unter Rückfluss wurde der Linker mit Natriumhydroxid (Tetrafluoroterephthalsäure 0.0837 g, 0.35 mmol / Natriumhydroxid 0.0289 g, 0.7 mmol) gelöst und anschließend das Metallsalz (Aluminiumsulfat 0.2348 g, 0.35 mmol) hinzugegeben und für 24 h zum Sieden erhitzt, in Reinstwasser (10 ml). Anschließend wurde das Produkt dreimal mit Wasser gewaschen und bei 80 °C unter Vakuum getrocknet. Die Ausbeute betrug 0.0689 g.
Bei der Autoklavensynthese wurden der Linker mit Natriumhydroxid (Tetrafluoroterephthalsäure 0.0831 g, 0.35 mmol / Natriumhydroxid 0.0312 g, 0.7 mmol) gelöst und anschließend das Metallsalz (Aluminiumsulfat 0.2332 g, 0.35 mmol) hinzugegeben und in den Autoklaven überführt. Anschließend wurde das Produkt dreimal mit Wasser gewaschen und bei 80 °C unter Vakuum getrocknet. Die Ausbeute betrug 0.0737 g.

Synthese mit Tetrafluoroterephthalsäure und Terephthalsäure (Mixed-Linker-Ansatz)

Bei der Rückflusssynthese mit zwei verschiedenen Liganden wurde analog zum Ansatz mit einem einzigen Liganden vorgegangen und die folgenden Einwaagen verwendet: Aluminiumsulfat 0.6661 g, 1.00 mmol / Terephthalsäure 0.0838 g, 0.5 mmol / Tetrafluoroterephthalsäure 0.1191 g, 0.55 mmol / Natriumhydroxid 0.0853 g, 2.0 mmol / Wasser 30 ml. Anschließend wurde das Produkt dreimal mit Wasser gewaschen und bei 80 °C unter Vakuum getrocknet. Die Ausbeute betrug 0.2322 g.

5.4.2 PXRDs und Sorptionsisothermen

Dieses Kapitel beinhaltet die PXRDs und die Stickstoffsorptionsisothermen der in Kapitel 5.4.1 Synthesen hergestellten MOFs und ist analog zu den anderen Kapiteln aufgeteilt in zwei Unterkapitel, die die beiden Themengebiete voneinander abgrenzen.

5.4.2.1 Sorptionsisothermen und PXRDs der UiO-MOFs

Die nachfolgenden Abbildungen zeigen jeweils das PXRD und die zugehörige Stickstoffsorptionsisotherme des jeweiligen MOFs.

UiO-66 (wenige Defekte)

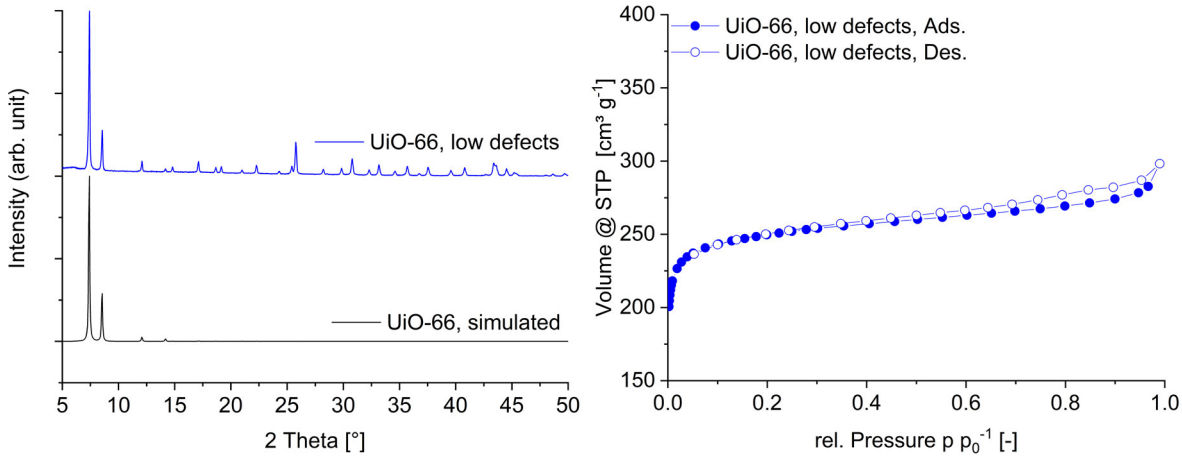

Abbildung 12: *Aufgenommenes PXRD, inklusive des simulierten PXRDs (CCDC: 733458, Ref.: 108) von UiO-66 mit wenigen Defekten und die zugehörige Stickstoffsorption.*

UiO-66 (viele Defekte)

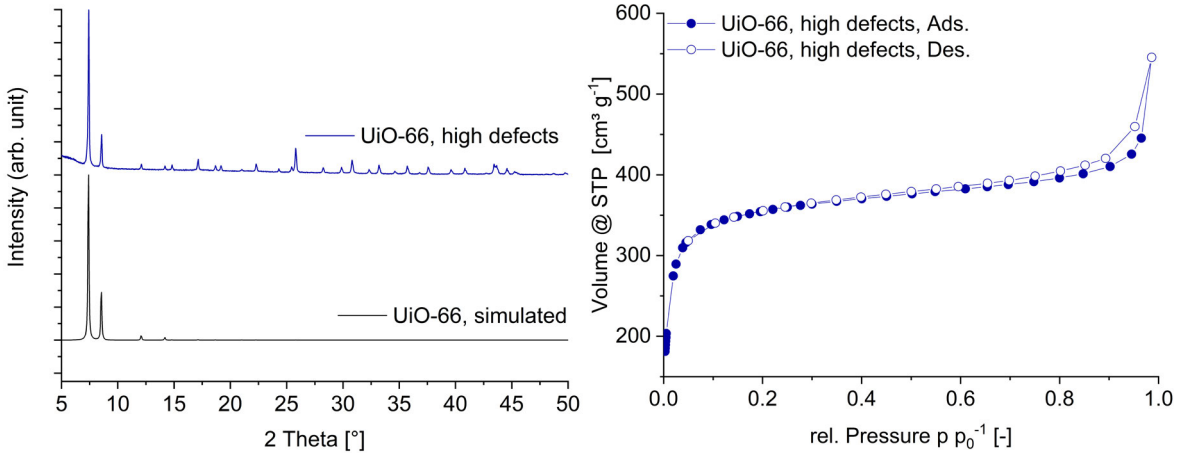

Abbildung 13: *Aufgenommenes PXRD, inklusive des simulierten PXRDs (CCDC: 733458, Ref.: 108) von UiO-66 mit vielen Defekten und die zugehörige Stickstoffsorption.*

UiO-66 (mittlere Defekte)

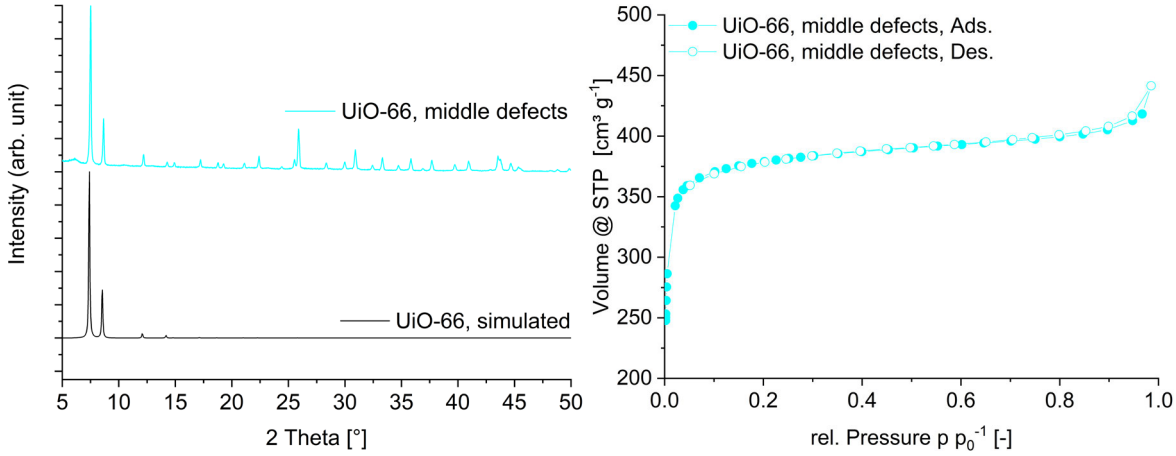

Abbildung 14: *Aufgenommenes PXRD, inklusive des simulierten PXRDs (CCDC: 733458, Ref.: 108) von UiO-66 mit mittleren Defekten und die zugehörige Stickstoffsorption.*

UiO-66-NH_2

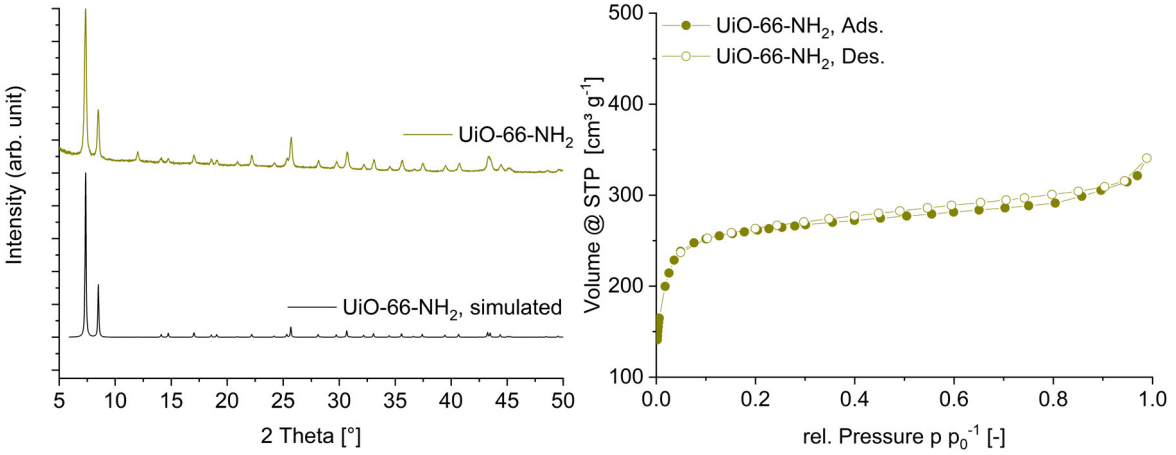

Abbildung 15: *Aufgenommenes PXRD, inklusive des simulierten PXRDs (CCDC: 1405751, Ref.: 256) von UiO-66-NH_2 und die zugehörige Stickstoffsorption.*

UiO-66-NO_2

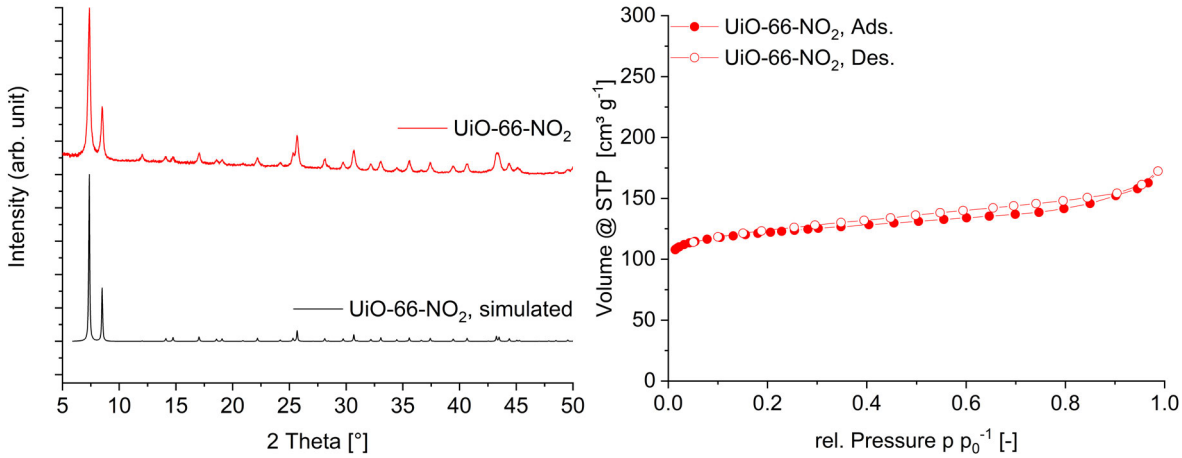

Abbildung 16: *Aufgenommenes PXRD, inklusive des simulierten PXRDs (CCDC: 1405752, Ref.: 256) von UiO-66-NO_2 und die zugehörige Stickstoffsorption.*

UiO-66-(OH)$_2$

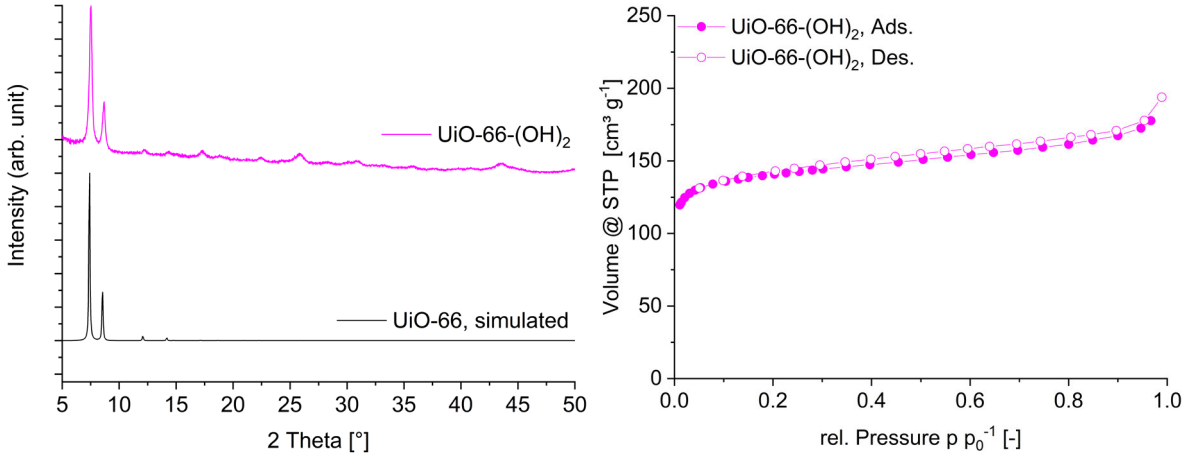

Abbildung 17: *Aufgenommenes PXRD, inklusive des simulierten PXRDs (CCDC: 733458, Ref.: 108) von UiO-66-(OH)$_2$ und die zugehörige Stickstoffsorption.*

UiO-67

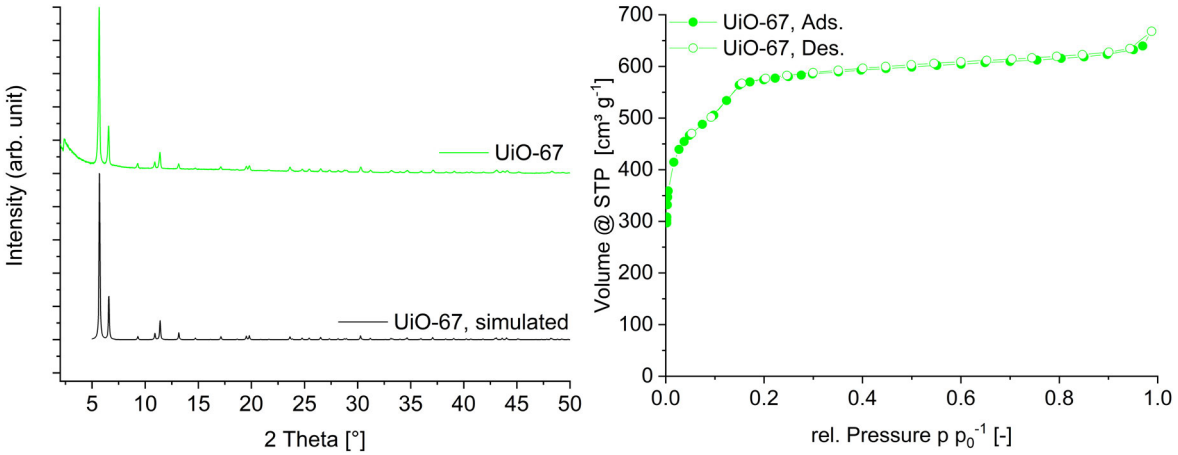

Abbildung 18: *Aufgenommenes PXRD, inklusive des simulierten PXRDs (CCDC: 1018032, Ref.: 257) von UiO-67 und die zugehörige Stickstoffsorption.*

MIL-140A (ohne Modulator)

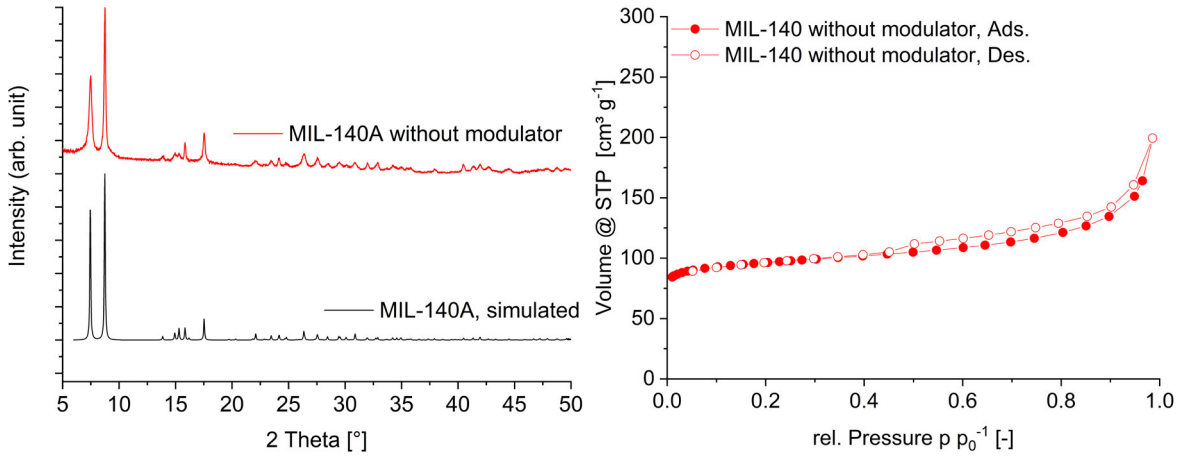

Abbildung 19: *Aufgenommenes PXRD, inklusive des simulierten PXRDs (CCDC: 905026, Ref.: 255) von MIL-140A ohne Modulator und die zugehörige Stickstoffsorption.*

MIL-140A (mit Modulator)

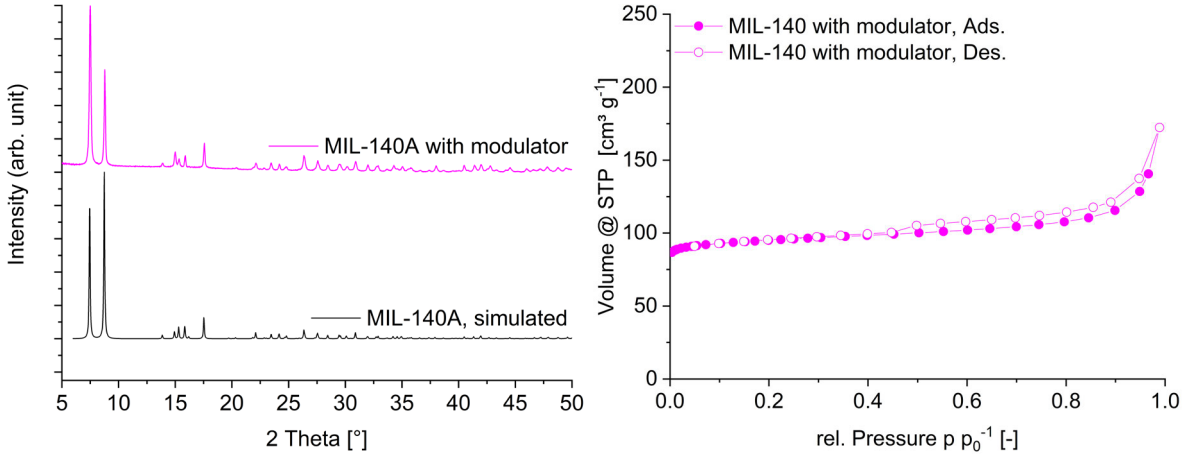

Abbildung 20: *Aufgenommenes PXRD, inklusive des simulierten PXRDs (CCDC: 905026, Ref.: 255) von MIL-140A mit Modulator und die zugehörige Stickstoffsorption.*

MIL-140B

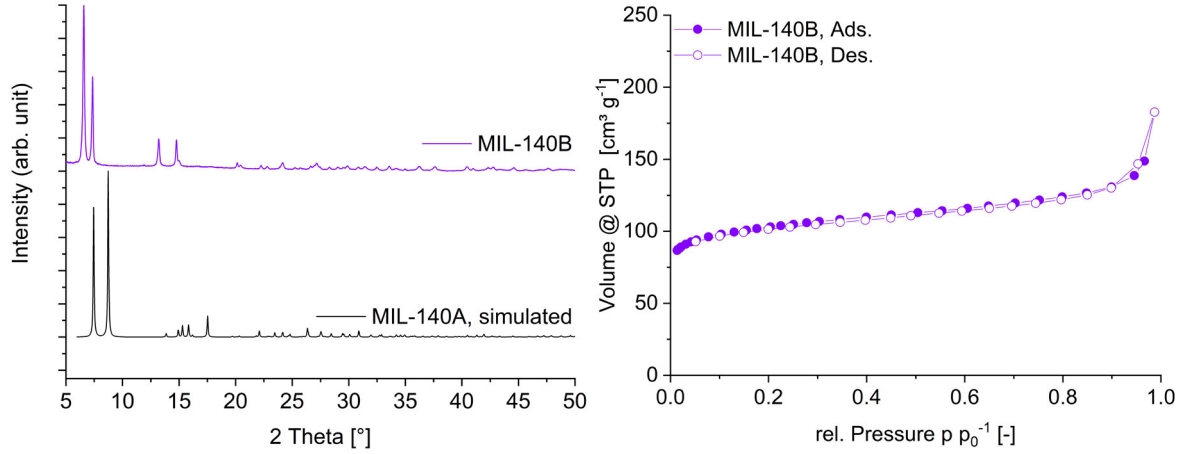

Abbildung 21: *Aufgenommenes PXRD, inklusive des simulierten PXRDs (CCDC: 905026, Ref.: 255) von MIL-140B und die zugehörige Stickstoffsorption.*

MIL-140C

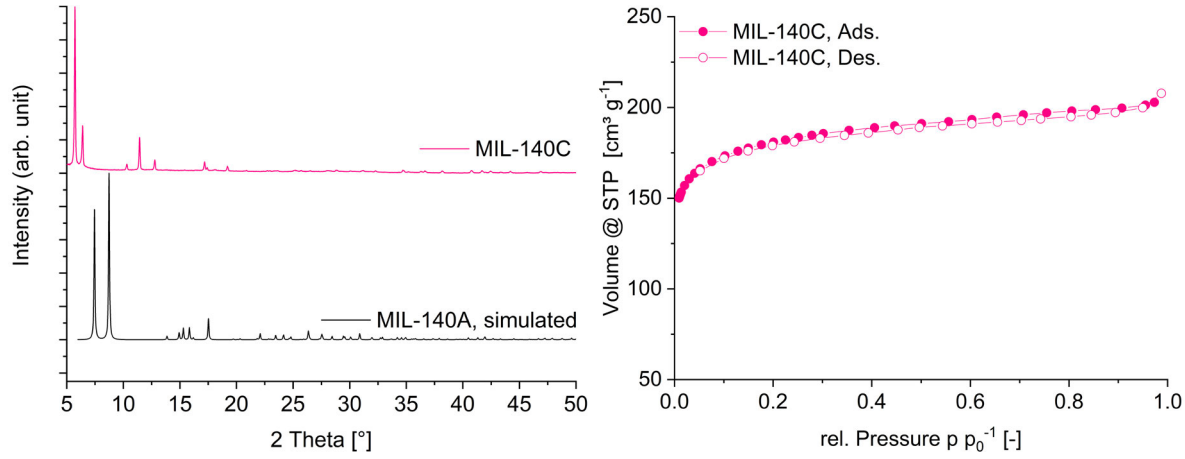

Abbildung 22: *Aufgenommenes PXRD, inklusive des simulierten PXRDs (CCDC: 905026, Ref.: 255) von MIL-140C und die zugehörige Stickstoffsorption.*

5.4.2.2 PXRDs zu den Al-MOFs mit Tetrafluoroterephthalsäure

Die entstandenen Materialien zeigen keine Porosität, weshalb an dieser Stelle auf das Abbilden der aufgenommenen Stickstoffsorptionsisothermen verzichtet wird. Dementsprechend sind nur die aufgenommen PXRDs in der nachfolgenden Abbildung 23 gezeigt.

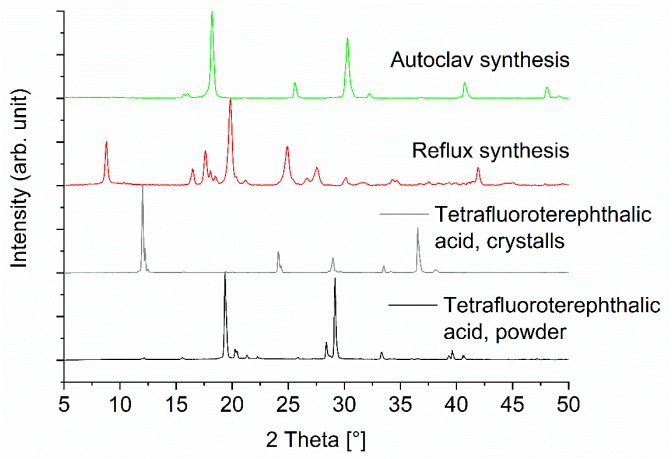

Abbildung 23: *PXRDs der Synthesen mit Tetrafluoroterephthalsäure, inklusive der reinen Säure.*

6. Zusammenfassung

Im Rahmen dieser Arbeit wurden die Sorptionseigenschaften von Metall-organischen Gerüstverbindungen und Kompositmaterialien, bestehend aus MOFs und verschiedenen Polymeren untersucht. Hierbei wurden sowohl die Eigenschaften von MOFs und den Kompositen gegenüber verschiedenen Gasen und Dämpfen untersucht als auch aufbauend auf diesen Ergebnissen theoretische Berechnungen für die Selektivität und die Wechselwirkungen der Materialien mit den Adsorptiven durchgeführt.
Diese Arbeit beschäftigte sich mit MOFs, die Bindungen beinhalten die nach dem HSAB-Konzept als stabil klassifiziert werden, wie in der Kurzzusammenfassung bereits erläutert wurde. Hierzu wurden in drei von fünf Publikation die Aluminium-MOFs in den Vordergrund gestellt und deren Verhalten von der Synthesen über die Charakterisierung bis hin zu den Sorptionseigenschaften detailliert untersucht.

Die erste der fünf Veröffentlichungen beschäftigte sich mit alternativen Syntheserouten für die stabilen Aluminium-MOFs und den Einfluss dieser auf die Kristallinität und die Porosität der Materialien. Hierzu wurde die sogenannte Trockengelsynthese nähergehend untersucht. Bei dieser Syntheseform wurden die Edukte oberhalb des Lösemittels auf einem Sieb eingewogen und es kam unter solvothermalen Bedingungen zur Reaktion im Dampfraum. Das Lösemittel kondensierte am Deckel des geschlossenen Systems aus und tropfte auf das Sieb und setzte die Edukte im Optimalfall zum gewünschten Produkt um. Die Menge an Lösemittel ist meistens ausreichend um die Synthese durchzuführen, aber zu wenig um das Produkt oder nicht reagierte Edukte vom Sieb zu waschen und in das Lösemittel zu spülen. Somit blieb nach dem Abkühlen des Reaktionsgefäßes das Lösemittel am Boden zurück und konnte wiederverwendet werden. So konnte Lösemittel eingespart werden, was ein wichtiger Aspekt für die Industrie ist. In dieser Veröffentlichung wurden im Einzelnen die MOFs Aluminiumfumarat, CAU-10-H und MIL-160 untersucht. Diese MOFs konnten mit kommerziell erhältlichen Liganden synthetisiert werden und zeigten alle eine hydrothermale Stabilität und sind für einen potenziellen Einsatz in adsorptionsgetriebenen Wärmetransformationsmaschinen geeignet. Für einen Materialvergleich wurden die MOFs einmal nach den literaturbekannten Synthesen hergestellt und ebenfalls mit der Methode der Trockengelsynthese. Hierbei ist hervorzuheben, dass die Synthesebedingungen bei der Trockengelsynthese variiert worden sind, um die optimalen Reaktionsbedingungen zu finden. Im Detail wurde die Reaktionszeit und die Reaktionstemperatur verändert und von den Literaturbedingungen ausgehend angepasst. Die optimalen Reaktionsbedingungen wurden durch die Eigenschaften der Produkte ermittelt, wobei hier der Fokus auf den ermittelten Oberflächen lag und das Produkt mit den höchsten Oberflächen zum Vergleich herangezogen wurde. Der größte Unterschied zwischen den nach Literatur hergestellten und den nach der Trockengelsynthese synthetisierten MOFs war das absolute Porenvolumen. Die MOFs, die

mittels Trockengelsynthese hergestellt wurden, zeigten ein höheres Porenvolumen und dies war auf eine Agglomeration der Partikel zurückzuführen, die bei den anderen ursprünglichen Syntheserouten nicht so stark ausgeprägt war. Dieses Phänomen ist in einer potenziellen Anwendung nicht besonders relevant für die Wasseraufnahme, da die maximale Aufnahme und vor allem der Aufnahmebereich durch die Mikroporen des Materials definiert wird. Daher sind die MOFs, die mittels der Trockengelsynthese hergestellt werden, eine Alternative bei der Herstellung von Aluminium-MOFs.

Die zweite der fünf Veröffentlichungen schließt an das erste Thema an und beschäftigte sich ebenfalls mit dem potenziellen Einsatz von MOFs im Bereich der adsorptionsgetriebenen Wärmetransformationsmaschinen. Jedoch wurde hier der Fokus mehr auf die Anwendung gelegt und schloss sich somit thematisch an die erste Publikation an. Es wurden ebenfalls die MOFs Aluminiumfumarat und MIL-160 betrachtet und deren Einbau in Kompositmaterialien. Diese Komposite sind für eine Formgebung des MOF-Pulvers in eine anwendungsgeeignete Form wichtig und diese Formgebung wird zum Beispiel durch den Einsatz von Polymeren erreicht. In dieser Veröffentlichung wurden MOF@Polymer-Kompositmaterialien mit Chitosan hergestellt. Chitosan ist ein Biopolymer, welches durch eine alkalische Deacetylierung von Chitin-Panzern verschiedener Meerestiere gewonnen werden kann und besitzt fungistatische Eigenschaften. Dies bedeutet, dass es Pilzwachstum hemmen kann und macht es somit interessant für verschiedene Anwendungen. In dieser Veröffentlichung wurden verschiedene MOF@Chitosan-Komposite mit unterschiedlichen MOF-Beladungen hergestellt und die fungistatischen Eigenschaften der Komposite mit einer MOF-Beladung von 90 % und die der jeweiligen Edukte gegenüber zwei verschiedenen Pilzen getestet (*Chaetomium globosum* und *Aspergillus falconensis*). Die Komposite wurden durch eine Tropfmethode der MOF-Polymer-Suspension in den gelösten Quervernetzer $Na_5P_3O_{10}$ hergestellt, was sich als schnelle und effektive Syntheseroute herausstellte, mit einer für die potenzielle Anwendung geeignete Form (Kügelchen).
Gegenüber *Chaetomium globosum* konnte keine fungistatische Wirkung des Chitosans festgestellt werden und die Kompositmaterialien wurden durch den aggressiven Pilz überwachsen. Jedoch zeigten die Komposite gegenüber dem Pilz *Aspergillus falconensis* einen gewissen Effekt, der durch das Chitosan bedingt wurde. Zusätzlich zu den reinen MOFs zeigten die MOF@Chitosan-Komposite ebenfalls eine deutlich erhöhte Resistenz gegenüber den Pilzen als die Vergleichsmaterialien, bestehend aus den MOFs und den synthetischen Polymeren PVA oder Silikophen®. Ein weiterer interessanter Aspekt war das unterschiedliche Verhalten der reinen MOFs unter den Testbedingungen. Hierbei zeigte MIL-160 eine deutlich höhere Stabilität als Aluminiumfumarat und lässt auf einen eventuellen Einfluss des Liganden schließen, was in nachfolgenden Veröffentlichungen untersucht werden könnte.

Die dritte der fünf Veröffentlichungen behandelt ebenfalls die Eigenschaften verschiedener MOF@Polymer-Komposite und fokussiert sich auf die Aufnahmen bei der Wassersorption. Hierzu wurden die fünf MOFs MIL-101(Cr), Aluminiumfumarat (Basolite® A520), MIL-53-TDC, Zirconiumfumarat und UiO-66 untersucht in Kombination mit verschiedenen Polyelektrolyten. Diese Kompositmaterialien wurden nach dem Kern-Hülle-Prinzip hergestellt und die MOFs mit verschiedenen Polymerschichten überzogen. Hierbei wurden bis zu drei Schichten und somit auch drei Syntheseschritte durchgeführt, um das endgültigen Kompositmaterial zu erhalten. Diese mehrschrittigen Beschichtungen des MOFs werden auch als Schicht-für-Schicht-Ansatz bezeichnet. Es können somit auch verschiedene Polymere eingesetzt werden, um die Eigenschaften des gewünschten Materials gezielt zu variieren.
In dieser Publikation konnten somit die Massenprozente des eingebauten Polymers bzw. der eingebauten Polymere von 0.6-2.5 bis zu 50 % variiert werden. Die erhaltenen Kompositmaterialien zeigten trotz der hohen Polymerbeladung einen S-typischen Isothermenverlauf bei der Wassersorption, was für reine MOFs üblich ist, beim Betrachten des relativen Druckbereichs bis hin zu $p\,p_0^{-1} = 0.9$. Dennoch zeigten die Komposite Veränderungen gegenüber den reinen MOFs und dies konnte auf die Kern-Hülle-Struktur und die eingesetzten Polymere zurückgeführt werden. Hierbei trat eine Veränderung der maximalen Aufnahme ein, ebenso wie eine Verschiebung der Aufnahme im relativen Druckbereich bei der Wassersorption. Diese Beobachtungen korrelierten mit der hydrophilen oder hydrophoben Oberfläche der jeweiligen Kompositmaterialien. Wichtig zu betonen bei all diesen Änderung war, dass die Struktur des MOFs unbeeinflusst hiervon war, was mit Pulverröntgendiffraktogrammen bestätigt werden konnte. Die dünnen Polymerschichten zeigten im Rasterelektronenmikroskop erst eine Veränderung der Partikel, wenn mehrere Schichten das MOF umschlossen, nicht schon bei einer einzelnen Polymerschicht.
In gewissen Einzelfällen konnte die maximale Wasseraufnahme durch den Einsatz von Polymeren über die Wasseraufnahme der reinen MOFs gesteigert werden und macht diese für eine potenzielle Anwendung interessant.

Die vierte der fünf Publikationen behandelt ein einzelnes MOF im Detail und ist die erste umfassende Charakterisierung der Sorptionseigenschaften dieses relativ neuen MOFs. Es handelt sich um das MOF CAU-23, ein Polymorph des länger literaturbekannten MOFs MIL-53-TDC. Diese Veröffentlichung untersuchte nicht nur die Sorptionseigenschaften dieses Aluminium-MOFs, sondern ordnete diese ebenfalls in die bereits literaturbekannten Daten ein und verglich diese mit denen für CAU-23.
Die Sorptionseigenschaften von CAU-23 wurden gegenüber den folgenden Gasen untersucht: CO_2, H_2, CH_4 und SO_2. Die Isothermen dieser Gase wurden bei verschiedenen Temperaturen aufgenommen, um anschließend die Adsorptionsenthalpien berechnen zu können und ebenso wurden die Selektivitäten eines binären Gemisches für CAU-23 analysiert. Für CO_2 wurde

zusätzlich eine Hochdrucksorption aufgenommen bis zu einem absoluten Druck von 20 bar bei Raumtemperatur. Die CO_2-Aufnahme von CAU-23 betrug 3.97 mmol g^{-1} bei 20 °C und die H_2-Aufnahme 10.25 mmol g^{-1} bei –196 °C und bedeutete im Vergleich mit den Aluminium-MOFs den zweitbesten Wert nach MIL-160. Die CH_4-Aufnahme bei 20 °C lag bei 0.89 mmol g^{-1} und war im gleichen Rahmen wie die anderen Aluminium-MOFs. Die SO_2-Aufnahme bei 20 °C von 8.4 mmol g^{-1} folgte sehr gut den mit Stickstoff ermittelten Porositäten der einzelnen Aluminium-MOFs. Eine höhere SO_2-Aufnahme zeigten nur die MOFs MIL-53 und MIL-100.

Im Vergleich zu den Werten bei Drücken bis 1 bar war der Wert der Hochdruckmessung für CO_2 von CAU-23 im Literaturvergleich besonders hervorzuheben mit einer Aufnahme von 33 wt-% bei 20 bar und 20 °C.

Im weiteren Verlauf dieser Arbeit wurden theoretische Rechnungen durchgeführt, die die umfassende Charakterisierung der Sorptionseigenschaften von CAU-23 abschließend in die Literatur der Aluminium-MOFs einordnen sollten. Hierzu wurden, wie bereits erwähnt, die Messungen eines Adsorptivs bei zwei Temperaturen bzw. die Messungen von zwei Adsorptiven bei derselben Temperatur herangezogen. Dadurch konnten die Adsorptionsenthalpien der Gase und die IAST-Selektivitäten kalkuliert und eingeordnet werden. Die Adsorptionsenthalpien bei Beladungen nahe Null ΔH_{ads}^0 für CO_2 und SO_2 lagen bei –22 kJ mol^{-1} für CO_2 und bei –38 kJ mol^{-1} für SO_2 und somit am unteren Ende des Literaturbereichs (für die anderen Aluminium-MOFs: –22 kJ mol^{-1} bis –39 kJ mol^{-1} für CO_2; –41 bis –51 kJ mol^{-1} für SO_2). Jedoch steigerten diese Werte sich für CO_2 zu –25 kJ mol^{-1}und für SO_2 zu –57 kJ mol^{-1}.

Die theoretische CO_2/CH_4- und die SO_2/CO_2-Trennleistung ermittelt mit den IAST-Selektivitäten lag bei 5 und 27-50 (je nach molarem Verhältnis und Kalkulationsmodel) und stimmte so mit der Literatur für die anderen Aluminium-MOFs überein, die im Bereich von 4.5-6.3 und 17-50 lagen. Lediglich MIL-53-TDC und MIL-160 zeigten bei einem molaren Verhältnis von 0.5 für SO_2/CO_2 deutlich höhere IAST-Selektivitäten von 83 bzw. 126 in der Literatur. Dennoch zeigte sich, dass CAU-23 ein interessanter Kandidat für potenzielle technische Anwendungen ist.

Die letzte der fünf Veröffentlichungen ist eine breite Übersicht von verschiedenen MOFs im Hinblick auf deren Sorptionseigenschaften gegenüber flüchtigen organischen Verbindungen, insbesondere Benzol, Cyclohexan und *n*-Hexan. In dieser Publikation wurden 18 verschiedene MOFs bzw. ZIFs mit verschiedenen Metallen (Aluminium, Zirconium, Titan, Chrom und Zink) und deren potenzieller Einsatz gegenüber den giftigen C_6-Kohlenwasserstoffen untersucht. Die in der Literatur und aufgrund des HSAB-Konzepts als stabil geltenden MOFs Aluminiumfumarat, MIL-160, DUT-4, DUT-5, MIL-53-TDC, MIL-53, UiO-66, UiO-66-NH_2, UiO-66$(F)_4$, UiO-67, DUT-67, NH_2-MIL-125, MIL-125, MIL-101(Cr), ZIF-8, ZIF-11 und ZIF-7

wurden für diese Experimente ausgewählt. Die verwendeten organischen Moleküle wurden aufgrund ihrer Relevanz in der Industrie und den damit einhergehenden Problemen ausgewählt, wie die schlechte Trennbarkeit von Benzol und Cyclohexan und ihrer generellen Toxizität. In dieser Arbeit wurde versucht durch eine umfassende Anzahl von verschiedenen MOFs und ZIFs einen generellen Trend für die Adsorptionseigenschaften gegenüber flüchtigen organischen Verbindungen zu finden. Es stellte sich jedoch heraus, dass eine einzelne einfache Korrelation, wie sie beispielsweise bei kleinen Gasmolekülen (bspw. SO_2) zu finden ist (Gasaufnahme und Porenvolumen), nicht für die deutlich größeren C_6-Moleküle anwendbar war. Im weiteren Verlauf dieser Arbeit sollten dann die erhaltenen Dampfsorptionsergebnisse als Ausgangspunkt für theoretische Berechnungen bezüglich der IAST-Selektivitäten der drei binären Gemische verwendet werden.

Im ersten Schritt wurden jedoch nur die reinen Aufnahmen der einzelnen drei Dämpfe für die verschiedenen MOFs betrachtet. Es konnte gezeigt werden, dass die Aufnahme nicht nur mit der Oberfläche oder dem Porenvolumen aus der Stickstoffsorption korrelierte, sondern vielmehr auch auf die komplexe Mikroporenstruktur der einzelnen MOFs einging und zusätzlich auch stark abhängig war von zugänglichen funktionellen Gruppen. Bei reiner Betrachtung der maximalen Aufnahme bei $p\,p_0^{-1} = 0.9$ zeigte sich DUT-4 für Benzol, MIL-101(Cr) für Cyclohexan und DUT-5 für *n*-Hexan am geeignetsten. Im niedrigen Druckbereich jedoch zeigte sich ein anderes Bild und verschiedene MOFs zeigten eine erhöhte Aufnahme für die verschiedenen Kohlenwasserstoffe. So hatten bei einem niedrigem relativen Druckbereich von $p\,p_0^{-1} = 0.1$ bis hin zu 0.05 DUT-5, DUT-67/UiO-67 und MIL-101(Cr) die höchsten Aufnahmen für Benzol, für Cyclohexan und *n*-Hexan jedoch DUT-5, UiO-67 und MIL-101(Cr). Dennoch ist hier ein deutlicher Trend zu erkennen für MOFs mit größeren Poren. Bei einem relativen Druck von $p\,p_0^{-1} = 0.02$ stach MIL-53 für Benzol, MIL-125 für Cyclohexan und DUT-5 für *n*-Hexan hervor. Bei detaillierter Betrachtung der einzelnen MOFs zeigte sich, dass DUT-5 und MIL-101(Cr) die MOFs mit dem größten Porenfenster sind, dennoch scheint die Aufnahme im gesamten niedrigen Druckbereich eine Kombination von mehreren Effekten zu sein. So war nicht nur das Porenfenster alleine ausschlaggebend, sondern musste immer in Kombination mit der gesamten Porengröße und der vollständigen MOF-Struktur gesehen werden, inklusive des jeweiligen Liganden. So spielte ebenfalls das mögliche Auftreten einer π···π-Bindung oder einer C-H···π-Bindung eine große Rolle bei der Dampfaufnahme. Diese Aspekte beeinflussten nicht nur die Adsorption, sondern auch die Desorption und führten in mehreren Fällen zum Auftreten von großen Hysteresen, die aber bei Dampfsorptionen auch zusätzlich auf einen Status der Kondensation in der Pore zurückgehen können. Dies kann aber nicht unterschieden werden, weshalb hierauf kein Fokus gesetzt wurde.

Die aus den reinen Adsorptionsdaten ermittelten IAST-Selektivitäten zeigten, dass diese

schwer vorherzusagen waren, aufgrund der gewonnenen Daten aus den Stickstoffsorptionsisothermen, wie die Porengröße oder dem Porenvolumen, selbst in Kombination mit Kristallstrukturdaten.

Generell konnte aber gezeigt werden, dass der Einfluss einer funktionellen Gruppe einen erheblichen zusätzlichen Einfluss haben kann. Dennoch zeigte sich im Vergleich mit der reinen Aufnahme bei den IAST-Selektivitäten ein umgekehrtes Bild. Hier zeichnete es sich ab, dass kleine Porenfenster oder kleine Porendurchmesser die Grundlage für höhere IAST-Selektivitäten waren, wie sie in den ZIFs (ZIF-8, ZIF-7 und ZIF-11) vorkommen. Diese schienen durch ihre Porenstruktur eine Beschränkung für eines der Adsorptive im binären Gemisch darzustellen. Dieses Phänomen konnte bedingt auch auf MOFs mit funktionellen Gruppen, wie $–NH_2$ oder $–(F)_4$ angewendet bzw. gezeigt werden, vor allem im Vergleich mit den unfunktionalisierten MOFs, die ebenfalls untersucht worden sind.

7. Anhang

TGAs

UiO-66 (wenige Defekte)

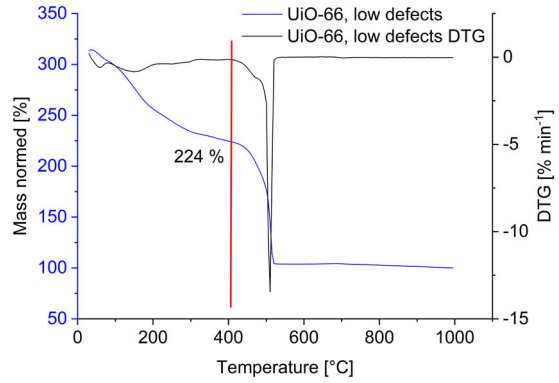

Abbildung 24: *TGA für UiO-66 mit wenigen Defekten unter Sauerstoff, inklusive der Normierung für die Defektstellenberechnung.*

UiO-66 (viele Defekte)

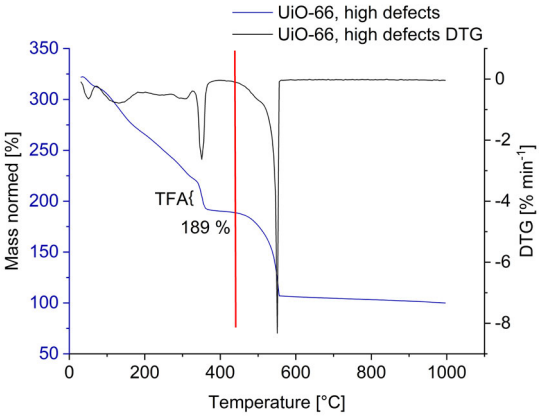

Abbildung 25: *TGA für UiO-66 mit vielen Defekten unter Sauerstoff, inklusive der Normierung für die Defektstellenberechnung.*

UiO-66 (mittlere Defekte)

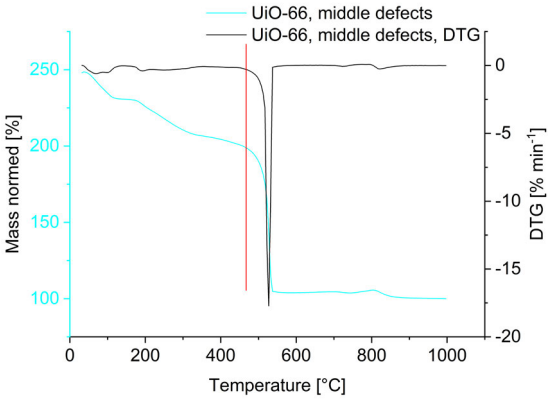

Abbildung 26: *TGA für UiO-66 mit mittleren Defekten unter Sauerstoff, inklusive der Normierung für die Defektstellenberechnung.*

UiO-66-NH_2

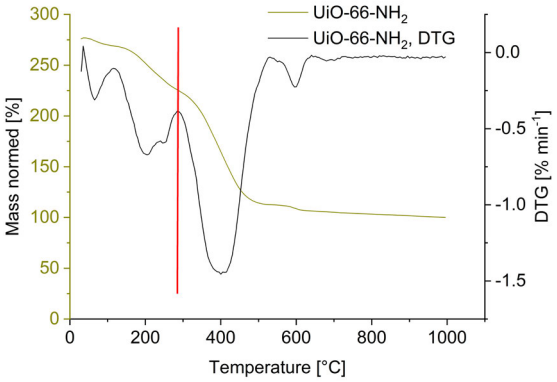

Abbildung 27: *TGA für UiO-66-NH_2 unter Sauerstoff, inklusive der Normierung für die Defektstellenberechnung.*

UiO-66-NO_2

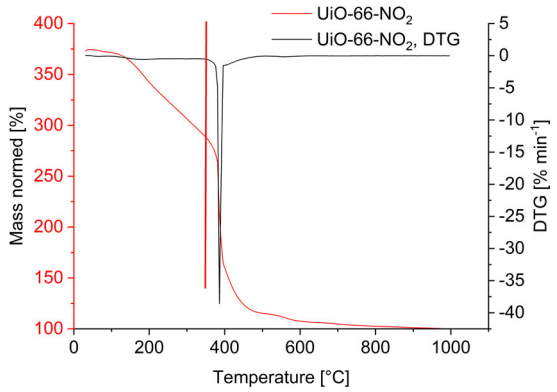

Abbildung 28: *TGA für UiO-66-NO_2 unter Sauerstoff, inklusive der Normierung für die Defektstellenberechnung.*

UiO-66-$(OH)_2$

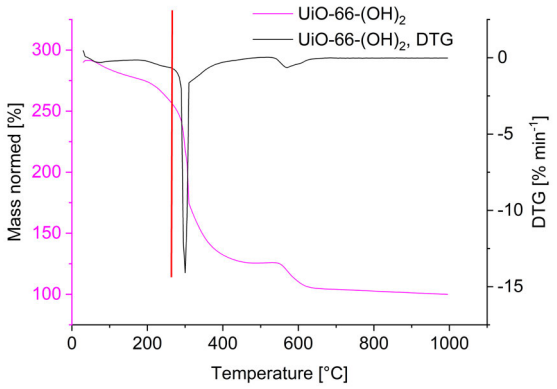

Abbildung 29: *TGA für UiO-66-$(OH)_2$ unter Sauerstoff, inklusive der Normierung für die Defektstellenberechnung.*

UiO-67

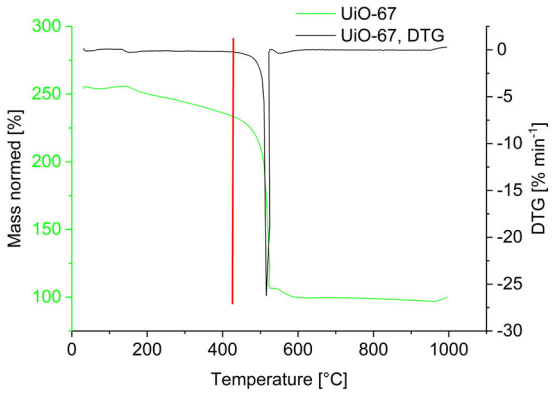

Abbildung 30: *TGA für UiO-67 unter Sauerstoff, inklusive der Normierung für die Defektstellenberechnung.*

MIL-140A (ohne Modulator)

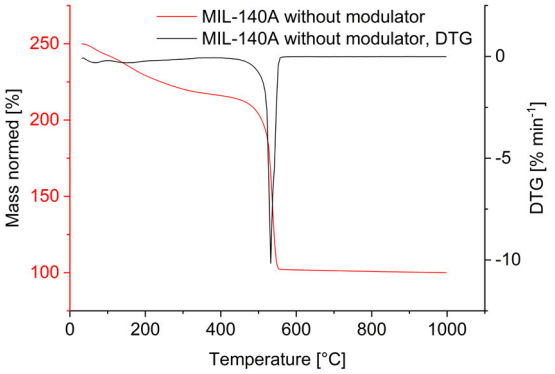

Abbildung 31: *TGA für MIL-140A ohne Modulator unter Sauerstoff, inklusive der Normierung für die Defektstellenberechnung.*

MIL-140A (mit Modulator)

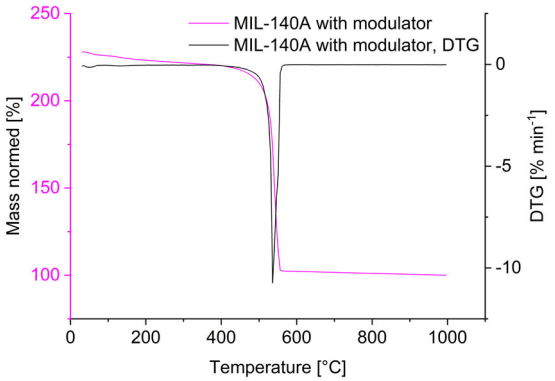

Abbildung 32: *TGA für MIL-140A mit Modulator unter Sauerstoff, inklusive der Normierung für die Defektstellenberechnung.*

MIL-140B

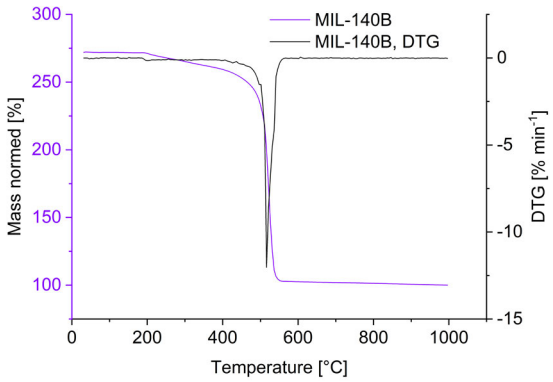

***Abbildung 33**: TGA für MIL-140B unter Sauerstoff, inklusive der Normierung für die Defektstellenberechnung.*

MIL-140C

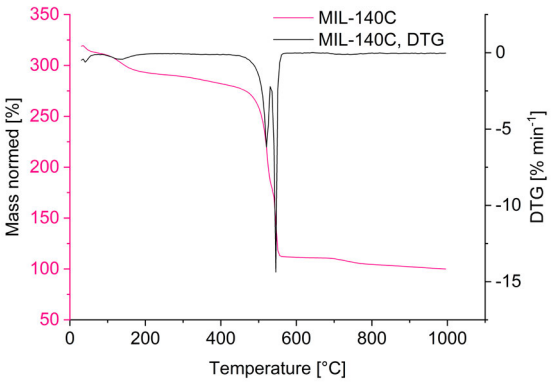

***Abbildung 34:** TGA für MIL-140C unter Sauerstoff, inklusive der Normierung für die Defektstellenberechnung.*

REM-Aufnahmen

UiO-66 (wenige Defekte)

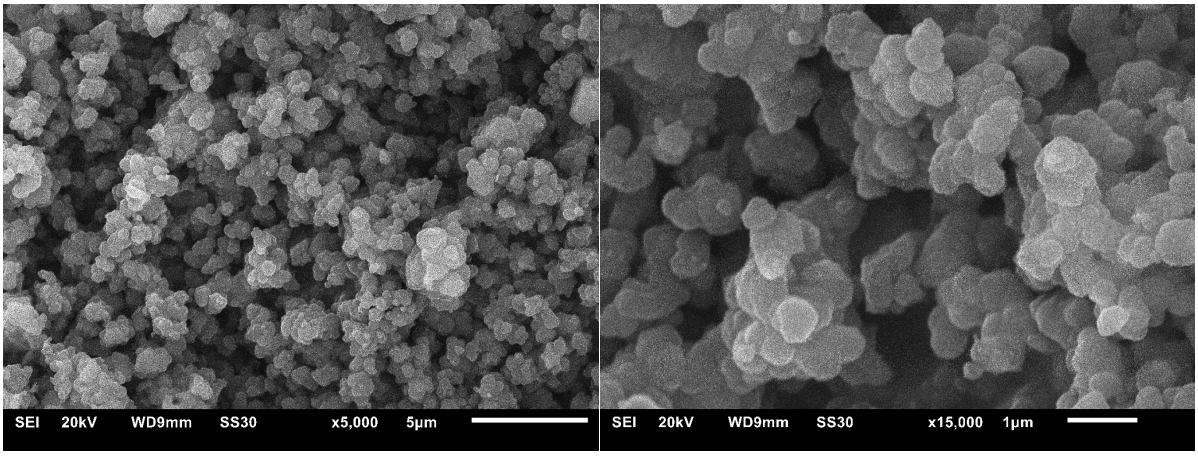

Abbildung 35: *REM-Aufnahmen von UiO-66 (wenige Defekte) bei zwei unterschiedlichen Vergrößerungen.*

UiO-66 (viele Defekte)

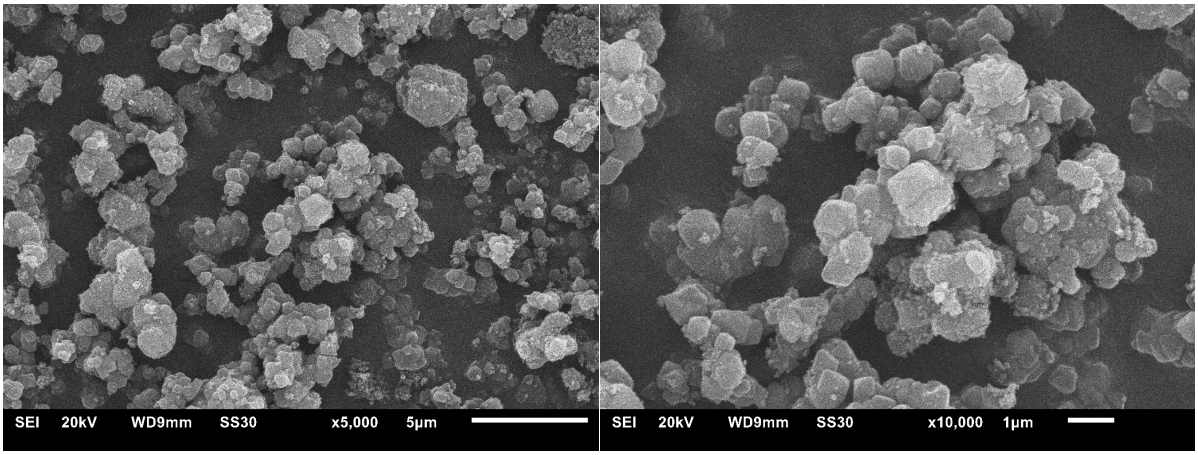

Abbildung 36: *REM-Aufnahmen von UiO-66 (viele Defekte) bei zwei unterschiedlichen Vergrößerungen.*

UiO-66 (mittlere Defekte)

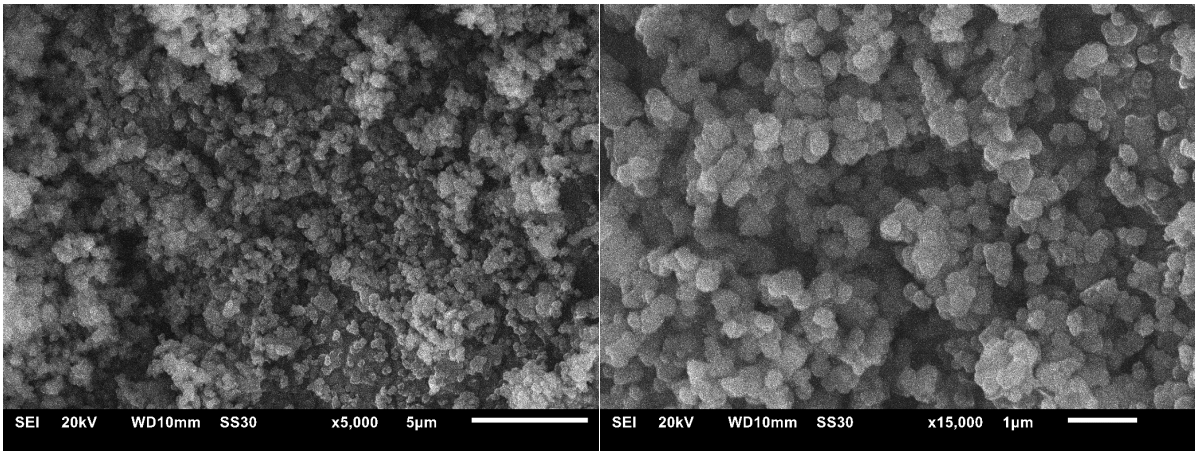

Abbildung 37: *REM-Aufnahmen von UiO-66 (mittlere Defekte) bei zwei unterschiedlichen Vergrößerungen.*

UiO-66-NH_2

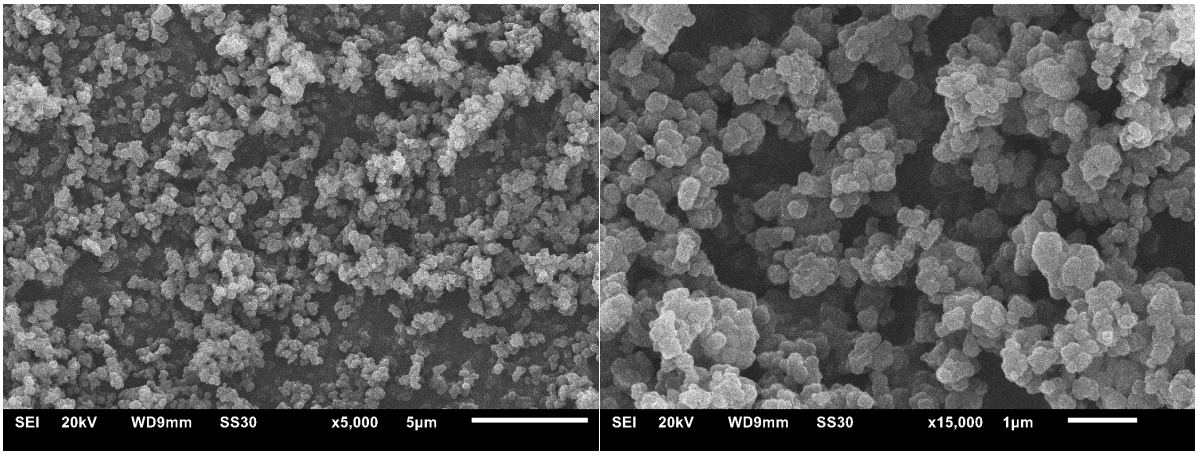

Abbildung 38: *REM-Aufnahmen von UiO-66-NH_2 bei zwei unterschiedlichen Vergrößerungen.*

UiO-66-NO_2

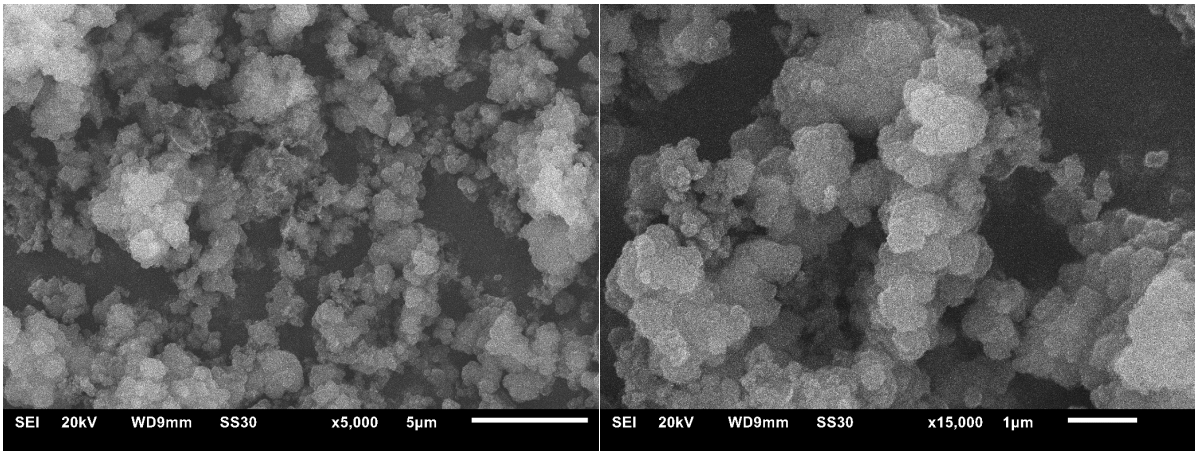

Abbildung 39: *REM-Aufnahmen von UiO-66-NO_2 bei zwei unterschiedlichen Vergrößerungen.*

UiO-66-$(OH)_2$

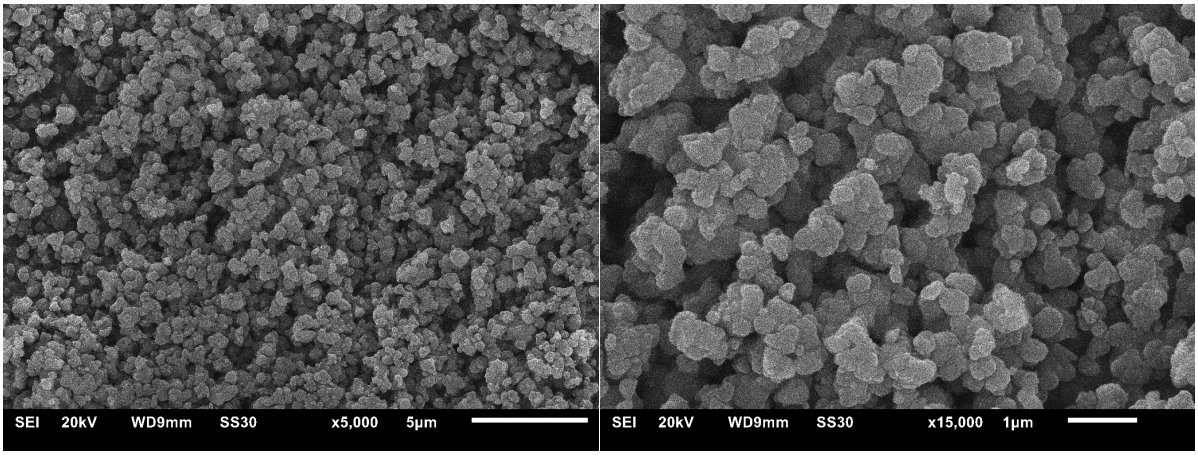

Abbildung 40: *REM-Aufnahmen von UiO-66-$(OH)_2$ bei zwei unterschiedlichen Vergrößerungen.*

UiO-67

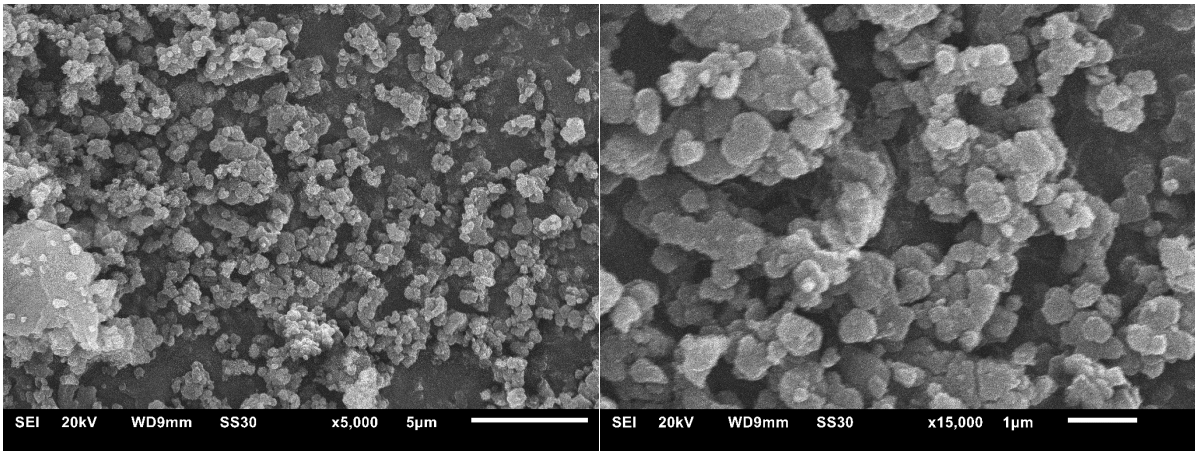

Abbildung 41: *REM-Aufnahmen von UiO-67 bei zwei unterschiedlichen Vergrößerungen.*

MIL-140A (ohne Modulator)

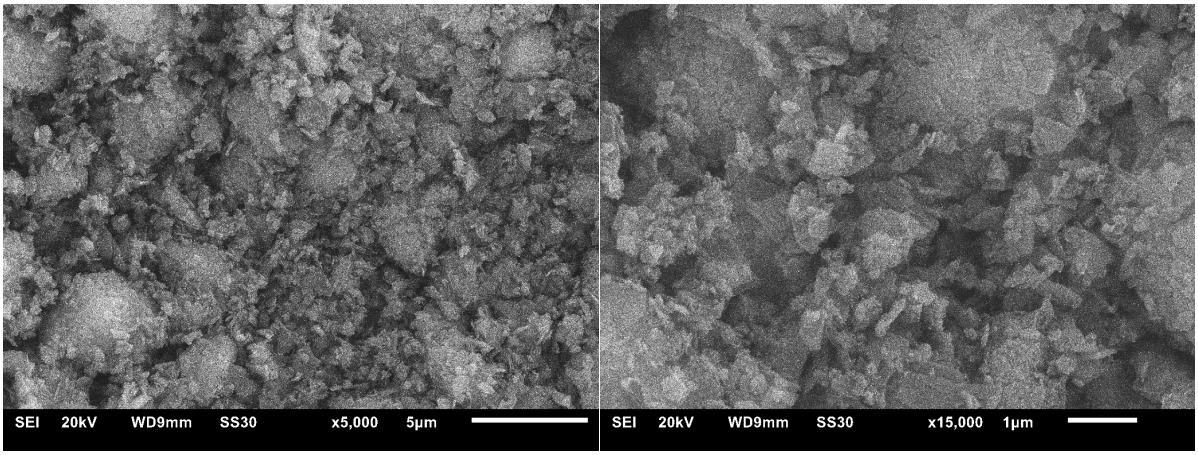

Abbildung 42: *REM-Aufnahmen von MIL-140A (ohne Modulator) bei zwei unterschiedlichen Vergrößerungen.*

MIL-140A (mit Modulator)

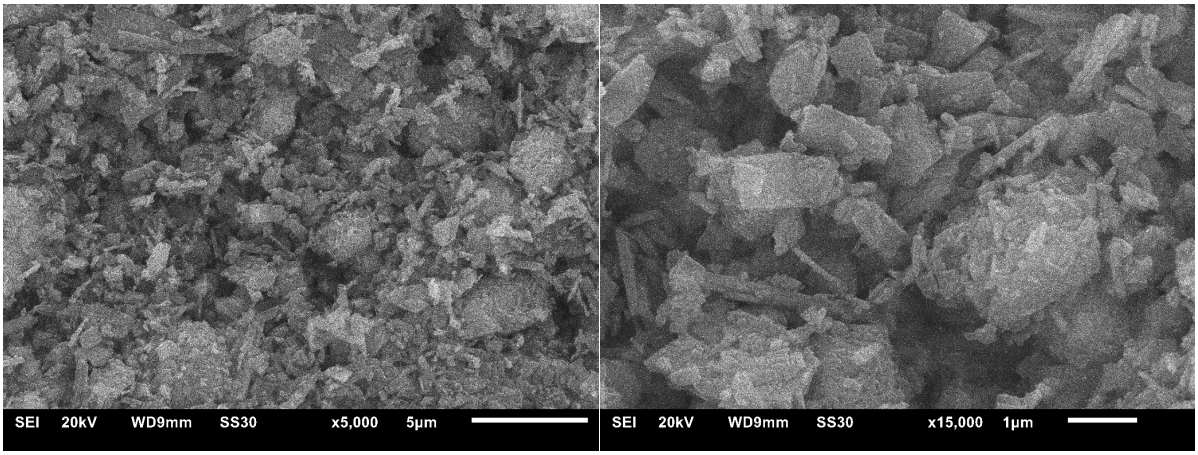

Abbildung 43: *REM-Aufnahmen von MIL-140A (mit Modulator) bei zwei unterschiedlichen Vergrößerungen.*

MIL-140B

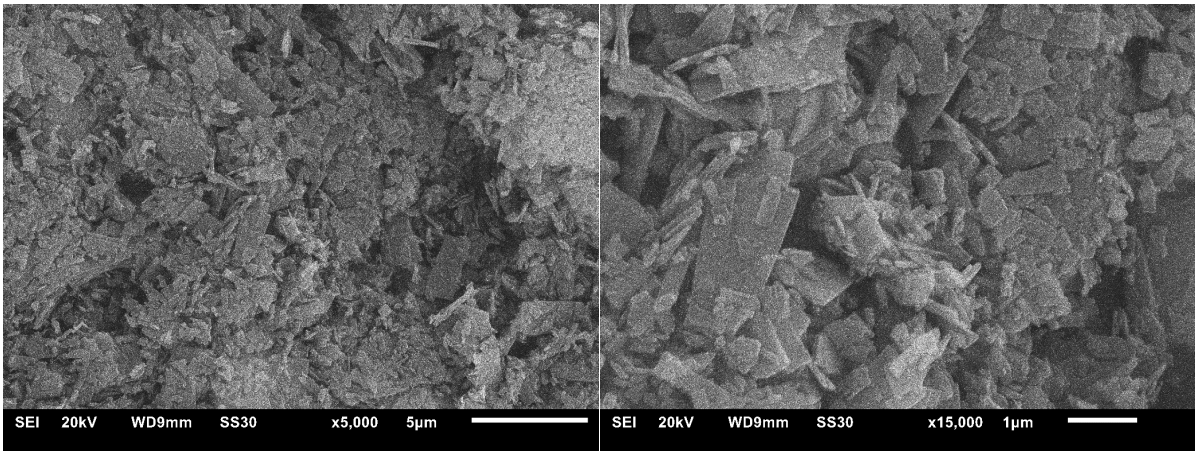

Abbildung 44: *REM-Aufnahmen von MIL-140B bei zwei unterschiedlichen Vergrößerungen.*

MIL-140C

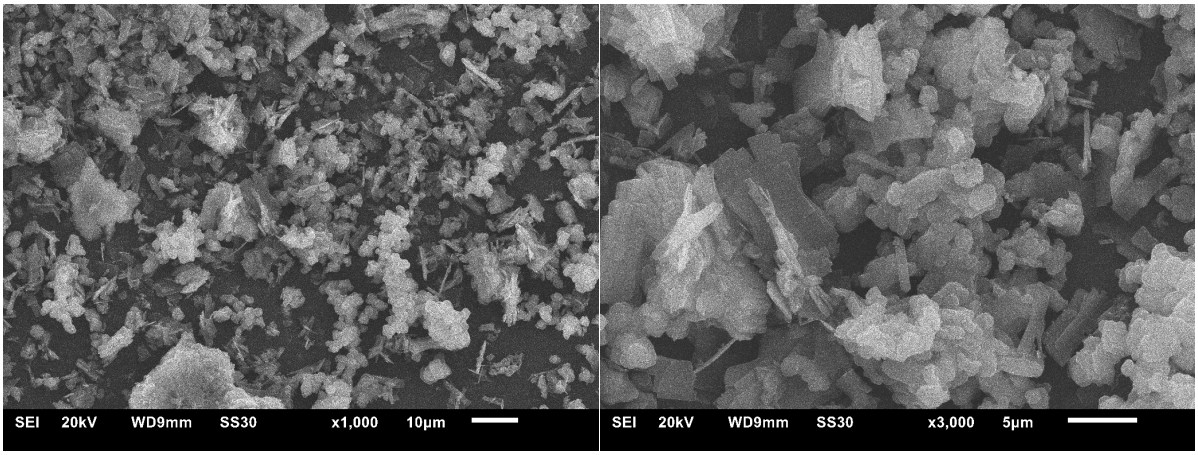

Abbildung 45: *REM-Aufnahmen von MIL-140C bei zwei unterschiedlichen Vergrößerungen.*

NMR

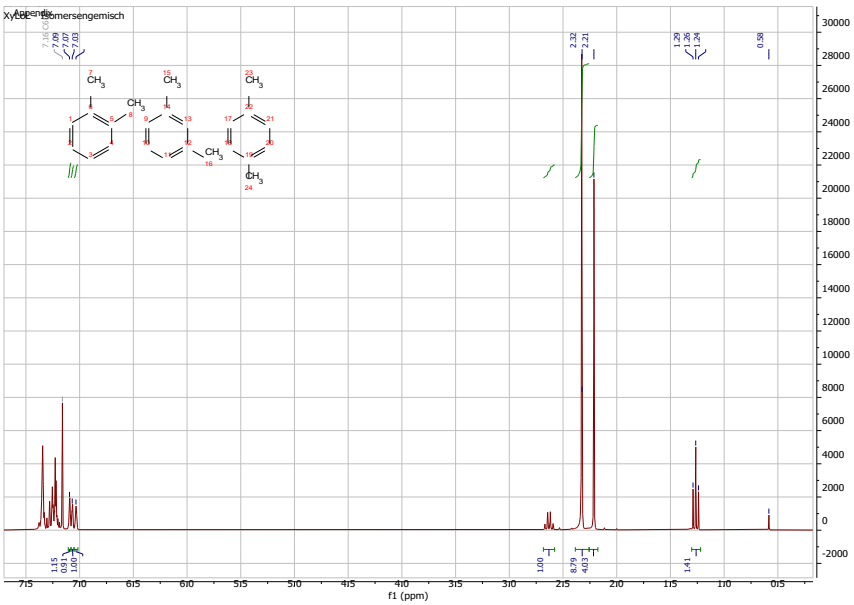

Abbildung 46: *^{1}H-NMR des Xyxlol-Isomerengemisches in deuteriertem Benzol.*

HPLC

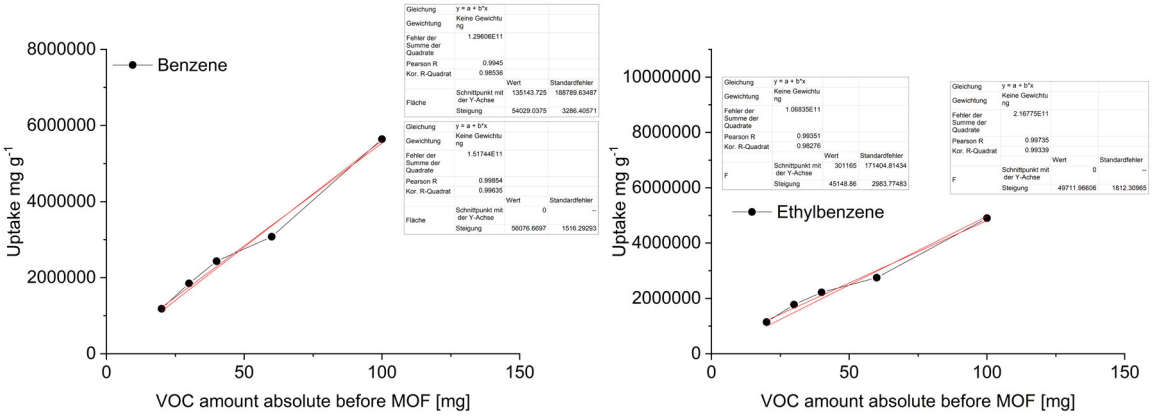

Abbildung 47: *Kalibriergeraden der HPLC-Messungen für Benzol und Ethylbenzol.*

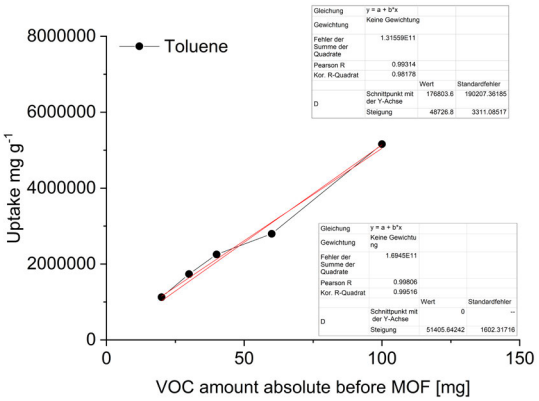

Abbildung 48: *Kalibriergerade der HPLC-Messungen für Toluol.*

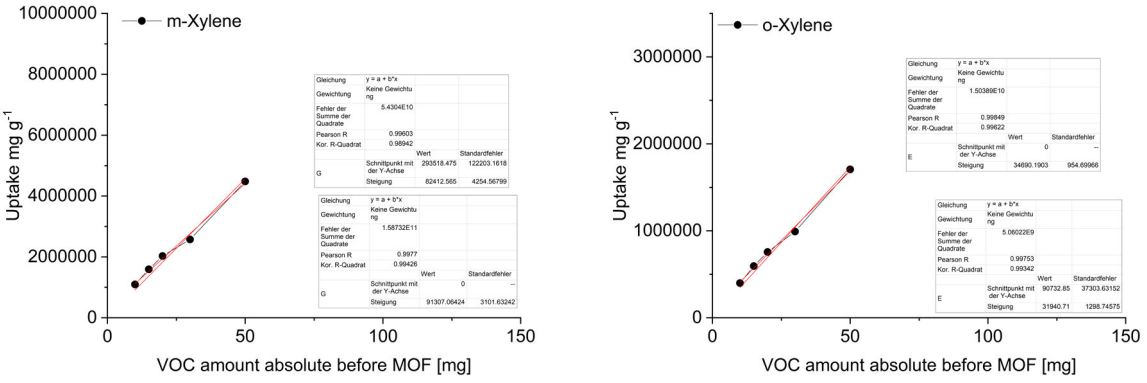

Abbildung 49: *Kalibriergeraden der HPLC-Messungen für die Xylole.*

Literaturverzeichnis

[1] S. Bauer, N. Stock, *Chem. Unserer Zeit* **2008**, *42*, 12–19.

[2] S. R. Batten, N. R. Champness, X.-M. Chen, J. Garcia-Martinez, S. Kitagawa, L. Öhrström, M. O'Keeffe, M. Paik Suh, J. Reedijk, Pure Appl. Chem. 2013, 85, 1715–1724.

[3] R. J. Kuppler, D. J. Timmons, Q.-R. Fang, J.-R. Li, T. A. Makal, M. D. Young, D. Yuan, D. Zhao, W. Zhuang, H.-C. Zhou, *Coord. Chem. Rev.* **2009**, *253*, 3042–3066.

[4] C. Janiak, J. K. Vieth, *New J. Chem.* **2010**, *34*, 2366–2388.

[5] M. J. Kalmutzki, N. Hanikel, O. M. Yaghi, *Sci. Adv.* **2018**, *4*, eaat9180.

[6] D. Zhao, D. J. Timmons, D. Yuan, H.-C. Zhou, *Acc. Chem. Res.* **2011**, *44*, 123–133.

[7] M. Ding, X. Cai, H.-L. Jiang, *Chem. Sci.* **2019**, *10*, 10209–10230.

[8] S. Yuan, L. Feng, K. Wang, J. Pang, M. Bosch, C. Lollar, Y. Sun, J. Qin, X. Yang, P. Zhang, Q. Wang, L. Zou, Y. Zhang, L. Zhang, Y. Fang, J. Li, H.-C. Zhou, *Adv. Mater.* **2018**, *30*, 1870277.

[9] K. J. Gagnon, H. P. Perry, A. Clearfield, *Chem. Rev.* **2012**, *112*, 1034–1054.

[10] S. Bhattacharjee, M.-S. Jang, H.-J. Kwon, W.-S. Ahn, *Catal. Surv. Asia* **2014**, *18*, 101–127.

[11] R. G. Pearson, *J. Am. Chem. Soc* **1963**, *85*, 3533–3539.

[12] A. M. Hamisu, A. Ariffin, A. C. Wibowo, *Inorg. Chim. Acta* **2020**, *511*, 119801.

[13] N. Li, J. Xu, R. Feng, T.-L. Hu, X.-H. Bu, *Chem. Commun.* **2016**, *52*, 8501–8513.

[14] J. Ren, Y. Huang, H. Zhu, B. Zhang, H. Zhu, S. Shen, G. Tan, F. Wu, H. He, S. Lan, X. Xia, Q. Liu, *Carbon Energy* **2020**, *2*, 176–202.

[15] S. M. Cohen, *Chem. Rev.* **2012**, *112*, 970–1000.

[16] F. A. A. Paz, J. Klinowski, S. M. F. Vilela, J. P. C. Tomé, J. A. S. Cavaleiro, J. Rocha, *Chem. Soc. Rev.* **2012**, *41*, 1088–1110.

[17] S. Ali Akbar Razavi, A. Morsali, *Coord. Chem. Rev.* **2019**, *399*, 213023.

[18] A. Kirchon, L. Feng, H. F. Drake, E. A. Joseph, H.-C. Zhou, *Chem. Soc. Rev.* **2018**, *47*, 8611.

[19] Z.-J. Lin, J. Lü, M. Hong, R. Cao, *Chem. Soc. Rev.* **2014**, *43*, 5867–5895.

[20] K. S. Park, Z. Ni, A. P. Côté, J. Y. Choi, R. Huang, F. J. Uribe-Romo, H. K. Chae, M. O'Keeffe, O. M. Yaghi, *PNAS* **2006**, *103*, 10186–10191.

[21] H. Furukawa, F. Gándara, Y.-B. Zhang, J. Jiang, W. L. Queen, M. R. Hudson, O. M. Yaghi, *J. Am. Chem. Soc.* **2014**, *136*, 4369–4381.

[22] T. Loiseau, C. Serre, C. Huguenard, G. Fink, F. Taulelle, M. Henry, T. Bataille, G. Férey, *Chem. Eur. J.* **2004**, *10*, 1373–1382.

[23] O. M. Yaghi, Hailian Li, *J. Am. Chem. Soc* **1995**, *117*, 10401–10402.

[24] O. M. Yaghi, G. Li, H. Li, *Nature* **1995**, *378*, 703–706.

[25] M. Eddaoudi, H. Li, O. M. Yaghi, *J. Am. Chem. Soc.* **2000**, *122*, 1391–1397.

[26] O. M. Yaghi, H. Li, T. L. Groy, *J. Am. Chem. Soc.* **1996**, *118*, 9096–9101.

[27] H. Li, M. Eddaoudi, M. O'Keeffe, O. M. Yaghi, *Nature* **1999**, *276*, 276–279.

[28] H. Li, M. Eddaoudi, T. L. Groy, O. M. Yaghi, *J. Am. Chem. Soc.* **1998**, *120*, 8571–8572.

[29] M. Eddaoudi, J. Kim, N. Rosi, D. Vodak, J. Wachter, M. O'Keeffe, O. M. Yaghi, *Science* **2002**, *295*, 469–472.

[30] B. Chen, Z. Yang, Y. Zhu, Y. Xia, *J. Mater. Chem. A* **2014**, *2*, 16811–16831.
[31] Y.-Q. Tian, C.-X. Cai, Y. Ji, X.-Z. You, S.-M. Peng, G.-H. Lee, *Angew. Chem.* **2002**, *114*, 1442–1444.
[32] N. Stock, S. Biswas, *Chem. Rev.* **2012**, *112*, 933–969.
[33] Y.-R. Lee, J. Kim, W.-S. Ahn, *Korean J. Chem. Eng.* **2013**, *30*, 1667–1680.
[34] D. Sud, G. Kaur, *Polyhedron* **2021**, *193*, 114897.
[35] P. Tundo, P. Anastas, D. Black, J. Breen, T. Collins, S. Memoli, J. Miyamoto, M. Polyakoff, W. Tumas, *Pure Appl. Chem.* **2000**, *72*, 1207–1228.
[36] H. Reinsch, *Eur. J. Inorg. Chem.* **2016**, *2016*, 4290–4299.
[37] D. Crawford, J. Casaban, R. Haydon, N. Giri, T. McNally, S. L. James, *Chem. Sci.* **2015**, *6*, 1645–1649.
[38] V. M. V., G. Nageswaran, *J. Electrochem. Soc.* **2020**, *167*, 155527–155537.
[39] A. Martinez Joaristi, J. Juan-Alcañiz, P. Serra-Crespo, F. Kapteijn, J. Gascon, *Cryst. Growth. Des.* **2012**, *12*, 3489–3498.
[40] I. Thomas-Hillman, A. Laybourn, C. Dodds, S. W. Kingman, *J. Mater. Chem. A* **2018**, *6*, 11564–11581.
[41] J. Y. Choi, J. Kim, S. H. Jhung, H.-K. Kim, J.-S. Chang, H. K. Chae, *Bull. Korean Chem. Soc.* **2006**, *27*, 1523–1524.
[42] A. K. Das, R. S. Vemuri, I. Kutnyakov, B. P. McGrail, R. K. Motkuri, *Sci. Rep.* **2016**, *6*, 28050–28057.
[43] N. Tannert, S. Gökpinar, E. Hastürk, S. Nießing, C. Janiak, *Dalton Trans.* **2018**, *47*, 9850–9860.
[44] Y. Liang, H. Huang, L. Kou, F. Li, J. Lü, H. Cao, *Cryst. Growth. Des.* **2018**, *18*, 6609–6616.
[45] P. Díaz, J. Benet-Buchholz, R. Vilar, A. J. P. White, *Inorg. Chem.* **2006**, *45*, 1617–1626.
[46] R. Seetharaj, P. V. Vandana, P. Arya, S. Mathew, *Arab. J. Chem.* **2019**, *12*, 295–315.
[47] C. Volkringer, D. Popov, T. Loiseau, G. Férey, M. Burghammer, C. Riekel, M. Haouas, F. Taulelle, *Chem. Mater.* **2009**, *21*, 5695–5697.
[48] C. Volkringer, D. Popov, T. Loiseau, N. Guillou, G. Férey, M. Haouas, F. Taulelle, C. Mellot-Draznieks, M. Burghammer, C. Riekel, *Nat. Mater.* **2007**, *6*, 760–764.
[49] T. Loiseau, L. Lecroq, C. Volkringer, J. Marrot, G. Férey, M. Haouas, F. Taulelle, S. Bourrelly, P. L. Llewellyn, M. Latroche, *J. Am. Chem. Soc* **2006**, *128*, 10223–10230.
[50] M. Haouas, C. Volkringer, T. Loiseau, G. Férey, F. Taulelle, *Chem. Mater.* **2012**, *24*, 2462–2471.
[51] D. Jiang, C. Huang, J. Zhu, P. Wang, Z. Liu, Di Fang, *Coord. Chem. Rev.* **2021**, *444*, 214064–214686.
[52] J. Hwang, A. Ejsmont, R. Freund, J. Goscianska, B. V. K. J. Schmidt, S. Wuttke, *Chem. Soc. Rev.* **2020**, *49*, 3348–3422.
[53] A. Schaate, P. Roy, A. Godt, J. Lippke, F. Waltz, M. Wiebcke, P. Behrens, *Chem. Eur. J.* **2011**, *17*, 6643–6651.
[54] S. Diring, S. Furukawa, Y. Takashima, T. Tsuruoka, S. Kitagawa, *Chem. Mater.* **2010**, *22*, 4531–4538.
[55] T. Tsuruoka, S. Furukawa, Y. Takashima, K. Yoshida, S. Isoda, S. Kitagawa, *Angew. Chem. Int. Ed.* **2009**, *48*, 4739–4743.
[56] I. Walton, C. Chen, J. M. Rimsza, T. M. Nenoff, K. S. Walton, *Cryst. Growth. Des.* **2020**, *20*, 6139–6146.

[57] F. Ragon, P. Horcajada, H. Chevreau, Y. K. Hwang, U.-H. Lee, S. R. Miller, T. Devic, J.-S. Chang, C. Serre, *Inorg. Chem.* **2014**, *53*, 2491–2500.

[58] G. C. Shearer, S. Chavan, S. Bordiga, S. Svelle, U. Olsbye, K. P. Lillerud, *Chem. Mater.* **2016**, *28*, 3749–3761.

[59] G. C. Shearer, S. Chavan, J. Ethiraj, J. G. Vitillo, S. Svelle, U. Olsbye, C. Lamberti, S. Bordiga, K. P. Lillerud, *Chem. Mater.* **2014**, *26*, 4068–4071.

[60] G. C. Shearer, J. G. Vitillo, S. Bordiga, S. Svelle, U. Olsbye, K. P. Lillerud, *Chem. Mater.* **2016**, *28*, 7190–7193.

[61] G. Férey, C. Mellot-Draznieks, C. Serre, F. Millange, J. Dutour, S. Surblé, I. Margiolaki, *Science* **2005**, *309*, 2040–2042.

[62] T. Zhao, F. Jeremias, I. Boldog, B. Nguyen, S. K. Henninger, C. Janiak, *Dalton Trans.* **2015**, *44*, 16791–16801.

[63] P. Vinaches, K. Bernardo-Gusmão, S. B. C. Pergher, *Molecules* **2017**, *22*.

[64] X. Huang, Y. Chen, Z. Lin, X. Ren, Y. Song, Z. Xu, X. Dong, X. Li, C. Hu, B. Wang, *Chem. Commun.* **2014**, *50*, 2624–2627.

[65] X. Zhang, Z. Chen, X. Liu, S. L. Hanna, X. Wang, R. Taheri-Ledari, A. Maleki, P. Li, O. K. Farha, *Chem. Soc. Rev.* **2020**, *49*, 7406–7427.

[66] O. K. Farha, J. T. Hupp, *Acc. Chem. Res.* **2010**, *43*, 1166–1175.

[67] B. Rungtaweevoranit, C. S. Diercks, M. J. Kalmutzki, O. M. Yaghi, *Faraday Discuss.* **2017**, *201*, 9–45.

[68] B. M. Connolly, J. P. Mehta, P. Z. Moghadam, A. E.H. Wheatley, D. Fairen-Jimenez, *Curr. Opin. Green Sustain. Chem.* **2018**, *12*, 47–56.

[69] Ü. Kökçam-Demir, A. Goldman, L. Esrafili, M. Gharib, A. Morsali, O. Weingart, C. Janiak, *Chem. Soc. Rev.* **2020**, *49*, 2751–2798.

[70] V. R. Remya, M. Kurian, *Int. Nano Lett.* **2019**, *9*, 17–29.

[71] X. Fang, B. Zong, S. Mao, *Nano-Micro Lett.* **2018**, *10*, 1–19.

[72] F. Demir Duman, R. S. Forgan, *J. Mater. Chem. B* **2021**, *9*, 3423–3449.

[73] M. C. Bernini, D. Fairen-Jimenez, M. Pasinetti, A. J. Ramirez-Pastor, R. Q. Snurr, *J. Mater. Chem. B* **2014**, *2*, 766–774.

[74] M. Bosch, S. Yuan, W. Rutledge, H.-C. Zhou, *Acc. Chem. Res.* **2017**, *50*, 857–865.

[75] M. B. Majewski, H. Noh, T. Islamoglu, O. K. Farha, *J. Mater. Chem. A* **2018**, *6*, 7338–7350.

[76] L. Feng, K.-Y. Wang, J. Willman, H.-C. Zhou, *ACS Cent. Sci.* **2020**, *6*, 359–367.

[77] C. Schlüsener, M. Xhinovci, S.-J. Ernst, A. Schmitz, N. Tannert, C. Janiak, *Chem. Mater.* **2019**, *31*, 4051–4062.

[78] C. Schlüsener, D. N. Jordan, M. Xhinovci, T. J. Matemb Ma Ntep, A. Schmitz, B. Giesen, C. Janiak, *Dalton Trans.* **2020**, *49*, 7373–7383.

[79] J. N. Hall, P. Bollini, *React. Chem. Eng.* **2019**, *4*, 207–222.

[80] J. H. Choe, H. Kim, C. S. Hong, *Mater. Chem. Front.* **2021**, *5*, 5172–5185.

[81] R. Freund, O. Zaremba, G. Arnauts, R. Ameloot, G. Skorupskii, M. Dincă, A. Bavykina, J. Gascon, A. Ejsmont, J. Goscianska, M. Kalmutzki, U. Lächelt, E. Ploetz, C. S. Diercks, S. Wuttke, *Angew. Chem. Int. Ed.* **2021**, *60*, 23975–24001.

[82] D. N. Bunck, W. R. Dichtel, *Chem. Eur. J.* **2013**, *19*, 818–827.

[83] B. Tan, Y. Luo, X. Liang, S. Wang, X. Gao, Z. Zhang, Y. Fang, *Cryst. Growth. Des.* **2020**, *20*, 6565–6572.

[84] T. He, X.-J. Kong, J.-R. Li, *Acc. Chem. Res.* **2021**, *54*, 3083–3094.

[85] N. Tannert, C. Jansen, S. Nießing, C. Janiak, *Dalton Trans.* **2019**, *48*, 2967–2976.

[86] T. Loiseau, C. Volkringer, M. Haouas, F. Taulelle, G. Férey, *C. R. Chim.* **2015**, *18*, 1350–1369.

[87] E. Laurenz, G. Füldner, L. Schnabel, G. Schmitz, *Energies* **2020**, *13*, 3003.

[88] A. Cadiau, J. S. Lee, D. Damasceno Borges, P. Fabry, T. Devic, M. T. Wharmby, C. Martineau, D. Foucher, F. Taulelle, C.-H. Jun, Y. K. Hwang, N. Stock, M. F. de Lange, F. Kapteijn, J. Gascon, G. Maurin, J.-S. Chang, C. Serre, *Adv. Mater.* **2015**, *27*, 4775–4780.

[89] K. Brandenburg, Diamond 4.0, Crystal and Molecular Structure Visualization, Crystal Impact - K. Brandenburg & H. Putz GbR, Bonn, Germany, 2009.

[90] E. Alvarez, N. Guillou, C. Martineau, B. Bueken, B. Van de Voorde, C. Le Guillouzer, P. Fabry, F. Nouar, F. Taulelle, D. de Vos, J.-S. Chang, K. H. Cho, N. Ramsahye, T. Devic, M. Daturi, G. Maurin, C. Serre, *Angew. Chem. Int. Ed.* **2015**, *54*, 3664–3668.

[91] M. Wahiduzzaman, D. Lenzen, G. Maurin, N. Stock, M. T. Wharmby, *Eur. J. Inorg. Chem.* **2018**, *2018*, 3626–3632.

[92] D. Lenzen, J. Zhao, S.-J. Ernst, M. Wahiduzzaman, A. Ken Inge, D. Fröhlich, H. Xu, H.-J. Bart, C. Janiak, S. Henninger, G. Maurin, X. Zou, N. Stock, *Nat. Commun.* **2019**, *10*, 3025.

[93] H. Reinsch, M. A. van der Veen, B. Gil, B. Marszalek, T. Verbiest, D. de Vos, N. Stock, *Chem. Mater.* **2013**, *25*, 17–26.

[94] I. Senkovska, F. Hoffmann, M. Fröba, J. Getzschmann, W. Böhlmann, S. Kaskel, *Microporous Mesoporous Mater.* **2009**, *122*, 93–98.

[95] C. B. L. Tschense, N. Reimer, C.-W. Hsu, H. Reinsch, R. Siegel, W.-J. Chen, C.-H. Lin, A. Cadiau, C. Serre, J. Senker, N. Stock, *Z. Anorg. Allg. Chem.* **2017**, *643*, 1600–1608.

[96] F. Jeremias, A. Khutia, S. K. Henninger, C. Janiak, *J. Mater. Chem.* **2012**, *22*, 10148–10151.

[97] S. Bourrelly, P. L. Llewellyn, C. Serre, F. Millange, T. Loiseau, G. Férey, *J. Am. Chem. Soc* **2005**, *127*, 13519–13521.

[98] Y. Bai, Y. Dou, L.-H. Xie, W. Rutledge, J.-R. Li, H.-C. Zhou, *Chem. Soc. Rev.* **2016**, *45*, 2327–2367.

[99] M. Dan-Hardi, C. Serre, T. Frot, L. Rozes, G. Maurin, C. Sanchez, G. Férey, *J. Am. Chem. Soc* **2009**, *131*, 10857–10859.

[100] Chui, Lo Charmant, Orpen, Williams, *Science* **1999**, *283*, 1148–1150.

[101] A. Buragohain, S. Couck, P. van der Voort, J. F.M. Denayer, S. Biswas, *J. Solid State Chem.* **2016**, *238*, 195–202.

[102] M. Lammert, S. Bernt, F. Vermoortele, D. E. de Vos, N. Stock, *Inorg. Chem.* **2013**, *52*, 8521–8528.

[103] A. Herbst, A. Khutia, C. Janiak, *Inorg. Chem.* **2014**, *53*, 7319–7333.

[104] M. Y. Zorainy, M. Gar Alalm, S. Kaliaguine, D. C. Boffito, *J. Mater. Chem. A* **2021**, *9*, 22159–22217.
[105] Y. Lin, C. Kong, L. Chen, *RSC Adv.* **2012**, *2*, 6417–6419.
[106] B. Liu, Y. Peng, Q. Chen, *Energy Fuels* **2016**, *30*, 5593–5600.
[107] S. Fei, A. Alizadeh, W.-L. Hsu, J.-J. Delaunay, H. Daiguji, *J. Phys. Chem. C* **2021**, *125*, 26755–26769.
[108] J. H. Cavka, S. Jakobsen, U. Olsbye, N. Guillou, C. Lamberti, S. Bordiga, K. P. Lillerud, *J. Am. Chem. Soc* **2008**, *130*, 13850–13851.
[109] X. Feng, H. S. Jena, C. Krishnaraj, K. Leus, G. Wang, H. Chen, C. Jia, P. van der Voort, *ACS Appl. Mater. Interfaces* **2021**, *13*, 60715–60735.
[110] M. Kandiah, M. H. Nilsen, S. Usseglio, S. Jakobsen, U. Olsbye, M. Tilset, C. Larabi, E. A. Quadrelli, F. Bonino, K. P. Lillerud, *Chem. Mater.* **2010**, *22*, 6632–6640.
[111] L. Valenzano, B. Civalleri, S. Chavan, S. Bordiga, M. H. Nilsen, S. Jakobsen, K. P. Lillerud, C. Lamberti, *Chem. Mater.* **2011**, *23*, 1700–1718.
[112] I. A. Lazaro, *Eur. J. Inorg. Chem.* **2020**, 4284–4294.
[113] M. Taddei, *Coord. Chem. Rev.* **2017**, *343*, 1–24.
[114] J. H. Cavka, C. A. Grande, G. Mondino, R. Blom, *Ind. Eng. Chem. Res.* **2014**, *53*, 15500–15507.
[115] P. Ghosh, Y. J. Colón, R. Q. Snurr, *Chem. Commun.* **2014**, *50*, 11329–11331.
[116] Z. Chen, X. Wang, H. Noh, G. Ayoub, G. W. Peterson, C. T. Buru, T. Islamoglu, O. K. Farha, *CrystEngComm* **2019**, *21*, 2409–2415.
[117] J. Aguilera-Sigalat, D. Bradshaw, *Chem. Commun.* **2014**, *50*, 4711–4713.
[118] Z. Hu, Y. Peng, Z. Kang, Y. Qian, D. Zhao, *Inorg. Chem.* **2015**, *54*, 4862–4868.
[119] G. W. Peterson, M. R. Destefano, S. J. Garibay, A. Ploskonka, M. McEntee, M. Hall, C. J. Karwacki, J. T. Hupp, O. K. Farha, *Chem. Eur. J.* **2017**, *23*, 15913–15916.
[120] F. Jeremias, V. Lozan, S. K. Henninger, C. Janiak, *Dalton Trans.* **2013**, *42*, 15967–15973.
[121] M. Sohail, Y.-N. Yun, E. Lee, S. K. Kim, K. Cho, J.-N. Kim, T. W. Kim, J.-H. Moon, H. Kim, *Cryst. Growth. Des.* **2017**, *17*, 1208–1213.
[122] G. Wen, Z. Guo, *Colloids Surf. A* **2018**, *541*, 58–67.
[123] S.-N. Kim, J. Kim, H.-Y. Kim, H.-Y. Cho, W.-S. Ahn, *Catal. Today* **2013**, *204*, 85–93.
[124] M. Martis, W. Meicheng, K. Mori, H. Yamashita, *Catal. Today* **2014**, *235*, 98–102.
[125] E. L. Bustamante, J. L. Fernández, J. M. Zamaro, *J. Colloid Interface Sci.* **2014**, *424*, 37–43.
[126] S. B. Novaković, G. A. Bogdanović, C. Heering, G. Makhloufi, D. Francuski, C. Janiak, *Inorg. Chem.* **2015**, *54*, 2660–2670.
[127] K. Kida, M. Okita, K. Fujita, S. Tanaka, Y. Miyake, *Cryst. Eng. Comm.* **2013**, *15*, 1794–1801.
[128] W. Morris, C. J. Stevens, R. E. Taylor, C. Dybowski, O. M. Yaghi, M. A. Garcia-Garibay, *J. Phys. Chem. C* **2012**, *116*, 13307–13312.
[129] K. Zhang, R. P. Lively, C. Zhang, W. J. Koros, R. R. Chance, *J. Phys. Chem. C* **2013**, *117*, 7214–7225.
[130] J.-R. Li, J. Sculley, H.-C. Zhou, *Chem. Rev.* **2012**, *112*, 869–932.
[131] M. He, J. Yao, Q. Liu, Z. Zhong, H. Wang, *Dalton Trans.* **2013**, *42*, 16608–16613.

[132] C. Gücüyener, J. van den Bergh, J. Gascon, F. Kapteijn, *J. Am. Chem. Soc.* **2010**, *132*, 17704–17706.

[133] J. van den Bergh, C. Gücüyener, E. A. Pidko, E. J. M. Hensen, J. Gascon, F. Kapteijn, *Chem. Eur. J.* **2011**, *17*, 8832–8840.

[134] B. R. Pimentel, M. L. Jue, E.-K. Zhou, R. J. Verploegh, J. Leisen, D. S. Sholl, R. P. Lively, *J. Phys. Chem. C* **2019**, *123*, 12862–12870.

[135] J. Sánchez-Laínez, B. Zornoza, Á. Mayoral, Á. Berenguer-Murcia, D. Cazorla-Amorós, C. Téllez, J. Coronas, *J. Mater. Chem. A* **2015**, *3*, 6549–6556.

[136] D.-L. Chen, N. Wang, F.-F. Wang, J. Xie, Y. Zhong, W. Zhu, J. K. Johnson, R. Krishna, *J. Phys. Chem. C* **2014**, *118*, 17831–17837.

[137] W. Cai, T. Lee, M. Lee, W. Cho, D.-Y. Han, N. Choi, A. C. K. Yip, J. Choi, *J. Am. Chem. Soc* **2014**, *136*, 7961–7971.

[138] W. Ma, Q. Jiang, P. Yu, L. Yang, L. Mao, *Anal. Chem.* **2013**, *85*, 7550–7557.

[139] Y.-T. Zhao, L.-Q. Yu, X. Xia, X.-Y. Yang, W. Hu, Y.-K. Lv, *Anal. Methods* **2018**, *10*, 4894–4901.

[140] S. Li, F. Huo, *Nanoscale* **2015**, *7*, 7482–7501.

[141] Q.-L. Zhu, Q. Xu, *Chem. Soc. Rev.* **2014**, *43*, 5468–5512.

[142] I. Ahmed, S. H. Jhung, *Mater. Today* **2014**, *17*, 136–146.

[143] M. Kalaj, K. C. Bentz, S. Ayala, J. M. Palomba, K. S. Barcus, Y. Katayama, S. M. Cohen, *Chem. Rev.* **2020**, *120*, 8267–8302.

[144] Y. Cheng, Y. Pu, D. Zhao, *Chem. Asian J.* **2020**, *15*, 2241–2270.

[145] E. Hastürk, C. Schlüsener, J. Quodbach, A. Schmitz, C. Janiak, *Microporous Mesoporous Mater.* **2019**, *280*, 277–287.

[146] Y. Khabzina, J. Dhainaut, M. Ahlhelm, H.-J. Richter, H. Reinsch, N. Stock, D. Farrusseng, *Ind. Eng. Chem. Res.* **2018**, *57*, 8200–8208.

[147] E. Hastürk, S.-P. Höfert, B. Topalli, C. Schlüsener, C. Janiak, *Microporous Mesoporous Mater.* **2020**, *295*, 109907.

[148] D. Wisser, F. M. Wisser, S. Raschke, N. Klein, M. Leistner, J. Grothe, E. Brunner, S. Kaskel, *Angew. Chem. Int. Ed.* **2015**, *54*, 12588–12591.

[149] L. Liu, E. Ping, J. Sun, L. Zhang, Y. Zhou, Y. Zhong, Y. Zhou, Y.-A. Wang, *Dalton Trans.* **2019**, *48*, 6951–6959.

[150] T. Azizi Vahed, M. R. Naimi-Jamal, L. Panahi, *New J. Chem.* **2018**, *42*, 11137–11146.

[151] W. Zhang, S. Shi, W. Zhu, L. Huang, C. Yang, S. Li, X. Liu, R. Wang, N. Hu, Y. Suo, Z. Li, J. Wang, *ACS Sustainable Chem. Eng.* **2017**, *5*, 9347–9354.

[152] F.-L. Mi, S.-S. Shyu, S.-T. Lee, T.-B. Wong, *J. Polym. Sci. B Polym. Phys.* **1999**, *37*, 1551–1564.

[153] O. A.C. Monteiro, C. Airoldi, *Int. J. Biol. Macromol.* **1999**, *26*, 119–128.

[154] Y. Kawamura, H. Yoshida, S. Asai, I. Kurahashi, H. Tanibe, *Sep. Sci. Technol.* **1997**, *32*, 1959–1974.

[155] J. Lim, E. J. Lee, J. S. Choi, N. C. Jeong, *ACS Appl. Mater. Interfaces* **2018**, *10*, 3793–3800.

[156] S. Li, M. Jia, H. Guo, X. Hou, *Anal. Bioanal. Chem.* **2018**, *410*, 6619–6632.

[157] X.-X. Liang, N. Wang, Y.-L. Qu, L.-Y. Yang, Y.-G. Wang, X.-K. Ouyang, *Molecules* **2018**, *23*, 1524.

[158] S. Dasgupta, S. Divekar, Aarti, A. I. Spjelkavik, T. Didriksen, A. Nanoti, R. Blom, *Chem. Eng. Technol.* **2015**, *137*, 525–531.

[159] X. Chang, D. Chen, X. Jiao, *J. Phys. Chem. B.* **2008**, *112*, 7721–7725.

[160] X.-H. Ma, Z. Yang, Z.-K. Yao, Z.-L. Xu, C. Y. Tang, *J. Membr. Sci.* **2017**, *525*, 269–276.

[161] Y. Wang, Y. Zhang, J. Cui, S. Li, M. Yuan, T. Wang, Q. Hu, X. Hou, *Anal. Chim. Acta.* **2018**, *1022*, 45–52.

[162] F. Devlieghere, A. Vermeulen, J. Debevere, *Food Microbiol.* **2004**, *21*, 703–714.

[163] M. Plascencia-Jatomea, G. Viniegra, R. Olayo, M. M. Castillo-Ortega, K. Shirai, *Macromol. Biosci.* **2003**, *3*, 582–586.

[164] N. Zhuo, Y. Lan, W. Yang, Z. Yang, X. Li, X. Zhou, Y. Liu, J. Shen, X. Zhang, *Sep. Purif. Technol.* **2017**, *177*, 272–280.

[165] Y. Xie, C. Chen, X. Ren, X. Wang, H. Wang, X. Wang, *Prog. Mater. Sci.* **2019**, *103*, 180–234.

[166] Q. Fu, L. Wen, L. Zhang, X. Chen, D. Pun, A. Ahmed, Y. Yang, H. Zhang, *ACS Appl. Mater. Interfaces* **2017**, *9*, 33979–33988.

[167] M.-X. Wu, Y.-W. Yang, *Adv. Mater.* **2017**, *29*, 1606134.

[168] S. Li, W. Zhang, F. Huo, *Physica E* **2015**, *69*, 56–60.

[169] X. Zhou, W. Huang, J. Shi, Z. Zhao, Q. Xia, Y. Li, H. Wang, Z. Li, *J. Mater. Chem. A* **2014**, *2*, 4722–4730.

[170] Z. Xiang, Z. Hu, D. Cao, W. Yang, J. Lu, B. Han, W. Wang, *Angew. Chem. Int. Ed.* **2011**, *50*, 491–494.

[171] S. Brunauer, P. H. Emmett, E. Teller, *J. Am. Chem. Soc* **1938**, *60*, 309–319.

[172] I. Langmuir, *J. Am. Chem. Soc* **1932**, *7*, 2798–2832.

[173] K. S.W. Sing, D. H. Everett, R. A. W. Haul, L. Moscou, R. A. Pierotti, J. Rouquerol, T. Siemieniewska, *Pure Appl. Chem.* **1985**, *57*, 603–619.

[174] K. D. Hammond, W. C. Conner in *Advances in Catalysis*, Elsevier, **2013**, S. 1–101.

[175] M. Thommes, K. Kaneko, A. V. Neimark, J. P. Olivier, F. Rodriguez-Reinoso, J. Rouquerol, K. S.W. Sing, *Pure Appl. Chem.* **2015**, *87*, 1051–1069.

[176] K. S. Walton, R. Q. Snurr, *J. Am. Chem. Soc.* **2007**, *129*, 8552–8556.

[177] Q.-Y. Yang, P. Lama, S. Sen, M. Lusi, K.-J. Chen, W.-Y. Gao, M. Shivanna, T. Pham, N. Hosono, S. Kusaka, J. J. Perry, S. Ma, B. Space, L. J. Barbour, S. Kitagawa, M. J. Zaworotko, *Angew. Chem. Int. Ed.* **2018**, *57*, 5684–5689.

[178] E. Barea, C. Montoro, J. A. R. Navarro, *Chem. Soc. Rev.* **2014**, *43*, 5419–5430.

[179] S. Mukherjee, Y. He, D. Franz, S.-Q. Wang, W.-R. Xian, A. A. Bezrukov, B. Space, Z. Xu, J. He, M. J. Zaworotko, *Chem. Eur. J.* **2020**, *26*, 4923–4929.

[180] Z. Li, P. Liu, C. Ou, X. Dong, *ACS Sustainable Chem. Eng.* **2020**, *8*, 15378–15404.

[181] R. Sabouni, H. Kazemian, S. Rohani, *Environ. Sci. Pollut. Res.* **2014**, *21*, 5427–5449.

[182] P. Rallapalli, K. P. Prasanth, D. Patil, R. S. Somani, R. V. Jasra, H. C. Bajaj, *J. Porous Mater.* **2011**, *18*, 205–210.

[183] D. Shade, B. Marszalek, K. S. Walton, *Adsorption* **2021**, *27*, 227–236.

[184] P. Brandt, A. Nuhnen, M. Lange, J. Möllmer, O. Weingart, C. Janiak, *ACS Appl. Mater. Interfaces* **2019**, *11*, 17350–17358.

[185] P. Brandt, A. Nuhnen, S. Öztürk, G. Kurt, J. Liang, C. Janiak, *Adv. Sustainable Syst.* **2021**, *122*, 2000285.

[186] P. Brandt, S.-H. Xing, J. Liang, G. Kurt, A. Nuhnen, O. Weingart, C. Janiak, *ACS Appl. Mater. Interfaces* **2021**, *13*, 29137–29149.

[187] A. López-Olvera, J. A. Zárate, E. Martínez-Ahumada, D. Fan, M. L. Díaz-Ramírez, P. A. Sáenz-Cavazos, V. Martis, D. R. Williams, E. Sánchez-González, G. Maurin, I. A. Ibarra, *ACS Appl. Mater. Interfaces* **2021**, *13*, 39363–39370.

[188] E. Martínez-Ahumada, A. López-Olvera, V. Jancik, J. E. Sánchez-Bautista, E. González-Zamora, V. Martis, D. R. Williams, I. A. Ibarra, *Organometallics* **2020**, *39*, 883–915.

[189] G. W. Peterson, J. B. DeCoste, F. Fatollahi-Fard, D. K. Britt, *Ind. Eng. Chem. Res.* **2014**, *53*, 701–707.

[190] E. Martínez-Ahumada, M. L. Díaz-Ramírez, M. d. J. Velasquez-Hernandez, V. Jancik, I. A. Ibarra, *Chem. Sci.* **2021**, *12*, 6722–6799.

[191] A. D. Wiersum, C. Giovannangeli, D. Vincent, E. Bloch, H. Reinsch, N. Stock, J. S. Lee, J.-S. Chang, P. L. Llewellyn, *ACS Comb. Sci.* **2013**, *15*, 111–119.

[192] C. Montoro, F. Linares, E. Q. Procopio, I. Senkovska, S. Kaskel, S. Galli, N. Masciocchi, E. Barea, J. A. R. Navarro, *J. Am. Chem. Soc.* **2011**, *133*, 11888–11891.

[193] A. M. Plonka, Q. Wang, W. O. Gordon, A. Balboa, D. Troya, W. Guo, C. H. Sharp, S. D. Senanayake, J. R. Morris, C. L. Hill, A. I. Frenkel, *J. Am. Chem. Soc* **2017**, *139*, 599–602.

[194] E. Hastürk, S.-J. Ernst, C. Janiak, *Curr. Opin. in Chem. Eng.* **2019**, *24*, 26–36.

[195] D. M. Steinert, S.-J. Ernst, S. K. Henninger, C. Janiak, *Eur. J. Inorg. Chem.* **2020**, *2020*, 4502–4515.

[196] H. Kim, S. Yang, S. R. Rao, S. Narayanan, E. A. Kapustin, H. Furukawa, A. S. Umans, O. M. Yaghi, E. N. Wang, *Science* **2017**, *356*, 430–434.

[197] S. K. Henninger, F. Jeremias, H. Kummer, C. Janiak, *Eur. J. Inorg. Chem.* **2012**, *2012*, 2625–2634.

[198] H. Kummer, F. Jeremias, A. Warlo, G. Füldner, D. Fröhlich, C. Janiak, R. Gläser, S. K. Henninger, *Ind. Eng. Chem. Res.* **2017**, *56*, 8393–8398.

[199] S. Gökpinar, S.-J. Ernst, E. Hastürk, M. Möllers, I. El Aita, R. Wiedey, N. Tannert, S. Nießing, S. Abdpour, A. Schmitz, J. Quodbach, G. Füldner, S. K. Henninger, C. Janiak, *Ind. Eng. Chem. Res.* **2019**, *58*, 21493–21503.

[200] Y. I. Aristov, *Appl. Therm. Eng.* **2013**, *50*, 1610–1618.

[201] D. Lenzen, P. Bendix, H. Reinsch, D. Fröhlich, H. Kummer, M. Möllers, P. P. C. Hügenell, R. Gläser, S. Henninger, N. Stock, *Adv. Mater.* **2018**, *30*, 1705869.

[202] Y. Sun, A. Spieß, C. Jansen, A. Nuhnen, S. Gökpinar, R. Wiedey, S.-J. Ernst, C. Janiak, *J. Mater. Chem. A* **2020**, *8*, 13364–13375.

[203] M. J. Kalmutzki, C. S. Diercks, O. M. Yaghi, *Adv. Mater.* **2018**, *30*, 1704304.

[204] F. Trapani, A. Polyzoidis, S. Loebbecke, C. G. Piscopo, *Microporous Mesoporous Mater.* **2016**, *230*, 20–24.

[205] S.-I. Kim, T.-U. Yoon, M.-B. Kim, S.-J. Lee, Y. K. Hwang, J.-S. Chang, H.-J. Kim, H.-N. Lee, U.-H. Lee, Y.-S. Bae, *Chem. Eng. J.* **2016**, *286*, 467–475.

[206] P. K. Tsobnang, E. Hastürk, D. Fröhlich, E. Wenger, P. Durand, J. L. Ngolui, C. Lecomte, C. Janiak, *Cryst. Growth. Des.* **2019**, *19*, 2869–2880.

[207] Code of Federal Regulation, 40: Chapter 1, Subchapter C, Part 51, Subpart F, 51100. Aufgerufen am 03.08.2022

[208] A. Krishnamurthy, B. Adebayo, T. Gelles, A. Rownaghi, F. Rezaei, *Catal. Today* **2020**, *350*, 100–119.

[209] Richtlinie 2004/42/EG des Europäischen Parlaments und des Rates vom 21.04.2004 Artikel 2 Absatz 5

[210] S. Bandehali, T. Miri, H. Onyeaka, P. Kumar, *Atmosphere* **2021**, *12*, 473.

[211] T. Gelles, A. Krishnamurthy, B. Adebayo, A. Rownaghi, F. Rezaei, *Catal. Today* **2020**, *350*, 3–18.

[212] N. A. Khan, Z. Hasan, S. H. Jhung, *J. Hazard. Mater.* **2013**, *244-245*, 444–456.

[213] C. Yang, G. Miao, Y. Pi, Q. Xia, J. Wu, Z. Li, J. Xiao, *Chem. Eng. Technol.* **2019**, *370*, 1128–1153.

[214] Umweltbundesamt, Nationale Trendtabellen für die deutsche Berichterstattung atmosphärischer Emissionen seit 1990, Emissionsentwicklung 1990 bis 2020 (Stand 02/2022)

[215] C. Lai, Z. Wang, L. Qin, Y. Fu, B. Li, M. Zhang, S. Liu, L. Li, H. Yi, X. Liu, X. Zhou, N. An, Z. An, X. Shi, C. Feng, *Coord. Chem. Rev.* **2021**, *427*, 213565.

[216] C. I. Ezugwu, S. Zhang, S. Li, S. Shi, C. Li, F. Verpoort, J. Yu, S. Liu, *Environ. Sci.: Nano* **2019**, *6*, 2931–2936.

[217] X. Li, L. Zhang, Z. Yang, P. Wang, Y. Yan, J. Ran, *Sep. Purif. Technol.* **2020**, *235*, 116213.

[218] E. Hunter-Sellars, J. J. Tee, I. P. Parkin, D. R. Williams, *Microporous Mesoporous Mater.* **2020**, *298*, 110090.

[219] H. Wu, Q. Gong, D. H. Olson, J. Li, *Chem. Rev.* **2012**, *112*, 836–868.

[220] J.-R. Li, R. J. Kuppler, H.-C. Zhou, *Chem. Soc. Rev.* **2009**, *38*, 1477–1504.

[221] S. Mukherjee, A. V. Desai, S. K. Ghosh, *Coord. Chem. Rev.* **2018**, *367*, 82–126.

[222] M. Woellner, S. Hausdorf, N. Klein, P. Mueller, M. W. Smith, S. Kaskel, *Adv. Mater.* **2018**, *30*, 1704679.

[223] M. Bahri, F. Haghighat, H. Kazemian, S. Rohani, *Chem. Eng. J.* **2017**, *313*, 711–723.

[224] B. Van de Voorde, B. Bueken, J. Denayer, D. de Vos, *Chem. Soc. Rev.* **2014**, *43*, 5766–5788.

[225] F. Yang, Q.-K. Liu, J.-P. Ma, Y.-A. Li, K.-X. Wang, Y.-B. Dong, *CrystEngComm* **2015**, *17*, 4102–4109.

[226] M. Agrawal, S. Bhattacharyya, Y. Huang, K. C. Jayachandrababu, C. R. Murdock, J. A. Bentley, A. Rivas-Cardona, M. M. Mertens, K. S. Walton, D. S. Sholl, S. Nair, *J. Phys. Chem. C* **2018**, *122*, 386–397.

[227] J.-Y. Cheng, P. Wang, J.-P. Ma, Q.-K. Liu, Y.-B. Dong, *Chem. Commun.* **2014**, *50*, 13672–13675.

[228] N. Chang, X.-P. Yan, *J. Chromatogr. A* **2012**, *1257*, 116–124.

[229] A. A. Sapianik, K. A. Kovalenko, D. G. Samsonenko, M. O. Barsukova, D. N. Dybtsev, V. P. Fedin, *Chem. Commun.* **2020**, *56*, 8241–8244.

[230] S. Mukherjee, B. Manna, A. V. Desai, Y. Yin, R. Krishna, R. Babarao, S. K. Ghosh, *Chem. Commun.* **2016**, *52*, 8215–8218.
[231] D.-D. Zhou, P. Chen, C. Wang, S.-S. Wang, Y. Du, H. Yan, Z.-M. Ye, C.-T. He, R.-K. Huang, Z.-W. Mo, N.-Y. Huang, J.-P. Zhang, *Nat. Mater.* **2019**, *18*, 994–998.
[232] L. K. Macreadie, O. T. Qazvini, R. Babarao, *ACS Appl. Mater. Interfaces* **2021**, *13*, 30885–30890.
[233] A. Santra, M. Francis, S. Parshamoni, S. Konar, *ChemistrySelect* **2017**, *2*, 3200–3206.
[234] P. S. Bárcia, D. Guimarães, P. A.P. Mendes, J. A.C. Silva, V. Guillerm, H. Chevreau, C. Serre, A. E. Rodrigues, *Microporous Mesoporous Mater.* **2011**, *139*, 67–73.
[235] D. Lv, H. Wang, Y. Chen, F. Xu, R. Shi, Z. Liu, X. Wang, S. J. Teat, Q. Xia, Z. Li, J. Li, *ACS Appl. Mater. Interfaces* **2018**, *10*, 6031–6038.
[236] B. Bozbiyik, T. Duerinck, J. Lannoeye, D. E. de Vos, G. V. Baron, J. F.M. Denayer, *Microporous Mesoporous Mater.* **2014**, *183*, 143–149.
[237] X. Zhang, Y. Yang, X. Lv, Y. Wang, N. Liu, D. Chen, L. Cui, *J. Hazard. Mater.* **2019**, *366*, 140–150.
[238] A. Nuhnen, C. Janiak, *Dalton Trans.* **2020**, *49*, 10295–10307.
[239] A. L. Myer, J. M. Prausnitz, *A. I. Ch. E. Journal* **1965**, *11*, 121–127.
[240] H. R. Abid, Z. H. Rada, J. Shang, S. Wang, *Polyhedron* **2016**, *120*, 103–111.
[241] S. Kavak, H. M. Polat, H. Kulak, S. Keskin, A. Uzun, *Chem. Asian J.* **2019**, *14*, 3655–3667.
[242] T. J. Matemb Ma Ntep, W. Wu, H. Breitzke, C. Schlüsener, B. Moll, L. Schmolke, G. Buntkowsky, C. Janiak, *Aust. J. Chem.* **2019**, *72*, 835.
[243] W. Fan, Y. Ying, S. B. Peh, H. Yuan, Z. Yang, Y. Di Yuan, D. Shi, X. Yu, C. Kang, D. Zhao, *J. Am. Chem. Soc.* **2021**, *143*, 17716–17723.
[244] A. Liu, X. Peng, Q. Jin, S. K. Jain, J. M. Vicent-Luna, S. Calero, D. Zhao, *ACS Appl. Mater. Interfaces* **2019**, *11*, 4686–4700.
[245] R. Krishna, J. M. van Baten, *ACS Omega* **2021**, *6*, 15499–15513.
[246] F.-X. Coudert, A. Boutin, M. Jeffroy, C. Mellot-Draznieks, A. H. Fuchs, *ChemPhysChem* **2011**, *12*, 247–258.
[247] S. M. J. Rogge, R. Goeminne, R. Demuynck, J. J. Gutiérrez-Sevillano, S. Vandenbrande, L. Vanduyfhuys, M. Waroquier, T. Verstraelen, V. van Speybroeck, *Adv. Theory Simul.* **2019**, *2*, 1800177.
[248] N. F. Cessford, N. A. Seaton, T. Düren, *Ind. Eng. Chem. Res.* **2012**, *51*, 4911–4921.
[249] J. McEwen, J.-D. Hayman, A. Ozgur Yazaydin, *Chem. Phys.* **2013**, *412*, 72–76.
[250] B. Manna, S. Mukherjee, A. V. Desai, S. Sharma, R. Krishna, S. K. Ghosh, *Chem. Commun.* **2015**, *51*, 15386–15389.
[251] H. Reinsch, B. Bueken, F. Vermoortele, I. Stassen, A. Lieb, K.-P. Lillerud, D. de Vos, *Cryst. Eng. Comm.* **2015**, *17*, 4070–4074.
[252] Z. H. Rada, H. R. Abid, H. Sun, S. Wang, *J. Chem. Eng. Data* **2015**, *60*, 2152–2161.
[253] M. J. Katz, Z. J. Brown, Y. J. Colón, P. W. Siu, K. A. Scheidt, R. Q. Snurr, J. T. Hupp, O. K. Farha, *Chem. Commun.* **2013**, *49*, 9449–9451.
[254] M. Schulz, N. Marquardt, M. Schäfer, D. P. Warwas, S. Zailskas, A. Schaate, *Chem. Eur. J.* **2019**, *25*, 13598–13608.

[255] V. Guillerm, F. Ragon, M. Dan-Hardi, T. Devic, M. Vishnuvarthan, B. Campo, A. Vimont, G. Clet, Q. Yang, G. Maurin, G. Férey, A. Vittadini, S. Gross, C. Serre, *Angew. Chem. Int. Ed.* **2012**, *51*, 9267–9271.

[256] C. A. Trickett, K. J. Gagnon, S. Lee, F. Gándara, H.-B. Bürgi, O. M. Yaghi, *Angew. Chem. Int. Ed.* **2015**, *54*, 11162–11167.

[257] S. Øien, D. Wragg, H. Reinsch, S. Svelle, S. Bordiga, C. Lamberti, K. P. Lillerud, *Cryst. Growth. Des.* **2014**, *14*, 5370–5372.